Editors: M. Rahman
and C.A. Brebbia

WIT PRESS

Advances in Fluid Mechanics VIII

Advances in Fluid Mechanics VIII

WIT PRESS

WIT Press publishes leading books in Science and Technology.
Visit our website for the current list of titles.
www.witpress.com

WIT eLibrary

Home of the Transactions of the Wessex Institute.
Papers presented at Advances in Fluid Mechanics VIII are archived in the WIT eLibrary in volume 69 of WIT Transactions on Engineering Sciences (ISSN 1743-3533). The WIT eLibrary provides the international scientific community with immediate and permanent access to individual papers presented at WIT conferences.
http://library.witpress.com.

EIGHTH INTERNATIONAL CONFERENCE ON
ADVANCES IN FLUID MECHANICS

Advances in Fluid Mechanics VIII

CONFERENCE CHAIRMEN

M. Rahman
Dalhousie University, Canada

C.A. Brebbia
Wessex Institute of Technology, UK

INTERNATIONAL SCIENTIFIC ADVISORY COMMITTEE

F. Barrera
R. Bourisli
P.C. Chu
S. D'Alessio
J. De Wilde
G. Micale
F. Morency
S. Sinkunas
L. Skerget
G. Swaters
R. Verhoeven

ORGANISED BY
The Wessex Institute of Technology, UK

SPONSORED BY
WIT Transactions on Engineering Sciences
Fluid Mechanics Book Series

WIT Transactions

Transactions Editor

Carlos Brebbia
Wessex Institute of Technology
Ashurst Lodge, Ashurst
Southampton SO40 7AA, UK
Email: carlos@wessex.ac.uk

Editorial Board

Advances in Fluid Mechanics VIII

Editors

M. Rahman
Dalhousie University, Canada

C.A. Brebbia
Wessex Institute of Technology, UK

WIT*PRESS* Southampton, Boston

Editors:

M. Rahman
Dalhousie University, Canada

C.A. Brebbia
Wessex Institute of Technology, UK

Published by

WIT Press
Ashurst Lodge, Ashurst, Southampton, SO40 7AA, UK
Tel: 44 (0) 238 029 3223; Fax: 44 (0) 238 029 2853
E-Mail: witpress@witpress.com
http://www.witpress.com

For USA, Canada and Mexico

WIT Press
25 Bridge Street, Billerica, MA 01821, USA
Tel: 978 667 5841; Fax: 978 667 7582
E-Mail: infousa@witpress.com
http://www.witpress.com

British Library Cataloguing-in-Publication Data

A Catalogue record for this book is available
from the British Library.

ISBN: 978-1-84564-476-5
ISSN: (print) 1746-4471
ISSN: (on-line) 1743-3533

The texts of the papers in this volume were set individually by the authors or under their supervision. Only minor corrections to the text may have been carried out by the publisher.

Printed in Great Britain by MPG Books Group, Bodmin and King's Lynn.

Preface

The field of fluid mechanics is vast and has numerous and diverse applications in everyday life. The papers in this book cover a wide range of topics in the area of advances in fluid mechanics. The papers were presented at the eighth International Conference on Advances in Fluid Mechanics held in Portugal in 2010. The meeting was organised by the Wessex Institute of Technology, UK.

The conference has reconvened every two years since 1996, and originated a very successful book series on the same topics which has resulted in over 60 volumes since then.

The first conference was held in New Orleans, USA (1996), and then followed by Udine, Italy (1998), Montreal, Canada (2000), Ghent, Belgium (2002), Lisbon, Portugal (2004), Skiathos, Greece (2006), and The New Forest, UK (2008).

The papers in the book are arranged in the following sections: Computational Methods in Fluid Mechanics; Environmental Fluid Mechanics; Experimental versus Simulation Methods; Multiphase Flow; Hydraulics and Hydrodynamics; Heat Transfer; Industrial Applications; Wave Studies; Bio-fluids; and Fluid Structure Interaction.

This volume is part of the Transactions of Wessex Institute series, published in paper and digital format and distributed throughout the world. In addition, all papers are archived within Wessex Institute electronic library (http://library.witpress.com) where they are permanently and easily available to the scientific community.

The Editors are indebted to all authors as well as the members of International Scientific Advisory Committee who helped review the papers.

The Editors,
The Algarve, Portugal, 2010

This page intentionally left blank

Contents

Section 1: Computational methods

Section 2: Experimental measurements

Section 3: Hydrodynamics

Section 4: Fluid structure interaction

Section 5: Multiphase flow

This page intentionally left blank

Section 1
Computational methods

This page intentionally left blank

Turbulence modeling with the boundary element method

J. Lupše, L. Škerget & J. Ravnik
University of Maribor, Faculty of Mechanical Engineering, Slovenia

Abstract

In the present article we were testing our flow solver for turbulent channel flow. Velocity-vorticity formulation of Navier-Stokes equations is applied, thus governing equations are given for the kinematic and kinetic aspects of flow instead of mass and momentum equations. The solution algorithm first solves the kinematics equation for unknown boundary vorticity values using the single domain boundary element numerical method. The next step of the solution algorithm is calculation of the domain velocity field, which is also achieved by solving the kinematics equation. In this and later cases we use the sub-domain boundary element method. After the velocity field is known, we calculate the turbulent kinetic energy and turbulent dissipation fields to obtain the turbulent viscosity. Finally, the vorticity field redistribution is calculated via the kinetics equation. For laminar solutions it was shown that the use of the boundary domain integral method accuracy of solutions for benchmark test cases is very high on coarse meshes. However, since this method is still limited, with high CPU and memory requirements, parallelization of the algorithm is a must for calculating turbulent flows. This was achieved with the use of a MPI (message passing interface) standard.

1 Introduction

In this paper we present the application of the boundary element method for solving planar turbulent flow problems with low-Reynolds-number turbulence models. Since viscosity now includes an additional, modeled part, governing equations have to be written in extended forms, which have to include this nonlinear behavior. The compressibility effect was neglected for simplifying an already highly nonlinear set of equations. For the same reason a zero gravity

WIT Transactions on Engineering Sciences, Vol 69, © 2010 WIT Press
www.witpress.com, ISSN 1743-3533 (on-line)
doi:10.2495/AFM100011

environment was applied. Governing equations are written in velocity-vorticity form, which eliminates pressure from equations that describe incompressible fluid flow. Instead of momentum conservation equations, velocity-vorticity formulation gives the equation for vorticity transport. The mass conservation equation is transformed into a kinematics equation with the help of vorticity definition. Kinematics equations represent compatibility and restriction conditions between velocity and vorticity field functions. These equations are derived from the mass conservation law with the help of vorticity definition. Kinetics equations are obtained by applying a curl differential operator to the momentum transport equation. For application of the turbulence model, the stress tensor has to be rewritten in such a way that we obtain appropriate form for the application of boundary elements. The Laplace fundamental solution was used for kinematics equations integral forms, which are then discretized by the single-domain boundary element method. As this method is very memory consuming, we applied the wavelet transform [1] of domain matrices in order to reduce its size. The resulting system of equations is then solved by direct solver using LU decomposition. The parabolic-diffusion fundamental solution was used in the integral form of kinetics equations, which are then discretized by the sub-domain boundary element method. This type of discretization yields an overdetermined system of equations, which is solved by a LSQR [2] type solver. Obtaining a solution is very challenging due to the strong nonlinearity of the vorticity equation.

2 Governing equations

Governing equations describing viscid fluid flow are conservation equations, e.g. mass, momentum and heat energy conservation equations. For isothermal flows, energy conservation equation may be omitted thus leaving us with only mass and momentum conservation equations. Equations are further simplified for incompressible flows. We can write those in Einstein notation as:

$$\frac{\partial v_j}{\partial x_j} = 0 \tag{1}$$

and

$$\rho_0 \frac{Dv_i}{Dt} = -\frac{\partial p}{\partial x_i} + \frac{\partial}{\partial x_j}\left(\nu \frac{\partial v_i}{\partial x_j}\right) + \rho_0 g_i, \tag{2}$$

where i is 1 or 2 for their planar forms, v_i or v_j are velocity vector components, x_j are spatial coordinates, g_i are gravity acceleration vector components, t is time, p is pressure and ρ_0 is density.

In equation (2), $\frac{Dv_i}{Dt}$ marks the material or Stokes derivative, which we can write in extended form as $\frac{Dv_i}{Dt} = \frac{\partial(\cdot)}{\partial t} + v_j \frac{\partial v_i}{x_j}$.

With some mathematical knowledge we can transform these equations to their velocity-vorticity form. By use of vorticity definition, the mass conservation equation can be transformed [3] to the following form:

$$\frac{\partial^2 v_i}{\partial x_j \partial x_j} + e_{ij}\frac{\partial \omega}{\partial x_j} = 0. \tag{3}$$

In equation (3) ω represents vorticity and e_{ij} is unit permutation tensor. Since equation (3) does not have a unique solution we have to apply compatibility and restriction conditions for velocity and vorticity fields, thus obtaining the following equation for the kinematics of planar flows.

$$\frac{\partial v_i}{\partial n} + e_{ij}\omega n_j = -e_{ij}\frac{\partial v_j}{\partial t}, \tag{4}$$

where n_j are unit normal vector components. Momentum transport equations transform into the vorticity transport equation by applying the curl operator to equations (2)

$$\frac{\partial \omega}{\partial t} + \frac{v_j \omega}{\partial x_j} = \nu_0 \left(\frac{\partial^2 \omega}{\partial x_j \partial x_j}\right) - \frac{1}{\rho_0} e_{ij}\frac{\partial f_i^m}{\partial x_j} \tag{5}$$

where f_i^m is the source term due to nonlinear viscosity and is equal to

$$f_i^m = -e_{ij}\frac{\partial \widetilde{\eta}\omega}{\partial x_j} + 2e_{ij}\frac{\partial \widetilde{\eta}}{\partial x_j}\omega + 2\frac{\partial \eta}{\partial x_j}\frac{\partial v_i}{\partial x_j}, \tag{6}$$

where nonlinear dynamic viscosity is decomposed into $\eta = \eta_0 + \widetilde{\eta}$.

Equation (5) is a scalar vorticity transport equation, since for planar flow, vorticity has only one component different from 0.

For turbulence model Spalart-Allmaras [4] one equation low-Reynolds turbulence model was used, where the trip term was omitted.

$$\frac{D\widetilde{\nu}}{Dt} = C_{b1}\left[1 - f_{t2}\right]\widetilde{S}\widetilde{\nu} + \frac{1}{\sigma}\left[\frac{\partial}{\partial x_j}\left(\left(\nu_0 + \widetilde{\nu}\right)\frac{\partial \widetilde{\nu}}{\partial x_j}\right) + C_{b2}\left(\frac{\partial \widetilde{\nu}}{\partial x_j}\right)^2\right] - \left[C_{w1} f_w - \frac{C_{b1}}{\kappa^2} f_{t2}\right]\left(\frac{\widetilde{\nu}}{d_n}\right)^2, \tag{7}$$

where d_n is normal distance from the wall and $\widetilde{\nu}$ is a viscosity-like variable. Turbulent eddy viscosity is computed from:

$$\nu_t = \widetilde{\nu} f_{v1}, \tag{8}$$

where

$$f_{v1} = \frac{\chi^3}{\chi^3 + C_{v1}^3} \tag{9}$$

and

$$\chi = \frac{\widetilde{\nu}}{\nu_0}. \tag{10}$$

The rest of the functions are defined as:

$$f_{t2} = C_{t3} e^{-C_{t4}\chi^2}, \tag{11}$$

$$f_w = g\left[\frac{1 + C_{w3}^6}{g^6 + C_{w3}^6}\right]^{\frac{1}{6}}, \tag{12}$$

$$g = r + C_{w2}\left(r^6 - r\right), \tag{13}$$

$$r = \frac{\widetilde{\nu}}{\widetilde{S}\kappa^2 d_n^2}, \tag{14}$$

$$\widetilde{S} = S + \frac{\widetilde{\nu}}{\kappa^2 d_n^2} f_{v2}, \tag{15}$$

$$f_{v2} = 1 - \frac{\chi}{1 + \chi f_{v1}} \tag{16}$$

and

$$S = \sqrt{2\Omega_{ij}\Omega_{ij}}, \tag{17}$$

where Ω_{ij} is a rotation tensor.

The values of the constants are as shown in table (1).

Table 1: Constants of the Spalart-Allmaras turbulent model.

σ	C_{b1}	C_{b2}	C_{w1}	C_{w2}	C_{w3}	C_{v1}	C_{t3}	C_{t4}	κ
$\frac{2}{3}$	0.1355	0.622	$\frac{C_{b1}}{\kappa^2} + \frac{(1+C_{b2})}{\sigma}$	0.3	2	7.1	1.2	0.5	0.41

3 Integral equations

Using ξ as the collocation point, the integral equations of kinematics [5] take the form

$$c(\xi)\vec{n}(\xi) \times \vec{v}(\xi) + \vec{n}(\xi) \times \int_\Gamma \vec{v}\vec{q^*} d\Gamma =$$

$$\vec{n}(\xi) \times \int_{\Gamma} \left(\vec{q^*} \times \vec{n}\right) \times \vec{v} d\Gamma + \vec{n}(\xi) \times \int_{\Omega} \vec{\omega} \times \vec{q^*} d\Omega, \tag{18}$$

$$c(\xi)\vec{n}(\xi) \cdot \vec{v}(\xi) + \vec{n}(\xi) \cdot \int_{\Gamma} \vec{v}\vec{q^*} d\Gamma =$$
$$\vec{n}(\xi) \cdot \int_{\Gamma} \left(\vec{q^*} \times \vec{n}\right) \times \vec{v} d\Gamma + \vec{n}(\xi) \times \int_{\Omega} \vec{\omega} \times \vec{q^*} d\Omega. \tag{19}$$

Ω and Γ denote domain and its boundary, c is the geometric parameter depending on the location of source point and q_* is the normal derivative of the fundamental solution.

Equations (18) and (19) are the tangential and normal forms of the kinematics integral equation, which we use for determining unknown boundary vorticity or tangential velocity component boundary values and unknown normal velocity component boundary values, respectively.

The integral equation of vorticity kinetics [3] is

$$c(\xi)\omega(\xi) + \int_{\Gamma} \omega Q^* d\Gamma = \frac{1}{\eta_0} \int_{\Gamma} \left(\eta_0 \frac{\partial \omega}{\partial n} - \rho_0 v_n \omega + f_t^m\right) U^* d\Gamma$$
$$+ \frac{1}{\eta_0} \int_{\Omega} \left(\rho_0 v_j \omega + e_{ij} f_i^m\right) Q_j^* d\Omega + \int_{\Omega} \omega_{F-1} u_{F-1}^* d\Omega. \tag{20}$$

For weighting function of equations (18) and (19), the elliptic Laplace fundamental solution was used. Its planar form is:

$$u^* = -\frac{1}{2\pi} ln(r), \tag{21}$$

where r is the distance between the source and the reference point. The normal derivative is written as $q^* = \frac{\partial u^*}{\partial n}$.

For equation (20) the parabolic diffusive fundamental solution was used, which is for planar flow in the form of:

$$u^* = \frac{1}{4\pi\alpha\tau}^{\frac{d}{2}} e^{\frac{-r^2}{4\alpha\tau}}, \tag{22}$$

where α is the relaxation parameter, d is the dimension of the problem and $\tau = t_F - t$. Assuming constant variation of all field functions within the individual time frame Δt, the time integrals may be evaluated analytically;

$$U^* = \alpha \int_{t_{F-1}}^{t_F} u^* dt \tag{23}$$

and

$$Q^* = \alpha \int_{t_{F-1}}^{t_F} q^* dt \tag{24}$$

The basic equation of the Spalart-Allmaras turbulent model (7) was partitioned to diffusive ($\nu_0 \frac{\partial^2 \widetilde{\nu}}{\partial x_j^2}$), accumulation ($\frac{\partial \widetilde{\nu}}{\partial t}$) and source term ($b$) in order to obtain the corresponding integral equation;

$$c(\xi)\widetilde{\nu}(\xi, t_F) + \int_\Gamma \widetilde{\nu} Q^* d\Gamma = \int_\Gamma \frac{\partial \widetilde{\nu}}{\partial n} U^* d\Gamma + \frac{1}{\alpha} b U^* d\Omega + \int_\Omega \widetilde{\nu}_{F-1} u^*_{F-1} d\Omega \tag{25}$$

3.1 Numerical algorithm

First, the laminar solution was obtained at some low Reynolds number [6]. Then calculation was restarted using the laminar results as initial conditions. The numerical algorithm calculates kinematics matrices first before entering the nonlinear loop. For laminar flows in the beginning of the nonlinear loop, the kinematics of flow is solved. The next step is obtaining a solution for vorticity transport, after that the loop begins anew. For turbulent flows, the algorithm first calculates turbulent viscosity by solving the turbulence model equation(s). After that, the nonlinear loop is the same as for laminar flows with the addition of calculating turbulent viscosity after the vorticity transport equation.

Kinematics is solved by a single-domain BEM. Kinetics is solved by a sub-domain BEM that uses quadrilateral elements for discretization of the domain.

4 Validation of the vorticity transport equation

The nonlinear vorticity transport equation was validated by calculating flows with various viscosity distributions as shown in table 2. Uniform meshes of different densities were used to test possibilities of capturing the nonlinearity of equations.

Table 2: Nonlinear dependence of viscosity for different test cases and values of the v_x component of velocity at channel half width; mesh a) 60x6 elements, mesh b) 70x20 elements, mesh c) 80x40 elements.

ν	$1+y$	$1+100 \cdot y$	y^3	y^5	$2-y$
Mesh a)	0.08515	0.00406	0.03729	0.01541	0.08515
Mesh b)	0.08499	0.00362	0.03700	0.01511	0.08499
Mesh c)	0.08500	0.00356	0.03713	0.01504	0.08500
Analytical	0.08496	0.00352	0.03704	0.01509	0.08496

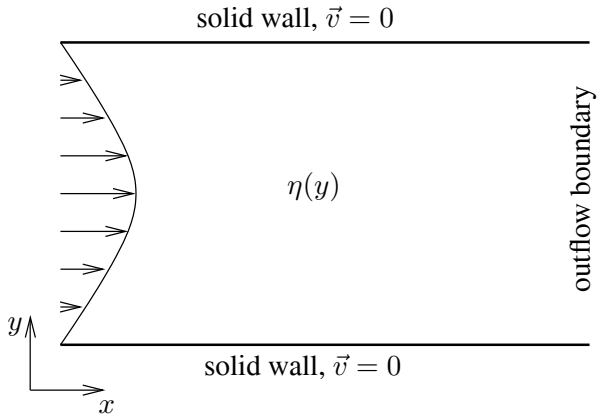

Figure 1: Boundary conditions for test cases.

The geometry for test cases was simple channel with a prescribed velocity profile at the inflow and zero flux boundary conditions at the outflow as shown in Figure 1.

The generalized equation in form $\frac{\partial}{\partial y}\left(\nu \frac{\partial v_x}{\partial y}\right) = -c$ was solved for different viscosity distributions and thus its behavior tested for nonlinear viscosity problems. First, viscosity was set to be the function of $1 + k \cdot y$. If $0 \leq y \leq< 1$, the general solution of this equation has the form:

$$v_x(y) = \frac{c}{k}\left[-y + \frac{ln(1+ky)}{ln(1+k)}\right] \tag{26}$$

Figures 2 and 3 show the results for two different values of k; 1 and 100. For low values of k governing equations are only weakly nonlinear, thus even coarse mesh describes the velocity profile quite well. At higher k values coarser meshes are simply not good enough, hence the need for much finer meshes. Since gradients for the first two cases of viscosity distributions are constant, we prescribed viscosity distribution dependant on y^3 and y^5. If $1 \leq y \leq 2$ analytical solutions have forms of

$$v_x(y) = c\left[\frac{1}{y} - \frac{2}{3y^2} - \frac{1}{3}\right], \tag{27}$$

$$v_x(y) = c\left[\frac{1}{3y^3} + \frac{14}{45}\left(-\frac{1}{y^4} + 1\right) - \frac{1}{3}\right]. \tag{28}$$

A comparison of the analytical and numerical results is shown in Figure 4 for y^3 dependance and in Figure 5 for y^5 dependance of viscosity.

To test negative gradients, the viscosity was set to be function $\nu = 2 - y$. The analytical solution for the velocity profile is

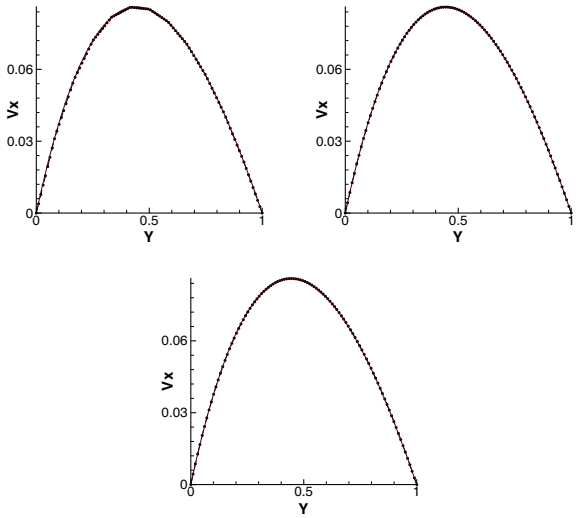

Figure 2: Velocity x component profiles for $\nu = 1 + y$ viscosity distribution; full circles represent numerical values, the full line represents analytical values; mesh a) top left, mesh b) top right and mesh c) bottom.

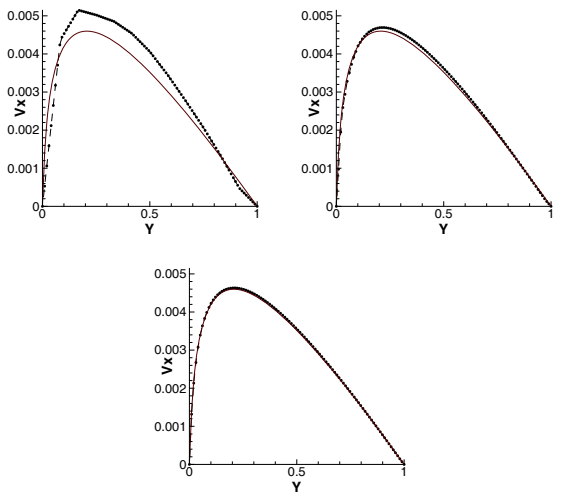

Figure 3: Velocity x component profiles for $\nu = 1 + 100 \cdot y$ viscosity distribution.

$$v_x(y) = c\left[1 - y\left(\frac{ln(2-y)}{ln2}\right)\right] \tag{29}$$

while y boundaries are the same as in cases of $\nu = 1 + k \cdot y$. The results for this test case are shown in Figure 6.

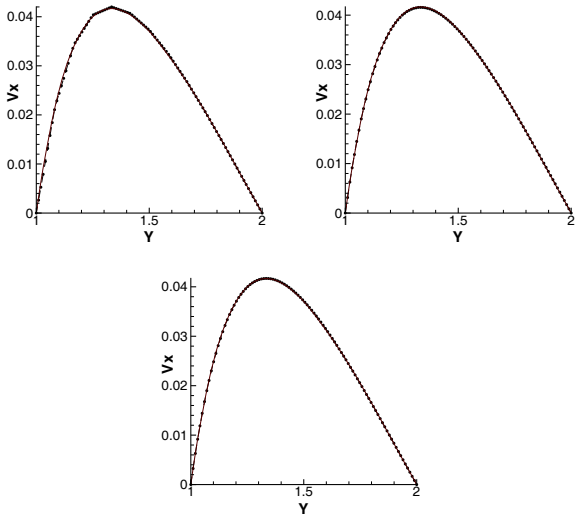

Figure 4: Velocity x component profiles for $\nu = y^3$ viscosity distribution.

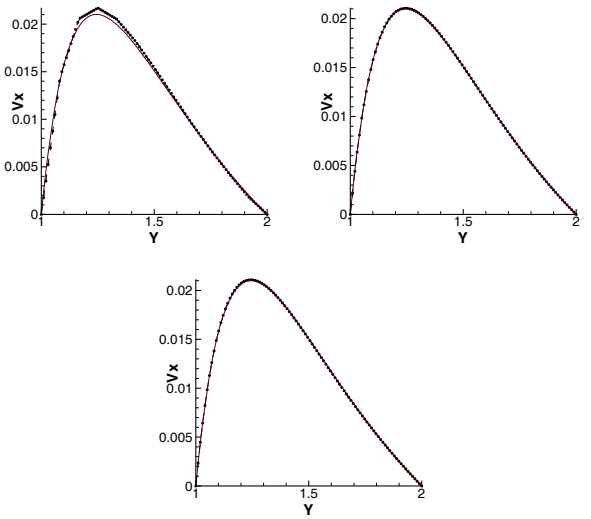

Figure 5: Velocity x component profiles for $\nu = y^5$ viscosity distribution.

5 Conclusion

The tested numerical algorithm was shown to be able to successfully cope with strong nonlinearities in the vorticity transport equation and it is able to predict the

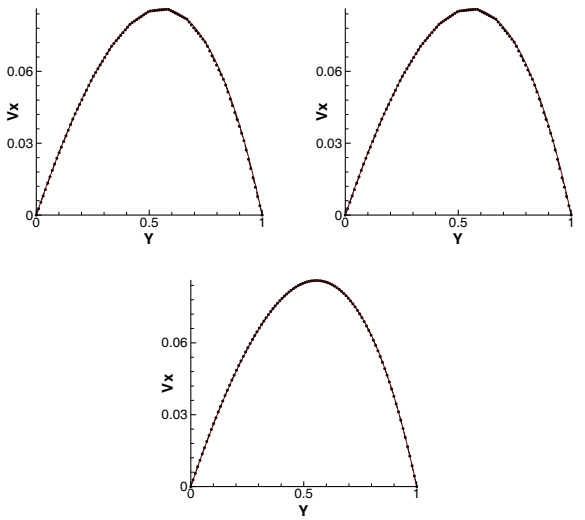

Figure 6: Velocity x component profiles for $\nu = 2 - y$ viscosity distribution.

corresponding velocity field accurately. In all test cases, except in the case with the strongest nonlinear viscosity distribution, even the coarsest mesh proved to be adequate. In the future, the developed numerical algorithm will be used to simulate turbulent fluid flow. DNS results of turbulent channel flow [7] will be used as a benchmark example to validate the algorithm. Furthermore, the algorithm will be tested on a backward-facing step example and compared with the DNS results of [8].

References

[1] Ravnik, J., Škerget, L. & Hriberšek, M., The wavelet transform for BEM computational fluid dynamics. *Eng Anal Bound Elem*, **28**, pp. 1303–1314, 2004.

[2] Paige, C.C. & Saunders, M.A., LSQR: An algorithm for sparse linear equations and sparse least squares. *ACM Transactions on Mathematical Software*, **8**, pp. 43–71, 1982.

[3] Škerget, L. & Samec, N., BEM for the two-dimensional plane compressible fluid dynamics. *Eng Anal Bound Elem*, **29**, pp. 41–57, 2005.

[4] Spalart, P. & Allmaras, S., A one-equation turbulence model for aerodynamic flows. *AIAA, Aerospace Sciences Meeting and Exhibit, 30 th, Reno, NV*, p. 1992, 1992.

[5] Škerget, L. & Ravnik, J., BEM simulation of compressible fluid flow in an enclosure induced by thermoacoustic waves. *Eng Anal Bound Elem*, **33**, pp. 561–571, 2009.
[6] Škerget, L., Hriberšek, M. & Žunič, Z., Natural convection flows in complex cavities by BEM. *Int J Num Meth Heat & Fluid Fl*, **13**, pp. 720–735, 2003.
[7] Kim, J., Moin, P. & Moser, R., Turbulence statistics in fully developed channel flow at low Reynolds number. *J Fluid Mech*, **177**, pp. 133–166, 1987.
[8] Lee, H., Moin, P. & Kim, J., Direct numerical simulation of turbulent flow over a backward-facing step. *J Fluid Mech*, pp. 330–349, 1997.

This page intentionally left blank

On properties of turbulence models

T. H. Moulden
The University of Tennessee Space Institute, USA

Abstract

Many applications of fluid mechanics are to turbulent flows. The practical computation of such flows call upon turbulence models to provide the information needed to close the mean motion equations. The present comments concern those properties of turbulence models that may be obtained by direct study of the field equations defining these models. The second moment model and the $k \sim \epsilon$ model are the focus of attention and norm inequalities are written for these models. The stability properties of the associated dynamical system are determined. Some difficulties associated with obtaining norm estimates are also discussed.
Keywords: turbulence models, energy estimates.

1 Background

It is generally accepted that the Navier–Stokes equations describe the motion of fluids under normal conditions of pressure and temperature. It is also accepted that these same equations describe turbulent fluid motion (the "sinuous motion" described by Stokes and studied by Reynolds). A caution is necessary at this point since the consistency of the Navier–Stokes equations has not been documented. In particular, there is no complete existence, uniqueness and regularity results available for these equations when provided with general boundary conditions.

Restrict attention to constant density fluid motion. Due to the lack of a complete theory for the constant density Navier–Stokes equations:

$$\frac{\partial v_i}{\partial x_i} = 0 \tag{1}$$

$$\frac{\partial v_i}{\partial t} + \frac{\partial (v_i v_j)}{\partial x_j} + \frac{\partial p}{\partial x_i} = \nu \nabla^2 (v_i) + f_i \tag{2}$$

noted above, it cannot be expected that a complete theory exists for the mean motion equations used to treat turbulent flow. Here $\mathbf{v}(\mathbf{x}, t)$ is the instantaneous

WIT Transactions on Engineering Sciences, Vol 69, © 2010 WIT Press
www.witpress.com, ISSN 1743-3533 (on-line)
doi:10.2495/AFM100021

velocity field and $p(\mathbf{x}, t)$ the corresponding pressure field (normalized by the constant fluid density). Turbulence models have, as a prequel, the existence of a Reynolds decomposition $\mathbf{v} \mapsto \mathbf{V} + \mathbf{u}$ where $\mathbf{V} = \mathcal{E}(\mathbf{v})$, denotes the mean velocity, and $\mathbf{u}(\mathbf{x}, t)$ a fluctuating velocity field. The resulting lack of closure found in the mean motion equations requires that a *turbulence model* be included. While such a model closes the field equations, it is not based upon any real physical principle and contains large empirical and heuristic content.

A turbulence model is said to be *meaningful* if it produces a closed set of mean motion equations for which a unique solution exists. This definition makes no mention of the predictive power of the turbulence model: that is a separate issue and not addressed herein (but see Gatski [1] for a discussion of turbulence models). Rather, the present interest focuses upon the mathematical properties of such models with special reference to energy estimates. The standard energy estimate for equations (1) and (2) gives:

$$|\mathbf{v}|_g^2(t) \leq |\mathbf{f}|_g^2/(\nu L_v^2)^2 \quad \text{as } t \to \infty \tag{E1}$$

when a body force, $\mathbf{f}(\mathbf{x})$, is present but independent of time. The global norm of some vector $\mathbf{p}$, $|\mathbf{p}|_g^2$, is defined to be $\int_{\mathcal{D}} \langle \mathbf{p}, \mathbf{p} \rangle \, dV$ where the standard inner product $\langle \mathbf{p}, \mathbf{p} \rangle \equiv p_i p_i$ (sum on i) is defined. $\mathcal{D}$ denotes the (bounded) domain occupied by the fluid with $\partial\mathcal{D}$ its boundary. In the absence of body forces, the velocity norm $|\mathbf{v}|_g^2(t)$, decays exponentially (see Foias et al. [2], for example):

$$|\mathbf{v}|_g^2(t) \leq exp[-\nu L_v^2 t] \, |\mathbf{v}|_g^2(t = 0) \tag{E2}$$

as $t \to \infty$. Here L_v is the constant in a Poincaré inequality of the form $\|\mathbf{L}\|_g^2 \geq L_v^2 |\mathbf{v}|_g^2$. These results hold for the instantaneous Navier–Stokes equations and hence apply to both laminar and turbulent flows. When the Reynolds decomposition is applied to the Navier–Stokes equations and the mean motion equations obtained, it follows that the same bounds on $|\mathbf{v}|_g$ must hold (but now $\mathbf{v} = \mathbf{V} + \mathbf{u}$ implies that $|\mathbf{v}|_g \leq |\mathbf{V}|_g + |\mathbf{u}|_g$ and a direct comparison between $|\mathbf{v}|_g$ and $|\mathbf{V}|_g$ is not possible). A valid turbulence model must produce a norm $|\mathbf{V}|_g$ that is consistent in properties with these estimates for the instantaneous equations: that is, $|\mathbf{V}|_g$ must decay exponentially as $t \to \infty$ in the absence of a body force. For example, it was shown in Moulden [3] that the classical Boussinesq model has this property simply because, in norm, it has the effect of augmenting the fluid viscosity as $\nu \mapsto \nu + \nu_\tau$ for some eddy viscosity coefficient ν_τ. As such the Boussinesq model does not reveal any physics associated with fluid turbulence other than an enhanced rate of dissipation.

The first axiom of Newtonian mechanics provides the foundation for the symmetry structure of the equations of fluid mechanics. That is, the equations must be covariant under the Galilean transformation group $\mathbb{G}_a$. All constructs in the theory must respect this symmetry. It is well known that the mean velocity field transforms as $\mathbf{V} \mapsto \mathbf{Q}\mathbf{V} + \mathbf{V}_B$ under $\mathbb{G}_a$ while the fluctuating velocity has the transformation $\mathbf{u} \mapsto \mathbf{Q}\mathbf{u}$. The Reynolds tensor $\boldsymbol{\mathcal{R}}$ is frame indifferent under $\mathbb{G}_a$. Here $\mathbf{Q}$ is a constant orthogonal matrix and $\mathbf{V}_B$ the constant Galilean boost velocity. Details of these transformations are given in Speziale [4]. It follows directly that

both $div(\mathbf{V}) \mapsto div(\mathbf{V})$ and $div(\mathbf{u}) \mapsto div(\mathbf{u})$: the mean and fluctuating continuity equations are both covariant under the transformation group $\mathbb{G}_a$. Turbulence models must be consistent with these transformations.

The mean motion equations can be extracted from the instantaneous equations (1) and (2) by means of the standard Reynolds decomposition noted above to give the system:

$$\frac{\partial V_i}{\partial x_i} = 0 \tag{3}$$

$$\frac{\partial V_i}{\partial t} + \frac{\partial (V_i V_j)}{\partial x_j} + \frac{\partial \mathcal{R}_{ij}}{\partial x_j} + \frac{\partial P}{\partial x_i} = \nu \nabla^2 (V_i) + f_i \tag{4}$$

In equation (4), P denotes the mean pressure field (again normalized by the fluid density) and $\mathbf{f}(\mathbf{x})$ a time independent body force. *A turbulence model* is taken to be a statement of the form:

$$\boldsymbol{\phi}(\boldsymbol{\mathcal{R}}, \mathbf{V}, \boldsymbol{\alpha}) = 0 \tag{5}$$

if $\boldsymbol{\mathcal{R}} \equiv \mathcal{E}(\mathbf{u} \otimes \mathbf{u})$ denotes the Reynolds tensor. The function $\boldsymbol{\phi}$ may be vector valued and may include partial derivatives as a set of evolutionary equations. $\boldsymbol{\phi}$ is referred to as a *representation* of a turbulent flow. $\boldsymbol{\alpha}$ represents a vector of model constants whose values are usually determined empirically. While equation (5) may close the set of equations (3) and (4), it leaves many questions unresolved. It is not known what, if any, bounds constrain the set of constants $\{\alpha_i\}$ for a given model to posses a stable physically realistic solution.

It is not clear, for example, that equations (3) and (4) have a solution for any arbitrary model contained in equation (5). This question is more fundamental than asking for equation (5) to reproduce the properties of turbulent flows since the existence of a unique solution is a pre-requisite for predictive performance. Formally:

> "*A meaningful turbulence model is one for which the system of equations (3), (4), (5) possesses a unique regular solution. In addition, the system should have stable fixed points and must be covariant under the group* $\mathbb{G}_a$."

No test is available to ascertain if equation (5) does, in fact, specify a meaningful turbulence model. The objective herein is to present the information that can be obtained from energy estimates for the equations of turbulence models (as introduced in Moulden [3] for a second moment closure model). A few comments are made about a second moment model and the well-known $k \sim \epsilon$ model is also considered.

Restricting attention to "meaningfulness" does not remove the importance of the criteria written by Hanjalić [5] for the construction of turbulence models. In particular: the model should satisfy the realizability constraints (the turbulence kinetic energy must be non-negative for example) and be computationally manageable. It must also satisfy the invariance requirements consistent with Newtonian continuum mechanics. That is, more is involved in the construction of a turbulence model than just the heuristic arguments required to select the functional form of modeled

terms. The norm estimates discussed below should be attended to at the same time as other computational issues are considered. Assessing the role of model constants in the stability properties of the model should be an essential feature of model development.

2 A uniqueness theorem

A uniqueness theorem for the mean motion equations, that follows the work of Gurtin [6], can be written for equations (3) and (4) without appeal to a turbulence model of the form given in equation (5). This result may be stated as:

Lemma I. *Let* $(\mathbf{V}_1, \overline{P}_1)$ *and* $(\mathbf{V}_2, \overline{P}_2)$ *be two solutions of the mean motion equations in (3) and (4) (with the same boundary conditions and body forces). Then:*

$$\mathbf{V}_1 = \mathbf{V}_2; \qquad \boldsymbol{\mathcal{R}}_1 + \overline{P}_1\mathbf{I} = [\boldsymbol{\mathcal{R}}_2 + \boldsymbol{\mathcal{C}}(\mathbf{x}, t)] + [\overline{P}_2 + Q(\mathbf{x}, t)]\mathbf{I}$$

such that the quantity $\boldsymbol{\mathcal{C}}(\mathbf{x}, t)$ *is an arbitrary divergence-free symmetric second order tensor and* Q *an arbitrary scalar field whose spatial gradient* $\boldsymbol{\nabla}(Q)$*, vanishes* $Q = Q(t)$ *only.*

and is valid provided that the regularity required by the proof holds. The result shows that while the mean velocity field is specified uniquely by the mean motion equations, the Reynolds tensor need not be unique. The same is true of the mean pressure field. The proof of this lemma, being given in Moulden [7], need not be repeated here. The lemma implies that equation (5) cannot define a *unique* representation, $\boldsymbol{\phi}$, of any particular turbulent flow model. However, the non-uniqueness in $\boldsymbol{\mathcal{R}}$ is of the form $\boldsymbol{\mathcal{R}} \mapsto \boldsymbol{\mathcal{R}} + \boldsymbol{\mathcal{C}}$ with $div(\boldsymbol{\mathcal{C}}) = \mathbf{0}$ so that the computation of the mean velocity is not compromised in equations (3) and (4). Such a finding is on the same footing as noticing that the mass invariance constraint $div(\mathbf{u}) = 0$ allows a gauge field, $\mathbf{w}(\mathbf{x}, t)$, from the condition $div(\mathbf{u} + \mathbf{w}) = 0$ *iff* $div(\mathbf{w}) = 0$. The role of gauge fields in turbulence models will be addressed elsewhere and can be adopted to describe the inactive component of the motion. For a discussion of this inactive motion, and other problems related to turbulence, see for example, Bradshaw [9].

In the proof of Lemma I it must be assumed that the mean velocity gradient $\overline{\mathbf{L}} = \partial\mathbf{V}/\partial\mathbf{x}$ has bounded eigenvalues (but, there is no proof that this assumed regularity is true). The local regularity results (ones that do not consider the influence of the initial conditions) for the Navier–Stokes equations are discussed in Seregin [8]. Of course, it is the non-linear terms that impede the progress in constructing a full theory. It is known that if the boundary data is smooth on a bounded domain then there is an "almost everywhere" restriction on solutions: sets of measure zero may contain singular behaviour. It is not clear how such a theory can be extended to the mean motion equations, (3) and (4), due to the lack of information about the properties of the Reynolds tensor, $\boldsymbol{\mathcal{R}}$, as defined by the turbulence model given in equation (5). The second moment equation has little to offer here due to the lack of closure of that equation (the $\boldsymbol{\Psi}$ term of equation (8) below must be

represented by a turbulence model). The present approach *assumes* sufficient regularity to obtain the results for the selected turbulence model: these assumptions are, however, stated as the discussion proceeds.

3 Energy estimates

Energy estimates start from the definition of norm quantities such as the velocity $|\mathbf{V}|^2 = \langle \mathbf{V}, \mathbf{V} \rangle$ and its global extension $|\mathbf{V}|_g^2 \equiv \int_{\mathcal{D}} \langle \mathbf{V}, \mathbf{V} \rangle \, dV$. The latter of which can be evaluated from the norm energy equation for the mean velocity:

$$\frac{1}{2}\frac{\partial}{\partial t}|\mathbf{V}|_g^2 + \nu \|\overline{\mathbf{L}}\|_g^2 = \langle\!\langle \overline{\mathbf{L}}, \boldsymbol{\mathcal{R}} \rangle\!\rangle_g + \langle \mathbf{V}, \mathbf{f} \rangle_g$$

a result obtained from equation (4) by means of an inner product with the mean velocity. Periodic boundary conditions have been assumed for this estimate and will be adopted throughout the following. The standard Poincaré inequality allows the statement $\|\overline{\mathbf{L}}\|_g^2 \geq L_L^2 |\mathbf{V}|_g^2$ to replace derivative norms by value norms. Hence there is the differential inequality:

$$\frac{\partial}{\partial t}|\mathbf{V}|_g^2 + 2\nu L_L^2 |\mathbf{V}|_g^2 \leq 2\|\overline{\mathbf{L}}\|_g \|\boldsymbol{\mathcal{R}}\|_g + 2|\mathbf{V}|_g |\mathbf{f}|_g \tag{6}$$

$\overline{\mathbf{L}}$ denotes the mean motion velocity gradient $\partial \mathbf{V}/\partial \mathbf{x}$. Herein, the notation $\langle\!\langle \mathbf{A}, \mathbf{B} \rangle\!\rangle_g = \int_{\mathcal{D}} trace(\mathbf{A}\mathbf{B}^T) \, dV$ is adopted for the global inner product of any pair of linear operators, $\mathbf{A}$ and $\mathbf{B}$, on $\mathbb{R}^3$. Locally, $\langle\!\langle \mathbf{A}, \mathbf{B} \rangle\!\rangle = trace(\mathbf{A}\mathbf{B}^T)$. Equation (6) requires an estimate for $\|\boldsymbol{\mathcal{R}}\|_g$ before anything can be said about the evolution of the mean velocity norm. This estimate must be prepared for each turbulence model considered. A class of invariant models were studied in Moulden [3] with the conclusion that a stable system was only possible for a restricted parameter vector $\boldsymbol{\alpha}$ in equation (5). A brief revue of such a model is included here to illustrate the problems involved.

It is important to recognize that regularity assumptions are included in equation (6) in that the norm $\|\overline{\mathbf{L}}\|_g^2 = \int_{\mathcal{D}} trace(\overline{\mathbf{L}}\,\overline{\mathbf{L}}^T) \, dV$ and the global inner product $\langle\!\langle \boldsymbol{\mathcal{R}}, \overline{\mathbf{L}} \rangle\!\rangle_g$ are both assumed to be bounded (which demands that both $\langle\!\langle \boldsymbol{\mathcal{R}}, \overline{\mathbf{L}} \rangle\!\rangle$ and $\langle\!\langle \overline{\mathbf{L}}, \overline{\mathbf{L}} \rangle\!\rangle$ be bounded everywhere and for all time). This requirement can be expressed as the need for the eigenvalues of both $\overline{\mathbf{L}}$ (a property of the mean motion) and $\boldsymbol{\mathcal{R}}$ (a property of the velocity fluctuations) to be bounded everywhere and for all time. The Cauchy–Schwarz inequality provides an upper bound:

$$\langle\!\langle \boldsymbol{\mathcal{R}}, \overline{\mathbf{L}} \rangle\!\rangle_g \leq \|\boldsymbol{\mathcal{R}}\|_g \|\overline{\mathbf{L}}\|_g \leq \left[\|\boldsymbol{\mathcal{R}}\|_g^2 + \|\overline{\mathbf{L}}\|_g^2 \right] / 2$$

This inequality and the Poincaré inequality allow inequality (6) to be expressed in the form:

$$\frac{\partial}{\partial t}|\mathbf{V}|_g^2 + \nu L_L^2 |\mathbf{V}|_g^2 \leq \frac{2}{\nu}\|\boldsymbol{\mathcal{R}}\|_g^2 + \frac{2}{\nu L_L^2}|\mathbf{f}|_g^2 \tag{6a}$$

to show the role that the norms of the Reynolds tensor and body force play in the stability of the mean motion. If regularity of the mean motion is assumed to the

extent that the mean velocity gradient, $\overline{\mathbf{L}}$, and its temporal and spatial gradients exist then equation (4) gives:

$$\frac{d\overline{\mathbf{L}}}{dt} + \overline{\mathbf{L}}^2 + \boldsymbol{\nabla}(div(\boldsymbol{\mathcal{R}})) = \nu\nabla^2(\overline{\mathbf{L}}) - \mathbf{P} + \mathbf{F}$$

where $\mathbf{F} = \boldsymbol{\nabla}(\mathbf{f})$ and $\mathbf{P}$ denotes the mean motion pressure Hessian. Both of which are assumed to exist. Then an energy equation for the mean velocity gradient emerges in the form:

$$\frac{\partial}{\partial t}\|\overline{\mathbf{L}}\|_g^2 + 2\nu\|\boldsymbol{\nabla}\overline{\mathbf{L}}\|_g^2 + 2\langle\!\langle \mathbf{K}, \overline{\mathbf{L}} \rangle\!\rangle_g = 2\langle\!\langle \mathbf{F}, \overline{\mathbf{L}} \rangle\!\rangle_g \tag{7}$$

if $\mathbf{K} = \overline{\mathbf{L}}^2 + \boldsymbol{\nabla}(div(\boldsymbol{\mathcal{R}}))$.

It was shown in Moulden [3] that there is no unique estimate available for the Reynolds stress models of the form discussed by Lewellen [10]. One reason for the lack of a unique estimate is the existence of a norm hierarchy for the mean motion equations. Estimates for turbulence models can use zero order norm closer based upon the level of equation (6), or can have first order norm closure using equation (7) with its additional regularity assumptions. In both cases conditional linear stability (depending upon model constants) was found at the origin of the phase space of the respective dynamical systems when body forces are absent. Physical significance of the estimates also needs to be considered. The process is illustrated below for zero order norm closure.

Second moment closure models are based upon the system of equations defined by:

$$\frac{\partial \mathcal{R}_{ij}}{\partial t} + V_k\frac{\partial \mathcal{R}_{ij}}{\partial x_k} + \mathcal{R}_{jk}\frac{\partial V_i}{\partial x_k} + \mathcal{R}_{ik}\frac{\partial V_j}{\partial x_k} - \nu\frac{\partial^2 \mathcal{R}_{ij}}{\partial x_k^2} = -\Psi_{ij} \tag{8}$$

(a set of six equations) for the Reynolds tensor $\boldsymbol{\mathcal{R}}$. Equation (8) makes use of the notation:

$$\Psi_{ij} = 2\nu\mathcal{E}\left[\frac{\partial u_i}{\partial x_k}\frac{\partial u_j}{\partial x_k}\right] + \frac{\partial}{\partial x_k}\mathcal{E}(u_iu_ju_k) + \psi_{ij} \equiv \mathbf{E}_T|_{ij} + \mathbf{D}_F|_{ij} + \psi_{ij}$$

with $\mathbf{E}_T$ the turbulence dissipation and $\mathbf{D}_F$ the velocity diffusion term. The linear combination:

$$\psi_{ij} = \left[\frac{\partial}{\partial x_i} - \mathcal{E}(u_jp) + \frac{\partial}{\partial x_j}\mathcal{E}(u_ip)\right] - \mathcal{E}\left[p\left(\frac{\partial u_j}{\partial x_i} + \frac{\partial u_i}{\partial x_j}\right)\right] \equiv \mathbf{D}_P|_{ij} + \mathbf{S}_P|_{ij}$$

of the pressure strain and pressure diffusion defines the tensor ψ_{ij}. Write the right hand side of equation (8) in the form: $\boldsymbol{\Psi} = \mathbf{E}_T + \mathbf{D}_F + \mathbf{D}_P + \mathbf{S}_P$ to allow the estimate:

$$\frac{\partial}{\partial t}\|\boldsymbol{\mathcal{R}}\|_g^2 + 2\nu\|\boldsymbol{\nabla}\boldsymbol{\mathcal{R}}\|_g^2 + 4\langle\!\langle \overline{\mathbf{L}}\boldsymbol{\mathcal{R}}, \boldsymbol{\mathcal{R}} \rangle\!\rangle_g + 2\langle\!\langle \boldsymbol{\Psi}, \boldsymbol{\mathcal{R}} \rangle\!\rangle_g = 0 \tag{9}$$

again for periodic boundary conditions. The case of zero order norm closure will illustrate some of the problems associate with the construction of meaningful estimates. The dynamical system for that estimate is given by:

$$\frac{\partial}{\partial t}\begin{pmatrix} |\mathbf{V}|_g^2 \\ \|\boldsymbol{\mathcal{R}}\|_g^2 \end{pmatrix} \leq \begin{pmatrix} -\nu L_L^2|\mathbf{V}|_g^2 + 2\|\boldsymbol{\mathcal{R}}\|_g^2/\nu + 2|\mathbf{f}|_g^2/(\nu L_L^2) \\ -2\nu L_R^2|\boldsymbol{\mathcal{R}}|_g^2 - 2(\nu + \Lambda^* - 2\overline{L})\|\boldsymbol{\mathcal{R}}\|_g^2 \end{pmatrix}$$

and is based upon equations (6a) and (9). The estimate:

$$\langle\!\langle \overline{\mathbf{L}}\boldsymbol{\mathcal{R}}, \boldsymbol{\mathcal{R}} \rangle\!\rangle_g \leq \|\overline{\mathbf{L}}\|_g \|\boldsymbol{\mathcal{R}}\|_g^2 \leq \overline{L}\|\boldsymbol{\mathcal{R}}\|_g^2$$

(with $\|\overline{\mathbf{L}}\|_g \leq \overline{L}$ assumed to be bounded) has also been introduced and has the effect of removing $\|\overline{\mathbf{L}}\|_g$ from the equation for $\|\boldsymbol{\mathcal{R}}\|_g$ as is consistent with zero order norm estimates. The turbulence model adopted in Moulden [3] placed:

$$\mathbf{E}_T = \alpha_e \boldsymbol{\mathcal{R}} + \alpha_i \, trace(\boldsymbol{\mathcal{R}})\mathbf{I}, \quad \mathbf{D}_F = \alpha_f \boldsymbol{\mathcal{R}}, \quad \mathbf{S}_P = \alpha_s[\boldsymbol{\mathcal{R}} - trace(\boldsymbol{\mathcal{R}})\mathbf{I}/3]$$

while the model for $\mathbf{D}_P$ was included in that for $\mathbf{D}_F$ (and was a simplified version of the model discussed in Lewellen [10]). The model satisfies the required Galilean covariance. Here, the set $\{\alpha_e, \, \alpha_f, \ldots\}$ are model constants (all greater than zero). The constant Λ^* in the dynamical system above is given by the sum $\Lambda^* = 2\alpha_s/3 + \alpha_e + \alpha_f + \alpha_i > 0$. The Reynolds tensor norm decays like:

$$\|\boldsymbol{\mathcal{R}}\|_g^2(t) \leq exp[-2(\nu(1 + L_R^2) + \Lambda^* - 2\overline{L})t] \, \|\boldsymbol{\mathcal{R}}\|_g^2(0)$$

provided that $\nu(1 + L_R^2) + \Lambda^* > 2\overline{L}$. In the limit as $t \to \infty$, the mean velocity norm then decays as:

$$|\mathbf{V}|_g^2(t) \leq exp[-\nu L_L^2 t/2] \, |\mathbf{V}|_g^2(0)$$

in the absence of a body force. Otherwise, $|\mathbf{V}|_g^2 \to 2|\mathbf{f}|_g^2/(\nu L_L^2)^2$ as $t \to \infty$. Note that this is twice the value found in estimate (E1) for the instantaneous velocity norm $|\mathbf{v}|_g^2$. With the removal of the mean velocity gradient from the $\|\boldsymbol{\mathcal{R}}\|_g$ equation any interaction of the Reynolds tensor with the mean motion is denied in this estimate. The estimate is not physically tenable. Hence first order norm closure, Moulden [3], must be adopted and an $\|\overline{\mathbf{L}}\|_g$ term retained in the $\|\boldsymbol{\mathcal{R}}\|_g$ equation. The limit $\|\boldsymbol{\mathcal{R}}\|_g \to 0$ is understood to mean that $|\mathbf{u}| \to 0$ locally and that $|\mathbf{V}|_g \to |\mathbf{v}|_g$. The finding above is another manifestation that the zero order norm closure estimate is unsatisfactory. The above has shown:

Lemma II. *Zero order norm closure for this model does not provide a useful estimate for* $|\mathbf{V}|_g$.

From Moulden [3], *first order* norm closure gave a limit for $|\mathbf{V}|_g$ that was consistent with estimate (E1) and was, in addition, linearly stable at the origin of phase space.

The present analysis does not carry epistemological content as far as the structure of the turbulence is concerned. The global norm quantities that enter the theory make no reference to the eddy sizes that contribute to the local motion. From the definition $|\mathbf{v}|_g^2 = \int_{\mathcal{D}} \langle \mathbf{v}, \mathbf{v} \rangle dV$ a global norm contains energy from all wave numbers. It also contains energy from all points of the flow domain $\mathcal{D}$. Only the time evolution of the norm is determined from the theory. The work of Foias et al. [2] and Henshaw et al. [11] for example does, however, make reference to some physical aspects of the flow in terms of small and large scale motions. It is not clear at this point how such information should be included in a turbulence model – if, indeed, it is of importance so to do. Certainly, these two disparate flow components play very different roles in the flow development. As noted below, it is

often necessary to modify turbulence models for application close to solid surfaces where eddy dissipation and production is a physically significant feature of the turbulence.

A comment can be made about the ubiquitous adoption of periodic boundary conditions in functional estimates. Such boundary conditions remove certain boundary integrals from the energy estimates. The flow region contained within the domain $\mathcal{D}$ is not totally arbitrary in the present theory since it can only contain solid boundaries if they have the required periodicity. This restriction is removed in Moulden [7].

4 The "$k \sim \epsilon$" model

As a turbulence model, the $k \sim \epsilon$ model is less complex than methods based upon the full second moment equation (8). The six equations contained in (8) is reduced to two equations, one for k and one for ϵ. However, the resulting $k \sim \epsilon$ model is algebraically more complex due to the definitions of P and the eddy viscosity ν_τ in equations (15) and (16) below. That is ratios such as ϵ^2/k and k^2/ϵ arise in the model. Herein, only an examination of the system is presented with the full theory to appear in Moulden [7]. First, introduce the variables:

$$k = trace(\boldsymbol{\mathcal{R}})/2 \qquad \text{(the turbulence kinetic energy)}$$

$$\epsilon = \nu\mathcal{E}[\partial u_i/\partial x_j)^2] \equiv \nu\mathcal{E}[trace(\mathbf{L}'\mathbf{L}'^T] \qquad \text{(the turbulence dissipation)}$$

both $k \geq 0$ and $\epsilon \geq 0$ are well defined physical quantities in the sense of being Galilean invariant and hence consistent with the Navier–Stokes equations.

Start the analysis with the adoption of a gradient transport model for the Reynolds tensor $\boldsymbol{\mathcal{R}} \equiv \mathcal{E}(\mathbf{u} \otimes \mathbf{u})$ (as discussed in Bradshaw [12] for example). That is, adopt the form:

$$\boldsymbol{\mathcal{R}} = 2\nu_\tau \overline{\mathbf{D}} - 2k\mathbf{I}/3 \tag{10}$$

which relates $\boldsymbol{\mathcal{R}}$ to both the mean motion, via the symmetric part, $\overline{\mathbf{D}}$, of the mean velocity gradient, $\overline{\mathbf{L}}$, and the turbulence kinetic energy, $k(\mathbf{x}, t)$. The eddy viscosity $\nu_\tau = \nu_\tau(k, \epsilon)$ is taken to be a function of both the kinetic energy k and the dissipation ϵ. As in the Boussinesq model, $\boldsymbol{\mathcal{R}}$ is related directly to the mean motion in equation (10), but this specification does not close the mean motion equations due to the inclusion of k in equation (10). Equation (10) leads to the global norm inequality:

$$\|\boldsymbol{\mathcal{R}}\|_g^2 \leq 2|\nu_\tau|_g^2 \|\overline{\mathbf{L}}\|_g^2 + 4|k|_g^2/3 \tag{11}$$

since the Korn inequality, see Horgan [13], shows that $\|\overline{\mathbf{D}}\|_g^2 = \|\overline{\mathbf{L}}\|_g^2/2$. Equation (11) may be compared with the inequality of Schumann [14] discussed in connection with the realizability conditions for the Reynolds tensor $\boldsymbol{\mathcal{R}}$. Equation (10) further implies that:

$$trace(\boldsymbol{\mathcal{R}}\overline{\mathbf{L}}^T) = \nu_\tau\, trace(\overline{\mathbf{D}}\,\overline{\mathbf{D}}) \equiv \nu_\tau \|\overline{\mathbf{D}}\|^2 = \nu_\tau \|\overline{\mathbf{L}}\|_g^2/2$$

and that:

$$\langle\!\langle \boldsymbol{\mathcal{R}}, \overline{\mathbf{L}} \rangle\!\rangle_g = \langle\!\langle \nu_\tau \overline{\mathbf{D}}, \overline{\mathbf{D}} \rangle\!\rangle_g \leq |\nu_\tau| \|\overline{\mathbf{D}}\|_g^2 \equiv |\nu_\tau| \|\overline{\mathbf{L}}\|_g^2/2 \tag{12}$$

from the Korn inequalities. Take the pair of equations:

$$\frac{\partial k}{\partial t} + V_j \frac{\partial k}{\partial x_j} + Q = \frac{\partial}{\partial x_j}\left[\nu_k \frac{\partial k}{\partial x_j}\right] \tag{13}$$

$$\frac{\partial \epsilon}{\partial t} + V_j \frac{\partial \epsilon}{\partial x_j} + P = \frac{\partial}{\partial x_j}\left[\nu_\epsilon \frac{\partial \epsilon}{\partial x_j}\right] \tag{14}$$

as defining the model $k \sim \epsilon$ (see Wilcox [15] for example). This pair of equations represent a standard form of the model and needs modification near solid surfaces and as the motion decays to a quiescent state. In the above:

$$P = c_1\,\epsilon^2/k + c_2\,\mathcal{R}_{ij}\overline{L}_{ij}\,\epsilon/k; \qquad Q = \epsilon + \mathcal{R}_{ij}\overline{L}_{ij} \tag{15a,b}$$

and:

$$\nu_k = \nu + \nu_\tau; \quad \nu_\epsilon = \nu + \nu_\tau/\sigma; \qquad \text{where } \nu_\tau = \alpha\,k^2/\epsilon \tag{16a,b,c}$$

the actual values of the constants $c_1,\ c_2,\ \sigma$ and α are not of importance at this point but do feature in the final stability result. It can also be noted that Lemma I suggests that P and Q are not uniquely defined since the transformation $\boldsymbol{\mathcal{R}} \mapsto \boldsymbol{\mathcal{R}} + \boldsymbol{\mathcal{C}}$ is permitted with $div(\boldsymbol{\mathcal{C}}) \equiv \mathbf{0}$. Hence equations (13) and (14) are not invariant under Lemma I. Equations (15a,b) take on the local form:

$$P = c_1\,\epsilon^2/k + \alpha\,c_2\,k\,\|\overline{\mathbf{D}}\|^2; \qquad Q = \epsilon + \nu_\tau\|\overline{\mathbf{D}}\|^2$$

with a $trace(\boldsymbol{\mathcal{C}}\,\overline{\mathbf{L}}^T)$ non-uniqueness possible in P and Q.

Look upon the system (13)–(16) as a set of equations for the four variables $k,\ \epsilon,\ P$ and ν_τ which augment the mean motion equations (3) and (4). Since P and Q involve the norm $\|\overline{\mathbf{L}}\|_g^2$ there should be first order norm closure with equation (7) included for a consistent estimate. With estimate (11), equation (6a) for the mean velocity norm reduces to the differential inequality:

$$\frac{\partial}{\partial t}|\mathbf{V}|_g^2 + \frac{\nu L_L^2}{2}|\mathbf{V}|_g^2 \le \frac{2}{\nu^3}|\nu_\tau|_g^2 + \frac{4}{3\nu}|k|_g^2 + \frac{1}{\nu L_L^2}|\mathbf{f}|_g^2 \tag{17}$$

when the Poincaré inequality is employed. The evolution of the mean velocity norm, $|\mathbf{V}|_g^2$, depends upon the norms $|\nu_\tau|_g^2$ and $|k|_g^2$ as well as the body force norm. The norms of $k,\ \epsilon$ and ν_τ are related by the inequality obtained from equation (16c):

$$\alpha|k|_g^2 \le |\nu_\tau|_g|\epsilon|_g \le [|\nu_\tau|_g^2 + |\epsilon|_g^2]/2$$

while the norms of P and Q relate to other norms as:

$$|P|_g^2 \le c_1|\mu_\tau|_g^2 + \alpha c_2|k|_g^2\|\overline{\mathbf{L}}\|_g^2/2; \qquad |Q|_g^2 \le |\epsilon|_g^2 + |\nu_\tau|_g^2\|\overline{\mathbf{L}}\|_g^2/2$$

if $\mu_\tau = \epsilon^2/k$ when $2|\epsilon|_g^2 \le |k|_g^2 + |\mu_\tau|_g^2$. Illustrate the process for zero order norm closure when these inequalities reduce to:

$$|P|_g^2 \le c_1|\mu_\tau|_g^2 + \alpha c_2|k|_g^2\,\overline{L}^2/2; \qquad |Q|_g^2 \le |\epsilon|_g^2 + |\nu_\tau|_g^2\,\overline{L}^2/2$$

using the bound $\|\overline{\mathbf{L}}\|_g \le \overline{L}$ as above.

Formally applying the Gronwall lemma to equation (17) (for which see Flavin and Rionero [16]) there is:

$$|\mathbf{V}|_g^2(t) \leq |\mathbf{V}|_g^2(0)\, exp[-\nu L_L^2 t/2] + \int_0^t F(t)\, exp[-\nu L_L^2 t/2]\, dt \tag{18}$$

if $F(t)$ denotes the right hand side of equation (17). The structure of equation (18) is the same as that for the instantaneous Navier–Stokes equations discussed earlier (from estimates (E1) and (E2)). However, the mean motion in estimate (18) decays as $exp[-\nu L_L^2 t/2]$ whereas the instantaneous motion decays as $exp[-\nu L_v^2 t]$. The meaning here was mentioned above in relation to equation (10). The turbulent flow decay in estimate (18) has additional contributions from the norms $|\nu_\tau|_g$ and $|k|_g$ which relate to the turbulent fluctuations. In the case where the body force is independent of time and the norm $|k|_g$ decays with time, the limit $t \to \infty$ in equation (18) gives the form:

$$|\mathbf{V}|_g^2(t) \leq 2|\mathbf{f}|_g^2/(\nu L_L^2)^2 \quad \text{as } t \to \infty$$

which is twice the body force contribution found for the instantaneous equations. It is again suggested that this can be attributed to the adoption of a zero order norm closure in the equations without appeal to equation (7) for the mean velocity gradient norm.

The $k \sim \epsilon$ model provides an evolution inequality for both $|k|_g^2$ and $|\epsilon|_g^2$ from equations (13) and (14).

$$\frac{\partial |k|_g^2}{\partial t} + (\nu + n) L_k^2\, |k|_g^2 \leq \frac{1}{4(\nu + n) L_k^2}\, |Q|_g^2 \tag{19}$$

$$\frac{\partial |k|_g^2}{\partial t} + (\nu + n/\sigma) L_\epsilon^2\, |\epsilon|_g^2 \leq \frac{1}{4(\nu + n/\sigma) L_\epsilon^2}\, |P|_g^2 \tag{20}$$

where the bounded constant $n = \nu_\tau|_{\text{max on } \mathcal{D}}$ has been introduced. From the definitions in equation (15), the norms $|P|_g^2$ and $|Q|_g^2$ are related by the inequality:

$$(2c_1 - 3c_2)|\epsilon|_g^2 \leq c_2|Q|_g^2 + |P|_g^2 + |k|_g^2$$

The model as treated herein is not intended to apply to wall bounded flows (some of the properties of which are discussed in Patel et al. [17] as well as in Nagano and Tagawa [18]). In particular, $k \to 0$ at a solid surface but ϵ does not: hence μ_τ is not well defined. Such wall bounded flows are examined in Moulden [7].

A system of equations has been obtained for the four unknown norm variables in the $k \sim \epsilon$ model. In actual estimates, it is required that values be given to the Poincaré constants $\{L_L;\, L_k;\, \cdots\}$. It is well known, see Moulden [19] for actual computations in a specific case, that the values of these constants can vary over a range of several orders of magnitude. This happenstance calls into question the actual *numerical* values adopted to determine the stability of the dynamical system.

The dynamical system of interest is constructed from equations (17), (19) and (20):

$$\frac{\partial}{\partial t}\begin{pmatrix} |\mathbf{V}|_g^2 \\ |k|_g^2 \\ |\epsilon|_g^2 \end{pmatrix} \leq \begin{pmatrix} -\nu\, L_L^2 |\mathbf{V}|_g^2/2 + 2|\nu_\tau|_g^2/\nu^3 + 4|k|_g^2/(3\nu) + |\mathbf{f}|_g^2/(\nu L_L^2) \\ -(\nu+n)\, L_k^2\, |k|_g^2 + [|\epsilon|_g^2 + |\nu_\tau|_g^2\, \overline{L}^2]/(8(\nu+n)L_k^2) \\ -\nu^*\, L_\epsilon^2\, |\epsilon|_g^2 + [c_1|\mu_\tau|_g^2 + \nu\, c_2 |k|_g^2\, \overline{L}^2]/(8\nu^* L_\epsilon^2) \end{pmatrix}$$

where $\nu^* = \nu + n/\sigma$. Robinson [20] discusses properties of dynamical systems which apply to the present situation. The fixed points of the corresponding differential system can be established. By definition *tenable* solutions cannot have negative values for the norms involved. Hence the fixed points (where the right hand side vanishes) defines an equilibrium state for the motion. Note that the limit $|k|_g^2 \to 0$ and $|\epsilon|_g^2 \to 0$ cannot be taken for this model for reasons discussed above. There is however:

Lemma III. *The $k \sim \epsilon$ model introduced above has a fixed point where the mean velocity norm, for example, has the value:*

$$|\mathbf{V}|_g^2 = \frac{2}{\nu L_L^2}\left[\frac{2}{\nu^3}|\nu_\tau|_g^2 + \frac{4}{3\nu}|k|_g^2 + \frac{1}{\nu L_L^2}|\mathbf{f}|_g^2\right]$$

in terms of turbulence quantities and the body force norm. This fixed point is linearly stable.

to complete the discussion of this model.

As a final note to this section there have been many modifications to the $k \sim \epsilon$ model and Nagano and Tagawa [18] being one such addition to allow for near wall effects. Such models call for additional functions, f_ν, f_ϵ and f_u, say, which allow for damping close to a solid wall. With these functions P is modified to:

$$P = c_1 f_\epsilon \epsilon^2/k + c_2 \mathcal{R}_{ij}\overline{L}_{ij}\, f_u\, \epsilon/k$$

while the eddy viscosity coefficient is changed to the form $\nu_\tau = \alpha f_\nu k^2/\epsilon$. The free turbulence limit requires a separate treatment.

5 Final comments

Some comments have been made concerning the structure of norm estimates and their application to both a second moment model and to the $k \sim \epsilon$ turbulence model. Without a body force present it was found that the second moment model predicts that the motion will decay to the origin of phase space. In the case of the $k \sim \epsilon$ model, there was a limitation to fixed points in a uniform flow where $\partial|\mathbf{V}|_g^2/\partial t \equiv 0$. That flow is linearly stable.

References

[1] Gatski, T. B: Constitutive equations for turbulent flows, *Th. and Comp. Fluid Dyn.*, **18**, No 5, pp 345–369, 2004.

[2] Foias, C. Manley, O. and Temam, R: Modeling of the interaction of small and large eddies in two-dimensional turbulence, *Math. Modeling and Num. Anal.*, **22**, pp 93–118, 1988.
[3] Moulden. T. H: Estimates for turbulence models, *Int. J. Pure and Appl. Math.*, **43**, pp 551–562, 2008.
[4] Speziale, C. G: Invariance of turbulence closure models, *Phys. Fluids*, **22**, pp 1033–1037, 1979.
[5] Hanjalić, K: Second-moment turbulence closures for CFD: needs and prospects, *IJCFD*, **12**, pp 67–97, [1999].
[6] Gurtin, M. E: *An Introduction to Continuum Mechanics*, Academic Press, New York, 1981.
[7] Moulden, T. H: *Viscous Fluid Motion*, Text in preparation.
[8] Seregin, G: Local regularity of the Navier Stokes equations, In: Friedlander, S. and Serre, D. (Eds). *"Handbook of Mathematical Fluid Mechanics"*, **4**, pp 159–200, North Holland, Amsterdam, 2007.
[9] Bradshaw, P: Turbulence: the chief outstanding difficulty of our subject, *Exp. in Fluids.*, **16**, pp 203–216, 1994.
[10] Lewellen, W. S: Use of invariant modeling, In: Frost, W. and Moulden, T. H. (Eds). *Handbook of Turbulence*, Plenum Press, New York, pp 237–280, 1977.
[11] Henshaw, W. D, Kreiss, H. O. and Reyna, L. G: Smallest scale estimates for the Navier–Stokes equations for incompressible fluids, *Arch. Rat. Mech. Anal.*, **112**, pp 21–44, 1990.
[12] Bradshaw, P. (Ed): *Turbulence*, 2nd Edition. Springer Verlag, Berlin, 1978.
[13] Horgan, C. O: Korn's inequalities and their application in continuum mechanics, *SIAM Review,* **37**, pp 491–511, 1995.
[14] Schumann, U: Realizability of Reynolds-stress turbulence models, *Phys. Fluids*, **20**, pp 721–725, 1977.
[15] Wilcox, D. C: *Turbulence Models for CFD*, DCW Industries, La Cafiada, 1998.
[16] Flavin, J. N. and Rionero, S: *Qualitative Estimates for Partial Differential Equations*, CRC Press, Boco Raton, 1996.
[17] Patel, V. C., Rodi, W. and Scheuerer, G: Turbulence models for near-wall and low Reynolds number flows: a review, *AIAA J.*, **23**, pp 1308–1319, 1985.
[18] Nagano, Y. and Tagawa, M: An improved $k \sim \epsilon$ model for boundary layer flows, *J. Fluids Eng.*, **112**, pp 33–39, 1990.
[19] Moulden, T. H: On the structure of Burgers' turbulence, *5th International Conference of Applied Mathematics*, Plovdiv, Bulgaria, 2008.
[20] Robinson, J. C: *Infinite Dimensional Dynamical Systems*, Cambridge University Press, Cambridge, 2001.

Turbulence combustion closure model based on the Eddy dissipation concept for large eddy simulation

B. Panjwani[1], I. S. Ertesvåg[1], A. Gruber[2] & K. E. Rian[3]
[1]*Department of Energy and Process Engineering, Norwegian University of Science and Technology(NTNU), Norway*
[2]*SINTEF Energy Research, Trondheim, Norway*
[3]*Computational Industry Technologies (ComputIT), Norway*

Abstract

Modeling of turbulence-chemistry interaction is still a challenge. Turbulence modeling with Large Eddy Simulation (LES) has been matured enough for industrial problems. In LES eddies up to the filter width are resolved on the grid scales, but the fine structures where combustion takes place are still not resolved, which calls for combustion modeling in LES. Combustion closure in LES is achieved through a Turbulence Chemistry Interaction Model (TCIM). Most of the developed TCIM are based on the already existing RANS model. In the present study, a TCIM based on the Eddy Dissipation Concept (EDC) is proposed for large eddy simulation. The model is formulated from subgrid viscosity and filtered strain rate tensor. EDC model constants are modified to account for the partial energy cascading in LES. The other model used in this study is the steady state Flamelet model. Another issue with reacting flows is the solution of the pressure correction Poisson's equation with density time derivative term, which causes severe time constraint per iteration. Density time derivative is the most destabilizing part of the calculation when the density from equation of state is used. In the present study density is formulated from species mass fraction, which is numerically stable and computationally less expensive. LES of the H2/N2 "FlameH3" non-premixed unconfined turbulent jet flame is performed using LES-EDC and Flamelet model. The Reynolds number based on nozzle diameter and jet bulk velocity is 10,000. The chemistry used for LES-EDC model is a fast-chemistry. Results of the simulations in the form of means and variances of

WIT Transactions on Engineering Sciences, Vol 69, © 2010 WIT Press
www.witpress.com, ISSN 1743-3533 (on-line)
doi:10.2495/AFM100031

velocity and scalars are compared to experimental data. All these quantities are in satisfactory agreement with experiments.
Keywords: LES, EDC, Flame H3, FLOWSI.

1 Introduction

Turbulence Chemistry Interaction Model (TCIM) is an approach where a combustion model for reaction rates is developed considering the major aspects of turbulence. In laminar flows a direct closure of the reaction rate is achieved by the Arrhenius reaction rate equation, but in turbulent flows having fluctuations, the direct closure leads to a difficulty due to non-linearity of the Arrhenius term. The challenging problem in the turbulent combustion is the wide range of length and time scales. The direct closure of a source term is only possible through Direct numerical simulation (DNS). DNS resolves all the reactive length scales, which makes DNS computationally expensive. Another approach is Large Eddy Simulation (LES), where large geometrically-dependent energy carrying eddies are resolved on the grid scales(GS), whereas effects of the smaller, more universal isotropic scales are modeled using a sub-grid scale (SGS) models. LES is a promising tool for understanding the physics of unsteady turbulent flows at comparatively reduced cost. Performance of the TCIM depends on the turbulence modeling. An accurate prediction of the turbulence leads to the better prediction of the combustion characteristics. In LES the small dissipative eddies where combustion takes place are not resolved on the grid scale. This calls for a combustion model in LES also, the combustion models in LES do not differ significantly from the already existing RANS models. An advantage with LES is that it captures the instantaneous quantities and mixing more accurately than RANS do.

Most widely used approaches for turbulence chemistry interaction are, a conserved variable approach and Eddy Dissipation Concept (EDC). In the conserved variable approach a transport equation for the conserved variable such as mixture fraction is solved. The mixture fraction represents the mixed ness of the fuel and oxidizer. In this approach turbulence and local equivalence ratio are represented by filtered mixture fraction, mixture fraction variance and scalar dissipation rate. Chemical kinetic is coupled with a flamelet equation which is solved in the mixture fraction space. A turbulence-chemistry interaction model based on presumed probability density functions (PDF) was presented by Landenfeld [1], which was capable of capturing major and minor species distribution features in turbulent diffusion flames. Branley and Jones [2], Forkel and Janicka [3] carried out a LES of hydrogen diffusion flame using the equilibrium chemistry model. Kempf [4] and Kempf et al. [5, 6] performed LES studies of the Sandia Flame D, a Bluff Body flame, a hydrogen diffusion flame and a counter flow diffusion flame using the steady state flamelet model and they obtained satisfactory agreement with experiments. A LES of the piloted Sandia-D flame using an unsteady Lagrangian flamelet model was performed by the Pitsch and Steiner [7] and they achieved an excellent agreement even

for minor species. The unsteady flamelet modeling is an expensive approach compared to the steady state approach, but some of the important unsteady phenomena such as extinction, re-ignition is possible through the unsteady approach. McMurtry et al. [8] formulated the Liner Eddy Model (LEM) developed by Kerstein [9] for LES reacting flows.

Hu et al. [10] carried out a LES simulation of swirling methane/air diffusion flames using the Second Order Moment (SOM) and EDC models. In SOM model the Arrhenius reaction rate equation was used for the direct closure of the source term. The non-linear terms, which arise due to the closure of the Arrhenius reaction rate equations, were modeled. The correlation functions between the temperature-species mass fraction and the fuel-oxidizer mass fraction were approximated using the gradient approach. The reaction mechanism used for the simulation was a single step. The SOM model also introduced some problem dependent constants. The predictions with SOM model were satisfactory but the predictions with EDC model did not agree well with the experimental results. The reason for the unsatisfactory prediction was that the EDC model employed by Hu et al. [10] was the earlier version of EDC model proposed by Magnussen and Hjertager [11], which uses the model constants based on the RANS. The model does not account for the fine structure region and mass fraction also. Yaga et al. [12] carried out a LES study of methane/air diffusion flame using a combustion model which was a combination of the Arrhenius reaction rate and EDC model. The overall reaction rate was the minimum of the Arrhenius reaction rate and the EDC model. The obtained results compared fairly well with experiments except for the CO concentration, that is because of the simple CO mechanism was used in their study. In the present study, a turbulence-chemistry interaction model based on EDC is extended from RANS to LES. A Proposal for modifying the model constant based on the partial cascading is discussed. Present methodology is validated by performing a Large Eddy simulation of the hydrogen diffusion flame "FlameH3" at a Reynolds number of 10,000. A formulation for density based on conservation of species mass fraction is also proposed [13].

1.1 Governing filtered equations

The governing filtered equation for LES are
The continuity equation

$$\frac{\partial \overline{\rho}}{\partial t} + \frac{\partial \overline{\rho}\widetilde{u}_i}{\partial x_i} = 0 \tag{1}$$

The momentum equation

$$\frac{\partial \overline{\rho}\widetilde{u}_i}{\partial t} + \frac{\partial \overline{\rho}\widetilde{u}_i\widetilde{u}_j}{\partial x_j} = -\frac{\partial \overline{p}}{\partial x_j} + \frac{\partial}{\partial x_j}\left(\mu\left(\frac{\partial \widetilde{u}_i}{\partial x_j} + \frac{\partial \widetilde{u}_j}{\partial x_i}\right)\right) - \frac{\partial \tau_{sgs}}{\partial x_j} \tag{2}$$

The mass fraction equation for species i

$$\frac{\partial \overline{\rho}\widetilde{Y}_i}{\partial t} + \frac{\partial \overline{\rho}\widetilde{Y}_i\widetilde{u}_j}{\partial x_j} = \frac{\partial}{\partial x_j}\left(\overline{\rho}D_i\left(\frac{\partial \widetilde{Y}_i}{\partial x_j}\right)\right) + \overline{\rho}\widetilde{\omega}_i \tag{3}$$

where $\overline{\rho}$ is a (Favre) filtered density, $\widetilde{u_i}$ is a filtered velocity component, $\overline{p}$ is pressure $\widetilde{Y_i}$ is a species mass fraction for species i, μ is the dynamic viscosity, t is time, τ_{sgs} is subgrid stress and $\widetilde{\omega}_i$ is the chemical source term. The incompressible governing equations Eqs (1-3) were discretized using the finite volume method (FVM) on a staggered cylindrical grid. A pressure correction Poisson's equation was solved at every time steps, and intermediate velocities and pressure were corrected. Now pressure corrected velocity field is divergence free. The Total Variation Diminishing (TVD) scheme was used for discretizing the convective terms in the species transport equation, and the second order central differencing scheme was used for discretizing the convective terms in the momentum equations. The diffusive terms were discretized using the second order central differencing scheme. The TVD schemes are preferred for discretizing the conserved variables because of their bounded nature. These schemes do not produce undershoot and overshoot in the conserved variables. A scheme is TVD if the total variations in the conserved variable is never increased by convections, the values of the conserved variable remains in between maximum and minimum. The TVD schemes are defined by the choice of a flux limiter function, in the present methodology the CHARM limiter is used [4]. The CHARM limiter is a smooth function which helps to stabilize the numerical scheme. The Smagorinsky subgrid model was used as a closure for the subgrid stress in filtered momentum equations. The transport equations were integrated in time by an explicit low storage three stage Runge–Kutta method. The numerical accuracy of the present finite volume technique is second-order in space. For further details, please refer [4–6, 13].

1.2 Theory and modeling of the filtered reaction rates in LES

The Eddy Dissipation concept for the turbulence combustion proposed by Magnussen and Hjertager [14], Magnussen [11] and Gran and Magnussen [15] is a mixing controlled model. Performance of the EDC is highly dependent on the turbulence model. Turbulence contains eddies of different length and time scale. Larger eddies extract energy from the mean flow, these eddies are highly unstable and breakdown in smaller eddies. This breakdown process continues until eddies are sufficient small and they can not transfer energy further down. Eventually, this process creates structures that are small enough that molecular diffusion becomes important and viscous dissipation of kinetic energy finally takes place. The scale at which this happens is the Kolmogorov length scale. These dissipative eddies are termed as fine structures. In DNS these structures are explicitly calculated on the grid and does not require the combustion modeling. In RANS none of the eddies or structures are computed on the grid and the fine structures length and velocity scales are evaluated using the turbulent kinetic energy k and its dissipation rate ε. The characteristic length $L^\star$ and velocity scale $u^\star$ of the fine structures based on the cascade theory of turbulence [16] are

$$L^\star = \frac{2}{3}\left(\frac{3C_{D2}^3}{C_{D1}^2}\right)^{1/4}\left(\frac{\nu^3}{\epsilon}\right)^{1/4} = 1.43\left(\frac{\nu^3}{\epsilon}\right)^{1/4} \tag{4}$$

$$u^\star = \left(\frac{C_{D2}}{3C_{D1}^2}\right)^{1/4} (\nu\epsilon)^{1/4} = 1.75\,(\nu\epsilon)^{1/4} \tag{5}$$

where $C_{D1} = 0.134$ and $C_{D2} = 0.5$ [11, 14, 16]. ν is the kinematic viscosity and ϵ is eddy dissipation rate. The scales $L^\star$ and $u^\star$ are the same order of magnitude as the Kolmogorov length scales. The constant associated with Eq. (4) and (5) are developed assuming the full cascade process at each numerical cell. A connection between the fine structure and the larger eddies is achieved through the cascade. Large eddy simulation although resolves most of the eddies or structures but fine dissipative structures are not calculated due to computational constraint. The smallest length scale available in LES is a filter width. The size of the fine structure eddies is much smaller than the filter width and need to be computed as a function of filter width. In principle, these fine structure regions are embedded within highly strained eddies.

The transport equation Eq. (3) requires a closure for the source term. In EDC model, it is assumed that each numerical cell consists of a reactor, with inflow equal to surrounding mass fraction and outflow equal to burnt fine structures. The source term in the transport equation Eq. (3) with EDC model is

$$\omega_i = \frac{\gamma_\lambda^2 \chi}{\tau_\star}(Y_i^0 - Y_i^\star),$$

where γ_λ is the fine structure region, $\gamma_\lambda^2/\tau_\star$ is the mass exchange between the surrounding and the fine structure region. Superscripts * and ^{0} refer the fine structure and the surrounding state respectively. $\tau_\star$ is a residence or mixing time. χ [13] is a fraction of the fine structure where reaction takes place. The fine structures state $Y^\star$ are estimated using the reactor modeling. In the present study a perfectly stirred reactor (PSR) is used assuming that the reactor mass is constant at each time step and reactants are perfectly mixed inside it. The chemistry in the reactor can be modeled either with fast chemistry, equilibrium or chemical kinetics. In order to save computational time the fast chemistry approach is used.

The fine structure region is estimated as a function of fine structure velocity and the eddy characteristic velocity u', $\gamma_\lambda = (u_\star/u')$. Characteristics of the larger eddies such as the velocity u' and length scale l' are evaluated using the turbulence model such as $k - \epsilon$. In LES most of the turbulent kinetic energy is resolved on the grid scale and only a small amount of the subgrid kinetic energy is available explicitly. The fine structures region γ_λ is evaluated using the subgrid eddy velocity u_{sgs} and fine structure velocity $u_\star$.

$$\gamma_\lambda = \left(\frac{u_\star}{u_{sgs}}\right) \tag{6}$$

and using the Eq.(5), the fine structure region can be expressed as

$$\gamma_\lambda = \left(\frac{3C_{D2}}{4C_{D1}^2}\right)^{1/4} \left(\frac{\nu\epsilon}{k_{sgs}^2}\right)^{1/4} \tag{7}$$

where k_{sgs} is the subgrid kinetic energy and is modeled $\nu_{sgs} = C_k \triangle {k_{sgs}}^{1/2}$ and similarly the subgrid eddy dissipation rate is modeled $\epsilon_{sgs} = C_\epsilon (k_{sgs})^{3/2}/\triangle$. The relationship between the subgrid viscosity, kinetic energy and dissipation is given by $\nu_{sgs} = C_{\nu sgs} k_{sgs}^2/\epsilon_{sgs}$. Most of the subgrid models in LES evaluate the eddy viscosity explicitly, and the subgrid kinetic energy and dissipation are calculated implicitly. Then the EDC model is formulated using the eddy viscosity ν_{sgs}, where the dimensionless model coefficients are $C_k = 0.05$ and $C_\epsilon = 1.00$ [17]. The fine structure region is represented as

$$\gamma_\lambda = \left(\frac{3 C_{\nu sgs} C_{D2}}{4 C_{D1}^2}\right)^{1/4} \left(\frac{\nu}{\nu_{sgs}}\right)^{1/4} \tag{8}$$

Equation (8) is a function of the molecular viscosity, the subgrid viscosity and the model constants. In case of LES a model constant $C_{EDC} = \left(3 C_{\nu sgs} C_{D2}/4 C_{D1}^2\right)^{1/4}$ is introduced. Value of the model constant is $C_{EDC} = 1.01$, where $C_{\nu sgs} = 0.05$ [17]. Using this value of the C_{EDC} overpredicts the temperature and the flame height is also under predicted. That is because the constant C_{EDC} has been developed using the standard value of CD_2 and CD_1 which are based on the full turbulence energy cascading. The model constant C_{EDC} has to be modified based on the partial cascading or no cascading in LES. In order to establish the constant C_{EDC} parametric studies were carried out, and it was found that the model constant C_{EDC} of 0.25 [13] gives better predictions. Although in the current formulation, EDC constant is assumed to be fixed, however in realistic problem the model constant has to be computed dynamically. In addition to that an upper limit of $(\gamma_\lambda < 1)$ is used wherever the fine structure velocity is larger than the subgrid velocity.

1.3 Density calculation for splitting the conserved variables

In reacting flows, solution of the pressure correction Poisson equation with density time derivative term causes a severe time constraint per iteration and is the most destabilizing part of the calculation. This stability problem mostly dominates near to the nozzle due to sudden heat release. A major issue discussed by Kempf et al. [4], was the splitting of ρf with density ρ in the flamelet approach. He proposed an Echt Konservativer Transport (EKT) scheme to alleviate this problem, which is based on the conservation of fuel ρf and oxidizer $\rho\,(1 - f)$. The EKT scheme assumes two pseudo species $X_A = f^+ = f$ and $X_B = f^- = (1 - f)$ and the transport equations for the pseudo species were solved in predictor and corrector steps. In the EKT approach the density was formulated as [4]

$$\overline{\rho} = \left(\overline{\rho}\widetilde{f^+}\right)^{n+1^\star} + \left(\overline{\rho}\widetilde{f^-}\right)^{n+1^\star} \tag{9}$$

A similar problem is also faced while splitting ρY_i with density in the EDC approach [13]. Then a method similar to EKT is proposed for calculation of the

density. In the present formulation, the species mass fractions were conserved instead of pseudo species:

$$\overline{\rho} = \sum_{i=1}^{i=n} (\rho Y_i)^{n+1^\star} / \sum_{i=1}^{i=n} (Y_i)^{n+1^\star} \tag{10}$$

where $\sum_{i=1}^{i=n} (Y_i)^{n+1^\star} = 1$. The time derivative density term in the pressure correction equation is evaluated at each time step using the chemical density and density from Eq. (10)

$$\frac{\partial \overline{\rho}}{\partial t} = \frac{\overline{\rho}_{chem} - \overline{\rho}}{\triangle t} \tag{11}$$

2 Results and discussion

In the present study, a LES of the H_2/N_2 diffusion flames Flame H3 [18] was carried out. The studied configuration has a fuel nozzle with a diameter (D) of 8mm, which was surrounded by an air co-flow of 0.2 m/s. The fuel jet consist of a mixture of 50% of H_2 and 50% of N_2 by volume. The fuel bulk velocity was 34.8m/s, which gave a Reynolds number of 10,000 based on the nozzle diameter. For the numerical simulation a cylindrical computational domain with 75D in axial direction and 25D in radial direction was employed. The numerical grids of $514 \times 32 \times 57$ were used axially, circumferentially and radially respectively. The grid was equidistant in the axial and circumferential directions. In the radial direction, 5 uniform cells were used in the nozzle, otherwise the grid was stretched linearly. The inflow boundary condition was Dirichlet condition. The mean velocity profiles superimposed with fluctuations were applied at the inflow. The fluctuations with specified length scales were generated using the turbulence inflow generator developed by Klein et al. [19]. On the downstream (outflow boundary) and the annular surface of the computational domain zero gradients for velocity components were posed. Periodicity was applied to all quantities in the circumferential direction.

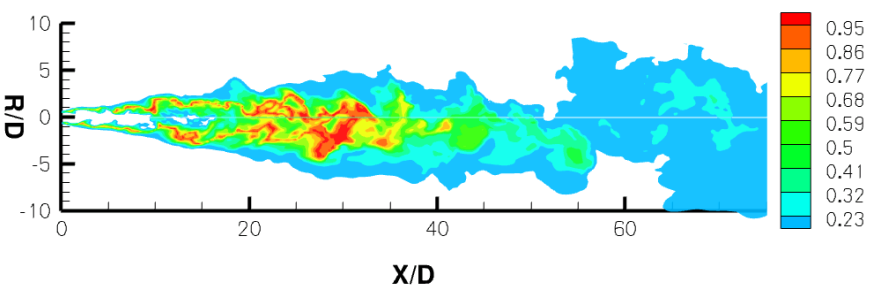

Figure 1: Instantaneous distribution of χ.

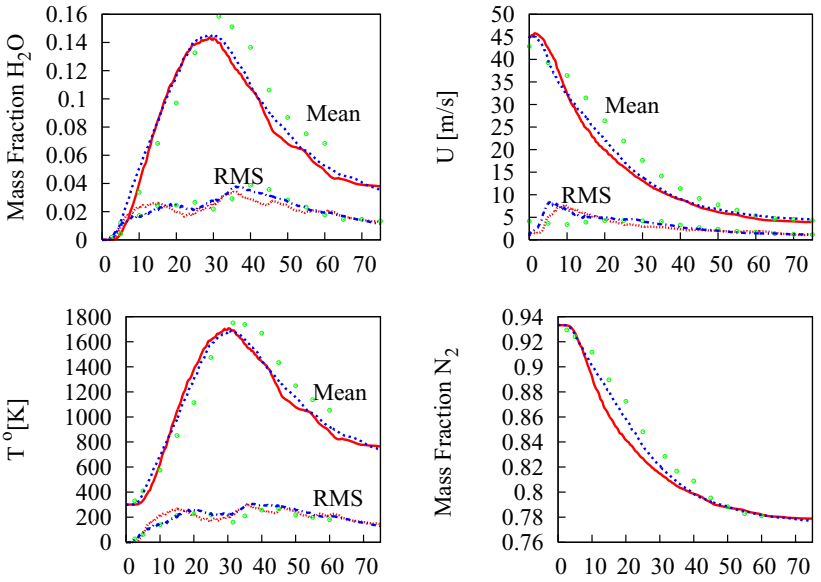

Figure 2: Mean and RMS centerline profiles of the mass fraction of H_2O, mass fraction of N_2, temperature and velocity, where ⊙, −− and ▬ represent experimental, Flamelet and EDC respectively.

The instantaneous plot for the χ is shown in fig. 1. It can be seen that the χ is comparatively higher, especially at the thin reaction zone between the jet and coflow. The main reaction zone which varies from 25D-40D is also well represented by χ. The concept of χ is very similar to the reaction progress variable approach of Pierce and Moin [20]. Where a mixture fraction controls the mixedness of the fuel and oxidizer and the progress variable estimates a global extent of the reaction. Similarly, in the EDC model the fine structure mass fraction represents an amount of the mixed fuel and oxidizer, the extent of the reaction is governed by χ. In the previous study [10, 21], where the earlier version of EDC model [11] without χ was used, the predictions were not satisfactory in comparison to the experiments. Simulations without χ tends to overpredict the temperature and major mass species fractions. LES, which is computationally demanding, reactor modeling of the fine structures with chemical kinetics makes still more expensive. The computational cost can be reduced by modeling the reactor with the fast chemistry assumption and with appropriate χ. The time averaged and variance of the temperature, velocities and mass fractions of species is depicted in figs 2 and 3. The calculated mean and RMS mass fractions of H_2O, N_2, and temperature profiles along the centerline is shown in fig. 2. The computed results are compared with the steady state flamelet model and experimental data base. The flame height with EDC model is predicted well. It is observed that the prediction of mean and variance is quite satisfactory with experiments.

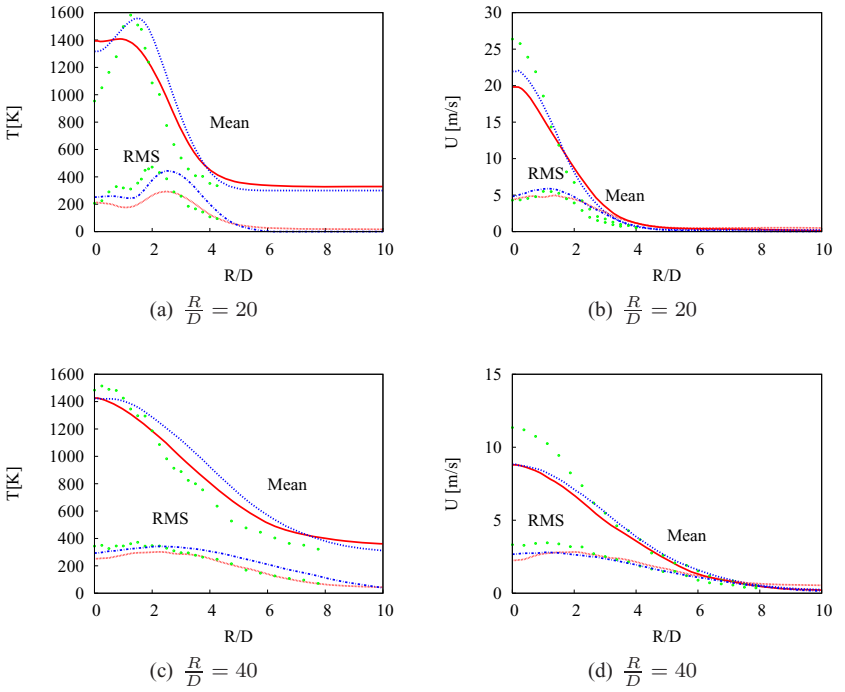

(a) $\frac{R}{D} = 20$ (b) $\frac{R}{D} = 20$

(c) $\frac{R}{D} = 40$ (d) $\frac{R}{D} = 40$

Figure 3: Mean and RMS radial profiles of the temperature and velocity , where ⊙, −− and ⎯ represent experimental, Flamelet and EDC results respectively.

It can be seen from fig. 2 that the peak of the variance of velocity is high compared to the experiment. The instantaneous mixing caused a sudden heat release and thus expansion near to the nozzle, which caused the deceleration in the fluid. The sudden heat release also caused the dilatation within the thin mixing layer between the fuel and oxidizer, thereby pushing apart the fuel and oxidizer when they try to mix. This process could be transient in nature. The boundary condition at the inflow is Dirichlet fixed velocity, which does not allow for relaxation of the upstream flow. In experiments the boundary condition at the inlet is not the Dirichlet fixed velocity, the fluctuation due to the heat release will be adjusted automatically. The Dirichlet boundary condition is known to work well for non reactive flows. All these effects caused increased of fluctuations or turbulent kinetic energy near to the nozzle [4, 13], as observed in fig. 2. In addition to that, the central differencing scheme used for the convective terms produces high fluctuations, especially close to the nozzle. Simulating upstream nozzle using immersed boundary condition along with a higher order convective diffusive scheme might improve the solution.

The mean and RMS radial profiles of the calculated temperature and velocities at $R/D = 20$ and $R/D = 40$ are shown in fig. 3. The calculated values are

compared with experiments and flamelet solutions and the comparison seems to be satisfactory. It is observed that the velocity was underpredicated at the core $R/D < 1.5$ which affected the overall spread. A similar behavior is also observed with the flamelet approach. It can be concluded that this behavior is not because of the combustion model used but because of the inflow boundary condition and modeling of the nozzle.

3 Conclusions

A Turbulence Chemistry Interaction Model (TCIM) based on the Eddy Dissipation Concept (EDC) is proposed for large eddy simulation. The proposed model estimates the fine structure mass fraction using the subgrid viscosity and kinematic viscosity. Modification of EDC model constants $C_{EDC} = 0.25$ was proposed to account for the partial turbulence energy cascading. The LES of the H2/N2 non-premixed unconfined turbulent jet flame is performed using LES-EDC and Flamelet model. The predicted means and variances of velocity and scalars are in satisfactory agreement to the experimental data and flamelet approach. A novel approach for estimating the density is proposed, where density is formulated from species mass fraction, which is numerically stable and computationally less expensive. Proper modeling of the inflow boundary conditions and nozzle is essential for obtaining the accurate predictions.

Acknowledgements

This work has been carried out as a part of Institution-based Strategic Project (ISP) funded by The Research Council of Norway. This support is gratefully acknowledged. We are indebted to Professor Emeritus Bjørn Magnussen for discussions and suggestions on the EDC model. We are also thankful to TU Darmstadt for providing the source code of FLOWSI code.

References

[1] Landenfeld, T., A turbulence-chemistry interaction model based on a multivariate presumed beta-pdf method for turbulent flames. *Applied Scientific Research*, **68**, pp. 111–135(25), March 2002.

[2] Branley, N. & Jones, W.P., Large eddy simulation of a turbulent non-premixed flame. *Combustion and Flame*, **127(1-2)**, pp. 1914 – 1934, 2001.

[3] Forkel, H. & Janicka, J., Large-eddy simulation of a turbulent hydrogen diffusion flame. *Flow, Turbulence and Combustion*, **65(2)**, pp. 163–175, 2000.

[4] Kempf, A., *Large Eddy Simulation of Non-Premixed Turbulent Flames*. Ph.D. thesis, Darmstadt University of Technology, Darmstadt, Germany, 2003.

[5] Kempf, A., Lindstedt, R.P. & Janicka, J., Large-eddy simulation of a bluff-body stabilized nonpremixed flame. *Combustion and Flame*, **144(1-2)**, pp. 170–189, 2006.
[6] Kempf, A., Malalasekera, W., Ranga-Dinesh, K. & Stein, O., Large eddy simulations of swirling non-premixed flames with flamelet models: A comparison of numerical methods. *Flow, Turbulence and Combustion*, **81(4)**, pp. 523–561, 2008.
[7] Pitsch, H. & Steiner, H., Large-Eddy Simulation of a turbulent piloted methane/air diffusion flame. *APS Meeting Abstracts*, 1999.
[8] McMurtry, P.A., Menon, S. & Kerstein, A.R., Linear eddy modeling of turbulent combustion. *Energy & Fuels*, **7(6)**, pp. 817–826, 1993.
[9] Kerstein, A., Linear-eddy modelling of turbulent transport. Part 7. Finite-rate chemistry and multi-stream mixing. *Journal of Fluid Mechanics*, **240**, pp. 289–313, 1992.
[10] Hu, L.Y., Zhou, L.X. & Zhang, J., Large-eddy simulation of a swirling diffusion flame using a som sgs combustion model. *Numerical Heat Transfer, Part B: Fundamentals: An International Journal of Computation and Methodology*, **50(1)**, pp. 41–58, 2006.
[11] Magnussen, B.F. & Hjertager, B., On mathematical modeling of turbulent combustion with special emphasis on soot formation and combustion. 16th Symp. (Int.) on Combustion (1976). Comb. Inst., Pittsburg, Pennsylvania, pp. 719–729.
[12] Yaga, M., Endo, H., Yamamoto, T., Aoki, H. & Miura, T., Modeling of eddy characteristic time in LES for calculating turbulent diffusion flame. *International Journal of Heat and Mass Transfer*, **45(11)**, pp. 2343–2349, 2002.
[13] Panjwani, B., Ertesvåg, I.S., Gruber, A. & Rian, K.E., Subgrid combustion modeling for large eddy simulation (les) of turbulent combustion using eddy dissipation concept. *Fifth European Conference on Computational Fluid Dynamics, ECCOMAS CFD 2010,Lisbon, Portugal*, 2010.
[14] Magnussen, B.F., On the structure of turbulence and a generalized eddy dissipation concept for chemical reaction in turbulent flow. *19 AIAA Aerospace Science Meeting*, 1981.
[15] Gran, I.R. & Magnussen, B.F., A numerical study of a bluff-body stabilized diffusion flame. part 2. influence of combustion modeling and finite-rate chemistry. *CombSciTech*, **119**, pp. 191–217, 1996.
[16] Ertesvåg, I.S. & Magnussen, B.F., The eddy dissipation turbulence energy cascade model. *Combustion Science and Technology*, **159(1)**, pp. 213–235, 2000.
[17] Fureby, C., Tabor, G., Weller, H.G. & Gosman, A.D., A comparative study of subgrid scale models in homogeneous isotropic turbulence. *Physics of Fluids*, **9(5)**, pp. 1416–1429, 1997.
[18] Http://www.tu-darmstadt.de/fb/mb/.

[19] Klein, M., Sadiki, A. & Janicka, J., A digital filter based generation of inflow data for spatially developing direct numerical or large eddy simulations. *J. Comput. Phys.*, **186(2)**, pp. 652–665, 2003.
[20] Pierce, C.D. & Moin, P., Progress-variable approach for large-eddy simulation of non-premixed turbulent combustion. *Journal of Fluid Mechanics*, **504(-1)**, pp. 73–97, 2004.
[21] Zhou, L.X., Hu, L.Y. & Wang, F., *Large-Eddy Simulation of Turbulent Combustion Using SOM and EBU SGS Combustion Models*, pp. 99–102, 2009.

Computational study on non-asymptotic behavior of developing turbulent pipe flow

W. A. S. Kumara[1], B. M. Halvorsen[1,2] & M. C. Melaaen[1,2]
[1]*Telemark University College, Norway*
[2]*Telemark R & D Centre (Tel-Tek), Norway*

Abstract

In general, developing turbulent pipe flow is a transition from a boundary layer type flow at the entrance to a fully developed flow downstream. The boundary layer thickness grows as the distance from the pipe inlet increases. An accurate description of the velocity and pressure distribution within the entrance region is very important to calculate the pressure drop for hydrodynamic inlets. More important perhaps, the velocity distribution is needed for an analysis of forced convection and mass transfer in a tube entrance. In the current study, we report the results of a detailed and systematic numerical investigation of developing turbulent pipe flow. Two-dimensional, axisymmetric computational scheme has been devised for determining the flow development in the entrance region of a circular pipe at different Reynolds numbers. The simulations are performed using commercial CFD software ANSYS FLUENT 12.0. Non-asymptotic behavior observed in developing turbulent pipe flow is discussed in detail. The predicted results are also compared with literature data.

Keywords: non-asymptotic behavior, turbulent flow, laminar flow, fully developed flow, computational simulations, axial velocity, velocity overshoot, wall shear stress.

1 Introduction

Turbulent pipe flow is one of the most common fluid motion in industrial and engineering applications. The importance of knowing the length of pipe required for the turbulent flow to fully develop, i.e., the velocity profile to become non-varying in the axial direction, has long been recognized. Consequently, several investigators have attempted to obtain solutions for incompressible turbulent

WIT Transactions on Engineering Sciences, Vol 69, © 2010 WIT Press
www.witpress.com, ISSN 1743-3533 (on-line)
doi:10.2495/AFM100041

flow development in pipes or ducts using numerical techniques [1-4]. The flow in the inlet region of a pipe is a transition from a boundary layer flow at the entrance to a fully developed flow downstream. Until recently, it is expected that the flow near the entrance of a pipe should resemble boundary layer flow over a flat plate [5]. Therefore, the peakiness of the velocity profile, defined as the ratio between the maximum value and the spatial mean, was thought to increase gradually until the boundary layers meet at the pipe centreline. According to the measurements quoted by Schlichting [6], this appeared to occur in turbulent flow after 25 to 100 pipe diameters, the exact length depending on the Reynolds number. Thereafter the flow was considered fully developed. In fact, however developing turbulent pipe flow is much more complex and there is a significant difference between the behavior of the free stream in flow over a plate and in a pipe [7]. Unlike that encountered in flat-plate boundary layer flow, the free stream in the inlet region of a pipe is completely surrounded by a growing boundary layer. Thus, the free stream accelerates as the displacement thickness of the boundary layer grows, and it loses its identity downstream as the boundary layer thickness reaches a value equal to the pipe radius. Following the disappearance of the free stream, further changes in the velocity profile and turbulence structure occur before a fully developed condition (i.e. uniform flow) is reached [7]. Bradley (quoted in [8]) appears to be the first who discovered that velocity profile peakiness might reach a maximum, which he found at about 40 pipe diameters, and then decreased again. Weir et al. [9] also obtained a maximum core velocity at 40 pipe diameters, while gradual velocity increase along the pipe were measured by Deissler [10] and Sale [11]. The latter type of velocity distribution was produced in [9] also, when a trip ring was inserted at the pipe entrance. Thus, it was shown that a change of inlet conditions might create substantial differences in flow development. Reichert and Azad presented detailed measurements of axial mean velocity profiles, in the inlet 70 diameters of the pipe, showing that the development of turbulent pipe flow is non-asymptotic [12]. The experiments were done at seven Reynolds numbers in the range 56 000-153 000. An axial velocity peak exceeding the fully developed values has been found to occur along the pipe centreline. Hot film measurements of the mean wall shear stresses in the inlet region also show a non-asymptotic development consistent with the mean velocity results. The Reynolds number behaviour of the peak position has been determined. They suggested that the peak position is a function of Reynolds number given by:

$$\frac{x_p}{D} = 30.80 + \frac{0.89}{10^{-5}\,\mathrm{Re}} + \frac{0.79}{\left(10^{-5}\,\mathrm{Re}\right)^2} \tag{1}$$

where x_p is the axial distance to the peak position, D is the pipe diameter and Re is Reynolds number. This equation implied a limit of x/D~31 for the peak position at the highest incompressible Reynolds numbers. On the other hand, the analysis implied that rather long entrance length would be required for low Reynolds number flows to become fully developed. Klein [5] has given a review of experimental results on velocity profile development in turbulent pipe flows.

In the current study, we report the results of a detailed and systematic numerical investigation of developing turbulent pipe flow. The present results also indicate that the development of the velocity profile to its fully developed value is not monotonic but displays a pronounced overshoot and consequently the fully developed state is not reached until some distance downstream. Since such flows are frequently used to provide reference or control inlet conditions for general flow investigations it is important that they should be better understood.

2 Turbulent pipe flow

In general, the major velocity changes take place very close to the body surface [13]. Nevertheless, there is generally some ambiguity in speaking of the "boundary layer thickness" if what is meant in the region in which velocity changes from zero to free stream velocity. It is convenient and far more useful to define boundary layer thickness parameters that are completely unambiguous [13]. They are called the displacement thickness (δ_1) and the momentum thickness (δ_2). The displacement thickness is defined as follows:

$$\delta_1 = R\int_0^1 \left(1-\frac{u}{u_c}\right)\frac{r}{R}d\left(\frac{r}{R}\right) \tag{2}$$

where R is the pipe radius, u is the mean axial velocity, u_c is the centreline velocity and r represents the radial location in the pipe. The momentum thickness is defined as:

$$\delta_2 = R\int_0^1 \frac{u}{u_c}\left(1-\frac{u}{u_c}\right)\frac{r}{R}d\left(\frac{r}{R}\right) \tag{3}$$

The measure of the flow development used in this paper is Sovran and Klomp's [14] blockage factor (b) which is defined by the ratio of the axisymmetric displacement thickness (δ_1) to pipe radius R. It can also be estimated by using bulk velocity (u_b) and centreline velocity (u_c) of the flow as given below:

$$b = 2\frac{\delta_1}{R} = 1-\frac{u_b}{u_c} \tag{4}$$

3 Computational scheme

The commercial CFD software package, FLUENT 12.0, which is based on the finite volume approach, is used for solving the set of governing equations. The discretized equations, along with the initial and boundary conditions, are solved using the pressure based solution method to obtain a numerical solution. Using the pressure based solver, the conservation of mass and momentum are solved iteratively and a pressure-correction equation is used to ensure the conservation of momentum and mass. Standard k-ω model is used for modelling turbulence. In addition, standard k–ε model and RNG k–ε model together with enhanced

wall treatment as the near-wall modelling method is used to investigate the effect of turbulence model on the flow development.

A schematic representation of the computational domain is given in Figure 1. At inlet (x=0), we apply a uniform velocity u_b. No-slip boundary condition is applied on the pipe wall and the pipe outlet is treated as a pressure outlet. One plane in the axisymmetric pipe is simulated and pipe centreline is considered as the axisymmetry axis. The length of the computational domain is dependent on the Reynolds number of the flow in question. In general, the domain was at least three times as long as the calculated development length.

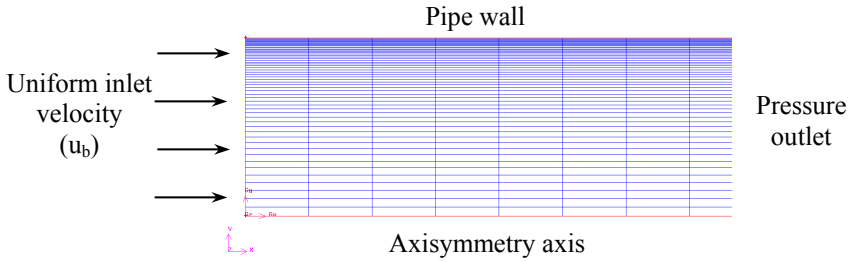

Figure 1: Computational domain.

Two-dimensional, axisymmetric grid system is used for the computations. The assumption of axisymmetry implies that there are no circumferential gradients in the flow. In this case, FLUENT used the cylindrical representation of the incompressible Navier-Stokes equations by taking the advantage of axisymmetry of the flow field. Enhanced wall treatment is a near-wall modeling method that combines a two-layer model with so-called enhanced wall functions [15]. A boundary layer mesh is used close to the wall, which is fine enough to be able to resolve the viscous sublayer (first near-wall node placed at $y^+<5$).

4 Results

4.1 Asymptotic behaviour of developing laminar flow

The development of laminar flow is investigated prior to the study of developing turbulent flows. Laminar flow (Re=557) in a pipe with internal diameter 56 mm is simulated and the results are given in Fig. 2. The uniform inlet velocity is 0.01 m/s and water is used as the working fluid. Fig. 2(a) shows the fully developed velocity profile at x/D=160. The velocity profile is parabolic and the maximum axial velocity is 0.02 m/s. In general, the axial velocity profile of laminar flow in pipes is given by the following expression:

$$u = 2u_b\left(1-\frac{r^2}{R^2}\right) \tag{5}$$

Eq. (5) suggests that the maximum axial velocity at the pipe center is 0.02 m/s and shows a good agreement with the simulated results. Fig. 2(b) shows the

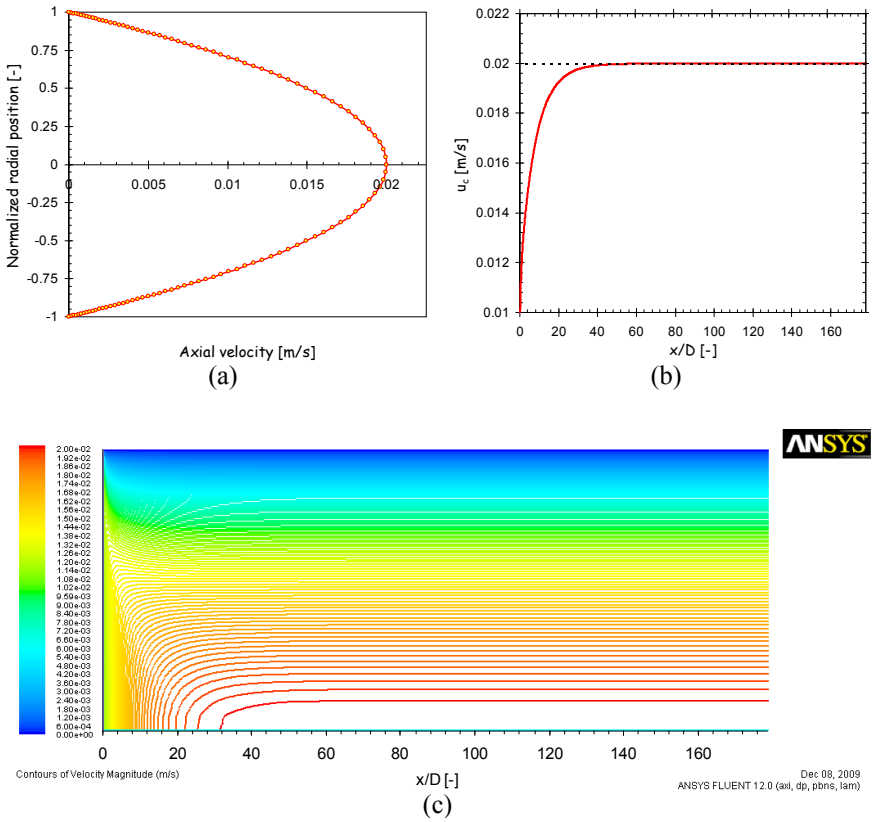

Figure 2: Asymptotic behavior of developing laminar flow (Re = 557): (a) Axial velocity, (b) Development of the axial velocity profile with non-dimensional distance from the inlet, (c) Contours of axial velocity.

evolution of the centreline velocity along the pipe. As the fluid moves down the tube, a boundary layer of low-velocity fluid forms and grows on the surface because the fluid immediately adjacent to the surface must have zero velocity. This retardation near the wall spreads inwards owing to viscous effects and the slowed-down fluid close to the wall causes the fluid in the center to move faster, since the cross-sectional mass flow rate at any axial location remains constant. A particular feature of viscous flow inside cylindrical tubes is the fact that the boundary layer must meet itself at the tube centerline, and the velocity distribution then establishes a fixed pattern that is invariant thereafter. The part of the tube in which the momentum boundary layer grows and the velocity distribution changes with length is referred as the hydrodynamic entry length (x_d). It is defined as the axial distance required for the centreline velocity to reach 99% of its fully developed value. As shown in Fig. 2(b), the centreline velocity gradually increases and reaches its fully developed value asymptotically. In this case, the hydrodynamic entry length is $x_d/D=31.78$. Durst et al. [16] have

conducted a detailed numerical study and proposed the following nonlinear correlation for hydrodynamic entry length:

$$\frac{x_d}{D} = \left[0.619^{1.6} + \left(0.0567\,\mathrm{Re}\right)^{1.6}\right]^{1/1.6} \tag{6}$$

The calculated entry length (x_d/D) according to Eq. (6) at Re=557 is 31.62. Therefore, the present predictions show a good consensus with the results presented by Durst et al. [16]. Contour plot of mean axial velocity field is given in Fig. 2(c). It clearly shows the asymptotic behavior of developing laminar flow in pipes.

4.2 Non-asymptotic behaviour of developing turbulent flow

The development of turbulent pipe flow is investigated in this section. Turbulent flow (Re=55776) in a pipe with internal diameter 56 mm is simulated and the results are given in Fig. 3. Water is used as the working fluid. The predictions are based on standard k-ω model. Fig. 3(a) shows the fully developed axial velocity profile at x/D=160. The velocity profile is flat compared to the laminar flow as expected. The maximum mean axial velocity is 1.189 m/s. The axial velocity profile of turbulent pipe flow is given by the power-law as follows:

$$\frac{u}{u_c} = \left(1 - r/R\right)^{1/n} \tag{7}$$

where n is the power-law exponent and determined by:

$$n = -1.7 + 1.8\log \mathrm{Re} \tag{8}$$

The power-law profile is much more blunt than the laminar profile, u_b~u_c, but is more generally determined by:

$$\frac{u_b}{u_c} = \frac{2n^2}{\left(n+1\right)\left(2n+1\right)} \tag{9}$$

In this case at Re=55776, Eq. (9) gives u_b/u_c = 0.813, while the simulated results gives u_b/u_c = 0.84.

Developing turbulent pipe flow is basically a transition from a boundary layer type flow at the entrance to a fully developed flow downstream. The boundary layer thickness grows as the distance from the pipe inlet increases. In order to maintain a constant bulk flow rate, the core region accelerates as it is being squeezed by the growing boundary layer. In the initial portion of the entrance flow, the boundary layers serve to squeeze fluid into the core causing the core velocity to increase. This core acceleration is the combined result of the deceleration near the wall and conservation of mass. As the flow evolves, the boundary layer grows and eventually merges. The flow subsequently evolves to its fully developed state. The initial core acceleration is so large for a turbulent flow that the centreline velocity overshoots its fully developed value as shown in Fig. 3(b). Hence, the development of turbulent pipe flow shows non-asymptotic behavior in contrast with the results of laminar flow. This velocity overshoot is more evident on the contour plot of axial velocity as shown in the Fig. 3(c). The

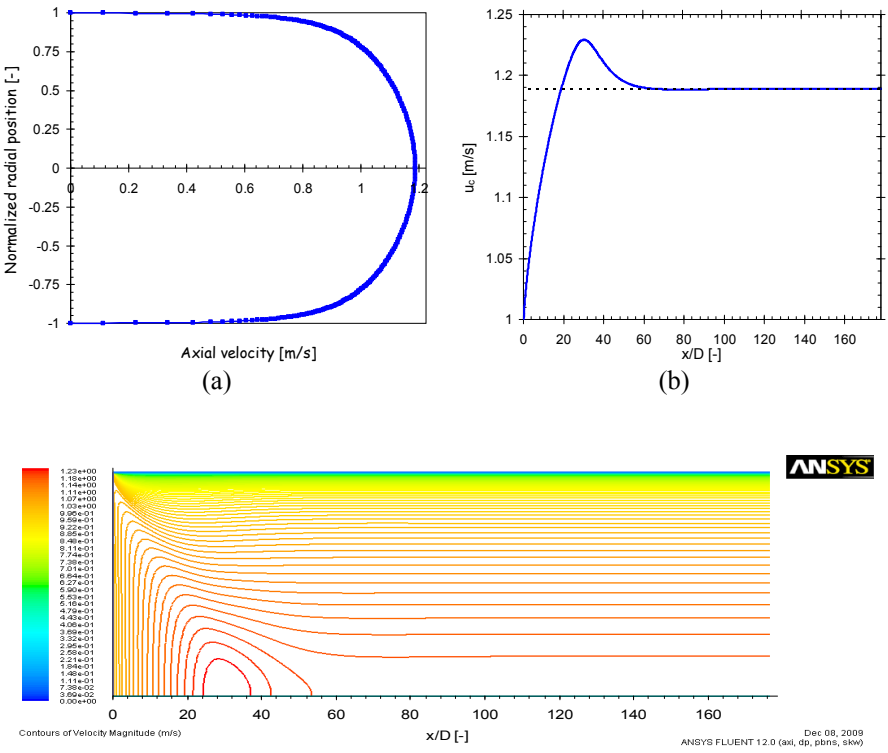

Figure 3: Non-asymptotic behavior of developing turbulent flow (Re = 55776): (a) Axial velocity, (b) Development of the axial velocity profile with non-dimensional distance from the inlet, (c) Contours of axial velocity.

centreline velocity increases up to about 30 pipe diameters, and followed by a decrease up to about 65 diameters, and then attains an approximately constant value. However, there is a very small undershoot of the centreline velocity profile compared to the fully developed value after the peak velocity. This waviness is due to the adjustment of the shear stress in the central region, an extremely complicated process since shear stresses of any direction exist [17]. The axial velocity contour plots are characterized by a narrowing core of accelerating fluid, which disappears after 24-37 pipe diameters. Outer regions are characterized by decelerating axial flow over approximately the first 20 diameters. This leads to axial velocities for radial positions near the wall, which undershoot the final fully developed values. The peak position of the centreline velocity is observed at $x_p/D=31.25$. The same position can be calculated by using Eq. (1) and it gives $x_p/D=34.93$ [18]. The reason that causes this discrepancy is uncertain. However, the differences of the inlet conditions used for experiments and simulations can influence the position of the centreline velocity overshoot.

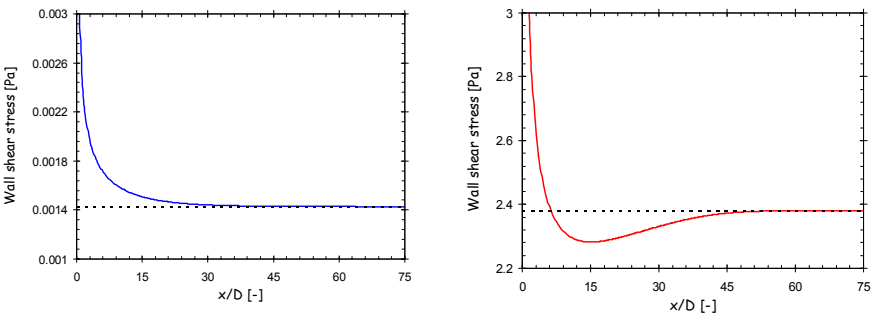

Figure 4: Wall shear stress: (a) Laminar flow (Re = 557), (b) Turbulent flow (Re = 55776).

Fig. 4 shows the wall shear stress distribution for developing laminar and turbulent flows. At the entrance of the pipe, there are larger shear rates by the wall giving higher wall shear stresses. As the boundary layer grows, shear rates close to the wall decreases. When the flow is fully developed, shear rates do not change along the pipe and constant wall shear stress is observed. As shown in Fig. 4(a), the wall shear stress decreases monotonically and attains its fully developed value for laminar flow. Fig. 4(b) shows wall shear stress distribution of developing turbulent flow. Significantly higher wall shear stresses are observed in turbulent flow compared to the laminar flow. The wall shear stress decreases as the boundary layer grows along the pipeline. However, wall shear stress undershoots its fully developed value compared to the laminar flow. It decreases up to 15 pipe diameters and then gradually increases up to 57 pipe diameters to reach its fully developed value. This may be attributed to the undershoot of the axial velocity gradient close to the wall around the position of peak centreline velocity.

4.3 Reynolds number effect on centerline velocity overshoot

In this section, the effect of Reynolds number on the position of centreline velocity overshoot is investigated. Fig. 5 shows contour plots of mean axial velocity at two different Reynolds numbers corresponding to the flows at bulk velocities 0.25 m/s and 1.50 m/s, respectively. Comparison of the axial velocity contour plots showed that the centreline velocity peak is more pronounced for the lowest Reynolds number. The maximum value of u_p/u_b approached 1.23 for Re=13994, while for Re=83664 the maximum u_p/u_b value just exceed 1.18.

An analysis of centreline velocities was undertaken to determine the effect of Reynolds number on the velocity overshoot position. Fig. 6 shows the flow development at seven different Reynolds numbers. The calculated blockage factor is plotted against the non-dimensional pipe length. The centerline peak overshoot position slightly moves downstream as the Reynolds number increases. Larger Reynolds numbers are seen to produce lower peak values and smaller Reynolds numbers higher peak values. The present predictions show a

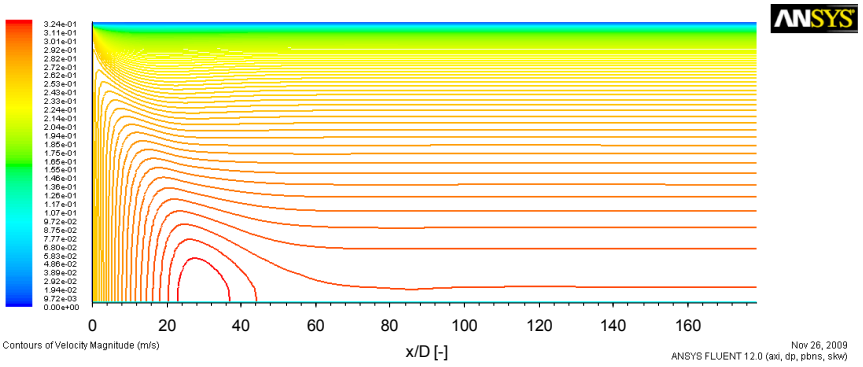

(a)

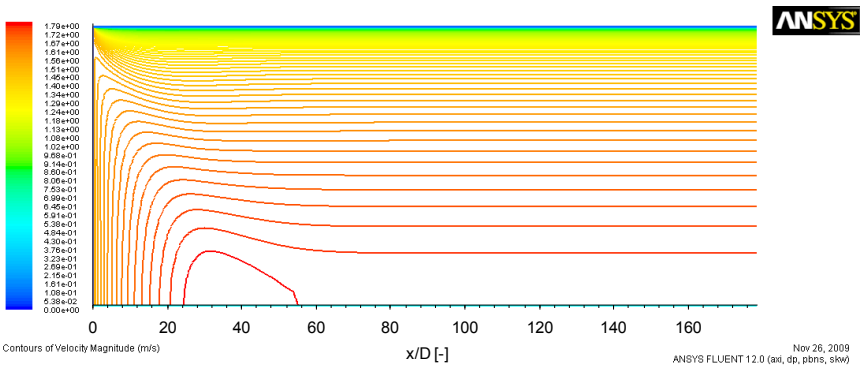

(b)

Figure 5: Contours of axial velocity: (a) U = 0.25 m/s (Re = 13994), (b) U = 1.50 m/s (Re = 83664).

good agreement with the experimental results presented by Klein [5]. The Reynolds number effect on the centerline peak position can be explained by considering integral boundary layer parameters. Axial displacement and momentum thicknesses (normalized by pipe diameter) have been computed by numerical integration of the axial velocity profiles and presented in Fig. 7. The behavior of these integral boundary layer parameters is significant in developing turbulent flow because the parameters are related to the momentum flux terms appearing in the boundary layer momentum balance equation [18]. As shown in the figure longitudinal derivatives of these integral parameters do not become zero monotonically providing a clear evidence of non-asymptotic character of the

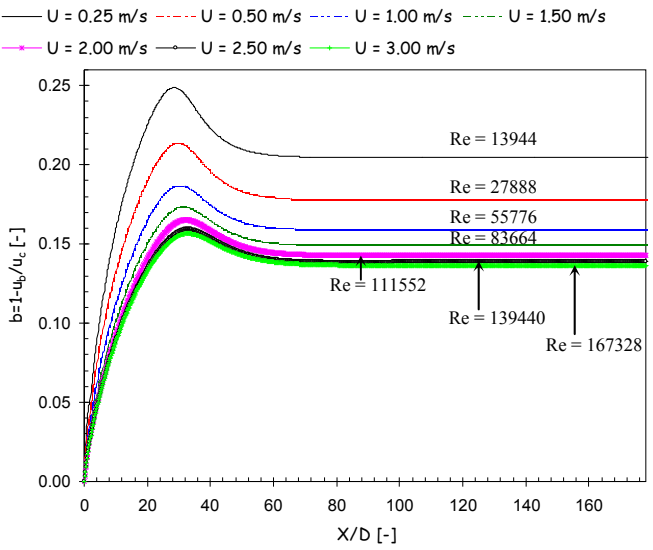

Figure 6: Development of the axial velocity profile with non-dimensional distance from inlet.

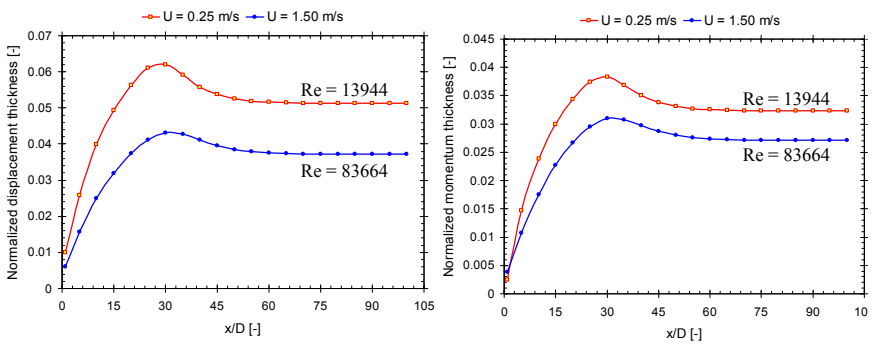

(a) (b)

Figure 7: Normalized displacement and momentum thicknesses: (a) displacement thickness, (b) momentum thickness.

flow development. Both displacement and momentum thickness curves show a distinct peak in their development along the pipe. The results show that more rapid boundary layer growth occurs for the lower Reynolds number since thicknesses for the lower Reynolds number are largest. This is the usual trend observed for turbulent boundary layer growth in other flows such as on a flat plate. As a result of rapid development of the boundary layer at low Reynolds numbers, centerline velocity overshoot can be observed close to the pipe entrance. As the Reynolds number increases the peaks of the displacement and

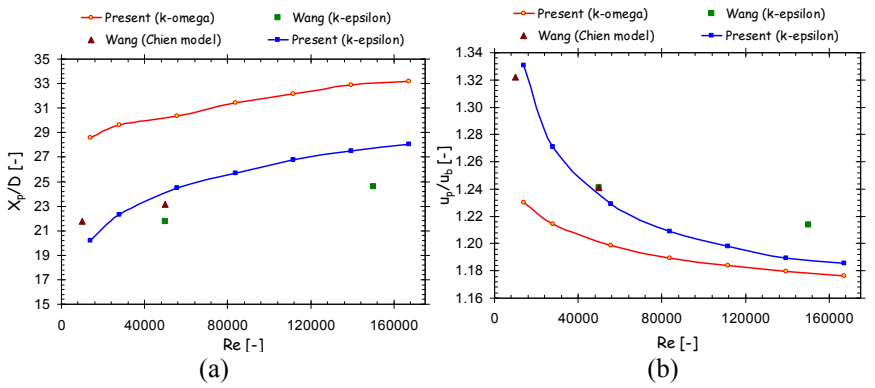

Figure 8: Overshoot of the axial velocity profile in developing turbulent flow: (a) x_p/D, (b) u_p/u_b.

momentum thickness curves moves towards the downstream. Therefore, the position where the centerline velocity overshoot is observed moves downstream as the Reynolds number increases. It should be mentioned that a discrepancy has been found between our observation and Reichert's [18] experimental data regarding the effect of Reynolds number on the location of the centerline overshoot position. Reichert suggested that the peak position is a function of Reynolds number given by Eq. (1) [18]. That means the peak overshoot position decreases as Reynolds number increases. The reason that causes this discrepancy is uncertain. However, the present predictions show a good agreement with the results presented by Wang [4] as shown in Fig. 8. Wang has reported that the peak overshoot position moves downstream as the Reynolds number increases. He has used standard k-ε model and Chien model [19] for turbulence modelling. The present predictions of centerline velocity overshoot position using standard k-ε model agree well with the results presented by Wang using same model as shown in Fig. 7(a). The magnitude of the velocity overshoot (u_p/u_b) decreases as the Reynolds number increases. The present predictions and the results presented by Wang using standard k-ε model show good consensus as shown in Fig. 7(b). The predicted behavior of the centerline velocity overshoot based on standard k-ω is also given in Fig. 7. There are significant deviations between the predictions based on standard k-ε and standard k-ω models. However, the predicted results show some similarities in their overall shape. The reason that causes this discrepancy is uncertain. Flow turbulence plays an important role in the physical process involved in the non-asymptotic mean flow development [18]. This suggested that the non-asymptotic behavior could be characteristic of both the mean velocity and turbulence stresses. These models handle turbulent quantities in different ways and it can be the reason for the observed deviations. A further investigation is needed in order to understand the effect of turbulence on the non-asymptotic turbulent flow development.

4.4 Comparison of predicted results with experimental data

The present predictions are compared with the experimental data presented by Reichert [18]. The wind tunnel installation used for the experiments has been described in detail by Reichert [18]. Briefly, air was blown through an 89:1 contraction cone, tripped by a strip of sandpaper (50.8 mm), and allowed to develop along a 76 diameter length of 101.6 mm inside diameter steel pipe, before being exhausted through an 8° included angle conical diffuser. Profiles of the axial component of the mean velocity were calculated using dynamic pressures, which were obtained from differential pressure measurements between a traversing total pressure tube and a ring of static pressure taps in the same plane. A Betz projection manometer with 0.1 mm of water scale intervals was used. No corrections were attempted to account for turbulence or displacement effects on the pressure tube. Present simulations are based on the RNG k-ε turbulence model. The simulated case has the flowing physical conditions: u_b=17.3 m/s, density = 0.118 kg/m^3, kinematic viscosity = 1.59x10^{-5} m^2/sec.

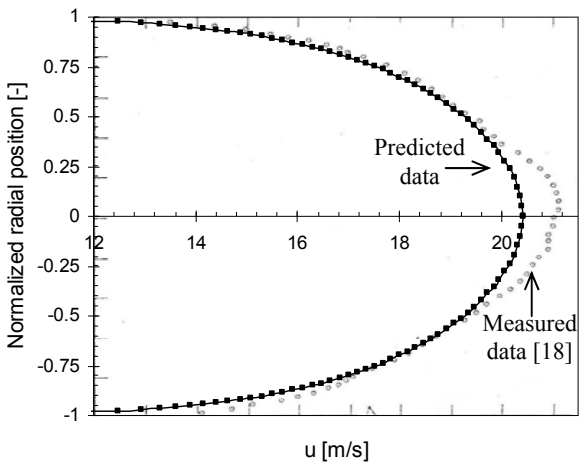

Figure 9: Comparison of mean axial velocity (x/D=61.9).

Fig. 8 gives a comparison of mean axial velocity profiles. A good comparison is observed between measurements [18] and predictions of axial velocity. However, there are some deviations close to the pipe center. The maximum deviation observed is about 1.45%. Fig. 9 shows a comparison of contour plots of axial velocity. It is notable that the simulation can predict the measured [18] behavior of the centerline velocity overshoot. However, there are some discrepancies. The measured maximum value of u/u_b approaches to 1.27. The predicted value approaches to 1.19. Hence, the experiments produce a larger velocity overshoot compared to the predicted data. The measured results shows that the centerline velocity overshoot is located around 34<x/D<35.5. However, the predicted data shows the corresponding location around 25<x/D<31.5. Hence, the predicted velocity overshoot position is located closer to the pipe inlet

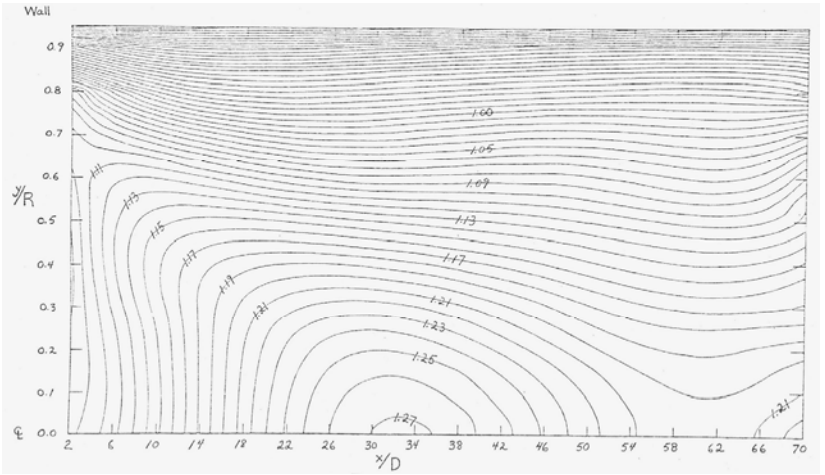

(a)

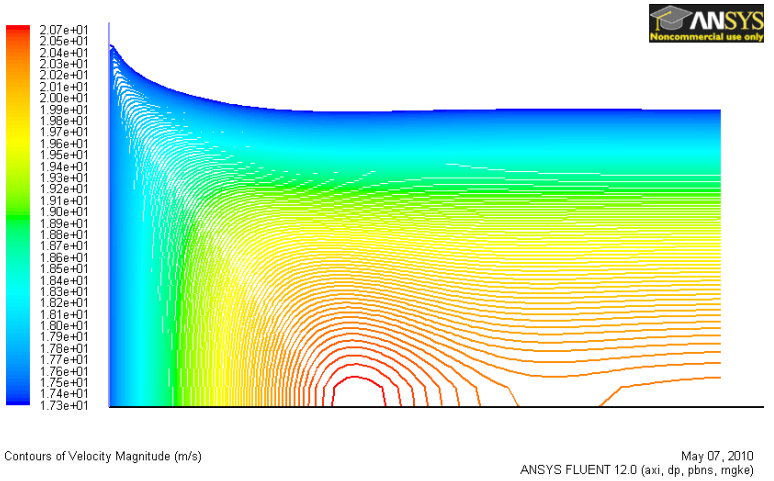

(b)

Figure 10: Comparison of contours of mean axial velocity: (a) measured data from Reichert [18], u/u_b (contour interval = 0.02), (b) predicted data, u, (contour interval = 0.10 m/s).

compared to the measured data. This can be attributed to the different inlet conditions employed in the experiments and simulations. In the simulations, a uniform velocity profile is used at the inlet while in the experiments, inlet boundary condition can be different from the simulations. The measurements show the waviness of the development of centerline velocity as shown in Fig. 9(a). It is notable that the simulations can capture the same physical phenomena even though there are some deviations between the magnitudes of

the velocity contours. In general, the present predictions show a satisfactory agreement with the experimental data presented by Reichert [18].

5 Conclusions

In the present study, we report the results of a detailed and systematic numerical investigation of developing turbulent pipe flow. Two-dimensional, axisymmetric computational scheme has been devised for determining the flow development in the entrance region of a circular pipe at different Reynolds numbers. Simulations are performed using commercial CFD software ANSYS FLUENT 12.0.

The present results indicate that the development of the mean velocity field of turbulent pipe flow is non-asymptotic. However, developing laminar flow shows an asymptotic behavior. Regions of overshoot and undershoot of axial velocity profiles are discernible in the developing region. In association with this mean velocity behavior, a non-asymptotic development has been found for the wall shear stress. It has been suggested that the flow development may take place in a damped oscillatory manner such that even after 60 diameters downstream some flow adjustment is still occurring.

Contrary to Reichert [18] observation, the present results show that the higher the flow Reynolds number is, the further downstream the centerline mean velocity peak overshoot position moves. The reason for this is unknown at present and more detailed study is required. However, the present predictions show a good agreement with results presented by Wang [4]. In addition, the behavior of the development of integral boundary layers supports the present argument. As the Reynolds number increases, the magnitude of the centerline velocity overshoot reduces. The predictions show satisfactory agreement with the experimental data presented by Reichert [18]. It is notable that the simulations can capture the complex oscillatory behavior of the turbulent flow development.

References

[1] Holdhusen, J.S., 1952. *Ph.D. Thesis, University of Minnesota, Minneapolis, Minnesota, 1952*.
[2] Bowlus, D.A. & Brighton, J.A., *Am. Soc. Mech. Eng. Trans*. **90**, D, 431, 1968.
[3] Azad, R.S. & Hummel, R.H., *Can. J. Phys*., **49**, 2917, 1971.
[4] Wang, Y.Q., Prediction of developing turbulent pipe flow by a modified k-ε-γ model, *Ph.D. Thesis, The University of Manitoba, 1999*.
[5] Klein, A., Review: Turbulent developing pipe flow, *Journal of Fluids Engineering*, **103**, pp. 243-249, 1981.
[6] Schlichting, H., Boundary layer theory, *6th edition, McGraw Hill*, 1968.
[7] Barbin, A.R. & Jones, J.B., Turbulent flow in the inlet region of a smooth pipe, *Journal of Basic Engineering*, pp. 29-34, 1963.

[8] Cockrell, D.J., Effect of inlet and outlet conditions on pipe and duct components, The 9th Members Conference, Cranfield, SP 929, The British Hydrodynamics Research Association, 1967.
[9] Weir, J., Priest, A.J. & Sharan, V.K., Research note: The effect of inlet disturbances on turbulent pipe flow, *Journal of Mechanical Engineering Science*, **16(3)**, pp. 211-213, 1974.
[10] Deissler, R.G., analytical and experimental investigation of adiabatic turbulent flow in smooth tubes, NACA T.N.2138, 1950.
[11] Sale, D.E., Entrance effects in incompressible diffuser flow, *M.Sc. Thesis, University of Manchester*, 1967.
[12] Reichert, J.K. & Azad, R.S., Nonasymptotic behaviour of developing turbulent flow, *Can. J. Phys*., **54**, pp. 268-278, 1976.
[13] Kays, W., Crawford, M., & Weigand, B., Convective heat and mass transfer, *4th edition, McGraw-Hill*, 2005.
[14] Sovran, G. & Klomp, E., Experimentally determined optimum geometries for rectilinear diffusers with rectangular, conical or annular cross-section, *Fluids mechanics of internal flow, Elsevier Publishing Company, Amsterdam*, 1967.
[15] FLUENT 12.0, User Manual, 2009.
[16] Durst, F., Ray, S., Unsal, B. & Bayoumi, O. A., The Development Lengths of Laminar Pipe and Channel Flows*, J. Fluids Eng*., **127**, pp. 1154-1160, 2005.
[17] Bradshaw, P., Review – Complex turbulent flows, *ASME Journal of Fluid Engineering*, **97(2)**, pp. 146-154.
[18] Reichert, J.K., A study of developing turbulent flow, *PhD Thesis*, The University of Manitoba, 1977.
[19] Chien, K. Y., Predictions of channel and boundary layer flows with a low-Reynolds-number turbulent Model, *AIAA Journal*, **20(1)**, pp. 33-38, 1982.

This page intentionally left blank

Vorticity Confinement method applied to flow around an Ahmed body and comparison with experiments

M. Forman[1], H. Jasak[2], J. Volavy[1], M. Jicha[1], C. Othmer[3] & H. P. Bensler[3]
[1]*Brno University of Technology, Faculty of Mechanical Engineering, Energy Institute, Czech Republic*
[2]*Wikki, Ltd., UK*
[3]*Volkswagen, Germany*

Abstract

In this paper, the Vorticity Confinement method (VC) is presented for the calculation of flow field around a bluff body. The VC method was originally proposed by Fan et al. ("Computing blunt body flows on coarse grids using vorticity confinement", *J. Fluids Engineering*, 124(4):1–18, Dec 2002) for the computation of thin vortical regions in the high Reynolds number incompressible flows. Steinhoff et al. (*Large Eddy Simulation: Computing Turbulent Flow Dynamics*, Chapter 12: Turbulent Flow Simulations Using Vorticity Confinement: Cambridge University Press, 2006) claim that VC is capable of capturing most of the main features of high-Re turbulent flows without the massive mesh resolution needed for Reynolds-Averaged Navier-Stokes (RANS) solutions or Large Eddy Simulation (LES). The aim of the method is to capture small-scale vortical structures efficiently. The presented study assesses the VC method (namely the first formulation, referred to as VC-1, which involves first derivatives of velocity), for external aerodynamics presented here on a well documented simplified car - Ahmed bluff body with different slant angles, namely 25° and 35°. These slant angles were chosen because the 35° slant angle supports the boundary layer separation and therefore stronger wake (also stronger oscillations of the wake), while at the 25° slant angle no separation takes part and the wake is much weaker and also more stable. The VC method was applied using different values for the diffusion parameter and confinement

WIT Transactions on Engineering Sciences, Vol 69, © 2010 WIT Press
www.witpress.com, ISSN 1743-3533 (on-line)
doi:10.2495/AFM100051

parameter, respectively. In addition, different a mesh size was tested. The comparison results are presented for RANS models. The RANS simulations were carried out using the k –ωSST model run in transience with second-order differencing in time and space. OpenFOAM code with wall functions was used. The experimental data used for validation were taken from Lienhart et al. (Flow and Turbulence Structures in the Wake of a Simplified Car Model (Ahmed Model), Measurements MOVA- project, online database: http://cfd.mace.manchester.ac.uk/ercoftac/) from the ERCOFTAC database. Compared are velocity profiles in different sections along the Ahmed body for both 25° and 35° slant angles, and forces acting on the body and drag coefficient.

Keywords: turbulent flow, Vorticity Confinement, Ahmed body, experiments.

1 Introduction

Many researchers and engineers are constantly looking for a rapid, yet correct method for external aerodynamics in turbulent flow with massive separation and vortexes. It is well known that standard CFD methods are not capable of conserving vortices over a sufficient period of time because of the numerical diffusion that is required to stabilize the numerical scheme. The solution obtained may be strongly dependent on the models and on the discretization used (e.g. turbulence model or grid) as soon as the flow is sufficiently complex with flow separation. Consequently, a large effort is still needed so that the flow physics is correctly represented. A natural way to tackle such a problem is to use high-order schemes and/or automatic grid refinement techniques in order to increase the accuracy of the resolution and thus avoid a too fast dissipation of the vortical structures [5–8]. However, such approaches are expensive and difficult to apply to realistic aerodynamic configurations with the present computer resources.

Until now there has been no universally acceptable turbulence model that can provide uniformly good results for engineering problems with separated flows. Algebraic models are simple to use, but are quite unreliable for separation flows because of the Boussinesq approximation. One-equation models have achieved closer agreement with experimental measurements for a limited number of separated flows than is possible with algebraic models, but the length scale for each new application needs to be specified. The k - ε model is the most widely used in the family of two equation models; unfortunately, it is inaccurate for flows with adverse pressure gradients, separation and recirculation. It appears that all two-equation models are inaccurate for the flows around surfaces with large curvatures, separations, sudden change in mean strain rate, rotation, vortex shedding, and 3D unsteady motions.

Alternative techniques capable to overcome these difficulties at reasonable cost have been developed. We have to mention an original Steinhoff's Vorticity Confinement method [9]. This technique modifies the incompressible Navier–Stokes equations by adding a well-chosen source term into the momentum equations, which concentrates vortices over a small number of grid cells and allows one to convect them without diffusion over a long period of time. This

confinement source term is aimed to be a model of the vortex flow structures. Such methodology has been successfully applied to very different types of flow-fields, from simple vortices up to complex rotor-fuselage interactions, using an extension of the method to general body surfaces with simple Cartesian grids and even to massively separated flows. The method has also been generalized to compressible flows considering the corresponding source term as a body force.

2 Vorticity confinement model

The vorticity confinement model is derived by adding a pair of terms to the transient incompressible laminar Navier-Stokes system, with the purpose of controlling the diffusive discretisation error and vorticity capturing. The idea of the model is that numerical discretisation methods introduce unacceptable levels of numerical diffusion and fail to resolve essential small-scale features of the flow. This can be clearly seen when a CFD code is used to transport an under-resolved vortex over a large distance or one attempts to track a wave along a large distance. Authors [2] claim that VC is capable of capturing most of the main features of high-Re turbulent flows without the massive mesh resolution needed for Reynolds-Averaged Navier Stokes (RANS) solutions or Large Eddy Simulation (LES). This is achieved by adding a negative eddy-type viscosity which saturates in a stable manner and counteracts the positive viscosity added by inappropriate discretisation.

There exist two formulations of the VC model. The first, referred to as VC-1, involves first derivatives of velocity, whereas the second (VC-2) involves second derivatives [10]. VC-1 was chosen for this study due to its robustness.

Modified Navier-Stokes system including the pair of VC terms reads as follows:

$$\nabla.\mathbf{u} = 0 \tag{1}$$

$$\frac{\partial \mathbf{u}}{\partial t} + \nabla.(\mathbf{uu}) - \nabla.(\nu_{vc}\nabla\mathbf{u}) = -\nabla p + \varepsilon \mathbf{s} \tag{2}$$

where ν_{vc} is the diffusive coefficient which controls the dissipation of the vorticity part εs. The second confinement term is calculated for the curl of velocity, using a user-defined constant **s** as follows:

$$\mathrm{s} = \frac{\nabla|\omega|}{|\nabla|\omega||}.\omega \tag{3}$$

where ω is curl of velocity defined as $\omega = \nabla \times \mathrm{u}$.

From the presented set of equations, two parameters need to be set. It is the diffusion parameter ν_{vc} and confinement parameter ε. The first confinement constant ν_{vc} is clearly related to fluid viscosity and numerical diffusion of the base (un-confined) solver. Its dependence of the *Re* number is clear. However, the second confinement constant ε is not dimensionless and its scaling with geometry, *Re* number and possibly other parameters is unknown. A consequence is that confinement tuning will be strictly problem-dependent, but presumably

constant over a range of related problems. In his paper, Vaughn [12] offers a way of estimating confinement parameters based on an analysis of the confinement parameter and the viscous terms. He suggested two ways how to calculate the parameters giving two different confinement parameters.

By assuming turbulence production to be homogenous and turbulent viscosity to be spatially constant for the local flow, it is possible to express the production in terms of vorticity. Since the laminar and turbulent viscous terms of the Navier-Stokes equations have the same form (due to Boussinesq approximation) the laminar components of the equation can likewise be articulated in terms of vorticity. Furthermore, it is assumed that ν_{vc} is a measure of local viscosity, combining its laminar and "turbulent" contribution. By performing an order-of-magnitude analysis, the first way how to calculate confinement parameter can be written in the form:

$$\varepsilon = \sqrt{2}\,\frac{\nu_{vc}}{uh} \tag{4}$$

where h is the representative dimension of local cell size (here cell size close to the bluff body) and u is free stream velocity (in our case mean velocity 40m/s). Second form is defined as:

$$\varepsilon = \frac{\sqrt{2}}{Re_L}\frac{L}{h}\left(1 + 0.1344\sqrt{Re_L}\right) \tag{5}$$

Both equations assume the diffusion coefficient ν_{vc} to consist of viscosity. While first form (4) takes only laminar viscosity into account, the second form (5) assumes the turbulence using turbulent Reynolds number calculated with respect to the global size L of the bluff body.

3 Model setup

3.1 Geometry

The presented study assesses the VC method for external aerodynamics presented here on a well documented simplified car – Ahmed bluff body [3]. The tunnel in which the Ahmed body was placed has 1.87 x 1.4m^2 in cross-section and is 6m long. The flow parameters are:
kinematic viscosity 15x10^{-6}m^2/s
bulk velocity U_b = 40m/s
height of the body h = 288mm
Reynolds number based on height of the bluff body Re = 768000.
The geometry of the bluff body is depicted in Figure 1.

The experimental data used for validation are from measurements of Lienhart et al. [4] and were downloaded from the ERCOFTAC online database.

3.2 Computational mesh

Computational mesh for all cases was created in program STAR-CCM+ using trimmed mesh (unstructured hexahedral mesh with "one to many" connections).

Such a mesh allows local refinement in the place of interest without affecting the mesh structure further from the place. The base size of the mesh in the free flow further away from the Ahmed body was held constant for all cases at value of 0.1m. To study the grid dependence of VC method, three grid sizes were used as shown in the Table 1. The mesh was refined from the base size in the vicinity of the bluff body as well as in the region of recirculation. Only on coarse mesh the front part of the body has mesh size of 2.5 cm to capture the curvature of the front part of the body as depicted in Figure 2. For the fine and extra fine mesh the surface size is kept constant along the body surface except the stubs where the mesh has the size of approx. 3mm (see Figure 3).

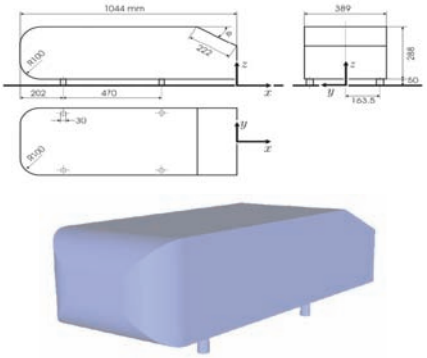

Figure 1: Ahmed body.

Table 1.

	Global mesh size	Local mesh size	cell number
Coarse	0.10 m	0.0250 m	227,046
Fine	0.10 m	0.0125 m	1,375,659
Extra fine	0.05 m	0.0050 m	2,186,569

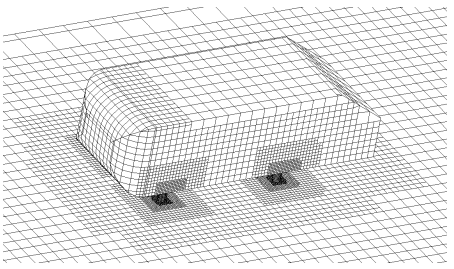

Figure 2: Surface mesh detail with coarse mesh settings.

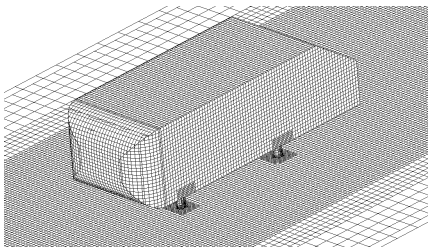

Figure 3: Surface mesh detail with extra fine mesh settings.

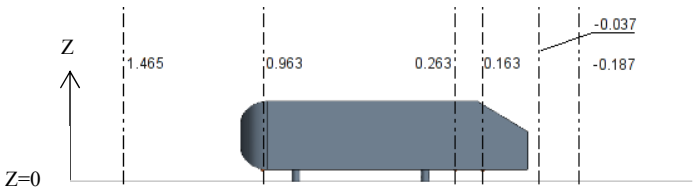

Figure 4: Cross section specification (X positions).

3.3 Solver settings in OpenFOAM

The VC solver developed by H. Jasak was used for all computations. The solver is transient by nature therefore all computations have been carried as transient. Hence the results presented in the study are averaged over several seconds to capture 4 and more cycles of vortex shedding behind the bluff body. For the solution version 1.5.x of OpenFOAM, the PISO algorithm was used using GAMG solver with FDIC preconditioner for pressure and PBiCG solver with DILU preconditioner for velocities. The coarse mesh has maximal non-orthogonality of 45 degrees and skewness of 3.5, while the fine mesh has maximal non-orthogonality of 50 degrees and maximum skewness of 2.9. The solver has been run with 2 non-orthogonal correctors.

4 Results

Results are presented for two geometries of the Ahmed body, namely for Ahmed body with 25° and 35° slant angles, respectively. These two geometries have been chosen for the different flow-field. The 35° slant angle supports the boundary layer separation and therefore stronger wake (also stronger oscillations of the wake) while at the 25° slant angle no separation takes part and the wake is much weaker and also more stable. As principle results, velocity profiles will be evaluated in several cross sections along the bluff body and close to slant angle. The locations of the cross sections are marked in Figure 4.

4.1 Ahmed body – 25° slant angle

Results are presented for fine mesh – for details see Tab.1. In the Figure 5, calculations are presented for velocity profiles with the fine mesh. Velocities are presented in the Z-direction perpendicular to the floor plane, with zero value on the floor. As we can see, the values of velocities are very close to the ones from the measurements (Ercoftac points) and the maximum error is only 3 per cent. However, from the figure there is no visible trend for the improvement with changing of vorticity parameter ε. Courant number Co, which is the measure of the time step, was kept 8. The results from these computations are encouraging, while the mesh, although having over 1 million of cells has the smallest cells only 1.25 cm in size. The only noticeable discrepancy can be detected close and after the stagnation point, in the location X = 0.963. Calculations were also done on the coarse mesh (not shown here), where - unlike for the fine mesh –an influence of different values of vorticity parameter ε can be seen, this mainly in

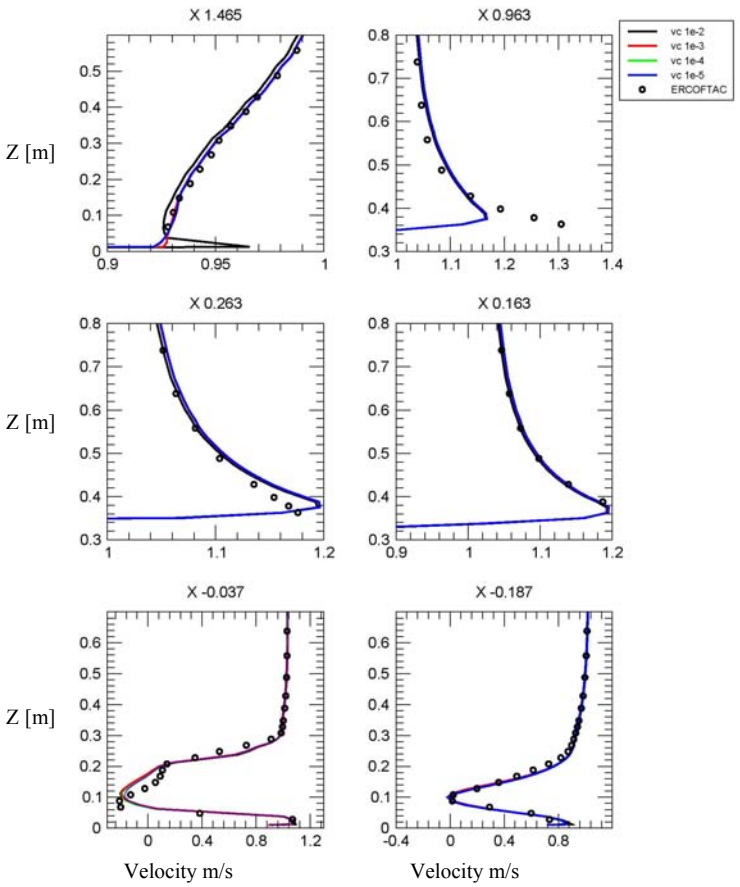

Figure 5: Velocity profiles on fine mesh, 25° slant angle, $Co_{max} = 8$.

the wake region for locations X = -0.037 and -0.187, where velocities are over predicted. Generally, lowest difference can be encountered for very low and very high vorticity parameter ε, namely $\varepsilon=10^{-5}$ and 10^{-2}. The largest error is for ε=0.01.

4.2 Ahmed body – 35° slant angle

The Ahmed body geometry with the stronger slant angle leads to stronger separation and mainly the wake behind the body. This type of flow is more realistic to the real car geometry and more challenging case to model. Series of ε parameter values were tested as well as time steps and mesh coarseness as for previous geometry. Here the results of velocity profiles for 35° slant angle are presented. For the nature of the flow with the separation at the rear of the bluff-body, the results are presented mainly concerning this region in a series of figures. Generally the behaviour of the VC model is the same as it is on the previous geometry with 25° slant angle, meaning there are not large differences in velocity profiles with respect to the changing ε parameter, as it could have been seen in Figure 6. The profiles for fine mesh are also shown in Figure 7 where very good fit could be seen for most of the profiles.

4.3 Comparison of VC and RANS simulations

Individual results of velocity profiles calculated with RANS models are not presented here, only comparison with VC. However, we can conclude that the velocity profiles at given cross sections show quite a good match for fine mesh in the wake region. In this case the resolution of the weak wake is sufficient. The problem is to capture the flow around the bluff body, where the mesh resolution is not capable of capturing the boundary layer. While the RANS on 25° slant angle geometry is capable to capture the wake even on rather coarse mesh, it is not capable to do so on the 35° geometry. Results obtained on fine mesh (the same as for VC calculations) are shown in Figures 8 and 9.

5 Conclusions

From all the computations we can conclude, that the VC method could be used for flows with small or no separation caused by adverse pressure gradient. It is also clear that the computational mesh for VC could be coarser compared to the RANS computations. Since the VC method is in principle transient, the resulting data must be averaged over reasonably long period of time. The method seems to be for the particular case of bluff body flow insensitive on the VC parameter ε value, at least not that much as on the mesh. This conclusion, however, applies only to the particular case tested. In more complicated flow situation the effect of the VC parameter would be probably higher. The method must also be tested for grid independence as its success is dependent on the flow structure. From the

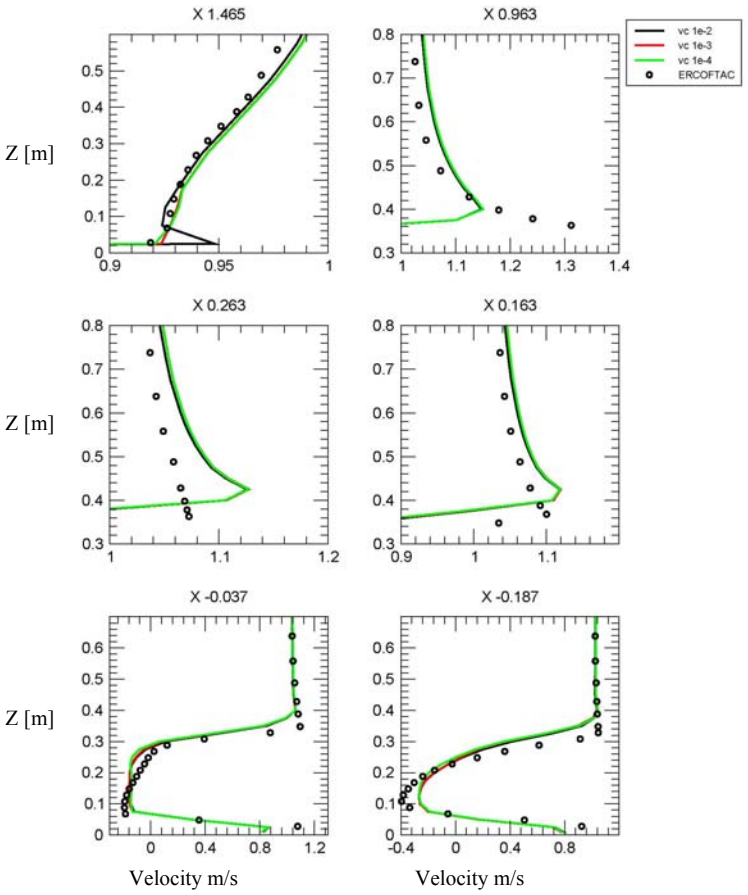

Figure 6: Velocity profiles on fine mesh, 35° slant angle, $Co_{max} = 8$.

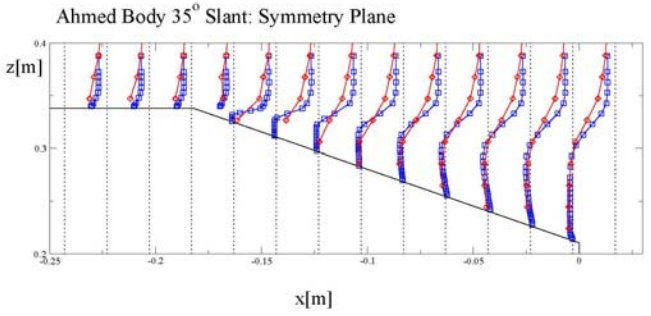

Figure 7: Velocity profiles on fine mesh; $\varepsilon = 1x10^{-3}$; Co = 10.

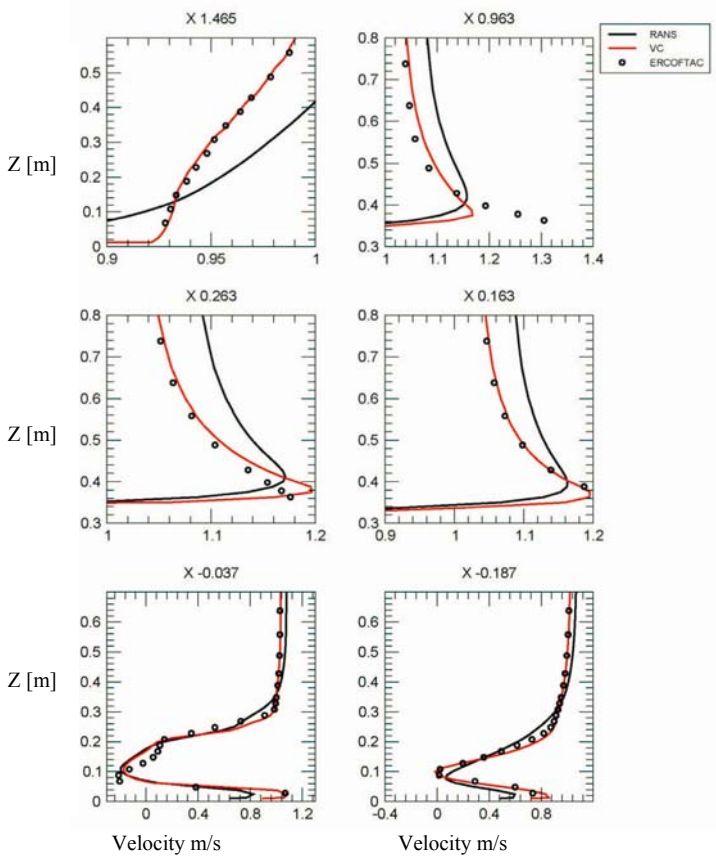

Figure 8: Velocity profiles; RANS and VC, 25° slant angle.

point of view of practical computation the VC method brings improvement. Mainly in cases featuring transient behaviour, the speed-up is significant over RANS methods. Still the computation of Ahmed body flow with fine mesh would last several hours on multiple CPUs. In language of numbers, the RANS computations took two times more time than the VC computations on the same hardware setup. The VC main speed-up effect could lie in much more complicated flows where RANS or URANS simulation would demand grid of several tens of millions. The VC method could lead to faster prediction of turbulent flow, but its potential may lie in more complicated geometries, hence more complicated flow and turbulence structure configurations.

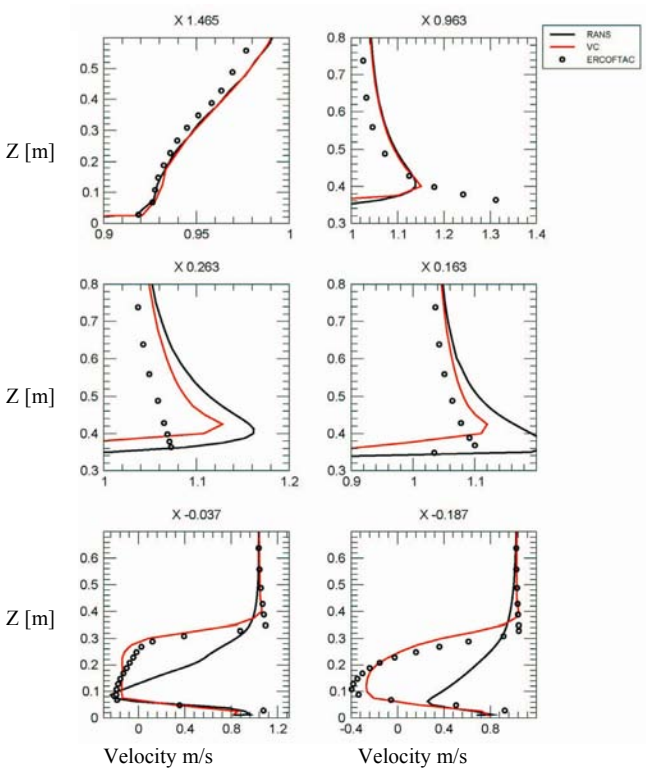

Figure 9: Velocity profiles; RANS and VC, 35° slant angle.

Acknowledgement

The work was performed under the support from the project GA 101/08/0096 of the Czech Grant Agency, which is gratefully acknowledged.

References

[1] Fan, M., Wenren, Y., Dietz, W., Xiao, M., and Steinhoff, J.: "Computing blunt body flows on coarse grids using vorticity confinement", *J. Fluids Engineering*, 124(4):1–18, Dec 2002.

[2] Steinhoff, J., Lynn, N., and Wenren, Y.: *Large Eddy Simulation: Computing Turbulent Flow Dynamics*, Chapter 12: Turbulent Flow Simulations Using Vorticity Confinement: Cambridge University Press, 2006.

[3] Ahmed, S.R., Ramm, G.: Some salient features of the time-averaged ground vehicle wake, SAE Technical Paper 840300, 1984.

[4] Lienhart H., Stoots C., Becker S., Flow and Turbulence Structures in the Wake of a Simplified Car Model (Ahmed Model), Measurements MOVA-project, online database: http://cfd.mace.manchester.ac.uk/ercoftac/.
[5] C. Benoit, Numerical simulation of 2D blade vortex interaction usány moving overset grids, in: 25th European Rotorcraft Forum, Roma, Italy, September 1999.
[6] C. Benoit, G. Jeanfaivre, 3D Inviscid isolated rotor and fuselage calculations using chimera and automatic Cartesian partitioning methods, in: AHS Aeromechanics 2000, Atlanta, GA, November 2000.
[7] A. Dadone, G. Hu, B. Grossman, Towards a better understanding of vorticity confinement methods in compressible flow, in: AIAA 2001 CFD Conference, Anaheim, CA, June 2001.
[8] A. Ochi, T. Aoyama, S. Saito, E. Shima, E. Yamakawa, BVI noise predictions by moving overlapped grid method, in: AHS 55th Annual Forum, Montréal, Québec, May 1999.
[9] M.R. Visbal, D.V. Gaitonde, High-order accurate methods for unsteady vortical flows on curvilinear meshes, in: AIAA 36th Aerospace Sciences, Meeting and Exhibit, Reno, NV, January 1998.
[10] J. Steinhoff, D. Underhill, Modification of the Euler equations for "vorticity confinement": Application to the computation of interacting vortex rings, Phys. Fluids 6 (8) (1994).
[11] Steinhoff, J., Dietz, W., Haas, S., Xiao, M., Lynn, M, and Fan, M: "Simulating Small Scale Features in Fluid Dynamics and Acoustics as Non-Linear Solitary Waves", In *41st AIAA Aerospace Sciences Meeting and Exhibit*, 2003: AIAA-2003-0078.
[12] Vaughn, M. E. Jr.: "An application of vorticity confinement to missile aerodynamic design", In 24th Applied Aerodynamics Conference. AIAA, June 2006: AIAA 2006-3866.

A new class of exact solutions of the Navier–Stokes equations for swirling flows in porous and rotating pipes

A. Fatsis[1], J. Statharas[2], A. Panoutsopoulou[3] & N. Vlachakis[1]
[1]*Technological University of Chalkis, Department of Mechanical Engineering, Greece*
[2]*Technological University of Chalkis, Department of Aeronautical Engineering, Greece*
[3]*Hellenic Defence Systems, Greece*

Abstract

Flow field analysis through porous boundaries is of great importance, both in engineering and bio-physical fields, such as transpiration cooling, soil mechanics, food preservation, blood flow and artificial dialysis. A new family of exact solution of the Navier–Stokes equations for unsteady laminar flow inside rotating systems of porous walls is presented in this study. The analytical solution of the Navier–Stokes equations is based on the use of the Bessel functions of the first kind. To resolve these equations analytically, it is assumed that the effect of the body force by mass transfer phenomena is the 'porosity' of the porous boundary in which the fluid moves.

In the present study the effect of porous boundaries on unsteady viscous flow is examined for two different cases. The first one examines the flow between two rotated porous cylinders and the second one discusses the swirl flow in a rotated porous pipe. The results obtained reveal the predominant features of the unsteady flows examined. The developed solutions are of general application and can be applied to any swirling flow in porous axisymmetric rotating geometries.

Keywords: exact solution, Navier–Stokes, porous, viscous flow, unsteady flow, laminar flow, swirl flow, Bessel functions.

WIT Transactions on Engineering Sciences, Vol 69, © 2010 WIT Press
www.witpress.com, ISSN 1743-3533 (on-line)
doi:10.2495/AFM100061

1 Introduction

In the previous years, problems of fluid flow through porous ducts have aroused the interest of Engineers and Mathematicians; the problems have been studied for their possible applications in cases of transpiration cooling, gaseous diffusion and drinking water treatment, as well as biomedical engineering. The cases where an exact solution for the Navier–Stokes equations can be obtained are of particular importance in order to describe the fluid motion of viscous flows. However, since the Navier–Stokes equations are non-linear, there cannot be a general method to solve analytically the full equations. Exact solutions on the other hand are very important for many reasons. They provide a reference solution to verify the accuracies of many approximate methods, such as numerical and/or empirical. Although, nowadays, computer techniques make the complete integration of the Navier–Stokes equations feasible, the accuracy of numerical results can be established only by comparison with an exact solution [1]. The Navier–Stokes equations were extensively studied in the literature. Exact solutions already known are one-dimensional or parallel shear flows, rectilinear motion flows, or duct flows [1–3]. The flow of fluids over boundaries of porous materials has many applications in practice, such as boundary layer control and transpiration processes. Exact solutions are generally easy to find when suction or injection is applied to a fluid flow. In the case of flows through porous media, a simple solution of the Navier–Stokes equations can be obtained for the flow over a porous plane boundary at which there is a uniform suction velocity [4]. Moreover, fully developed laminar flow through porous channel with a porous pipe for low Reynolds numbers was investigated in [5] and the flow in a duct of rectangular cross-section in [6]. This problem was extended in [7] to high Reynolds numbers. The exact solution of the Navier–Stokes equations for the case of steady laminar flow between two porous coaxial cylinders with different permeability was obtained using the perturbation technique [8]. The cylinders were assumed to rotate with different angular velocities and the fluid between them was flowing with a constant axial pressure gradient. A mathematical model for particle motion in viscous flow between two rotating porous cylinders was also presented [9]. In that paper, a steady flow of a mixture of fluid and particles was assumed. The mass fraction of particles in the flow was small, so the perturbations of the mean liquid flow due to the presence of particles were negligible. An analytical approximate solution for decaying laminar swirling flows within a narrow annulus between two concentric cylinders was also obtained. It was found that the swirl velocity exhibits a Hagen-Poiseuille flow profile decaying downstream [10]. An exact solution of the Navier–Stokes equation was obtained in [11] for the laminar incompressible flow in a uniformly porous pipe with suction and injection. In this study the velocity field was expressed in a series form in terms of the modified Bessel function of the first kind of order n. For large values of the non-dimensional time, the unsteady flow solution approaches its asymptotic value of the steady state problem. Laminar flow over pipes with injection and suction through the

porous wall was studied by means of analytic solutions for the case of low Reynolds numbers [12].

In the present study the full unsteady three-dimensional Navier–Stokes equations are considered for the case of incompressible porous flow. An exact solution is obtained by employing the Bessel functions for the case of three-dimensional unsteady flow between rotated porous cylinders and for the case of unsteady swirl flow in rotated porous pipes.

2 Mathematical and physical modelling

Assuming for the first case study the flow of a Newtonian fluid through an annulus formed between two rotating cylinders, figure 1a, and, for the second case study the flow within a rotating cylindrical pipe, figure 1b, the basic equations are the mass conservation equation and the equations of motion (Navier–Stokes), in a cylindrical system of coordinates (r,θ,z) where the $z-$axis lies along the centre of the pipe, r is the radial distance and θ is the peripheral angle.

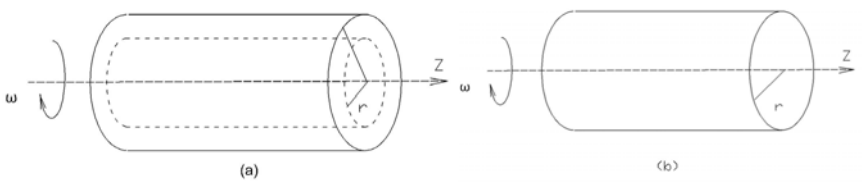

Figure 1: (a) Flow between two rotating porous cylinders; (b) flow within a rotating porous pipe.

2.1 Governing equations

Considering that the flow modelling describes the motion of a homogeneous Newtonian fluid the incompressible Navier–Stokes equations are the governing equations, while the following simplified assumptions are made:
a) the rotating cylinders or the rotating pipe are considered of finite length
b) the permeable wall boundary is treated as a `fluid medium'.
c) the gravitational forces due to the fluid weight are negligible.
The continuity equation is:

$$\frac{u_r}{r}+\frac{\partial u_r}{\partial r}+\frac{\partial u_z}{\partial z}+\frac{1}{r}\cdot\frac{\partial u_\theta}{\partial \theta}=0 \tag{1}$$

The system of the Navier–Stokes equations can be written:

$$\frac{\partial u_r}{\partial t}+u_r\frac{\partial u_r}{\partial r}-\frac{u_\theta^2}{r}+u_z\frac{\partial u_r}{\partial z}=-\frac{1}{\rho}\cdot\frac{\partial p}{\partial r}+\omega^2 r+2\omega u_\theta+$$

$$\frac{\mu}{\rho}\left[\frac{\partial^2 u_r}{\partial r^2}+\frac{1}{r}\cdot\frac{\partial u_r}{\partial r}-\frac{u_r}{r^2}+\frac{\partial^2 u_r}{\partial z^2}\right] \tag{2}$$

$$\frac{\partial u_\theta}{\partial t}+u_r\frac{\partial u_\theta}{\partial r}+\frac{u_r\cdot u_\theta}{r}+u_z\frac{\partial u_\theta}{\partial z}=-\frac{1}{\rho}\cdot\frac{1}{r}\cdot\frac{\partial P}{\partial r}-2\omega u_r+$$

$$\frac{\mu}{\rho}\left[\frac{\partial u_\theta^2}{\partial r^2}+\frac{1}{r}\cdot\frac{\partial u_\theta}{\partial r}-\frac{u_\theta}{r^2}+\frac{\partial^2 u_\theta}{\partial z^2}\right] \tag{3}$$

$$\frac{\partial u_z}{\partial t}+u_r\frac{\partial u_z}{\partial r}+u_z\frac{\partial u_z}{\partial z}=-\frac{1}{\rho}\cdot\frac{\partial p}{\partial z}+\frac{\mu}{\rho}\left[\frac{\partial^2 u_z}{\partial r^2}+\frac{1}{r}\cdot\frac{\partial u_z}{\partial r}+\frac{\partial^2 u_z}{\partial z^2}\right] \tag{4}$$

3 Solution methodology

3.1 Unsteady flow between two coaxial porous rotating cylinders

An incompressible fluid of dynamic viscosity μ and density ρ is considered between two rotating cylinders of length *L*. The inner cylinder can rotate with peripheral velocity $\omega\cdot R_i$ and the outer can rotate with peripheral velocity $\omega\cdot R_o$. At time level $t=t_0$ the fluid enters the cylinders gap uniformly at $z^*=0$ and exits at $z^*=L$ or at non-dimensional axial distance $z=1$.

The following boundary conditions are satisfied:

For $r=R_i$ $\quad u_r\big|_{r=R_i}=u_{ri}$ $\quad u_\theta\big|_{r=R_i}=u_{\theta i}=\omega\cdot R_i$ $\quad u_z\big|_{r=R_i}=1$

For $r=R_o$ $\quad u_r\big|_{r=R_o}=u_{ro}$ $\quad u_\theta\big|_{r=R_o}=u_{\theta o}=\omega\cdot R_o$ $\quad u_z\big|_{r=R_o}=0$

For the test case selected, the value of the axial velocity was set equal to zero at the outer radius. Resolving the system of equations (1) to (4), it was found that the axial velocity u_z, the radial velocity u_r and the tangential velocity u_θ, can be expressed in terms of the functions:

$$u_z=J_0(rb)e^{-bz}e^{kt}+A\cdot(1-r^2) \tag{5a}$$

$$u_r=J_1(rb)e^{-bz}e^{kt}+\frac{C}{r} \tag{5b}$$

$$u_\theta=\frac{D}{r}e^{kt} \tag{5c}$$

where A, C, D are integration constants and $J_0(rb)$ and $J_1(rb)$ are the Bessel functions of the First kind given in detail in [13].

The constant D is defined as $D = \omega_1 - \omega_2$, so it covers the case of counter-rotating cylinders or cylinders rotated in the counter-clockwise direction.

The static pressure field is then calculated analytically as:

$$p(r,z,\theta,t) = \frac{k}{b} J_0\, e^{-bz} e^{kt} - \frac{1}{2}\left(J_1^2 + J_0^2\right) e^{-2bz} e^{2kt} - \frac{CJ_1}{r} e^{-bz} e^{kt} -$$

$$\frac{2A}{b} J_1 r\, e^{-bz} e^{kt} + 2ACz - \frac{4}{\mathrm{Re}} z - AJ_0\, e^{-bz} e^{kt} + AJ_0\, r^2 e^{-bz} e^{kt} - kD\, e^{kt}\theta \quad (6)$$

where the Reynolds number is defined as: $\mathrm{Re} = \dfrac{\rho \cdot U \cdot L}{\mu}$

The proposed solution was validated for the case of the laminar fully developed swirling flow in the annulus between two coaxial cylinders. For this case, one can find in the literature numerical solutions as well as analytical ones [10]. Figure 2 presents the comparison between the axial velocity obtained by the present analytical method (solid line) and the analytical solution obtained in [10] (dashed line). The comparison is considered satisfactory to validate the present method, since the maximum difference between these results does not exceed 5%.

The solution of the Navier–Stokes equations defined by equations (5) and (6) does satisfy the continuity equation (1) and momentum equations (2) to (4).

Figure 3 shows the radial velocity distribution for three different time levels, namely for $t = 0, 1, 2$ along the radius. It was assumed that the inner non-dimensional (by the cylinders length L) radius is $R_i = 0.1$, while the outer

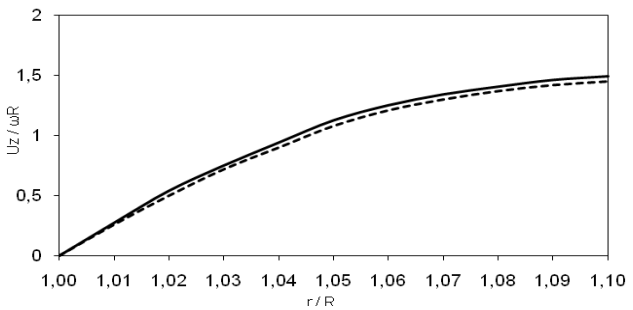

Figure 2: Distribution of the axial velocity for the case of swirling flow between two cylinders. (solid line: present results, dashed line: results from [10]).

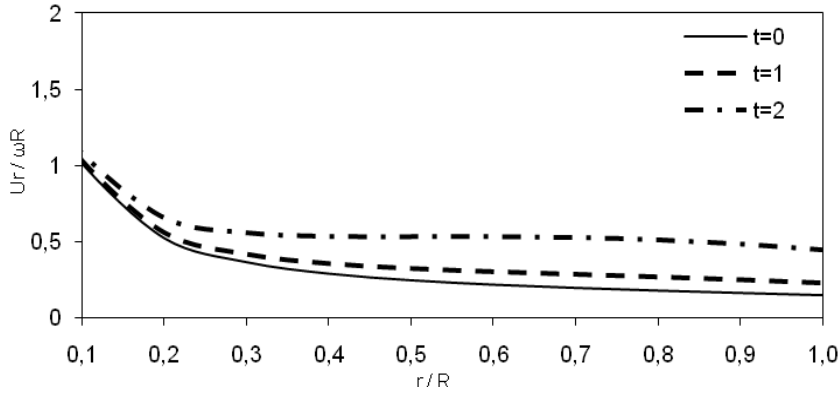

Figure 3: Distribution of the radial velocity in terms of radius for different time levels.

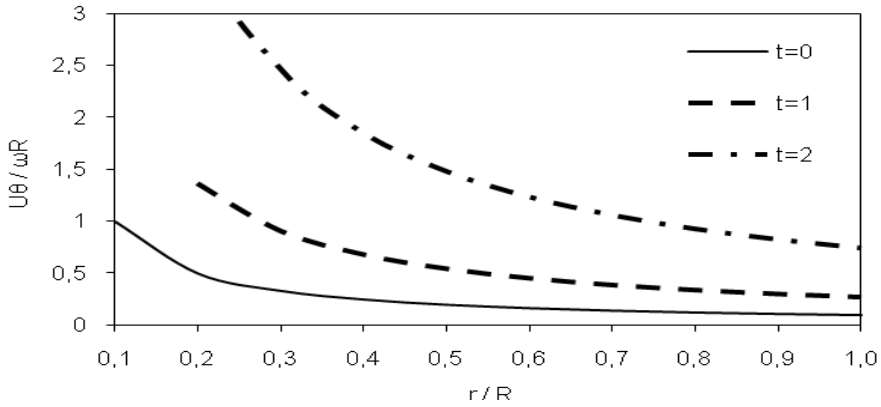

Figure 4: Distribution of the tangential velocity in terms of radius for different time levels.

non-dimensional radius is $R_o = 0.8$ for specific values of the constants A, C, D, k. A decaying behaviour is observed along the radial gap.

The tangential velocity distribution shows in figure 4 a reduction from the inner to the outer cylinder for $t = 0, 1, 2$. As the time level increases more fluid is moving tangentially, thus tangential velocity values increase.

The axial velocity has a decaying distribution from the inner to the outer radius, figure 5.

Figure 6 shows the radial velocity distribution for a given time level for different non-dimensional axial positions, namely for $z = 0, 0.3, 0.8$.

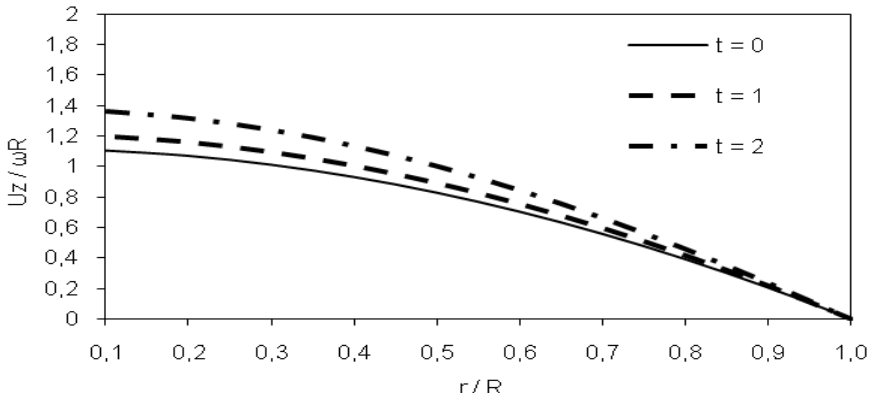

Figure 5: Distribution of the axial velocity in terms of radius for different time levels.

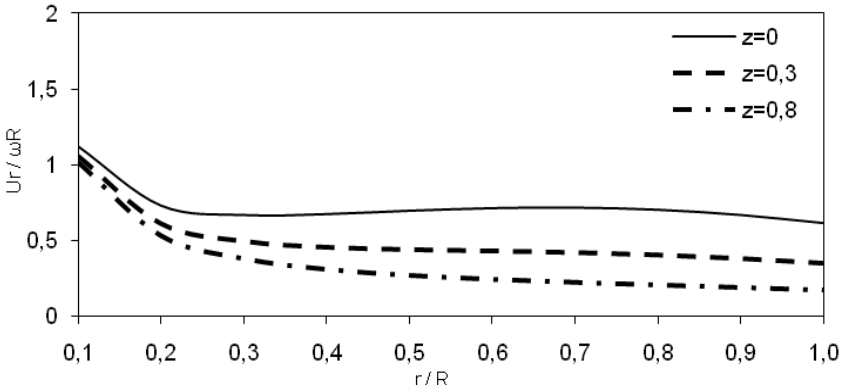

Figure 6: Distribution of the radial velocity in terms of radius for different axial positions.

The radial velocity decreases from the inlet to the outlet. The distribution of the tangential velocity found to satisfy the system of equations of motion is not a function of the axial distance, z according to equation (5c). So at any axial position, the tangential position has a constant radial distribution at given time levels.

Figure 7 presents the axial velocity distribution for a given time level for different axial positions $z = 0, 0.3, 0.8$. The axial velocity shows an increase along the gap of the cylinders from the inlet to the outlet.

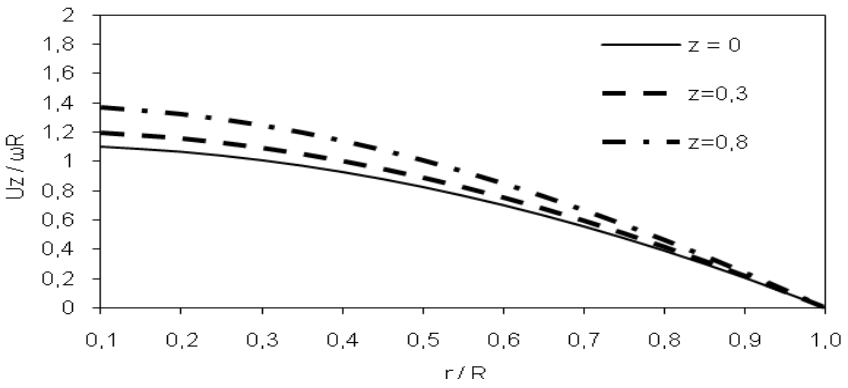

Figure 7: Distribution of the axial velocity in terms of radius for different axial positions.

3.2 Unsteady swirling flow in a rotated porous pipe

An incompressible fluid of dynamic viscosity μ and density ρ is considered within a rotating pipe of length *L*. The inner pipe can rotate along its axis with peripheral velocity $\omega \cdot R$. At time level $t = t_0$ the fluid enters the pipe uniformly at $z^* = 0$ and exits at $z^* = L$ or at non-dimensional axial distance $z = 1$.

The following boundary conditions are satisfied:

For $r = 0$ $\quad u_r\big|_{r=R_i} = 0 \quad u_\theta\big|_{r=R_i} = 0 \quad u_z\big|_{r=0} = 1$

For $r = R_o$ $\quad u_r\big|_{r=R_o} = u_{ro} \quad u_\theta\big|_{r=R_o} = u_{\theta o} = \omega \cdot R_o \quad u_z\big|_{r=R_o} = 0$

For the test case selected, the value of the axial velocity is zero at the outer radius.

The axial velocity u_z, the radial velocity u_r and the tangential velocity u_θ, can expressed in terms of the functions:

$$u_z = J_0(rb)e^{-bz}e^{kt} + A \cdot (1 - r^2) \tag{7a}$$

$$u_r = J_1(rb)e^{-bz}e^{kt} + \frac{B}{r} \tag{7b}$$

$$u_\theta = C \cdot r \tag{7c}$$

where $J_0(rb)$ and $J_1(rb)$ are the Bessel functions of the First kind and A, B, C are integration constants.

The static pressure field is then calculated analytically as:

$$p(r,z,\theta,t)=\frac{k}{b}J_0\,e^{-bz}e^{kt}-\frac{1}{2}\left(J_1^2+J_0^2\right)e^{-2bz}e^{2kt}+\frac{BJ_1}{r}e^{-bz}e^{kt}-$$
$$\frac{2A}{b}J_1 r\,e^{-bz}e^{kt}-AJ_0\,e^{-bz}e^{kt}+AJ_0\,r^2e^{-bz}e^{kt}+2ABz+Az \qquad (8)$$

The solution of the Navier–Stokes equations defined by equations (7) and (8) does satisfy the continuity equation (1) and momentum equations (2) to (4).

Figure 8 shows the radial velocity distribution for three different time levels, namely for $t=0,1,2$ along the radius. A decaying behaviour is observed in this figure. The tangential velocity distribution found in equation (11c) is independent of the time variable *t*.

The axial velocity has a decaying distribution towards the outer radius, figure 9.

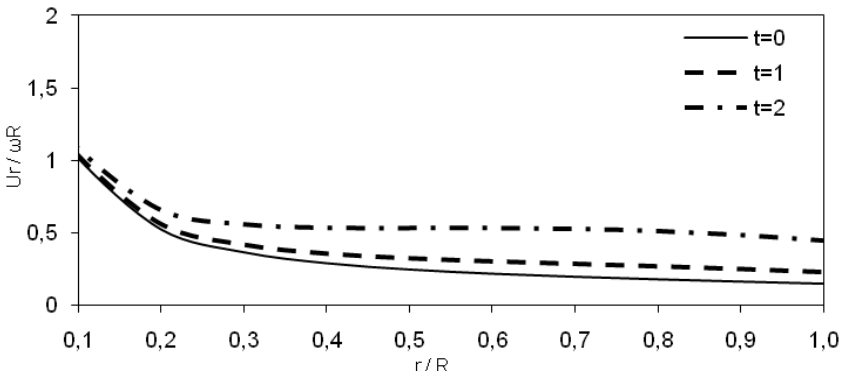

Figure 8: Distribution of the radial velocity in terms of radius for different time levels.

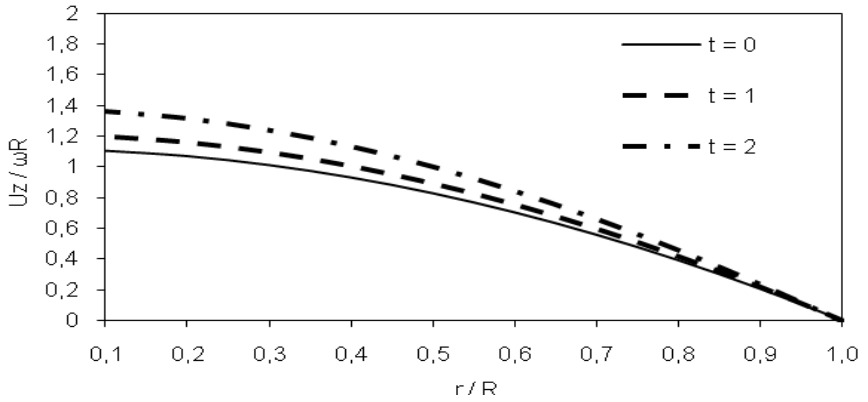

Figure 9: Distribution of the axial velocity in terms of radius for different time levels.

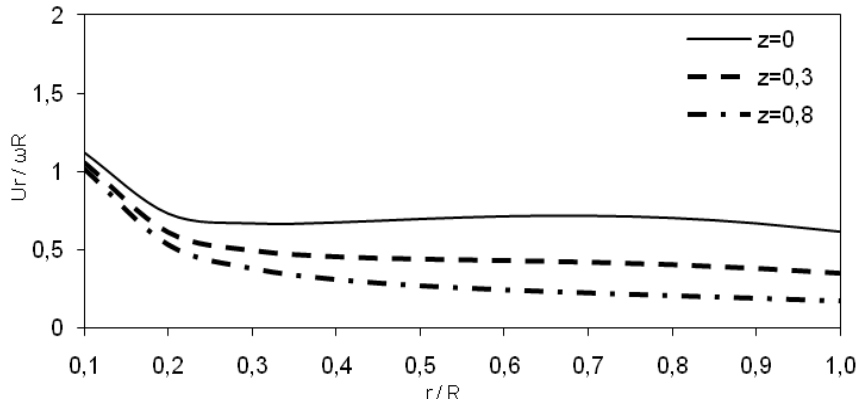

Figure 10: Distribution of the radial velocity in terms of radius for different axial positions.

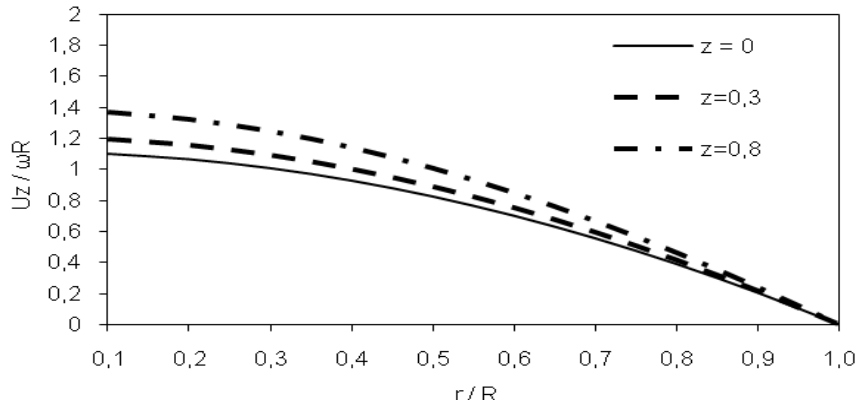

Figure 11: Distribution of the axial velocity in terms of radius for different axial positions.

Figure 10 shows the radial velocity distribution for a given time level for different non-dimensional axial positions, namely for $z = 0, 0.3, 0.8$.

The distribution of the tangential velocity found to satisfy the system of equations of motion is not a function of the axial distance, *z*. So at any axial position, the tangential position has a constant radial distribution at given time levels.

Figure 11 presents the axial velocity distribution for a given time level for different axial positions $z = 0, 0.3, 0.8$. The axial velocity shows an increase along the gap of the cylinders from the inlet to the outlet.

4 Conclusions

In this article, an original work presenting exact solutions of the Navier–Stokes equations in the presence of porous boundaries of axisymmetric rotating geometries is proposed. Such flows have significant industrial applications including filtration and particle separation.

Two cases were examined. The first one is the unsteady flow between two rotating porous cylinders and the second one is the unsteady flow inside rotating porous pipes. In both cases, the Bessel functions of the first kind were used to compute the axial and radial components of the flow velocities, while the tangential flow velocity was found to depend only on the radius. For both cases, the velocity and pressure fields were found by means of analytical methods to satisfy the Navier–Stokes equations for laminar, incompressible unsteady flows.

For the case of the unsteady flow inside two rotating cylinders, it was found that the maximum of the axial velocity shifts towards the inner cylinder. The axial and radial velocity components are independent of the rates of rotation of cylinders. The tangential flow velocity having the form of "free vortex" type of flow was found to satisfy the equations of motion.

For the case of the swirl flow inside rotating pipes, it was found that the maximum of the axial velocity is at the centre of the pipe and decays towards the porous boundary at the maximum radius. Variations were observed also for the radial velocity component which also has a maximum close to the centre of the pipe. The linear variation of the tangential velocity having the form of "forced vortex" type of flow along the radius was found to satisfy the equations of motion.

References

[1] Turkyilmazoglu, M, *Exact solutions for the incompressible viscous fluid of a porous rotating disk*, International Journal of Non-Linear Mechanics, 44 (2009), pp. 352-357.

[2] Batchelor, G.K., *An Introduction to Fluid Dynamics,* Cambridge University Press, Cambridge, 1967.

[3] Polyanin A.D., *Exact solution to the Navier-Stokes equations with generalized separation of variable*s, Dokt. Phys. 46 (2001), pp. 726-731.

[4] Sherman, R.S., *Viscous Flow,* McGraw-Hill Inc., New York, 1990.

[5] Berman, A.S., *Laminar flow in channels with porous walls,* J. Appl. Phys., 24 (1953), pp. 1232-1235.

[6] Jain, R.K. Metha, K.N., *Laminar hydrodynamic flow in a rectangular channel with porous walls,* Proc. Nat. Inst. Sci. India, 28 (1962), pp. 846-856.

[7] Terril R.M., *Laminar flow in a uniformly porous channel,* The Aeronautical Quarterly **15**, 1964, pp.299.

[8] Gupta, M.C., Goyal, M.C., *Viscous incompressible steady laminar flow between two porous coaxial rotating circular cylinders with different*

permeability, Indian Journal of pure applied Mathematics, Vol. 3, No. 3, pp.402-425.

[9] Gumerov, N. A., Dureiswami, R., *Modeling of particle motion in viscous swirl flow between two porous cylinders,* ASME Paper FEDSM98-5110 in the Proceedings of 1998 ASME Fluids Engineering Division Summer Meeting, June 21-25, 1998.

[10] Jawarneh, A.M., Vatistas, G.H., Ababneh, A., *Analytical approximate solution for decaying laminar swirling flows within a narrow annulus,* Jordan Journal of Mechanical and Industrial Engineering, 2 (2008), pp. 101-109.

[11] Erdogan, M.E., Imrak, C.E., *On the flow in a uniformly porous pipe,* International Journal on Non-Linear Mechanics, 43 (2008), pp. 292-301.

[12] Moussy, Y., Snider, A.D., *Laminar flow over pipes with injection and suction through the porous wall at low Reynolds number*, Journal of Membrane Science, 327 (2009), pp. 104-107.

[13] N. Vlachakis, A. Fatsis, A. Panoutsopoulou, E. Kioussis M. Kouskouti V. Vlachakis, *An exact solution of the Navier-Stokes equations for swirl flow models through porous pipes*, Proceedings of the 6th International Conference on Advances in Fluid Mechanics, Wessex Institute of Technology, (2006), pp. 583-591.

Implementation of an LES mixed subgrid model for the numerical investigation of flow around a circular cylinder at Re = 3,900 and 140,000

J. Wong & E. Png
Marine Systems, DSO National Laboratories, Singapore

Abstract

Flows around ships, autonomous underwater vehicles, and other marine structures are often complicated and highly three-dimensional. For accurate flow prediction, large eddy simulation (LES) is a promising alternative which is more accurate than Reynolds-averaged (RANS) turbulence modelling and computationally less intensive than direct numerical simulation (DNS). The flow over a cylinder at Re = 3900 and Re = 140,000 is investigated using the commercial Ansys-Fluent CFD solver and the performance of two different LES subgrid models is evaluated. In particular, we have incorporated the scale similarity term of Bardina into the conventional Smagorinsky model using User-Defined Functions, to form what is known as a Mixed subgrid model. The Mixed subgrid model gives the best agreement with measurements, especially for higher Reynolds numbers where the grid is correspondingly coarser with respect to the flow. This has important implications for the LES modelling of marine engineering applications, where the Reynolds numbers involved are typically extremely large and fine meshes are computationally expensive.
Keywords: large eddy simulation, cylinder, mixed subgrid model, scale similarity, smagorinsky, FLUENT, user-defined functions.

1 Introduction

Flows around ships, autonomous underwater vehicles, and other marine structures are often complicated and highly three-dimensional. The traditional approaches of using facility testing to measure the performance of marine vessels

WIT Transactions on Engineering Sciences, Vol 69, © 2010 WIT Press
www.witpress.com, ISSN 1743-3533 (on-line)
doi:10.2495/AFM100071

have been complemented with computational fluid dynamics predictions in recent years. Simulations have the benefits of cost-savings and also serve to elucidate on certain details of flow physics which cannot be easily measured. For highly unsteady turbulent flows, large anisotropic eddies are generated which are important in the turbulent transport of flow variables. A wide range of time and length scales are involved and Reynolds-averaged (RANS) models are often unable to give accurate predictions in such situations. These situations might include instances when the marine vessel is undergoing turning maneuvers, or when the flow noise, both self- and radiated, needs to be computed. Theoretically, direct numerical simulation is able to resolve all the length and time scales inherent in the flow; however, the computational cost for practical simulations would be exorbitant. Large Eddy Simulation (LES) is a promising approach in which the large eddies are accurately resolved while the smaller eddies are modeled via a subgrid turbulent model. Thus it is able to predict the flow more accurately than RANS methods while providing cost savings compared to DNS.

The flow around a circular cylinder at various Reynolds numbers has been the subject of extensive measurements and numerical studies. Although the geometry is simple, it possesses flow features which are common in many marine structures such as submarine periscopes, ship rudders, marine pipelines, and offshore platform support legs. Such flows typically include curved boundary layers, boundary layer separation, laminar-turbulent transition, unsteady shear layers, and vortex shedding. It is therefore important to be able to predict the flow around the circular cylinder at high Reynolds numbers accurately. To this end, numerous experimental studies have been conducted [1–11].

With the advent in computing power over the years, the use of LES for engineering applications is becoming increasingly common [12–15]. The practicing engineer in industry can now turn to commercially available CFD software such as Ansys-Fluent, for their LES computing needs [16]. These solvers contain robust numerics, a wide range of prediction modules, as well as user-friendly graphical user-interfaces for easy usage. However, the LES models available on the commercial market currently are solely of the pure eddy-viscosity type. These functional models (see section 2.1) are unable to adequately capture the flow physics, especially at the high Reynolds numbers which are of practical importance to industry. To this end, we have incorporated a structural model, known as a Mixed subgrid model, which contains the scale-similarity term of Bardina's. This, and the constant-coefficient Smagorinsky model, which is available in FLUENT, are then tested for the flow past a circular cylinder at two Reynolds numbers, Re = 3900 and Re = 140,000.

2 LES modelling technique

In LES the flow is divided into two regimes $\mathbf{v} = \overline{\mathbf{v}} + \mathbf{v}'$, where $\overline{\mathbf{v}}(\mathbf{x},t) = G * \mathbf{v}(\mathbf{x},t)$ denotes the large-scale (resolvable) component and $\mathbf{v}'(\mathbf{x},t)$

the small-scale component. Here, $G = G(\mathbf{x}, \Delta)$ is a filter function and $\Delta(\mathbf{x})$ is the characteristic grid spacing. Convolving the incompressible NSE with G yields,

$$\partial_t(\bar{\mathbf{v}}) + \overline{\nabla \cdot (\mathbf{v} \otimes \mathbf{v})} = -\overline{\nabla p} + \overline{\nabla \cdot \mathbf{S}} + \bar{\mathbf{f}}, \quad \overline{\nabla \cdot \mathbf{v}} = 0, \tag{1}$$

where **v** is the velocity, p the pressure, **S**= 2ν**D** the viscous stress tensor, ν the viscosity, $\mathbf{D} = \frac{1}{2}(\nabla \mathbf{v} + \nabla \mathbf{v}^T)$ the rate-of-strain tensor and **f** the body force. Recognizing that filtering and derivative operators do not generally commute, i.e. $[G*, \nabla]\rho = \overline{\nabla \rho} - \nabla \overline{\rho} \neq 0$, [17], and that the advection term in (1) gives rise to unclosed terms,

$$\partial_t(\bar{\mathbf{v}}) + \nabla \cdot (\bar{\mathbf{v}} \otimes \bar{\mathbf{v}}) = -\nabla \bar{p} + \nabla \cdot (\bar{\mathbf{S}} - \mathbf{B}) + \bar{\mathbf{f}} + \mathbf{m}, \quad \nabla \cdot \bar{\mathbf{v}} = m, \tag{2}$$

where $\mathbf{B} = (\overline{\mathbf{v} \otimes \mathbf{v}} - \bar{\mathbf{v}} \otimes \bar{\mathbf{v}})$ is the subgrid stress tensor and $\mathbf{m} = [G*, \nabla](\mathbf{v} \otimes \mathbf{v} + p\mathbf{I} - \mathbf{S})$ and $m = [G*, \nabla]\mathbf{v}$ are the commutation error terms. Although both terms contribute to the closure problem of LES, these are often neglected since they are expected to be smaller than the effect of the unresolved transport.

2.1 Subgrid stress modelling

Many analyses performed in the framework of fully isotropic turbulence reveal two main mechanisms which govern the interactions between large and small scales: the forward energy cascade, in which the subgrid scales drain energy from the resolved scales, and the backward energy cascade, in which there is a weak feedback of energy, proportional to k^4, to the resolved scales. Correspondingly, there exist two main modelling approaches. In functional modelling, it is assumed that the action of the subgrid scales on the resolved scales is mainly energetic in nature so that the balance of the energy transfers between the two scale ranges is sufficient to describe the subgrid scale effects. Structural modelling focuses on modelling **B** without incorporating any knowledge of the nature of interactions between subgrid and resolved scales [18]. Most LES modelling for high Reynolds flows today are of the functional type and are able to account for the forward energy cascade while structural models (based on either scale similarity or mixed subgrid models, series expansion techniques, and other techniques) which attempt to model the backscatter of energy from the subgrid to the resolved scales, are not widely used [17]. Although structural models are able to capture more of the relevant flow physics, they are not popular because the same mechanism which predicts the backward cascade can sometimes lead to numerical instability. Here we will compare the performance of two LES models, the conventional Smagorinsky model belonging to the class of functional models, and the Mixed subgrid model

belonging to the class of structural models, incorporated via the use of FLUENT User-Defined Functions.

2.1.1 Smagorinsky model

The Smagorinsky model is an eddy-viscosity type model which models the subgrid stress tensor **B** using the Boussinesq hypothesis:

$$\mathbf{B} = -2\nu_{sgs}\overline{\mathbf{D}} \tag{3}$$

where ν_{sgs} is the subgrid viscosity and $\overline{\mathbf{D}}$ is the resolved rate-of-strain tensor. The subgrid viscosity is in turn calculated as

$$\nu_{sgs} = \left[\min(0.42d, C_s V^{1/3})\right]^2 \left|C_s\sqrt{2\overline{D_{ij}D_{ij}}}\right| \tag{4}$$

where d is the distance from the closest wall, V is the volume of the computational cell, $\overline{D_{ij}}$ is the rate of strain tensor, and C_s is the Smagorinsky constant with a default value of 0.1 [19].

2.1.2 Mixed subgrid model

The use of the Boussinesq hypothesis in the Smagorinksy subgrid model means that **B** is necessarily aligned with $\overline{\mathbf{D}}$. However, tests performed on databases generated by DNS have shown that there is in fact a low level of correlation between the two tensors. Bardina's model, in which the subgrid tensor is calculated by applying the filter twice, shows a much better correlation [17]. In our implementation, following Fureby et al. [20], we first define the subgrid velocity as $\mathbf{v}' = \mathbf{v} - \overline{\mathbf{v}}$. Applying the filter a second time gives $\overline{\mathbf{v}'} = \overline{\mathbf{v}} - \overline{\overline{\mathbf{v}}}$. Then **B** can be further decomposed as

$$\begin{aligned}\mathbf{B} &= (\overline{\overline{\mathbf{v}}\otimes\overline{\mathbf{v}}} - \overline{\overline{\mathbf{v}}}\otimes\overline{\overline{\mathbf{v}}}) + (\overline{\overline{\mathbf{v}}\otimes\mathbf{v}'} - \overline{\overline{\mathbf{v}}}\otimes\overline{\mathbf{v}'} + \overline{\mathbf{v}'\otimes\overline{\mathbf{v}}} - \overline{\mathbf{v}'}\otimes\overline{\overline{\mathbf{v}}}) + (\overline{\mathbf{v}'\otimes\mathbf{v}'} - \overline{\mathbf{v}'}\otimes\overline{\mathbf{v}'}) \\ &= \mathbf{L} + \mathbf{C} + \mathbf{R}\end{aligned} \tag{5}$$

where **L** is the modified Leonard term, and **C+R** is modelled by a subgrid viscosity model; for this, we choose the Smagorinsky model (Eqns (3) and (4)). For practical reasons, it is also necessary to include this because tests have shown that the modified Leonard term alone is only slightly dissipative, and therefore might not be able to drain sufficient energy from the resolved scales, resulting in an underestimation of the forward energy cascade and numerical instability. The Leonard term appears as an explicit source term in the LES momentum equations, and linear interpolation is used to obtain the twice filtered velocities.

2.2 Near-wall treatment

Special treatment is needed to address the boundary layer flow due to the formation and growth of small but important eddies in the near-wall region. Two

approaches exist: the first consists of resolving the near-wall flow directly. In practice, this requires the first computational cell to be within the viscous sublayer. However, this is clearly not possible for high Reynolds number flows, and thus we have to rely on modelling the wall dynamics instead. A number of such wall-models exist: these include Deardorff's model, which work by enforcing boundary conditions on second-order derivatives, and wall stress models, which work by modifying the subgrid viscosity of the LES models. Several such models exist, for example the Schumann model, used with good results for the case of an inclined prolate spheroid by Wikstrom et al. [21], the Grotzbach model, the model of Werner and Wengle, which is available in FLUENT, and others. A third class of wall-models modify the subgrid viscosity according to the distance from the wall to provide the correct scaling; a well known example is the Van Driest's damping function.

As the purpose of the simulations is to highlight the effect of the scale-similarity term, we use FLUENT's ad-hoc wall model (belonging to the third class of wall models) which comes with the basic Smagorinsky model. In this wall model, the turbulent viscosity is reduced for the first cell adjacent to the wall in the manner

$$\nu_{sgs} = \left[\min(0.42d, C_s V^{1/3})\right]^2 \left| C_s \sqrt{2\overline{D_{ij} D_{ij}}} \right|$$

through the wall-distance variable d.

2.3 Numerical methods

FLUENT uses a finite volume method and a segregated approach to discretize and solve the incompressible LES equations. Pressure-velocity coupling is achieved using the PISO scheme, and the equations are iterated using a second-order spatial accurate central-differencing scheme and a second-order accurate implicit time-stepping scheme [refer to 19 for details]. It is known that central-differencing schemes give rise to numerical oscillations on coarse grids; however, for the current simulations, these oscillations do not seem to affect the computed results in any significant manner. The residuals drop to at least 10^{-6} at the end of each time step, and the Courant number, defined here as $Co = V\Delta t / \Delta x$, is kept below 0.8 to ensure a good resolution of the temporal flow dynamics.

3 Computational set-up

The computational domain used is rectangular, with the inflow set at 10D (cylinder diameters) upstream of the cylinder and the outlet at 20D downstream (see fig. 1). The vertical extent is 20D, giving a blockage ratio of 5%. The spanwise extent of the domain is πD. This has the same dimensions as that used by Franke and Frank [22], and Persson et al. [23], amongst others. The velocity is set to a fixed value at the inflow, while a zero gradient is enforced at the outlet. The top and bottom of the domain are slip walls, while the spanwise planes are set as symmetry planes. Finally, the cylinder itself is set to a no-slip wall

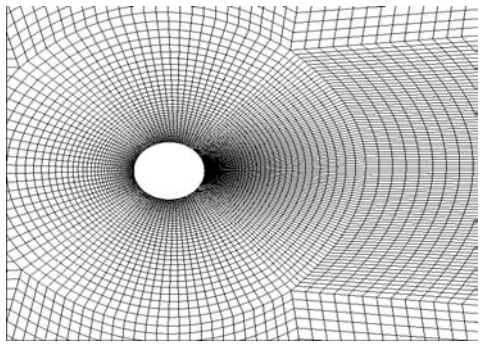

Figure 1: Close-up view of computational mesh close to cylinder.

boundary condition. The cells are clustered in the vicinity of the cylinder as well as the wake, and the grid is stretched in the direction normal to the cylinder wall with a stretching factor of 1.08. The total number of cells used in the domain is 1.1 Million, which gives a near-wall resolution of y^+ ~8 for Re = 3900 and y^+~100 for Re = 140,000. A y^+ of 100 is chosen (instead of a finer grid) for the higher Re simulations because this is typical (and necessary) for practical LES computations in which compromises have to be made between grid sizes and computational time. It is also thought that the coarse grid would provide a better comparison of the different subgrid models used.

4 Results and discussion

4.1 General flow physics

Figure 2. shows a perspective view of the iso-surfaces of the second invariant of the velocity gradient Q for the Re = 3900 flow case. It can be seen that the wake separating from the cylinder consists of curved shear layers with vortices being shed from alternate sides of the cylinder. The initial vortical structures consist of spanwise rollers resulting from the Kelvin-Helmholtz instability in the shear layers. Further downstream, these undergo helical pairing and vortex stretching to form longitudinal vortices which persist as far as 10D behind the cylinder. The Re = 140,000 flow is similar, although the wake is now smaller due to later flow separation. Figure 3 shows the time-averaged streamlines on the centre plane for Re = 3900 and Re = 140,000. It is seen that at the lower Reynolds number, there is not much difference between the models. At the higher Reynolds number, it is seen that the constant-coefficient Smagorinsky model overpredicts the extent of the recirculation region, while the Mixed subgrid model gives better agreement with experiment. This is related to the wake statistics and will be further discussed in the following section.

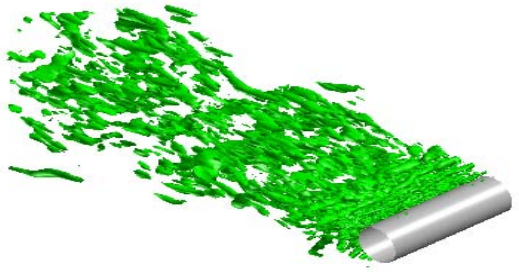

Figure 2: Iso-surfaces of Q behind cylinder for Re = 3900.

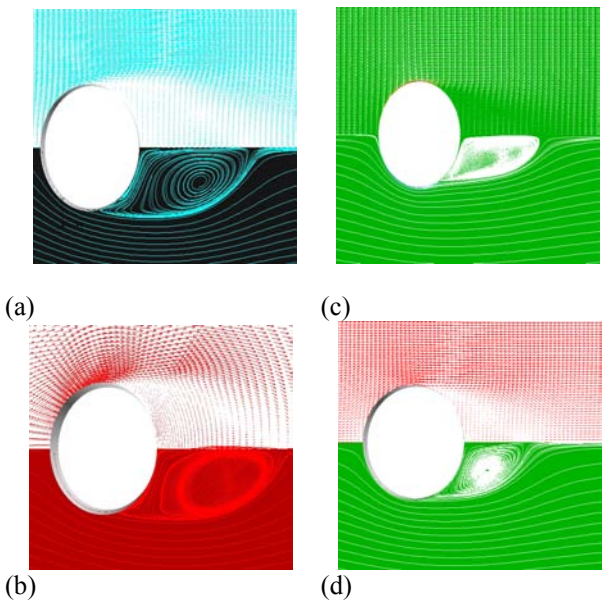

Figure 3: Time-averaged streamlines on centre plane for Re = 3900 and Re = 140,000 for smagorinsky (a, c) and mixed subgrid models (b, d).

4.2 Wake statistics

Time averaged profiles of the streamwise velocity are plotted in fig. 4. For Re = 3900, comparisons are made at locations given by Lourenco and Shih [6] and Ong and Wallace [8]. At the first measurement position, x/D = 1.06, the velocity profile is U-shaped, which is an indication that a sufficiently long sampling time for the velocity has been achieved. Good agreement is obtained in terms of both the centreline velocities and the width of the wake at the first two downstream positions, x/D = 1.06 and x/D = 1.54, whereas LES overpredicts the centreline velocity at about 3% for the position x/D = 2.02. Further downstream, good agreement is again obtained between LES and experiment. That the width of the

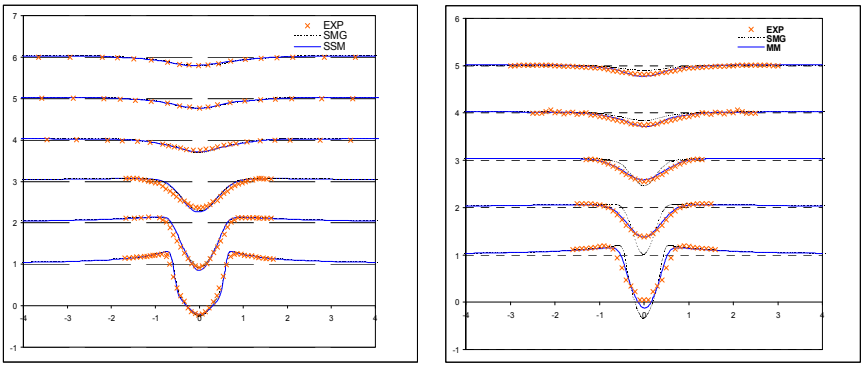

(a) (b)

Figure 4: Time-averaged streamwise velocity at x/D = 1.06, 1.54, 2.02, 4, 7 and 10 for (a) Re = 3900 and x/D = 1, 1.5, 2, 4 and 7 for (b) Re = 140,000.

predicted wake is in good agreement with experiment is also an indication that the flow separation angle on the cylinder is captured correctly. The difference between the conventional Smagorinsky model and the Mixed subgrid model is negligible, indicating that the effect of the subgrid model is not so important at this low Reynolds number. For Re = 140,000, comparisons are made with the measurements by Cantwell and Coles [5]. Significant differences between the subgrid models can now be seen. At stations x/D = 1, 1.5, and 2, the conventional Smagorinsky model greatly underpredicts the magnitude of the centreline velocity and also predicts a wake which is much too narrow compared to the experiment. This under-prediction of the centreline velocity results in a computed recirculation region that is much larger than measured, as noted in the previous section. The Mixed subgrid model shows better agreement with experimental data, although it still slightly underpredicts the centreline velocity at x/D = 1. The wake width is also captured more accurately, which indicates that the predicted flow separation angle is also closer to experiment. Here, the computational grid is the same one that was used for Re = 3900. As a result, the grid is correspondingly coarser with respect to the much higher Reynolds number. The influence of the subgrid model is thus more important.

The streamwise rms velocity fluctuations are presented in fig. 5. For Re = 3900, we again see negligible differences between the LES models and experiment. In addition, the measured profiles are slightly asymmetrical, which perhaps indicates that the experimental statistics is insufficient. At Re = 140,000, a significant difference between the LES models can be seen. The Mixed subgrid model overpredicts the peak rms values while the conventional Smagorinsky model underpredicts it. However, the width of the rms fluctuations is much better captured by the Mixed subgrid model, while the conventional Smagorinsky model consistently gives a too-narrow wake. In addition, the computed LES profiles show a bimodal character which is also seen for

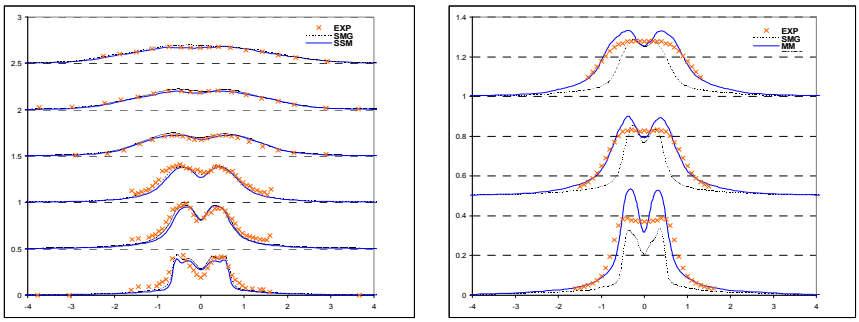

(a) (b)

Figure 5: Time-averaged streamwise rms fluctations for x/D = 1.06, 1.54, 2.02, 4, 7 and 10 for (a) Re = 3900 and x/D = 1, 1.5 and 2 for (b) Re = 140,000.

Re = 3900, whereas this is absent in the measured profiles. One would expect this bimodal character as it represents velocity fluctuations in the shear layer.

4.3 Mean integrated quantities

Next, the mean integrated quantities are shown in table 1. The following quantities are compared:

$$\mathrm{CP} = \frac{\iint C_p \cos\theta d\theta dz}{L}, \tag{6}$$

$$-C_{pb} = \frac{p_{\theta=\pi} - p_{ref}}{\frac{1}{2}\rho U_{ref}^2}. \tag{7}$$

L is the length of the cylinder, taken to be πD in this case. For the calculation of the skin friction coefficient, it is assumed that the first cell adjacent to the wall is embedded well within the viscous sublayer since the wall y^+~8 for Re = 3900. Employing the law of the wall, we have :

$$\langle \tau_w \rangle = \frac{\mu \langle \overline{U} \rangle}{y}. \tag{8}$$

At Re = 140,000, the wall y^+ is ~100, i.e., the log-law region. Hence no similar simple formula for obtaining the mean shear stress is available during postprocessing. It is seen that for Re = 3900, both LES models overpredict slightly the mean integrated pressure and the base pressure coefficient, with the Mixed subgrid model giving results that are slightly closer to experiment. Both

Table 1: Mean integrated cylinder quantities.

Re= 3900	CP	$-C_{pb}$	ϕ_s (^{0})	L_r/D
Smagorinsky	1.047	1.05	94.5	1.1332
Mixed subgrid model	0.987	0.99	97.4	1.2085
Expt	0.942	0.84	85	1.1583
Re= 140,000	CP	-Cpb	ϕs (^{0})	Lr/D
Smagorinsky	0.4673	0.589	-	0.997
Mixed subgrid model	0.9491	1.15	-	0.620
Expt	1.2346	1.21	78	0.4421

models overpredict the mean flow separation angle, but not to the extent where the computed wakes differ significantly from the experimental results. The computed recirculation lengths are also in good agreement with experiment, with the conventional Smagorinsky model slightly underpredicting, and the Mixed subgrid model slightly overpredicting, the actual value. At Re = 140,000, significant differences can be seen between the two LES models. The integrated pressure coefficient predicted by the Smagorinsky model is more than 50% lower than the actual value, while the Mixed subgrid model gives a much better result with around 20% discrepancy. The differences become even more significant when one compares the base pressure coefficients. Again, the Smagorinsky model computes a value which differs from the measured by more than 50%, while the Mixed subgrid model gives much better agreement, predicting a value which is only 5% lower than the experimental result. Likewise, the recirculation length predicted by the Smagorinsky model exceeds the measured value significantly, in part due to the high value of Cs (= 0.1) used in the current computations, as noted by Ma et al. [7]. The Mixed subgrid model is able to rectify this to a certain degree, and reduces the computed recirculation length discrepancy from L_r/D = 0.997 to L_r/D = 0.620, which is more in line with the measured value of L_r/D = 0.4421.

5 Conclusions

In this study, we have performed Large Eddy Simulations of the flow over a cylinder for Re = 3900 and Re = 140,000. We compare the predictive capability of the constant-coefficient Smagorinsky model with the Mixed subgrid model, which consists of an additional Leonard stress tensor term. For the lower Reynolds number, the agreement between LES models and experiment is very good. This implies that most of the energetic vortices are fully resolved by the grid and therefore the difference between subgrid models is small. At the higher Reynolds number of 140,000, significant differences exist between LES models and experiment. In particular, the proposed Mixed subgrid model gives flow prediction which are in much better agreement with experimental data. The predicted time-averaged streamwise velocity is in good quantitative agreement and while the rms fluctuations overpredict the peak values, the mixed subgrid model is at least able to capture the width of the wake. The recirculation length

and the mean integrated cylinder quantities are also much better predicted. For example, the integrated pressure coefficient predicted by the mixed subgrid model has a discrepancy of 20% while the Smagorinsky model differs by more than 50%, and the base pressure coefficient computed by the mixed subgrid model differs from experiment by only 5% while the Smagorinsky value differs by more than 50%. The reason for this improvement is thought to be due to the handling of the smallest resolved scales, as well as the inter-scale energy transfer, in particular the backward energy cascade, offered by the Leonard stress tensor term. This has important practical implications for the ability to conduct high Reynolds number LES computations. This mixed subgrid model will allow the practicing engineer to conduct good quality hydrodynamic analysis at a fraction of the computational cost that would be required for a much finer mesh if the constant-coefficient Smagorinsky model is used.

References

[1] Achenbach E., Distribution of local pressure and skin friction around a circular cylinder in cross-flow up to Re = 5 x 10^6,*J. Fluid Mech,* vol 34, 625-39, 1968.

[2] Norberg, C., Effects of Reynolds number and a low-intensity freestream turbulence on the flow around a circular cylinder *Publ 87/2, Dept. applied Thermo science & fluid mechanics, Chalmers University of Technology, Sweden,* 1987.

[3] Norberg, C., LDV-measurements in the near wake of a circular cylinder, *Advances in Understanding of Bluff Body Wakes and Vortex-Induced Vibration*, Washington D.C., 1998.

[4] Roshko, A., Experiments on the flow past a circular cylinder at very high Reynolds number, *J. Fluid Mech.,* **10(3),** 345-56, 1961.

[5] Catwell, B. & Coles, D., An experimental study of entrainment and transport in the turbulent near wake of a circular cylinder, *J. Fluid Mech*, **136** 321-74, 1983.

[6] Lourenco, L. M. & Shih, C., Characteristics of the plane turbulent near wake of a circular cylinder. A particle image velocimetry study. Data taken from [7].

[7] Ma. X, Karamanos, G. S. & Karniadakis, G.E., Dynamics and low-dimensionality of a turbulent near wake, *J. Fluid Mech*, **410** 29-65, 2000.

[8] Ong, L. & Wallace, J., The velocity field of the turbulent very near wake of a circular cylinder, *Exp. In Fluids*, **20** 441-53, 1996.

[9] Beaudan, P. & Moin, P., Numerical experiments on the flow past a circular cylinder at a sub-critical Reynolds number, *Report No. TF-62*, Thermosciences Division, Dept. Mechanical Engineering, Stanford University, USA, 1994.

[10] Mittal, R. & Moin, P., Suitability of upwind-biased finite difference schemes for large-eddy simulation of turbulent flow, *AIAA J.*, **35** (8) 1415-1417, 1997.

[11] Breuer, M., Towards technical application of large eddy simulation, *Z. Angew. Math. Mech*, 81 (suppl 3), S461-S462, 2001.
[12] Liefvendahl, M., Bensow, R. & Wikstrom, N., Propeller flow field analysis using Large Eddy Simulation, *26th Symp. On Naval Hydrodynamics,* Rome, Italy, 2006.
[13] Grinstein et al, Implicit Large Eddy Simulation, Computing Turbulent Fluid Dynamics, Cambridge University Press, 2007.
[14] Fureby, C., Large Eddy Simulation of Ship Hydrodynamics, *27th Symposium on Naval Hydrodynamics,* Korea, 2009.
[15] Felice, D.F., Felli, M. & Liefvendahl, M., Numerical and Experimental Analysis of the Wake Behavior of a Generic Submarine Propeller, *First International Symposium on Marine Propulsors,* 22-24 June, Trondheim, Norway, 2009.
[16] Wong, J. & Png, E., Numerical Investigation of the Wing-Body Junction Vortex using various Large Eddy Simulation Models, *39th AIAA Fluid Dynamics Conference,* 22-25 June, San Antonio, Texas, 2009.
[17] Sagaut, P., *Large Eddy Simulation for Incompressible Flows*, Springer, 2000.
[18] Alin, N., Fureby, C., & Svennberg, U., LES of the Flow past Simplified Submarine Hulls, *8th International Conference on Numerical Ship Hydrodynamics*, Sept 22-25, 2003, Busan, Korea.
[19] ANSYS-FLUENT v6.3, User's Guide.
[20] Fureby, C., Bensow, R. & Persson, T., Scale Similarity Revisited in LES, *Turbulent Shear Flow Phenomena IV,* p1077, 2005.
[21] Wikstrom, N., Svennger, U., Alin, N. & Fureby, C., Large eddy simulation of the flow around an inclined prolate spheroid, *Journal of Turbulence,* 2004.
[22] Franke, J. & Frank, W., Large eddy simulation of the flow past a circular cylinder at Re_D = 3900, *J. Wind Engineering & Industrial Aerodynamics,* **90** p1191-1206, 2002.
[23] Persson, T., Bensow, R. & Fureby, C., Flow around a Circular Cylinder at Re = 3900 and 140,000, *7th Numerical Towing Tank Symposium,* Hamburg, Germany, 2004.

Adaptive meshfree method for thermo-fluid problems with phase change

G. Kosec & B. Šarler
University of Nova Gorica, Slovenia

Abstract

In the present paper, the recently developed local meshfree method solution of thermo-fluid problems is modified from the collocation to the combined collocation and weighted least squares approach and upgraded with an h-adaptive strategy. A one domain enthalpy formulation is used for modelling the solid-liquid energy transport and the liquid phase is assumed to behave as an incompressible Newtonian fluid modelled by the Boussinesq hypothesis. The involved temperature, enthalpy, velocity and pressure fields are represented on overlapping local sub-domains through weighted least squares approximation (by a truncated Gaussian weight in the domain nodes) and collocation (at the boundary nodes) by using multiquadrics Radial Basis Functions (RBF). The transport equations are solved through explicit time stepping. The pressure-velocity coupling is calculated iteratively through a novel local pressure correction algorithm. The node adaptivity is established through a phase-indicator and a node refinement strategy that takes into account the dynamic number of neighbouring nodes. The proposed approach is used to solve the standard Gobin Le Quéré melting benchmark with tin at Stefan number (Ste) 0.01, Prandtl number (Pr) 0.02, and Rayleigh number (Ra) 2.5e4. The node distribution changes through the simulation as the melting front advances. The solid is consequently computed at much lower node distribution density in comparison with the liquid, which speeds up the simulation and at the same time preserves accuracy. The latter issue has been demonstrated by comparison with the results of other combinations of numerical methods and formulations that attempted this benchmark in the past.

Keywords: meshfree, RBF, weighted least squares, collocation, convective-diffusive problems, adaptation, refinement, melting, fluid flow, Newtonian fluids.

WIT Transactions on Engineering Sciences, Vol 69, © 2010 WIT Press
www.witpress.com, ISSN 1743-3533 (on-line)
doi:10.2495/AFM100081

1 Introduction

The computational modelling of multiphase systems has become a highly popular research subject due to its pronounced influence in the better understanding of nature, as well as in the development of the advanced technologies. Melting of the polar ice caps, the global ocean dynamics, various weather systems, water transport, soil erosion and denudation, magma transport, ...; and manufacturing of nano-materials, improving casting processes, fossil and renewable energy studies, exploitation of natural resources..., are two typical contemporary research fields where multiphase systems play an important role. In most cases even the simplest useful multiphase physical models cannot be solved in a closed form and therefore numerical solution is required. The classical numerical methods, such as the Finite Volume Method (FVM) [4], Finite Difference Method (FDM) [5, 6], Boundary Elements Method (BEM) [7] and the Finite Element Method (FEM) [8], are used for solving these problems in the majority of the simulations [9, 10]. Despite the powerful features of these methods, there are often substantial difficulties in applying them to realistic, geometrically complex three-dimensional transient problems. A common drawback of the mentioned methods is the need to create a polygonisation, either in the domain and/or on its boundary. This type of meshing is often the most time consuming part of the solution process and is far from being fully automated. The numerical simulations of engineering multiphase systems are mainly based on the averaged or mixture equations, defined on the arbitrary phases, with the interphase conditions, incorporated into the non-linearity of the governing equations. The proper numerical solution of these equations requires adaptation of the discretization in the vicinity of the moving boundary. The principal bottleneck in these types of numerical methods is the time consuming re-meshing of the evolving interphase boundaries and phase domains. The polygonisation problem is thus even more pronounced. The application of the alternative numerical methods to FVM and FEM, such as the mesh reduction [11–13] or meshless [14] methods, for phase change problems is relatively rare at the present, however the number of respective meshless publications is steadily growing. Different adaptive node distributions strategies have been used in the past for different numerical methods in order to enhance the numerical effectives at physical intense behaviour or boundaries [15–21]; however, this paper is focused on the local h-refinement in a meshfree context. The nodes are simultaneously added on the computational domain in order to improve the numerical approach. The local refinement approach is proposed and demonstrated in this paper.

2 Problem definition

The physical model solved in this paper is based on the classical De Vahl Davis natural convection benchmark test [22] with the phase change phenomena added. The phase change splits the domain into two different connected areas, occupied by the different phases. The liquid phase is described by an incompressible

Newtonian fluid while the solid phase is stationary. The energy transport is the same for both phases. The benchmark case was originally proposed by Gobin and Le Quéré [3]. The problem is modelled by three coupled PDEs and the Boussinesq approximation. The PDEs are mass, momentum and energy conservation equations where all material properties are considered to be constant.

$$\nabla \cdot \mathbf{v} = 0 \tag{1}$$

$$\frac{\partial \mathbf{v}}{\partial t} + \nabla \cdot (\rho \mathbf{v}\mathbf{v}) = -\nabla P + \nabla \cdot \left(\mu \nabla \mathbf{v}\right) + \mathbf{b} \tag{2}$$

$$\frac{\partial \left(\rho h\right)}{\partial t} + \nabla \cdot (\rho h \mathbf{v}) = \nabla \cdot \left(\lambda \nabla T\right) \tag{3}$$

$$\mathbf{b} = \rho_{ref} \left[1 - \beta_T (T - T_{\text{ref}})\right] \mathbf{g}, \tag{4}$$

$$h(T) = c_p T + f_L^V L \tag{5}$$

with $\mathbf{v}(v_x, v_y)$, t, ρ, P, μ, $\mathbf{b}$, h, λ, T, ρ_{rer}, β_T, T_{ref}, $\mathbf{g}$, c_p, f_L^V and L standing for velocity, time, density, pressure, viscosity, body force, enthalpy, thermal conductivity, temperature, reference density, thermal expansion coefficient, reference temperature, gravitational acceleration, specific heat, liquid volume fraction and latent heat, respectively. The pure substance phase change occurs at constant temperature and thus the enthalpy is discontinuous at the melting temperature. To avoid the numerical instabilities the enthalpy jump is smoothed by implementing a temperature interval similar to that in the multicomponent phase change process. The liquid fraction is therefore formulated as

$$f_L^V(T) = \begin{cases} T \geq T_F + \delta T_L; & 1 \\ T_F + \delta T_L > T > T_F; & T - T_m / \delta T_L \\ T \leq T_F; & 0 \end{cases} \tag{6}$$

with δT_L, T_F standing for smoothing interval and melting temperature, respectively. The results obtained with such phase-change interval smoothing are physically reasonable as long as the interval is small enough [23]. The introduced smoothing represents a standard approach for solving such problems [3]. We limit our subsequent discussion to 2D Cartesian coordinates $p_\xi = \mathbf{p} \cdot \mathbf{i}_\xi; \xi = x, y$ with orthogonal base vectors $\mathbf{i}_\xi$ and coordinates p_ξ. The boundary conditions and the initial state are set on a rectangular domain $0 \leq p_x = \Omega_W$, $0 \leq p_y = \Omega_H$

$$\tilde{\mathbf{v}}\left(\Gamma,\tilde{t}\right)=0 \tag{7}$$

$$T\left(p_x=0,t\right)=T_H,\ T\left(p_x=\Omega_W,t\right)=T_C=T_F,\ \frac{\partial}{\partial\tilde{p}_y}\tilde{T}\left(\tilde{p}_y=[0,1],\tilde{t}\right)=0 \tag{8}$$

$$\tilde{\mathbf{v}}\left(\Omega,t=0\right)=0,\ T\left(\Omega,t=0\right)=T_F \tag{9}$$

with dimensionless quantities introduced as

$$\tilde{p}_{x,y}=\frac{p_{x,y}}{\Omega_W},\ \tilde{v}_{x,y}=\frac{v_{x,y}\Omega_{W,H}\rho c_p}{\lambda},\ \tilde{T}=\frac{T-T_C}{T_H-T_C}, \tag{10}$$

where T_H, T_C, Γ, Ω, Ω_W, Ω_H and $\mathbf{p}(p_x,p_y)$ stand for hot side temperature, cold side temperature, domain boundary, domain interior, domain width, domain height and position vector. The problem is characterized by four dimensionless numbers: the thermal Rayleigh number, Prandtl number, Stefan number and domain aspect ratio, defined as

$$\mathrm{Ra}_T=\frac{|\mathbf{g}|\beta_T\left(T_H-T_C\right)\Omega_H{}^3\rho^2c_p}{\lambda\mu},\ \mathrm{Pr}=\frac{\mu c_p}{\lambda},\ \mathrm{Ste}=\frac{\left(T_H-T_C\right)cp}{L},\ \mathrm{A_R}=\frac{D_W}{D_H}. \tag{11}$$

The problem is schematically presented in Figure 1.

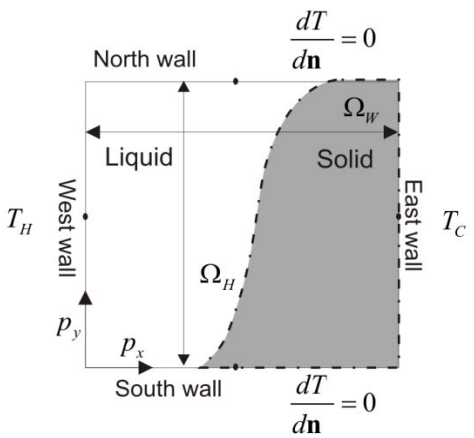

Figure 1: Problem schematics.

3 Solution procedure

A two level Euler explicit time stepping scheme is used for time discretization. The domain and boundary are discretized into $N = N_\Omega + N_\Gamma$ nodes of which N_Ω nodes are distributed in the domain and N_Γ at the boundary. The spatial discretization is performed by using the local meshfree method where overlapping local subdomains are used. An arbitrary scalar function θ is represented on each of the local subdomains as

$$\theta(\mathbf{p}) = \sum_{n=1}^{N_{Basis}} \alpha_n \Psi_n(\mathbf{p}) \tag{12}$$

where N_{Basis}, α_n and Ψ_n stand for the number of basis functions, interpolation coefficients and basis functions, respectively. The basis could be selected arbitrary however in this work only Hardy's Multiquadrics (MQs) $\Psi_n(\mathbf{p}) = \sqrt{(\mathbf{p}-\mathbf{p}^n)\cdot(\mathbf{p}-\mathbf{p}^n)/\sigma_C^2 + 1}$ with σ_C standing for basis function free shape parameter are used. For non refined node distributions even smallest five nodded subdomain collocation works fine but with introduction of more complex refined nodes distributions small subdomain computations do not behave convergent anymore. To circumvent the problem, larger subdomains are selected with more stable weighted least squares approximation to determine coefficients α_n. The subdomains are weighted by truncated Gauss weight function

$$W(\mathbf{p}) = \begin{cases} \exp(-\dfrac{\|\mathbf{p}\|^2}{\sigma_w^2}) & \|\mathbf{p}-\mathbf{p}^0\| \le \sigma_T \\ 0 & \|\mathbf{p}-\mathbf{p}^0\| > \sigma_T \end{cases} \tag{13}$$

where σ_T, σ_W and $\mathbf{p}^0$ stand for weight function truncation parameter, weight function shape parameter and central subdomain node position vector, respectively. The subdomain size is thus determined by the weight function truncation radius, where all nodes within this radius are used as subdomain nodes. With the constructed approximation function an arbitrary spatial differential operator (L) can be computed

$$L\theta(\mathbf{p}) = \sum_{n=1}^{N_{Basis}} \alpha_n L\Psi_n(\mathbf{p}) \,. \tag{14}$$

In the boundary nodes collocation instead of WLS is used in order to satisfy the boundary condition exactly [24]. In this paper five nodded subdomains are

used in Neumann boundary nodes. In such nodes boundary node collocation equation is replaced by the boundary condition equation

$$\sum_{n=1}^{N_{Basis}} \alpha_n \frac{\partial}{\partial \mathbf{n}} \Psi_n(\mathbf{p}) = 0 \,. \tag{15}$$

The spatial discretization problem is formulated in a vector form

$$\boldsymbol{\alpha} = \boldsymbol{\Psi}^{-1}\boldsymbol{\Theta} \,. \tag{16}$$

with matrix dimension $\dim(\boldsymbol{\Psi}) = [N_{Sub}, N_{Basis}]$ where N_{Sub} stands for number of subdomain nodes. To maintain the general formulation both, the WLS and the collocation are considered through equation (16) where pseudo inverse of the non square WLS matrix $\boldsymbol{\Psi}$ is computed by singular value decomposition and square collocation matrix is inverted by LU decomposition.

With defined time and spatial discretization schemes the general transport equation under the model assumptions can be written as

$$\frac{\theta_1 - \theta_0}{\Delta t} = D\nabla^2 \theta_0 - \nabla \Theta_0 \cdot (\rho \mathbf{v}_0) + S_0 \tag{17}$$

where $\Theta_{0,1} = \Theta([t_0, t_1])$ stands for the field value in the interior node with index Ω at current and next time step, D for general diffusion coefficient and S_Ω^0 for source term. To couple the mass and momentum conservation a special treatment is required. The intermediate velocity is computed by

$$\hat{\mathbf{v}} = \mathbf{v}_0 + \frac{\Delta t}{\rho}\left(-\nabla P_0 + \nabla \cdot (\mu \nabla \mathbf{v}_0) + \mathbf{b}_0 - \nabla \cdot (\rho \mathbf{v}_0 \mathbf{v}_0)\right). \tag{18}$$

The equation (18) did not take in account the mass continuity and therefore pressure and velocity corrections are added

$$\hat{\mathbf{v}}^{m+1} = \hat{\mathbf{v}}^m + \hat{\mathbf{v}} \qquad \hat{P}^{m+1} = \hat{P}^m + \hat{P} \tag{19}$$

where m, $\hat{v}$ and $\hat{P}$ stand for pressure velocity iteration index, velocity correction and pressure correction, respectively. Combining the momentum and mass continuity equations the pressure correction Poisson equation emerges

$$\nabla \hat{\mathbf{v}}^m = \frac{\Delta t}{\rho} \nabla^2 \hat{P} \tag{20}$$

Instead of solving the global Poisson equation problem the pressure correction is directly related to the intermediate velocity divergence

$$\hat{P} = \ell^2 \frac{\rho}{\Delta t} \nabla \cdot \hat{\mathbf{v}}^m \tag{21}$$

The proposed assumption enables direct solving of the pressure velocity coupling iteration and thus is very fast due to only one step needed in each node to evaluate the new iteration pressure and the velocity correction. With computed pressure correction the pressure and the velocity can be corrected as

$$\hat{\mathbf{v}}^{m+1} = \hat{\mathbf{v}}^m - \zeta \frac{\Delta t}{\rho} \nabla \hat{P} \qquad \hat{P}^{m+1} = \hat{P}^m + \zeta \hat{P} \tag{22}$$

where ζ stands for relaxation parameter. The iteration is performed until the criteria $\nabla \cdot \hat{\mathbf{v}} < \varepsilon_V$ is met in all computational nodes.

Each simulation starts with the uniformly distributed initial nodes. At every predefined number of time steps $\sigma_R^{N_t}$ all nodes are checked if refinement/derefinement is needed. If the refinement criterion is met, additional nodes are added or removed from the vicinity of the node. At each refinement maximum four nodes are symmetrically added around the refined node. Maximum allowed difference in the refinements between neighbouring nodes is set to one in order to keep the numerical approach as stable as possible. Important part of CPU complexity of the meshfree methods represents the selection of proper subdomain. The problem becomes even more important when working with dynamic node distribution. Truly meshfree methods should not use any topological information about the nodes connectivity, however in order to utilize fast subdomain selection the information about the local node neighbourhood (four symmetric neighbours) is stored within the node. The example of once and four times refined node is presented in Figure 2 where the arrows point to each node neighbourhood.

4 Results

The melting of a metal like material is considered as a benchmark test. A detailed comparison of other cases proposed in the call [3] can be found in [1]. The present paper is focused on the application of a dynamic node distribution in such cases. The comparison of the melting front position after $\tilde{t} = 10$ to the previously published data is shown in Figure 4.

The solid part of the domain is kept at initial node distribution density while the liquid part is $\sigma_R^{\max}$ times refined. As the melting front advances with the time, nodes are added to the area with governed liquid phase. Solution at

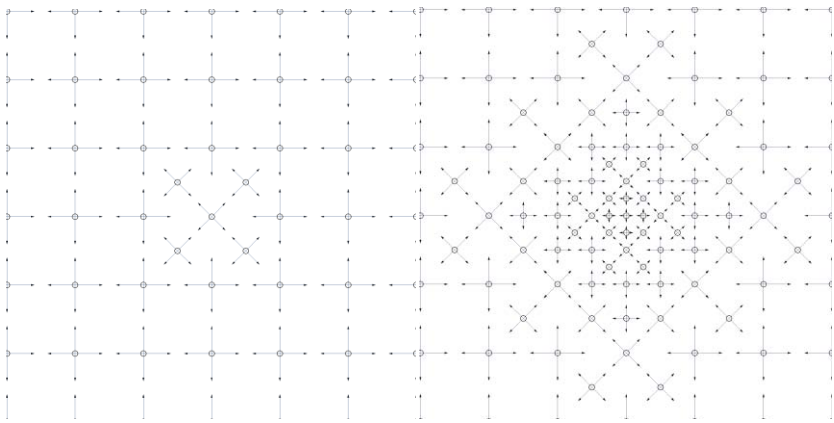

Figure 2: An example of one refined node (left) and four time refined node (right).

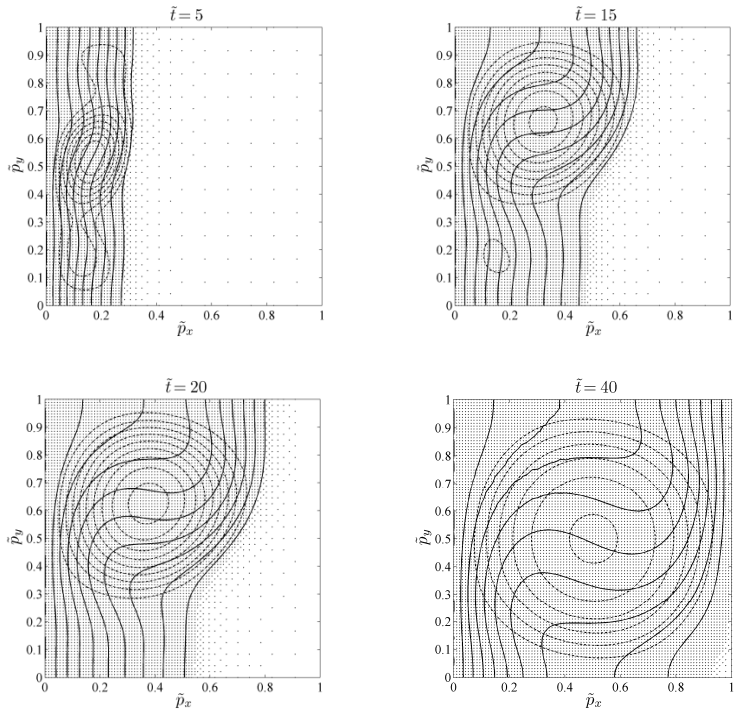

Figure 3: Solution at different times.

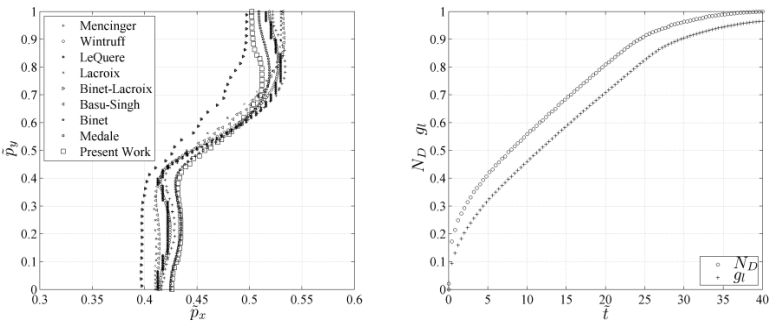

Figure 4: Melting front comparison at $\tilde{t} = 10$ and domain average liquid fraction (left). Relative number of computational nodes with respect to the fully refined liquid phase (right).

different time is represented in Figure 3 where streamlines are plotted as dotted lines and temperature contours as solid lines. In Figure 3 the nodes distribution is plotted as well. At the beginning most of the domain is covered only with initial nodes due to its solid state. The advancing melting front leaves liquid phase behind it. The liquid phase is refined in order to handle much more complex fluid flow computations and the phase change phenomena. The number of computational nodes is therefore directly related to the domain average liquid fraction. In Figure 4 the comparison of average liquid fraction with relative number of domain nodes

$$N_D(\tilde{t}) = N(\tilde{t}) / N(40) \tag{23}$$

where N and N_D stand for the number of the nodes and relative number of nodes is represented. The comparison gives the expected results. The case has been computed with $\zeta = \Delta\tilde{t} = 10^{-6}$, $\delta T_L / T_F = 0.01$, $\varepsilon_V = 0.1$, $N(\tilde{t} = 0) = 144$, $N_{basis} = 6$, $\sigma_C = 90$, $\sigma_T = 1.7$, $\sigma_w = 0.7$, $\sigma_R^{N_t} = 50$ and $\sigma_R^{\max} = 6$.

5 Conclusions

In this paper an application of the dynamic node distribution strategy in the thermo-fluid problems with phase change has been explored. The local meshfree method based on the weighted least squares approximation has been used for spatial discretization with two level Euler explicit time stepping for time discretization. To optimize the numerical effectiveness the computational nodes are added to domain based on the phase indicator. The liquid phase is covered with much denser nodes distribution in comparison with the solid phase of the domain thus the most complex computations are in the liquid part of the domain and its boundary. Nodes are constantly refined as the melting front is advancing

from the hot side to the cold side of the domain assuring the appropriate node coverage of the liquid part. The nodes refinement algorithm is local as well as subdomain selection. The proposed solution procedure is completely local and therefore numerically very effective. The parallelization of the numerical code is almost trivial.

Future work will be focused on more complex physical situations as well as more involved node refinement/derefinement criteria that would take into account also the flow structure.

Acknowledgements

The authors would like to express their gratitude to Slovenian Research Agency for support in the framework of the projects Young Researcher Program 1000-06-310232 (G.K.), and project J2-0099 Multiscale Modelling and Simulation of Liquid-Solid Systems (B.Š.).

References

[1] Kosec, G. & Šarler, B., Solution of phase change problems by collocation with local pressure correction. *CMES: Computer Modeling in Engineering and Sciences,* **47**, pp. 191-216, 2009.

[2] Kosec, G. & Šarler, B., Solution of thermo-fluid problems by collocation with local pressure correction. International Journal of Numerical Methods for Heat and Fluid Flow, 18, pp. 868-882, 2008.

[3] Gobin, D. & Le Quéré, P., Melting from an isothermal vertical wall, synthesis of a numerical comparison exercise. Comp. Assist. Mech. Eng. Sc., 198, pp. 289-306, 2000.

[4] Ferziger, J. H. & Perić, M., Computational Methods for Fluid Dynamics, Springer: Berlin, 2002.

[5] Ozisik, M. N., Finite Difference Methods in Heat Transfer CRC Press: 2000.

[6] Shashkov, M., Conservative Finite-Difference Methods on General Grids, CRC: Boca Raton, 1996.

[7] Wrobel, L. C., The Boundary Element Method: Applications in Thermo-Fluids and Acoustics, John Wiley & Sons: West Sussex, 2002.

[8] Rappaz, M., Bellet, M. & Deville, M., Numerical Modeling in Materials Science and Engineering, Springer-Verlag: Berlin, 2003.

[9] Dantzig, J.A., Liquid-solid phase changes with melt convection. International Journal of Numerical Methods in Engineering, 28, pp. 1769-1785, 1989.

[10] Viswanath, R. & Jaluria, R., A comparison of different solution methodologies for melting and solidification problems in enclosures. Numerical Heat Transfer, Part B, 24, pp. 77-105, 1993.

[11] Šarler, B. & Kuhn, G., Primitive variable dual reciprocity boundary element method solution of incompressible Navier-Stokes equations. Engineering Analysis with Boundary Elements, 23, pp. 443-455, 1999.

[12] Šarler, B. & Kuhn, G., Dual reciprocity boundary element method for convective-diffusive solid-liquid phase change problems, Part 2: Numerical Examples. Engineering Analysis with Boundary Elements, 21, pp. 65-79, 1998.
[13] Šarler, B. & Kuhn, G., Dual reciprocity boundary element method for convective-diffusive solid-liquid phase change problems, Part 1: Formulation. Engineering Analysis with Boundary Elements, 21, pp. 53-63, 1998.
[14] Šarler, B., Towards a mesh-free computation of transport phenomena. Engineering Analysis with Boundary Elements, 26, pp. 731-738, 2002.
[15] Kovačević, I. & Šarler, B., Solution of a phase-field model for dissolution of primary particles in binary aluminum alloys by an r-adaptive mesh-free method. Materials Science and Engineering A, 413–414, pp. 423–428, 2005.
[16] Perko, J. & Šarler, B., Weigh function shape parameter optimization in meshless methods for non-uniform grids. CMES: Computer Modeling in Engineering and Sciences, 19, pp. 55-68, 2007.
[17] Li, S., Petzold, L. & Ren, Y., Stability of moving mesh systems of partial differential equations. Journal of Scientific Computing, 20, pp. 719-738, 1998.
[18] Bourantas, G.C., Skouras, E.D. & Nikiforidis, G.C., Adaptive support domain implementation on the moving least squares approximation for mfree methods applied on elliptic and parabolic pde problems using strong-form description. CMES: Computer Modeling in Engineering and Sciences, 43, pp. 1-25, 2009.
[19] Berger, M. J., Adaptive mesh refinement for hyperbolic partial differential equations. Journal of Computational Physics, 53, pp. 484-512, 1983.
[20] Berger, M. J. & Colella, P., Local adaptive mesh refinement for shock hydrodynamics. Journal of Computational Physics, 82, pp. 64-84, 1989.
[21] Mencinger, J., Numerical simulation of melting in two-dimensional cavity using adaptive grid. Journal of Computational Physics, 198, pp. 243-264, 2003.
[22] De Vahl Davis, G., Natural convection of air in a square cavity: a bench mark numerical solution. International Journal of Numerical Methods in Fluids, 3, pp. 249-264, 1983.
[23] Dalhuijsen, A.J. & Segal, A., A comparison of finite element techniques for solidification problems. International Journal of Numerical Methods in Engineering, 23, pp. 1829-1986, 1986.
[24] Kosec, G. & Šarler, B., Solution of heat transfer and fluid flow problems by the simplified explicit local radial basis function collocation method. 14th international Conference on FE in Flow Problems, pp. 2007.

This page intentionally left blank

Particle level set implementation on the finite volume method

M. Elmi & M. Kolahdouzan
Department of Civil and Environmental Engineering,
Amirkabir University of Technology (Tehran Polytechnic), Iran

Abstract

Prediction of free surface elevation is one of the most important phenomena in the field of free surface flow modelling. To date different procedures have been introduced to capture the free surface. In the current study, a Eulerian-Lagrangian Method named Particle Level Set (PLS) is developed to predict the location of free surface. The first implementation of this scheme was on the Finite Difference Method. This paper deals with the implementation of Particle Level Set on the Finite Volume mesh. IN the PLS scheme, computational particles were deployed in conjunction with LS function to raise the accuracy of function values. Results obtained from the developed model were compared with experimental and numerical results of dam break cited in the literature which represent the capability of method to predict high gradient free surface changes accurately.

Keywords: free surface flow, particle level set method, finite volume method.

1 Introduction

Multi-phase flow modelling is one of the most practical issues and many researchers try to implement it on their own area of expertise. Prediction of water surface elevation especially in the high gradient situations (i.e. Dam Break and Wave Breaking), is an example of multiphase flow. Different approaches have been introduced to have an accurate prediction of free surface which can be classified into two categories namely free surface tracking and free surface capturing [1].

According to free surface tracking methods, the location of free surface can be predicted by the use of Lagrangian characteristics of the flow. Although the

WIT Transactions on Engineering Sciences, Vol 69, © 2010 WIT Press
www.witpress.com, ISSN 1743-3533 (on-line)
doi:10.2495/AFM100091

implementation of these types of methods in the numerical model is simple and accurate enough in terms of modelling purposes, some limitations have been recognized for complex flows (wave reflection). Different research has been carried out using free surface tracking methods [2–5].

Interface capturing methods are based on the variation of a scalar quantity according to the advection equation. Volume of Fluid (VOF) can be classified in this category. A lot of research has been carried out according to the VOF method [6–10], each of which tries to explore the possibility and raise the accuracy of this method for free surface prediction. Osher and Fedkiw [11] introduced another method in this category called Level Set (LS). This method is not satisfying mass conservation even with the high resolution techniques [12], Therefore it is not so popular in Computational Fluid Dynamics. Different researchers try to combine methods to overcome the problem which was existing in each one individually. Sussmam and Puckett [13] tried to combine LS and VOF methods. In recent years an attempt has been made to improve the LS method in a way that it can be used for free surface prediction. Particle Level Set (PLS) is the result of recent researches in this field [14, 15]. The first implementation of the PLS Scheme was on the Finite Difference method. In this research an attempt has been made to implement the PLS method in the Finite Volume Method mesh.

2 Governing equations

Governing equations of incompressible viscous fluid flow are expressed by the Navier-Stokes equations which can be shown as follows [1]:

$$\frac{\partial \boldsymbol{u}}{\partial t} + \boldsymbol{u}.\boldsymbol{\nabla}\boldsymbol{u} = \nu\nabla^2\boldsymbol{u} - \frac{1}{\rho}\boldsymbol{\nabla}P + S \qquad \nabla.\mathrm{u} = 0 \tag{1}$$

where: $\boldsymbol{u}$ is the velocity vector, ν is the fluid viscosity, P is the pressure and S is the body forces.

To discretize governing differential equations based on the Finite Volume method, it is essential to integrate these equations over the control volume. In the current study, discretization of advection and viscous terms in equations (1) were carried out by the use of a central difference scheme (CDS). In order to prevent non-physical oscillation in the pressure field due to CDS application, it was suggested to use a special interpolation scheme for advection acceleration terms in the momentum equation which can be shown as [16]:

$$\boldsymbol{u}_f = LI(\boldsymbol{u}) + \frac{\Delta t}{\rho}\frac{\partial P}{\partial \boldsymbol{n}} \tag{2}$$

where: $LI(\boldsymbol{u})$ is the linear interpolation of velocity components, Δt is the time step and $\boldsymbol{n}$ is the normal vector to control volume face.

In order to couple momentum and continuity equations, a Fractional Step method was applied [17]. In the first step, a momentum equation was solved to

obtain velocity components in the absence of pressure terms (mid-term velocities):

$$\frac{\tilde{u}_i - u_i^n}{\Delta t} + \frac{\partial u_i u_j}{\partial x_j} = \nu \frac{\partial^2 u_i}{\partial x_j \partial x_j} + S_i \tag{3}$$

In order to include pressure effect on the velocity components in the new time step the following relationship was used [17]:

$$u_i^{n+1} = \tilde{u}_i - \frac{1}{\rho}\frac{\partial p^{n+1}}{\partial x_i} \tag{4}$$

By which can be reformulated as equation (5):

$$\nabla^2 p^{n+1} = \rho \nabla . \tilde{\boldsymbol{u}} \tag{5}$$

Equation (5) is a Poisson type equation which was used to obtain pressure field in the study area. Solution algorithm for governing equations of fluid flow can be summarized as:

1) Solving equation (3) to obtain mid-term velocity components ($\tilde{\boldsymbol{u}}$).
2) Equation (5) was solved to obtain pressure field.
3) To correct the velocity components values equation (4) was deployed.

To satisfy conservation of momentum, it is essential to correct velocity components obtained from step (1) in step (3) using pressure gradient. In multi-phase flow, the discretization procedure for Poisson equation is very important as the density of fluid is suddenly changes on the free surface. In the current study to discretize Poisson equation, the broken line method was deployed [18]. According to broken line method (Figure 1), in free surface grids, fluid density was calculated by the following relationship [18]:

$$\rho = \alpha\rho_1 + (1-\alpha)\rho_2 \tag{6}$$

where: α is the volumetric ratio of two fluids and ρ is the fluid density. The pressure values in the side centre of each computational grid can be evaluated by equation (7):

$$P_f = \frac{P_A\rho_B\delta_B + P_B\rho_A\delta_A}{\rho_B\delta_B + \rho_A\delta_A} \tag{7}$$

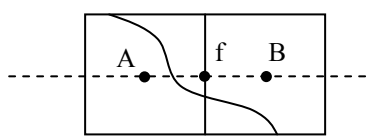

Figure 1: Broken line discretization method in each computational grid cell.

3 Particle level set method

The level set function magnitude in each computational point is the smallest distance between free surface and that point. In addition, this function has different sign in each phase of fluid (Figure 2). Computational particles were deployed in conjunction with LS function to raise the accuracy of function values [11].

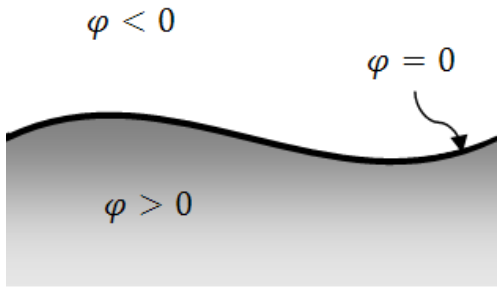

Figure 2: LS function.

The level set function has different geometrical properties like as [11]:

$$|\nabla\varphi| = 1 \tag{8}$$

$$\boldsymbol{n} = \frac{\boldsymbol{N}}{|\boldsymbol{N}|} = \frac{\nabla\varphi}{|\nabla\varphi|} = \nabla\varphi \tag{9}$$

where: $\boldsymbol{n}$ is the normal vector to the free surface and φ is the LS function. The governing equation of LS function is the advection type and can be written as [11]:

$$\frac{\partial\varphi}{\partial t} + \boldsymbol{u}.\nabla\varphi = 0 \tag{10}$$

In order to transfer the LS function in the PLS method, a semi-Lagrangian approach was used. According to this approach, to obtain the new value for the LS function in each grid cell, it is essential to assume that the cell centre was moved equal to $-\boldsymbol{u}.\Delta t$ and the LS value in this new position was considered as the LS value for the specified grid cell. In the current study, LS function gradient have been calculated through equation (11):

$$\nabla\varphi = \frac{\sum_{faces}\varphi_f \boldsymbol{n}_f A_f}{V} \tag{11}$$

where: A_f is the computational cell area, V is the cell volume and $\boldsymbol{n}_f$ is the unit vector normal to the surface.

It is essential to point out that the LS function is solved in a very thin band close to the free surface. Computational errors where produced in the transport of each LS function, which in turn cause uncertainty on the free surface position. Many techniques were introduced to overcome this problem [11]. In the current study, the Fast Marching method was deployed to reduce inaccuracy in the prediction of free surface elevation [19].

Computational particles were used to correct the LS function transfer in the computational domain. These particles are distributed close to the initial free surface in a way that each particle radius introduces the distance of particle and free surface. In addition, the radius of each particle can be positive or negative according to its placement in different phase. To obtain more accurate results, these particles can have overlap in terms of their placement near the water surface (Figure 3). In Figure 3 the hatched area represents the difference between the real situation and model prediction for a straight line.

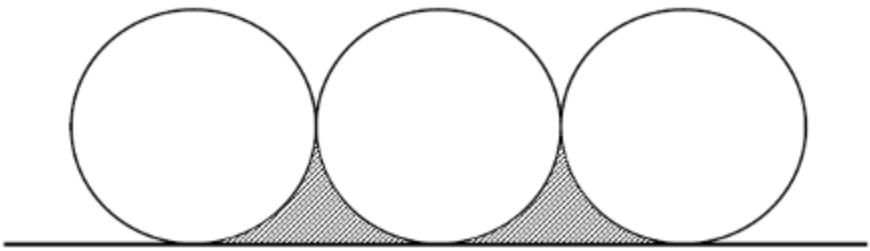

(a) Three particles without overlap

(b) Six particles with overlap

Figure 3: Illustration of a straight line with particles.

In each time step, the placement of each particle was calculated by the 3rd order TVD-Runge Kutta method and then, the value of the LS function was corrected with these particles. The step by step method of correction can be summarized as [14]:

1) Those particles which have distance more than their radius outside of their own fluid phase with free surface, considered as an escaped particle. These particles are used to correct the free surface position.

2) By generating a mesh for computational domain, the placement of each particle in the grid generation was investigated and the value of LS function for surrounding grid cells was calculated as follows:

$$\varphi_p = r_p - \left|\boldsymbol{x} - \boldsymbol{x}_p\right|.\mathrm{sgn}(r_p) \tag{12}$$

3) LS function is corrected according to equations (13)-(15):

$$\varphi^+ = \max\left(\varphi_p, \varphi_{\mathrm{old}}\right), \forall p \in E^+ \tag{13}$$

$$\varphi^- = \min\left(\varphi_p, \varphi_{\mathrm{old}}\right), \forall p \in E^- \tag{14}$$

$$\varphi_{\mathrm{new}} = \begin{cases} \varphi^+ \text{ if } |\varphi^+| \le |\varphi^-| \\ \varphi^- \text{ if } |\varphi^+| > |\varphi^-| \end{cases} \tag{15}$$

where E^+ is all positive-radius escaped particles and E^- is all negative-radius escaped particles. It is essential to point out that the difference between above method and main PLS method is on the selection of surrounding mesh cells in order to correct LS function. It is worth to point out that this method can be used on the unstructured finite volume mesh which raised the capability of the method for using in complex geometry.

4 Model verification

In order to represent capability of model to represent free surface elevation, a dam break problem has been chosen (Figure 4). The uniform 100*75 grid mesh with 0.0001sec time step has been used for modelling purposes. A no-slip boundary condition was applied for all of solid boundaries. Initial free-surface elevation and initial particle distribution are shown in figure 5. The predicted model results for free surface elevation and also experimental measurements are presented in figure 6. From the comparison of predicted and measured values for free surface elevation, it can be concluded that the developed model which consists of the PLS approach can well predict the free surface. In addition model results were compared with experimental results and other numerical models cited in the literature (Figure 7). From figure 7 it can be concluded that in the early stages of modelling, the numerical model results based on the Lagrangian approach are more accurate while close to the end of modelling simulation time, the LS approach is more accurate in terms of predicting free surface elevation.

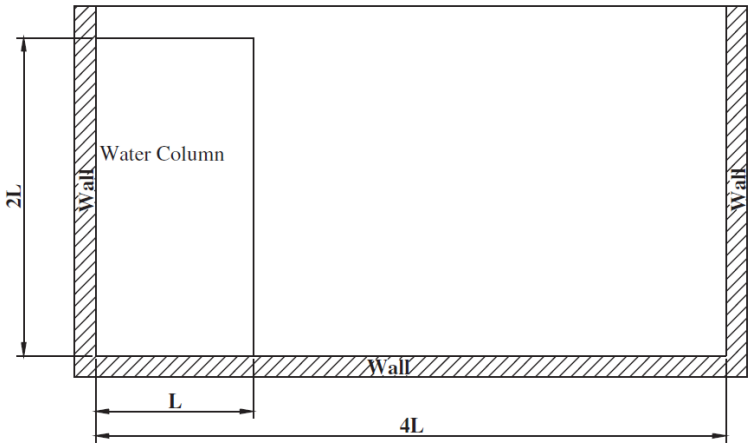

Figure 4: Geometry of dam break problem.

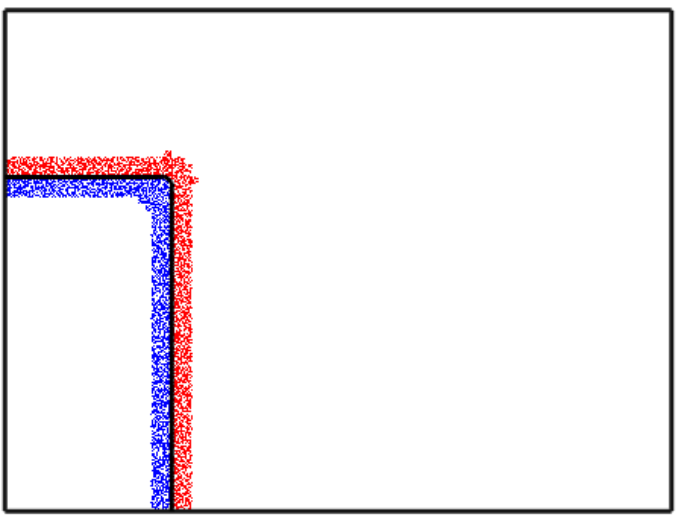

Figure 5: Initial particle distribution in dam break problem.

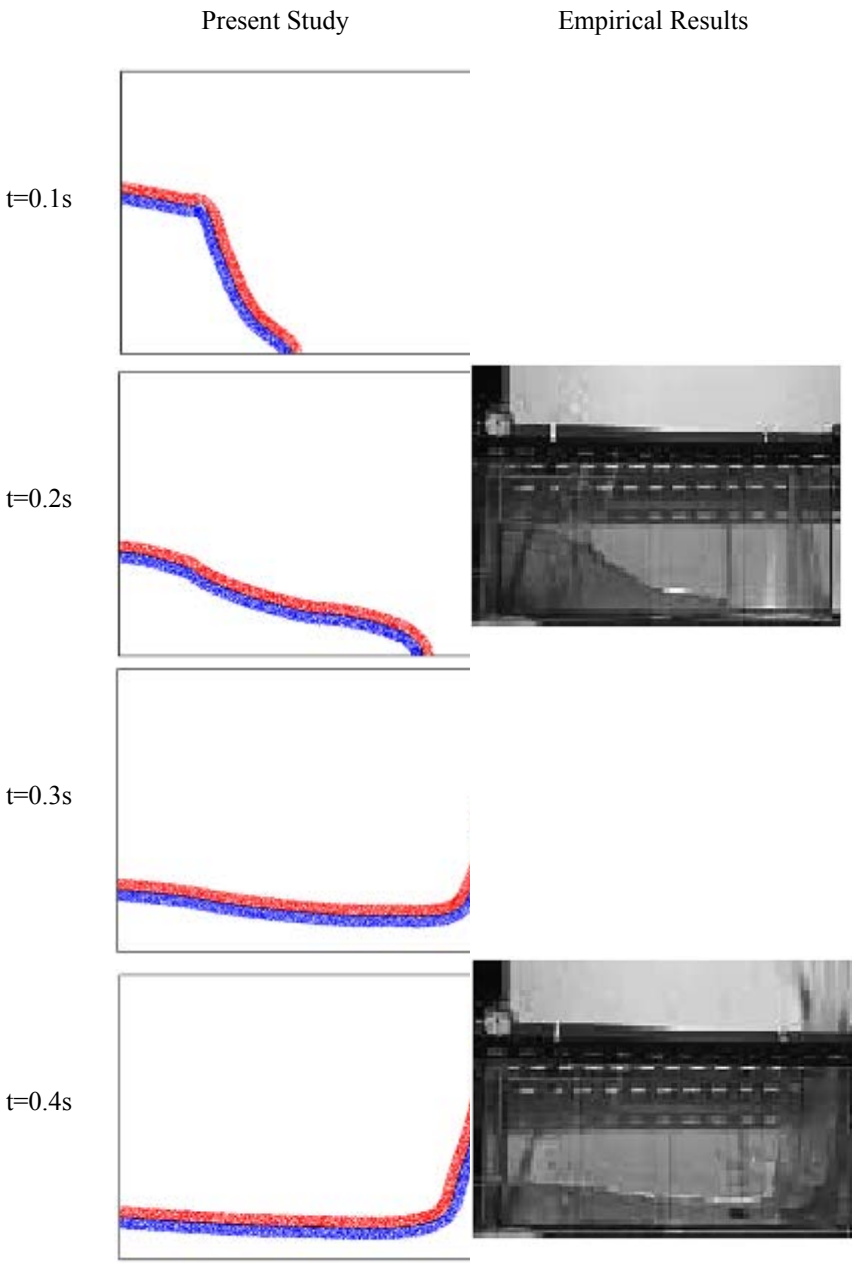

Figure 6: Free surface variation and computational particles.

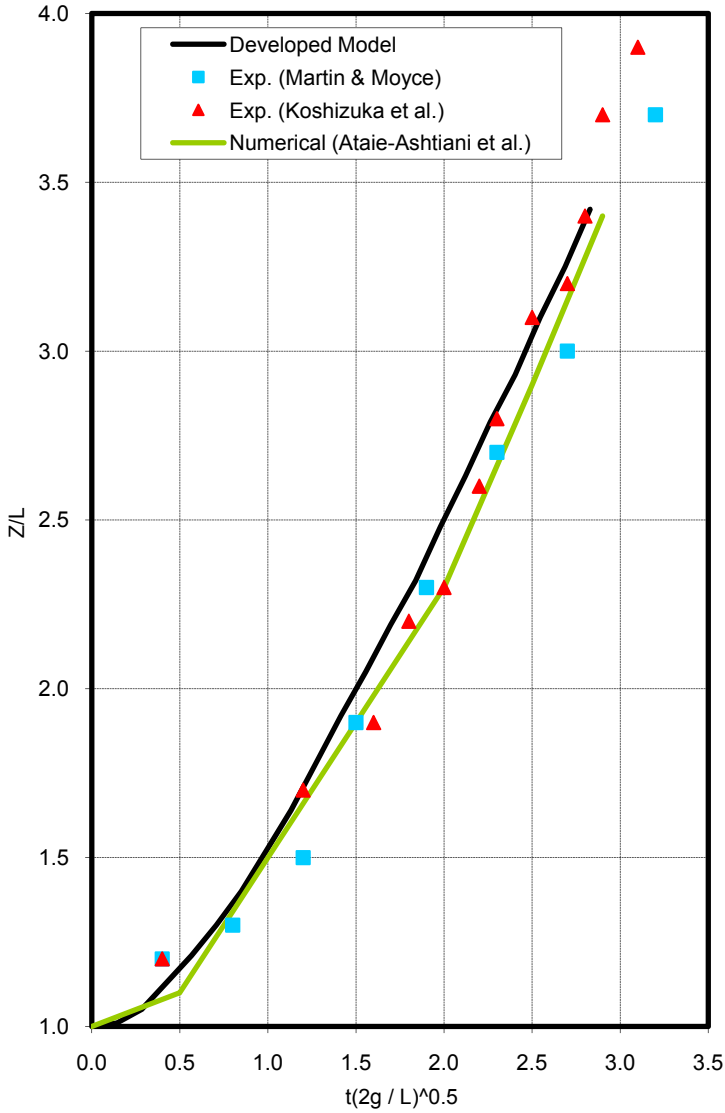

Figure 7: Comparison of measured and predicted values of water in front.

5 Conclusion

Free surface prediction is one of the most important issues in the field of fluid dynamics. The problem is more critical in coastal area were the short waves are the most dominant hydrodynamic phenomena. In this research study the PLS

method has been chosen to investigate its capability on the free surface prediction. Results obtained from the developed model show that the PLS method can well predict the free surface elevation in comparison with measurements and other numerical models cited in the literature.

References

[1] Ferziger, J., Peric, M., 1996. Computational methods for fluid dynamics. Springer Verlag.
[2] Raad, P., Chen, S. and Johnson, D., 1995. The Introduction of Micro Cells to Treat Pressure in Free Surface Fluid Flow Problems. J. Fluids Eng. 117, 683–690.
[3] Torres, D. and Brackbill, J., 2000. The Point-Set Method: Front Tracking without Connectivity. J. Comp. Phys. 165, 620–644.
[4] Tryggvason, G., Bunner, B., Esmaeeli, A., Juric, D., Al-Rawahi, N., Tauber, W., Han, J., Nas, S. and Jan, Y.-J., 2001. A Front-Tracking Method for the Computations of Multiphase Flow. J. Comp. Phys. 169, 708–759.
[5] Unverdi, S.-O. and Tryggvason, G., 1992. A Front-Tracking Method for Viscous, Incompressible, Multi-fluid Flows, J. Comp. Phys. 100, 25–37.
[6] Ubbink, O., Issa, R. I., 1999. A method for capturing sharp fluid interfaces on arbitrary meshes. J. of computational physics 153, 26-50.
[7] Puckett, E., Almgren, A., Bell, J., Marcus, D. and Rider, W., 1997. A High-Order Projection Method for Tracking Fluid Interfaces in Variable Density Incompressible Flows. J. Comp. Phys. 130, 269–282.
[8] Hirt, C. and Nichols, B., 1981. Volume of Fluid (VOF) Method for the Dynamics of Free Boundaries. J. Comp. Phys. 39, 201–225.
[9] Williams, M., Kothe, D. and Puckett, E., 1999. Approximating Interfacial Topologies with Applications for Interface Tracking Algorithms. 37th AAIA Aerospace Sciences Meeting, 99–1076, AIAA.
[10] Williams, M., Kothe, D. and Puckett, E., 1999. Convergence and Accuracy of Kernal-Based Continuum Surface Tension Models. Fluid Dynamics at Interfaces, pp. 347–356, Cambridge University Press.
[11] Osher, S., Fedkiw, R., 2002. Level Set Methods and Dynamic Implicit Surfaces, Springer.
[12] Jiang, G.-S. and Peng, D., 2000. Weighted ENO Schemes for Hamilton-Jacobi Equations. SIAM J. Sci. Comput 21, 2126–2143.
[13] Sussmam, M. and Puckett, E., A Coupled Level Set and Volume of Fluid Method for Computing 3D and Axisymmetric Incompressible Two-Phase Flows, J. Comp. Phys. 162, 301–337 (2000).
[14] Enright, D., Fedkiw, R., Ferziger, J. and Mitchell, I., 2002. A Hybrid Particle Level Set Method for Improved Interface Capturing. J. Comput. Phys. 183, 83-116.
[15] Enright, D., Losasso, F. and Fedkiw, R., 2005. A Fast and Accurate Semi-Lagrangian Particle Level Set Method. Computers and Structures 83, 479-490.

[16] Zang, Y., Street, R.L. and Koseff, J.R., 1994. A non-staggered fractional step method for time-dependent incompressible Navier-Stokes equations in curvilinear Coordinate. J. of computational physics 114, 18-33.
[17] Kim, D., Choi, H., 2000. A second-order time-accurate finite volume method for unsteady incompressible flow with hybrid unstructured grids. J. of computational physics 162, 411-428.
[18] Jahanbakhsh, E., Panahi, R., Seif, M.S., 2007. Numerical simulation of three-dimensional interfacial flows. International Journal of Numerical Methods for Heat & Fluid Flow 17, 384-404.
[19] Tsitsiklis, John N., 1995. Efficient Algorithms for Globally Optimal Trajectories. IEEE TRANSACTIONS ON AUTOMATIC CONTROL 40.
[20] Ataie-Ashtiani, B., Farhadi, L., 2006. A stable moving-particle semi-implicit method for free surface flows. Fluid Dynamics Research 38, 241-256
[21] Koshizuka, S., Nobe, A., Oka, Y., 1998. Numerical analysis of breaking waves using the moving particle semi-implicit method. Int. J. Numer. Methods Fluids 26, 751–769.
[22] Martin, J.C., Moyce, W.J., 1952. An experimental study of the collapse of liquid columns on a rigid horizontal plane. Philos. Trans. R. Soc. London Ser. A, 244–312.

This page intentionally left blank

Bidimensional modeling for incompressible viscous flow using the Circumcenter Based Approach in an unstructured grid

A. L. Fazenda[1] & J. S. Travelho[2]
[1]*Department of Science and Technology,*
Federal University of São Paulo, São José dos Campos-SP, Brazil
[2]*Computing and Applied Mathematics Laboratory,*
National Institute for Space Research, São José dos Campos-SP, Brazil

Abstract

A possible approach for modeling two-dimensional convection-diffusion problems in a cell-centered scheme with an unstructured triangular grid is the use of the Circumcenter, that is the center of the circumference that passes through the vertices of the triangular volume. This point is used to calculate all variables involved in the numerical simulation, and a Finite Volume Method was use to discretize the equations of an Incompressible Viscous Flow. This work analyzes classical problems of bidimensional flow, such as the inlet region of a Poiseuille flow, lid-driven cavity, backward-facing step and free convection with Boussinesq approximation. The application of the method has been shown to be a simple and flexible scheme and the results fit the analytical, experimental or numeric data presented in the literature.

Keywords: unstructured grid, cell-centered scheme, incompressible flow, Circumcenter Approach.

1 Introduction

The numerical modeling of incompressible viscous flow has received special attention in recent decades, in particular because of the Velocity–Pressure relationship. Therefore, numerous different strategies to create equations that model the phenomena have been developed.

WIT Transactions on Engineering Sciences, Vol 69, © 2010 WIT Press
www.witpress.com, ISSN 1743-3533 (on-line)
doi:10.2495/AFM100101

In this work, a co-located cell-centered scheme in the primitive variables is developed, under a triangular unstructured grid. The viscous term of the Navier-Stokes equation is discretized with the "Circumcenter Based Approach" (CBA) [9], and an up-wind scheme is used in the convective term.

The pressure field is calculated with an artificial equation, created by applying a divergent operator in the Momentum equation, and considers Neumann boundary conditions. The final algorithm is easy to use and understand, without equations to correct or under-relax any of the primitive variables used. The Linear System Equations involved are calculated by a specific solver, according to the form of the matrix resulting.

Computational benchmarks were realized in classical 2D flow problems, considering an incompressible, viscous and laminar flow. The problems are: flow under flat plates (Poiseuille Flow), Lid-driven cavity flow, suddenly expansion in a step (Backward-facing step) and natural or free convections problems (with Boussinesq modeling approach).

2 Basic equations

The equations used, in this document, for the numerical simulation of an uncompressible flow in steady state, will be:

$$\nabla \cdot \left(\rho \vec{V}\right) = 0, \tag{1}$$

$$\rho \nabla \cdot \left(\vec{V}\vec{V}\right) = \mu \nabla^2 \vec{V} + \rho \vec{g} - \nabla P, \tag{2}$$

$$\nabla \cdot \left(\rho \vec{V} T\right) = \nabla \cdot \left(\frac{k}{c_P} \nabla T\right), \tag{3}$$

The equation (1) represents the continuity equation; the equation (2) represents the *momentum* equation and (3) represents the energy equation. In above equations, the symbol ρ defines the fluid density; the vector $\vec{V}$ defines the velocity vector; μ represents the viscosity; P represents the Pressure field; T defines the temperature; κ the thermal conductibility and C_p the specific heat at constant pressure.

It is important to mention that in all numerical simulations presented in this paper we consider an incompressible laminar flow with constant density and viscosity.

In the case of free convection, the flow is not isothermal; however, this temperature buoyancy should not cause significant changes in density and viscosity of the fluid.

3 The relationship between velocity and pressure in incompressible flows

In incompressible flows, there is not an explicit equation to calculate the pressure evolution, and it is common to use the momentum and continuity equations to derive a new equation to determine the required pressure values.

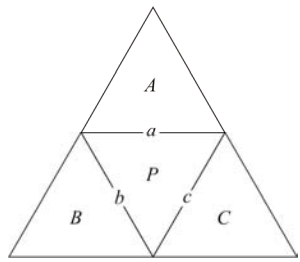

Figure 1: Stencil for the calculation of each triangular element.

In this case, primitive variables with a Poisson equation will be used to allow pressure determination, following Gresho and Sani [1]. It can be obtained through the application of a divergent operator in the momentum equation (2). After some rearrangements, it can be defined as:

$$\nabla^2 P = \nabla \cdot \left[-\rho \nabla \cdot \left(\vec{V}\vec{V} \right) + \mu \nabla^2 \vec{V} + \rho \vec{g} \right] \tag{4}$$

So, the equations to be used in the numerical simulation will be: (1), (2) and (4). For non-isothermal cases the equation (3) must be added and solved also.

4 Circumcenter Based Approach (CBA)

To discretize the partial differential equations defined by (1), (2), (3) and (4) the Finite Volume Method [10] will be used. With the unstructured triangular grid used, it is necessary to integrate each PDE of the problem in the triangular cell. Considering the stencil in figure 1, each central control volume will be called "*P*" and the three neighbors' cells will be called *A, B, C*. The cell faces for *P* will be defined *a, b, c,* and each of them share the *P* cell with *A, B* and *C* cell, respectively.

The resultant discretized equation for (2) will be:

$$\rho \oint_S \left(\hat{n} \cdot \vec{V} \right) \vec{V} dS = \mu \oint_S \hat{n} \cdot \left(\nabla \vec{V} \right) ds + \rho \vec{g} A - \left(\hat{n}_a P_a S_a + \hat{n}_b P_b S_b + \hat{n}_c P_c S_c \right) \tag{5}$$

where n_x define the normal vector to face x, S_x define the length of face x and A is the area of the cell P.

The solution for diffusive problems in structured grid is very simple because the cell faces are perpendicular to the line linking the two neighbor cell centers. These characteristics, generally, are not found in a triangular unstructured grid. The use of a vertex centered scheme with Voronoi Diagrams causes a return to this facility.

Another way to maintain these characteristics in triangular unstructured grids is the use of CBA [9], i.e., the use of the circumcenter of each triangular cell like the center of the element. Remembering that the center of a circle or sphere that

touches each cell vertex is the point where the respective mediatrices crosses each other. So the term $\oint_S \hat{n} \cdot \left(\nabla \vec{V}\right) ds$ can be approximated by:

$$\oint_S \hat{n} \cdot \left(\nabla \vec{V}\right) ds = \sum_{i=a,b,c} \frac{\partial\left(\vec{V}\right)}{\partial n_i} S_i \cong \sum_{i=a,b,c} \frac{\vec{V}_{i_i} - \vec{V}_P}{d_i} S_i \tag{6}$$

where *d* defines the distance between the center of cell *P* and the neighbor *X*. For the convective term, an upwind scheme has been used.

5 Boundary conditions

5.1 Velocity with the Dirichlet condition

In this first case the velocity on face *"a"*, of the triangular cell, in the boundary will be predefined:

$$\vec{V}_a \cdot \hat{n}_a = C \tag{7}$$

A special and very common case, of Dirichlet condition, to be noticed is the no slip condition:

$$\vec{V}_a \cdot \hat{n}_a = 0 \tag{8}$$

In both situations the convective contribution of face *"a"* is defined like a constant or null, respectively to (7) and (8). The pressure at the boundary, with no slip condition (8), can be considered to be constant. In the case of non-null value (7) the pressure at the boundary can be approximated in another way.

5.2 Null velocity gradient (Neumann condition)

This kind of boundary condition is applied specially in the outlet of a Hagen-Poiseuille flow. Assuming that the face *"a"* of a cell is at the boundary, we have:

$$\left.\frac{\partial \vec{V}}{\partial n}\right|_a = 0 \tag{9}$$

In this case, the value of the velocity vector in the center of *A, B* or *C* cell, is equal to the value in the cell center *P*. The value of the pressure in the boundary can be determined by an extrapolation in the adjacent cells.

5.3 Adiabatic boundary with the no slip condition

The first derivate of *T* in the face *"a"* of a cell will be null:

$$\left.\frac{\partial T}{\partial n}\right|_a = 0 \tag{10}$$

The condition defined in equation (8) will be applied. The contribution of the diffusive term in Energy equation (3) for the face *"a"* will be null, and, because of (8), the contribution of the convective term in (3) will be null too.

5.4 Boundary with predefined temperature and the no slip condition

The value of temperature at the boundary is predefined:

$$T_a = C \tag{11}$$

The condition defined in equation (8) must be applied like in the previous case.

6 Results

In this section the result for the application of Circumcenter Based Approach for Poiseuille flow, lid-driven cavity flow, backward-facing step flow and free or natural convection are presented.

6.1 Poiseuille flow

The results presented here were obtained solving an incompressible laminar viscous flow in steady state considering isothermal conditions. Brodkey [2] called the flow in a channel formed by two flat plates by Poiseuille flow, and in this case, in a fully developed flow, the maximum of the velocity parallel to the plates are obtained in the middle of the boundary distance, and corresponds to 150% of the medium velocity.

The two dimensional domain can be viewed in figure 2.

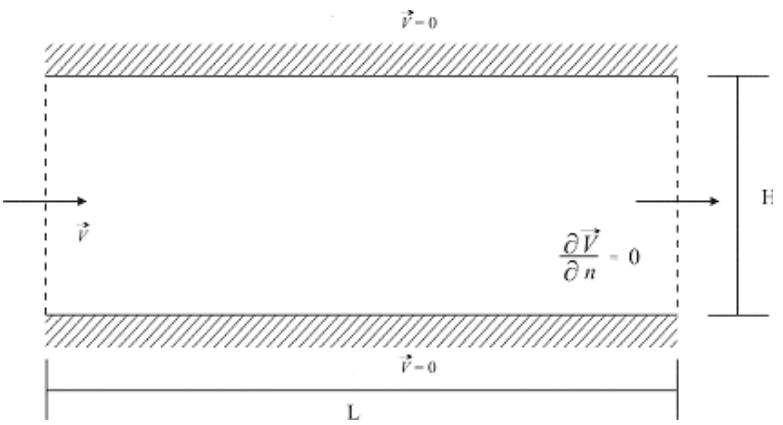

Figure 2: Poiseuille flow domain.

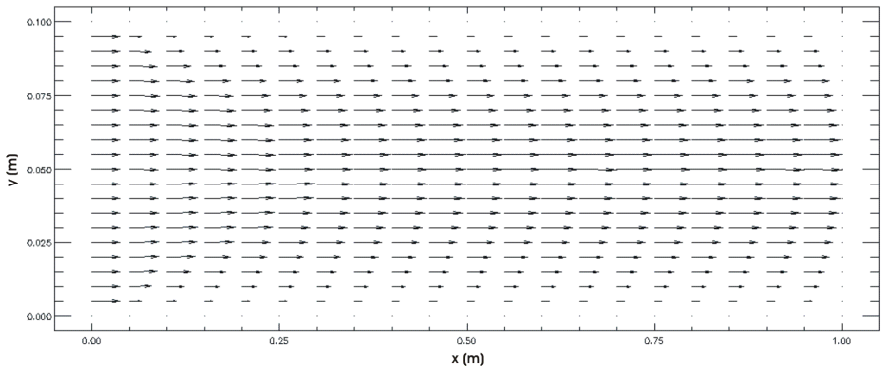

Figure 3: Flow for Re = 100.

The length L is 10 times larger than the height H. The triangular unstructured grid uses 18864 vertex and 36846 triangular cells. The velocity in the inlet of the domain is a flat profile. The result showing the velocity vector for Reynolds 100 (fully developed) can be viewed in figure 3.

The position where the fluid can be considered as fully developed $\left(\partial \vec{V} / \partial x \cong 0\right)$ depends upon the Reynolds number. For simulations with Reynolds 400 and 800 the flow is not fully developed at the outlet of the domain. In Schlichting [3] is defined a simple equation to estimate the length of the developing area (Le):

$$\frac{Le}{H} = 0.04\,\mathrm{Re} \tag{12}$$

The simulation shows that for Reynolds 100 the relative medium value for $\partial \vec{V} / \partial x$ is lower than 0.1% in the cell with the longitudinal coordinate is located after 0.35m and for Reynolds 200 the same value is obtained for 0.75m, which agrees with (12).

6.2 Lid-driven cavity flow

In this case the interior of a cavity is filled with fluid and, in the upper boundary, there is a layer of the same fluid moving with parallel uniform velocity. The 2D domain, with equal length L and height H, can be viewed in figure 4.

In figure 5 it is possible to see three vortexes in the streamlines visualization for Reynolds 1000.

Using Ghia et al. [4] to compare the results of the method, it is possible to see in figures 6 and 7, the velocity profile at the line that crosses $x = L/2$ and $y = H/2$, for Reynolds 100 and 1000, respectively. Remembering that the data in the lines x and y are obtained with a linear interpolation.

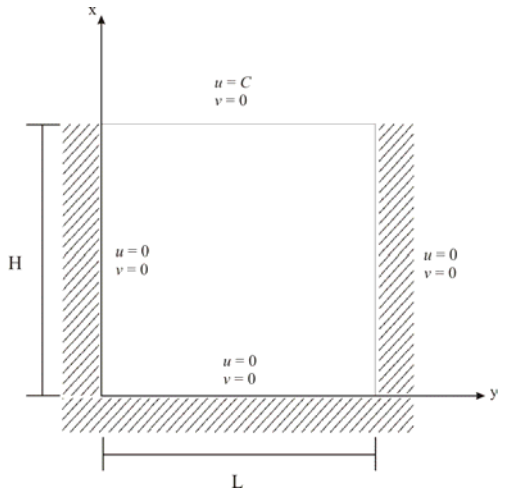

Figure 4: Lid-driven cavity flow domain.

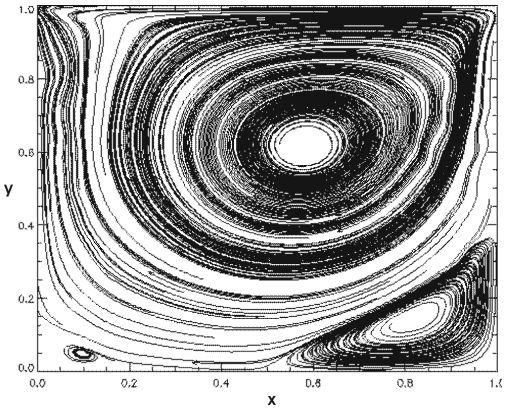

Figure 5: Streamlines for Reynolds 1000 in a lid-driven cavity.

6.3 Backward-facing step flow

This problem consists of a flow with inlet in a straight channel (height h) that suddenly opens in a larger channel (height H). The relationships between the different heights are: $H/h = 2$ and the length L will be $2H$. The tests are performed with Reynolds 150, and the direction of the velocity vector can be viewed in figure 8:

In Zhao and Zhang [12] it is possible to found physical and numerical results for Reynolds 150. The location of the main vortex after the step and the re-attachment point in [13] experimental results can be compared with the numerical data obtained in this work in table 1.

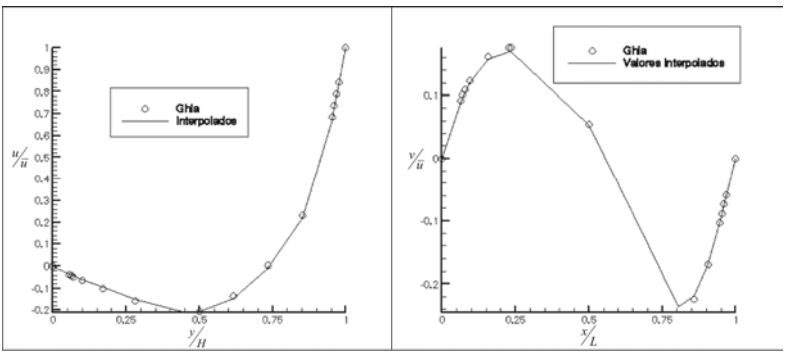

(a) (b)

Figure 6: Velocity profile interpolated at $x = L/2$ (a) and $y = H/2$ (b) for Reynolds 100.

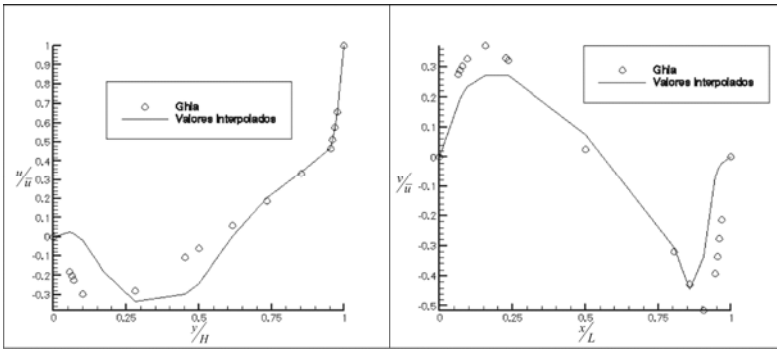

(a) (b)

Figure 7: Velocity profile interpolated at $x = L/2$ (a) and $y = H/2$ (b) for Reynolds 1000.

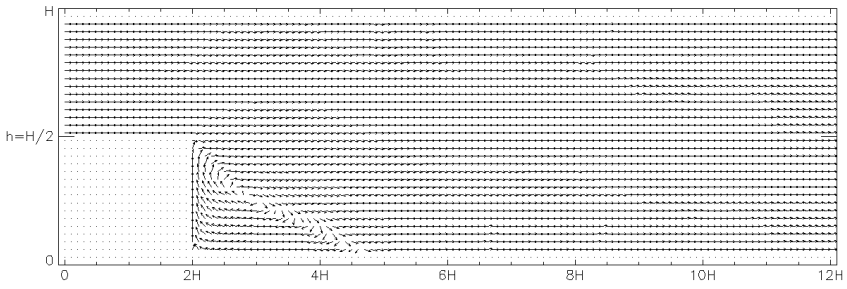

Figure 8: Direction of the velocity vector in Reynolds 150.

Table 1: Location of the main vortex and re-attachment point.

	X coordinate for vortex	Y coordinate for vortex	Re-attachment point
Zhao & Zhang [12]	0,925 H	0,29 H	2,25 H
CBA	0,9 H	0,24 H	2,6 H

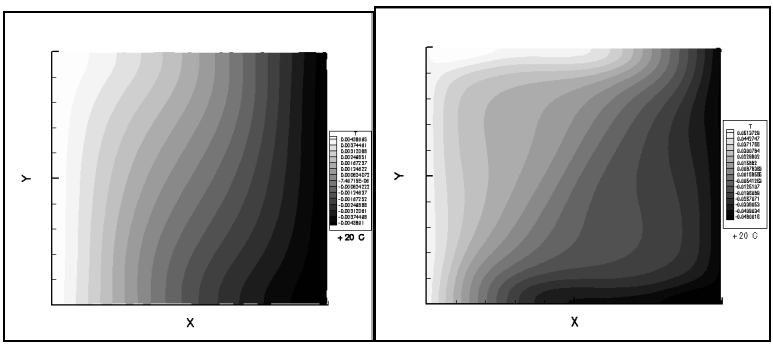

(a) (b)

Figure 9: Temperature field for Ra = 10^3 (a) and Ra = 10^4 (b).

Table 2: Nusselt number in free convection.

	Ra = 10^3	Ra = 10^4
Vahl Davis [5]	1,116	2,234
Actual simulation	1,06005	2,01911

6.4 Free or natural convection

The main characteristics of free convection are a natural flow of the fluid because of density buoyancy when submitted to temperature or pressure variations. In this problem the density buoyancy occurs because of temperature gradient in a bidimensional domain with a box shape, where the horizontal boundaries are adiabatic, the right vertical boundary is consider hotter than medium temperature and the left vertical boundary is colder than the same reference value, and remembering that the Boussinesq approximation for the body force ρg is used in momentum equation.

The shaded graphic of temperature field for Rayleigh number (Ra) equal 10^3 and 10^4 can be checked in figures 9(a) and 9(b).

Table 2 allows checking the Nusselt number calculated by the current method and the Nusselt number numerically calculated by Vahl Davis [5].

7 Conclusions

The Pereira Filho [13] work is the first use of CBA to solve incompressible flow problems, however, in his last work, only the Hagen-Poiseuille flow are solved.

The 3D grid used was triangular and unstructured in x and y directions, and structured in the z direction (the direction of the main stream). In this work there is no structured grid in any direction and it is possible to notice recirculation vortices in almost of cases tested, including a new variable (temperature) calculation in one of them (free convection).

Analyzing the results presented, it is possible to conclude that the CBA can be used in an alternative way to modeling 2D incompressible laminar flow problems under triangular unstructured grids. The resulting discrete equations, in primitive variables, are easy to obtain and understand, without use of staggered grids, corrections or under-relax procedures.

Because of simplicity, the CBA method presents a small algorithm complexity and a low computational costs when comparing other methods used with the same purpose and characteristics, like Frink [6], Mathur and Murthy [7], Despotis and Tsangaris [8], because needs a minor arithmetic operations per "timestep".

The benchmarks performed shows promising behavior, agreeing with classical 2D incompressible problems. However, numerical instabilities were found with flows with higher Reynolds Numbers. The future inclusion of a turbulent modeling scheme in CBA needs to be investigated with this kind of 2D flows. Another problem encountered shows that the method is grid dependent, needing efficient grid generators, specially to prevent the generation of triangular element with internal angles bigger than 90º, like depicted in Date [11]. In this case, Delaunay triangulations minimize the problem.

This kind of problem (triangular element with internal angles bigger than 90º) makes the circumcenter be localized outside the control volume. However, the problem affects also Voronoi schemes (Vertex centered), creating polygons with sides that do not cross triangular faces. In 3D flows similar problems can occurs with tetrahedral elements (circumsphere localized outside the control volume).

For the future the authors suggests a better investigation of 3D case (preliminary analyzes shows numerical precision lose), and comparative tests with other classical approaches, like Voronoi schemes and Frink [6] scheme. A compressible modeling case and an inclusion of turbulent scheme can be explored too.

References

[1] Gresho, P.M.; Sani, R.L. On pressure boundary conditions for the incompressible Navier-Stokes equations. *International Journal for Numerical Methods in Fluids,* v. 7, p. 1111-1145, 1987.

[2] Brodkey, R.S. *The phenomena of fluid motions*. Massachusetts: Addison-Wesley, 1967. 737 p.

[3] Schlichting, H. *Boundary layer theory*. 7. ed. New York: McGraw-Hill, 1979. 817 p.

[4] Ghia, U.; Ghia, K.N.; Shin C.T. High-Re solutions for incompressible flow using the Navier-Stokes equations and a multigrid method. *Journal of Computational Physics,* v. 48, p. 387-411, 1982.

[5] Vahl Davis, G. Natural convection of air in a square cavity: a bench mark numerical solution. *International Journal for Numerical Methods in Fluids,* v. 3, p.249-264, 1983.
[6] Frink, N.T. Recent progress toward a three-dimensional unstructured Navier-Stokes flow solver, Reno: NASA Langley Research Center, 1994. *AIAA Paper* 94-0061. 24 p.
[7] Mathur, S.R.; Murthy, J.Y. A pressure-based method for unstructured meshes. *Numerical* Heat *Transfer, Part B*, v. 31, n. 2, p. 195-215, 1997.
[8] Despotis, G.K.; Tsangaris, S. Fractional step method for solution of incompressible Navier-Stokes equations on unstructured triangular meshes. *International Journal for Numerical Methods in Fluids*, v. 20, p. 1273-1288, 1995.
[9] Travelho, J.S.; Fazenda, A.L.; Enari, E.H. Abordagem pelo circuncentro para malhas não estruturadas em transferência de calor (The Circumcenter Based Approach for unstructured grid in heat transfer). In: *Congresso Brasileiro de Engenharia Mecânica (Brazilian Congress in Mechanical Engineering)*, 15., Águas de Lindóia, 1999. *Proceedings*.
[10] Patankar, S.V. *Numerical heat transfer and fluid flow.* New York: Hemisphere, 1980. 197 p.
[11] Date, A.W. Solution of transport equations on unstructured meshes with cell-centered colocated variables. Part I: Discretization. *International* Journal *of Heat and Mass Transfer*, V. 48, p. 1117–1127, 2005
[12] Zhao, Y.; Zhang, B. A high-order characteristics upwind FV method for incompressible flow and heat transfer simulation on unstructured grids. *Computational Methods Applied Mechanics Engineering*, v. 190, p. 733-756, 2000.
[13] Pereira Filho, N. Simulação de escoamentos incompressíveis tridimensionais com uso da abordagem baseada no circuncentro (Tridimensional incompressible flow simulation with circumcenter based approach). São José dos Campos. 126 p. PHD Thesis (Applied Computing) – National Institute for Space Research, 2000

This page intentionally left blank

Pressure-enthalpy coupling for subsonic flows with density variation

M. Emans[1], S. Frolov[2], B. Lidskii[2], V. Posvyanskii[2],
Z. Žunič[3] & B. Basara[3]
[1]*IMCC, Linz, Austria*
[2]*N. N. Semenov Institute of Chemical Physics, Moscow, Russia*
[3]*AVL List GmbH, Graz, Austria*

Abstract

The method we present is derived from the SIMPLE algorithm. Instead of solving the linear equations for each variable and the pressure-correction equation separately in a so called segregated manner it relies on the solution of a linear system that comprises the discretisation of enthalpy and pressure-correction equation that are linked through physical coupling terms. These coupling terms are deduced from a more accurate approximation of the density update (compared to standard SIMPLE method) that is reasonable with respect to the thermodynamic formulation of the density increment. The method leads to a considerable acceleration of the non-linear SIMPLE convergence not only in cases characterised by a global density change due to the rise of the pressure, but also if the enthalpy is merely spatially distributed in the computational domain. In this contribution we will first discuss the key idea of the new method and compare it to established techniques. Then we will demonstrate its advantages in terms of computational efficiency and robustness for industrial CFD applications, e.g. combustion and engine flow calculations on unstructured grids.
Keywords: finite volumes, pressure-enthalpy coupling, variable-density flow, CFD.

1 Introduction

Robust methods that provide an appropriate approximation of the solution of the Navier–Stokes equations for CFD (computational fluid dynamics) applications employ finite volumes for the spatial discretisation and master the non-linearity of


WIT Transactions on Engineering Sciences, Vol 69, © 2010 WIT Press
www.witpress.com, ISSN 1743-3533 (on-line)
doi:10.2495/AFM100111

the system as well as the coupling of the momentum equations and the continuity equation by iterative algorithms derived from SIMPLE ("semi-implicit method for pressure-linked equations"); they are used to calculate the velocity and the pressure field.

Many ways have been proposed to accelerate the convergence of the SIMPLE algorithm in the genuine formulation of Patankar and Spalding [1] that tends to be unsatisfactory in some situations. Among the most important ones are SIMPLER, SIMPLEC, and PISO, see van Doormal and Raithby [2] for an overview. Whereas genuine SIMPLE requires the solution of one linear system per unknown and time step, the enhanced methods require the solution of more than one linear system per unknown and time step. The size of the systems always corresponds to the number of finite volumes; despite occasional convergence problems these methods are applied with great success in many important engineering applications.

Coupling equations and calculating two or more variables at the same time is an alternative to obtain accelerated convergence compared to the established approaches that are referred to as segregated. It seems, however, that until very recently one tends to prefer segregated approaches in CFD simulation tools for engineering applications On the other hand, long references for methods that couple momentum equations and continuity equation can be easily listed, e.g. Tai et al. [3] and Chen et al. [4]. The increased availability of parallel computers with large memory makes it possible and attractive to apply methods with coupled solution of linear systems to practical engineering problems. This includes methods that couple other equations than momentum equations and continuity equation.

For compressible flows the pressure-correction equation (that represents the mass conservation in SIMPLE algorithm) depends not only on the velocity field, but also on the density field, see Demirdžić et al. [5]. The segregated methods improve velocity update with respect to the mass conservation, but the error introduced by the density field, calculated based on the pressure of the previous iteration, is not reduced. Since the density depends strongly on the temperature, this error can be large if the actual guess of the temperature is not yet close to the solution. As a matter of fact the right-hand-side of the pressure-correction equation strongly depends on the enthalpy changes through the density field and, on the other hand, the pressure change as a result of this pressure-correction equation contributes significantly to the right-hand side of the enthalpy equation. A stronger link between enthalpy and pressure allows to employ a better approximation to the density in the pressure-correction equation. This motivated us to couple these two equations within the context of the SIMPLE algorithm.

2 Conventional SIMPLE method

In this contribution we consider a finite volume approach with collocated variable arrangement for the spacial discretisation of the governing equations and an implicit first order time discretisation. The discretised momentum, continuity, and energy equations for the discrete unknown velocity field $\vec{u}$, the pressure field $\vec{p}$,

and the (static) enthalpy field $\vec{h}$ read

$$A(\hat{\vec{u}})\vec{u} + M\vec{p} = \vec{b} \tag{1}$$

$$C\hat{\vec{u}} = \vec{c} \tag{2}$$

$$G(\hat{\vec{u}})\vec{h} = \tilde{\vec{g}}. \tag{3}$$

Here, A denotes the discretised and linearised operator that acts on the velocity field in the momentum equations, i.e. it expresses convective, diffusive, and inertia components. M is the discretisation of the pressure term, $\vec{b}$ the body force term, C represents the discretised continuity equation, $\vec{c}$ the corresponding right-hand side; the energy equation is represented by G and $\tilde{\vec{g}}$. The hat ($\hat{}$) on top of the vectors indicates that the vector is discretised on the grid that corresponds to the cell faces. The discretisation of the operators requires that both, the velocity in the cell centre $\vec{u}$ and the velocity at the cell faces $\hat{\vec{u}}$ appear in the system of equations. Both variables are linked by a linear interpolation operator S. The above system is completed by a relation between density and two thermodynamic variables, e.g. pressure and temperature

$$\varrho = \frac{p}{R \cdot T} \tag{4}$$

where R is the gas constant and $T = T(h)$.

The iterative SIMPLE algorithm uses updates for pressure and velocity, $\vec{p}\,' = \vec{p}^{\,(m)} - \vec{p}^{\,(m-1)}$ and $\vec{u}\,' = \vec{u}^{\,(m)} - \vec{u}^{\,*}$ where m denotes the iteration count and $\vec{u}^{\,*}$ is the solution of the momentum equations with the pressure taken from the previous iteration. A stable and robust algorithm for collocated grids is obtained if the technique of Rhie and Chow [6] is applied to the formulation of the pressure-correction equation. For this we introduce the operator

$$\hat{A}_M := [SA_D^{-1}\vec{1}] \tag{5}$$

where $A_D := \mathsf{diag}(A)$ and the square brackets $[\vec{x}]$ denote a diagonal matrix that has the element of value x_j (j-th component of vector $\vec{x}$) in the j-th row, i.e. $[\vec{x}] = \mathsf{diag}(\vec{1}\vec{x}^{\,T})$. The pressure-correction equation can be derived ,see Demirdžić et al. [5], as

$$\left\{C_c\left([\hat{\tilde{\varrho}}^{(m-1)}](-\hat{A}_M\hat{M}) + [\hat{\vec{u}}^{\,*}]S[\vec{r}]\right) + [\vec{o}][\vec{r}]\right\}\vec{p}\,' = \\ -[\vec{o}](\vec{\varrho}^{\,(m-1)} - \vec{\varrho}_0) - C_c[\hat{\tilde{\varrho}}^{(m-1)}]\hat{\vec{u}}^{\,*} \tag{6}$$

where the vector $\vec{o}$ is composed of $o_j = V_j/\delta t$ with the cell volume V_j and the time step δt, the vector $\vec{r}$ contains the components $r_j = 1/(R_j \cdot T_j)$ and the continuity operator is split as $C \equiv C_c[\hat{\tilde{\varrho}}]$. ϱ_0 is the density of the previous time step. The pressure-correction equation contains as a central assumption the relation

$$\hat{\vec{u}}\,' = -\hat{A}_M\hat{M}\vec{p}\,' \tag{7}$$

that uses the gradient operator $\hat{M}$ on the cell faces.

The segregated SIMPLE algorithm for compressible flows with temperature variation on collocated grids is:

1. compute density field $\vec{\varrho}^{(m-1)}$ using $\vec{p}^{(m-1)}$ and $\vec{T}^{(m-1)}$ with eqn. (4) or, alternatively, from tabulated material data
2. evaluate A in eqn. (1) with $\hat{\vec{u}}^{(m-1)}$ and solve for $\vec{u} = \vec{u}^*$
3. interpolate $\vec{\varrho}^{(m-1)}$, accumulate left-hand side operator of eqn. (6), compute right-hand side and solve for $\vec{p}\,'$
4. compute $\hat{\vec{u}}\,'$ with eqn. (7)
5. update $\hat{\vec{u}}$ and $\vec{p}$ to obtain $\hat{\vec{u}}^{(m)}$ and $\vec{p}^{(m)}$
6. compute coefficients and solve eqn. (3) for $h^{(m)}$

3 Pressure-enthalpy coupling

Apart from the special actions taken for pressure and velocity that have been highlighted above, in a segregated approach, the solution of a coupled system is approached iteratively. For each unknown, a linear system

$$B\vec{\phi} = \vec{b} \tag{8}$$

is solved; the coupling is achieved through the usage of the latest available values for the computation of the matrix coefficients and the right-hand sides. This is referred to as segregated approach. Coupling n variables, on the other hand, means that systems like

$$\begin{pmatrix} B_{11} & B_{12} & \cdots & B_{1n} \\ B_{21} & B_{22} & \cdots & B_{2n} \\ \vdots & \cdots & \ddots & \vdots \\ B_{n1} & \cdots & \cdots & B_{nn} \end{pmatrix} \begin{pmatrix} \vec{\phi}_1 \\ \vec{\phi}_2 \\ \vdots \\ \vec{\phi}_n \end{pmatrix} = \begin{pmatrix} \vec{b}_1 \\ \vec{b}_2 \\ \vdots \\ \vec{b}_n \end{pmatrix} \tag{9}$$

are solved. The matrices on the main diagonal are identical to those matrices that are used in the segregated approach. The off-diagonal matrices reflect the coupling, i.e. the mutual influences.

From thermodynamics the relation

$$\vec{\varrho}\,' = [\vec{r}](\vec{p}\,' + [\vec{k}]\vec{h}\,') \tag{10}$$

is derived where the components of $\vec{k}$ are $k = -p/(c_p \cdot T)$. Note that the difference to standard SIMPLE is that in the latter the second term (or an equivalent contribution) is neglected. If now the enthalpy equation is equivalently reformulated for an enthalpy update $\vec{h}\,' = \vec{h}^{(m)} - \vec{h}^{(m-1)}$ and coupled to the pressure-correction equation such that in eqn. (9) $n = 2$, the four needed matrices can be determined in the following way:

$$B_{11} = C_c \left([\hat{\vec{\varrho}}^{(m-1)}](-\hat{A}_M \hat{M}) + [\hat{\vec{u}}^{\,*}] S[\vec{r}] \right) + [\vec{o}][\vec{r}] \tag{11}$$

$$B_{12} = C_c [\hat{\vec{u}}^{\,*}] S[\vec{r}][\vec{k}] + [\vec{o}][\vec{r}][\vec{k}] \tag{12}$$

$$B_{21} = -[\vec{\sigma}] \tag{13}$$

$$B_{22} = G \tag{14}$$

The right-hand side vectors are

$$\vec{b}_1 = -[\vec{\sigma}](\vec{\varrho}^{(m-1)} - \vec{\varrho}_0) - C_c[\hat{\vec{\varrho}}^{(m-1)}]\hat{\vec{u}}^* \tag{15}$$

$$\vec{b}_2 = \vec{g} + [\vec{\sigma}](\vec{p}^{(m-1)} - \vec{p}_0) \tag{16}$$

where $\vec{g} = \tilde{\vec{g}} - [\vec{\sigma}](\vec{p}^{(m)} - \vec{p}_0)$ and $\vec{p}_0$ is the pressure of the previous time step.

This is integrated into the SIMPLE algorithm for compressible flows. For the pressure-enthalpy coupling scheme, step 3 of above form of this algorithm has been replaced by

3. interpolate $\vec{\varrho}^{(m-1)}$, accumulate left-hand side operator for $n = 2$ of eqn. (9) using the relations (11), (12), (13), and (14), compute right-hand side according to relations (15) and (16) and solve for $\phi_1 = \vec{p}\,'$ and $\phi_2 = \vec{h}\,'$

and step 5 by

5. update $\hat{\vec{u}}$, $\vec{p}$, and $\vec{h}$ to obtain $\hat{\vec{u}}^{(m)}$, $\vec{p}^{(m)}$ and $\vec{h}^{(m)}$.

Step 6 has become obsolete.

4 Numerical experiments

The pressure-enthalpy coupling has been implemented into the CFD package FIRE$^{(R)}$ (distributed by AVL) that uses the SIMPLE method as the standard algorithm. It has been demonstrated in Emans et al. [7] that the pressure-enthalpy coupling accelerates the SIMPLE method by a factor of up to five. While the examples in that publication were rather simple in terms of geometry, we will demonstrate here the efficiency of the pressure-enthalpy scheme in a simulation of industrial relevance.

The implementation of the SIMPLE method is that of a commercial code. The employed discretisation practice was explored in other publications starting with Demirdžić and Muzaferija [8], and continuing with Ferziger and Perić [9], Marthur and Murthy [10], Basara [11], Basara et al. [12] etc. Hence the method has been applied and proved on various applications and a comparison of the obtained results to measurements or to analytical solutions is skipped here. We observe throughout that the proposed pressure-enthalpy coupling method yields essentially the same results as the SIMPLE method.

The pressure-correction equation of the segregated SIMPLE is solved by an AMG-preconditioned conjugate gradient method where the AMG is of Smoothed Aggregation type of Vaněk et al. [13], for details about the implementation see Emans [14]. The coupled system is solved by an AMG-preconditioned GMRES that is restarted each 10 iterations. The preconditioning is done as v-cycle with two Gauß-Seidel sweeps for both, pre- and post-smoothing. The grid hierarchy is setup by aggregation of pairs where the selection of the pairs follows the algorithm described in detail by Notay [15]. All other non-symmetric systems are

solved by a BiCGstab algorithm that is preconditioned by an incomplete Cholesky factorisation.

4.1 Test cases from the simulation of an engine cycle

Our two benchmark cases are short but representative periods taken from an unsteady simulation of a full cycle of a four cylinder gasoline engine. The variation of the position of the piston during the engine cycle as well as some characteristic results of the simulation are shown in figure 1.

The simulation comprises the gas flow and the combustion in one of the cylinders. The stroke of the cylinder is $81.4\ mm$, the bore is $79.0\ mm$ yielding a (maximum) volume of $0.4\ l$ (per cylinder). Each benchmark case consists of a few time-steps. The three-dimensional computational domain is subject to change in time: It contains the interior of the cylinder and the parts of the ducts through which the air is sucked into the cylinder or hot gas is expelled from it. The piston surface is a moving boundary. The engine runs at 5500 rpm. A three-dimensional simulation of a full engine cycle comprises the simulation of the (compressible) flow of cold air into the cylinder while the piston is moving downward, the subsequent compression after the valves are closed, the combustion of the explosive mixture, and the discharge of the hot gas while the piston moves upward. In the simulation the modelling by the above discussed system of equations is amended by a standard k-ε turbulence model; the fluid properties are those of air. The model fuel that is burnt is octane; an eddy break-up model is used to simulate the combustion process. The simulation is carried out with the FIRE$^{(R)}$ code that has been validated for this type of problem many times, see e.g. Priesching et al. [16]. Further information about the setup can be found in Emans [17].

Example 1a comprises 4 degree crank angle α within the compression phase, i.e. we observe a closed system with adiabatic walls; the unstructured mesh consists of 238000 mostly hexagonal cells. This period is simulated with four different

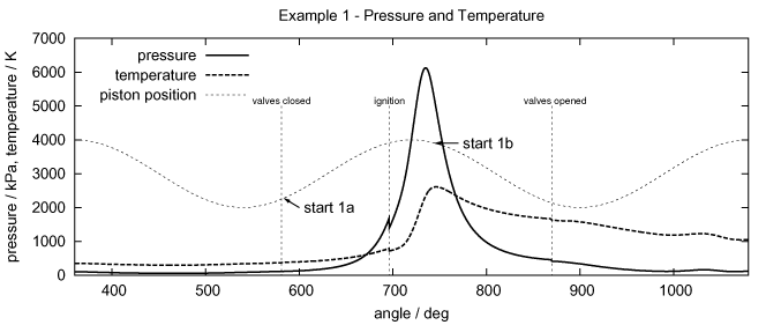

Figure 1: Scheme of the engine cycle and characteristic simulation results; the arrows point to the start of the benchmark cases.

Figure 2: Slices through the first meshes of the benchmark cases: example 1a (compression) right, example 1b (combustion) left.

time resolutions: $\delta\alpha_1 = 0.4^o$, $\delta\alpha_2 = 0.2^o$, $\delta\alpha_3 = 0.05^o$, and $\delta\alpha_4 = 0.01^o$ This corresponds to time steps of $\delta t_1 = 1.2 \cdot 10^{-6}s$, $\delta t_2 = 0.60 \cdot 10^{-6}s$, $\delta t_3 = 0.15 \cdot 10^{-6}s$ $\delta t_4 = 0.03 \cdot 10^{-6}s$; with these time steps we cover the range that is relevant for applications in engineering. Each calculation has been carried out once with segregated SIMPLE (SIM) that uses block-pressure adjustment, see Ahmadi-Befrui [18], and with SIMPLE with pressure-enthalpy coupling (PH). The hardware consisted of one node of a Linux-cluster equipped with 2 quad-cores (Intel Xeon CPU X5365, 3.00GHz, main memory 16 GB, L1-cache 2·4·32 kB, L2-cache 2·4 MB).

Example 1b comprises 4 degree crank angle within the combustion phase, i.e. here, additionally to fluid flow, combustion is modelled; the unstructured mesh consists of 254000 mostly hexagonal cells. Other settings as well as the hardware are identical. The first meshes used in example 1a and example 1b are shown in figure 2.

4.2 Convergence and performance

The data shown in figure 3 demonstrates that the pressure-enthalpy coupling improves the convergence of SIMPLE significantly in all cases. The computing time is reduced to a lower extent than the number of iterations since the solution of the coupled system is more expensive than the solution of the systems in the segregated approach. For the largest part this is due to the more expensive solution of the linear system: The pressure-correction equation is a semi-definite or definite system in the case of the conventional SIMPLE algorithm, but it has no beneficial properties apart from the sparseness that can be exploited by the solver in the case of pressure-enthalpy coupling algorithm. In most cases, however, the computing time is still reduced significantly. The exception is the coarsest time resolution of example 1b.

It can be seen from the data in figure 4 that the savings in terms of SIMPLE iterations increase with decreased time step. The savings range from 63% ($\delta\alpha = 0.01^o$, example 1b) to 26% ($\delta\alpha = 0.4^o$, example 1b). The maximum saving in

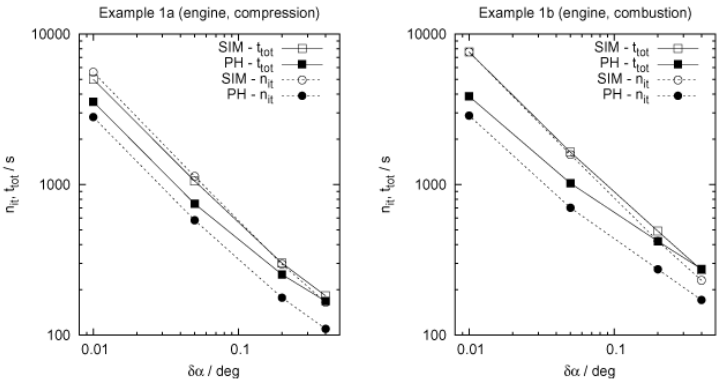

Figure 3: Total computing time t_{tot} and number of SIMPLE-iterations n_{it} of the benchmarks of examples 1a and 1b.

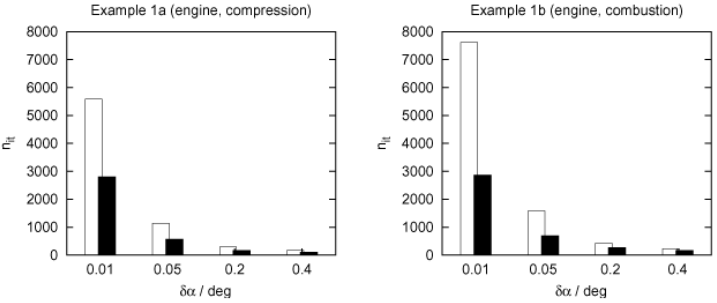

Figure 4: Comparison or the number of SIMPLE iterations n_{it} of the benchmarks of examples 1a and 1b.

terms of computing time is 49% ($\delta\alpha = 0.01^o$, example 1b). Note that in Emans et al. [7] the maximum acceleration through the pressure-enthalpy coupling is obtained in cases where the segregated SIMPLE algorithm could not be amended by block-pressure adjustment. The acceleration observed here confirms the data reported in Emans et al. [7] for the comparison between SIMPLE without block-pressure adjustment and pressure-enthalpy coupling.

5 Conclusions

The presented pressure-enthalpy coupling scheme accelerates the convergence of the SIMPLE algorithm significantly. The method is particularly efficient if small time steps are chosen. The disadvantage of the method is that the computational effort to solve linear systems for the pressure correction mechanism is increased

compared to segregated SIMPLE. Despite this we can show that the computations of a complex engine simulation using the pressure-enthalpy coupling scheme are faster by a factor of up to two compared to those of segregated SIMPLE.

References

[1] Patankar S.V. & Spalding, D.B., *A calculation procedure for heat, mass and momentum transfer in three-dimensional parabolic flows*, International Journal Heat Mass Transfer, **15**, pp. 1787–1806, 1972

[2] van Doormal J.P. & Raithby G.D., *Enhancements of the SIMPLE Method for Predicting Incompressible Flows*, Numerical Heat Transfer, **7**, pp. 147–163, 1984

[3] Tai, C.H., Zhou, Y. & Liew, K.M., *Parallel-multigrid computations of unsteady incompressible viscous flows using a matrix-free implicit method and high-resolution characteristics-based scheme*, Computational Methods in Applied Mechanics and Engineering, **194**, pp. 3949–3983, 2005

[4] Chen, Z.J., Marella S.V. & Przekwas A.J., A finite volume method of pressure-coupled solver for incompressible/compressible flows, *Proc. of the 47^{th} AIAA Aerospace Sciences Meeting Including The New Horizons Forum and Aerospace Exposition*, AIAA 2009-600, Orlando, Florida (USA), 2009

[5] Demirdžić I., Lilek Ž. & M. Perić, *A Collocated Finite Volume Method for Predicting Flows at All Speeds*, International Journal for Numerical Methods in Fluids, **16**, pp. 1029–1050, 1993

[6] Rhie, C.M. & Chow, W.L., *Numerical Study of the Turbulent Flow past an Airfoil with Trailing Edge Separation*, AIAA Journal, **21**, pp. 1525–1532, 1983

[7] Emans M., Frolov, S., Lidskii, B. Posvyanskii, V. & Basara, B., *A finite volume pressure-enthalpy coupling scheme for compressible flows*, Journal of Computational Physics, submitted

[8] Demirdžić, I. & Muzaferija, S., *Numerical Method for Coupled Fluid Flow, Heat Transfer and Stress Analysis Using Unstructured Moving Meshes With Cells of Arbitrary Topology*, Computational Methods in Applied Mechanical Engineering **125**, pp. 235–255, 1995

[9] Ferziger, J.H. & and Perić, M., *Computational Methods for Fluid Dynamics*, Springer-Verlag: Berlin and New York, 1996

[10] Marthur, S.R. & Murthy, J.Y., *A Pressure Based Method for Unstructured Meshes*, Numerical Heat Transfer B **31**, pp. 195–215, 1997

[11] Basara, B., *Employment of the second-moment turbulence closure on arbitrary unstructured grids*, International Journal for Numerical Methods in Fluids, **44**, pp. 377–407, 2004

[12] Basara, B., Alajbegovic, A., & Beader, D., *Simulation of single- and two-phase flows on sliding unstructured meshes using finite volume method*, International Journal for Numerical Methods in Fluids, **45**, pp. 1137–1159, 2004

[13] Vaněk, P., Brezina M. & Mandel, J., *Algebraic Multigrid by Smoothed Aggregation for Second and Fourth Order Elliptic Problems*, Computing, **56**, pp. 179–196, 1996
[14] Emans M.: *Performance of Parallel AMG-Preconditioners in CFD-Codes for Weakly Compressible Flows*, Parallel Computing, **36**, pp. 326–338, 2010
[15] Notay, Y., *An aggregation-based algebraic multigrid method*, Electronic Transactions on Numerical Analysis, **37**, pp. 123–146, 2010
[16] Priesching P., Wanker R., Cartellieri P. & Tatschl R., *CFD Modelling of HCCI Engine Combustion – Validation and Application*, Proceedings of ICE 2003, Capri, 2003
[17] Emans M.: *AMG for linear systems in engine flow simulations*, Proceedings of PPAM09, Lecture Notes in Computer Science, Springer Verlag: Berlin and New York, 2010, to appear
[18] Ahmadi-Befrui, B., *Analysis of flow evolution in the cylinders of motored reciprocating engines*, PhD Thesis, Imperial College of Science & Technology, University of London, 1985

Study of ventilation reversion of airflow in mining roadways and tunnels by CFD and experimental methods

S. Torno, J. Toraño & J. Velasco
School of Mines, University of Oviedo, Spain

Abstract

When a mining roadway and tunnel is being advanced or has already been carried out, the air circulation direction can be inverted for different reasons, the most frequent being, the outburst of pollutant gases and the effect of a fire.

This reversion effect can become serious for the workers. The behaviour analysis of this ventilation by conventional methods presents deficiencies which can be improved by CFD (Computational Fluid Dynamics) by using Ansys CFX 10.0 software with the establishment of prediction models.

The CFD modelling were validated by mining roadway measurements using anemometers, methanometers and oxymeters.

It has been proved that the mining roadway or tunnel longitude reached by the reversion of airflow is reduced by installing an auxiliary forcing ventilation overlapped with the main ventilation. Additionally, it has been determined that the longitude is not reduced by increasing the main ventilation velocity.

Likewise, different tests to check the effect of different types of auxiliary ventilation system over the roadway longitude reduction, have been carried out.

Keywords: underground ventilation, reversion of airflow, CFD3D (Computational Fluid Dynamics), mining roadway.

1 Introduction

In the driving tunnel with a longitudinal type of ventilation, the air flows along intake airway (tunnel or roadway 1) to the working area and the contaminated air passes back along return airways (parallel tunnel or mining roadway 2). The roadway (3) joins (1) and (2), it can be seen in figure 1. In this working area, a significant pollutant gas (methane) emission has been produced [1, 2] which has

WIT Transactions on Engineering Sciences, Vol 69, © 2010 WIT Press
www.witpress.com, ISSN 1743-3533 (on-line)
doi:10.2495/AFM100121

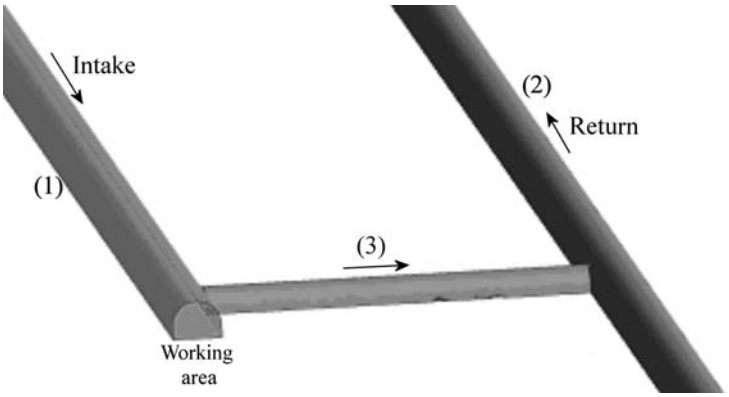

Figure 1: Geometry and model description.

caused the circulation flow direction of intake in the roadway or tunnel (1) to become inverted instead of flowing out through the roadway or tunnel (2), causing a great danger to the workers [3–5].

The study and analysis of the latter and the possible solutions by mean of conventional methods present clear deficiencies which should be improved through computational numerical methods, Computational Fluid Dynamics (CFD).

The flow behaviour is modelized by software Ansys CFX-10.0 utilizing the K-epsilon turbulence model, as has already been carried out by other [6–9].

In this paper, the effect of the reversion on the workers working at the end tram of the roadway is analysed. In addition, as the roadway or tunnel longitude of reversion (1) varies when safety measures such us ventilation duct outlet airflow modification are introduced, since in this case the use of methane drainage installing systems are not possible.

The study and analysis of the latter and the possible solutions by mean of conventional methods present clear deficiencies which should be improved through computational numerical methods, CFD.

The flow behaviour is model zed by software Ansys CFX-10.0 utilizing the K-epsilon turbulence model, as has already been carried out by other [6–9].

In this paper, the effect of the reversion on the workers working at the end tram of the roadway is analysed. In addition, as the roadway or tunnel longitude of reversion (1) varies when safety measures such us ventilation duct outlet airflow modification are introduced, since in this case the use of methane drainage installing systems are not possible.

2 CFD Modelling and underground field measurement

The CFD based on the resolution of set of equations which describe the processes of momentum, heat and mass transfer in a moving fluid are known as the Navier–Stokes equations, [12] eqn (1), Continuity, eqn (2) and Energy eqn (3).

$$\rho \frac{D\overline{V}}{Dt} = -\overline{\nabla} p + \rho \overline{g} + \mu \nabla^2 \overline{V} \tag{1}$$

$$\frac{D\rho}{Dt} + \rho \overline{\nabla} \cdot \overline{V} = 0 \tag{2}$$

$$\rho \frac{D\tilde{u}}{Dt} = K \nabla^2 T - p \overline{\nabla} \cdot \overline{V} \tag{3}$$

where ρ is the density, $\nabla \cdot$ is the operator divergence, ∇ is the gradient, μ is the viscosity, T is the temperature, t is the time, V is the velocity, $\tilde{u}$ is the specific heat and K is the conductivity.

These partial differential equations have no known general analytical solution but can be discretized and solved numerically.

These expressions form a partial differential equation system, which is coupled for linear form, and therefore CFD is used for the solutions.

This is a multiphase problem, where a two phase flow, air and pollutant (methane) is modelled. The software Ansys CFX-10.0 has two multiphase flow models available, the Eulerian–Eulerian multiphase model and the Lagrangian Particle Tracking multiphase model. In other researches carried out where one of the phases is dust particle, the Lagrangian Tracking multiphase model has been used, whereas in this paper, Eulerian–Eulerian multiphase model is used.

Within this model, certain interphase transfer terms used in interphase transfer models, are modelled using the Mixture Model, which symmetrically deals with the phases, but merely for continuous phases.

The CFD Modelling commence with a geometry carried out by SolidWorks, which is posteriorly meshed by ICEMCFD-10.0 with approximately 500000 elements and a finer meshing for the auxiliary ventilation duct area.

The resulting model is characterised in software Ansy CFX-10.0, by 3 different boundary conditions, Inlet, Opening and Wall. In this model, there are 3 Inlets, one fresh air inlet and two pollutant inlets. The Opening corresponds to the model flow outlet and the remaining surfaces are Wall.

In figure 2 the coloured streamlines in velocity function according to longitudinal direction of the roadway are shown. Furthermore, the reversion areas can be seen as streamline interaction, represented by two arrows.

Having carried out the modelling, the results are compared to real data, which have been collected in the mining roadway by means of various instruments Miniar Junior Macro-MIE handheld anemometers, Trolex 6383.01 methane detectors and Trolex 6531 oxygen detectors.

The comparison between CFD values and (EXP) Experimental values, giving us a correlation $R^2 = 0.9833$, which is adjusted to the following equation, Eqn (4), have been developed:

$$CFD = 0.7168 \cdot EXP + 12.681 \tag{4}$$

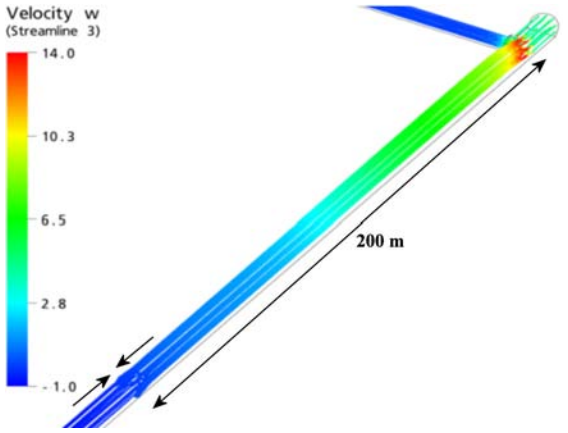

Figure 2: Longitude of reversion.

3 Effect of roadway (3) for ventilation reversion

The effect of the reversion of airflow for the final roadway tram has been studied for its repercussion for the security of workers and it is also a significant reason for the use of CFD model adjusted by experimental tests.

The importance of this study being carried out away from the pollutant emission source is due to the fact that two workers were working in the roadway at the time of the incident.

However, these workers were not affected by the oxygen reduction produced during the reversion. Additionally, data collected by a methanometer (at that time) have been used to validate modelization for this roadway tram.

In figure 3, the obtained results by CFD modelling for the final roadway tram where the reversion of airflow was produced is shown. A papallel plane to floor at 1 m high can be seen where the velocity distribution for both the roadway longitudinal direction and the streamlines, are shown. In tram (I), the velocity

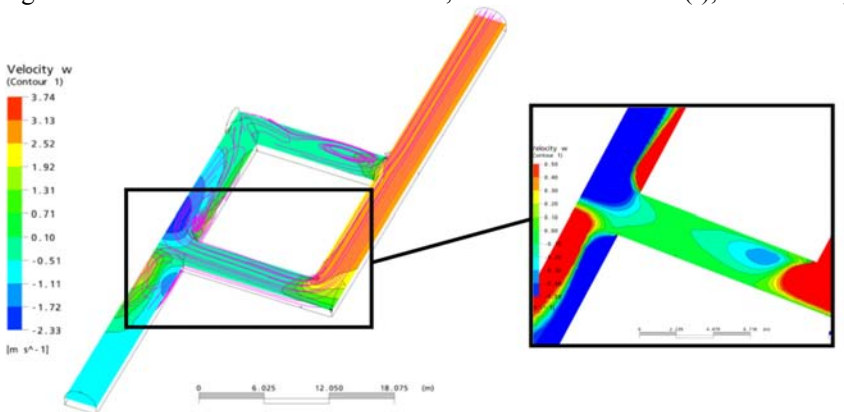

Figure 3: Modelization of roadway final tram.

flow (3.74 m/s), which diminishes when the flow is divided by the two roadways, even causing a change of direction resulting in negative values.

If cross-sections are analyzed in figure 3, the flow distribution for tram (I) can be studied.

The study cross-sections are S1, S2, S3, S4.1, S4.2, S5, S6 and S7, are shown in figure 4. In this figure, cross-section of the roadway longitudinal direction velocity is shown.

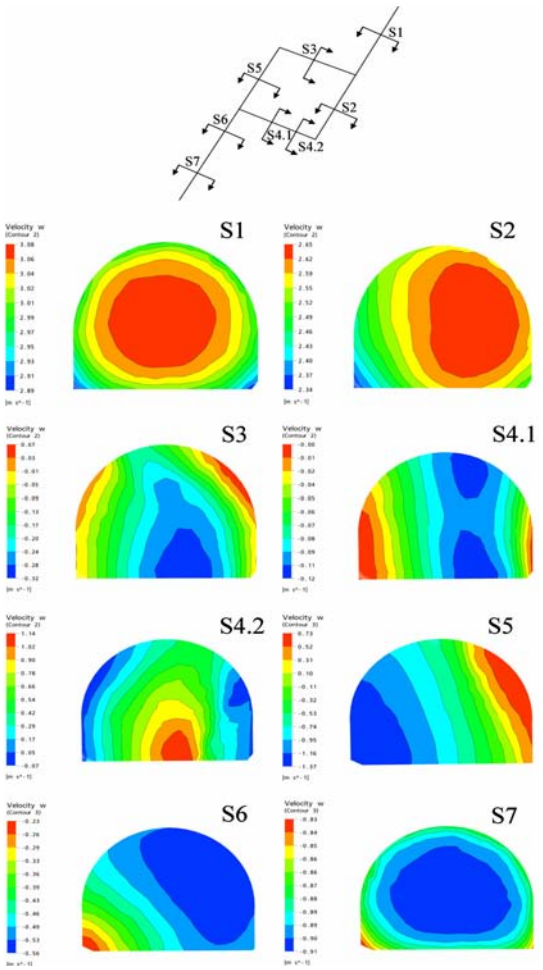

Figure 4: Velocity cross-section for the roadway final tram.

For cross-sections S1 and S2, the high velocity is found in the central area of the roadway, where the greater amount of pollutant is concentrated. When the flow is divided by cross-section S3 and S4 its distribution changes, lower and even negative velocities are present in the central roadway areas. It is considered to be of great significance for cross-section S4 (S4.1 and S4.2), since the latter workers were working in this area at the time of the incident.

In cross-section, S5, S6 and S7, the amount of fresh air increases, reaching a total flow recovery for cross-section.

As it can be proved, the obtained and adjusted model coincides with the facts, observed in the mine where a greater ventilation reversion is produced. Therefore, the methane influence is found in the central zone of the roadway. In this way, it has been indicated that the workers were not affected by the methane emerging from the reversion of airflow.

4 Effect of an auxiliary forcing ventilation system over the reversion of airflow

An auxiliary forcing ventilation system overlapped with the main ventilation in roadway (1) has been incorporated in order to diminish the roadway longitude where the reversion of airflow is produced. This auxiliary ventilation consists of a 400 mm diameter and 60 m long duct.

Two different modellings with 12 and 20 m/s velocity at the auxiliary duct outlet have been carried out.

The results have shown a 74m reversion reduction for 12 m/s velocity, whereas for 20 m/s velocity a 78 m reduction was shown, (the reversion being 120m from the roadway 3). The 20 m/s velocity has been chosen to be installed in the underground coal mine.

In figure 5, the streamline flow distribution for the 20 m/s velocity is shown, where the streamline of auxiliary forcing ventilation reduce the velocity of the pollutant streamline (dark colour), allowing the main ventilation streamline (clear colour) to reach a greater longitude (158 m).

In order to validate the results of this 20 m/s auxiliary forcing ventilation modelling, they have been compared to real data according to Eqn (5) with a R^2 =0.90 value.

$$CFD = 1.4247 \cdot EXP - 0.124 \quad (5)$$

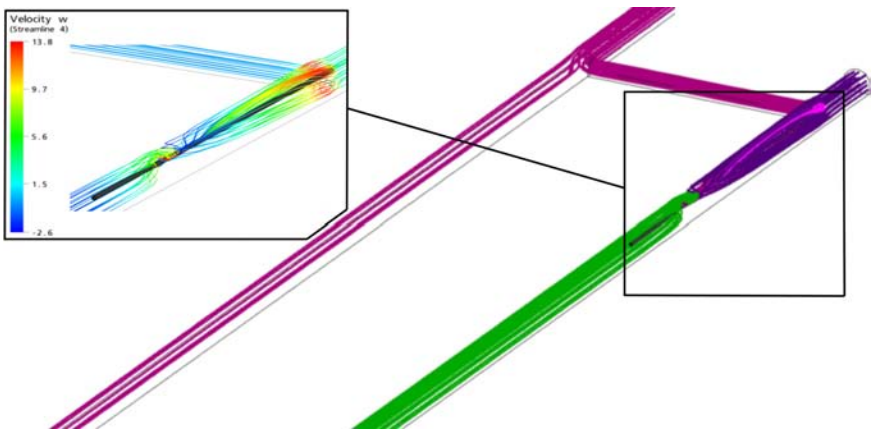

Figure 5: Streamline flow for the 12 m/s auxiliary forcing ventilation output.

This reduction in the roadway longitude, where the reversion is produced, can be achieved by using the 20 m/s auxiliary forcing ventilation with favourable results. On the other hand, if the main ventilation velocity increases a good reversion reduction is not achieved.

In Table 1, a 200 m reversion reduction from the roadway (3) for main ventilation of 2, 3, 5 and 8 m/s is shown. The Spanish Regulation establishes a tunnel or roadway velocity between (0,2 - 8 m/s).

The 5 and 8 m/s velocity, which most reduces the reversion longitude, is scarcely used, as they are unfavourable for the workers. Even with these high values, the reversion is not reduced as much as by introducing a 20 m/s auxiliary ventilation over the main ventilation.

Table 1: Reversion longitude for several main velocities.

Main ventilation (m/s)	Reversion longitude (m)
1	200
2	140
3	118
5	92
8	82

5 Conclusions

In this paper, the use of Computational Fluid Dynamics for the underground mining ventilation study, is widely proved. Additionally, a widespread study of safety measures can be carried out when a significant methane outburst occurs in tunnel or mining roadway construction.

In order to avoid ventilation reversion during the significant methane outburst, different CFD options, such as an increase in the main ventilation velocity and the incorporation of an auxiliary forcing ventilation, have been studied.

In the first case, 2, 3, 5 and 8 m/s velocities were used with no sufficiently effective velocity findings, which are a danger to the workers.

In the second case, two 12 and 20 m/s auxiliary fans were used, achieving more favourable results for the 20 m/s.

The chosen safety measures is the 20 m/s auxiliary forcing ventilation overlapped with the main ventilation, reducing the reversion longitude to 150 m. This safety measure has been placed in the real tunnel achieving the expected results.

References

[1] Vandeloise, R., Compte rendu du Colloque International sur les Dégagements Instantanés. Harkany (Hungrie), Annales des Mines de Belgique. Nº 2 Février, 1969.

[2] Belin, J. & Vandeloise, R, Résultats des recherches efectúes en Belgique et en France sur les dégagements instantanés Dans les mines de charbon. Annales des Mines de Belgique. Nº 2 Février, 1969.
[3] Kissell, F. N., *Handbook for Methane Control in Mining*. U.S. Department of Health and Human Services. Public Health Service. Centers for Disease Control and Prevention. National Institute for Occupational Safety and Health. Pittsburgh Research Laboratory, 2003.
[4] Wasilewski, S., Methods and means of monitoring of gas hazards in polish underground hard coal mines. *Mine Hazards Prevention and Control Technology*, 17, pp. 650-654, 2007.
[5] McPherson, M.J., *Subsurface Ventilation Engineering*. Chapter 12 Methane, Mine Ventilation Services, Inc., 2009.
[6] Norton, T., Sun, D.W., Grant, J., Fallon, R. & Dodd, V., Applications of computational fluid dynamics (CFD) in the modelling and design of ventilation systems in the agricultural industry. *Bioresource Technology*, 98, pp. 2386-2414, 2007.
[7] Moloney, K.W., Lowndes, I.S. & Hargrave, Analysis of flow patterns in drivages with auxiliary ventilation. *Transaction of the Institution of Mining and Metallurgy (Section A: Mining Industry)*, 108, pp. 105-114, 1999.
[8] Moloney, K.W. & Lowndes, I.S., Comparison of measured underground air velocities and air flows simulated by computational fluid dynamics. *Transaction of the Institution of Mining and Metallurgy (Section A: Mining Industry)*, 108, pp. 105-114, 1999.
[9] Toraño, J., Rodríguez, R. & Diego, I., Computational Fluid Dynamics (CFD) used in the simulation of the death end ventilation in tunnel and galleries. *Transaction: Engineering Sciences*, 52, pp. 2006.
[10] Brunner, D.J., Schwoebel, J.J. & Brinton, J.S., *Modern CMMM strategies*. 11th North American Mine Ventilation Symposium., Eds Mutmansky and Ramani, Penn State University, 2006.
[11] Karacan, C.O., Diamond, W.D. & Schatzel, S.J., Numerical analysis of the influence of in-seam horizontal methane drainage boreholes on longwall face emission rates. *International Journal of Coal Geology,* 72, pp. 15-32, 2007.
[12] Ansys CFX ANSYS CFX- Solver. Release 10.0 ANSYS CFX-Solver, Release 10.0: Modelling pp 327.

Dam break Smoothed Particle Hydrodynamic modeling based on Riemann solvers

L. Minatti[1] & A. Pasculli[2]
[1]*Department of Civil and Environmental Engineering, University of Florence, Italy*
[2]*Department of Sciences, University of Chieti-Pescara, Italy*

Abstract

The Smoothed Particle Hydrodynamic (SPH) method, originally developed during the 1970s to solve astrophysical problems, has shown many attractive features that have led many authors to try to use it to solve fluid flows problems. Its free surfaces tracking capabilities and its straightforward implementation of multi-materials interactions make it well suited for complex flows modeling.

The first part of the paper is devoted to a general overview of the method. In particular, a brief description of a recently proposed flux term, implemented in this paper, is introduced. The addition of the flux terms, based on a Riemann solvers approach, enhances the stability and smoothness of field variables, leading to more accurate pressure fields.

In order to test the effectiveness of the selected approach, in the second part of the paper, the Dam break problem is discussed. Furthermore, the classical Poiseuille flow problem is considered as well.

The numerical results are very satisfactory, exhibiting the effectiveness of the implemented approach regarding, at least, the selected kind of problems.

Keywords: SPH method, Riemann solvers, Dam break, Poiseuille flow.

1 Overview of the SPH method

The Smoothed Particle Hydrodynamic (SPH) method is a numerical technique that was initially developed during the 1970s to solve astrophysical problems (Monaghan [1]). It is a fully meshless particle method that is easy to code. Its meshless and Lagrangian nature make it very attractive for solving fluid flow problems where free surface boundary conditions and large strain rates may be

WIT Transactions on Engineering Sciences, Vol 69, © 2010 WIT Press
www.witpress.com, ISSN 1743-3533 (on-line)
doi:10.2495/AFM100131

involved. The computational domain is filled with particles carrying flow field information (e.g. pressure, velocity, density) and is capable of moving in space. Particles are the computational frame used in the method to solve the flow describing PDEs, as a grid or a mesh to calculate spatial derivatives is not needed.

We shall refer to 2D cases throughout the rest of the paper, even though all the assumptions and results can be extended to a 3D case with little effort. The key idea on which the method is based is the well-known use of a convolution integral with a Dirac delta function to reproduce a generic function $f(\underline{x})$:

$$\hat{f}(\underline{x}) = \int_D f(\underline{x}') \cdot \delta(\underline{x} - \underline{x}') d\underline{x}' \tag{1}$$

In the SPH method, the Dirac function is replaced by a "bell-shaped" kernel function W (it 'mimics' the Dirac delta function), and the generic function $f(\underline{x})$ is reproduced with the following convolution integral:

$$\hat{f}(\underline{x}) = \int_{\Omega_x} f(\underline{x}') \cdot W(\underline{x} - \underline{x}') d\underline{x}' \tag{2}$$

The kernel function is chosen to be non-negative, even and with a support domain Ω_x (usually circular) whose radius is a multiple of a length h, named *smoothing length*. The kernel function is zero outside the support domain and the smoothing length serves as a scaling parameter for its arguments. It also has the property of converging to the Dirac function as the smoothing length approaches to zero.

The kernel function must satisfy some conditions in order to correctly reproduce functions up to a given order k, in a Taylor series expansion. Let us consider a 1D case where a function $f(x)$ is approximated about point x by a Taylor series up to the order k:

$$f(x') = \sum_{i=0}^{k} \frac{f^{(i)}(x)}{i!} \cdot (x' - x)^i \tag{3}$$

If eqn (3) is substituted in eqn (2), the SPH approximation of function $f(x)$ takes the form:

$$\begin{aligned} \hat{f}(x) &= \int_{\Omega_x} \sum_{i=0}^{k} \frac{f^{(i)}(x)}{i!} \cdot (x' - x)^i \cdot W(x - x') dx' = \\ &= \sum_{i=0}^{k} \frac{f^{(i)}(x)}{i!} \cdot \int_{\Omega_x} (x' - x)^i \cdot W(x - x') dx' \end{aligned} \tag{4}$$

If a correct reproduction of function $f(x)$ is searched up to the order k, then the kernel must satisfy the following conditions:

$$M_i(x) = \int_{\Omega_x} (x - x')^i \cdot W(x - x') dx' = \delta^{i0} \quad i = 0 \ldots k \tag{5}$$

i.e. every kernel moment has to be equal to zero (except for the 0 order one that has to be equal to 1).

It is possible to obtain the expression for the SPH approximation of a function gradient by using eqn (2) and the Gauss-Green formula:

$$\nabla \hat{f}'(\underline{x}) = \int_{\Omega_x} \nabla f(\underline{x}') \cdot W(\underline{x} - \underline{x}') d\underline{x}' = \int_{\partial\Omega_x} f(\underline{x}') \cdot W(\underline{x} - \underline{x}') \cdot \underline{n} ds - \int_{\Omega_x} f(\underline{x}') \cdot \nabla' W(\underline{x} - \underline{x}') d\underline{x}' \tag{6}$$

where:

- the kernel is differentiated with respect to the $\underline{x}'$ coordinate;
- $\underline{n}$ represents the normal to the support domain boundaries;

The first term of the RHS of eqn (6) can be zero if the support domain is not truncated by the computational domain boundaries, as the kernel is zero on the support domain boundaries. Another case when the term can be zero is when the support domain is truncated by the computational domain boundaries but there exists a boundary condition forcing the function $f(\underline{x})$ to vanish on the boundaries (it may be the case when $f(\underline{x})$ represents a velocity and a no-slip condition has to be enforced on the computational domain boundaries). If the first term of the RHS of eqn (6) is zero, then the SPH approximation of $f(\underline{x})$ gradient takes the form:

$$\nabla \hat{f}(\underline{x}) = -\int_{\Omega_x} f(\underline{x}') \cdot \nabla' W(\underline{x} - \underline{x}') d\underline{x}' \tag{7}$$

Eqn (7) is often used, even when the first term of the RHS of eqn (6) does not vanish.

It is possible to find the conditions the kernel must meet in order to correctly reproduce the first derivative of a given function $f(x)$, up the order k of its Taylor series expansion. They are similar to the conditions of eqn (5) and it can be shown that they are related. The reproducing conditions for a function first derivative are expressed as follows:

$$M_i^{'}(x) = \int_{\Omega_x} (x - x')^i \cdot W'(x - x') dx' = \delta^{i1} \quad i = 0...k \tag{8}$$

The most frequently used kernels involve truncated Gaussian and spline curves. The kernel used in this paper is the cubic spline function with compact support, whose expression is as follows (see also the plot reported in Figure 1):

$$\begin{aligned} W(R) &= \frac{2}{3} - R^2 + \frac{1}{2} R^3 \quad 0 \le R < 1 \\ W(R) &= \frac{1}{6} (2\text{-}R)^3 \quad 1 \le R \le 2 \\ R &= \frac{|\underline{x}\text{-}\underline{x}'|}{h} \end{aligned} \tag{9}$$

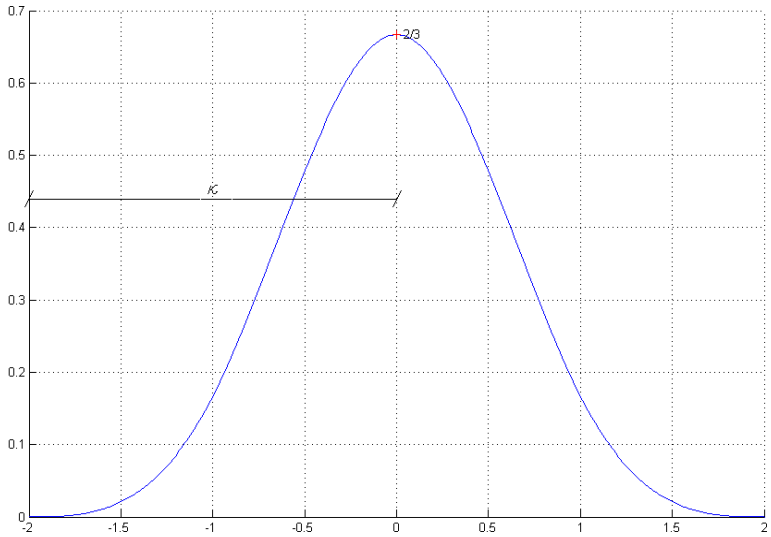

Figure 1: Third order cubic spline kernel plot.

The condition forcing the kernel to be non-negative makes it impossible to meet condition of eqn (5) for k = 2 and condition of eqn (8) for k = 3. Furthermore, the use of an even function as a kernel automatically satisfies conditions for exact reproduction of linear functions and second order function derivatives. Therefore, it is possible to correctly reproduce this kind of functions only with a non-negative kernel like the cubic spline.

2 Particle approximation related problems

The previous equations need to be evaluated in a discrete manner in order to develop a numerical technique from the theoretical framework shown above. In the SPH method, the discrete evaluation is made by means of the particle approximation. The continuous space is then replaced by a finite set of particles, each one of them carrying a mass, an area and other problem related information.

Hence, particle approximations of eqns (2) and (7) take the form:

$$\hat{f}_h(\underline{x}_i) = \sum_{j=1}^{n} f(\underline{x}_j) \cdot W(\underline{x}_i - \underline{x}_j) \cdot \Delta A_j \tag{10}$$

$$\nabla \hat{f}_h(\underline{x}_i) = -\sum_{j=1}^{n} f(\underline{x}_j) \cdot \nabla_j W(\underline{x}_i - \underline{x}_j) \cdot \Delta A_j \tag{11}$$

where:

- $\underline{x}_i$ and $\underline{x}_j$ represent the i and j particle positions in the given frame of reference;
- ΔA_j represents the tributary area associated with particle j;

- Summations are extended to all the particles located within the support domain of particle *i*;

The ability of the kernel to exactly reproduce a function and its derivative up to a certain order vanishes when the particle approximations shown in eqns (10) and (11) are performed. This means that the particle approximations of the consistency conditions of eqns (5) and (8), which are shown below for a 1D case:

$$m_p(x_i) = \sum_{j=1}^{n} (x_i - x_j)^p \cdot W\left(x_i - x_j\right) \cdot \Delta x_j = \delta^{p0} \quad p = 0...k \tag{12}$$

$$m_p'(x_i) = \sum_{j=1}^{n} (x_i - x_j)^p \cdot W'\left(x_i - x_j\right) \cdot \Delta x_j = \delta^{p1} \quad p = 0...k \tag{13}$$

are no longer exactly satisfied. The afore-mentioned problem is often referred to as the *particle inconsistency* problem.

Another issue related -but not limited to the particle inconsistency problem arises when particle approximation of eqn (11), for evaluating a function gradient, is performed at a particle whose support domain overlaps with the computational domain boundaries. As the first term of the RHS of eqn (6) is often neglected, the particle approximation shown in eqn (11), besides suffering from the particle inconsistency related errors, suffers from the ones arising from this further approximation. This problem is often referred to as the *particle deficiency* problem and it may cause relevant errors both in evaluating a function derivative close to boundaries and in imposing a boundary condition on a field variable.

Many authors have proposed corrective strategies to tackle particle approximation related problems. Randles and Libersky [2] used ghost particles to treat a symmetrical surface boundary condition. Ghost particles have also been used in a various manners for particle approximations near boundaries by Takeda *et al.* [3], Morris *et al.* [4] and Ferrari *et al.* [5].

An approach that tries to overcome these issues without the use of any kind of ghost particles has been proposed by Liu *et al.* [6]. The method proposed by the authors (briefly named RKPM) consists in multiplying the kernel function by corrective coefficients in the particle approximation, in order to restore the particle approximation of the consistency conditions of eqns (12) and (13). By using the RKPM method, it is possible to find corrective coefficients to attain higher order consistency. The computational cost of the SPH simulation increases as it is necessary to solve least squares problem and to invert symmetrical square matrixes.

Another corrective approach is the one proposed by Liu and Liu [7]. The authors use the Taylor expansion series to offset and correct the standard particle approximations of eqns (10) and (11) for reproducing a function and its first derivative. Computational cost is increased even in this case, as it is necessary to perform matrix inversion in order to obtain a corrective matrix for the standard SPH approximation.

Nevertheless, it is possible to obtain realistic and accurate simulations with SPH despite these issues. The main reasons relies on the fact that the momentum

equation can be set up so that the interaction terms between each pair of particles are symmetrical, thus allowing for momentum conservation.

3 SPH for fluid flow problems

In this paper, uncompressible fluids are treated using the weakly compressible fluid approximation. This means that pressure is not obtained by solving a Poisson equation, as in the uncompressible case but using a stiff equation of state instead. The equation used here has successfully been employed before by Monaghan [8] and Ferrari *et al.* [5], among others, and computes the particle pressure p_i this way:

$$p_i = k_0 \cdot \left(\left(\frac{\rho_i}{\rho_0} \right)^7 - 1 \right) \tag{14}$$

where:

- k_0 is a reference pressure;
- ρ_i represents the density at particle i;
- ρ_0 represents a reference density of the fluid when relative pressure is zero.

The k_0 value must be chosen in order to have a speed of sound, which is at least ten times higher than the highest fluid velocity involved in the problem: in this way it is possible to limit the density variations to around 1% of reference density and to not introduce prohibitively small time steps (see Monaghan [8]). Finally, please note that if eqn (14) is employed then particle sound speed c_i has the following expression:

$$c_i = \sqrt{\frac{7k_0}{\rho_0} \cdot \left(\frac{\rho_i}{\rho_0} \right)^6} \tag{15}$$

The particle approximation used for the continuity equation is the following:

$$\frac{D\rho_i}{Dt} = \rho_i \sum_{j=1}^{n} \frac{m_j}{\rho_j} \cdot (\underline{v}_i - \underline{v}_j) \cdot \nabla_i W_{ij} \tag{16}$$

where:

- $\underline{v}_j$ represents the velocity for particle j;
- m_j represents the mass of particle j.

In eqn (16), velocity derivatives are calculated slightly differently from what would be suggested by equation (11). It is possible to show that with this modification, involving velocity differences in the equation instead of just the term $\underline{v}_j$, it is possible to exactly reproduce gradients of constant velocity fields. It can also be shown that using equation (15) is like using a modified kernel, which satisfies the particle approximation for consistency conditions (13) up to the 0^{th} order. The use of such equation, which has proved to be successful in many cases, enhances the accuracy in velocity field divergence calculations, especially near boundaries (see Liu and Liu [9]).

In this paper, we also selected an approach proposed by Ferrari *et al.* [5], which uses a Riemann solvers based modification of the continuity equation

where a central Rusanov flux term is added to the equation. Adding the Rusanov central flux term to eqn (16) leads to the following form for the continuity equation:

$$\frac{D\rho_i}{Dt} = \rho_i \sum_{j=1}^{n} \frac{m_j}{\rho_j} \cdot (\underline{v}_i - \underline{v}_j) \cdot \nabla_i W_{ij} + \sum_{j=1}^{n} \frac{m_j}{\rho_j} \cdot (\underline{n}_{ij} \cdot \nabla_i W_{ij}) \cdot c_{ij} \cdot (\rho_j - \rho_i) \tag{17}$$

where:

- $\underline{n}_{ij}$ is the unit vector pointing from particle i towards particle j;
- c_{ij} represents highest sound speed between particle i and j.

The addition of the flux terms results in more accurate and smoother density field calculations, which lead to more accurate pressure fields. The correction acts also as a penalty term for density fluctuations helping in enforcing weak compressibility condition.

Finally, the particle approximation that has been used throughout the computations for momentum equation is the following one:

$$\frac{D\underline{v}_i}{Dt} = \underline{f}_i + \sum_{j=1}^{n} m_j \cdot \left(\frac{\underline{\underline{\sigma}}_i}{\rho_i^2} + \frac{\underline{\underline{\sigma}}_j}{\rho_j^2} \right) \cdot \nabla_i W_{ij} \tag{18}$$

where:

- $\underline{f}_i$ is the force/mass ratio of the external forces for particle i;
- $\underline{\underline{\sigma}}_i$ is the stress tensor at particle i.

It is possible to show that this form of momentum equation does not satisfy the particle consistency conditions of eqn (13), neither for the 0^{th} order: therefore, it cannot be used to reproduce gradients of constant stress fields exactly. However, if the terms in the summation of the right hand side of eqn (18) are interpreted as forces (per unit of mass) exchanged by each pair of interacting particles, it is easy to notice that they are symmetrical, thus allowing for particle momentum conservation (when no external forces are present).

3.1 Inviscid flows computations

In order to simulate the behavior of inviscid flows we use the following isotropic constitutive equation for the stress tensor:

$$\underline{\underline{\sigma}}_i = -p_i \cdot \underline{\underline{I}} \tag{19}$$

where:

- $\underline{\underline{I}}$ is the unit tensor.

By using eqn (19), the momentum eqn (18) takes this form:

$$\frac{D\underline{v}_i}{Dt} = \underline{f}_i - \sum_{j=1}^{n} m_j \cdot \left(\frac{p_i}{\rho_i^2} + \frac{p_j}{\rho_j^2} \right) \cdot \nabla_i W_{ij} \tag{20}$$

As it has been pointed out in paragraph 3, the momentum equation conserves momentum exactly, when there are no external forces acting on the system.

3.2 Viscous flows computations

In order to simulate the behavior of a Newtonian viscous fluid at a laminar regime, we use the well-known constitutive equation:

$$\underline{\underline{\sigma}}_i = -p_i \cdot \underline{\underline{I}} + \mu \cdot \underline{\underline{\varepsilon}}_i \tag{21}$$

where:

- $\underline{\underline{\varepsilon}}_i$ is the strain rate tensor at particle i;
- μ is the dynamic viscosity of the fluid.

We then used the following expression for the particle approximation of the strain rate tensor components (see Liu and Liu [9]):

$$\varepsilon_i^{\alpha\beta} = \sum_{j=1}^{n}(v_j^\beta - v_i^\beta)\cdot\frac{\partial W_{ij}}{\partial x_i^\alpha}\cdot\Delta A_j + \sum_{j=1}^{n}(v_j^\alpha - v_i^\alpha)\cdot\frac{\partial W_{ij}}{\partial x_i^\beta}\cdot\Delta A_j - \left(\sum_{j=1}^{n}(\underline{v}_i - \underline{v}_j)\cdot\nabla_i W_{ij}\cdot\Delta A_j\right)\delta^{\alpha\beta} \tag{22}$$

By using eqn (21), the momentum eqn (18) takes this form:

$$\frac{D\underline{v}_i}{Dt} = \underline{f}_i - \sum_{j=1}^{n} m_j \cdot \left(\frac{p_i}{\rho_i^2} + \frac{p_j}{\rho_j^2}\right)\cdot\nabla_i W_{ij} + \sum_{j=1}^{n} m_j \cdot \left(\frac{\mu\cdot\underline{\underline{\varepsilon}}_i}{\rho_i^2} + \frac{\mu\cdot\underline{\underline{\varepsilon}}_j}{\rho_j^2}\right)\cdot\nabla_i W_{ij} \tag{23}$$

4 Numerical examples

In the following paragraphs we show numerical examples regarding the solution of two test cases, one for inviscid flow and the other for a laminar viscous flow.

4.1 Water column

The test case regards the solution of the classical Water column (or Dam break) problem where a column of water collapses under the effect of gravity and a breaking wave impinging on a vertical wall is created thereafter.

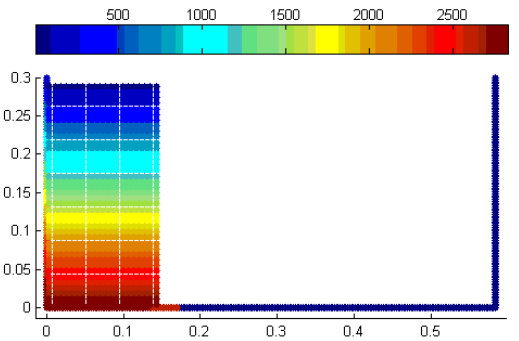

Figure 2: Initial particles distribution for the SPH solution of the water column problem.

The SPH scheme used to solve this numerical test is the inviscid scheme given by eqns (14), (17) and (20). A free-slip boundary condition has been enforced on the boundaries by using special ghost particles that are created via point symmetry about a layer of boundary particles as in Ferrari *et al.* [5].

Time integration has been performed by using a Runge-Kutta third order TVD scheme (see Gottlieb and Shu [10]).

At the initial time step, particles are placed on the left side of the tank with zero velocity and a hydrostatic pressure distribution, which has been calculated analytically according to the equation of state of eqn (14). The initial particle distribution can be seen in Figure 2, where the particles are color coded according to pressure values (measured in Pa) and distances are in meters.

The water column size is 14.6 cm x 28.9 cm, while the tank length is 58.4 cm. 800 particles have been used in the simulation with spacing of 7.3 mm in both vertical and horizontal directions.

In Figures 3–5, the results obtained with SPH are shown. Particles are color coded according to pressure values (measured in Pa).

Even though no comparison with experiments or other numerical solutions has been made at this stage, the results, in terms of pressure and particles displacement seem very realistic and reasonable.

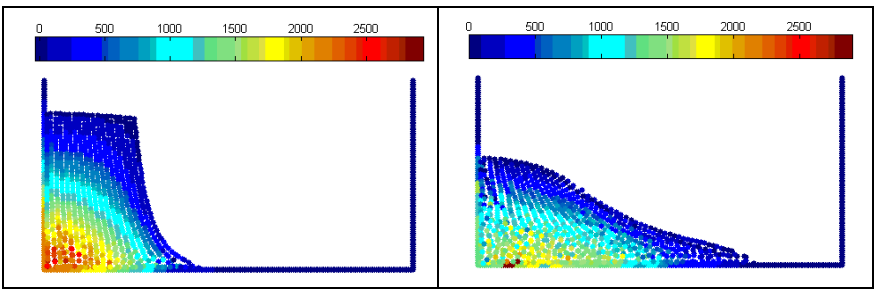

Figure 3: SPH solution at time 0.10 s (left) and 0.20 s (right) (color online only).

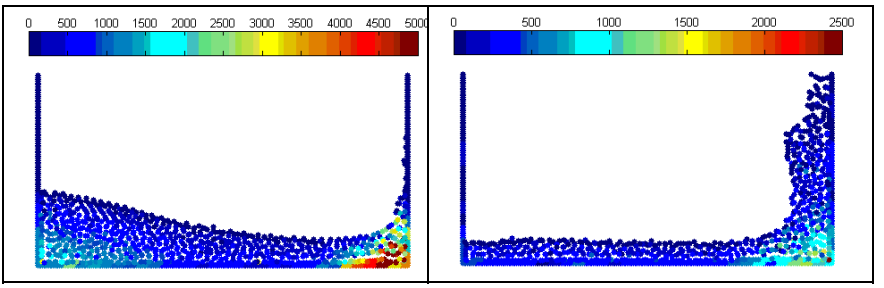

Figure 4: SPH solution at time 0.30 s (left) and 0.60 s (right) (color online only).

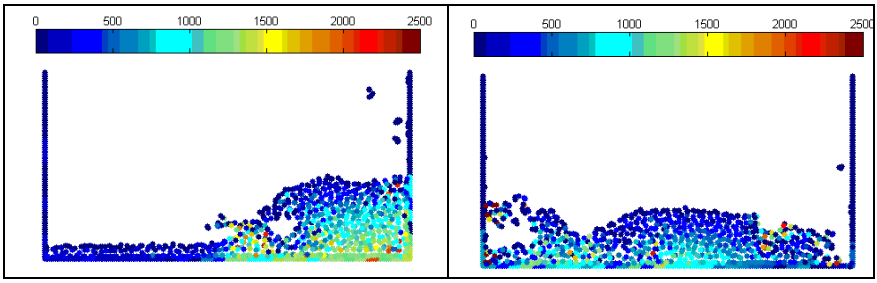

Figure 5: SPH solution at time 0.80 s (left) and 1.00 s (right).

4.2 Poiseuille viscous flow

The test case is the classical Poiseuille flow problem, solved with a layer of water flowing between two infinite parallel planes. Motion is created by a horizontal body force/mass $\underline{F}$, whose module has been set to $2 \cdot 10^{-4}$ m/s in the SPH simulation.

The analytical solution of the problem is known as a series solution. Its expression for horizontal velocity v_x as a function of time and space is as follows:

$$v_x(z,t) = \frac{F}{2\nu} z(z-L) + \sum_{n=0}^{+\infty} \frac{4FL^2}{\nu\pi^3(2n+1)^3} \cdot \exp\left(-\frac{(2n+1)^2\pi^2\nu}{L^2}t\right) \cdot \sin\left(\frac{\pi z}{L}(2n+1)\right) \quad (24)$$

where:

- L is the distance between the two planes (set to 10^{-3} m in the SPH simulation);
- ν is the kinematic viscosity of water (10^{-6} m^2/s);
- z is the transversal coordinate between the planes (z=0 on the lower plane).

From the first spatial derivative of eqn (24), it is possible to obtain the analytical expression for the tangential stresses.

The SPH scheme used to solve this numerical test is the viscous scheme given by eqns (14), (16), (22) and (23). Boundary conditions have been enforced by using ghost particles that are being created by mirroring the liquid particles about the boundaries as in Morris *et al.* [4]. For viscous flows, a no-slip condition is required and so ghost particles are assigned an opposite velocity to the liquid particles they are created from. To simulate an infinite extension of the domain on the horizontal direction, periodic boundary conditions have been used, where particles exiting the domain on one side are re-entered in the system from the opposite side.

Time integration has been performed by using the simple Euler forward-in-time scheme.

At the initial time step, particles are placed between the two planes with zero velocity and a uniform zero pressure distribution. The motion is triggered by the horizontal body force/mass component $\underline{F}$, which is constant in every instant of the simulation. Four hundred particles have been used in the simulation with spacing of 0.025 mm in both vertical and horizontal directions.

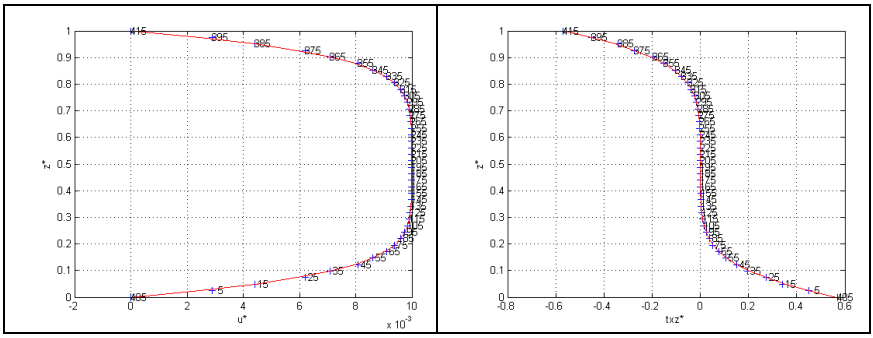

Figure 6: SPH solution of unsteady Poiseuille flow at an intermediate time step.

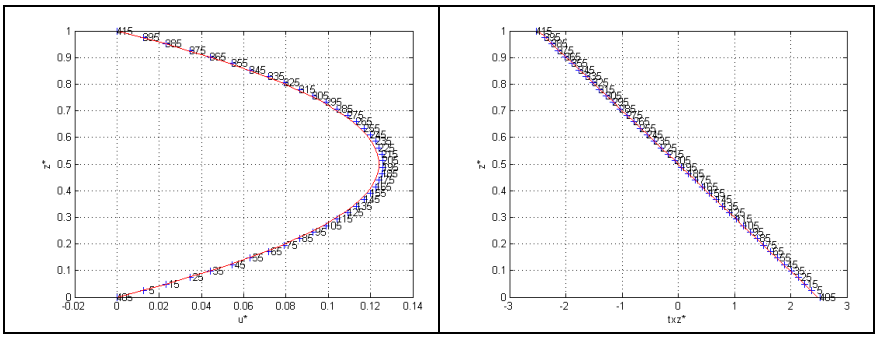

Figure 7: SPH solution of unsteady Poiseuille flow at the steady state.

In Figures 6 and 7, a comparison between the SPH solution of the problem and the analytical solution of the problem is shown, both for the horizontal velocity component (left hand side) and the tangential stresses (right hand side). Variables values are non-dimensional and scaled, with $l_0 = 1 \cdot 10^{-3}$ m being the scaling length, $u_0 = 2 \cdot 10^{-4}$ m/s being the scaling velocity and $\tau_0 = 4 \cdot 10^{-5}$ Pa being the scaling tension.

As can be seen from Figures 6 and 7, the SPH solution well agrees with the analytical solution. Steady state was considered reached when the average SPH solution error was lower than 2%. The error was also lower than this bound during all the intermediate instants of the simulation, except for the first ones, when the error was found to be higher.

5 Conclusions

SPH is a powerful and easy to code numerical tool that can be useful in order to solve many fluid flow problems. Its Lagrangian nature makes it particularly suitable for simulating free surface flows, but some drawbacks still wait to be solved. To this purpose, in order to enhance stability and smoothness of field

variables, a Riemann based modification approach of continuity equation has been selected and implemented. The numerical elaborations show the capability of the method to capture the general features of the Dam break problem. Poiseuille test has shown very satisfactory behavior as well.

Next step will be the comparison of the results obtained with the selected method with experimental and other kind of numerical approaches.

References

[1] Monaghan J.J., Smoothed particle hydrodynamics. *Reports on Progress in Physics*, **68**, pp. 1703-1759, 2005.
[2] Randles P.W., Libersky L.D., Smoothed particle hydrodynamics: some recent improvements and applications. *Computer Methods in Applied Mechanics and Engineering*, **138**, pp 375-408, 1996.
[3] Takeda H., Miyama S.M., Sekiya M., Numerical simulation of viscous flow by Smoothed particle hydrodynamics. *Progress of Theoretical Physics*, **92(5)**, pp. 939-960, 1994.
[4] Morris J.P., Fox P.J., Zhu Y., Modeling low Reynolds number incompressible flows using SPH. *Journal of Computational Physics*, **136**, pp. 214-226, 1997.
[5] Ferrari A., Dumbser M., Toro E.F., A new 3D parallel scheme for free surface flows. *Computers & Fluids*, **38**, pp. 1203-1217, 2009.
[6] Liu W.K., Jun S., Zhang Y.F., Reproducing kernel particle methods. *International Journal for Numerical Methods in Fluids*, **20**, pp. 1081-1106, 1995.
[7] Liu M.B., Liu G.R., Restoring particle consistency in smoothed particle hydrodynamics. *Applied Numerical Mathematics*, **56**, pp.19-36, 2006.
[8] Monaghan J.J., Simulating free surface flows with SPH. *Journal of Computational Physics*, **110**, pp. 399-406, 1994.
[9] Liu G.R., Liu M.B., *Smoothed Particle Hydrodynamics a meshfree particle method*, World Scientific Publishing, pp. 114-117, 2003.
[10] Gottlieb S., Shu C.-W., Total Variation Diminishing Runge-Kutta Schemes. *Mathematics of Computation*, **67(221)**, pp. 73-85, 1998

Numerical modelling of the filling of formworks with self-compacting concrete

S. Tichko[1], J. Van De Maele[2], N. Vanmassenhove[2],
G. De Schutter[1], J. Vierendeels[3], R. Verhoeven[4] & P. Troch[5]
[1]*Magnel Laboratory for Concrete Research, Ghent University, Belgium*
[2]*Ghent University, Belgium*
[3]*Dept. of Flow, Heat & Combustion Mechanics, Ghent University, Belgium*
[4]*Laboratory for Hydraulics, Ghent University, Belgium*
[5]*Department of Civil Engineering, Ghent University, Belgium*

Abstract

This paper describes the numerical modelling of the flow of self-compacting concrete (SCC) in column and wall formworks during the filling process. It is subdivided into four main parts. In the first part, the rheological properties of SCC and the theory regarding the pressure exerted by the SCC on the formworks are shortly described. In the second part, the formwork filling tests, which have been carried out at the Magnel Laboratory for Concrete Research of the Ghent University, are presented. The general layout of the tests and the measurement set-up are clearly described. In the third part, the numerical modelling of the flow of SCC using a commercially available solver is explained as well as the obtained results from the CFD simulations. Finally in the last part, a comparison is made between the measurements and the simulation results. The formwork pressures are hydrostatic for SCC pumped from the base of the formworks.
Keywords: CFD, numerical modelling, laminar flow, self-compacting concrete.

1 Rheology of SCC and the theory of formwork pressure

1.1 Rheology of SCC

According to De Schutter et al [1], SCC can be defined as a concrete which needs to possess sufficient fluidity in order to be able to fill a formwork

WIT Transactions on Engineering Sciences, Vol 69, © 2010 WIT Press
www.witpress.com, ISSN 1743-3533 (on-line)
doi:10.2495/AFM100141

completely (filling ability) without the aid of other forces than gravity, even when having to flow through narrow gaps (passing ability), but also showing a sufficient resistance to segregation, during flow and in stationary conditions (stability).

In order to achieve sufficient fluidity in SCC, without increasing the water content, super-plasticizers must be applied. Only adding super-plasticizers to traditional concrete is not sufficient to create SCC, due to the large amount of coarse aggregates, which can form particle bridges when flowing through a narrow gap, causing blocking. Therefore in order to fulfil the passing ability condition, the amount of coarse aggregates is reduced. On the other hand, extra amounts of fine materials, like limestone filler, fly ash, silica fume are added in order to increase the stability of SCC [1, 2].

According to Feys [2] and Roussel and Lemaître [2, 3], the behaviour of fresh concrete may be described using a yield stress model such as the Bingham model or the Herschel-Bulkley model, which are formulated mathematically by eqn (1) and eqn (2) respectively.

$$\tau_B = \tau_{0,B} + \mu_{p,B}.\dot{\gamma} \tag{1}$$

$$\tau_{HB} = \tau_{0,HB} + K_{HB}.\dot{\gamma}^{n_{HB}} \tag{2}$$

where: the indices B, HB stand for Bingham, Herschel-Bulkley, resp.

τ = shear stress in the material (Pa)

$\dot{\gamma}$ = shear rate in the material (1/s)

τ_0 = yield stress (Pa)

$\mu_{p,B}$ = plastic viscosity (Pa s)

K_{HB} = consistency factor (Pa s^n)

n_{HB} = consistency index (-)

SCC is further characterized by two specific phenomena, thixotropy and shear thickening. Thixotropy can be defined as a reversible build-up and breakdown of internal structure due to flocculation or coagulation of cement particles for which the influence of inter-particle forces is still significant, whereas shear thickening is an increase in apparent viscosity with increasing shear rate.

In order to capture the effect of shear thickening in SCC, Feys [2] proposed a modification of the standard Bingham material model. This modified Bingham model is defined by the following equation.

$$\tau_{MB} = \tau_{0,MB} + \mu_{p,MB}.\dot{\gamma} + c_{MB}.\dot{\gamma}^2 \tag{3}$$

where: the indices MB stands for modified Bingham

c_{MB} = second order parameter (Pa s^2)

The effect of shear thickening becomes very important at high shear rates. This is captured in the modified Bingham model by the extra quadratic term in eqn (3).

Roussel [4] proposed the following model for describing thixotropy in SCC. He introduced a structure parameter λ, the flocculation state of the material, which influences the apparent rheological properties of the material. It is defined by two equations, where three parameters have to be identified.

$$\tau = (1+\lambda).\tau_{0,B} + \mu_{p,B}.\dot{\gamma} \tag{4}$$

$$\frac{\partial\lambda}{\partial t} = \frac{1}{T} - \alpha.\lambda.\dot{\gamma} \tag{5}$$

where: λ = the flocculation state of the material (-)
T = flocculation characteristic time (s)
α = de-flocculation parameter (-)

Eqn (4) is a constitutive equation and eqn (5) describes the rate of change of the internal structure.

It is assumed that the characteristic time of flocculation is long compared to the characteristic time of de-flocculation [5]. Eqn (5) then simplifies to:

$$\frac{\partial\lambda}{\partial t} = -\alpha.\lambda.\dot{\gamma} \tag{6}$$

After integration of eqn (6), and introducing the resulting flocculation state in eqn (4), the shear stress then writes:

$$\tau = \left(1+\lambda_0.e^{-\alpha\dot{\gamma}t}\right).\tau_{0,B} + \mu_{p,B}.\dot{\gamma} \tag{7}$$

At rest, the shear rate equals zero and the evolution of the apparent yield stress is described by eqn (8).

$$\tau = \tau_0(t) = (1+\lambda).\tau_0 = \tau_0 + \tau_0.\frac{t}{T} = \tau_0 + A_{thix}.t \tag{8}$$

Based on the experience of Roussel [4] with formwork pressure measurements, a classification of SCC according to their flocculation rate A_{thix} can be made. This classification is presented in Table 1.

Table 1: Classification of SCC according to their flocculation rate.

Flocculation rate A_{thix} (Pa/s)	SCC type
Less than 0,1	Non-thixotropic SCC
Between 0,1 and 0,5	Thixotropic SCC
Higher than 0,5	Highly thixotropic SCC

1.2 Theory of formwork pressure

In practice, two types of filling processes are encountered, namely filling from the top of the formwork and filling from the base of the formwork. When the formwork is filled from the top, due to thixotropy the SCC starts to build up a structure able to withstand pressure from the concrete above, without increasing the horizontal pressure against the form [5]. For this type of formwork filling, the horizontal formwork pressure can be calculated using eqn (9) [4].

$$p_{hor} = \left(1 - \frac{A_{thix}.H}{\rho_{SCC}.g.R.e}\right)\rho_{SCC}.g.H \tag{9}$$

where: e = the casted wall thickness (m)
H = height of the casted element (m)
ρ_{SCC} = density of the SCC (kg/m³)
g = gravity acceleration (m/s²)
R = casting rate (m/s)

For the case where the SCC is pumped from the base of the formwork, the formwork pressure is mainly hydrostatic [5]. The reason is because the SCC is in motion during the whole casting procedure, without any possibility for the concrete shear strength to develop. The resulting formwork pressure can then be determined using eqn (10).

$$p_{hor} = \rho_{SCC}.g.H \tag{10}$$

2 Full-scale formwork filling tests

In this part, the four full-scale formwork filling tests that have been performed by Van De Maele and Vanmassenhove [6] at the Magnel Laboratory for Concrete Research of the Ghent University in Belgium are described. During these tests, two columns and two walls were cast, as shown in Fig. 1.

The two columns are identical and have a height of 2 m, a depth of 21 cm and a width of 17,4 cm. The SCC is pumped from the base of the formwork. The two walls are also identical regarding the dimension (a height of 2 m, a length of 4 m and a thickness of 21 cm), but not regarding the positioning of the SCC inlet.

Figure 1: Layout of the formwork filling tests.

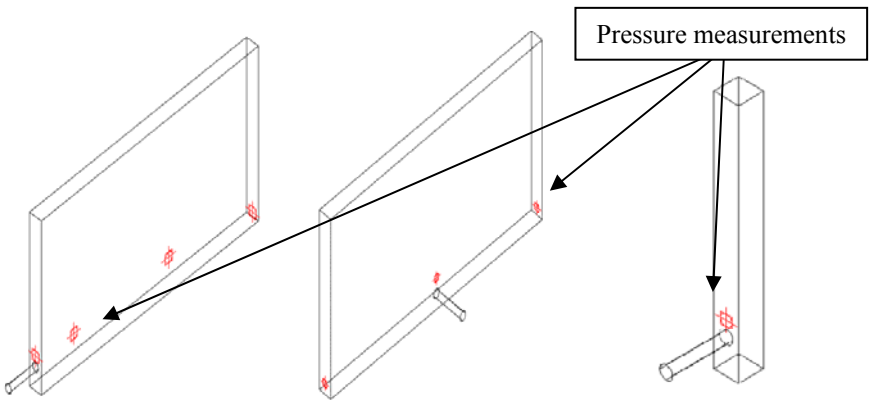

Figure 2: Connections of the SCC inlet for wall type A and B.

Fig. 2 shows the two different pumping connections. For both walls, the SCC is also pumped from the base of the formwork.

During the filling of the formworks, the flow of the SCC was measured at the concrete pump, the time was recorded and the progression of the filling process was monitored with several cameras. The formwork pressure was also measured on several positions at the base of the formwork, where the maximum pressure was expected. Two types of pressure measurements were used: manometers and electronic pressure transducers. Both devices were fixed on an intermediate water chamber, sealed with a rubber membrane, and flush mounted on the formwork. The locations of the pressure measurements (red cross-haired squares) are shown on fig. 2 for the walls and for the columns. At the beginning of each filling process and at the end of the casting test period, a sample of concrete has been taken in order to investigate the fresh properties, by means of a Tattersall Mk-II rheometer and standard tests on SCC like slump flow, V-funnel, L-box, sieve stability and air content.

3 Numerical modelling of the formwork filling tests

3.1 Governing equations

The most general description of a fluid flow is obtained from the well known Navier-Stokes equations. They represent mass conservation, conservation of motion and conservation of energy [7, 8]. Due to fact that the density and the viscosity of the SCC remains constant during the isothermal filling process, the conservation of energy is not considered in the numerical simulations. For unsteady, isothermal, laminar flows these equations take on the following forms:

Conservation of mass:

$$\frac{\partial \rho}{\partial t} + \nabla(\rho.\vec{v}) = 0 \tag{11}$$

Conservation of momentum:

$$\frac{\partial(\rho.\vec{v})}{\partial t} + \nabla(\rho.\vec{v} \otimes \vec{v}) = -\nabla p + \nabla \bar{\tau} + \rho.\vec{g} \tag{12}$$

where:
- ρ = density or specific mass of the fluid (kg/m³)
- $\vec{v}$ = velocity vector (m/s)
- $\bar{\tau}$ = stress tensor (Pa)
- $\vec{g}$ = gravity acceleration vector (m/s²)
- $\otimes$ = tensor product of two vectors

Due to the fact that the shear rates remain relatively low during the formwork filling process, no shear thickening is occurring. Therefore the stress tensor τ is modelled using the Herschel-Bulkley material model (see also eqn (2)). These Navier-Stokes equations are solved for the pressures and the velocities over the entire computational domain for each time step with the aid of the Fluent v.6.3 software. In order to simulate a free surface flow, as in the formwork filling process, the *Volume of Fluid* (VOF) method developed by Hirt and Nichols [9], is used. The VOF method can model two or more immiscible fluids by solving a single set of momentum equations and tracking the volume fraction of each of the fluids throughout the domain.

3.2 Computational domain

In order to perform the numerical simulation of the SCC flow through the formworks shown in fig. 1, a 3D geometry is constructed for each cast element and meshed with the Fluent Gambit v.2.3.16 pre-processor [10]. Fig. 3, fig. 4 and fig. 5 show the resulting high quality meshes for the columns and the walls.

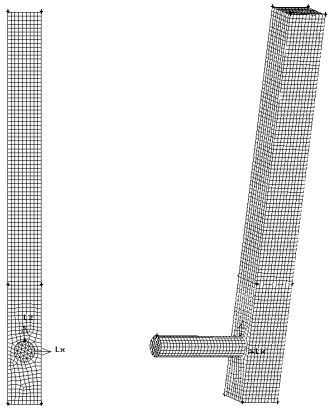

Figure 3: Computational domain for the column filling process.

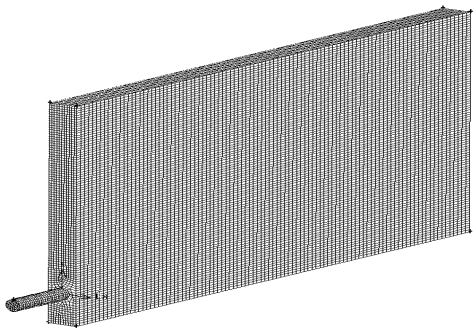

Figure 4: Computational domain for wall type A filling process.

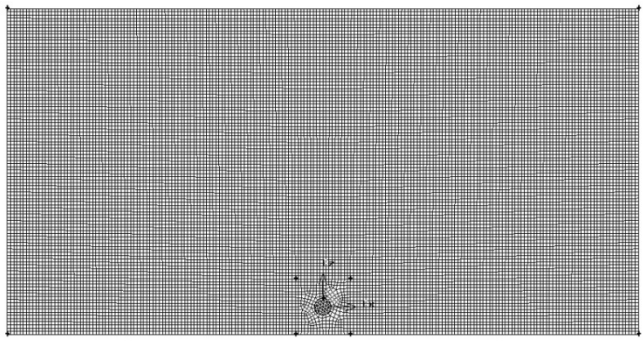

Figure 5: Computational domain for wall type B filling process.

3.3 Boundary conditions

In order to obtain solutions for the stated Navier-Stokes equations, a set of boundary conditions needs to be applied to the computational domain. At the flow inlet, a uniform velocity profile of the incoming SCC and the volume fraction of the SCC phase is imposed. At the top of the formwork, the pressure is atmospheric, resulting in a zero gauge pressure condition at the outlet. At the pipe walls, a no-slip condition is assumed.

3.4 Solution of the governing equations

The governing flow equations are discretized using the Finite Volume Method and solved with a 3D, double precision, implicit pressure-based solver [8]. In table 2 the solver settings of the numerical model are summarized.

Table 2: Solver controls.

Controls	Columns	Wall type A and B
Multiphase VOF model/scheme	2 phases	2 phases
VOF scheme	Explicit	Explicit
Transient controls	NITA[1]	NITA[1]
Unsteady formulation	1st order implicit	1st order implicit
Body force formulation	Implicit body force	Implicit body force
Momentum discretization	2nd order upwind	2nd order upwind
Volume fraction discretization	Geo-reconstruct	CICSAM[2]
Pressure discretization	Body force weighted	Body force weighted
Pressure-velocity coupling	Fractional step method	Fractional step method

[1] Non-Iterative Time Advancement
[2] Compressive Interface Capturing Scheme for Arbitrary Meshes

3.5 Formwork filling simulations

The fresh properties of the SCC used in the formwork filling tests are the presented in table 3.

Table 3: Fresh properties of the SCC used in the tests.

Property	Value
Density ρ_{SCC} (kg/m³)	2314,4
Viscosity $\mu_{p.HB}$ (Pa s)	28,3
Yield stress $\tau_{0.HB}$ (Pa)	10,3
Consistency index n_{HB} (-)	1,385
Consistency factor K_{HB} (Pa s^n)	17,7

Fig. 6 show the simulated formwork filling of the columns, while the simulated casting process of the walls are presented in fig. 7 and fig. 8.

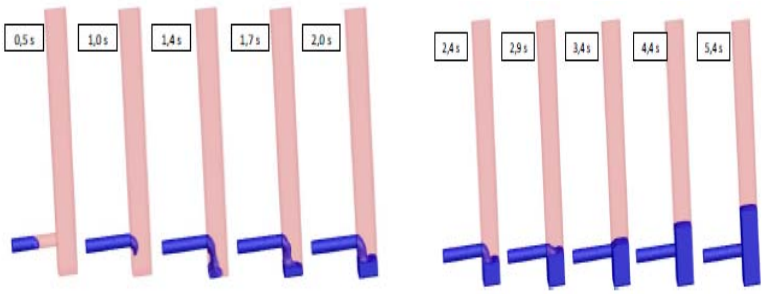

Figure 6: Simulated filling process of the columns.

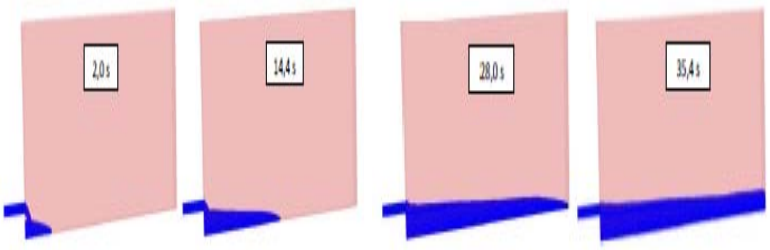

Figure 7: Simulated filling process of wall type A.

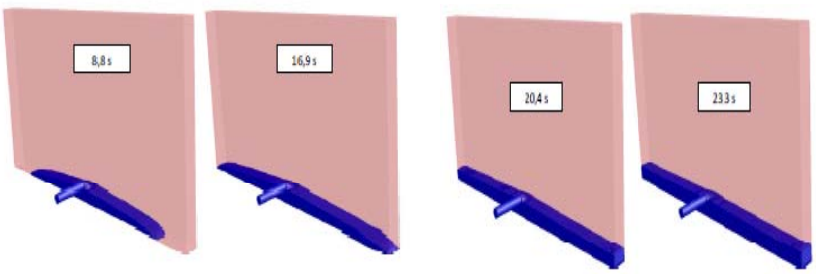

Figure 8: Simulated filling process of wall type B.

4 Comparison of the results and conclusions

4.1 Comparison of the results

Without the presence of thixotropic build-up, the formwork pressures are expected to be hydrostatic, and therefore they can be calculated analytically using eqn (10). The measured formwork pressures are compared with the hydrostatic pressures and presented in fig. 9 for the columns and in fig. 10 for the two wall types.

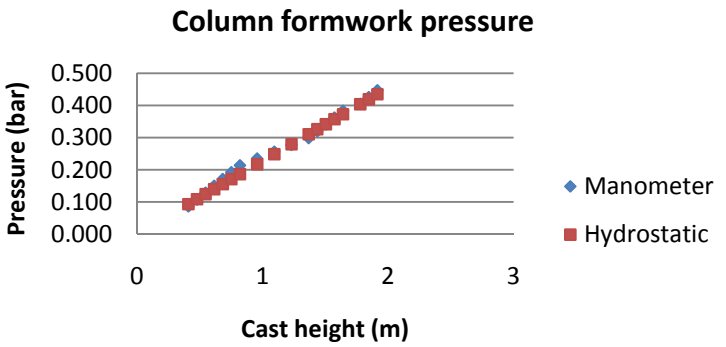

Figure 9: Formwork pressure of the columns.

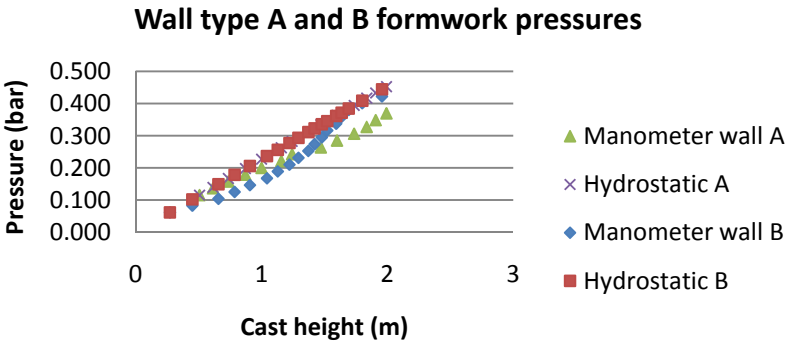

Figure 10: Formwork pressure of the wall type A and B.

The formwork pressures obtained from the numerical simulations are shown in fig. 11 for the columns and in fig. 12 for the two wall types.

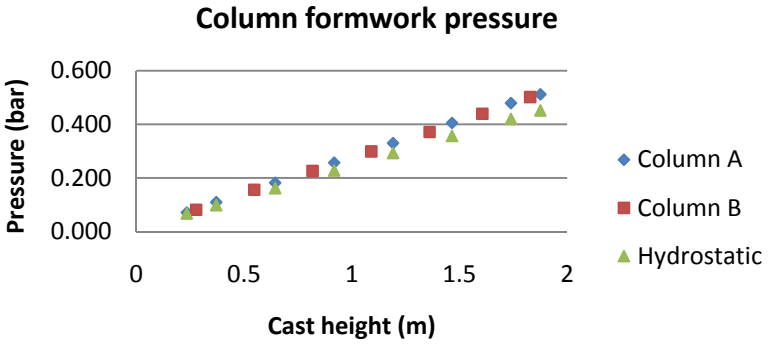

Figure 11: Column formwork pressure from CFD simulation.

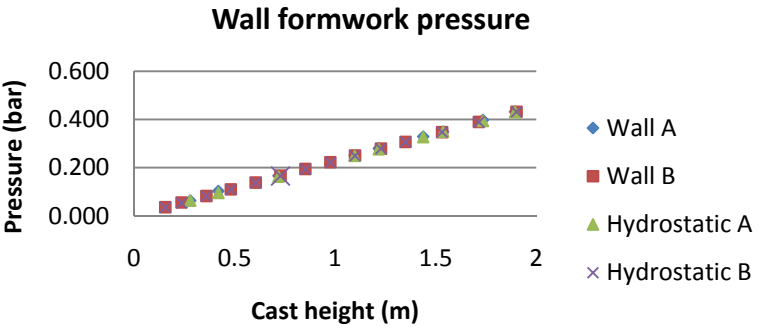

Figure 12: Wall formwork pressure from CFD simulations.

4.2 Conclusions

From the comparison of the measurements, the analytical results and the results from the CFD simulations, we can conclude that the formwork pressures are hydrostatic as expected [2]. The small differences that can be observed between the measured pressures and the hydrostatic pressures for the same cast heights is related to the experienced shortcomings of the pressure measurement units used in the tests. The non-linear deformation of the plastic membranes due to exerted concrete pressure, the variable surface tension of the used membranes and the unavoidable inclusion of air bubbles into the water chambers have lead to these small differences in the formwork pressure measurements.

Nevertheless, it can be concluded that there is a very good agreement between all the obtained results. The VOF method has proved to very effective in capturing the time evolution of a formwork filling process, as shown in fig. 13.

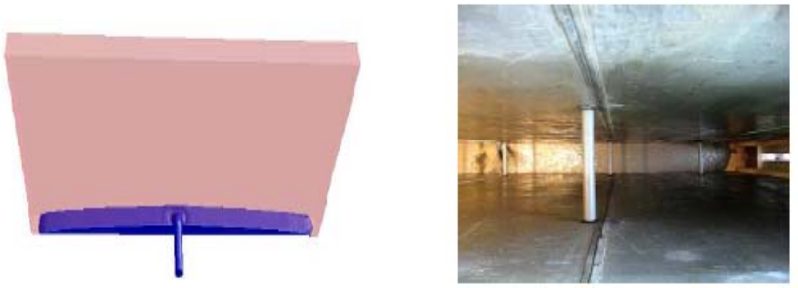

Figure 13: Simulated and real formwork filling evolution.

The real position and form of the free surface of the SCC, during the filling of the formwork of wall type B, is compared with the simulated position and form of the SCC-air interface at the same time.

For this type of casting processes, where the SCC is pumped from the base of the formwork to the top, as such avoiding thixotropic build-up, the formwork pressures can easily be estimated using the simple formula for the hydrostatic pressure, eqn (10). When more details on the formwork filling process are required, numerical simulations can be carried out using the implemented Herschel-Bulkley material model, describing the relation between the applied shear rate and the resulting shear stress in the SCC, in combination with the VOF method. These CFD simulations will predict the formwork pressures and the time evolution of the casting process accurately.

References

[1] De Schutter, G. and Bartos, P. and Domone, P. and Gibbs, J., *Self-Compacting Concrete,* Whittles Publishing, Caithness, 2008.
[2] Feys, D., *Interactions between Rheological Properties and Pumping of Self-Compacting Concrete,* Ph-D dissertation, Ghent University, 2009.
[3] Roussel, N. and Lemaître, A., *Steady state flow of cement suspensions,* Cem. Conc. Res., vol. 40, pp. 77-84, 2010.
[4] Roussel, N., *A thixotropy model for fresh fluid concretes,* Cem. Conc. Res., vol. 36, pp. 1797-1806, 2006.
[5] Billberg, P., *Form pressure generated by SCC - Influence of Thixotropy and Structural Behaviour at Rest,* Ph-D dissertation, Royal Institute of Technology, Stockholm, 2006.
[6] Van De Maele, J. and Vanmassenhove, N., *Vullen van een bekisting met zelfverdichtend beton door het pompen van onderaan,* Master thesis (in Dutch), Ghent University, 2010.
[7] Hirsch, Ch., *Numerical Computations of Internal and External Flows, Volume 1 – Fundamentals of Numerical Discretization,* John Wiley & Sons, New York, 1989.
[8] Fluent 6.3 User's Guide, Fluent Inc, 2006.
[9] Hirt, C.W. and Nichols, B.D., *Volume of Fluid Method for the Dynamics of Free Boundaries,* J. Comput. Phys., vol. 39, pp. 201-225 1981.
[10] Gambit 2.3 Modelling Guide, Fluent Inc, 2006.

Analysis of tunnel compression wave generation and distortion by the lattice Boltzmann method

K. Akamatsu & M. Tsutahara
Graduate School of Engineering, Kobe University, Japan

Abstract

The finite difference lattice Boltzmann method was applied to investigate the generation of the compression wave produced when a high-speed train enters a tunnel and the distortion of the wave front as it travels in the tunnel. The discrete Boltzmann equation for the 3D39Q thermal BGK model is solved in three-dimensional space using a second-order Runge-Kutta scheme in time and a third order upwind finite difference scheme in space. The arbitrary Lagrangian-Eulerian formulation is applied to model the interaction of the moving train nose and the tunnel portal. Numerical calculations are carried out for axisymmetric trains with various nose profiles entering a long circular cylindrical tunnel with straight and stepwise flared portals. The generation of the compression wave can be described in terms of flow parameters along the train nose and the interaction with the tunnel portal. The train speed and the train to tunnel area dependence of the predicted wave strength are found to be in good agreement with an analytic linear prediction. The distortion of the compression wave front that travels within an acoustically smooth tunnel is consistent with the time-domain computation of the one-dimensional Burgers equation. The non-linear steepening is confirmed to be dependent on the initial steepness of the wave front, which is determined by the interaction of the train nose and the tunnel portal. The tunnel entrance with flared portals is shown not only to decrease the initial steepness of the compression wave front but also to counteract the effect of non-linear steepening.

Keywords: lattice Boltzmann method, high speed train, compression wave, micro-pressure wave, nonlinear steepening, aerodynamic noise.

WIT Transactions on Engineering Sciences, Vol 69, © 2010 WIT Press
www.witpress.com, ISSN 1743-3533 (on-line)
doi:10.2495/AFM100151

1 Introduction

A high-speed train entering a tunnel compresses the air in front of it and generates the compression wave, which travels within the tunnel at the speed of sound toward the exit of the tunnel. The compression wave is reflected as an expansion wave at the exit of the tunnel being accompanied by the emission of an impulsive sound wave so-called 'micro-pressure wave' or 'tunnel bang' which causes the environmental annoyance in the nearby area (Ozawa et al [1]).

The strength of the micro-pressure wave is proportional to the steepness of the arriving compression wave, i.e. the gradient of the pressure across the wave front at the exit. The initial steepness of the wave front is determined primarily by the train speed and the geometries of train nose and tunnel portal. For a tunnel with acoustically smooth concrete slab tracks, and with the length comparable to the shock formation distance, which depends on the initial steepness of the compression wave, the wave front forms a shock wave due to the 'non-linear steepening'. This non-linear effect of acoustic propagation causes the strength of the micro-pressure wave to become comparable to the sonic bang from a supersonic aircraft. Fukuda et al [2] found that the compression wave in a tunnel longer than the shock formation distance once develops a shock profile, and then reverts by friction to a waveform with reduced steepness causing less subjective effects on the environment. Integrated numerical simulations will be necessary to investigate the propagation of compression wave and the radiation of micro-pressure wave such that the progressive characteristics of compression wave are interconnected to the original waveform.

A number of investigations on the generation and propagation of the compression wave have been carried out including scale model experiments by Aoki et al [3], theoretical analysis by Sugimoto and Ogawa [4] and by Howe [5], and numerical simulations by Ogawa and Fujii [6] and by Mashimu et al [7]. Howe has developed a linear theory of the compression wave. The head wave is expressed as a convolution product of the sources dependent on the nose shape and speed of the train, and an acoustic Green's function whose form depends on the geometry of the tunnel entrance. In the numerical calculations of Mashita et al, one-dimensional Euler's equation and the equation of state are solved to simulate the distortion of compressive wave front in the tunnel giving measured waveform as initial conditions.

The lattice Boltzmann method is now a very powerful tool of computational fluid dynamics. Tsutahara et al [8] have reported successful applications of the finite difference lattice Boltzmann method (FDLBM) to the direct numerical simulation of the sound generated a body immersed in fluids. Akamatsu et al [9] has demonstrated that the FDLBM is also a useful approach for studying problems in the non-linear acoustics. In this paper, we present direct numerical simulations of the generation of compression wave using the FDLBM. The arbitrary Lagrangian-Eulerian (ALE) formulation developed by Hirt et al [10] is applied to model the interaction of the moving train nose and the tunnel portal giving the local equilibrium distribution function in Eulerian form and moving the train and grids in Lagrangian manner.

2 Numerical method

2.1 Discrete BGK equation

The lattice Boltzmann model we use is a single relaxation time discrete BGK scheme on a three dimensional cubic lattice called D3Q39 model. The basic equation is written considering the arbitrary Lagrangian-Eulerian moving frame as:

$$\frac{\partial f_i}{\partial t}+\left(c_{i\alpha}-V_\alpha\right)\frac{\partial f_i}{\partial x_\alpha}-\frac{A}{\phi}c_{i\alpha}\frac{\partial\left(f_i-f_i^{\mathrm{eq}}\right)}{\partial x_\alpha}=-\frac{1}{\phi}\left(f_i-f_i^{\mathrm{eq}}\right), \tag{1}$$

where f_i and f_i^{eq} are the velocity distribution function and the local equilibrium distribution function respectively, which represent the number density of particles having velocity $c_{i\alpha}$ at each lattice node. Subscript i represents the direction of particle translation and α indicates the Cartesian coordinates. V_α is the velocity of moving grid in ALE formulation, which is same as the speed of train translation. ϕ is the relaxation time and A is a constant of an additional term introduced to make the calculation of high Reynolds number flows fast and stable. These two parameters ϕ and A determine the viscosity of fluid.

The macroscopic variables of flow: density, velocity and internal energy are defined by the moment of velocity distribution function as follows:

$$\rho=\sum_i f_i\,, \tag{2}$$

$$\rho u_\alpha=\sum_i f_i c_{i\alpha}\,, \tag{3}$$

$$\frac{1}{2}\rho u^2+\rho e=\sum_i\frac{1}{2}f_i c_{i\alpha}^2\,. \tag{4}$$

The local equilibrium distribution function f_i^{eq} is dependent on the macroscopic variables and is given by a polynomial of the flow velocity up to the third order. The pressure p and the sound velocity c_{s} are given by:

$$p=\frac{2}{3}\rho e\,, \tag{5}$$

$$c_{\mathrm{s}}=\sqrt{\frac{10}{9}e}\,. \tag{6}$$

Eqn (1) is discretized in a finite difference scheme and the time integration is evaluated by the second-order Runge-Kutta scheme. The second and third terms on the left-hand side of eqn (1) are estimated using a forth-order central difference scheme added by a numerical viscosity term. The described LBM approach recovers the compressible Navier-Stokes equation. More details of the discrete BGK formulation and numerical procedure are referred to [8].

2.2 Numerical models

A cross section of the axisymmetric computational domain is shown in fig. 1, where the radius of tunnel normalizes the dimensions. The train is formed by a part of the inner boundary where a body fitted grid is employed. The no-slip boundary condition is applied to the train surface and slip boundary condition to the tunnel wall. The train travels in the negative x direction where the origin is at the centre of the tunnel entrance plane. The thick dotted line indicates the boundary of the moving frame being the grid nodes below the line to move with the same speed as the train.

The computations were made for three different train nose profiles: cone, paraboloid, ellipsoid and three different tunnel portals: unflared and two flared. The configurations of train nose profiles and tunnel portals are shown in fig. 2. The cross section of the train becomes uniform with constant area $A_0 = \pi h^2$ at a distance L from the nose of the train. The aspect ratio h/L of the nose is 0.2 for all profiles. The blockage A_0/A is 0.2 for the paraboloidal and ellipsoidal train, and is set to 0.12, 0.16, 0.2 and 0.25 for the conical train, where A is the cross-sectional area of the tunnel. The train Mach number is fixed to 0.25 for the paraboloidal and ellipsoidal train, but is changed to 0.15, 0.2, 0.25, and 0.3 for the conical train. The acoustic pressure was calculated at six microphone positions located on the tunnel wall (5) and in the outlet space (1). The microphone positions on the tunnel wall are x/R = -10, -30, -50, -70 and -90 where R is the radius of tunnel. The microphone position in the outlet space is at a distance r/R = 10 in the direction of 45 degree from the centre of the tunnel exit.

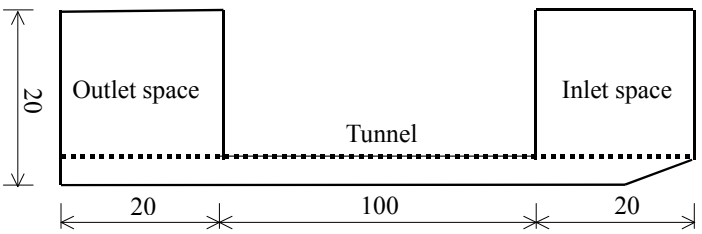

Figure 1: Cross section of axisymmetric computational domain.

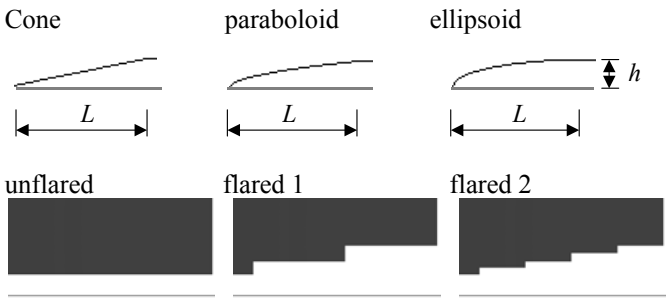

Figure 2: Configuration of train nose profiles and tunnel portals.

3 Results and discussion

3.1 Flow field along the train nose

A train travelling at constant speed pushes aside the stationary air ahead and builds up a frozen flow field along the train. No sound wave is produced by the steady straight translation of train through a homogeneous environment. But the flow pattern changes and pressure waves are generated when the train nose sweeps past the variable geometry of the tunnel portal. Fig. 3 shows a variation of the flow field along a conical train nose at three relative positions to the tunnel portal. The pressure rise contour lines are shown in the left-hand side and the velocity vector plots in the right-hand side. Just before the train approaches the tunnel portal the air in tunnel starts to flow in the direction of train progression and a compressive head wave is observed to propagate as a plane wave with an initially small pressure rise fig. 3(a), when the train nose enters halfway into the tunnel air starts to flow out of portal fig. 3(b), and after the nose has passed into the tunnel and the uniform section of train passes the tunnel entrance plane, most of air flows out of the tunnel fig. 3(c). The hydrodynamic pressure is always the highest at the stagnation point of nose throughout the train progression.

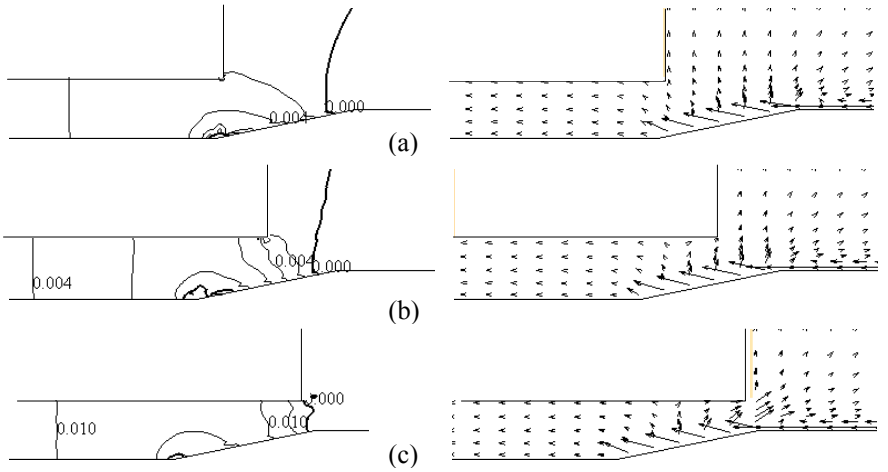

Figure 3: Flow field along a conical train nose.

Spatial distributions of the pressure rise along the tunnel are plotted on a frame moving with a speed of sound in fig. 4. The parameters x_0 are the x-coordinates of train nose at each time step. The pressure ahead of the train nose gradually increases until the nose has passed into the tunnel. The pressure behind the nose section rapidly decreases to the ambient pressure at the tunnel entrance. Variations of axial flow velocity u in the axial and radial directions are shown in figs. 5 and 6. The air ahead of the nose flows forward to the train, but the air behind the nose flows backward toward the tunnel entrance except in the boundary layer enveloping the train. The branch is in the middle of nose.

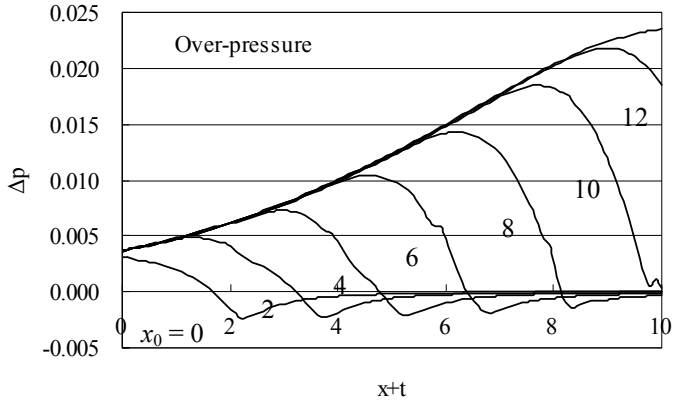

Figure 4: Variation of pressure rise along the tunnel.

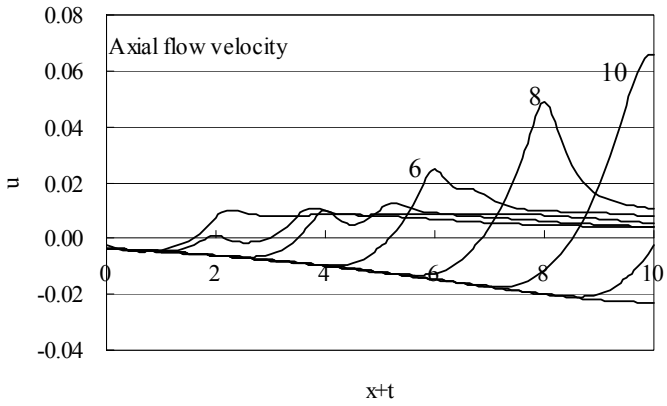

Figure 5: Variation of axial flow velocity along the tunnel.

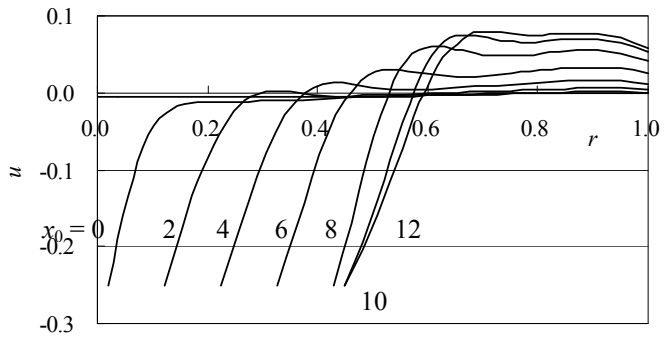

Figure 6: Variation of axial flow velocity across the tunnel.

3.2 Initial wave profile at tunnel entrance

Fig. 7 shows a typical pressure rise waveform observed at a fixed position in tunnel (x = -10) and a time–distance diagram for the compression wave propagation and the train translation. The pressure at point "a" is same as the pressure at x = 0 when the nose passes the tunnel entrance plane. Air in the tunnel has been compressed before the train arrives at the entrance. The pressure at point "b" is that when the end of nose passes the entrance plane. The pressure increases rapidly between "a" and "b" due to the change of the cross-sectional area of the train. The head of train passes the fixed point at the time of "c". The gradual increase of pressure between "b" and "c" is attributed to the growth of boundary layer on the train surface. The end of nose passes the point at the time of "d" and the pressure dives when the middle of nose has passed the point.

Howe has developed a formula for the pressure rise across the compression wave front based on a linear theory. The net pressure rise Δp across the wave front and the maximum pressure gradient are given by:

$$\Delta p = \frac{\rho_0 U^2}{1-M^2}\frac{A_0}{A}, \tag{7}$$

$$\left(\frac{\partial p}{\partial t}\right)_{\max} \propto \frac{\rho_0 U^3 A_0}{R\,A}. \tag{8}$$

The formulas are valid for any nose profiles. The pressure rise $p/(\rho_0 U^2 A_0/A)$ and the pressure gradient $dp/dt/(\rho_0 U^3 A_0/RA)$ are plotted in fig. 8 against the non-dimensional retarded position of the train $U[t]/R$, where $[t]$ is the retarded time t-x/c_0, for train Mach numbers M between 0.15 and 0.3. The pressure rises in the

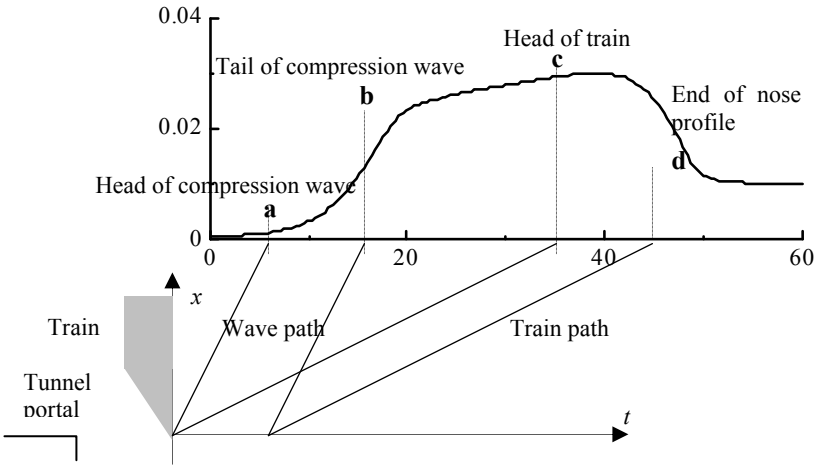

Figure 7: Wave profile observed at a fixed position in the tunnel and diagram for compression wave propagation and train translation.

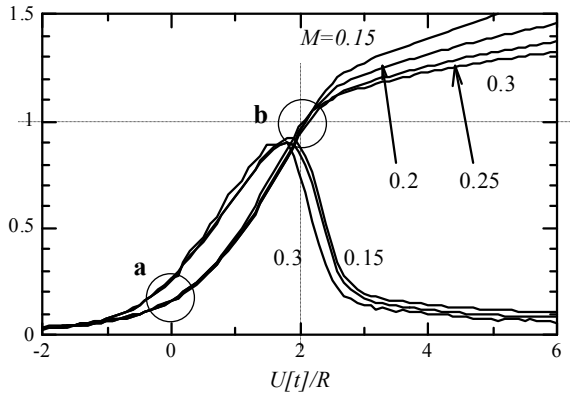

Figure 8: Comparison of the pressure rise $p/(\rho_0 U^2 A_0/A)$ and the pressure gradient $dp/dt/(\rho_0 U^3 A_0/RA)$ for different Mach numbers $M = U/c_0$.

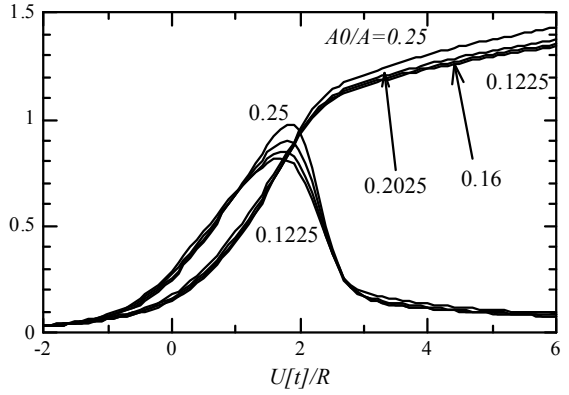

Figure 9: Comparison of the pressure rise $p/(\rho_0 U^2 A_0/A)$ and the pressure gradient $dp/dt/(\rho_0 U^3 A_0/RA)$ for different blockages A_0/A.

circles are referable to the pressures at "a" and "b" in fig. 7. It is found that the compression wave rise time is independent of Mach number, being equal to the effective transit time $\sim 2R/U$ of the nose across the entrance plane of the tunnel. The pressure rise and the pressure gradient are plotted against $U[t]/R$ for the blockages A_0/A between 0.1225 and 0.25 in fig. 9. The pressure rise and the pressure gradient are essentially independent of blockage except the peak value of the pressure gradient. As a whole, these results confirm that the train speed and area ratio dependence on the pressure rise and the pressure gradient is consistent with the linear theory prediction for the wave initially produced at the tunnel entrance.

3.3 Comparison of nose profiles and tunnel portals

According to the linear theory [5], the pressure rise is expressed as a convolution product of the source term proportional to $\partial A_{\mathrm{T}}(s)/\partial s$ and an acoustic Green's function, where $A_{\mathrm{T}}(s)$ is the cross-sectional area of the train at distance s from the nose. The acoustic Green's function for the tunnel portal with an infinite flange is approximately given by a unit step function so that the initial waveform is primarily determined by $\partial A_{\mathrm{T}}(s)/\partial s$. The area ratio A_{T}/A_0 and the rate of area change $\partial A_{\mathrm{T}}/\partial s\, L/A_0$ are given for cone, ellipsoid and paraboloid respectively as:

$$\frac{A_T(s)}{A_0} = \frac{s^2}{L^2},\ \frac{s}{L}\left(2-\frac{s}{L}\right),\ \frac{s}{L}, \tag{9}$$

$$\frac{\partial A_T(s)}{\partial s}\frac{L}{A_0} = \frac{2s}{L},\ 2\left(1-\frac{s}{L}\right),\ 1 \ \text{ for } 0 < s < L. \tag{10}$$

A comparison of the pressure rise and the pressure gradients is made for a conical, an ellipsoidal and a paraboloidal train in fig. 10. The peak values of the pressure gradients for the conical and ellipsoidal trains are almost the same, but the time of peak for the conical train is later by approximately 8 in non-dimensional time than the peak of ellipsoidal train. This time lag corresponds to the ratio L/U, where L is the length of nose and U is the speed of train. The pressure gradient of the paraboloidal train is flat and the value is smaller by approximately 30 % than other two trains.

Fig. 11 presents the pressure rise and pressure gradients predicted at x/R = -20 for the ellipsoidal train entering two and four step flared portals, comparing with the predictions for the unflared portal. The pressure rises for the flared portals are essentially linear with superposed ripples. It can be seen that the flared portal prevents the non-linear steepening of compression wave front.

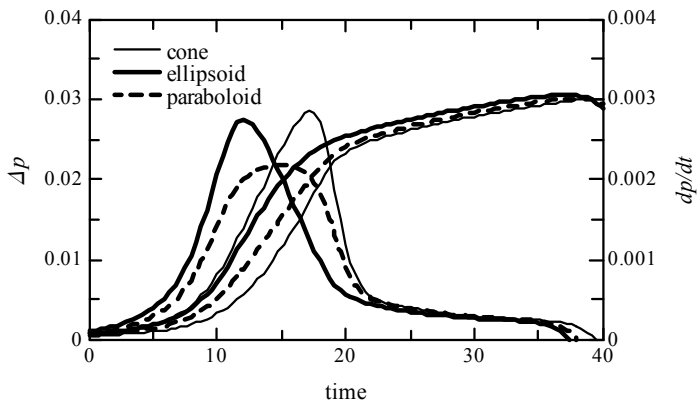

Figure 10: Comparison of over-pressure and pressure gradient.

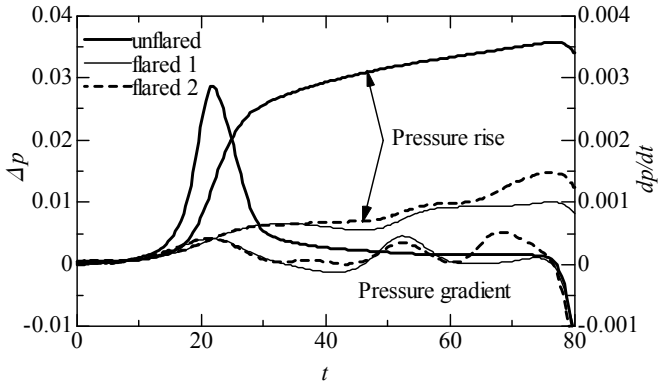

Figure 11: Pressure gradients for flared and unflared portals.

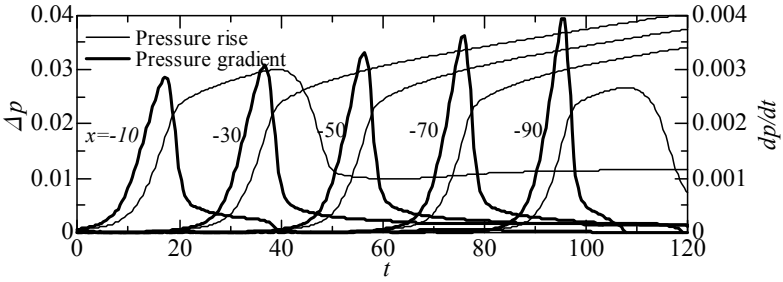

Figure 12: Variation of pressure gradients along the tunnel (cone).

3.4 Non-linear steepening in tunnel

Fig. 12 illustrates variations of the pressure rise and pressure gradients along the tunnel for the conical train. The waveform at x/R = -90 is deformed by the expansion wave reflected at the open end of tunnel. The peak values increase continuously as the distance from the tunnel entrance increases, demonstrating the deformation and steepening of the waveform in the tunnel. The non-linear deformation of waveform is verified by evaluating the following dimensionless form of Burgers equation (Cleveland et al [11]):

$$\frac{\partial P}{\partial \sigma} = AP\frac{\partial P}{\partial \theta} + \frac{1}{\Gamma}\frac{\partial^2 P}{\partial \theta^2}, \tag{11}$$

where $P(\sigma,\theta) = p/p_0$, p_0 is a reference pressure, $\sigma = x/\bar{x}$, $\bar{x}$ is the shock formation distance, $\theta = \omega\tau$, τ is the retarded time, Γ is the Gol'dberg number, and A is a coefficient. The LBM waveform at x = -10 is sampled as an initial waveform and the waveform evaluated by eqn (11) is compared with the LBM waveform at x = -90 in fig. 13. The agreement of both waveforms is excellent.

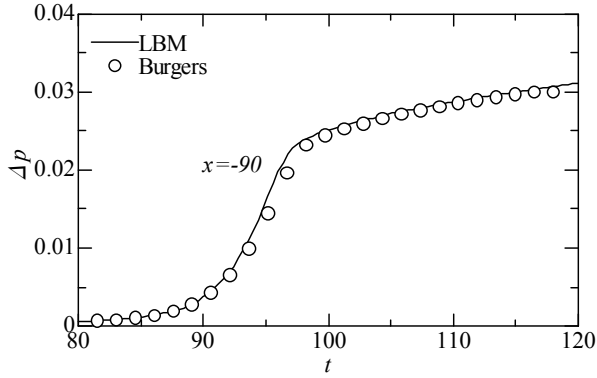

Figure 13: Comparison of LBM and Burgers prediction (cone).

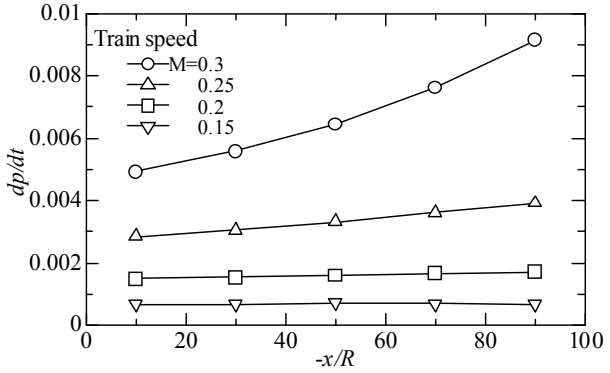

Figure 14: Variation of pressure gradient as a function of distance from tunnel entrance for train Mach numbers M between 0.15 and 0.3 (cone).

The maximum pressure gradient $\left(\partial p/\partial t\right)_{\max}$ is plotted in fig. 14 against the distance from the tunnel entrance plane for the train Mach numbers between 0.15 and 0.3. The result confirms that the rate of non-linear steepening depends on the initial value of the maximum pressure gradient.

4 Conclusions

The FDLBM was applied to the direct numerical simulations of the compression wave generated by a high-speed train entering a tunnel and the distortion of wave front in the tunnel. Numerical calculations were carried out for axisymmetric trains with various nose profiles entering a circular cylindrical tunnel. The predicted pressure rise across the compression wave front and the maximum pressure gradient near the tunnel entrance are in good agreement with the linear theory. The distortion of the compression wave front travelling within an

acoustically smooth tunnel is consistent with the time-domain computation of one-dimensional Burgers equation. The non-linear steepening was confirmed to be dependent on the initial steepness of the wave front, and the tunnel entrance with flared portals was shown not only to decrease the initial steepness of the compression wave front but also to counteract the effect of non-linear steepening.

References

[1] Ozawa, S., Maeda, T., Matsumura, T., Uchida, K., Kajiyama, H. & Tanemoto, K., Countermeasures to reduce micro-pressure waves radiating from exits of Shinkansen tunnels. *Proc. of 7th Int. Symp. On Aerodynamics and Ventilation of Vehicle Tunnels*, ed. A. Haeter, Elsevier Applied Science, pp. 253-266, 1991.

[2] Fukuda, T., Ozawa, S., Iida, M., Takasaki, T. & Wakabayashi, Y., Distortion of compression wave propagation through very long tunnel with slab tracks. *JSME Int. J.* Ser. B, **49(4)**, pp. 1156-1164, Japan Society of Mechanical Engineers, 2006.

[3] Aoki, T., Matsuo, K., Hidaka, H., Noguchi, Y. & Morihara, S., Attenuation and distortion of propagating compression wave in a high-speed railway model and real tunnels. *Proc. Int. Symp. Shock Waves*, pp. 347-352, 1995.

[4] Sugimoto, N. & Ogawa, T., Acoustic analysis of the pressure field in a tunnel, generated by entry of a train. *Proc. R. Soc. Lond.* A **454**, pp. 2083-2112, 1998.

[5] Howe, M. S., The compression wave produced by a high-speed train entering a tunnel. *Proc. R. Soc. Lond.* A **454**, pp. 1523–1534, 1998.

[6] Ogawa, T. & Fujii, K., Numerical investigation of three-dimensional compressible flows induced by a train moving into a tunnel. *Computers & Fluids* **26 (6)**, pp. 565-585, 1997.

[7] Mashimo, S., Nakatsu, E., Aoki, T. & Matsuo, K., Attenuation and distortion of compression wave Propagating in a high-speed railway tunnel. *JSME Int. J.* Ser. B, **40(1)**, pp. 51-57, Japan Society of Mechanical Engineers, 1997.

[8] Tsutahara, M., Tamura, A., Tajiri, S. & Long W., Direct simulation of fluid dynamic sounds by the finite difference lattice Boltzmann method. *Computational Methods and Experimental Measurements XIII*, eds C. A. Brebbia & G. M. Carlomagno, WIT press: UK, pp. 3-12, 2007.

[9] Akamatsu, K., Tamura, A. & Tsutahara, M., A numerical simulation for finite amplitude sound waves using finite difference lattice Boltzmann method (in Japanese). *Trans. JSME* Ser. B, **75(752)**, pp. 718-723, 2009.

[10] Hirt, C. W., Amsden, A. A., Cook, J. L., An arbitrary Lagrangian-Eulerian computing method for all flow speeds. *J. Comp. Phys.*, **14**, pp. 227-253, 1974.

[11] Cleveland, R. O. Hamilton, M. F. & Blackstock, D. T., Time-domain modeling of finite-amplitude sound in relaxing fluids. *The Journal of the Acoustical Society of America*, **99**(**6**), pp. 3312-3318, 1996.

A universal multi-dimensional charge and mass transfer model

G. Kennell & R. W. Evitts
Department of Chemical Engineering, University of Saskatchewan, Canada

Abstract

A new approach has been developed for modelling the transport of charge and mass through electrolytes. This approach utilizes a dynamically computed electric field that contributes to the transport of charged species in much the same way a flow field contributes to the transport of mass. Since a multidimensional electric field is computed, the effects of this field on redox reactions occurring in the electrolyte or at the interface of an electronic and ionic conductor can be modelled. Transport of species due to diffusion and convection is also considered, and the overall transport system is modelled using a control volume technique with a modified Peclet number. Electroneutrality and the conservation of species are incorporated into the model. This method produces a universal model capable of predicting one, two, or three-dimensional mass and charge transport for electrochemical phenomena where macroscopic anodic and cathodic couples exist. This model has the potential to simulate forms of localized corrosion and energy storage and generation applications such as batteries and fuel cells. The theoretical development and validation of this new model for a two dimensional case study is presented.

Keywords: electrochemistry, modelling, computational fluid dynamics, control volume technique, polarization, electric field, electrolyte.

1 Introduction

The open literature contains many articles on modelling of charge and mass in numerous electrochemical systems. Some examples of these systems include: fuel cells, batteries, pitting corrosion, and crevice corrosion. In such systems the transport of charged species is usually significantly affected by the electric field.

WIT Transactions on Engineering Sciences, Vol 69, © 2010 WIT Press
www.witpress.com, ISSN 1743-3533 (on-line)
doi:10.2495/AFM100161

However, the transport of charged species can also affect the electric field, which in turn affects the further transport of charged species. In crevice corrosion many important phenomena depend upon the electric field caused by the transport (or resistance to transport) of charged ions between predominantly anodic and cathodic areas. Even the rate of electrochemical reactions occurring at cathodic and anodic areas has been shown to be dependent on the electric field [1]. The methods presented in this paper represent the development of a multi-dimensional model that simultaneously considers the dynamic electric field, its affect on transport and redox reaction kinetics, and the interaction of these with the field.

One of the major applications of this model is the simulation of crevice corrosion. This model has been developed to simulate crevice corrosion by considering not only the crevice, but also the coupled reactions occurring along the bold surface, using a single set of equations that spans the whole computational domain. However, the application of this multi-dimensional model is not limited to localized forms of corrosion. Although not presented here, the method outlined in this paper may be applied to model crevice corrosion and other electrochemical systems, such as batteries and fuel cells.

2 Modelling transport and the electric potential field

The model utilizes the comprehensively developed control volume technique described by Patankar [2]. Infinitely dilute solution theory is used as the basis of the equation describing the electric field. Two main equations are numerically solved for the multi-dimensional transport:

$$\frac{\partial C_i}{\partial t} - \left(z_i u_i \mathrm{F} \nabla \mathbf{\Phi} - \mathbf{V}\right) \nabla C_i = D_i \nabla^2 C_i + S_i \,, \tag{1}$$

and

$$\nabla^2 \mathbf{\Phi} = -\frac{\mathrm{F}}{\kappa} \sum_i z_i D_i \nabla^2 C_i - \frac{\mathrm{F}}{\kappa} \sum_i z_i S_i - \frac{\mathrm{F}}{\kappa} \sum_i z_i \frac{C_i}{\partial t} \,. \tag{2}$$

Eqn (1) describes the transport of charged species due to concentration and potential gradients. Eqn (2) describes the electric field established due to concentration gradients of charged species (diffusion potential), physically separated but electrically conserved anodic and cathodic reactions, and electroneutrality. These two equations are solved independently. Eqn (1) is solved utilizing established techniques [2], and the development of its numerical representation is shown in Section 2.1. Eqn (2) is solved using the Alternating-Direction Implicit Method, although other methods could be used. During the numerical solution of eqn (1) a differencing scheme, such as The Upwind Scheme, The Hybrid Scheme, or The Power-Law Scheme, utilizes a Peclet number [2]. (The Power-Law Scheme was utilized during the numerical predictions presented in this paper.) However, since the Peclet number does not consider the transport of species due to migration, a new Peclet number is

defined. This Peclet number is similar to the Peclet number proposed by Heppner [3], but also considers convection, as well as migration and diffusion:

$$P = \frac{\left(z_i u_i \mathrm{F} \nabla \mathbf{\Phi} - \mathbf{V}\right)\Delta x}{D_i}. \tag{3}$$

Similar to eqn (1), the migration term in eqn (3) acts as an amendment to the flow field that is specific to the charge and mobility of each species. This does not significantly increase the complexity of the numerical solution of eqns (1) or (3).

2.1 Solving the transport equation

The development of the two-dimensional transport model is shown below. Effort has been taken to present this development and associated nomenclature in a manner that corresponds to that described by Patankar [2]. This new transport model (easily capable of being developed in three dimensions) is particularly easy to solve using numerical methods due to the manner in which the flux is integrated over each control volume. This integration method maintains the expression describing the migration of ions in its simplest form with only two variables to be solved for: the concentration of species and gradient of potential. The term describing the migration of ions is the first term on the right hand side of eqn (4). The flux of each dissolved species under the influence of a potential field (assuming infinitely dilute solution theory) can be given as [4]:

$$\mathbf{N}_i = -z_i u_i \mathrm{F} C_i \nabla \mathbf{\Phi} - D_i \nabla C_i + C_i \mathbf{V}. \tag{4}$$

The subscript, *i*, indicating an individual species is dropped in the following development for clarity. It is, however, assumed that each of the following equations in this sub-section can be written for each dissolved species. From eqn (4) it can be seen that the flux in the *x*-dimension and *y*-dimension can be expressed by:

$$J_x \equiv \left(U - zu\mathrm{F}\frac{d\mathbf{\Phi}}{dx}\right)C - D\frac{dC}{dx}, \tag{5}$$

$$J_y \equiv \left(V - zu\mathrm{F}\frac{d\mathbf{\Phi}}{dy}\right)C - D\frac{dC}{dy}, \tag{6}$$

and the integration of eqn (4) gives:

$$\frac{\left(C_P - C_P^0\right)\Delta x \Delta y}{\Delta t} + J_n + J_e - J_s - J_w = \left(S_c + S_p C_P\right)\Delta x \Delta y. \tag{7}$$

Eqn (7) is the equation developed in Patankar [2] for convective-diffusive problems. However, in this paper the fluxes in eqn (7) include the migration terms expressed by eqns (5) and (6). Thus, the numerical techniques that have evolved during the development of the Control Volume method may be utilized to solve convective-diffusive problems with electromigration. Eqn (7) is the discretized form of eqn (1). The mass flow rates through the faces of a control volume are given by:

$$F_n = \left(V - zu\mathrm{F}\frac{d\mathbf{\Phi}}{dy} \right)_n \Delta x\,, \tag{8}$$

$$F_s = \left(V - zu\mathrm{F}\frac{d\mathbf{\Phi}}{dy} \right)_s \Delta x\,, \tag{9}$$

$$F_e = \left(U - zu\mathrm{F}\frac{d\mathbf{\Phi}}{dx} \right)_e \Delta y\,, \tag{10}$$

$$F_w = \left(U - zu\mathrm{F}\frac{d\mathbf{\Phi}}{dx} \right)_w \Delta y\,. \tag{11}$$

The migration term in the current development occurs as an amendment to the flow field term. The addition of these two terms creates a flow field that does not satisfy the volume continuity equation for the case of incompressible flow. This is realistic when considering the migration of a single species. However, conservation of species due to transport is assured in this model because any flux leaving a control volume is the flux entering a neighbouring control volume. This is a property of the Control Volume technique. For a flow field that does not satisfy the volume continuity equation, eqn (7) can be rearranged to be:

$$\begin{aligned} \frac{\left(C_P - C_P^0\right)\Delta x\Delta y}{\Delta t} + \left(F_n + F_e - F_s - F_w\right)C_P + \left(J_n - F_n C_P\right) \\ + \left(J_e - F_e C_P\right) - \left(J_s - F_s C_P\right) - \left(J_w - F_w C_P\right), \\ = \left(S_c + S_p C_P\right)\Delta x\Delta y \end{aligned} \tag{12}$$

$$\begin{aligned} \frac{\left(C_P - C_P^0\right)\Delta x\Delta y}{\Delta t} + \left(F_n + F_e - F_s - F_w\right)C_P + a_N\left(C_P - C_N\right) \\ + a_E\left(C_P - C_E\right) - a_S\left(C_S - C_P\right) - a_W\left(C_W - C_P\right), \\ = \left(S_c + S_p C_P\right)\Delta x\Delta y \end{aligned} \tag{13}$$

$$a_P C_P = a_N C_N + a_E C_E + a_S C_S + a_W C_W + b\,, \tag{14}$$

where:

$$a_P = \left(\frac{\Delta x \Delta y}{\Delta t} + F_n + F_e - F_s - F_w + a_N + a_E - a_S - a_W + S_P \Delta x \Delta y \right), \quad (15)$$

$$a_N = D_n A\left(\left|P_n\right|\right) + [[-F_e, 0]], \quad (16)$$

$$a_E = D_e A\left(\left|P_e\right|\right) + [[-F_e, 0]], \quad (17)$$

$$a_S = D_s A\left(\left|P_s\right|\right) + [[F_s, 0]], \quad (18)$$

$$a_W = D_w A\left(\left|P_w\right|\right) + [[F_w, 0]], \quad (19)$$

and

$$b = \left(S_c + \frac{C_P^0}{\Delta t} \right) \Delta x \Delta . \quad (20)$$

The calculation of the function, $A\left(\left|P_n\right|\right)$, depends on the differencing scheme as indicated earlier in this paper.

2.2 Development of an equation for the electric potential field

The following is the development of an equation that describes the electric field in the electrolyte. This equation does not include effects very close to the electrode surface in the charge double layer. A material balance for a single species shows that the change in concentration of a species depends on the divergence (due to flux) and production of that species [4]:

$$\frac{\partial C_i}{\partial t} = -\nabla \cdot \mathbf{N}_i + S_i . \quad (21)$$

Multiplying eqn (21) by $z_i \mathrm{F}$ gives:

$$\frac{\partial}{\partial t}\left(\mathrm{F} \sum_i z_i C_i \right) = -\nabla \cdot \mathrm{F} \sum_i z_i \mathbf{N}_i + \mathrm{F} \sum_{\mathrm{i}} z_i S_i . \quad (22)$$

This model is designed to predict concentration profiles that are electrically neutral. The electroneutrality assumption has been shown to be a very good approximation of reality [4]:

$$\sum_i z_i C_i = 0 \,. \tag{23}$$

Substituting eqn (23) into eqn (22) gives eqn (24).

$$\nabla \cdot \mathrm{F} \sum_i z_i \mathbf{N}_i = \mathrm{F} \sum_i z_i S_i \,. \tag{24}$$

Current in an electrolyte solution is:

$$\mathbf{i} = \mathrm{F} \sum_i z_i \mathbf{N}_i \,. \tag{25}$$

Substituting eqn (25) into eqn (24) gives:

$$\nabla \cdot \mathbf{i} = \mathrm{F} \sum_i z_i S_i \,. \tag{26}$$

Eqn (26) implies there is no divergence of electrical current except for the transport of charge created by physically separated anodic and cathodic reactions. Current density is given by [4]:

$$\mathbf{i} = -\mathrm{F}^2 \nabla \mathbf{\Phi} \sum_i z_i^2 u_i C_i - \mathrm{F} \sum_i z_i D_i \nabla C_i + \mathrm{F} \mathbf{v} \sum_i z_i C_i \,. \tag{27}$$

From eqn (27), the divergence of current is therefore:

$$\nabla \cdot \mathbf{i} = -\nabla \cdot \left(\kappa \nabla \mathbf{\Phi} \right) - \mathrm{F} \sum_i z_i \nabla \cdot D_i \nabla C_i + \mathrm{F} \mathbf{v} \sum_i z_i C_i \,, \tag{28}$$

where the conductivity is:

$$\kappa = \mathrm{F}^2 \sum_i z_i^2 u_i C_i \,. \tag{29}$$

The last term of eqn (28) is zero since the system is assumed to be electrically neutral. Substituting eqn (26) into eqn (28) and assuming constant conductivity and diffusion coefficients over a control volume yields an equation that describes the electrical field:

$$\nabla^2 \mathbf{\Phi} = -\frac{\mathrm{F}}{\kappa} \sum_i z_i D_i \nabla^2 C_i - \frac{\mathrm{F}}{\kappa} \sum_i z_i S_i \,. \tag{30}$$

2.3 Electroneutrality

An analogous equation to eqn (1) can be derived as follows; substituting eqn (4) into eqn (21) gives:

$$\frac{\partial C_i}{\partial t} = -\nabla \cdot \left(- z_i u_i \mathrm{F} C_i \nabla \mathbf{\Phi} - D_i \nabla C_i + C_i \mathbf{V}\right) + S_i \,. \tag{31}$$

Using the chain rule to differentiate eqn (31) and rearranging:

$$\frac{\partial C_i}{\partial t} - \left(z_i u_i \mathrm{F} \nabla \mathbf{\Phi} - \mathbf{V}\right) \nabla C_i = D_i \nabla^2 C_i + S_i + z_i u_i \mathrm{F} \nabla^2 \mathbf{\Phi} C_i \,. \tag{32}$$

Comparison of eqn (32) with eqn (1) shows that there is an additional term on the right hand side of eqn (32). The absence of this term in eqn (1) is one of the inherent strengths of the model presented in this paper. Numerically, this extra term is a species source term dependent on charge density. This previous statement is made assuming a more rigorous definition of near-electroneutrality for a medium with uniform dielectric constant [4]:

$$\nabla^2 \Phi = -\frac{\mathrm{F}}{\varepsilon} \sum_i z_i C_i \,. \tag{33}$$

If eqn (32) was solved using the actual potential field in the system, and no errors were introduced during the numerical procedure, conservation of species should occur; however, the guarantee of species conservation for all situations (assured for the model presented in this paper) is not evident for the numerical solution of eqn (32) i.e., when rounding errors occur.

There is one disadvantage of the new model. In deriving eqn (30) electroneutrality was assumed. However, discretization of eqns (1) and (30) will introduce errors in their solution and therefore there is no guarantee of electroneutrality. A predicted concentration that differs significantly from electroneutrality would be unreasonable. However, if the derivation presented in section 2.2 is repeated with all affects on the Laplacian of the electric field neglected except for non-electroneutrality (in the current model any non-electroneutrality would be caused by numerical error):

$$\nabla^2 \mathbf{\Phi} = \frac{\mathrm{F}}{\kappa} \sum_i z_i \frac{\partial C_i}{\partial t} \,. \tag{34}$$

Therefore, the Laplacian of the electric potential expressed in eqn (34) may be thought of as a representation of the numerical error generated over the previous time step. Then the Laplacian of the electric potential needed to cause the

transport of charge that will eliminate any error (in regards to electroneutrality) that has occurred up to the current time step over the next time step is:

$$\nabla^2 \mathbf{\Phi} = -\frac{\mathrm{F}}{\kappa} \sum_i z_i \frac{C_i}{\partial t} . \tag{35}$$

Adding eqn (35) to eqn (30) yields eqn (2). Thus, eqn (2) ensures an electrically neutral system is predicted. Eqn (2) is also generally not a stiff equation, unlike eqn (33), due to the significantly larger value of conductivity when compared with the dielectric constant, for most systems.

2.4 Boundary conditions

For the numerical solution of eqns (1) and (2) boundary conditions are needed. Three situations existing at the boundary have been considered for the simulation presented in Section 3: bulk electrolyte, a barrier through which no mass or charge is transported, or a barrier through which charge and mass is only transported via an electrochemical reaction (i.e. an electroactive surface). For the situation that involves bulk electrolyte the boundary condition for eqn (1) may be given as

$$C_i = A , \tag{36}$$

and for eqn (2)

$$\mathbf{\Phi} = B . \tag{37}$$

For the situation where a barrier through which no charge or mass is transported exists at the boundary, the boundary condition for eqn (1) is

$$\frac{\partial C_i}{\partial x} = 0 , \tag{38}$$

and for eqn (2) is

$$\frac{\partial \mathbf{\Phi}}{\partial x} = 0 . \tag{39}$$

For the situation where an electroactive area is present at the boundary, the boundary condition for eqn (1) is eqn (38), and for eqn (2) it is eqn (37).

3 Validation and discussion

The model presented in this paper was used to model the moving boundary experiment of Fu and Chan [5]. The experiment consisted of a small diameter glass tube filled with 0.1 M KNO_3. One end of the tube was open to a beaker containing a platinum cathode and the other end of the tube was plugged with an

Ag anode. Upon application of a 1 mA current silver ions were dissolved into the electrolyte and were transported along the glass tube. During this process a transition zone was formed between areas containing mostly Ag^+ or K^+. This transition zone, or boundary, was made visible by a small addition of ascorbic acid and its progression along the glass tube was measured. Fig. 1 shows this experimental data along with the movement of the boundary predicted by the current model and an excellent fit is evident. For this simulation 200 nodes in the direction of migration and 10 nodes in the radial direction were used along with a time step of 0.001 s. The width of a control volume was 0.0002 m in both directions. A grid dependency study has been completed. The numerical model is stable when simulating using a coarser spatial and temporal grid; however, as the grid size is increased the rate of predicted transport also increases. For simulations conducted using a finer spatial and temporal grid than the validation simulation no change in the rate of transport was evident and the results corresponded with the validation results.

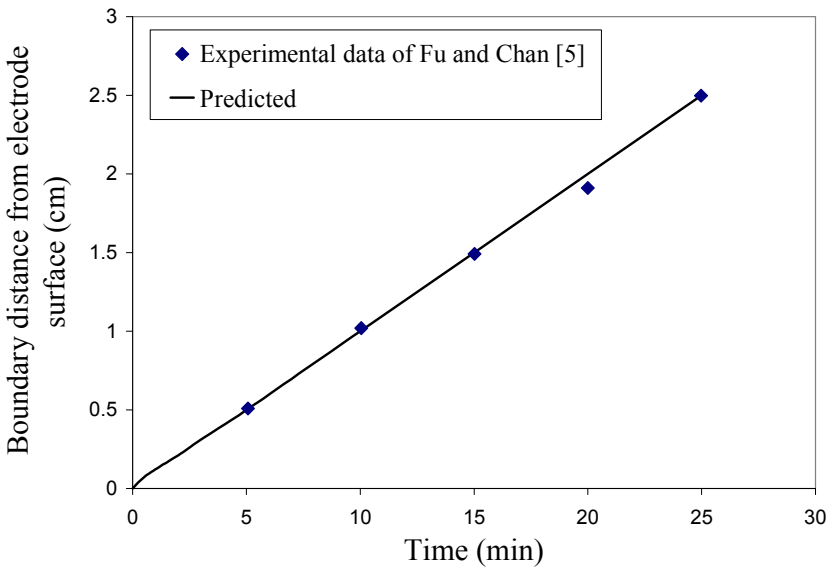

Figure 1: Experimentally determined and predicted boundary position.

The concentration of Ag^+, as predicted by the model over two dimensions, can be seen in fig. 2. Although significant concentration gradients are only established along the length of the tube during the simulation, the validation is considered to be successful in two dimensions. This is because the prediction of insignificant radial concentration gradients matches experimental observations and verifies that errors did not propagate in the radial direction during the coupled solution of eqns (1) and (2). In fig. 2 the transition region, where the concentration of Ag^+ approaches zero, can be seen at approximately 1 cm from

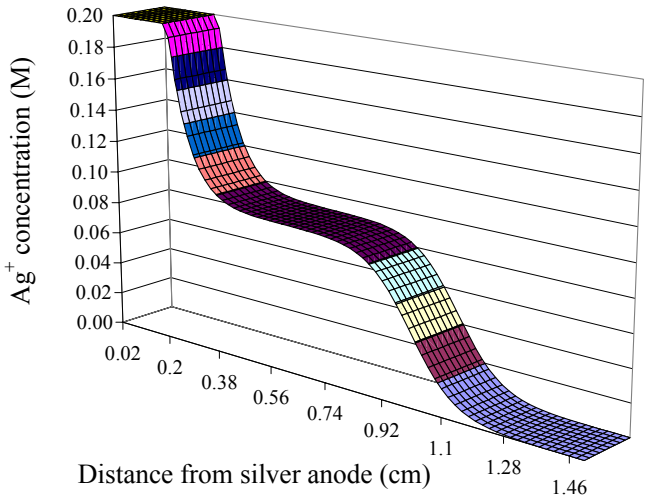

Figure 2: Predicted Ag^+ concentration after 10 mins.

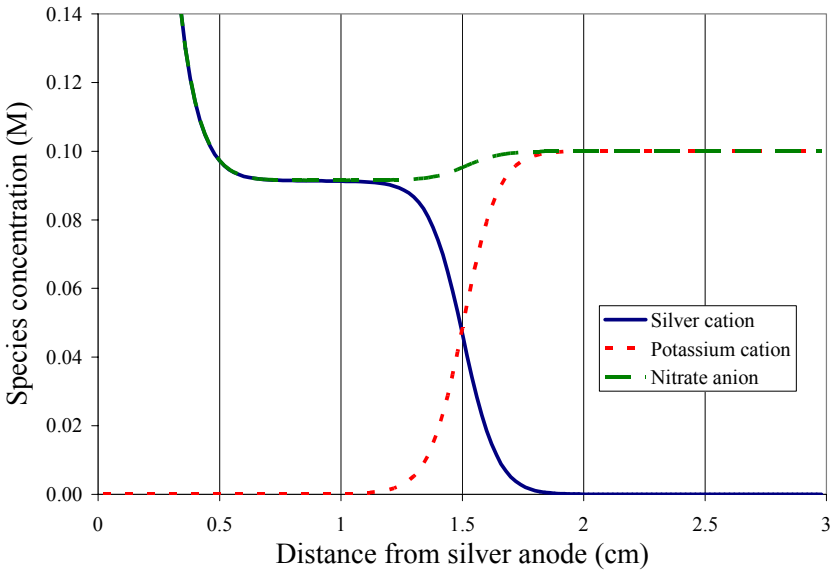

Figure 3: Predicted ion concentrations after 15 mins.

the silver anode. Also, a region of relatively constant concentration of Ag^+ exists from approximately 0.5 cm to the start of the transition region at about 0.75 cm from the anode. This region of relatively constant concentration expands in length at later times; however the concentration of Ag^+ in this region is steady at approximately 0.09 M. Since the model predicts no significant concentration gradients in the radial direction at any time, predicted concentrations can be

expressed (at a set time) as a function of distance from the anode (fig. 3). Fig. 3 shows the predicted concentrations of all species in the electrolyte after 15 mins. The boundary between Ag^+ and K^+ can clearly be established at 1.5 cm from the anode. Fig. 3 also shows predicted concentrations that result in electroneutrality of the electrolyte and dissolved species.

It was found that the numerical solution of this model was relatively computationally inexpensive and stable when compared with other electrolyte transport models the authors have worked with [1, 6]. A notebook PC equipped with a 1.5 GHz Intel Celeron M processor with 504 MB of RAM was able to solve the model presented here in approximately ten hours. Since the model is relatively computationally inexpensive it is expected that simulations times for much more complex systems will be short. This illustrates the usefulness of the methods outlined here, and the possible applicability of these methods to the transport of charge and mass through many different electrolytes in many different industrial settings.

4 Conclusions

A new method was presented for modelling the transport of charge and mass through electrolytes. This utilizes a control volume technique coupled with the predicted electric field. This method was validated against the experimental data of Fu and Chan [5] and excellent agreement was found. It is proposed that this new method may be useful to simulate a wide variety of electrochemical systems where multi-dimensional mass and charge transport is important, due to the stability and computational ease of the numerical solution outlined here.

References

[1] Kennell, G.F. & Evitts, R.W., Crevice Corrosion Cathodic Reactions and Crevice Scaling Laws. *Electrochimica Acta*, **54**, pp. 4696-4703, 2009.
[2] Patankar, S.V., *Numerical Heat Transfer and Fluid Flow*, Hemisphere: New York, 1980.
[3] Heppner, K.L., *Development of Predictive Models of Flow Induced and Localized Corrosion*, Ph.D. Thesis, University of Saskatchewan: Saskatoon, 2006.
[4] Newman, J.S., *Electrochemical Systems*, Prentice Hall, New Jersey, 1991.
[5] Fu, J.W. & Chan, S., A Finite Element Method for Modeling Localized Corrosion Cells. *Corrosion*, **40**, pp. 540–544, 1984.
[6] Kennell, G.F., Heppner, K.L., Evitts, R.W., A Critical Crevice Solution and iR Drop Crevice Corrosion Model. *Corrosion Science*, **50**, pp. 1716-1725, 2008.

This page intentionally left blank

Numerical investigation of the jet formation through the oscillation of a bubble between a couple of parallel walls

R. M. B. Teymouri[1] & G. Ahmadi[2]
[1]*Center of Smart Interfaces, Darmstadt University of Technology, Germany*
[2]*Department of Mechanical and Aeronautical Engineering, Clarkson University, USA*

Abstract

The jet formation through the oscillation of a bubble between a couple of parallel rigid walls was numerically investigated. The Navier-Stokes and energy equations accompanying with the proper constitutive relations were numerically solved to predict the flow and thermal conditions inside and outside the bubble. The volume of fluid method was incorporated to capture the bubble surface applying a piecewise linear interface reconstruction method. For the bubble to walls distances less than certain limits, the bubble underwent a necking process after reaching to its maximum volume. The necking process led to splitting of the bubble and the formation of a couple of round jets toward the walls. The velocity of each jet was higher than the velocity of a jet induced through the oscillation of a bubble near a single wall. Also it was found that keeping the position of one of the walls fixed, the velocity of the jet toward that wall increases with increasing the other wall distance from the bubble, up to a certain limit. These analyses were performed for several initial inside to outside pressure ratios of the bubble. The results can be used for increasing the performance of the devices for which the jet induced through the near wall bubble oscillation is applied.

Keywords: oscillating bubble, wall, jet, VOF.

WIT Transactions on Engineering Sciences, Vol 69, © 2010 WIT Press
www.witpress.com, ISSN 1743-3533 (on-line)
doi:10.2495/AFM100171

1 Introduction

Bubble dynamics is one of the main subjects in the phenomenological studies of cavitation and boiling. Some of the discovered features have seemed to be useful for inventing new devices. One of the invented devices is the ink-jet printer. In this type of printers, the ink droplets are generated through the collapse of the boiling bubbles [1]. Another invented device is a micro-pump that does not use any moving element. In this pump, the jet induced through the near wall bubble oscillation is applied [2]. It should be reminded that this induced jet that leads to the bubble collapse, is the main mechanism of the cavitation damaging effects in the turbomachineries and hydraulic structures [3–5].

The jet formation through the near wall bubble oscillation is the subject of the present numerical study. To briefly describe the physics of this phenomenon, a high-pressure bubble is considered near a rigid wall. The bubble grows spherically to reach its maximum volume. During the expansion, the bubble potential energy that is related to its gas content, is transferred to the surrounding liquid in the form of kinetic energy. The momentum of the outgoing liquid however causes the bubble to over-expand. This energy transfer accompanies with the pressure decrease inside the bubble and results the deceleration of the expansion. At the end of the expansion, the pressure difference between inside and outside the bubble has an opposite sign with respect to the start of this process and leads to initiation of the compression. The compression is also a result of the surface tension. During the compression, the surrounding liquid kinetic energy is transferred to the bubble gas content in the form of potential energy, but with a lower amount as a result of the viscous damping effects. The main effect of the wall is that the surrounding liquid kinetic energy in the regions away from the wall is much higher than the region adjacent to the wall. Consequently a part of the ingoing liquid penetrates into the bubble as a high velocity round jet toward the wall. The jet destroys the bubble spherical shape and makes a hole and finally impacts the wall. Sequence of the jet formation through the oscillation of a bubble near a wall is shown in Fig. 1.

Figure 1: Jet formation through the oscillation of a bubble near a wall.

Lauterborn and Bolle [6] carried out several experiments on the near wall bubble oscillation and observed the instantaneous bubble shapes using the high-speed photography. The method for generating the bubble was firing a focused short laser pulse. It should be pointed that one of the problems in performing such experiments is the lack of possibility to measure the initial pressure inside the bubble as well as the equilibrium bubble radius. Consequently, for the

numerical simulations one is confronted with making assumptions on the initial conditions.

In the experiments carried out by Ishida et al. [7] the jet formation through the oscillation of a bubble between a couple of parallel walls was investigated. The bubble was generated by an electric charge. According to their observations, when the distances between the bubble and the walls are less than a certain limit, the bubble undergoes a necking process during the compression. The necking process leads to splitting of the bubble into a couple of compressing daughter bubbles. In turn, a couple of jets toward the walls are induced. They found that keeping one of the walls position fixed, the velocity of the jet toward that wall increases with increasing the other wall distance from the bubble.

The necking process is the result of the fact that the surrounding liquid kinetic energy in the regions away from the walls is much higher than the regions adjacent to the walls. Consequently a part of the ingoing liquid penetrates into the bubble as a plane jet parallel to the walls, leading to necking of the bubble. At the moment of the bubble splitting, a stagnation point is created at the splitting point. Therefore the plane jet is converted to a couple of round jets toward the walls. The round jets intensify the jets induced during the compression of the daughter bubbles. Consequently, the jets impact the walls with the velocities higher than the velocity of the jet induced through the oscillation of a bubble near a single wall. Sequence of the jet formation through the oscillation of a bubble between a couple of parallel walls is shown in Fig. 2.

Figure 2: The jet formation through the oscillation of a bubble between a couple of parallel walls.

The numerical studies about the jet formation through the near wall bubble oscillation can be divided into two categories. At the first category, the fluid flow is assumed to be inviscide and irrotational. To calculate the flow field variables, a Laplace equation governing the velocity potential is solved [1]. This approach is simple for implementation. But the inviscide fluid assumption is no longer acceptable in the small scales [5]. The irrotational flow assumption is also incorrect because of the vortical flow structure inside the bubble during the jet formation. In the second category, Navier-Stokes equations are solved accompanying with the different methods to capture the bubble surface [5].

In the present study the second approach is selected to model the jet formation through the oscillation of a bubble between a couple of parallel walls. The simulations are performed for several initial inside to outside pressure ratios of the bubble. One of the walls position is kept fixed and the effects of changing the other wall position are investigated.

2 Mathematical modelling

The fluid flow field under consideration contains two immiscible phases with a sharp interface across which, no mass transfer occurs. The primary phase is compressible air inside the bubble and the secondary phase is incompressible water outside the bubble.

2.1 Interface capturing approaches

The recent numerical methods developed to precisely capture the sharp interfaces between the immiscible fluids on Eulerian grids, can be divided into a couple of approaches called the surface approach and the volume approach.

In the surface approach, the interface is represented by the marker points. The most important advantage of this approach is that the interface remains sharp as it is advected across the domain. This results precisely calculation of the interface curvature. There are a couple of mostly used methods that can be categorized in this approach, including the front tracking method and the level set method. In the front tracking method the interface is represented by a set of connected massless marker particles and explicitly tracked in a Lagrangian manner using the flow field local velocity. By using this method, some difficulties arise in modelling the coalescence or break up of the interfaces. In the level set method a scalar advection equation is solved for a distance function from the interface. The interface is defined as the zero level set of the distance function and implicitly captured during its advection across the domain. The disadvantage of the level set method is that there is no guaranty for the mass conservation during the interface advection [8].

In the volume approach, the immiscible fluids on either sides of the interface are marked instead of marking the interface itself. Consequently some special techniques are needed to reconstruct the sharp interface. There are a couple of mostly used methods that can be categorized in this approach, including the marker and cell method (MAC) and the volume of fluid method (VOF). In the MAC method the marker particles that are used to mark the fluids, are transported in a Lagrangian manner as the interface is advected across the domain. The interface is reconstructed using the marker particle density in the mixed numerical cells where the marker particles of both of the fluids exist. The disadvantage of this method is the computational cost due to the requirement of many particles. In the VOF method an indicator function that is the local volume fraction of one of the fluids, is used to distinguish between two different fluids. The indicator function is locally calculated solving a scalar equation. The interface is reconstructed using the indicator function in the mixed cells where its values are in the range of zero to one. The disadvantage of this method is the difficulties to precisely calculate the interface local curvature [8].

2.2 VOF method

For the present research the VOF method is used to numerically capture the bubble surface. In this method an indicator function that is the local volume

fraction of one of the fluids, is initialized in each cell. As a result of the fact that the fluids are immiscible, each fluid element does not change its material in time. Therefore the indicator function satisfies eqn (1) that is called the volume fraction equation [9]. In the present study this equation is written in term of the volume fraction of water.

$$\frac{D}{Dt}\left(\alpha_{water}\right)=\left(\rho_{water}\alpha_{water}\right)_{t}+\left(\rho_{water}\alpha_{water}v_{i}\right)_{,i}=0 \tag{1}$$

where ρ is the density, α is the volume fraction and v is the velocity. In this paper the equations are written in the tensor form.

Solving eqn (1) using the lower order schemes, leads to losing the interface sharpness due to the numerical diffusion. Using the higher order schemes is also not suitable because they make the solution unstable. Several techniques have been proposed to precisely predict a sharp interface using the VOF method. One of the accurate techniques is to represent the interface by a piecewise linear surface. In this geometrical technique the interface in each cell is represented by a plane in 3D or a line in 2D that is perpendicular to the local gradient of the volume fraction. At the present study, Young's method is used to calculate the local gradient of the volume fraction. After calculating the orientation of the linear surface in each cell, its position can be obtained by knowing the volume fractions of both of the fluids.

2.3 Governing equations

In the VOF method the fluid flow equations are written in terms of the mixture properties to make a single set of the governing equations for both of the fluids. The mixture properties can be calculated using eqn (2) that is written in terms of a general fluid property φ.

$$\varphi_{mix}=\alpha_{air}\varphi_{air}+\alpha_{water}\varphi_{water} \tag{2}$$

Equation (3) is the continuity equation.

$$\left(\rho_{mix}\right)_{t}+\left(\rho_{mix}v_{i}\right)_{,i}=0 \tag{3}$$

Equation (4) is the momentum equation.

$$\left(\rho_{mix}v_{j}\right)_{t}+\left(\rho_{mix}v_{j}\right)_{,i}v_{i}+p_{,j}-\tau_{ij,i}-F_{j}=0 \tag{4}$$

where p is the pressure, F is the body force due to the surface tension and τ is the viscous stress. Equation (5) is used to calculate the viscous stress tensor.

$$\tau_{ij}=\mu_{mix}\left(v_{ij}+v_{ji}\right) \tag{5}$$

where μ is the viscosity.

At the present study, the total energy and temperature are treated as mass-averaged variables. The mass-averaged variables are calculated using eqn (6) that is written in term of a general variable X [10].

$$\mathrm{X} = \frac{\alpha_{air}\rho_{air}\mathrm{X}_{air} + \alpha_{water}\rho_{water}\mathrm{X}_{air}}{\alpha_{air}\rho_{air} + \alpha_{water}\rho_{water}} \tag{6}$$

Equation (7) is the energy equation.

$$\left(\rho_{mix}E\right)_t + \left(v_i\left(\rho_{mix}E + p\right)\right)_{,i} = \left(k_{mix}T_{,i}\right)_{,i} \tag{7}$$

where E is the total energy, T is the temperature and k is the thermal conductivity.

The total energy and temperature fields are related together using eqn (8).

$$E = c_{P\_mix}T - \frac{p}{\rho_{mix}} + \frac{1}{2}v_i v_i \tag{8}$$

where c_P is the constant pressure specific heat.

The ideal gas equation is used to calculate the variable air density.

2.4 Surface tension

A continuum surface force model (CSF) is used to take the surface tension effects into account [11]. The surface tension is written in term of the pressure jump across the interface. The pressure jump is related to the interface curvature that is the divergence of the interface unit normal. Applying the divergence theorem, the surface tension can be expressed as a volume force. This volume force that can be calculated using eqn (9) is added to the momentum equation as a source term.

$$F = \sigma\frac{\rho_m\kappa\alpha_{water,i}}{0.5\left(\rho_{air} + \rho_{water}\right)} \tag{9}$$

where σ is the surface tension and κ is the interface curvature.

2.5 Numerical schemes

FLUENT CFD software is used to numerically solve the governing equations applying the finite volume method. SIMPLE pressure based algorithm is applied to solve the set of governing equations. A first order implicit time integration method is used for the temporal discretization. The power law first order scheme is used for discretization of the convective terms.

According to the axisymmetry of the flow field, the equations are written in a cylindrical coordinate system. The line that is perpendicular to the walls and passes the bubble center is chosen as the axis of the cylindrical coordinate.

Because of the symmetry with respect to this axis, the equations are solved in a plane passing the axis. Therefore the solution domain is simply a rectangle.

The upper and lower sides of the rectangular solution domain are the walls for which, the no-slip boundary condition is imposed. The axis boundary condition is imposed on the right side of the domain and a constant static pressure is imposed on the left side. The constant static pressure boundary is sufficiently away from the axis. Therefore the variable pressure field around the oscillating bubble is not affected by the constant pressure boundary.

GAMBIT grid generation software is used to generate the two-dimensional structured numerical grids. The numbers of the cells used for the different cases are in the range of 8500 to 15000. The numerical grids are examined to result grid independent solutions.

3 Problem description

A bubble with the initial diameter of 1mm is considered between a couple of parallel rigid walls that are large in comparison with the bubble size. Therefore the flow field is axisymmetric with respect to an axis that is perpendicular to the walls and passes the bubble center. For the different cases, the values of 20, 40, 60, 80 and 100 are assigned for the initial inside to outside pressure ratio of the bubble. This parameter is represented by $(p_{in}/p_{out})_{initial}$. For each value of $(p_{in}/p_{out})_{initial}$, the distance from the bubble center to each wall is non-dimensionalized with the maximum bubble radius. The non-dimensional distances from the bubble center to the lower and upper walls are represented by γ_1 and γ_2 respectively. The value of γ_1 is kept 1 for all of the cases. The values of γ_2 are in the range of 1 to 2.5 for the different cases.

To find the bubble maximum radius, a free bubble oscillation is simulated for each value of $(p_{in}/p_{out})_{initial}$. For the initialization of the numerical solution, the initial temperature inside the bubble should be calculated. Assuming an isentropic process between the initial and equilibrium conditions, eqns (10) and (11) can be used:

$$\frac{p_{in,initial}}{p_{in,equilibrium}} = \left(\frac{R_{equilibrium}}{R_{initial}} \right)^{3k} \tag{10}$$

$$\frac{T_{in,initial}}{T_{in,equilibrium}} = \left(\frac{R_{equilibrium}}{R_{initial}} \right)^{3(k-1)} \tag{11}$$

where R is the bubble radius and k is a constant value that is 1.4 for the present study.

Equation (12) is obtained by applying a force balance at the equilibrium condition.

$$p_{in,equilibrium} - p_{out} = \frac{2\sigma}{R_{equilibrium}} \tag{12}$$

Eliminating $p_{in,equilibrium}$ in relating eqns (10) and (12), the equilibrium bubble radius can be obtained for the different values of $(p_{in}/p_{out})_{initial}$. Assuming that the inside and outside temperatures of the bubble have the same values at the equilibrium condition, eqn (11) can be used to find the temperature inside the bubble at the initial condition.

To indicate the importance of the buoyancy force in analyzing the bubble oscillation, a non-dimensional parameter is usually used in the literature. This parameter that is represented by Δ is defined by eqn (13).

$$\Delta^2 = \frac{\rho_{water} g R_{\max}}{p_{out} - p_V} \tag{13}$$

where g is the gravity acceleration and p_V is the vapor pressure. The effects of the buoyancy force are negligible as long as the value of Δ is less than 0.3 [12]. For the present study the effects of buoyancy force are negligible.

4 Numerical results

Figure 3 shows the numerical simulation of a bubble oscillation between a couple of parallel walls. The initial inside to outside pressure ratio of the bubble is 100 and the non-dimensional distances from the bubble center to both of the walls are 1. The necking process, splitting and formation of the round jets toward the walls are successfully simulated. The instantaneous bubble shapes are qualitatively in good agreement with the experimental observations performed by Ishida et al. [7]. The numerical and experimental results cannot be

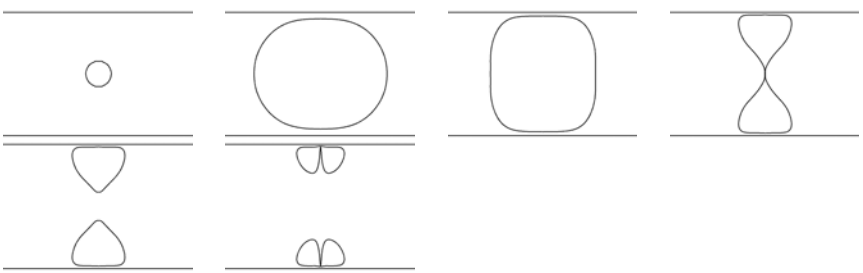

Figure 3: Simulation of a bubble oscillation between a couple of parallel walls, $(p_{in}/p_{out})_{initial} = 100$, $\gamma_{1,2} = 1$.

Figure 4: Experimental observation of a bubble oscillation between a couple of parallel walls, $\gamma_{1,2} = 1.1$, [7].

quantitatively compared, because neither the initial pressure inside the bubble is possible to be measured nor the equilibrium bubble radius.

Figure 4 shows the experimental observations carried out by Ishida et al. In the experiment, the non-dimensional distances of the bubble center to both of the walls are 1.1.

Figures 5 and 6 show the velocity vector field obtained by the numerical simulation of the case for which $(p_{in}/p_{out})_{initial}$ is 100 and both of γ_1 and γ_2 are 1. Figure 5 demonstrates the creation of a stagnation point at the point of splitting and the formation of the round jets toward the walls. Figure 6 shows the velocity vector field around one of the daughter bubbles at the moment of the creation of a hole by the round jet.

Figure 7 shows the bubble shapes at the moment of splitting, obtained by the numerical simulation of the different cases. For each value of γ_2, the different bubble shapes corresponding to the different values of $(p_{in}/p_{out})_{initial}$, are shown in a single picture. The bigger bubble shapes correspond to the higher values of $(p_{in}/p_{out})_{initial}$. In this figure the bubble shapes are shown just for the values of γ_2 which are in the range of 1 to 1.5, because the splitting process does not occur for the higher values. For the value of γ_2 equal to 1.5, the splitting process does not occur if the value of $(p_{in}/p_{out})_{initial}$ is higher than 20. It is also demonstrated from fig. 7 that for the higher values of γ_2, the upper daughter bubble has the smaller sizes, but the size of the lower daughter bubble remains fixed. This behaviour is consistent with the other experimental observations carried out by Ishida et al. [7]. In that experiment, the value of γ_1 is 1.3 and the value of γ_2 is 0.9. The experimental observations are shown in fig. 8.

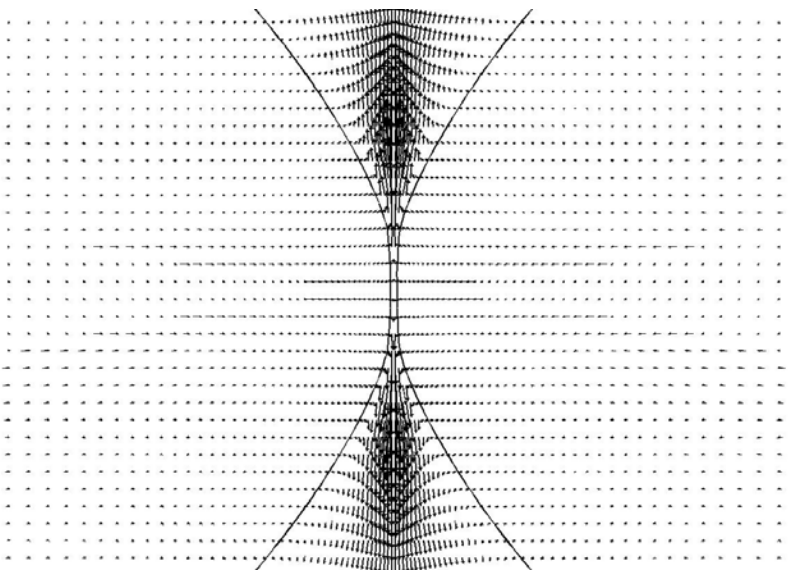

Figure 5: Velocity vector field at the moment of splitting, $(p_{in}/p_{out})_{initial} = 100$, $\gamma_{1,2} = 1$.

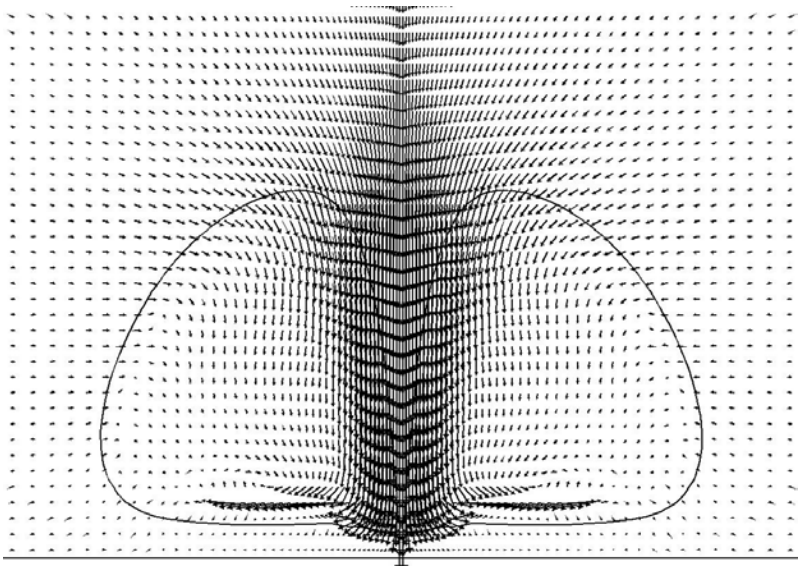

Figure 6: Velocity vector field at the moment of the creation of a hole, $(p_{in}/p_{out})_{initial} = 100$, $\gamma_{1,2} = 1$.

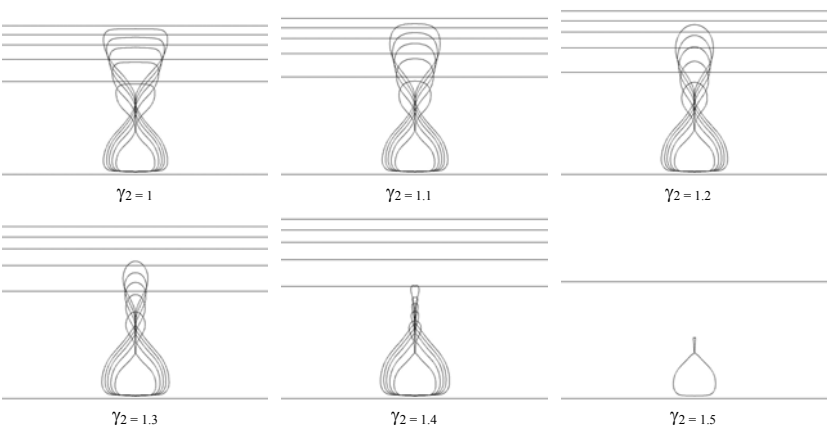

Figure 7: The bubble shapes at the moment of splitting for the different cases.

Figure 8: Experimental observation of a bubble oscillation between a couple of parallel walls, $\gamma_1 = 1.3$ and $\gamma_2 = 0.9$, [7].

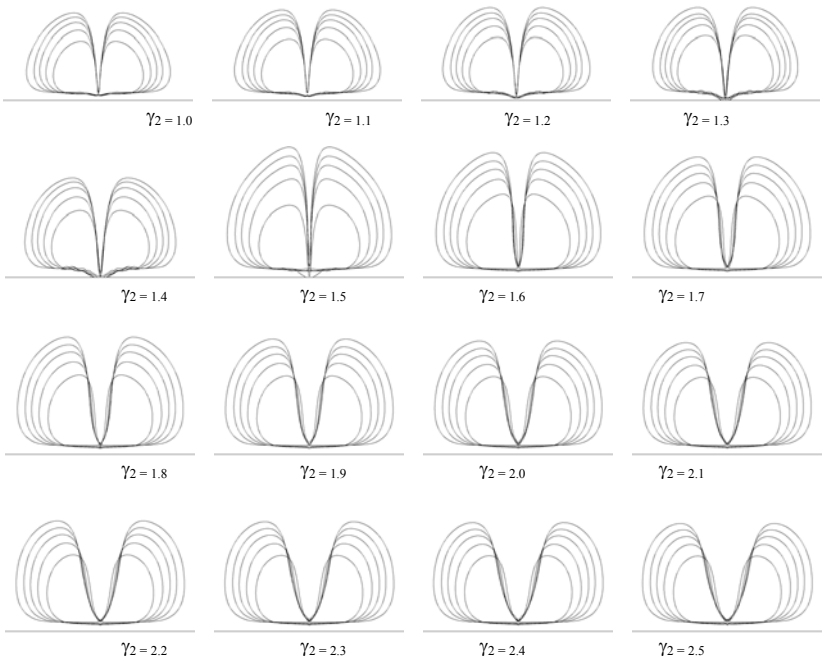

Figure 9: Bubble shapes at the moment of creation of a hole for the different cases.

Figure 9 shows the bubble shapes near the lower wall at the moment of creation of a hole. The results are obtained by the numerical simulation of the different cases. For each value of γ_2, the different bubble shapes corresponding to the different values of $(p_{in}/p_{out})_{initial}$, are shown in a single picture. The bigger bubble shapes correspond to the higher values of $(p_{in}/p_{out})_{initial}$. It is demonstrated from this figure that as the value of γ_2 increases, the diameter of the induced round jet toward the lower wall decreases. Also for the cases without splitting, the bubble near the lower wall has bigger sizes than the cases with splitting.

Figure 10 shows the effect of the value of $(p_{in}/p_{out})_{initial}$ on the jet velocity for the cases for which γ_2 tends to infinity. The velocities are measured at the moment of the creation of a hole. The jet velocity of the case for which the value of $(p_{in}/p_{out})_{initial}$ is 20, is used to non-dimensionalize the velocities of the other cases. This figure demonstrates that increasing the value of $(p_{in}/p_{out})_{initial}$ leads to increasing the jet velocity.

Figure 11 shows the effect of the values of γ_2 and $(p_{in}/p_{out})_{initial}$ on the jet velocity toward the lower wall at the moment of the creation of a hole. For each value of $(p_{in}/p_{out})_{initial}$, the jet velocities are non-dimensionalized with the jet velocity of the case for which γ_2 tends to infinity. All of the non-dimensional velocities have the values higher than 1. Therefore it is demonstrated from this figure that the upper wall increases the jet velocity toward the lower wall. For

each value of γ_2, the higher values of $(p_{in}/p_{out})_{initial}$ result the higher increases in the jet velocity, because the kinetic energy of the surrounding liquid is higher for the higher pressure ratios. For each value of $(p_{in}/p_{out})_{initial}$, the jet velocity toward the lower wall increases with increasing the value of γ_2 up to a certain limit. It can be a result of the fact that for the values of γ_2 higher than 1, most of the plane jet kinetic energy is transferred to the round jet induced toward the lower wall. For the value of $(p_{in}/p_{out})_{initial}$ equal to 20, this limit is 1.6. But for the higher values of $(p_{in}/p_{out})_{initial}$ this limit is 1.5. One of the features of the cases for which the value of $(p_{in}/p_{out})_{initial}$ is 20, is that the splitting process occurs also at the value of γ_2 equal to 1.5. Therefore it can be concluded that as long as the splitting process occurs, the jet velocity toward the lower wall increases with increasing the value of γ_2. To interpret this result, it can be stated that for the cases without the splitting process, the induced plane jet is weak and can not sufficiently intensify the induced round jet during the bubble compression.

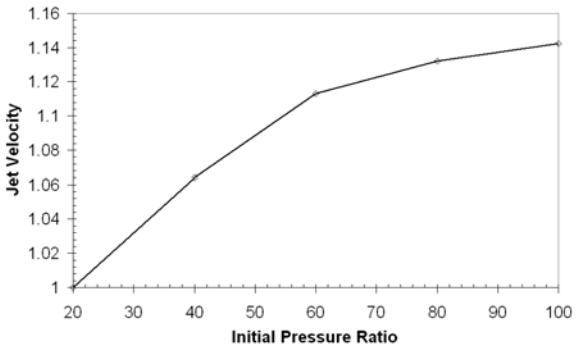

Figure 10: The jet velocity versus the value of $(p_{in}/p_{out})_{initial}$ at the moment of the creation of a hole for the cases for which γ_2 tends to infinity.

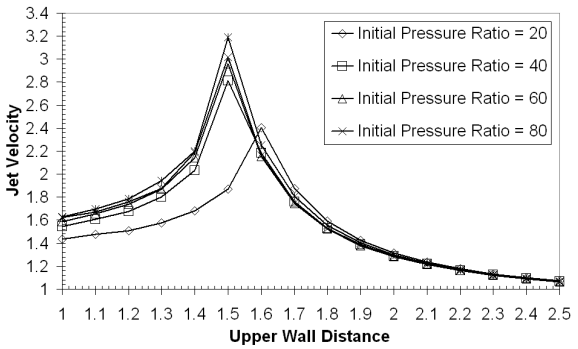

Figure 11: The jet velocity versus the value of γ_2 at the moment of the creation of a hole for the different values of $(p_{in}/p_{out})_{initial}$.

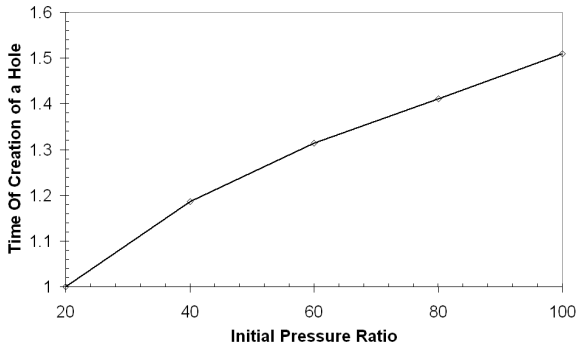

Figure 12: The time of the creation of a hole versus $(p_{in}/p_{out})_{initial}$ for the cases for which γ_2 tends to infinity.

Figure 12 shows the effect of the value of $(p_{in}/p_{out})_{initial}$ on the time of the creation of a hole, for the cases for which γ_2 tends to infinity. In this figure, the times are non-dimensionalized with the time of the creation of a hole for the case for which the value of $(p_{in}/p_{out})_{initial}$ is 20. It is demonstrated from this figure that for the higher values of $(p_{in}/p_{out})_{initial}$ the process that leads to the creation of a hole takes more time.

Figure 13 shows the effects of $(p_{in}/p_{out})_{initial}$ and γ_2 on the time of the creation of a hole. For each value of $(p_{in}/p_{out})_{initial}$, the times are non-dimensionalized with the time of the creation of a hole for the case for which γ_2 tends to infinity. Figure 13 demonstrates that for each value of $(p_{in}/p_{out})_{initial}$, the process that leads to the creation of a hole takes more time for the lower values of γ_2.

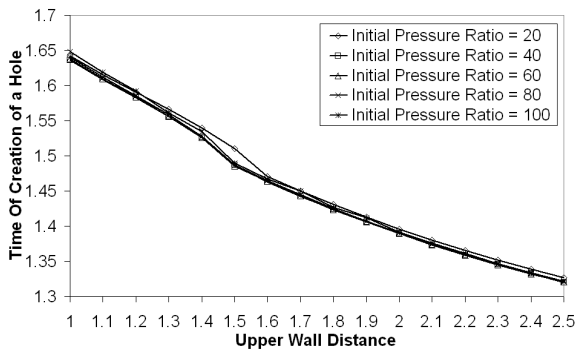

Figure 13: The time of the creation of a hole versus the value of γ_2 for the different values of $(p_{in}/p_{out})_{initial}$.

5 Conclusion

The jet formation through the oscillation of a bubble between a couple of parallel walls is numerically simulated using FLUENT CFD software. The volume of fluid method is used to capture the bubble surface applying a geometric reconstruction method. The simulations are performed for several initial inside to outside pressure ratios of the bubble and different distances from the walls to the bubble center. The results are qualitatively in good agreement with the experimental observations performed by Ishida et al. [7]. It is concluded that the existence of each wall increases the velocity of the round jet induced toward the other wall. Keeping the position of one of the walls fixed, the velocity of the jet toward that wall increases with increasing the other wall distance from the bubble center up to a certain limit. For the distances larger than this limit, the bubble splitting does not occur. Also it can be concluded that for the smaller distances from the walls to the bubble center, the process that leads to the jet formation takes more time.

References

[1] Wikipedia Free Encyclopedia, http://en.wikipedia.org/wiki/Inkjet_printer
[2] Khoo, B. C., Klaseboer, E. and Hung, K. C., A collapsing bubble-induced micro-pump using the jetting effect, J. Sensors and Actuators A, **118**, pp. 152-161, 2005
[3] Brennen, C. E., Cavitation and bubble dynamics, Book, Oxford Univ. Press, 1995
[4] Benjamin, T. B. and Ellis A. T., The collapse of cavitation bubbles and pressure thereby produced against solid boundaries, Phil. Trans. Royal Soc. London A, **260**, pp. 221-240, 1966
[5] Popinet, S. and Zaleski, S., Bubble collapse near a solid boundary: A numerical study of the influence of viscosity, J. Fluid Mech., **464**, pp. 137-163, 2002
[6] Lauterborn, W. and Bolle, H., Experimental investigation of cavitation-bubble collapse in the neighborhood of a solid boundary, J. Fluid Mech., **72**, pp. 391-399, 1975
[7] Ishida, H., Nuntadusit, C., Kimoto, H., Nakagava, T. and Yamamoto, T., Cavitation bubble behavior near solid boundaries, CAV2001 Conf., 2001
[8] Gopala, V. R., van Wachen, B. G. M., Volume of fluid methods for immiscible-fluid and free-surface flows, Chem. Eng. J., **141**, pp. 204-221, 2008
[9] Aulisa, E., Manservisi, S., Scardovelli, R., Zaleski, S., Interface reconstruction with least-squares fit and split advection in three-dimensional Cartesian geometry, J. Comp. Phys., **225**, pp. 2301-2319, 2007
[10] FLUENT 6.3 documentation
[11] Brackbill, J. U. and Kothe, D. B. and Zemach, C., A continuum method for modeling surface tension, J. Comp. Phys., **100**, pp. 335-354, 1992
[12] Brujan, E. A., Pearson, A., Blake, J. R., Pulsating, buoyant bubbles close to a rigid boundary and near the null final Kelvin impulse state, Int. J. Multiphase Flow, **31**, pp. 302-317, 2005

The VOF method applied to the numerical simulation of a 2D liquid jet under gravity

G. Rocco[1], G. Coppola[2] & L. de Luca[1]
[1]*Dipartimento di Ingegneria Aerospaziale (DIAS), Università degli Studi di Napoli "Federico II", Italia*
[2]*Dipartmento di Energetica, Termofluidodinamica e Condizionamenti ambientali (DETEC), Università degli Studi di Napoli "Federico II", Italia*

Abstract

Numerical simulations of a two-dimensional gravitational liquid sheet injected in another immiscible fluid are performed. The steady state of the liquid sheet has been calculated by solving the two-dimensional Navier-Stokes equations for variable density incompressible flows and the interface between the two fluids has been determined by using the Volume of Fluids method . The analysis takes into account viscous, inertial, gravitational and surface tension forces and different regimes of motion are identified according to the values of Reynolds and Stokes numbers. Velocity, pressure and shape of the sheet are investigated and the results are in well agreement with previous numerical and experimental results.

Keywords: VOF method, liquid jet, die-swell effect.

1 Introduction

The numerical simulation of free surface flows represents a very hard challenge due to the complex physical phenomena involved in the liquid-gas or liquid-liquid interface dynamics, such as changes in topology (coalescence, break-up), instability, surface tension effects. A variety of engineering applications, concerning atomization, drops impact and liquid jets dynamics have motivated much research on this topic.

In particular, laminar liquid jets injected from a rectangular slot (liquid sheets) in an immiscible fluid have been studied extensively in the last years.

WIT Transactions on Engineering Sciences, Vol 69, © 2010 WIT Press
www.witpress.com, ISSN 1743-3533 (on-line)
doi:10.2495/AFM100181

The qualitative behaviour of a steady liquid sheet is well known. In the absence of gravity, at high Reynolds numbers the sheet contracts, whereas at low Reynolds numbers due to the sudden change of the boundary conditions on the viscous stresses, the sheet expands in the near field (die-swell effect, see Georgiou *et al.* [1]). Other important effects affecting the dynamics of the jet are surface tension and gravity. Among several contributions in the literature, two accurate references for the numerical simulation of the relevant flow field are represented by the works of de Luca and Costa [2] and Richards *et al*. [3]. In the former the numerical simulation of the liquid sheet is addressed by means of the so-called orthogonal Boundary-Fitted Coordinate Transformation (BFCT), while in the latter a Volume Of Fluids method (VOF) is applied to simulate a round liquid jet issuing into another liquid.

In the present paper a two-dimensional second order finite difference VOF-code, named MultiFluids, is developed to investigate the behaviour of a two-dimensional liquid sheet issuing from a rectangular slot under the influence of the gravitational field. The aim of the present paper is to carry out wide spectrum numerical simulations concerned with various flow regimes. This application is still lacking in the VOF literature.

The remainder of this paper is organized as follows. In section 2 we give a brief description of the VOF method and we introduce the numerical peculiarities of MultiFluids code. In section 3 the liquid sheet problem is set out. Finally, in section 4 and 5 we report the results of the numerical simulations and some conclusions.

2 Numerical method

In this section we describe the method for tracking the interface between two fluids in a two-dimensional, nonreacting, incompressible flow. In recent years a number of methods have been developed for the solution of problems involving the motion of interfaces in multiphase flows. A possible classification of these methods is based on the type of grid used. From this point of view the various methods for interface simulation can be divided into two great classes. In the first class, the interface is treated as a boundary between two sub-domains. This approach requires a deformable grid in order to follow the motion of the interface. The principal disadvantage in the use of these methods is that the grid can undergo a considerable distortion. The second class of methods uses a predefined fixed grid that does not move with the interface. In this case, a specific advection scheme, able to convect the interface, is employed. These last schemes can be divided into explicit and implicit if the interface is explicitly or implicitly represented. Among the implicit methods there are the Level Set (LS) and VOF methods. The first one, introduced by Osher and Sethian [4], describes the interface as the zero level of a continuous scalar field, named level set function. This method consists updating the level set function at each time step by means of a transport equation. The principal advantage of this method, with respect to the VOF method, is that the approximation of the interface is globally continuous. Unfortunately, this method does not enforce the mass balance in a

natural way. In the VOF method, introduced by Hirt and Nichols [5], the interface is represented by means of a Heaviside function, named volume of fraction function. In contrast to the LS method, the main advantage of this method is that it enforces the mass balance in a natural way, even for a relatively coarse grid. Furthermore, as in the LS method, no special treatments are required to model the topological changes of the interface or break-up phenomena. Unfortunately, this method uses a discontinuous function to describe the interface, thus the solution is affected by numerical diffusion and all topological information of the interface as, for example, the normal and the curvature, are approximated by smoothing the Heaviside function.

In the VOF methods, as well as in LS methods, the Navier-Stokes equations are used in a "one-fluid formulation" which requires solving only one set of equations for two immiscible fluids with different densities and viscosity. In order to identify the topology of the interface advected by the velocity field, a transport equation for the volume fraction function f is coupled to the Navier-Stokes equations. This function is used to compute physical properties and local curvature of the interface. The equations of motion to be solved are:

$$\nabla \cdot \underline{V} = 0 . \tag{1}$$

$$\rho \frac{\partial \underline{V}}{\partial t} + \rho \nabla \cdot \underline{V}\underline{V} = -\underline{\nabla} p + \nabla \cdot (2\mu \underline{\underline{D}}) + \underline{F}_s + \underline{F}_b . \tag{2}$$

$$\frac{\partial f}{\partial t} + \underline{V} \cdot \underline{\nabla} f = 0 . \tag{3}$$

where $\underline{F}_b$ is a body force, $\underline{\underline{D}}$ is the symmetric part of the strain tensor and $\underline{F}_s$ is the surface tension force. In eqns. (2), density and viscosity are not constant in all physical domain, but their value depends on the volume fraction function:

$$\rho = \rho_l f + (1-f)\rho_g , \qquad \mu = \mu_l f + (1-f)\mu_g .$$

where ρ_l, μ_l are the density and the viscosity of the liquid phase and ρ_g, μ_g are the density and the viscosity of the gas phase.

In last years many numerical methods have been proposed in order to model the effects of surface tension forces $\underline{F}_s$ in VOF codes. This is an important topic since in many free surface flows, such as fluids with high surface tension (or with surfactant), flows with convolute interfaces (high curvature) and pendant drops, surface tension forces are the dominant forces. The surface tension term in the Navier-Stokes equations creates the principal difficulties, since it is a singular term. In several implementations of the VOF method these difficulties can produce spurious currents and numerical instability (Renardy and Renardy [6]). In our code many of the most popular schemes for surface tension

modelling have been tested, the numerical simulations here presented have been obtained by means of the Continuum Surface Force (CSF) model (Brackbill *et al.* [7]) because of its low computational cost and wide diffusion in many commercial and *home-made* numerical codes. In CSF model, the effects of surface tension forces are modelled by means of an explicit term in the Navier-Stokes equations:

$$\underline{F}_s = \sigma k \delta_s \underline{n}_s .$$

where k is the curvature of the interface, δ_s is the Dirac function, σ is the surface tension coefficient and $\underline{n}_s$ the normal unit vector to the interface. The curvature is calculated by evaluating the divergence of the normal unit vector to the interface and this vector is calculated by implementing finite differences of the volume fraction function smoothed with the filter defined in Lafaurie *et al.* [8]. Thus the surface tension effects are implemented in a simple way, by distributing it over neighbouring grid points.

In MultiFluids code, the Navier-Stokes equations are solved by means of the projection method on staggered uniform grid due to Chorin [9]. The special features of our code are: it is based on a explicit fourth order Runge-Kutta method; a second order lagrangian scheme for the volume fraction equation is used (Gueyffier *et al.* [10]); a CSF method is adopted in order to model the surface tension forces. A modified Neumann boundary condition is employed for the special treatment of the normal component of the velocity at the outflow boundary (Sander *et al.* [11]).

3 Problem definition and numerical setup

A stationary jet of water is ejected vertically in the gravitational field by means of a rectangular slot in an environment of quiescent air (figure 1(a)). The slot width is 2b, whereas along the z direction the slot is infinite and the flow can be considered two-dimensional. The main dimensionless numbers governing the motion of the liquid sheet are Reynolds (Re), Stokes (St) and Capillary (Ca) numbers:

$$\mathrm{Re} = \frac{2u\rho_l b}{\mu_l}, \qquad St = \frac{4\rho_l g b^2}{\mu_l u}, \qquad Ca = \frac{\mu_l u}{\sigma}.$$

where ρ_l, μ_l are the density and the viscosity of the water, u is the mean inflow velocity and σ is the surface tension coefficient.

3.1 Computational domain

A sketch of computational domain is shown in Figure 1(b). The flow is assumed to be symmetric with respect to the slot symmetry plane (*x*-*z* plane in figure 1(a)), so the computational domain is a rectangle bounded by the symmetric plane of the slot at its west side, wall at north and open edges at east and south sides. The dimensions of the computational domain depends on the slot width.

We assume that the dimension, in axial direction, is equal to $L_x = 30b$; whereas in the normal direction it is set to $L_y = 10b$. Numerical experiments carried out on different domain size confirm that these dimensions are sufficient to obtain a full-developed flow. The spatial resolution of computational domain was defined by a uniform grid spacing of b/10 spatial step.

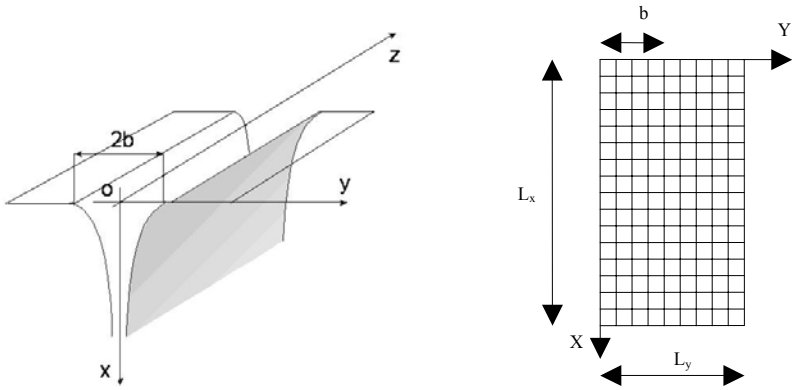

Figure 1: Schematic description of the (a) physical and (b) computational domain.

3.2 Boundary and initial conditions

Regarding the initial conditions, we use a rectangular form for the initial shape of the jet, whereas for the initial velocity conditions a Poiseuille profile is employed in the liquid phase and a zero velocity condition is imposed in the gaseous phase (quiescent ambient). For what it concerns boundary conditions, a Poiseuille velocity profile has been adopted for the inflow, whereas at the west edge of the computational domain a symmetry condition has been imposed. The treatment of the boundary conditions at east and south edges is more complex. In fact, in order to take into account the lateral inflow of the gas due to the typical entrainment effect occurring during the spread of the liquid jet, an open boundary condition is imposed on east edge of the computational domain. This condition consists in homogeneous Neumann conditions for both velocity components. At the outflow, in order to suppress numerical difficulties arising from the backflow, a modified Neumann boundary condition for the streamwise component of the velocity has been applied. The modification is based on the idea that if the streamwise component of the velocity, in the last computational cell, is positive, then classic homogeneous Neumann boundary condition is adopted. On contrary, if this velocity is negative (backflow), a Dirichlet boundary condition is adopted and the streamwise component of the velocity is set to zero.

4 Results

In this section we present some results obtained by means of MultiFluids code. In order to give a better physical interpretation of the results we introduce a classification of different regimes of motion for various Reynolds and Stokes numbers. All the possible flow regimes are reported in table 1; for example, a liquid jet with high Reynolds and Stokes numbers is in Inertial–Gravitational regime, whereas a liquid jet, with low Reynolds and Stokes numbers is in Viscous regime. Capillary number can be seen as an additional governing parameter for each regimes identified in table 1. Note that in the figures, the adopted Cartesian coordinate system (x, y) denoting the axial and lateral coordinates are made dimensionless with respect to the half slot width.

Table 1: Classification of different flow regimes.

	Re << 1 *Creeping*	*Re = O(1)*	*Re >> 1* *Inertial*
St << 1 No gravity regime	Viscous	Viscous Inertial	Inertial
St = O(1)	Viscous Gravitational	Viscous Inertial Gravitational	Inertial
St >> 1 Gravitational regime	Gravitational	Gravitational	Inertial Gravitational

4.1 Vertically falling liquid sheet

Figure 2 shows the solution during the transient evolutions of the liquid sheet without surface tension force at various time step computed at Reynolds number equal to 50 and Stokes number equal to 25. Figure 3 refers to the same simulation of figure 2 and shows the steady shape of the computed interface (continuous line) together with the inviscid, or torricellian, solution (dotted line). This simulation refers to Inertia – Gravity regime for which the jet contracts and uncovers downstream the torricellian solution. The numerical solution appears more slender than the inviscid one in the near field according with literature results. Nevertheless, the contraction of the jet in the present simulations appears more pronounced than in de Luca and Costa [2]. Figure 4 shows the pressure field when the stationary conditions are reached.

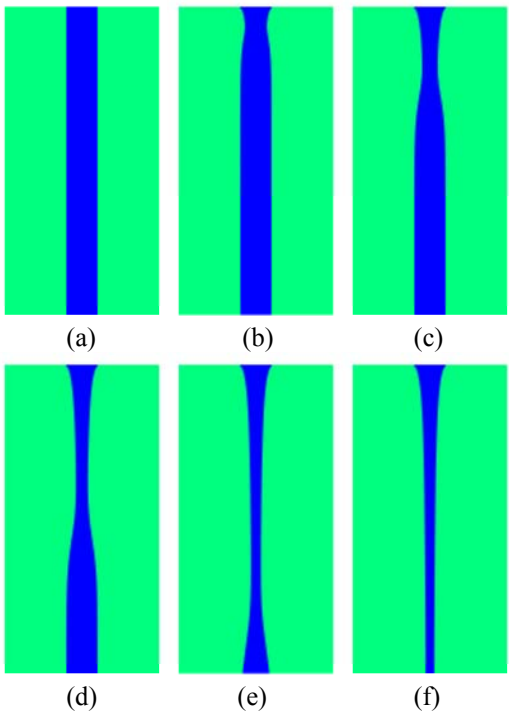

Figure 2: Transient evolution of the liquid sheet with Ca = ∞, Re = 50 and St = 25. $\Delta t = 10^{-5}$ s (a) time step 1, (b) 10000, (c) 20000, (d) 30000, (e) 40000, (f) 50000.

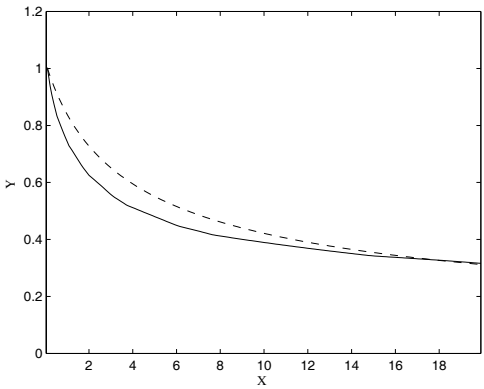

Figure 3: Stationary shape of the liquid sheet: (—) Ca = ∞, Re = 50 and St = 25; (---) torricellian solution.

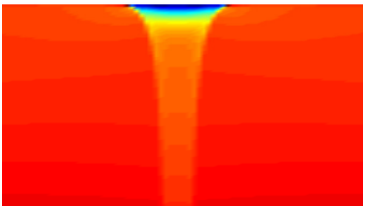

Figure 4: Pressure field in stationary condition at Ca = ∞, Re = 50 and St = 25.

4.2 No-gravity or low gravity jet swell problem

A simulation of the jet behaviour in the Viscous – Inertial regime is represented in figure 5. In this regime, in the absence of gravity, the jet exhibits a very large swelling due to high viscous effects. According to Nickell *et al.*[12] the extrudate swell for this case approaches to 1.19. Figure 6 shows the classic die-swell phenomenon computed at Re = 2 and St = 1. This simulation refers to the Viscous–Inertial–Gravitational regime. In this regime the jet exhibits a remarkable swelling only in the entrance region. This behaviour is due to the combination of high viscous and low gravity local effects. Subsequently the gravitational effects produce a contraction of the jet that approaches the torricellian solution (dotted line). The comparison between figures 7(a) and 7(b) emphasizes the different behaviour between the jet in the gravitational and in the viscous regime and the role of the velocity fields on the deformed shape of the curtain. As we can see in figure 7(a), the velocity field causes a contraction of the jet in the Inertial regime, whereas in figure 7(b) a remarkable swelling due to velocity field is clearly evident.

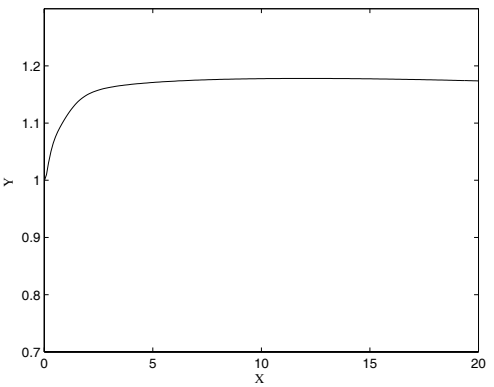

Figure 5: A detail of the liquid sheet at Ca = ∞, Re = 4 and St = 0.

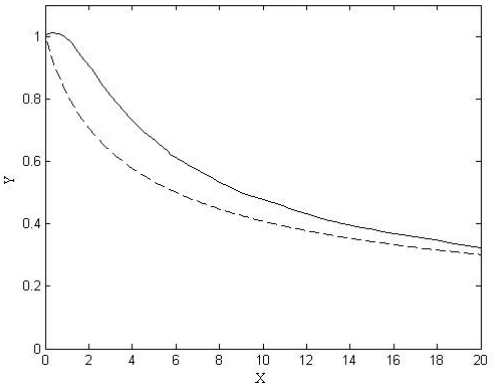

Figure 6: Stationary shape of the liquid sheet: (—) Ca = ∞, Re = 2 and St = 1; (---) torricellian solution.

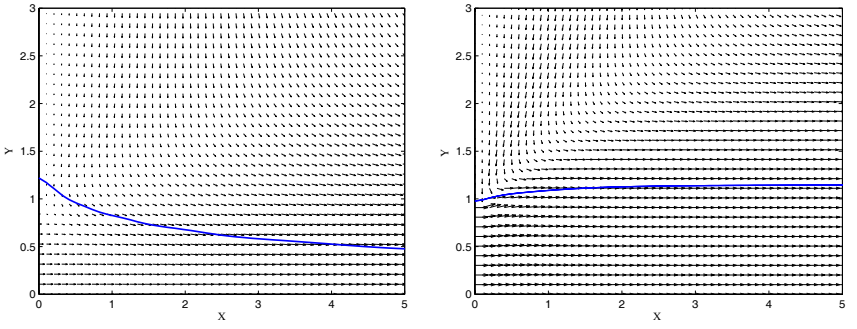

(a) (b)

Figure 7: Velocity field and stationary shape of the liquid sheet (—) at Ca = ∞. (a) Re = 50 and St = 25, (b) Re = 4 and St = 0.

4.3 Influence of the capillary number

A comparison of the jet behaviour with and without surface tension effects is reported in figure 8. In this figure we can see that the jet without surface tension forces (red line) appears more slender than the jet computed in the case including the effects of the surface tension force (black line). As a conclusion, the surface tension, in inertial gravity regime, tends to reduce the contraction of the sheet.

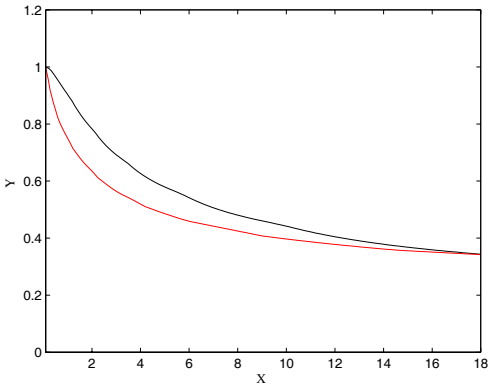

Figure 8: Influence of the capillary number on the stationary shape of the liquid sheet at Re = 50 and St = 25: (—) Ca = 10^{-2}; (—) Ca = ∞.

5 Conclusion

The stationary free surface flow of a two-dimensional plane liquid jet evolving in quiescent air in presence of gravity has been numerically determined by means of a VOF code. Inertia, viscous, gravity and surface tension are all included in the present model.

The results show that at low Stokes numbers (low gravity) the jet expands issuing from the slot and, subsequently, it contracts along the streamwise direction, whereas, at zero gravity, the jet expands and, if the Reynolds number is very low, the contraction is not present. The dynamics of die-swell phenomena is recovered. In the gravitational regime, the effect of the gravity is dominant and the jet contracts monotonically along the streamwise direction uncovering far downstream the inviscid solution.

The results are in good agreement with previous numerical simulations. This paper constitutes a preliminary step towards the numerical simulation of breakup phenomena, whose task is currently in progress.

Reference

[1] Georgiou G. C., Papanastasiou T. C. and Wilkes J. O., "Laminar Newtonian jets at high Reynolds number and high surface tension," *AIChE Journal*, v. 34, p. 1559-1562, 1988.

[2] de Luca L. and Costa M., "Two-dimensional flow of a liquid sheet under gravity," *Computers & Fluids*, v. 24, p. 401-414, 1995.

[3] Richards J. R., Beris A. N., and Lenhoff A. M., "Steady laminar flow of liquid-liquid jets at high Reynolds numbers," *Physics of Fluids*, v. A 5, p. 1703-1717, 1993.

[4] Osher S., Sethian J., "Fronts propagating with curvature-dependent speed: Algorithms based on Hamilton-Jacobi formulations," *Journal of Computational Physics*, v. 79, p. 12-49, 1988.
[5] Hirt C. W., Nichols B. D., "Volume of fluid (VOF) method for the dynamics of free boundaries," *Journal of Computational Physics*, v. 39, p. 201-235, 1981.
[6] Renardy Y., Renardy M., "PROST: A Parabolic Reconstruction of Surface Tension for the Volume-of-Fluid Method," *Journal of Computational Physics*, v. 183, p. 400-421, 2002.
[7] Brackbill J. U., Kote D. B., and Zemach C., "A continuum method for modelling surface tension," *Journal of Computational Physics*, v. 100, p. 335-354, 1992.
[8] Lafaurie B., Nardone C., Scardovelli R. and Zaleski S., "Modelling, merging and fragmentation in multiphase flow with SURFER," *Journal of Computational Physics*, v. 113, p. 134-147, 1994.
[9] Chorin A., "A numerical solution of the Navier-Stokes equations," *Mathematics of Computation*, v. 22, p. 745-762, 1968.
[10] Gueyffier D., Nadim A., Li J., Scardovelli R., Zaleski S., "Volume of fluid interface tracking with smoothed surface stress methods for three-dimensional flows," *Journal of Computational Physics*, v. 152, p. 423-456, 1999.
[11] Sander W. and Weigand B., "Direct numerical simulation and analysis of instability enhancing parameters in liquid sheets at moderate Reynolds number," *Physics of Fluids*, v. 20 053301, p. 1-18, 2008.
[12] Nickell R. E., Tanner R. I. and Caswell B., "The Solution of Viscous Incompressible Flow Jet and Free-Surface Flows Using Finite-Element Methods," *Journal of Fluid Mechanics*, v. 65, p. 189-206, 1974.

This page intentionally left blank

Large eddy simulation of particle laden jet flow with aerodynamic three-way coupling

A. Jadoon & J. Revstedt
Lund University, Department of Energy Sciences, Sweden

Abstract

A model to incorporate for aerodynamic 3-way (indirect) coupling between mono dispersed particles is proposed. The model is applied on particle laden jet flow and the results are compared with 2-way coupling. The particle drag coefficients are corrected based on the relative position of the particles. The correction factor is obtained from the pre-computed lookup tables. The particles are tracked by Lagrangian particle tracking (LPT), whereas the continuous phase is modelled by Large eddy simulation (LES). Particle mean axial velocity is found to be large in 3-way coupling which results in more particle penetration in the streamwise direction due to less momentum transfer of the particles to the fluid phase. The fluid velocity is also observed to be higher in case of 3-way coupling due to high mass loading which results in reduced axial fluid velocity fluctuations. The void faction is also found to be higher in 3-way coupling due to particle entrainment and less interaction with turbulence.
Keywords: LES/LPT, turbulent jet, three-way coupling, drag correction.

1 Introduction

Particle laden jet flows remained an interesting and important topic due to its industrial and engineering applications like pulverized-coal combustors, cyclone separators, combustion etc. An important issue often neglected in the moderately dense flows is the aerodynamic (indirect) interaction between the particles i.e. three-way coupling. The addition of particles to turbulent flows can change the flow characteristics like turbulent intensities even at very low volume fraction. Therefore taking the particle interaction into account in such flows still needs to be addressed.

Previously most of the research both experimentally and numerically has been carried out considering one-way and two-way coupling. Longmire and Eaton [1]

WIT Transactions on Engineering Sciences, Vol 69, © 2010 WIT Press
www.witpress.com, ISSN 1743-3533 (on-line)
doi:10.2495/AFM100191

studied experimentally the dispersion of particles when they interact with turbulent jet dominated with vortex ring structures. They further confirmed that the local dispersion and concentration of particles are governed by convection due to large scale structures. Kulick et al. [2] experimentally investigated the gas phase turbulent flows with heavy particles of mass loading up to 80%. The fluid turbulence is found to be attenuated when particles are added depending on particle relaxation time to turbulent scale and solid mass loading. Boivin et al. [3] investigated the feasibility of using Large eddy simulation (LES) when the gas flow turbulence is modified due to momentum exchange of particles. They conducted a priori tests of sub-grid scale models by using the results obtained from DNS. He found a good agreement with DNS data by using dynamic sub-grid models. Jin et al. [4] using LES predict the particle dispersion patterns when particles with different Stokes number (based on particle diameter) are injected. Their results are in good agreement with the experimental work.

Regarding the inter-particle interaction, Tanaka and Tsuji [5] simulated the two phase (gas-solid) flow considering inter-particle collisions. They used the deterministic method to calculate the inter-particle collision where inter-particle collision is described by hard sphere model. They reported that even in dilute conditions (volume fraction (10^{-4})), the inter-particle collision has large effect on particle diffusion. Sommerfeld and Zivkovik [6] applied the stochastic collision model in a dilute phase pneumatic conveying through pipe systems. They also showed that the effect of inter-particle collision is significant even at low overall mass loading for the development of particle concentration profiles. Oesterle and Petitjean [7] simulated the gas-solid flow to demonstrate the significance of inter-particle collision in horizontal pipes. The other contribution concluding the importance of inter-particle collision are Lun and Lui [8], Sakiz and Simonin [9], Sommerfeld [10]. Sommerfeld [11] also applied the stochastic model of particle collision to isotropic homogeneous turbulence flow and obtained reliable results. More recently Yan et al. [12], conducted the Direct numerical simulation (DNS) of three dimensional two phase jet. The inter-particle collision was described by deterministic hard-sphere model. The study was only focused on inter-particle collision by neglecting the two-way coupling. They found that occurrence of inter-particle collision correlates well with local particle concentration, though average concentration of the particles is lower in the whole field. They also reported that the relation between the average inter-particle collision number and stokes number is not a linear but has a local maximum.

In the present studies, only the effect of three-way aerodynamic coupling (indirect collision) in gas-solid flow is accounted by considering the flows in which number density of the particles is not high enough to have an equilibrium in interaction among particles, secondly the inter-particle distance is not large enough to neglect the particle interaction. However the direct inter-particle collisions are neglected in this study. It has been shown for particle Reynolds number < 200, that drag of particle placed in the wake of reference particle is affected even up-to $6d_p$ (d_p is the diameter of the particle) distance, Prahl et al. [13]. Prahl et al [14], Jadoon et al. [15] also found that even for high particle Reynolds number

i.e. up-to 600, the drag of trailing particle in the wake of reference particle is still 90 percent of the drag of the single particle at $9d_p$. Hence the particle interaction is important in dilute flows also. A model is proposed to account the three-way coupling. Salewski and Fuchs [16] applied this drag correction technique to a spray in cross-flow. They corrected the drag of the particles up to particle Reynolds number of 200. They found 40% decrease in the average drag of particles in the near-field (dense) jet due to aerodynamic interaction. However it decreases to 10% at $15D_N$ (D_N is the diameter of the nozzle) downstream. The technique is applied to particle laden jet flow in order to analyze the effect of the model on velocities of both discrete and continuous phase, particle dispersion, velocity fluctuations etc. The current study is the step towards the complete parameterization of the model which includes the effect of particle size, stokes number, turbulent Reynolds number and mass loading. The data is available for particles Reynolds number up-to 600, however in the current study the only particle Reynolds numbers up to 200 are achieved.

2 Mathematical models

The continuous phase is modelled by LES whereas the particles are tracked by Lagrangian particle tracking (LPT)

2.1 Modelling of continuous phase

In LES, the large scales are resolved and small scales are modelled. As large scales are assumed to be most important ones because of energy and momentum transport in turbulent flows. The space filtered non-dimensional Navier-Stokes equation for incompressible flows can be written as:

$$\frac{\partial \bar{u_i}}{\partial x_i} = 0 \tag{1}$$

$$\frac{\partial \bar{u_i}}{\partial t} + \bar{u_j}\frac{\partial \bar{u_i}}{\partial x_j} = -\frac{\partial \bar{p}}{\partial x_i} + \frac{1}{Re}(\frac{\partial^2 \bar{u_i}}{\partial {x_j}^2}) - \frac{\partial \tau_{ij}}{\partial x_j} \tag{2}$$

Equations (1) and (2) govern the resolved scale motion. The effect of the small scales are modelled through sub-grid scale (SGS) stresses.

$$\tau_{ij} = \overline{u_i u_j} - \bar{u_i}\bar{u_j} \tag{3}$$

In the current study, no explicit SGS model is applied instead the properties of the numerical scheme are used to achieve the necessary dissipation of energy at small scales, Rai and Moin [17].

2.2 Particle equation of motion

Lagrangian particle tracking based on momentum equation for particle is stated as:

$$m\frac{d\vec{u}_p}{dt} = \vec{F} \tag{4}$$

In the above equation, F is the forces acting on the particle and m is its mass. As the ratio of particle to air density is high i.e. approx 2000, therefore only the drag and the gravity forces are considered. The equation for the drag force in non-dimensional form:

$$F_D = -\frac{3}{4}\frac{\rho_c}{\rho_p}\frac{1}{d_p^*}C_D \mid U_r^* \mid U_r^* \tag{5}$$

where ρ_c and ρ_p are the densities of continuous (fluid) and dispersed (particle) phase respectively. d_p^* is the non-dimensional diameter of the particle scaled with the diameter of the nozzle D_N and U_r^* is non-dimensional relative velocity scaled with inlet air velocity U_o. C_D is the drag coefficient and the correlation is given by Schiller and Nauman [18] as:

$$C_D = \frac{24}{Re_p},\ for\ Re_p << 1 \tag{6}$$

$$C_D = \frac{24}{Re_p}(1 + 0.15{Re_p}^{0.687}),\ for\ Re_p \leq 1000 \tag{7}$$

$$C_D = 0.44,\ for\ 1000 \leq Re_p \leq 100000 \tag{8}$$

Here Re_p is the particles Reynolds number and defined as:

$$Re_p = \frac{d_p \mid V_i - u_i \mid}{\nu_c} \tag{9}$$

Similarly the non-dimensional gravity term is as follows:

$$F_{grav} = (1 - \frac{\rho_c}{\rho_p})\frac{1}{Fr^2} \tag{10}$$

where Fr is the Froud number defined as ratio between inertial to gravitational forces and expressed as $U_o/\sqrt{gD_N}$, where g is the acceleration due to gravity.

3 Numerical methods

The numerical scheme used in this current study is based on Olsson and Fuchs [19]. The Governing equations are discretized on a staggered cartesian grid. Fourth order central finite difference scheme is used for approximation of the equation except for convective term. The convective terms are discretized using third order upwind based schemes Rai and Moin [17]. The governing equations are solved

using a split solver; explicit and implicit. The momentum equations are integrated explicitly in time using fourth order Runge-Kutta type method. A Poison equation is solved for the pressure correction. A multi-grid scheme is used to accelerate the solution of the Poisson equation.

4 Problem description

In all simulations, a rectangular domain of $[8, 14, 8]D_N$ (D_N is the diameter of the nozzle) corresponding to $[x, y, z]$ directions respectively is used. The jet enters at the center of the $x - z$ plane (x and z being lateral coordinates) and flows in the y (stream-wise) direction. The four Multi-grid levels with 96, 290 and 96 cells corresponding to x,y and z directions respectively on the finer level are used. Grid stretching is used in all three coordinates for high spatial resolution ensuring that order of accuracy is maintained. At inflow, fluctuations are introduces in the radial velocities as $\pm 10\%$ of the stream wise velocity and no slip boundary conditions at walls. At outflow both Neumann convective or non-reflective boundary conditions are tested and no difference is observed.

4.1 Two-way coupling

In the two-way coupling, the results are validated with the experimental work of Longmire and Eaton [1]. The jet is forced with a strouhal number $St = 0.43$. The jet Reynolds number of 19000 based on jet diameter D_N, fluid inlet velocity U_o and fluid kinematic viscosity is used. The particle mean diameter of 0.00275 and particle to fluid density ratio of 2000 are used. The velocity of the particle is $0.55U_o$. The mass loading ratio of 9% is used.

4.2 Three-way coupling

The aerodynamic three-way coupling is introduced by correcting the drag coefficient of the particle depending upon their relative position. The correction is done up-to particles' Reynolds number of 200. In order to achieve the particle's Reynolds number of 200, the particle velocity is set twice the air velocity at inlet, diameter of the particle is set to 0.01, mass loading ratio is 1.11 and Reynolds number based on air velocity and diameter of the jet is 19000. Uniform inflow conditions are applied in 3-way coupling. The modelling of the aerodynamic three-way is achieved by using the precomputed drag correction factor f, and the drag coefficient in equation is then adjusted by this factor. The drag correction factors are used from the precomputed look up tables [13, 16].

Thus the drag force term after adjusting with correction factor f becomes:

$$F_D = -\frac{3}{4}\frac{\rho_c}{\rho_p}\frac{1}{d_p^*}C_D f \mid U_r^* \mid U_r^* \tag{11}$$

5 Results

In the result section, all velocities are scaled with the inlet velocity U_o and the length of the domain are scaled with the diameter of the nozzle D_N.

5.1 Validation

The results for two-way coupling are presented in order to validate the code. The mean properties of the discrete phase i.e. particles are compared with the experimental work of Longmire and Eaton [1]. Fig. 1(a) shows the axial mean velocity of the particles along the centerline of the jet. The velocity of the particle is under predicted by 8% in the range of shear layer ($\approx 4 - 6D_N$) where the potential core ends and the jet starts to spread. A high radial velocity is observed at this point i.e $Y/D_N = 4$ which results in more spreading of particles compared to experimental data which explains the decrease in axial velocity at the end of potential core along the center line Fig. 1(b).

Fig. 1(c), (d) shows the axial velocity along the radius at different axial positions of $Y/D_N = 2$ and $Y/D_N = 4$ respectively. At $Y/D_N = 2$, the results agree well with the experimental data but at $Y/D_N = 4$ the velocity is somewhat under predicted compared to experimental data, which may be due to difference in the inlet condition of the particle velocity. Longmire and Eaton [1] do not present particle velocities at the nozzle. Therefore, instead the measured velocities at $Y/D_N = 0.5$ are used as boundary conditions, whereas in the current simulations, the boundary conditions are set at the nozzle, which of course may be one of the reason for the discrepancies seen in Fig. 1.

The radial velocities at $Y/D_N = 2$ and 4 are shown in Fig. 1(b). The radial velocities at $Y/D_N = 2$ is negative for $r/D_N < 0.35$ compared to Longmire and Eaton [1]. This may be caused by difference in entrainment between the simulation and the experiment of Longmire and Eaton [1], which in turn caused by geometrical difference. The jet is coming out from a flat surface compared to thin, sharp edged converging nozzle used in the experiments. The entrainment in the main flow is only from sides in the present case in contrast to experimental conditions where the entrainment is both from sides and from the upstream of the nozzle. This may leads to the negative radial velocity at $Y/D_N = 2$. However, the results are in good agreement downstream at $Y/D_N = 4$. The particles have higher radial velocities at $r/D_N > 0.4$ showing more dispersion of the particles. Fig. 1(e), (f) shows the comparison of standard deviation of the particle axial velocity fluctuations along the radius at $Y = 2D_N$ and $Y = 4D_N$ downstream.

5.2 Three-way coupling

The results for the three-way coupling are presented in this section. Fig. 2(a) shows the fluid axial velocity along the centerline of the jet. The fluid velocity is found to be greater in 3-way coupling compared to 2-way coupling. However the particles experience less drag in 3-way due to drag correction and therefore less momentum

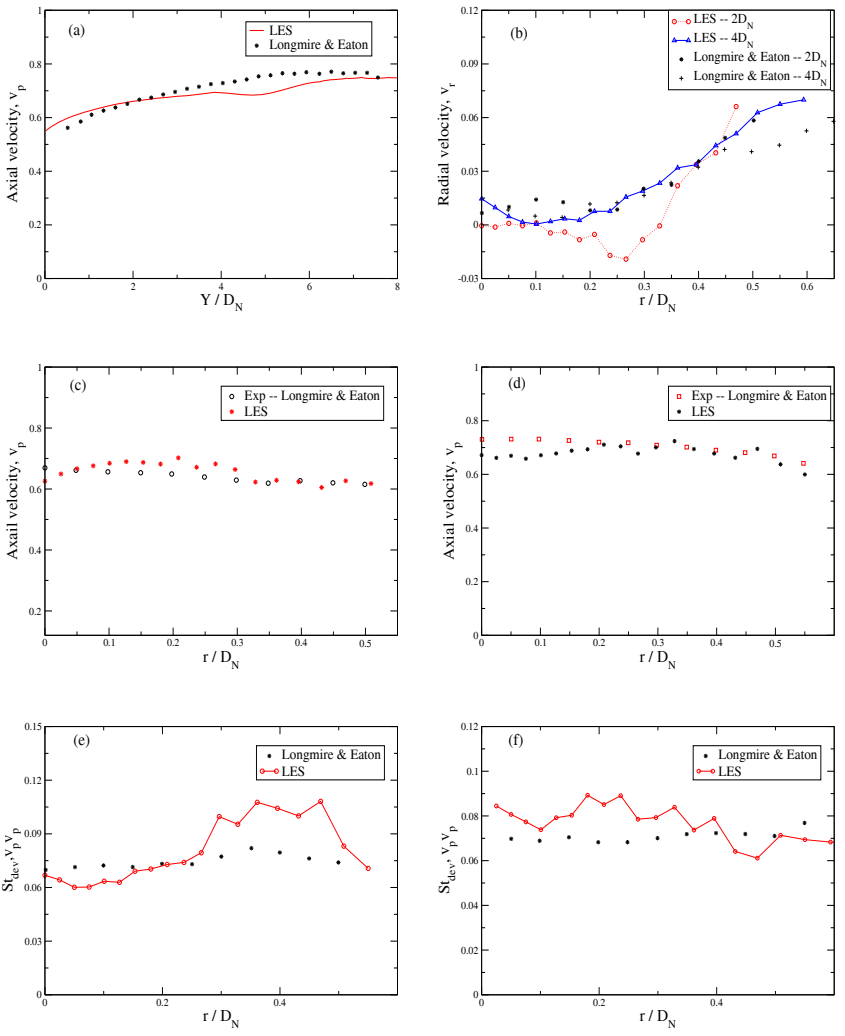

Figure 1: Particle axial velocity along the center line of the jet (a) and particle radial velocity along radius at $Y = 2D_N$ and $Y = 4D_N$ downstream (b), Particle axial velocity along the radius of the jet at axial distance of $Y = 2D_N$ (c) and $Y = 4D_N$ (d), Standard deviation of the particle axial velocity fluctuations along the radius of the jet at axial distance of $Y = 2D_N$ (e) and $Y = 4D_N$ (f).

of particles is transferred to the fluid phase but on the other hand, greater volume fraction (mass loading) is found in 3-way coupling compared to 2-way (Fig. 3(a)) and it is well known conclusion that the presence of particles reduces the decay

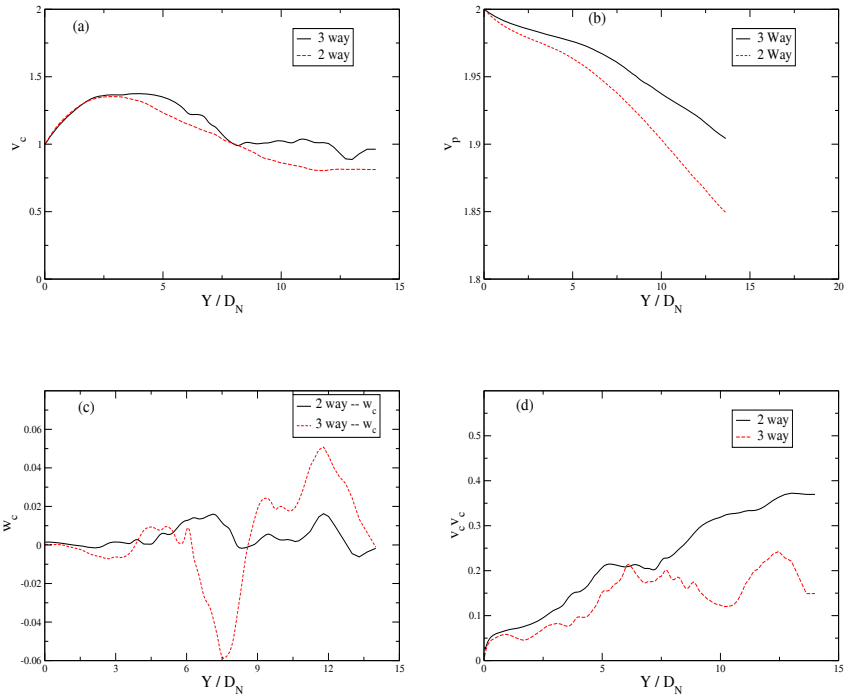

Figure 2: Fluid axial velocity (a), particle axial velocity (b), fluid radial velocity (c) and fluid axial velocity fluctuations (d) along the centerline of the jet.

of centreline air velocity. Therefore average momentum transfer in 3-way is still higher (due to high mass loading) which results in increase in gas velocity in 3-way.

The effect of less momentum transfer from particles in 3-way coupling can be seen in the mean particle velocity in Fig. 2(b), the particles penetrate more in the 3-way coupling compared to 2-way. It can be seen in Fig. 3(a) that the average number of particle (void fraction) along the center line is also greater in 3-way coupling. This is due to the negative radial velocity attained by the fluid in 3-way coupling Fig. 2(c), therefore particles are entrained towards the center of the jet. The other reason for high mass loading may be consequence of smaller lateral diffusion due to less interaction with turbulence for 3way coupling which results in smaller source terms in the NS equations. Fig. 3(b) shows the particle Reynolds number along the centerline of the jet for 3-way coupling. The difference between the particle velocities in 2-way and 3-way coupling is greater in the region of high particle Reynolds number as the drag correction is more active in this region. The standard deviation of fluctuations of the mean axial velocity of the fluid along the center line is shown in Fig. 2(d), the fluctuations are reduced in 3-way coupling compared to 2way as the average number of particles along the centerline in greater in 3-way coupling which helps in attenuating the turbulent

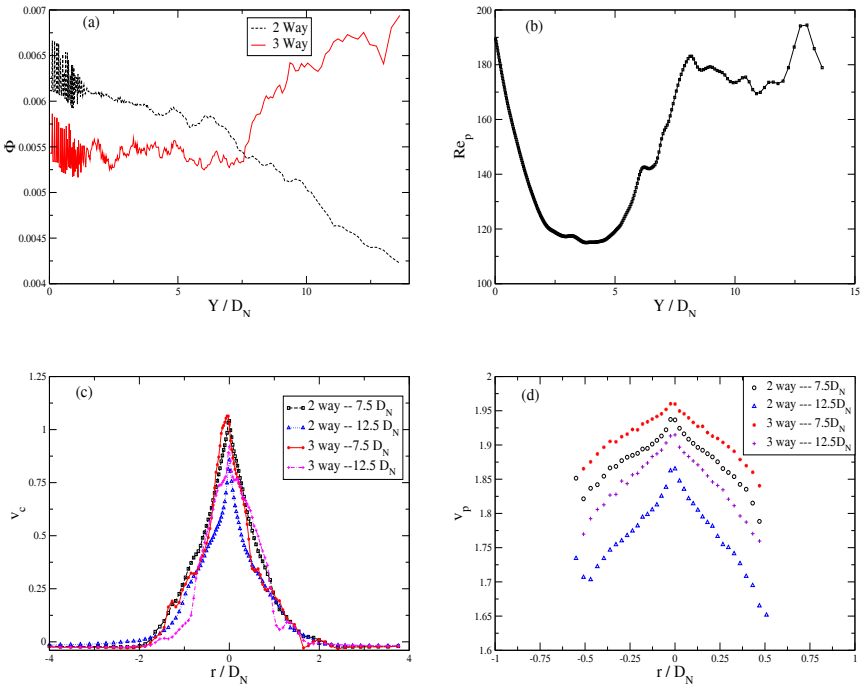

Figure 3: Void fraction (a) and particle Reynolds number (b) along the centerline of the jet, fluid axial velocity (c) and particle axial velocity (d) at $Y = 7.5D_N$ and $12.5D_N$.

intensity in 3-way case. The radial velocity component is plotted in Fig. 2(c), it can be seen that the decrease in fluid axial velocity at $7.5D_N$ in Fig. 2(a) is due to the negative radial velocity gained by the fluid at this point which interferes to the axial velocity progress. However the radial velocity becomes positive afterwards and as a result axial velocity also increases again.

The mean axial velocities of both fluid and particles are shown in the Fig. 3(c) and Fig. 3(d) respectively. The difference in the particle velocities in 2-way and 3-way coupling can be easily observed. However, there is no difference along the radius of the jet is observed in both 2-way and 3-way coupling. The particles used in the simulation are heavy and bigger in size with Stokes number > 170. The particles are merely affected by the continuous phase as they have very little time to respond to the fluid and tend to keep their initial velocity. However even with such high stokes number, the difference between the 2-way and 3-way coupling is obvious.

6 Conclusion

A model based on aerodynamic 3-way coupling is applied to a particle laden jet flow. The mean particle and fluid velocities are compared with the 2-way coupled

flow. The results shows difference in mean properties of both particle and fluid properties when 3-way coupling is applied. Particles penetrate more downstream in the 3-way coupled flow as the particles experience less drag compared to 2-way coupled flow. The fluid axial velocity increases whereas the fluctuations decreases due to high mass loading in 3-way coupling. The average number of particles tend to increase along the centerline in the 3-way coupled flow. The results gives the insight to further investigate and parameterize the model by varying the stokes number, density, Reynolds number etc.

References

[1] Longmire, E.K. & Eaton, J.K., Structure of particle laden jet. *J Fluid Mech*, **236**, pp. 217–258, 1992.
[2] Kulick, J.D., Fessler, J.R. & Eaton, J.K., Particle response and turbulent modification in fully developed channel flow. *J Fluid Mech*, **277**, pp. 109–134, 1994.
[3] Boivin, M., Simonin, O. & Squires, K., On the prediction of gas-solid flows with two-way coupling using large eddy simulation. *Phys Fluids*, **12(8)**, pp. 2080–2090, 2000.
[4] Jin, H.H., Luo, K., Fan, J.R. & Cen, K., Large eddy simulation of a particle laden turbulent plane jet. *Journal of Zhejiang Uni Sci*, **4(2)**, pp. 175–180, 2003.
[5] Tanaka, T. & Tsuji, Y., Numerical simulation of gas solid two phase flow in vertical pipe: on the effect of inter-particle collision. *ASME/FED gas-solid flows*, **121**, pp. 123–128, 1991.
[6] Sommerfeld, M. & Zivkovic, G., "Recent advancements in numerical simulations of pneumatic conveying through pipe system". *In: Hirsch, Ch., Periaux, J., Onate, E. (Eds), Comp Meth in Appl Sci, invited lectures and special tech sessions of the First European Comp Fluid Dynamics Conf and the First European Conf on N Methods in Engg*, pp. 201–212, 1992.
[7] Oesterle, B. & Petitjean, A., Simulation of particle to particle interaction in gas solid flows. **19**, pp. 199–211, 1993.
[8] Lun, C.K.K. & Lui, H.S., Numerical simulation of dilute turbulent gas solid flows in horizontal channels. **23**, pp. 575–605, 1997.
[9] Sakiz, M., Simonin, O., 2001 "Continuum modelling and Lagrangian simulation of massive frictional colliding particles in a vertical gas-solid channel flow". *In: Michaelides, E. (Ed.), Proceedings of the Fourth International Conference on Multiphase Flow, New Orleans, USA* (CD-ROM proc. ICMF_2001, Paper 186).
[10] Sommerfeld, M., Analysis of collision effects for turbulent gas particle flow in horizontal channel: Part1. particle transport. **29**.
[11] Sommerfeld, M., Validation of stochastic Lagrangian modelling approach for inter-particle collisions in homogeneous isotropic turbulence. **27**.

[12] Yan, J., Luo, K., Tsuji, Y. & Cen, K., Direct numerical simulation of particle dispersion in a turbulent jet considering inter-particle collisions. *Int J Multiphase Flow*, **34**, pp. 723–733, 208.
[13] Prahl, L., Holzer, A., Arlov, D., Revstedt, J., Sommerfeld, M. & Fuchs, L., A study of the interaction between two fixed spherical particles. *Int J Multiphase Flow*, **33**, pp. 707–725, 2007.
[14] Prahl, L., Jadoon, A. & Revstedt, J., Interaction between two spheres placed in tandem arrangement in steady and pulsating flow. *Accepted for publication in Int J of Multi-phase flows*, May 2009.
[15] Jadoon, A., Prahl, L. & Revstedt, J., Dynamic interaction of fixed dual spheres for several configurations and inflow conditions. *Submitted for publication in Eurpeon J of Mech*, 2008.
[16] Salewski, M. & Fuchs, L., Effects of aerodynamic particle interaction in turbulent non-dilute particle laden flow. *J of Turbulence*, **9**, pp. N–46, 2008.
[17] Rai, M.M. & Moin, P., Direct simulations of turbulent flow using finite-difference schemes. *J Comput Phys*, **96**, pp. 15–53, 1991.
[18] Schiller & Nauman, A.Z., A drag coefficient correlation. *Ver Deut Ing*, **77**, pp. 318–320, 1933.
[19] Olsson, P.J. & Fuchs, L., Large eddy simulation of the proximal region of spatially developing circular jet. *Phys Fluids*, **8**, pp. 2125–2137, 1996.

This page intentionally left blank

High quality triangular grid generation for the risk analysis of a special lagoon

B. Tansel
Istanbul Technical University, Maritime Faculty, Turkey

Abstract

Much of the world's open coasts are formed by estuaries and lagoons which are highly important for ecological reasons. Since the rich organic materials are carried in by the stream water, a favorable environment gets formed for plankton, the other creatures thriving on planktons and the fish feeding on them. On the other hand, the water, the reeds and other vegetation, the fish and the organic material that has settled provide the birds with an ideal environment. In this context, the problems with pollution in lagoon systems are important risk factors for the ecological balance. The purpose of the study is to generate a high quality computational network for the risk analysis of a special lagoon in order to construct a solid foundation for the next step in our study. A reduction of the number of elements is aimed at while the underlying physical domain is adequately represented via several grid refinement criteria. Furthermore, standardizing the method to be used as the calculation network, and utilizing its highly accurate risk predictions for all lagoon systems are also aimed at.

Keywords: lagoon quality, risk analyses, grid generation.

1 Introduction

Istanbul, one of the largest and crowded metropolitan cities of Turkey, affects coastal fields negatively in terms of city development, as is the case in many examples throughout the world. We performed our study for the Tuzla Kamil Abdus Lagoon (TKAL) in the Tuzla District of Istanbul. Although the fishery and the hosted birds were important ecological elements and also sources of income before the 1970's in the region, it was completely dried out in 2001 as a result of the relocation of the shipyards in this region (which blocked the natural opening of the lagoon), the highway construction, the modified paths of rivers,

WIT Transactions on Engineering Sciences, Vol 69, © 2010 WIT Press
www.witpress.com, ISSN 1743-3533 (on-line)
doi:10.2495/AFM100201

and various other reasons after 1978. The lagoon, which is extremely important in the environmental ecology and from the socio-economical aspects for Tuzla, was rehabilitated and resuscitated by the Municipality of Tuzla and converted into a beneficial facility. Some of the studies on predicting the necessary risks, which are required for the healthy management of TKAL, were summarized in this paper. The purpose of the study related to TKAL is the determination of the security risks, the dimension of these risks and the cases where taking a precaution is necessary in the lagoon. The results of the performed study are not specific to TKAL, but they can be used for all ecologically important lagoons. In our paper, studies on the generation of a mesh structure, which is the basic and the most important phase in the application of this method, was presented. The first phase of the necessary study was completed by obtaining the bathymetry information of the lagoon, and the data on the wind properties and the current data on the region. The second and the most important stage was to construct the mesh structure of the lagoon, which constitutes a basis for the whole analysis. Our next study will be the computerized solution of the equations (the Navier-Stokes equation and its derivations), by making use of digital methods defining water mass-movements in computer-based models, and following this, the calculation of the fluid free water surface movements and the flow areas will be our next goal. The construction of TKAL mesh structure, which constitutes an important part of this study and the basic results of the first test-run will be presented in our paper.

2 The triangular grid generation method

As is known, the coastal areas constitute a rather difficult setup in comparison to a rigid body meshing, due their very complex geometries. Particularly, in order to perform the risk analysis with various wind and current configurations, it is very important to mesh these regions in a correct and meaningful manner. In our study the high quality triangular mesh generation program BatTri was used, which is a public domain meshing program working under Matlab and developed to meet the needs of the ocean modeling researchers [1].

The actual grid generation is performed by Triangle while BatTri does pre and post processing. The Software's stronger part is its Delaunay refinement algorithm (DRAs) during its triangular grid generation. DRA is a method that is used to produce the refined Delaunay triangulation in point sets [2]. According to the Delaunay feature, there are peripheral circles for every triangle, and the triangles are refined in their peripheral circles with certain restrictions. Indeed, BatTri manages the input and output functions with Triangle [1], which performs meshing according to optimizing the conditions on element creation. That is to say, for grid generation and optimization of produced grids, the main program between input and output is the Triangle, which performs re-meshing according to BatTri conditions. In Figure 1 a very general algorithm is shown related to the BatTri meshing loop.

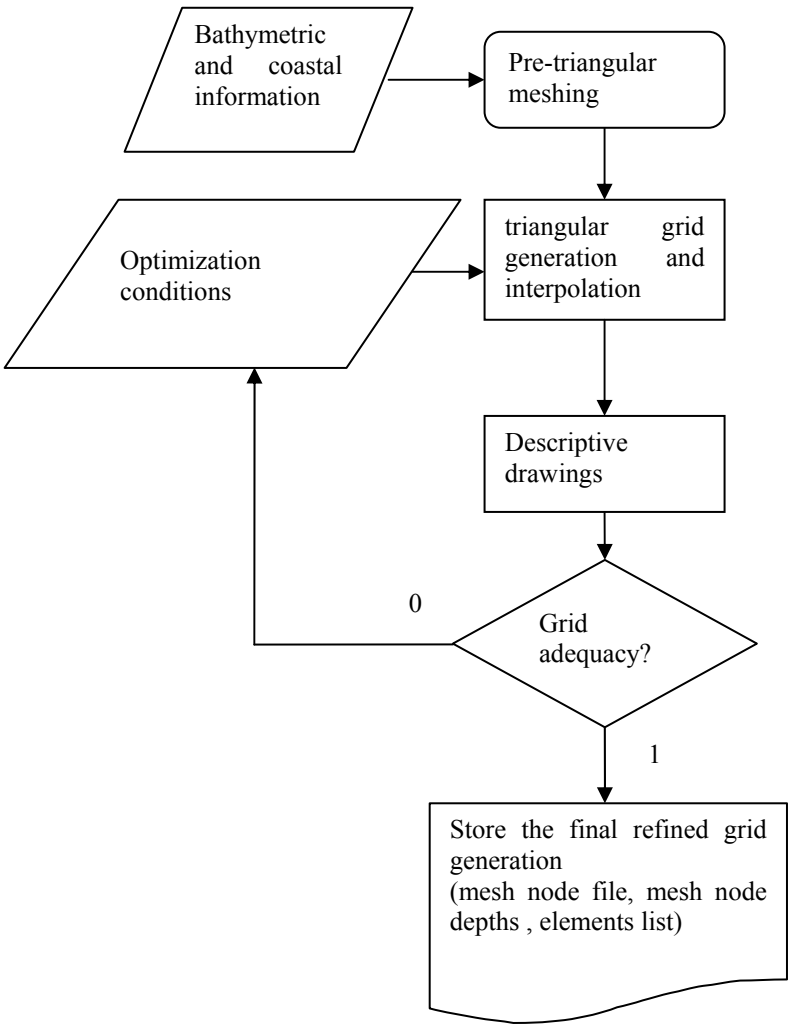

Figure 1: The BatTri Algorithm.

There are BatTri mesh optimization functions for refined grids. Some of these functions are defined below.

$$\frac{h}{\nabla h}\frac{1}{\alpha} \geq A \tag{1}$$

h; average element depth, ▼h; depth gradient value of element verticals, A; maximum element area, α;limiting ratio stated by the user.

$$\frac{h}{\alpha} \geq A \tag{2}$$

The refinement condition related to the tide height and the grid dimension in as of the Courant-Friedrichs-Levy (CFL) type; and for the maximum element area (A),

$$\frac{ght^2}{R^2} \geq A \text{ or } \frac{\sqrt{3}}{4}\frac{ght^2}{R^2} \geq A \tag{3}$$

where g;m/sn^2 gravity dimension, t; time step of the model in minutes, R; it's the ration tide height of the ebb and the flow to the grid dimension.

The refinement condition as in the Pecklet type; if the current speed and diffusion area are known, this condition can be applied for the restriction of the element area restriction.

$$\left(\frac{PeD}{V}\right)^2 \geq A \text{ or } \frac{\sqrt{3}}{4}\left(\frac{PeD}{V}\right)^2 \geq A \tag{4}$$

where *Pe*; Peclet number, *D*; diffusion constant, *V*; speed.

All of these optimization conditions are the functions chosen selected for converting the triangular element into a more refined form [1].

3 TKAL grid generation studies

Figure 2 shows the TKAL configuration. As is seen, there are three islands and channels inside the lagoon. The connection of the lagoon with the sea is provided by two openings.

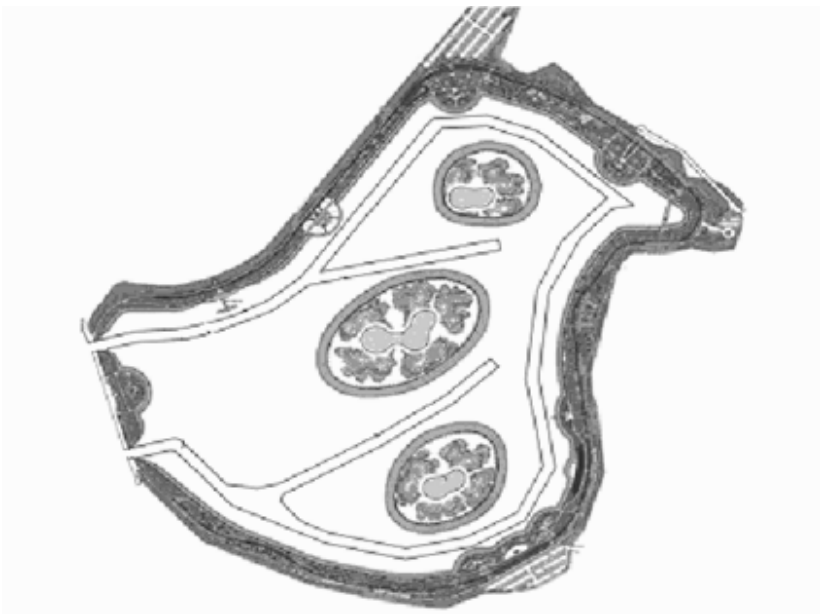

Figure 2: The TKAL configuration.

The deeper channels were set to be 2.5 m deeper than the mean sea level and the shallows surrounding the channels were configured to be 1.2 m. Openings were configured to be 20 m wide and 3.5 m deep. The transition zone between the inner lagoon channels and the shallows is defined to be 10 m wide. The depths in this area were randomly selected around a straight line connecting the endpoints of the transition zone with a slope of 0.8 and an average depth of 1.85 m, within a standard variation of 0.492 m. The depths of the intermediate grid points were calculated using linear interpolation. Considering the small tidal range on the order of centimeters (≈ 6 cm) [3], the absence of fresh water input and the shallowness of the lagoon, it can be assumed that the dominant forces behind the particle exchange with the coastal sea will be caused by the wind stress and the wave action. The dominant winds in the region are southwesterly and northeasterly. In order to effectively resolve the current field in the lagoon and around the lagoon openings where the exchange will occur, two grid resolution zones are defined using the 5 m isobath. The landward zone contains triangular elements whose areas are always less than 1,000 m^2. The open-sea zone contains elements whose areas are less than 10,000 m^2. The first base of the analysis of risk examination is created with the high quality meshing via BatTri. On top of this, the deeper channels in the lagoon were marked by nodes that were 5 m apart along the 2.5 m isobath. These nodes whose presence is enforced

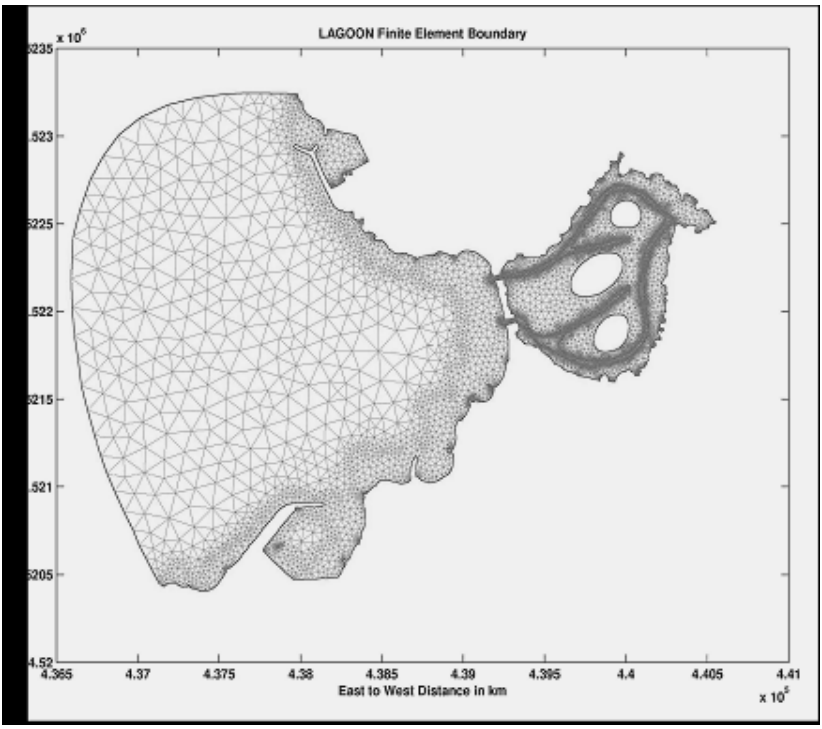

Figure 3: The overall view of the model domain grid.

in the triangulation assure that the transition zone between the channels and the flats is appropriately resolved by a larger number of elements to simulate the relatively steeper gradients. Also, the larger elements in the open-sea region make sure that the forcing signals are appropriately transferred to the coastal zone and the lagoon, while keeping the number of elements low for obvious computational reasons. The finite element mesh is shown in Figure 3. Bathymetry is shown in Figure 4. The grid consists of 15,347 nodes and 29,287 triangular elements.

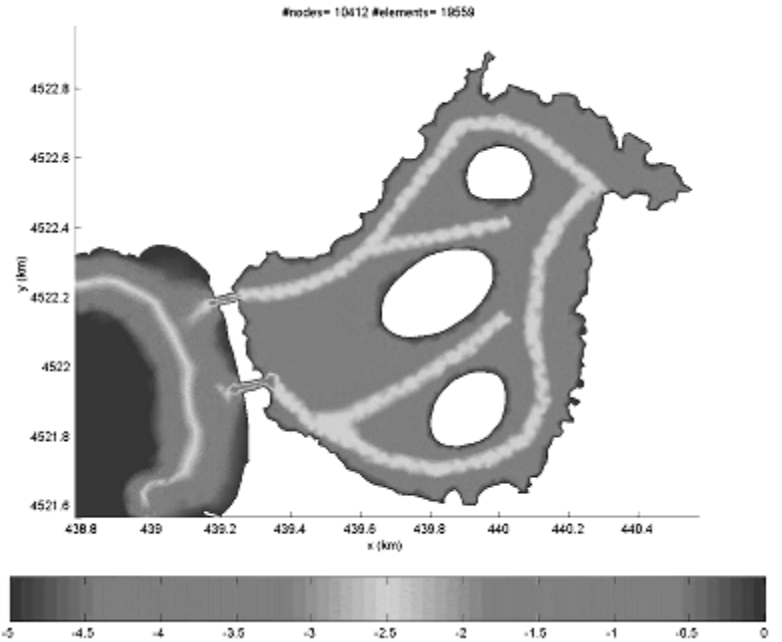

Figure 4: Bathymetric map of the inside and the outside of the lagoon. Scale shows depth in meters.

Figure 5 shows that the element quality is enforced by a minimum 30º inside angle constraint. This condition is met for a majority of the elements in the domain, except for the regions where the presence of certain nodes are enforced. In these regions, the minimum inside angle may rarely drop down to 25º.

Another requirement that the mesh should meet is the CFL (Courant-Friedrichs-Levy) condition, which directly affects the stability of the calculations in the explicit formulations. Assuming equilateral triangles, this can be written as

$$\frac{\sqrt{3}}{4} \cdot \frac{g \cdot h \cdot t^2}{R^2} > A \qquad (5)$$

Here, g is the gravitational acceleration, h is the depth of the water, t is the time step, A is the element area and R is a constant. The values of R may range

between 25 on flat bottoms and 500 on high bathymetry gradients. R = 100 would be an optimized choice for many situations. Assuming that the maximum current velocities in the TKAL model domain are in the vicinity of 0.5 m/sec, the time steps on the order of 25 seconds may be needed to meet the CFL condition. Figure 6 shows the time steps.

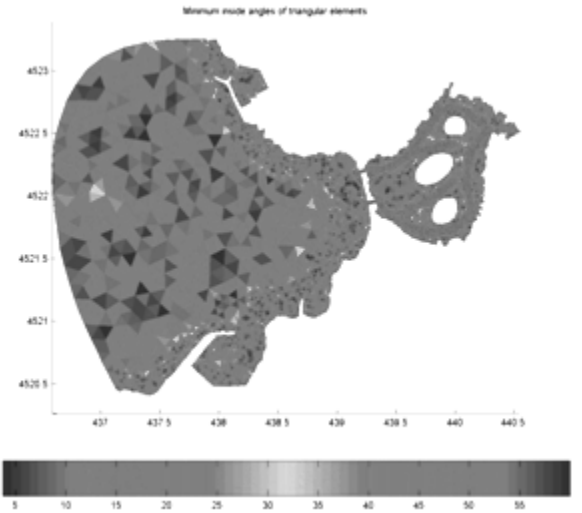

Figure 5: The representation of the Lagoon inner mesh structure based on the inner angles, refined according to the BatTri program.

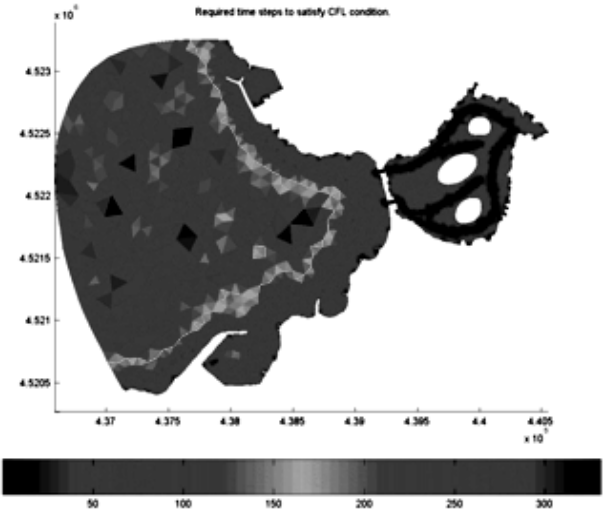

Figure 6: The regional time steps determined according to the BatTri.

Figure 7 shows the element quality measure as defined by:

$$q = \frac{4 \cdot \sqrt{3} \cdot A}{L_1^{\,2} + L_2^{\,2} + L_3^{\,2}} \tag{6}$$

Here, q is the element quality measure, A is the element area and L_1, L_2, L_3 are the element edge lengths. It is usually assumed that the element quality is acceptable for all q ≥ 0.6. Please note that in the ideal situation where an element is an equilateral triangle, $q = 1$ since, $L_1 = L_2 = L_3$.

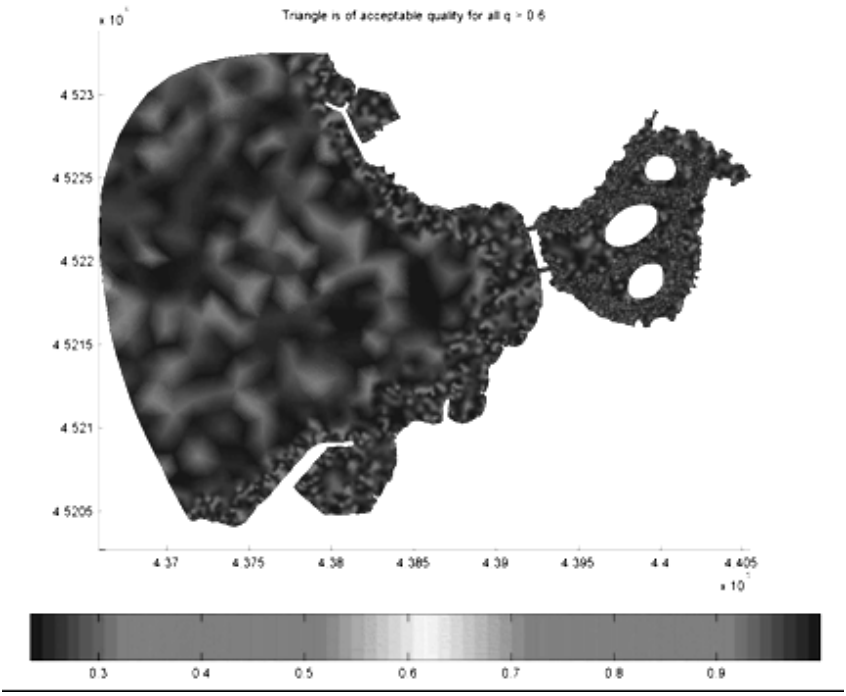

Figure 7: The quality map of the calculation mesh elements. The scale shows the element quality measure q. The dark part, represents $q=1$.

The characteristic element length of the grid, as calculated by $\sqrt{2 \cdot A}$, where A is the element area, ranges from 0.10 m in the lagoon to 153 m in the open-sea, with an average of 11.17 m and a standard variation of 16.9 m.

A model run with the standardized input performed on the generated grid showed no overall qualitative problems in the calculated current fields. For the quantitative evaluations, a field work is planned to acquire the current profiles in and out of the lagoon for the summer of 2010. Two examples of the resulting current vector fields are shown in Figures 8 and 9. The findings demonstrated in Figures 8 and 9 were obtained with the calculation network standard inputs by

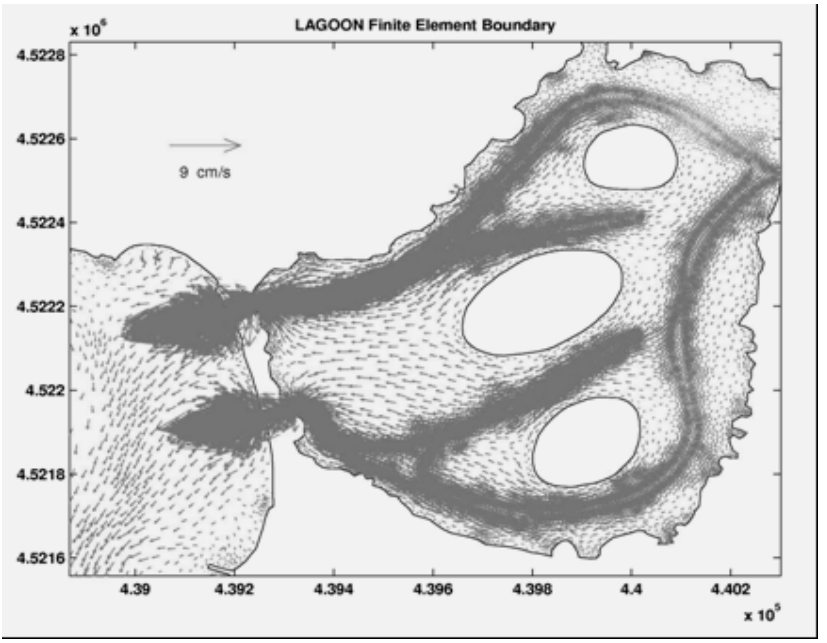

Figure 8: Characteristic example flow vectors obtained as a result of test run around the lagoon.

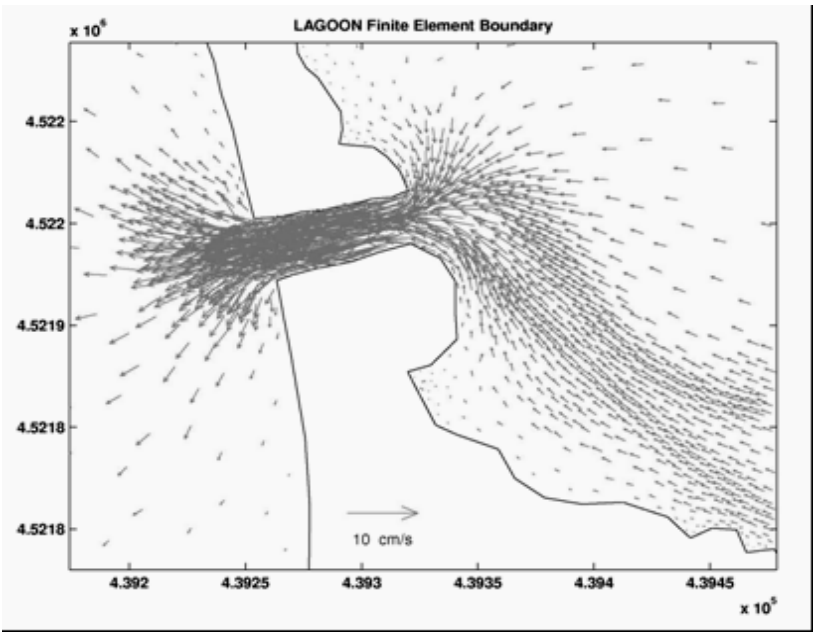

Figure 9: The characteristic example flow vectors obtained as a result of the test run for the southern lagoon opening.

running in the Cygwin environment using a laptop computer with 3.20 MHz and 1 GB RAM. A simulation of 24 hours was completed in 51 minutes with a time step of 144 seconds. In conclusion, no anomaly connected with the calculation network has been observed in the analysis of the calculated velocity vectors. The network transfers the signals that belong to the open-sea free-water level and wind pressure to the coastal area and the lagoon, and vectors in these areas react to these actions. In the phase of real-time modelling, it is estimated that no problem in terms of the calculation network will be experienced in order to ensure the statistical validity of the findings to be obtained through the optimization of input parameters. The current vector maps of test conditions were only provided as characteristic examples.

4 Conclusion

A base grid on which the hydrodynamic finite element simulations are going to be performed has crucial importance on the quality of results. Several factors such as the choice of the model time steps (via CFL condition) and the dispersion coefficients (via Peclet number) actually depend on the characteristics of the grid, combined with the hydrodynamic vector field properties. The optimization here is of utmost importance: an excessive number of elements should be eliminated while the domain discretization is ensured adequately. In this study, a high quality finite element grid is generated for the Tuzla Kamil Abdus Lagoon in Istanbul, Turkey using the public domain triangular finite element grid generator BatTri. Several important parameters such as the quality of the triangular elements and the model time step were examined and determined for later simulations. A test simulation performed on the grid showed no qualitative problems.

Simulations of the lagoon water quality using statistically proven computer models is much cheaper than making a number of measurements, and has the benefit of examining effects of different input parameters in a quick, easy and reliable way. The fast generation of a reliable grid will help in not only normal cases but also in emergency situations for quick decision making.

References

[1] Bilgili, A. & Smith, K.W., *BatTri: A two-dimensional bathymetry-based unstructured triangular grid generator for finite element circulation modeling*. Lynch Computers and Geosciences 32:632-642. 2006.

[2] Lee, D.T. & Schachter, B.J., *Two algorithms for constructing a Delaunay triangulation.* International Journal of Computer Information Science 9, 219–242. 1980.

[3] Alpar, B. &, Yüce H. , *Sea-level Variations and their Interactions between the Black Sea and the Aegean Sea*. Estuarine, Coastal and Shelf Science 46, 609-619, 1998.

Section 2
Experimental measurements

This page intentionally left blank

Validation of airflow measurement in ducts using Laser Doppler Anemometry and Computational Fluid Dynamics modelling

A. Mayes[1], S. Mitchell[1], J. Missenden[1] & A. Gilbert[2]
[1]*London South Bank University, UK*
[2]*BSRIA Instrument Solutions, UK*

Abstract

The problem of airflow measurement is of interest to Building Services Engineers to allow for the effective commissioning and validation of predictive procedures. The velocity distribution in a square section duct (400 mm x 400 mm) was investigated using a Laser Doppler Anemometer (LDA) to determine the velocity distribution and volumetric flow rate in the system, and to compare it with CFD and theoretical predictions (for both square and circular sections). The procedure has revealed a number of practical issues involved in the measurement of such air flows involving an LDA, including boundary flow measurement issues, and the consistency of results. A standard Computational Fluid Dynamics (CFD) package was also used to model the same flow regime, and agreement was obtained with the LDA results for a range of flow rates. Of particular interest was the detailed distribution of modelled and measured velocities across the duct, and the ways in which these compared with the commonly assumed one-seventh power law relationship for turbulent flows. The detailed nature of the observations made allowed investigation of the suitability of power laws for the circular case, and enabled assessment of whether an alternative exponent or method of predicting such flows would be more appropriate in air flow modelling. The study shows the comparison of velocity distribution in a square duct and theoretical similarly sized circular duct.

Keywords: Laser Doppler Anemometer, LDA, airflow, Computational Fluid Dynamics, CFD, log-tchebycheff, one-seventh power law, turbulent flow, boundary layer, internal flow.

WIT Transactions on Engineering Sciences, Vol 69, © 2010 WIT Press
www.witpress.com, ISSN 1743-3533 (on-line)
doi:10.2495/AFM100211

1 Introduction

The provision of good quality experimental data is essential for calibrating and validating mathematical models of airflow. Such models may be used for important applications in building services engineering, including airtightness, ventilation, air conditioning and refrigeration. Reliable data improves confidence in the use of mathematical models (generally Computational Fluid Dynamics, or CFD models), and enables design engineers to investigate the effects of installing, removing or altering the arrangement of fans, ducts and other ventilation devices, without expensive physical testing. A Laser Doppler anemometer (LDA) allows the non-intrusive measurement of air velocity. When used in a confined environment such as a duct, in which the air velocities are reasonably constant over time, measurements at a series of points across the section of flow can be integrated to give the volumetric flow rate. In addition, such results can provide important information about the variation in velocity across the duct, including near the edges (duct surfaces). Care must be taken to allow for the variation between instantaneous and time-averaged velocities, due to turbulence, by extended measurement. In order to verify the results from the LDA, CFD models can be used to picture the flow processes that occur throughout the cross section for a range of flow conditions. These models have enjoyed considerable exposure in recent years to a wide variety of flow problems in a range of engineering disciplines, beyond building services engineering. In this study, a LDA (Dantec FlowExplorer BSA F60) was used to observe the distribution of velocity in a duct of square cross section, in order to obtain the velocity distribution and so deduce volumetric flow rates for a range of airflow conditions. Comparisons were made of some of the results with the output of the CFD model (FLUENT, ANSYS, v12.0). The aim of the study was to see if the results of the CFD model were sufficiently in agreement with measurement to allow its use in studies of ducted air flow, supplemented where appropriate by the proper use of an LDA. In addition, the commonly assumed power law relationship of the turbulent flow region of a circular duct was considered.

2 Duct sections investigated

Airflow through a square duct of cross-section 400 x 400 mm was investigated using both LDA and CFD methods. In addition, a circular section was examined using CFD only. The experimental apparatus is shown in Figure 1. An Air Supply Rig provided air to the square duct. The rig consisted of a variable speed fan that directed air through an orifice plate, and into a box containing three resistance screens beyond which was a square opening. The duct was placed at the opening creating a step-change in the cross sectional area into the duct. In order to reduce the effects of jetting, hexagonal mesh sections of 100 mm overall length were incorporated to condition the flow at the inlet and outlet of the duct.

The LDA was used to measure the velocity profile in the duct, and was controlled using a PC interfaced with the LDA as well as with the 3-dimensional traverse controller, allowing for accurate and repeatable positional control of the

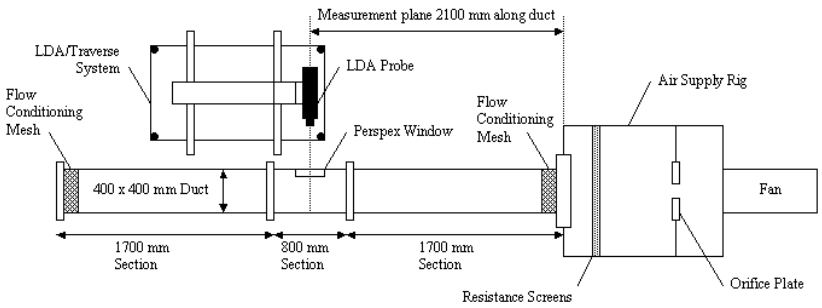

Figure 1: Experimental apparatus.

LDA probe. The probe was projected into the duct through a clear Perspex window to capture precise measurements of airflow without any intrusive disruptions. In order to acquire the experimental LDA data, a traverse of individual velocity measurements according to the Log-Tchebycheff rule was made [1]. This method creates a profile of measuring points such that the average velocity of the internal flow, over the whole cross section, is equal to the arithmetic mean of the measured points. This can then be converted into a volumetric flow rate by multiplying by the cross sectional area. Two flow rates were considered during this investigation: a low flow rate (with an average velocity of 0.620 m/s) and a high flow rate (5.761 m/s). This range is typical of those found in air supply and extract ducts within buildings.

3 CFD model

A CFD calculation is essentially the application of Newton's Law, with friction, to fluid discrete elements. This requires three items to be set; the mesh size, the steadiness of the flow and the viscosity model. Firstly, the mesh is specified which contains the number of cells. Each of these cells possesses a value for the properties of the fluid at that position (for example, velocity, pressure, or temperature). Broadly speaking, a mesh with a larger number of cells provides a more accurate solution. However, this is also more expensive computationally [2] so preliminary tests were performed to find an optimum mesh arrangement (and see Section 3.1). Secondly, to allow the flow profile to develop without the aid of simulating the flow conditioners, the duct was modelled to be arbitrarily long. A length of 20m was deemed sufficient; this equates to 50 duct (hydraulic) diameters. Thirdly, the turbulence characteristics of the airflow at the outlet and inlet were specified. The characteristics can be defined in a number of ways, one of which is to use the turbulence intensity and hydraulic diameter. The hydraulic diameter is defined as shown below (Section 4). According to [3], the turbulence intensity for internal flow can be specified as:

$$I = 0.16 \times \mathrm{Re}^{(-1/8)} \tag{1}$$

where 'I' is the turbulence intensity and 'Re' is the Reynolds Number of the flow (see Section 4.1).

3.1 Boundary layer

In preliminary tests, the wall-adjacent boundary layer had been simulated using a 'non-equilibrium wall function'. This involved using a large cell size to capture this region. However, the boundary layer is of interest and, as such, the mesh has been refined to capture this region in multiple smaller cells. Instead of using a simple wall function, an enhanced wall treatment was used. This allowed the boundary layer behaviour to be captured. However, the problem with this approach is the number of cells required and the quality of these cells. Naturally, to make the cells small enough in one dimension to capture sufficient detail in the few mm of the boundary layer is at odds with the relatively long cells required to model a long duct. This leads to cells possessing a very large aspect ratio, which is undesirable as it could affect convergence and accuracy. However, length-wise partitioning of the cells would quickly lead to a model containing a huge number of cells. The greater the number of cells, the more demanding the model will be in terms of computing power and time. A preliminary investigation was performed to deduce a suitable CFD mesh. This had to be fine enough to include the near-wall behaviour where, due to the length of the duct, fine meshes at the boundary could easily lead to either long and thin cells, or far too many cells. The double-precision solver was activated to help deal with cells with high aspect ratio [3]. The k-ε realizable turbulence model was used to calculate the solution.

4 Theory

4.1 Square and circular duct relationship

For two ducts to have full similitude, they must have the same geometry and the same Reynolds Number, relating inertial to viscous forces. A square duct and a circular duct do not share geometries. However, to compare the flows the Reynolds Numbers could be equated:

$$\mathrm{Re}_s = \frac{\rho \overline{u_s} D_{hs}}{\mu} = \mathrm{Re}_c = \frac{\rho \overline{u_c} D_{hc}}{\mu}, \tag{2}$$

where 'Re_s' and 'Re_c' are the Reynolds Numbers of the square and circular ducts, respectively; '$\bar{u}_s$' and '$\bar{u}_c$' are the average velocities; and 'Dh_s' and 'Dh_c' are the hydraulic diameters (see eqn (4)). At constant atmospheric conditions, density, 'ρ', and viscosity, 'μ', are constant. Therefore, the above equation reduces to a mean velocity, diameter equation:

$$\overline{u_s} D_{hs} = \overline{u_c} D_{hc}. \tag{3}$$

The hydraulic diameter, used to allow non-circular ducts to be treated as such, is given by:

$$D_h = \frac{4A}{P} \tag{4}$$

where A is the cross sectional area, and P is the contact perimeter (also known as the wetted perimeter) of the duct. Eqn 4 provides the same hydraulic diameter for both a square and a circle when the sides of the square are equal to the diameter of the circle. For the square duct, this means that approximately 27% more air (the difference in areas of a square and a circle), by mass or by volume, is required in a square duct than a circular duct for the same amount of turbulence. However, the mean velocity will be the same.

4.2 Theoretical power law in circular ducts

For fully turbulent flow in a circular duct, the central region, away from the laminar boundary layer and the transitional region at the walls, is said to obey a power law [4]. That is:

$$\frac{u(r)}{u_{cl}} = \left(1 - \frac{r}{R}\right)^{\frac{1}{n}} \text{ OR } \frac{u(y)}{u_{cl}} = \left(\frac{y}{R}\right)^{\frac{1}{n}} \tag{5}$$

where y is the distance from the wall, r is the distance from the centreline, R is the distance between the wall and the axial centreline, and 'u_{cl}' is the velocity at the axial centreline. The CFD data, at a virtual duct distance such that the flow was fully developed, and the theoretical power law fit were compared. This analysis used the standard error, normalised by velocity, and was calculated for different values of 'n' (see Section 5.3), where n is the denominator of the power (see eqn (5)). For example, n = 7 in the one-seventh power law. Since the power law only applies to the central turbulent region of the flow, the extent of the boundary layers must be identified. In the universal velocity profile [4], the boundary layers extend to when the dimensionless wall distance, y^+, is approximately equal to 30. Where:

$$y^+ = \frac{1}{\nu}\sqrt{\frac{\tau_\omega}{\rho}} \tag{6}$$

where, 'τ_ω' is the wall shear stress and 'υ' is the dynamic viscosity [4].

5 Results

5.1 LDA - CFD comparison

The experimental LDA data measurement points were dictated by the 7-by-7 Log-Tchebycheff profile. The CFD model had a region of symmetry, as shown in Figure 2, which contained ten measuring points. This implies that there are equivalent points throughout the cross section. In order to assess the agreement of the LDA data to the CFD data at each point along the duct, the LDA data was first converted into the same form consisting of the ten data points. Each point consisted of the mean of the LDA readings at each occurrence of an equivalent point. For example, the four corner-points were averaged to provide the converted LDA data for 'Point 1'.

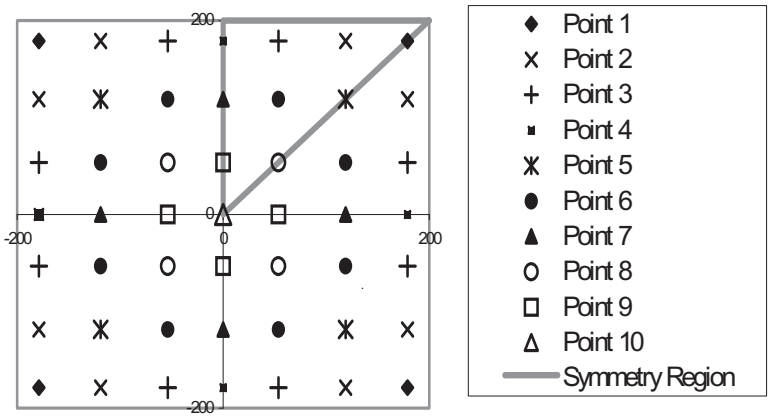

Figure 2: Symmetries and point locations with the CFD model.

The normalised standard error for each duct distance was found by comparing the corresponding ten points. However, each contribution was weighted by the number of instances of that point (for example, the four 'Point 1's and eight 'Point 6's). This enabled identification of the duct distance at which there was a highest agreement between CFD and experimental LDA data. By plotting how the normalised standard error changes over the length of the virtual duct, the distance at which this value is smallest can be found. This implies that this virtual duct distance has the best agreement with the experimental LDA data. The distance was found to be at 2.75 m and 5 m for the low speed and high speed tests respectively. These normalised standard error results shown in Figure 3.

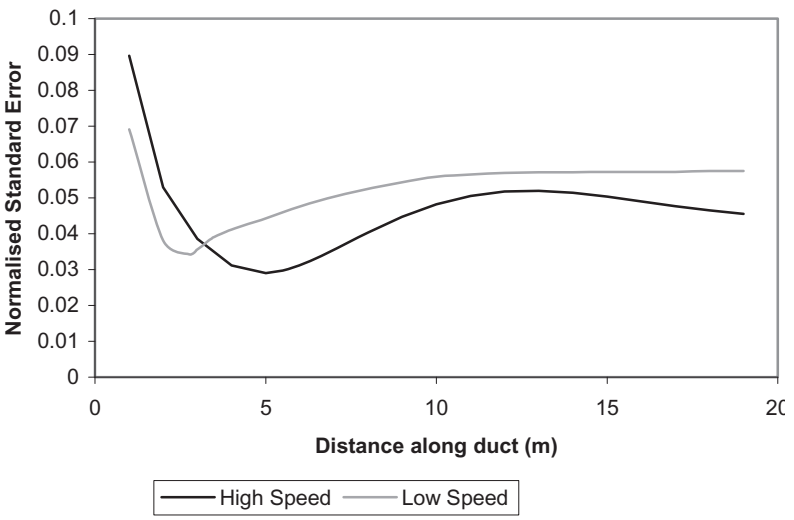

Figure 3: Normalised standard errors between CFD and LDA data.

The measured flow profiles across the square duct cross sections determined by LDA are shown in Figure 4. The equivalent calculated flow rates using CFD are shown in Figure 5. As can be seen, the CFD data (at the derived duct distances) has symmetry, as described above. In contrast, the experimental data is less stable, although, the overall distribution of LDA-measured velocities is comparable.

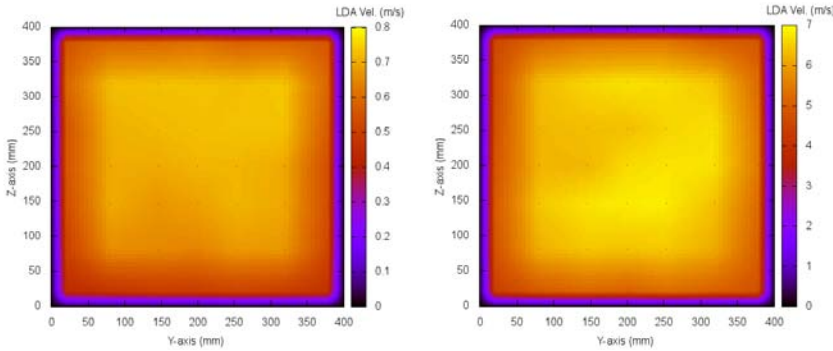

Figure 4: LDA results at low (left) and high (right) flow rates.

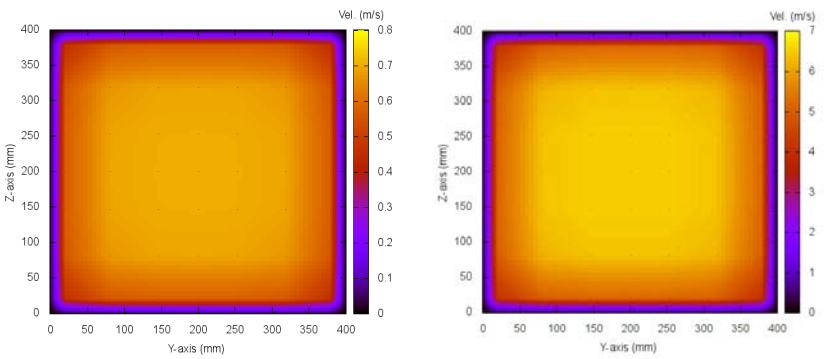

Figure 5: CFD results at low (left) and high (right) flow rates.

5.2 Equal Areas - Log-Tchebycheff comparison using CFD

The CFD inlet velocity is known because it was defined, as a boundary condition for the CFD problem initialisation, to match with the experimental data (the low speed average velocity of 0.620 m/s and the high speed of 5.761 m/s). Furthermore, the velocity at the inlet is uniform across the whole cross-section of the duct. Since the cross-sectional area is known, so is the volumetric flow rate, which is a conserved quantity in every cross-sectional plane. Since the cross-section is also known and constant, the average velocity is also conserved in every cross-sectional plane. Therefore, if the inlet velocity is taken as the 'true'

average velocity, then traverse methods can be analysed based upon the CFD predictions. Two possible methods for computing the volumetric flow rate in the duct are the Equal Areas profile and the Log-Tchebycheff profile. The former simply involves splitting the duct area into 'equal areas' and taking a single measurement at the centre of each area (in this case, 64 measurement points were used). Using this method could underestimate the effects of the boundary layer, where the velocities are considerably lower. The aim of the Log-Tchebycheff profile is to consider the boundary effect by positioning the measuring points to give a relatively greater weight to the near-edge velocities. From the CFD data, points can be extracted corresponding to the required 49 measuring positions in order to emulate each profiling method. As mentioned previously, the Log-Tchebycheff profile will give a lower value for the mean velocity than the Equal Areas profile due to the consideration of edge effects.

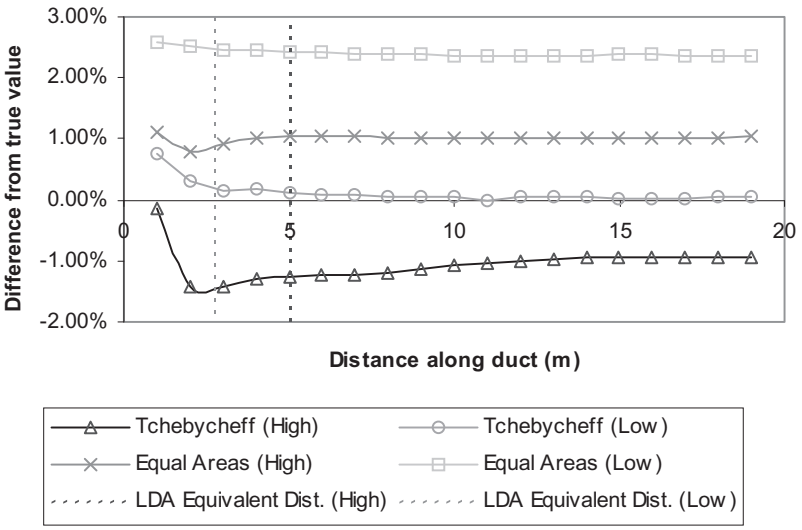

Figure 6: The disagreement between the average velocities, calculated by the Tchebycheff and equal areas methods, and the actual average velocity. Also shown is the distance along the CFD duct which is equivalent to the experimental LDA data.

The behaviour of the experimental LDA data can be compared with the CFD predictions to find the equivalent distance along the axis of the duct, as described above. At high speeds (when the 5 m CFD cross section corresponds to the LDA data), the Equal Areas profile is just over 1% higher than the true value (see Figure 6), however the Log-Tchebycheff profile gives a value that is -1.25% higher, implying that the Equal Areas profile is actually slightly more accurate in this case. However, at low speeds (when the CFD data at 2.75 m duct distance corresponds to LDA data) the Equal Areas profile gives a value that is 2.5% higher, whereas the Log-Tchebycheff profile gives a value that is just 0.16% higher, which is considered to be very close to the actual value. It seems that the

percentage error changes along the duct, approaching a constant value (see Figure 6). This figure also shows that the Tchebycheff method always estimates a lower value than the Equal Areas method. This is expected, see [5] and as described above.

5.3 Theoretical power law

As mentioned in Section 4.2, a power law can be used to approximate the velocity profile in the turbulent region of circular ducts. For the low speed simulation, the boundary layer extends to 25.16 mm from the wall (see Section 4.2). Therefore, the power law is only applicable outside this range. To find the value of n, in eqn (5), which provides the lowest normalised standard error, a quartic, polynomial curve was fitted to eleven data points between n = 9.2 and n = 10.2. The minimum of this curve occurred at n = 9.740 with a normalised standard error of 0.018. Table 1 shows the normalised standard error between the CFD data and the theoretical power law for varying values of 'n'.

Table 1: Normalised standard errors for high and low speeds at integer values of 'n' (where 'n' is the power denominator in eqn (5)).

Low Speed		High Speed	
n	Normalised Standard Error	n	Normalised Standard Error
8	0.029	5	0.057
9	0.020	6	0.021
10	0.018	7	0.043
11	0.023	8	0.072

For the high speed simulation, the boundary layer extends to 2.73 mm from the wall. The value of n that provides the lowest normalised standard error, the polynomial curve was fitted to eleven data points between n = 5.75 and n = 6.25. The minimum of the curve in this case occurred at n = 6.035, with a normalised standard error of 0.021 (see Table 1). Figure 7 shows the normalised data for both power laws compared with the corresponding CFD data. It can be seen that the power laws match the velocity profiles of the CFD data in the turbulent flow region.

Table 2: Flow properties for both flow speeds.

Air Speed	Reynolds Number	Best Fit Value of 'n'	Theoretical Average Tchebycheff Velocity
Low (0.620 m/s)	15840	9.740	0.635 m/s
High (5.761 m/s)	146100	6.035	5.627 m/s

The results found in the present investigation seem to be at odds with the results of Nikuradse as reported by De Chant [6]. Log-Tchebycheff point velocities in a circular duct can be generated using [1] and the above theoretical power-law profiles. At the low speed, the Tchebycheff average velocity is 2.4% higher than the actual value, whereas the Tchebycheff average velocity at the high speed case is 2.4% lower (see Table 2).

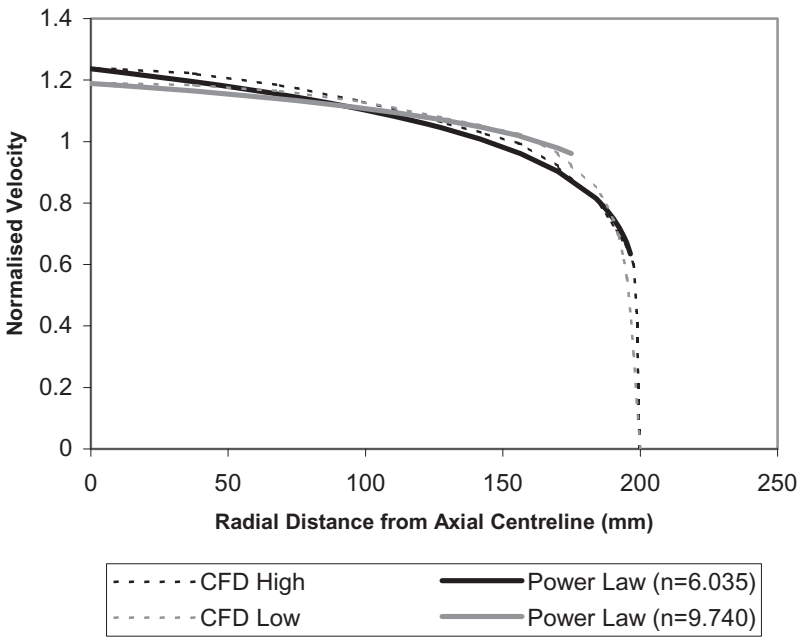

Figure 7: The radial CFD data in a circular duct at both high and low flow rates with overlaid best-fitted power laws.

6 Conclusions

An experimental study of the velocity profiles obtained in a square duct using an LDA device has provided velocity profiles for a range of air flow rates that are typical of those used within the building services industry. These results compared favourably with data obtained from a CFD model. Two methods were compared to compute the volumetric flow rate using the velocity profile data obtained from the LDA. It was shown that the Log-Tchebycheff method provided an improved estimate over the Equal Areas method using fewer measurement locations. This validates the Log-Tchebycheff method as an accurate and efficient solution for measurement profiles of ducts of the size investigated. Comparison of the circular duct CFD results with a velocity power law relationship revealed a contrast with the value of 1/7 normally used for prediction of velocity profiles in such cases. In this study, powers of

approximately 1/6 (low speed) and 1/10 (high speed) were found to be more appropriate. This has implications for the application of the 1/7 power law in the prediction of the velocity profiles in circular ducts. In addition, the use of the derived power laws to extract theoretical Log-Tchebycheff velocity values produces encouraging results (Section 5.3). Further work would help develop the methods for using the LDA, such as spacing and near-wall reflection and combination with CFD modelling, in order that greater confidence can be obtained in prediction of the flow data in air ducts of this kind. This study has shown that there is a definite correlation between the experimental, computational and theoretical data; the span at low speed is 0.015 m/s and at high speed is 0.134 m/s. Assuming the LDA measurement is the true value, this equates to a maximum disagreement of 2.4% above at low speed and 2.4% below at high speed. Deviations from the ideal in level of agreement could be attributed to the complex nature of turbulent flow, assumptions used in the computational modelling process and possible inadequacies in the experimental setup. However, this work does validate the use of CFD as a tool for predicting airflow within ducts of the sizes considered.

Acknowledgements

This work was part funded by the UK Government via the Technology Strategy Board under its Knowledge Transfer Partnership programme [KTP 7139]. BSRIA Instrument Solutions provided the laboratory facilities including the LDA.

References

[1] BS ISO 3966:2008, Measurement of fluid flow in closed conduits. Velocity area method using Pitot static tubes, 2008.
[2] Versteeg, H.K. & Malalasekera, W., *An Introduction to Computational Fluid Dynamics*, Pearson Education Limited, 2007.
[3] *FLUENT 12.0 User's Guide,* ANSYS, 2009.
[4] Benedict, R.P., *Fundamentals of Pipe Flow*, Wiley, 1980.
[5] ISO 5802:2009, *Industrial fans - Performance testing in situ,* 2009.
[6] De Chant, L.J., The venerable 1/7th power law turbulent velocity profile: a classical nonlinear boundary value problem solution and its relationship to stochastic processes, *Applied Mathematics and Computation*, **161**, pp. 463-474, 1985.
[7] Albrecht, H.-E., Borys, M., Damaschke, N. & Tropea, C., *Laser Doppler and Phase Measurement Techniques*, Springer-Verlag Berlin Heidelberg, 2003.
[8] Sherwin, K., Horsley, M., *Thermofluids*, Chapman & Hall, 1996.
[9] Rae, W.H., Jr., Pope, A., *Low-speed wind tunnel testing*, Wiley, 1999.
[10] LMNO Engineering, Research and Software Ltd. website, www.lmnoeng.com/index.shtml

This page intentionally left blank

Flow field assessment in a vertical axis wind turbine

R. Ricci, S. Montelpare, A. Secchiaroli & V. D'Alessandro
Dipartimento di Energetica, Università Politecnica delle Marche, Italy

Abstract

In this work, flow field features in a vertical axis Savonius wind rotor were investigated by means of a specially developed CFD method validated using wind tunnel testing data.

The Savonius rotor exhibits a strong variation of its angular velocity during the rotation. The solution of the second cardinal equation of dynamics is then needed to obtain a high-fidelity physical modelling of the device and an accurate performance prediction.

The proposed methodology is based on the integration between a commercial CFD code and custom MatLab routines. The former is used for the flow field computations, while the latter are used for the time integration of the second cardinal equation of dynamics. Unsteady RANS equations closed with the v2-f turbulence model were solved to consider the turbulent flow behaviour.

This procedure allows one to numerically evaluate the dimensionless parameters used in the performance characterization of wind turbines. Moreover, the flow field around the rotor can be evaluated, at every solved angular position (with respect to the incoming wind direction), taking into account the effect of the angular velocity variations of the rotor. An extended wind tunnel testing campaign was conducted on a rotor model in order to validate the computational procedure. A very good agreement between experimental and numerical data can be observed.

The main features of the flow field at different operating points of the rotor are presented in this paper. An evaluation of the characteristic of the wake behind the rotor obtained by means of a spectral analysis of the velocity magnitude signal is reported too.

Keywords: computational fluid-dynamics, Savonius wind rotor, wind energy.

WIT Transactions on Engineering Sciences, Vol 69, © 2010 WIT Press
www.witpress.com, ISSN 1743-3533 (on-line)
doi:10.2495/AFM100221

1 Introduction

Nowadays, vertical axis wind turbines are under the study of several research groups because they are very attractive for the integration of wind turbines in urban environments.

Two main types of vertical axis wind turbines exist: Darrieus rotor and Savonius rotor. In the first case, the lift force is responsible for the motion whereas in the second case the drag force is the main force which makes the turbine to spin.

In this study, a detailed numerical analysis of the flow field developing around a Savonius wind rotor is presented in order to gain insight into the basic mechanisms on which torque release is based.

Previous numerical studies about Savonius rotor aerodynamic performance are available in literature [5–10]. Numerical computations which take into account the rotor rotation following two different approaches: locating the rotor in a non-inertial frame or in an inertial one. In the first case, the solution obtained is strictly connected with the angle of attack of the rotor (angle between the cord of the rotor and the wind direction). Moreover, Coriolis force effect is completely neglected in Eddy-Viscosity Models (EVM) using the transport equation for TKE. This is directly related to the scalar nature of the TKE [3].

Locating the rotor in a inertial reference frame with constant angular velocity a not high-fidelity physical modelling is performed because the Savonius during its rotation exhibits a strong variation in angular velocity due to its torque release; for this reason in this work an approach based on an inertial frame with variable rotor angular velocity was used. RANS equations (closed using $\overline{\upsilon^2} - f$ turbulence model) were solved in order to obtain accurate information about the flow field. The rotor blades were treated as rigid bodies and their behaviour was modelled by means of the Second Cardinal Equation of Dynamics.

An extended wind tunnel testing program was also conducted at the Environmental Wind Tunnel of the Polytechnic University of Marche [4]. The experimental facilities allowed to evaluate rotor performance expressed by means of the dimensionless parameters usually used in the aerodynamics of wind turbines [1]. The experimental data were used to validate the developed computational methodology.

2 Mathematical model

The Savonius rotor analyzed in this work is a split-type as clearly shown in Fig. 1 and it has the characteristic angle of the helix fixed to zero. This allows one to build a computational 2D domain named Ω.

A crucial issue in the analysis of the flow field around the Savonius rotor is the treatment of the fluid-solid coupling and its modelling. In this work the structure (rotor) was treated as a rigid body while the fluid was modelled as incompressible and viscous.

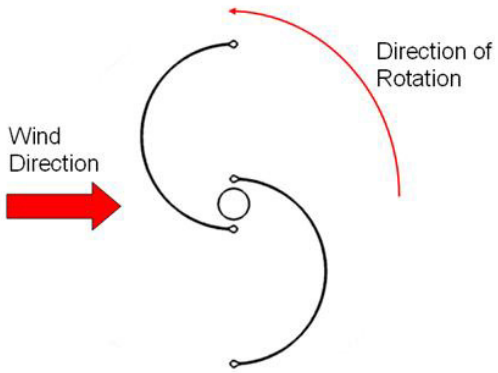

Figure 1: Savonius rotor analyzed in this work.

The fluid-structure coupling algorithm presented in this paper provides, for each time-step, the solution of the fluid-dynamic field (by means of the finite volume code FLUENT) and then evaluates the angular velocity of the rotating system. These analyses were performed by a numerical algorithm written in MatLab language. A flow chart of the algorithm is shown in Fig. 2.

The fluid flow induces the motion of the solid body by means of aerodynamic interactions. Only the rigid body kinematics was considered; hence the motion of the solid is evaluated integrating the second cardinal equation of dynamics for 1-DOF (Degree of Freedom) rotating system (1)

$$I\dot{\omega} = \sum_k M_{G,k}^{ext} \tag{1}$$

which is referred to the fixed rotation axis of the system. Torques acting on the rotor are the aerodynamic moment M_a and resistant torque M_r. The first is expressed per unit of rotor length by (2), in which n_k are the components of the outward normal unit vector while the second one can be expressed as a linear function of the angular velocity in order to reproduce the experimental conditions described in [4].

$$M_a^{'} = \int_{\partial\Omega_s} \varepsilon_{3ij}\left(x_i - x_{G,i}\right)\tau_{jk} n_k d\Gamma \tag{2}$$

with

$$\tau_{ij} = (\mu + \mu_T)\left(\partial_i u_j + \partial_j u_i\right) - p\delta_{ij} \tag{3}$$

$$M_r = a_k \omega \tag{4}$$

Second cardinal equations of dynamics can be written as:

$$I\dot{\omega} = LM_a^{'} - M_r \tag{5}$$

where L is the rotor height. The initial condition adopted in solving (5) is given by:

$$\omega(0) = \omega_0 \tag{6}$$

The rotor moment of inertia resulted from a CAD evaluation of the model geometry. ω_0 was assumed to be 16 rad/s in order to achieve a suitable time-step size in the first time-step solved for flow governing equations numerical solution.

The strategy used in this work in order to solve the fluid-structure interaction problem was a SMM (Sliding Mesh Model) approach. Hence, in Ω an inner sub-domain K is defined.

K represents a rotating frame around a fixed axis normal to the represented plane and passing for the point (x_G, y_G) with radium R_{mg} (red area represented in Fig. 2).

In other words, the computational grid is decomposed into two sub-grids, where the inner K domain is able to rigidly rotate with respect to the outer one.

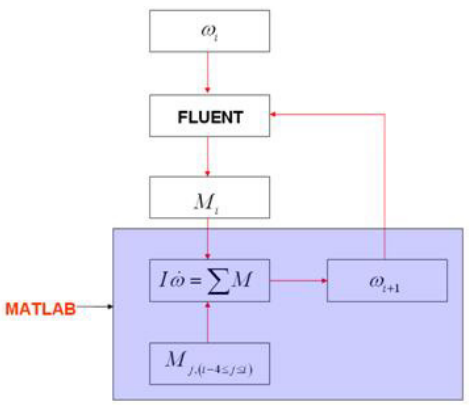

Figure 2: Flow chart of the computational methodology.

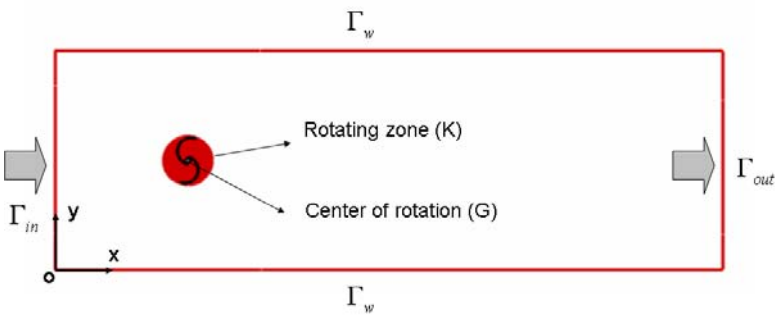

Figure 3: Sketch of the computational model.

The commonly used Fluid-Dynamics conservation laws (i.e. momentum, mass and turbulence quantities) must be suitably modified in order to take into account the grid motion. At this purpose a mesh motion flux term, related to mesh motion velocity $\mathbf{u_g}$, was introduced. Hence, the transport equation for a generic fluid flow variable ϕ becomes:

$$\int_{\Omega} \partial_t \left(\rho\phi\right) d\Omega + \oint_{\partial\Omega} \rho\left(\mathbf{u} - \mathbf{u}_{\mathbf{g}}\right)\phi \cdot \mathbf{n} d\Gamma - \oint_{\partial\Omega} \left(\Gamma \nabla\phi\right) \cdot \mathbf{n} d\Gamma + \int_{\Omega} s d\Omega = 0 \qquad (7)$$

the main problem due to the relative motion between the mesh elements of the K and {Ω\K} domains is related to the fluxes at the boundaries. The adopted solution procedure provides an appropriate choice of time-step size (8) obtained by fixing the number of nodes that slide in each time-step and knowing the distance between two consecutive nodes on the grids interface Δs, the angular velocity at the previous time-step solved $\omega^{(n-1)}$ and the radius of the rotating frame R_{mg}. In this way there are not overlapped cells at the sliding boundary and a conformal grid is assured in every time-step solved.

$$\Delta t^{(n)} = \frac{\Delta s \cdot N}{\omega^{(n-1)} \cdot R_{mg}} \qquad (8)$$

Moreover, regarding the meshing strategy, inside the K domain an unstructured triangular mesh having a curvilinear orthogonal refinement near the walls (Fig. 3) was adopted, in $\{\Omega_F \backslash K\}$ (the white area inside the rectangle) both curvilinear and orthogonal structured elements were used.

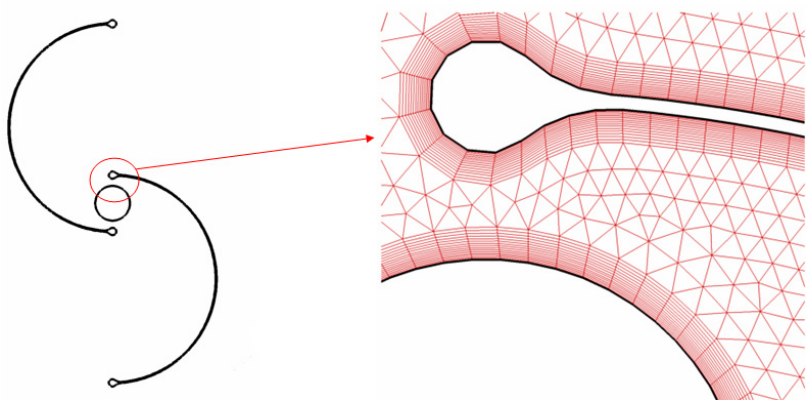

Figure 4: Meshing strategy used near the rotor blades.

RANS equations closed with $\overline{\upsilon^2} - f$ model must be, obviously, completed with a set of boundary conditions. The imposed boundary conditions are:

- a fixed inflow velocity at the inflow section (see Fig. 2) ;
- a zero normal pressure gradient at the inflow section;
- no-slip at the rotor blades (9);

$$\mathbf{u}(\mathbf{x}) = \omega \mathbf{e}_{\mathbf{k}} \wedge (\mathbf{x} - \mathbf{x}_{\mathbf{G}}) \quad \forall \mathbf{x} \in \partial\Omega_s \tag{9}$$

- Γ_w is treated as wall in order to reproduce the test chamber of the Environmental Wind Tunnel Laboratory of the Polytechnic University of Marche and to create a virtual wind tunnel.
- an outflow physical boundary condition was used at Γ_{out} [11].
- the turbulent intensity and the hydraulic diameter were fixed on Γ_{in} (the same values used in the experimental tests were reproduced).
- At Γ_{in}, Γ_w and on the rotor blades a zero normal gradient condition for the turbulent quantities was fixed
- For the fluid domain the following initial condition was set:

$$\mathbf{u}(\mathbf{x}, t = 0) = \mathbf{0} \quad \forall \mathbf{x} \in \Omega \setminus K \tag{10}$$

3 Numerical methods

RANS equations coupled with the turbulence model, were solved by means of a second order Finite Volume Method [13]. An extended dissertation about the numerical schemes used in the solution of the equations can be found in [2] and [3]. The fluid-structure coupling algorithm, presented in this paper, implies that the aerodynamic torque is known only from previous time-step. This requires an explicit scheme for the time-integration of the second cardinal equation of dynamics with a time-step size fixed for mesh conformity reasons, see (9). The code able to manage the fluid-structure interaction in this moment provides an explicit four stage Runge-Kutta method, a two point and a three point explicit Adams-Bashfort schemes. It was showed as an increasing in the scheme order produce a better agreement between and experimental data [3].

4 Results

Savonius wind rotor performance, obtained from numerical computations, was evaluated for every angular position occupied by the rotor using the parameters usually used in Aerodynamics of wind turbines [1]:

$$C_m = \frac{M}{\frac{1}{2}\rho u_\infty^2 A \cdot R} \tag{11}$$

$$C_P = \frac{P}{\frac{1}{2}\rho u_\infty^3 A} \tag{12}$$

$$\lambda = \frac{\omega R}{u_\infty} \tag{13}$$

where R is the rotor radius and A is the rotor frontal area. The rotor performance is evaluated averaging on the single rotor rotation (12) and (13).

$$\langle \lambda \rangle = \frac{1}{2\pi} \int_0^{2\pi} \lambda(\theta) d\theta \tag{14}$$

$$\langle C_P \rangle = \frac{1}{2\pi} \int_0^{2\pi} C_P(\theta) d\theta \tag{15}$$

The integrals (14) and (15) were calculated using a second order accurate method [3]. In Fig. 4 the effect of the average on the instantaneous tip speed ratio is shown. In Fig. 5 the mean power coefficient trend is reported.

The Savonius rotor mean performance, at the operating point, was evaluated averaging the parameters reported in Figs. 4 and 5 once the asymptotic behaviour was reached. The average was performed on the samples number corresponding to the steady condition. These data were used for numerical/experimental data comparison as reported in Fig. 6 and Fig. 7.

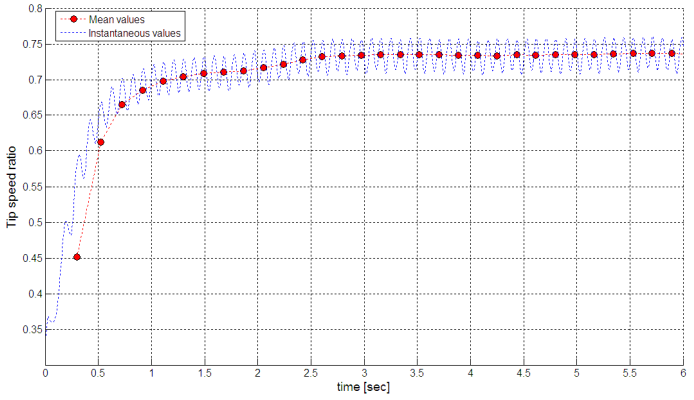

Figure 5: Instantaneous and averaged tip-speed ratio.

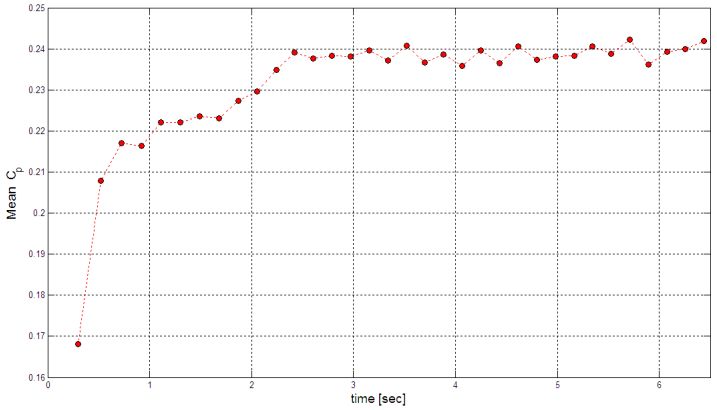

Figure 6: Mean power coefficient.

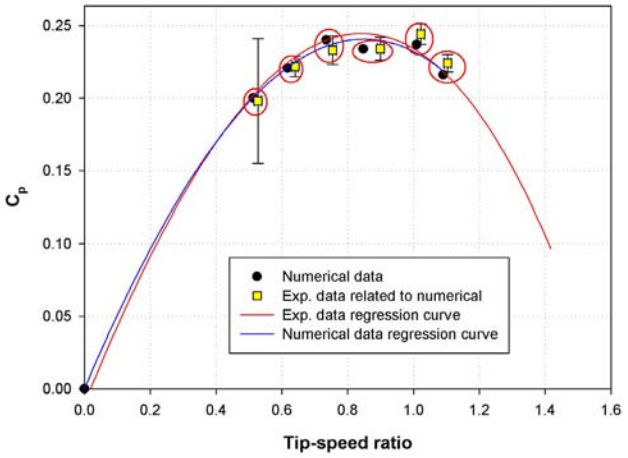

Figure 7: Comparison between numerical and experimental power.

Numerical and experimental data are reported in Fig. 6 and Fig. 7. Aerodynamic performance, obtained by the numerical simulations, shows a very good agreement with experimental data. This allows one to use the computational model for a fluid dynamic analysis of a Savonius wind rotor.

In all the simulations reported in this paper, the inflow wind velocity has been fixed to 9 m/sec and the turbulent intensity at the inflow section was fixed to 0.2% as in the experimental set-up.

In order to gain an insight into the main feature of the flow field developing around the Savonius rotor several contours were produced and reported in

Figs. 8, 9 and 10. Data related to the rotor with and AOA of about 45 degrees respect the incoming wind velocities were reported. TSRs reported are 0.735, 0.847 and 1.1.This angular position was identified as the position of the rotor maximum torque release [3].

An increasing of the stagnation region on the returning blade can be observed going beyond the unitary tip-speed ratio. The stagnation region on the pressure side of the advancing undergoes a shift near the blade tip with the increase of the TSR. On the suction side of the advancing blade, the increase of the TSR produces a larger size of the depression zone. This feature causes a more important contribution of the lift force on the rotor torque release. A separation bubble is located on the suction side of the advancing blade; its extension seems to be independent by the TSR. The wake zone behind the returning blade is clearly more affected by the TSR values. The increase of TSR produces the born of complex structures behind the returning blade.

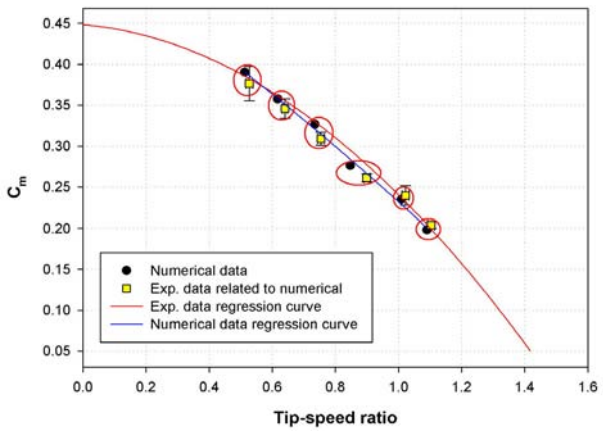

Figure 8: Comparison between numerical and experimental torque curve.

A crucial issue regarding the structural of design of this object is related to the vortex shedding frequencies. A PSD analysis of the absolute velocity magnitude signal was conducted on a grid of point reported in Fig 11. In the point located at (3D, -D) energy peak an in correspondence to the rotation frequency can be observed. This feature was found for point (3D, D) too. In this case the energy peak related to the blade passage frequency is less pronounced. Moreover, this frequency corresponds with the vortex shedding frequency.

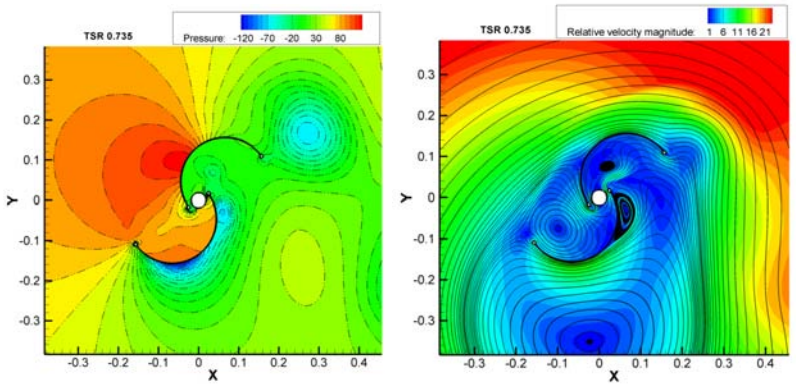

Figure 9: Contour of relative pressure and relative velocity magnitude. TSR = 0.735.

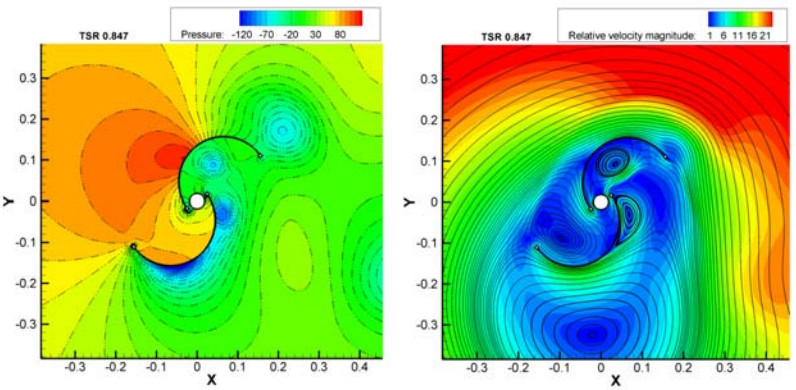

Figure 10: Contour of relative pressure and relative velocity magnitude. TSR = 0.847.

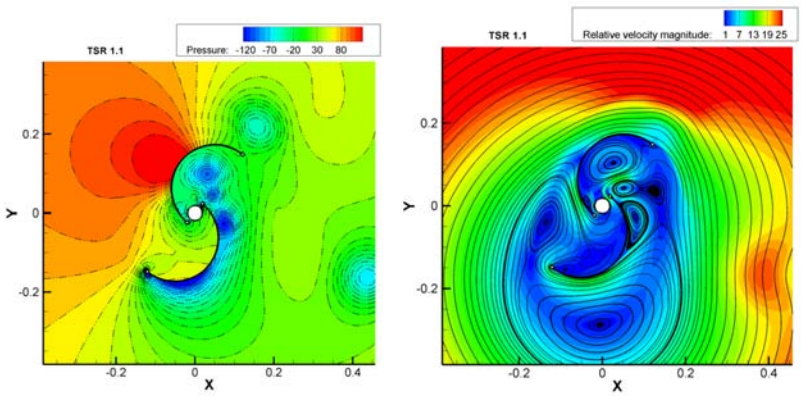

Figure 11: Contour of relative pressure and relative velocity magnitude. TSR = 1.1.

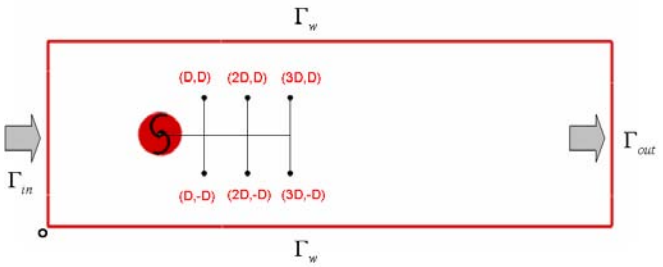

Figure 12: Layout of the points used for PSD calculation.

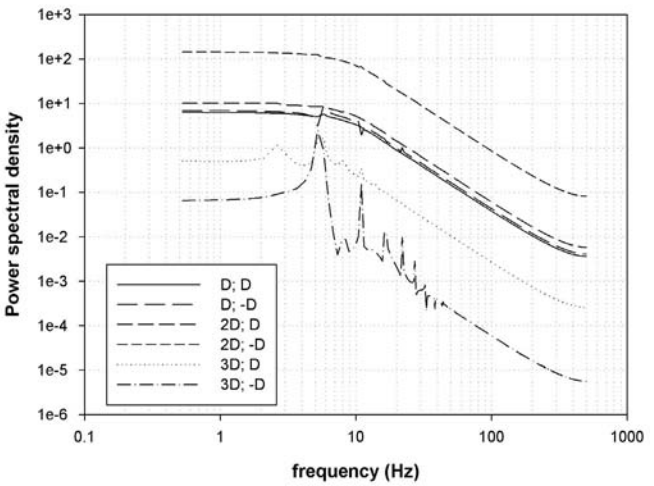

Figure 13: PSD data for the points showed in Fig. 11.

5 Conclusions

An efficient computational producer able to analyze the fluid-dynamic behaviour of vertical axis wind turbine was developed. For this purpose an integration between custom routines and a commercial code was performed in order to obtain a good physical model of the phenomenon. The case study presented is related to a Savonius wind rotor. The main features of the flow field developing around the rotor were outlined by means of pressure, relative velocity magnitude contours, relative velocity streamlines and PSD a velocity signal in the rotor wake.

References

[1] Hansen, M.O.L. Aerodynamics of Wind Turbines, 2nd edition, Earthscan – London, Sterling VA, 2008

[2] S. Montelpare, R. Ricci, V. D'Alessandro, G. Di Giovine. Aerodynamics of a Savonius wind rotor. 4th Symposium on Integrating CFD and Experiments in Aerodynamics, September 14-16, 2009, Ed. by P. Rambaud & Ph. Planquarat, ISSN 0377-8312, Von Karman Institute for Fluid Dynamics – Rhode-Saint-Genèse, Belgium
[3] V. D'Alessandro, S. Montelpare, R. Ricci, A. Secchiaroli. Unsteady Aerodynamics of a Savonius wind rotor: a new computational approach for the simulation of energy performance. *Energy, ISSN 0360-5442,* (*Accepted*. DOI: 10.1016/j.energy.2010.04.021).
[4] R. Ricci, S. Montelpare, G. Borrelli, V. D'Alessandro. Experimental analysis of a Savonius wind rotor for street lighting systems. ASME-ATI-UIT Conference on Thermal and Environmental Issues in Energy Systems, May 16-19, 2010, Sorrento, Italy.
[5] Fujisawa, N. Velocity measurements and numerical calculations of flow fields in and around Savonius rotors. J. of Wind Eng. and Ind. Aerod., **59**, pp. 39-50, 1996.
[6] Fernando, M.S.U.K., Modi, V.J. A numerical analysis of the unsteady flow past a Savonius wind turbine. J. of Wind Eng. and Ind. Aerod. , **32**, Issue 3, pp. 303-327.
[7] Shinohara, T., Ishimatsu, K. Simulation of flow around rotating Savonius rotors. Proc. of the 6th National Symposium on Computational Fluid Dynamics, 691-694 (SEE N94-34731 10-34).
[8] Redchyts, D., Prykhodko, O. Numerical modelling of dynamics and aerodynamics processes of Darrieus and Savonius rotors. Geophysical Research Abstract, 8, 03083, 2006.
[9] Altan, B.D., Atilgan, M. An experimental and numerical study on the improvement of the performance of Savonius wind rotor. En. Conv. and Man., **49**, pp., 3425-3432, 2008.
[10] Gupta, R., CFD analysis of a two-bucket Savonius rotor using Fluent package. EWEC 2009, Marseille.
[11] FLUENT users' guide release 6.3.26, Ansys Inc., USA, 2006.
[12] Durbin, P., Near-wall turbulence closure modelling without damping functions. Theoretical and Computational Fluid Dynamics, **3**, pp. 1-13, 1991.
[13] Jasak, H., Error analysis and estimation of the finite volume method with applications to fluid flows. PhD thesis – Imperial College of Science, Technology and Medicine, London, UK, 1996.
[14] H.K. Versteeg, W. Malalasekera. An Introduction to Computational Fluid Dynamics, The Finite Volume Method. Longman Scientific & Technical, 1995.

Characteristics of boundary layer flow induced by a solitary wave

C. Lin[1], S. C. Hsieh[1], S. M. Yu[1] & R. V. Raikar[2]
[1]*Department of Civil Engineering, National Chung Hsing University, Taiwan*
[2]*Department of Civil Engineering, K. L. E. S. College of Engineering and Technology, India*

Abstract

The experimental results on the characteristics of bottom boundary layer flow induced by a solitary wave, obtained using high speed particle image velocimetry (HSPIV) and particle trajectory techniques, are presented in the paper. The particle trajectory technique is particularly used near the bottom boundary to visualize the flow field. The velocity distribution in the bottom boundary layer is classified into two types from the point of view of similarity analysis: one pre-passing and another post-passing of the crest of solitary wave across the measuring section. The velocity distribution in the bottom boundary layer before the passing of solitary wave-crest was regressed using two hyperbolic tangent functions. The free stream velocity u_∞ and the boundary layer thickness δ are found to be the suitable characteristic velocity and length scales to obtain the similarity profile. However, other characteristic properties of the boundary layer such as displacement thickness, momentum thickness and energy thickness were also used in the analysis, but they are proved to be mere multiples of boundary layer thickness δ. On the other hand, to attain the similarity profile for the velocity distribution for post-passing of the crest of solitary wave, the characteristic velocity scale ($u_\infty - U_m$), where U_m is the maximum negative velocity, and length scale: maximum thickness of reverse flow b_0 is used.

Keywords: bottom boundary flow, solitary waves, flow visualization, high speed particle image velocimeter, similarity profile.

WIT Transactions on Engineering Sciences, Vol 69, © 2010 WIT Press
www.witpress.com, ISSN 1743-3533 (on-line)
doi:10.2495/AFM100231

1 Introduction

Solitary waves as first observed by Russell [1] can travel over large distances and exhibit the property of stable state of motion. They propagate steadily without either steepening their wave height or widening their wave length but maintaining constant wave length and relative wave height. In addition, they also do not loose their energy so much and structure as well. These solitary waves to some extent resemble to a tsunami because of shallow water depth, before they undergo changes near the shores. Therefore, the solitary waves are often studied due to their simple and permanent wave form and also the study of solitary waves (or combinations of negative and positive solitary-like waves) help in simulating the run-up and shoreward inundation. Keulegan [2] was the pioneer to present the effects of viscous damping on solitary waves. Later, Mei [3] used perturbation method to obtain the similar results. However, the study of Keulegan [2] and Mei [3] mainly concentrate on the estimation of damping rate. Recently, Liu and Orfila [4] obtained analytical solutions for viscous boundary layer flows under transient long waves, including the damping rates for the solitary waves. Further, the perturbation analysis of Liu and Orfila [4] for linear boundary layer solution was extended by Liu *et al.* [5] for fully nonlinear boundary layer condition.

The objective of the present study is to emphasize mainly on the measurement of flow structure within the bottom boundary layer induced by a solitary wave using HSPIV and particle trajectory techniques. The particle trajectory technique is particularly used to enhance the flow field near the bottom boundary layer.

2 Experimentation

2.1 Experimental setup and conditions

A glass-walled and glass-bottomed wave flume 14 m long, 0.25 m wide and 0.5 m deep located at the Hydraulics Laboratory of the Department of Civil Engineering, National Chung Hsing University, Taiwan was used to conduct the experiments. The wave flume was fitted with a piston-type wave maker at one of its end, which was driven by a servo motor; while at the other end the wave dissipater was fixed to dampen the waves. An electromagnetic clutch installed inside the wave maker allowed a rapid start and stop of the wave paddle thereby facilitating the generation of the desired solitary waves. The servo motor used to trigger the wave paddle made it possible to generate an individual solitary wave without followed by any dispersive tail wave train. The validation of generated solitary waves is discussed later. However, the generated solitary waves, being highly repeatable, were clean enough with certain combinations of wave height and water depth.

The measuring section was located at 8 m from the wave board and two fields of view (FOV) were used for the flow visualization. FOV A located near the boundary area has the size of 2 cm × 1 cm with 1 cm of its width on either side of the measuring section and FOV B with its effective size 12 cm × 12 cm

covering the potential area. Fig. 1 shows the schematic view of the wave flume with location of measuring section, two FOV's and the coordinate system used in the study. The origin of the coordinate system is located at the bottom center of the FOV A with X measured along the flume bed in the direction of the wave motion and Y normal to the flume bed. The time $t = 0$ indicated the moment when the crest of the solitary wave reaches the position $X = 0$. In all 7 experimental runs were taken with the wave height H in the range between 1.1 cm to 3 cm, water depth h between 7 cm to 10 cm so that the relative wave height ratio H/h is between 0.11 to 0.414. Table 1 furnishes the details of all experimental runs. In the present study, the maximum Reynolds number defined by $(R_e)_{max} = Uh/\nu$ is about 18,750, where U is the maximum free stream velocity at the edge of bottom boundary layer [i.e., $(u_\infty)_{max}$], and ν is the kinematic viscosity.

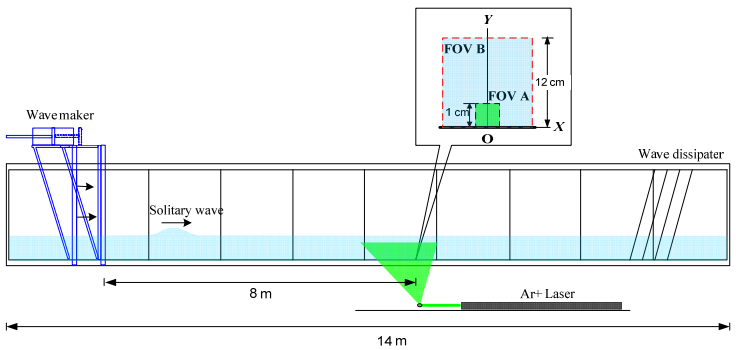

Figure 1: Schematic view of wave flume showing location of measuring section, FOV's and coordinate system.

Table 1: Details of experimental conditions.

Case	Wave height H (cm)	Water depth h (cm)	$\frac{H}{h}$	Measured wave celerity c (cm/s)
A	1.1	10	0.110	108.42
B	1.1	7	0.157	92.79
C	1.4	7	0.200	93.44
D	2.0	8	0.250	100.44
E	1.9	7	0.271	92.48
F	3.0	8	0.375	102.28
G	2.9	7	0.414	96.14

2.2 Velocity measurement

HSPIV system used to measure the velocity field. The laser light sheet spread for the flow visualization is made use of in HSPIV. The image recording system was a 10 bit Complementary Metal-Oxide (CMO) high speed camera (Phantom V5.1) having resolution of 1024 × 1024 pixel and 1200 Hz maximum framing rate (aperture opening rate of 10 – 47000 μs). Velocity fields were determined by cross-correlation analysis using commercial software (TSI Insight). The interrogation windows of 32 × 32 pixels with 50% overlap were used in the cross-correlation analysis. In parallel to HSPIV system, a fiber laser Doppler velocimeter (FLDV) was also used to verify the velocity field measured by HSPIV system.

2.3 Validation of solitary wave generation

The wavemaker was fitted with high precision servo motor system, which could generate a perfect solitary wave nearly without any dispersive tail wave train. The generated solitary waves in this study followed the procedure described by Goring [6]. Initially, the validation of the solitary wave generation by the wavemaker system was carried out for the experimental case D having wave height H = 2.0 cm and water depth h = 8 cm. Along with the comparison of free surface elevation, the associated wave celerity was also assessed. Fig. 2(a) presents the comparison of free surface profile between the generated solitary wave and theoretical wave form of

$$\eta(X,t) = H \sec h^2\left[\sqrt{\frac{3H}{4h^3}}(X - ct)\right] \tag{1}$$

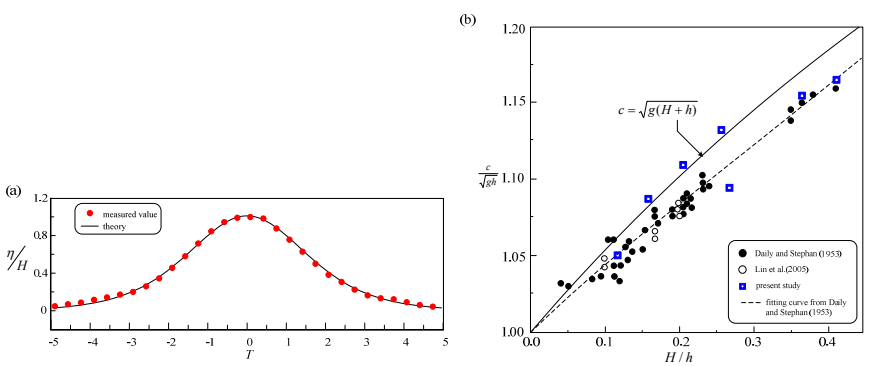

Figure 2: Validation of target solitary wave for experimental case D: (a) comparison of free surface profile; (b) comparison of wave celerity.

where c = wave celerity, can be obtained as $\sqrt{g(H+h)}$. It is interesting to observe a good conformity of the generated wave with the theoretical one. Fig. 2(b) shows the comparison of the wave celerity. There is a satisfactory agreement between the generated waves and the data of Daily and Stephan [7] and Lin *et al.* [8], both exhibiting slightly lower celerity than the theoretical.

3 Result and discussions

The images obtained by particle trajectory technique using the high speed digital camera in the boundary area of size 2 cm × 1 cm (FOV A) with 1 cm width on either side of the measuring section for the non-dimensional time $-3.0 \le T \le 4.0$ are captured. The bottom boundary layer can be distinctly visualized in these images. It is supported by the corresponding phase-averaged velocity field depicted in Fig. 3 for $T = -3.0 \sim 4.0$. The velocity field looks similar to the free stream velocity up to $T < 1.00$; however, for $T \ge 2.00$ it is interesting to observe the reversal of flow velocity. The velocity distribution after $T \ge 2.00$ resembles that of velocity profile due to wall jet. This indicates the development of negative or adverse pressure gradient after passing of the solitary wave at the measuring section ($T = 0$), particularly after $T \ge 1.00$. The exact non-dimensional time T, when the flow reversal occurs and adverse pressure gradient develops at the measuring section can be viewed by Fig. 4, which illustrates the velocity field in potential area at the measuring section for $-5.0 \le T \le 5.0$ for experimental case D. From Fig. 4, the occurrence of flow reversal can be found to be at $T = 1.60$ at location very close to the boundary. However, the zone of flow reversal increases with the passage of solitary wave (for $T \ge 1.60$) as seen from Fig. 4. The vertical position of center of flow reversal near the boundary is found to be within $Y/h < 0.025$. Fig. 4 also depicts another horizontal scale $5.0 \ge X/h \ge -5.0$ corresponding to the same velocity field. However, the values of X/h are obtained by parametric transformation using the theoretical wave form (Eq. (1)). Using this X/h scale, it could be seen that the position where the flow reversal occurs is at $X/h = -2.00$.

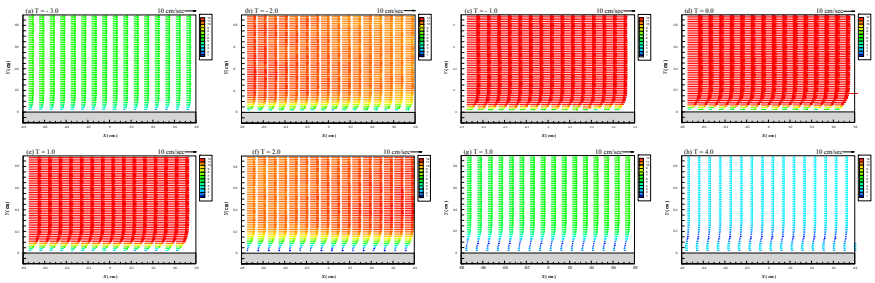

Figure 3: HSPIV velocity vectors measured near and in the boundary area for case D at non-dimensional time T: (a) –3.0; (b) –2.0; (c) –1.0; (d) 0.0; (e) 1.0; (f) 2.0; (g) 3.0; (h) 4.0.

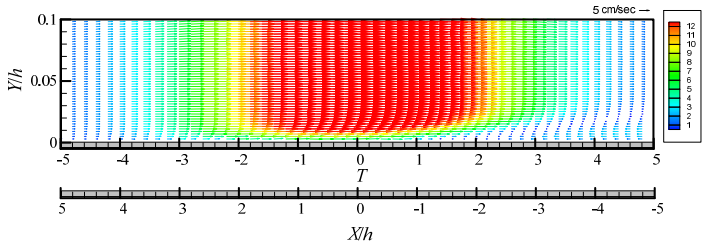

Figure 4: Velocity field obtained at measuring section near and in the boundary area for case D at $-5.0 \le T \le 5.0$.

By obtaining the non-dimensional time T and position X/h of occurrence of adverse pressure gradient (flow reversal) for different experimental cases, their variation is plotted as shown in Fig. 5. Fig. 5(a) presents the variation of non-dimensional time T of occurrence of adverse pressure gradient with the relative height H/h. It shows a linear relationship between non-dimensional time T and relative height H/h, depicting the decrease in T with increase in relative height H/h following Eq. (2). On the other hand, the variation between the position X/h of occurrence of adverse pressure gradient with relative height H/h is plotted in Fig. 5(b). Fig. 5(b) indicates the increase in X/h with increase in relative height H/h following Eq. (3).

$$T = -1.794\left(\frac{H}{h}\right) + 2.315 \tag{2}$$

$$\frac{X}{h} = 2.366\left(\frac{H}{h}\right) - 2.717 \tag{3}$$

The distribution of horizontal velocity u measured by HSPIV at the measuring section for the experimental case D with non-dimensional $-5.0 \le T \le 5.0$ at every $T = 0.5$ are presented in Fig. 6. The movement of solitary wave at the measuring section is illustrated in Fig. 6(a) showing various T (= 0.5) at points numbered 1 to 21. The horizontal velocity profiles for pre-passing of the solitary wave ($-5.0 \le T \le 0.0$) at the measuring section are shown in Fig. 6(b) as indicated by number 1 – 11 and for post-passing of the solitary wave ($0.0 \le T \le 5.0$) in Fig. 6(c) with number 11 – 21. It is interesting to observe that the horizontal velocity profiles follow certain specific trends for each of the case of pre-passing and post-passing of solitary wave. Hence, they are grouped into two classes, which would help in attaining the similarity profiles.

From horizontal velocity profiles shown in Fig. 6(b) before passing of the solitary wave ($T \le 0.0$) at the measuring section, it can be seen that they follow a particular trend of increasing horizontal velocity u and then reaching a uniform distribution representing the free stream velocity after certain value of Y. The

position Y corresponding to the location of free stream velocity $u = u_\infty$ depends on T. However, the distance Y increases with increase in T approximately from Y = 0.1 cm (at T = -5.00) to 0.25 cm (at T = 0). The corresponding value of free stream velocity are u_∞ = 1.2 cm/s at T = -5.00 to u_∞ = 20 cm/s at T = 0. That is the free stream velocity u_∞ increases with the approach of solitary wave towards the test section and reaches its maximum value $(u_\infty)_{max}$. This can be evidenced from Fig. 6(b) in which the free stream velocity at non-dimensional time T, $u_\infty(T)$ increases as T increases from -5.0 to 0.0.

The profiles of horizontal velocity u after passing of the solitary wave ($T \geq$ 0.0) are shown in Fig. 6(c). After passing of the solitary wave ($T \geq 0.0$), the profiles of horizontal velocity u continue to exhibit the same trend as those of pre-passing of solitary wave ($T \leq 0.0$). However, the free stream velocity u_∞ starts decreasing with increase in T (0.0 ~ 2.0). After $T \geq 2.0$, the profiles of horizontal velocity u depict the flow reversal within the zone close to the boundary. In this zone, the horizontal velocity u increases in the negative direction reaching its maximum negative value U_m and then decreases to become positive and increases towards the top to reach free stream velocity u_∞. It is pertinent to mention that the free stream velocity at non-dimensional time T, $u_\infty(T)$ continues to decrease with T and reaches its minimum value $(u_\infty)_{min}$. The characteristic nature of the velocity distribution is similar to that of the case of wall jet. The thickness of this zone where the velocity reversal occurs, the location of maximum negative value U_m from the boundary and the magnitude of U_m depend on the non-dimensional time T.

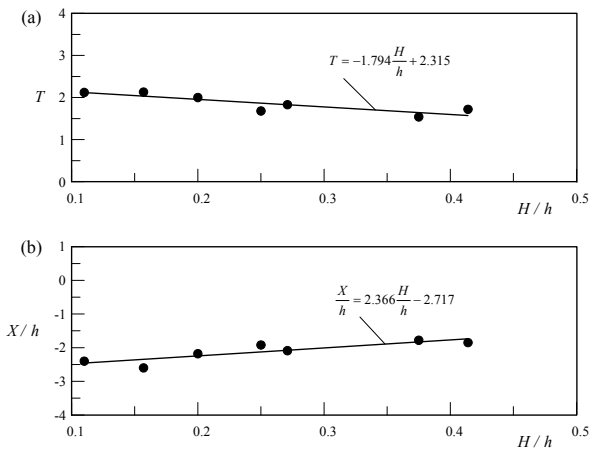

Figure 5: (a) Dependency of non-dimensional time T of occurrence of adverse pressure gradient on the relative height H/h; (b) dependency of non-dimensional position X/h of adverse pressure gradient on the relative height H/h.

The nonlinear regression analysis was performed for the measured velocity profiles to obtain the equation for the horizontal velocity u distributions. The distribution of the horizontal velocity u in the boundary layer was classified into two types as mentioned in the previous section: one for the pre-passing of the solitary wave ($T \leq 0.0$) and another for post-passing of the solitary wave ($T \geq 0.0$) at the section.

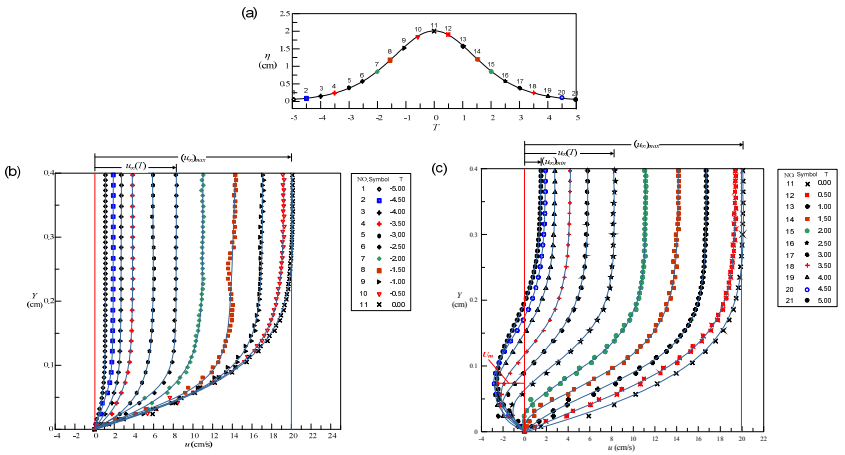

Figure 6: (a) Solitary wave showing the measuring instants of horizontal velocity; (b) horizontal velocity u profiles at measuring section for pre-passing of solitary wave ($T \leq 0.0$); (c) horizontal velocity u profiles at measuring section for post-passing of solitary wave ($T \geq 0.0$), for case D.

By observing the velocity profiles shown in Fig. 6(b), the characteristic nature of velocity profile is sketched as illustrated in Fig. 7(a). The horizontal velocity u increases in the boundary layer and reaches free stream velocity u_∞ at the end of boundary layer. To obtain the velocity distribution for the horizontal velocity u for the pre-passing of the solitary wave ($T \leq 0.0$), three types of nonlinear regression equations having two hyperbolic tangent functions (Eq. (4)) were attempted.

$$u(Y) = C_1 \times \left[\tanh\left(C_2 Y + C_3\right) - \tanh(C_3)\right] \tag{4a}$$

$$u(Y) = C_4 \times \tanh\left(C_5 Y^2 + C_6\right) - \tanh(C_7 Y^2 + C_8) \tag{4b}$$

$$u(Y) = C_9 \times \tanh\left(C_{10} Y + C_{11}\right) \times \tanh\left(C_{12} Y + C_{13}\right) + C_{14} \tag{4c}$$

where C_1 to C_{14} are constants. Amongst these three equations, Eq. (4c) is found to be the most appropriate one to fit all the measured velocity profiles before

passing of the solitary wave ($T \leq 0.0$). Hence, Eq. (4c) is considered as the suitable velocity distribution for the horizontal velocity u for pre-passing of the solitary wave having R^2 value of fitting as 0.993. Fig. 6 (b) also demonstrates the satisfactory fitting of the velocity profiles obtained by Eq. (4c) to the experimental data.

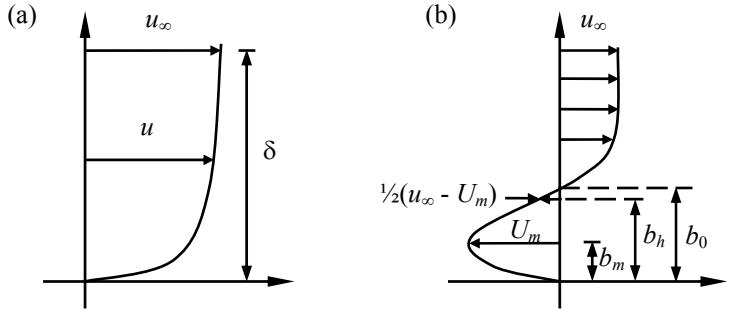

Figure 7: Schematic diagram illustrating characteristic profiles of horizontal velocity: (a) for pre-passing of solitary wave ($T \leq 0.0$); (b) for post-passing of solitary wave ($T \geq 0.0$).

On the other hand, for post-passing of solitary wave ($T \geq 0.0$) at the section, the velocity profiles gradually change their trend as a result of flow reversal that occurs near the boundary for T exceeding nearly 1.60 (depends on the experimental case). From Fig. 6(c) for experimental case D, it can be evidenced that the horizontal velocity profile at $T = 2.00$ shows the distinct reversal of flow. After $T \geq 2.00$, all profiles follow the same trend. However, as T increases the maximum negative value U_m increases, while the free stream velocity at non-dimensional time T, $u_\infty(T)$ decreases. The value of U_m reaches its maximum value corresponding to non-dimensional time $T = 5.00$ and correspondingly, the free stream velocity reaches its minimum value $(u_\infty)_{min}$. The details are illustrated in Fig. 6(c). Following this nature of velocity profile, the definition sketch illustrating the characteristic of the horizontal velocity after passing of solitary wave at the test section is drawn as shown in Fig. 7(b). In Fig. 7(b), b_m represents the height of the maximum negative velocity, b_h represents half-velocity-deficit [where $u = (u_\infty - U_m)/2$] and b_0 represents maximum thickness of reverse flow. To match this specific nature of horizontal velocity, the nonlinear equation consisting of a hyperbolic tangent function and a cosine function of the form Eq. (5) is selected to attain the velocity distribution. It is very interesting to mention that it fits very well for the horizontal velocity u profiles after passing of the solitary wave with its R^2 value 0.95.

$$u(Y) = C_{15} \times \left[\tanh\left(C_{16}Y + C_{17}\right) - C_{15}\right] \times \cos\left(C_{18}Y + C_{19}\right) + C_{20} \qquad (5)$$

where C_{15} to C_{20} are constants. The fitting of the velocity profiles to the experimental data are represented in Fig. 6(c). By observing the similar trend of

velocity profiles before passing of the solitary wave ($T \leq 0.0$) at the section presented in Fig. 6(b), the fitting of the similarity profile for the horizontal velocity u distribution was thought of. To decide on the length scale for obtaining the similarity profile, four length scales corresponding to boundary layer theory, such as boundary layer thickness δ, displacement thickness δ_*, momentum thickness θ and energy thickness δ_e were considered. On the other hand, the free stream velocity u_∞ at the edge of bottom boundary layer is used as characteristic velocity. Fig. 8 show the similarity profile for the horizontal velocity u considering boundary layer thickness δ. The corresponding regression equation is expressed as in Eq. (6).

$$\frac{u}{u_\infty} = 1 - \exp\left[-4.29\left(\frac{Y}{\delta}\right)\right] \tag{6}$$

By observing the similarity profile and considering various conditions, the authors found that the boundary layer thickness δ and the free stream velocity u_∞ are the appropriate characteristic length and velocity scales for defining the similarity profile for the horizontal velocity u before passing of the solitary wave ($T \leq 0.0$) at the section.

Similarly, to obtain the similarity profile for the horizontal velocity u after passing of the solitary wave ($T \geq 0.0$), three length scales such as height of the maximum negative velocity b_m, half-velocity-defect b_h and maximum thickness of reverse flow b_0 were considered. Along with these, the velocity defect ($u_\infty - U_m$) is used as the velocity scale. However, it is important to mention that the velocity profiles those depict the flow reversal were considered in obtaining the similarity profile. Out of the three length scales attempted, the maximum thickness of reverse flow b_0 was found to give good result with the respective R^2 value being 0.998. The similarity profile is defined by Eq. (7).

$$\frac{u - U_m}{u_\infty - U_m} = \left[-1.78 \times \tanh\left(1.33\frac{Y}{b_0} - 0.35\right) + 1.78\right] \times \cos\left(-1.40\frac{Y}{b_0} - 1.77\right) + 1.00 \tag{7}$$

Fig. 9 presents the similarity profile for the horizontal velocity u for post-passing of the solitary wave ($T \geq 0.0$) with respective length scale as maximum thickness of reverse flow b_0 and ($u_\infty - U_m$) as the velocity scale. Both the similarity profiles shown depict the promising self-preservation, except slight variation in R^2 value. However, as the horizontal velocity profiles are comparable with those of the case of a wall jet, the flow phenomenon within boundary layer after passing of the solitary wave (with velocity profiles depicting the flow reversal) could be related to wall jets. With this point of view, the maximum thickness of reverse flow b_0 is considered as the most suitable

length scale. Hence, Eq. (7) is considered as the ideal similarity profile for post-passing of solitary wave ($T \geq 0.0$) with the velocity defect ($u_\infty - U_m$) and the thickness of maximum reverse flow b_0 as the characteristic velocity and length scales.

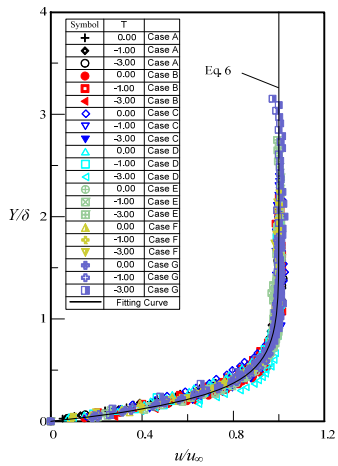

Figure 8: Similarity profile for horizontal velocity u for pre-passing of solitary wave ($T \leq 0.0$) with the length scale using boundary layer thickness δ.

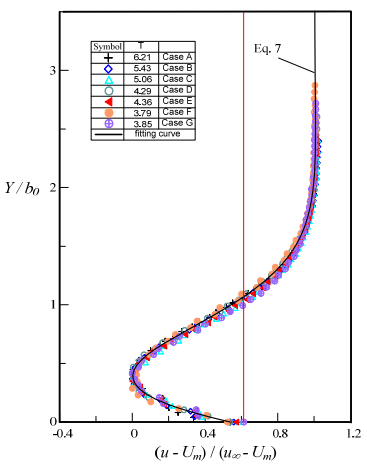

Figure 9: Similarity profile for horizontal velocity u for post-passing of solitary wave ($T \geq 0.0$) with length scale using maximum thickness of reverse flow b_0.

4 Conclusions

The characteristics of bottom boundary layer flow induced by a solitary wave are investigated using high speed particle image velocimetry (HSPIV) and particle trajectory techniques. The important results are summarized as follows:

1. Based on the nature of horizontal velocity profiles in the bottom boundary layer, the velocity distribution is classified into two types: one for pre-passing and another for post-passing of the crest of solitary wave across the measuring section.
2. Two hyperbolic tangent functions were used in nonlinear regression analysis to fit the anticipated velocity distribution to the measured horizontal velocity profiles in the bottom boundary layer before passing the crest of solitary wave. Further, to obtain the similarity profile for the velocity distribution, various characteristics properties of the boundary layer such as boundary layer thickness, displacement thickness, momentum thickness and energy thickness were considered as length scales in the analysis along with the free stream velocity u_∞ as velocity scale. However, the boundary layer thickness δ and the free stream velocity u_∞ are found to be the appropriate characteristic length and velocity scales to obtain the similarity profile. Other length scales (displacement thickness, momentum thickness and energy thickness) proved to be simple multiple of boundary layer thickness.
3. On the other hand, for post-passing of the crest of solitary wave, the velocity profile is fitted using both hyperbolic tangent and cosine functions in the nonlinear regression analysis. In addition, the height of maximum negative velocity b_m, maximum thickness of reverse flow b_0 and half-velocity-defect b_h were considered as length scales along with velocity deficit ($u_\infty - U_m$) as the velocity scale, in attaining the similarity profile. Amongst the three length scales, the maximum thickness reverse flow b_0 and half-velocity-deficit b_h are found to be suitable. Considering the flow phenomena after passing of the solitary wave following the trend of wall jets, the maximum reverse flow layer thickness b_0 is considered as the appropriate length scale. Hence, the similarity profile is obtained using b_0 and ($u_\infty - U_m$) as the characteristic length and velocity scales.

Acknowledgement

The writers gratefully acknowledge the support of this work by National Science Council, Taiwan, under Grant Nos. NSC 96-2221-E-005-078-MY3 and NSC 99-2811-E-005-003.

References

[1] Russell, J. S. "Report of the committee on waves", *Rep. 7th Meet.* Brit. Assoc. Adv. Sci., Liverpool, John Murray, London, 417-496, 1838.

[2] Keulegan, G. H., Gradual damping of solitary wave. *Journal of Research,* National Bureau of Standards, 40, pp. 607-614, 1948.
[3] Mei, C. C., *The applied dynamics of ocean surface waves*. John Wiley and Sons, 1983.
[4] Liu, P. L. F., and Orfila, A., Viscous effects on transient long waves. *Journal of Fluid Mechanics,* 520, pp. 83-92, 2004.
[5] Liu, P. L. -F., Park, Y. S., and Cowen, E. A., Boundary layer flow and bed shear stress under a solitary wave. *Journal of Fluid Mechanics,* 574, pp.449-463, 2007.
[6] Goring, D. G., *Tsunamis – The propagation of long waves onto a shelf*. Rep. No. KH-R-38, California Institute of Technology, Pasadena, California, 1978.
[7] Daily, J. W., & Stephan, S. C., Characteristics of solitary wave. *Transactions ASCE*, 118, pp. 575- 587, 1953.
[8] Lin, C., Ho, T. C., Chang, S. C., Hsieh, S. C., and Chang, K. A.,Vortex shedding induced by a solitary wave propagating over a submerged vertical plate. *International Journal of Heat and Fluid Flow*, 26, pp. 894-904, 2005.

This page intentionally left blank

Section 3
Hydrodynamics

This page intentionally left blank

Peculiarities of hydrodynamics in the evaporation of hydrocarbon droplets

G. Miliauskas, S. Sinkunas, J. Talubinskas & K. Sinkunas
Department of Thermal and Nuclear Energy,
Kaunas University of Technology, Lithuania

Abstract

Combustion of liquid fuel generally is going on in the sprayed form. The combustion effectiveness is influenced by the evaporation rate of droplets, which determine heat and mass transfer intensity between droplets and the gas and peculiarities of combined heat spread in warming semitransparent droplets. Modeling of complex heat transfer raises the assessment problem of the potential liquid instability within droplets. Free liquid circulation in warming liquid droplets can occur under the influence of Archimedes forces and forced circulation inside them can be forced by sliding gas friction forces acting on the droplet surface. Under the influence of these forces, droplets liquid starts to flow on its surface and emerged vortices pass into the interior layers of the droplets. Hydrodynamic regime of the liquid droplets determines the solution methodology of the inner "droplet" problem. A combined analytical and numerical method of investigation is applied. A system of parabolic type second order integral-differential equations describing complex heat transfer in the droplet by conduction and radiation is transformed into an infinite series of integral equations. Securing balance of energy fluxes in the droplet with confidence of one hundredth of percent and using the fastest sinking the droplet surface temperature is selected. The change of thermal state and phase transformation intensity of warming hydrocarbons droplets heated in air is modeled under different boundary conditions of heat and mass transfer. The influence of forced liquid circulation on the droplet thermal state evaluated using effective heat conduction coefficient. Free liquid circulation in the droplets is evaluated by Rayleigh number.

Keywords: hydrocarbon droplets, combined heat and mass transfer, heating and evaporation of droplets, hydrodynamics.

WIT Transactions on Engineering Sciences, Vol 69, © 2010 WIT Press
www.witpress.com, ISSN 1743-3533 (on-line)
doi:10.2495/AFM100241

1 Introduction

Liquid fuel is generally combusted in the sprayed form. Its combustion efficiency determines droplet evaporation speed. Heat and mass transfer processes non-stationarity and their interactions are important factors in the sprinkle liquid fuel heating and evaporation process. High-temperature two-phase flow multiple heat and mass transfer processes additionally affect the interaction of translucent droplets absorbed radiation flux. Experimentally investigate the multiple heat transmission of droplets rather difficult, so widely used theoretical methods [1]. Modeling multiple heat spread of the droplets of liquid existence instability assessment problem in its. Spontaneous circulation of liquid warming droplets can occur when Archimedes forces is on, and they forced circulation can lead to gas sliding friction force acting on the surface. The exposure of the liquid droplets flowing on the surface and formed vortices passes into the interior layers of the droplets. Hydrodynamic mode of the liquid droplets determines the solution methodology of "drop" inner problem. The simplest form of droplets heat transfer models that deny the influence of radiation. Suggesting that the droplets while maintaining a uniform temperature is warming up their volume, they concluded "the infinite heat conductivity", or "infinite fluid mixing" strain [2, 3]. These droplets heat transfer models to define the effective conductivity model [4], which additionally take into account the fluid-flow finite intensity of thermal impact on the spread of the droplets. Translucent droplets radiation absorbed by the flow describing the spectral radiation models [5–9] enables the evaluation of the combination of heat spreading droplets. Recently developed combined analytical and numerical models of droplet non-stationary evaporation [5, 10]. Then the temperature field of droplets of a multiple their heating case describing integral equation the endless lines. Despite their numerical solution schemes, convergence control is convenient, but inconvenience causes the need to know the evaporating droplet surface temperature. When trying to save the counting machine time and avoid this temperature calculation by iterative methods, doing that task simplification assumption [10]. Correctness case the droplet surface temperature is calculating by iterative methods for solving the energy flow balance droplets on the surface of describing an additional equation. In this case, the heat conductivity effective coefficient consider and to hydrodynamic mode impact on the liquid droplets thermal state [5].

The aim of this work is to assess spontaneous fluid flow increases possibility of evaporative and warming pure liquid fuel droplets.

2 Formulation of the Problem

Natural circulation of fluid within a droplet is induced by non-uniformity of temperature field, which has been expressed by difference of temperatures at droplet surface and in the center of it: $\Delta T_l \equiv T_R - T_C$. The intensity of natural circulation in the droplet is described by Rayleigh number:

$$Ra = \frac{\beta_l g R^3}{\nu_l a_l} \Delta T_l \,. \tag{1}$$

The circulation of liquid is said to onset when the Rayleigh number exceeds the critical value i.e. $Ra > Ra_{cr}$. Otherwise the processes in the droplet are dominated by diffusion. Research of fluid behavior in spherical volume with non-uniform temperature field [11] demonstrates that critical values of the Rayleigh number are strongly dependent on the method of volume heating. For asymmetric heating the critical value is in the range of 200 to 300, and for symmetric heating it can reach few thousands. The fluid temperature profile in the droplet under heating is described by the following equation [1]:

$$T_r = T_R + \frac{2}{r} \sum_{n=1}^{\infty} \sin \frac{n\pi r}{R} \int_0^t f_n(\tau) \exp\left[-a \left(\frac{n\pi}{R} \right)^2 (t-\tau) \right] d\tau \,, \tag{2}$$

where the heat source is described by the function

$$\begin{aligned} f_n(\tau) &= (-1)^n \frac{R}{n\pi} \frac{dT_R}{d\tau} \\ &+ \frac{1}{\rho c_p R} \int_0^R \left(\sin \frac{n\pi r}{R} - \frac{n\pi r}{R} \cos \frac{n\pi r}{R} \right) q_r \, dr \end{aligned} \,. \tag{3}$$

The function takes into account radiant heat absorption in the semi-transparent droplet and the dynamics of its surface temperature. The model of the droplet does not consider the slippage between two phases i.e. droplet and its environment. In this scenario the effect of gaseous phase to fluid circulation in the droplet are not considered as the forces inducing such circulation are absent. The droplet is heated by conductivity. The surface temperature of the evaporating droplet is calculated using energy conservation principle and has been implemented using the method of the steepest descent:

$$\lambda_{vg} \frac{T_g - T_R}{2R} f_{B_T} - \lambda_{ef} \left. \frac{\partial T_r}{\partial r} \right|_{r \equiv R} - m_v L \equiv 0 \,. \tag{4}$$

Spalding heat transfer parametric function f_{B_T} in eq. (4) takes into account Stephan hydrodynamic effect to in-droplet convection of the droplet in the gas stream. It is defined as [4]

$$f_{B_T} \equiv \frac{\ln(1 + B_T)}{B_T} \,, \tag{5}$$

■

where Spalding heat transfer parameter for non-stationary evaporation of droplet is defined as [12]

$$B_T \equiv \frac{c_{p,vg}\left(T_g - T_R\right)}{L}\left(1 - \lambda_{ef}\left.\frac{\partial T}{\partial r}\right|_{r\equiv R} / q_{c,R}\right). \tag{6}$$

Non-stationary temperature gradient in eq. (4) and (6) is described by the following equation (2):

$$\left.\frac{\partial T_r}{\partial r}\right|_{r\equiv R} = \frac{2\pi}{R^2}\sum_{n=1}^{\infty} n(-1)^n \int_0^t f_n(\tau)\exp\left[-a\left(\frac{n\pi}{R}\right)^2(t-\tau)\right]d\tau\,. \tag{7}$$

Assuming that there is no forced circulation in the droplet and that the effect of natural circulation to droplet heating is negligible the effective thermal conductivity coefficient in (4) and (6) will be defined by the thermal conductivity coefficient of fluid $\lambda_{ef} \equiv \lambda_l$. Vapor mass flux is calculated based on the Shorin-Kuzikovskij model [13, 14]

$$m_v = \frac{D_{vg}}{T_R}\frac{\mu_g}{R\cdot R_\mu}\, p \ln\frac{p - p_{v,\infty}}{p - p_{v,R}}\,. \tag{8}$$

System of equations (1)–(8) can be solved numerically. Using iterative method number J of the control droplet cross-section is selected arbitrary. The position of the cross-section is defined by the dimensionless droplet coordinate η_j (η_j=0, when $j\equiv 1$ and η_j=1, when $j\equiv J$). Control time t is selected and number I of time coordinate steps is provided ($\tau = 0$, when $i \equiv 1$ and $\tau = t$, when $i \equiv I$). Temperature field in the droplet is determined from eq. (2) iteratively varying droplet surface temperature on the basis of energy conservation principle at the surface and using the method of the steepest descent. The final result is achieved when the energy balance error (4) from the previous iteration is no greater than 0.01 percent. The local radiation flux density in a semi-transparent droplet is calculated using the technique described in ref. [5]. It requires the updated temperature field in the droplet from the previous iteration, takes into account light absorption by the droplet and effects at the surface of the droplet.

3 Results and discussion

To investigate the influence of fluid natural circulation in the hydrocarbon droplet the droplet heating and evaporation in air flow has been modelled. The n-hexane, n-heptane and n-decane have been chosen. The complex droplet heating by conduction and radiation has bean modelled. It is assumed the absolutely black-body radiation heat source with the temperature of the droplet environment exists. The droplet is internally heated by conduction to the temperature of

equilibrium evaporation $T_{e,k}$, which does not alter during such evaporation mode (fig. 1).

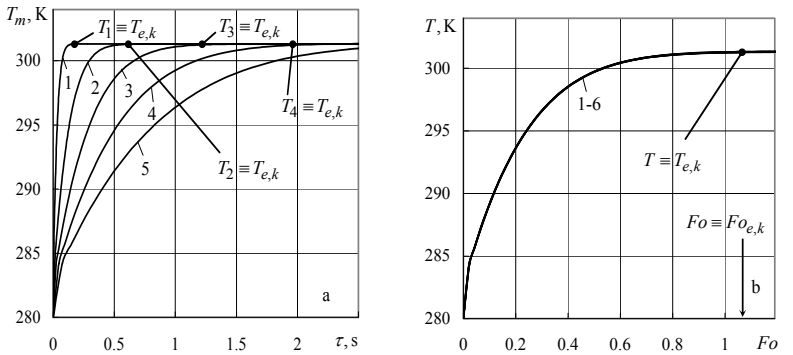

Figure 1: n-hexane droplet internal heating by conduction in air environment. Mean droplet temperature in time (a) and Fourier criterion (b) domains. $R \cdot 10^6$, m: 1 – 50, 2 – 100, 3 – 200, 4 – 300, 5 – 400, 1 – 600; T_g=473K.

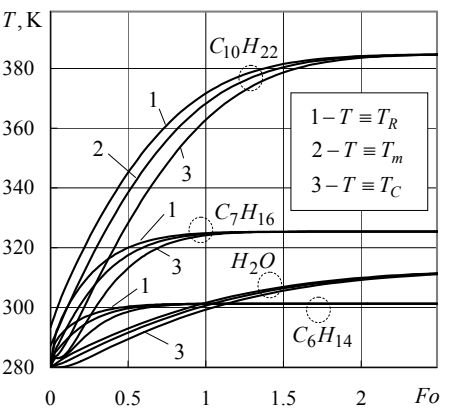

Figure 2: Hydrocarbons n-hexane (C_6H_{14}), n-heptane (C_7H_{16}), n-decane ($C_{10}H_{22}$) and water (H_2O) droplet heating in 473K air temperature.

Dynamics of droplet mean temperature, when internally heating by conduction only, for the same liquid droplets is invariant of droplet size in the domain of Fourier criterion (fig. 1b). For each type of liquid the characteristic curves of droplet surface temperature $T_R(Fo)$, center temperature $T_C(Fo)$ and mean temperature $T_m(Fo)$ dynamics can be established (fig. 2). It allowed optimization of the numerical model for droplet heating and evaporation processes. The characteristic droplet temperature non-uniformity curves are

established based on the droplet surface temperature and droplet center temperature dynamics. They clearly depict that liquid properties have influence to temperature non-uniformity (fig. 3). The intensive temperature increase of droplet external fluid layers during the initial droplet heating stage causes rapid rise of the droplet temperature non-uniformity. Later the temperature non-uniformity reduces and eventually vanishes when droplet equilibrium evaporation mode is entered. The results show that water droplets establish equilibrium evaporation earlier than hydrocarbon droplets. Therefore, non-uniformity in water droplets vanishes earlier, as well. In the modeled case (fig. 3) non-stationary evaporation of hydrocarbon droplets lasts up to 80% of phase transformation duration, but for water droplets it is just 20%.

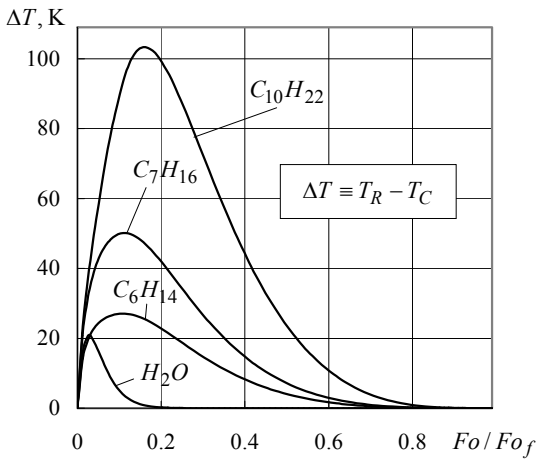

Figure 3: The dynamics of non-uniformity of temperature field for droplets in 1073K air environment.

Droplet temperature non-uniformity is significantly influenced by gas phase temperature, which has effect on droplet equilibrium evaporation temperature. For air temperature of 473K droplet equilibrium evaporation temperature is 301.3K for n-hexane, 325.4K for n-heptane, 384.8K for n-dekane and 313K for water. Droplet equilibrium evaporation temperature increases to 311.3K, 337.8K, 406.4K and 332.1K correspondingly when air temperature is increased by 1000K to 1473K. For hydrocarbons with higher saturation temperature (in this instance it was n-dekane) droplet equilibrium evaporation temperature is higher and the spike of temperature non-uniformity is more pronounced (fig. 3). Therefore, conditions for fluid natural circulation are favorable. For sprinkled of liquid temperatures close to droplet equilibrium evaporation temperature droplet temperature non-uniformity will be smaller and will last shorter compared to sprinkled of liquid with temperatures significantly below it.

The research results show and quantify that the size of droplet has an effect to droplet natural circulation (fig. 4).

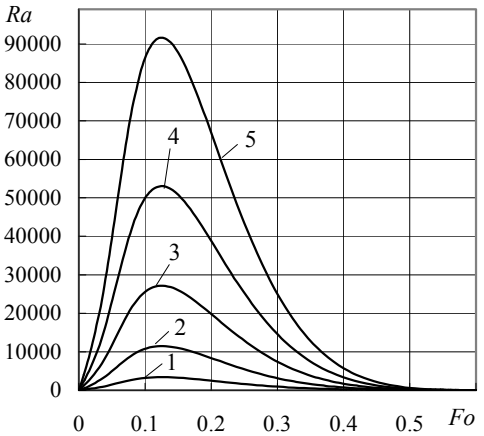

Figure 4: Droplet size influence to droplet internal natural circulation for n-decane. $R \cdot 10^6$, m: 1 – 500, 2 – 750, 3 – 1000, 4 – 1250, 5 – 1500; $T_{l,0}$=283K, T_g=1073K.

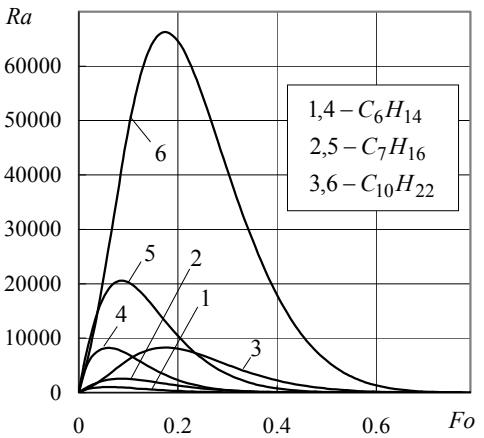

Figure 5: Influence of liquid properties to droplet internal natural fluid circulation. $R \cdot 10^6$, m: 1-3 – 750, 4-6 – 1500; $T_{l,0}$=283K, T_g=873K.

Larger droplets have better conditions to stimulate droplet natural circulation. The results of this research show that when the size of droplets is the same, the fluid natural circulation will depend on liquid properties. In the case of hydrocarbons, the results show (fig. 5) that out of three hydrocarbons n-dekane (the highest hydrocarbon out of three) had the best properties to stimulate natural circulation.

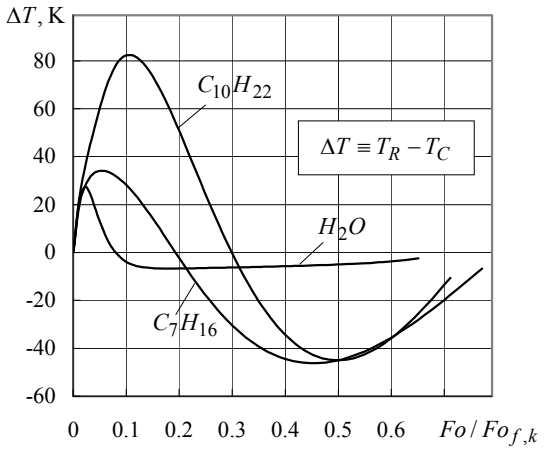

Figure 6: The effect of fluid radiation absorption property to non-uniformity of droplet heating. R_0=500·10^{-6}m, $T_{l,0}$=283K, T_g=1073K.

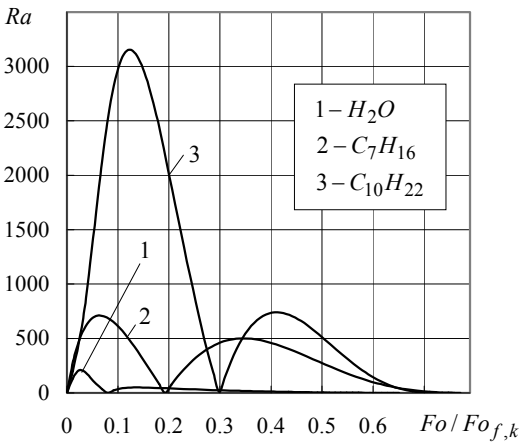

Figure 7: The effect of fluid properties and radiation to droplet internal natural fluid circulation. R_0=500·10^{-6}m, $T_{l,0}$=283K, T_g=1073K.

Absorbed radiation by semitransparent droplet is essential to droplet heating (fig. 6). In the case of complex conduction-radiation droplet heating, the temperature profile in the droplet and the heating process has new features introduced. The process changes quantitatively as well as qualitatively. In the complex heating case two spikes of temperature non-uniformity are observed. The first one is the consequence of conduction and has been discussed above. The second spike is the result of radiation absorption by liquid and results in temperature increase of internal liquid layers. The maximum of this non-

uniformity spike occurs when droplet equilibrium evaporation is established. The temperature gradient in the droplet balances heat transfer due to radiation and conduction if the fluid internal circulation is insignificant. The second temperature non-uniformity spike is smaller than the first. Therefore, conditions for fluid natural circulation are determined by the first spike (fig. 7).

4 Conclusions

On the basis of Rayleigh number utilization to classify water droplets and research results for n-decane, hydrocarbon droplets can be divided into such categories:

- small (less than 100μm in diameter);
- medium (50-1000μm in diameter);
- large (more than 1mm in diameter).

Fluid natural circulation in small hydrocarbon droplets is practically impossible. It is unlikely that natural circulation will be significant in medium size droplets, as well. The only category of hydrocarbon droplets, where fluid natural circulation might be sensible is of large droplets, i.e. with diameters of droplets exceeding 1mm. In general, the larger the droplet size the more likely that natural circulation in the droplet will be observed.

Radiation absorbed by semitransparent droplets has a significant effect on their heating, evaporation and process dynamics by the formation of the secondary spike in temperature non-uniformity. It is smaller than the first spike originating due to conduction, and does not dominate determination of conditions for fluid natural circulation.

Droplet sizes in technologies utilizing the principle of liquid sprinkle of mostly fall into small and medium categories. Therefore, fluid natural circulation in the droplets is insignificant and is not necessary to be modeled.

Nomenclature

a – thermal diffusivity, m^2/s; B – Spalding transfer number; c_p – specific heat, $J/(kg\ K)$; D – mass diffusivity, m^2/s; Fo – Fourier number; L – latent heat of evaporation, J/kg; m – vapour mass flux, $kg/(s\,m^2)$; n – number of the term in infinite sum; p – pressure, Pa; q – heat flux, W/m^2; R – radius of a droplet, m; r – coordinate of a droplet, m; Ra – Rayleigh number; Nu – Nusselt number; T – temperature, K; η – non-dimensional coordinate; λ – thermal conductivity, $W/(m\ K)$; μ – molecular mass, $kg/kmol$; ρ– density, kg/m^3; τ – time, s;

Subscripts: C – droplet centre; cr – critical; e – equilibrium evaporation; g – gas; i – time index; I – index of control time; j – index of droplet cross-section; J – index of droplet surface; k – conductive; l – liquid; m – mass average; r – coordinate of a droplet; R – droplet surface; v – vapour; vg – vapour-gas mixture; 0 – initial state; ∞ – far from a droplet.

References

[1] Sazhin S.S., Advanced models of fuel droplet heating and evaporation. *Progress in Energy and Combustion Science*, **32**, pp 162–214, 2006.
[2] Law C.K., Unsteady droplet combustion with droplet heating. *Combust. Flame*, **26**, pp. 17-22, 1976.
[3] Law C.K., Multicomponent droplet combustion with rapid internal mixing. *Combust. Flame*, **26**, pp. 219-233, 1976.
[4] Abramzon B., Sirignano W.A., Droplet vaporization model for spray combustion calculations. *Int. J. Heat Mass Transfer*, **32**, pp.1605-1618, 1989.
[5] Miliauskas G, Regularities of unsteady radiative-conductive heat transfer in evaporating semitransparent liquid droplet. *Int. J. Heat Mass Transfer*, **44**, pp. 785-798, 2001.
[6] Lage P.L.C., Rangel R.H., Single droplet vaporization including thermal radiation absorption. *J. of Thermophysics and Heat Transfer*, **7**, pp. 502-509, 1993.
[7] Harpole G.M., Radiative absorption by evaporating droplets. *Int. J. Heat Mass Transfer*, **22**, pp.17-26, 1980.
[8] Dombrovsky L.A., Thermal radiation form no isothermal spherical particles of a semitransparent material. *Int. J. Heat Mass Transfer*, **43**, pp. 1661-1672, 2000.
[9] Tseng, C.C., Viskanta R., Enhancement of water droplet evaporation by radiation absorption. *Fire Safety J,* 41, pp 236–247, 2006.
[10] Sazhin S, Modeling of heating, evaporation and ignition of fuel droplets: combined analytical, asymptotic and numerical analysis. *J. of Physics: Conference Series*, **22**, pp 174-193, 2005.
[11] Gershuni G.Z., Zhukovickiy E.M*., Konvektivnaja ustoicivost neszimaemoi zidkosti,* Nauka, Moskva, 1972.
[12] Miliauskas G., Interaction of the transfer processes in semitransparent liquid droplets. *Int. J. Heat Mass Transfer*, **46**, pp. 4119-4138, 2003.
[13] Shorin S.N. *Teploperedacha*, Vishaja Shkola, Maskva, 1964.
[14] Kuzikovskij A.V. Dynamic of spherical particle in powerful optical field, *Izv. VUZ Fizika*,. **5**, pp 89–94, 1970.

Exact solutions of the two-dimensional Boussinesq and dispersive water waves equations

F. P. Barrera[1], T. Brugarino[2] & F. Montano[1]
[1] *Dip. di Ingegneria dei Trasporti, Italy*
[2] *Dip. di Metodi e Modelli Matematici Università di Palermo, Facoltà d'Ingegneria Viale delle Scienze, 90128 Palermo, Italy*

Abstract

In this paper two-dimensional Boussinesq and dispersive water waves equations are investigated in exact solutions. The Exp-function method is used for seeking exact solutions of the equations through symbolic computation.
Keywords: analytical solutions, nonlinear waves equations, Exp-function method.

1 Introduction

Recently new methods have been presented to solve the analytical solutions of the nonlinear wave equations, tanh-function method [1, 2], homotopy method [3] and Adomian decomposition method [4]. The Exp-function method was proposed by He and Wu to obtain solutions of nonlinear evolution equations arising in many physic problems [5]. It is simple to find numerical solutions of linear systems using computers, but this is not true for nonlinear problems. Indeed, numerical methods are connected to initial solutions and it is not easy to have convergent results for strong nonlinearity.

The procedure of the Exp-function method for the solution of PDE is straightforward. The symbol computation is an essential tool to apply the presented method.

The examination of two-dimensional Boussinesq equation arises when we consider the propagation of gravity waves on the surface of water. The structure of this equation leads to consider the propagation of waves in opposite directions.

WIT Transactions on Engineering Sciences, Vol 69, © 2010 WIT Press
www.witpress.com, ISSN 1743-3533 (on-line)
doi:10.2495/AFM100251

The dispersive long wave equations govern the propagation of long waves in shallow water. This problem consists of pair of coupled partial differential equations.

2 Exp-function method

We consider nonlinear partial differential equations:

$$H(u, u_x, u_y, u_t, u_{xx}, u_{xy}, u_{yy}, \ldots) = 0 \tag{1}$$

To find solutions the following transformation needs to be introduced:

$$u(x, y, t) = u(\eta), \qquad \eta = kx + hy - \omega t$$

where k, h and ω are constants and so we can convert Eq. (1) into ordinary differential equation:

$$G(u, u', u'', u''', \ldots) = 0 \tag{2}$$

the prime denoting differentiation respect to η.

According to the Exp-function method, we assume that the solution of Eq. (2) can be expressed in the following form:

$$u(\eta) = \frac{\sum_{n=-c}^{d} a_n \exp(n\eta)}{\sum_{m=-p}^{q} b_m \exp(m\eta)} \tag{3}$$

In order to determine the values of c and p, balancing the linear term of the highest order of Eq. (1) with the highest order nonlinear term, we obtain:

$$d = c$$

Similarly, to determine the values of d and q we balance the linear term of the lowest order of Eq. (1) with the lowest order nonlinear term. So we obtain:

$$q = p$$

Substituting Eq. (3) into Eq. (2) we have a system of algebraic equations for a_n and b_m.

Solving this system using *MATHEMATICA* we carry out the values of the coefficients.

3 Two-dimensional Boussinesq equation

We consider the two-dimensional Boussinesq equation:

$$v_{tt} - v_{xx} + 3(v^2)_{xx} - v_{xxxx} - v_{yy} = 0 \tag{4}$$

This equation describes the propagation of waves in opposite directions in (2+1) dimensions [6]. Using the wave variable:

$$\eta = kx + hy - \omega t$$

it is possible to lead Eq. (4) to an ordinary differential equation:

$$(\omega^2 - k^2 - h^2)v'' + 3k^2(v^2)'' - k^4 v^{(iv)} = 0 \tag{5}$$

According to the Exp-function method, we assume that the solution of Eq. (5) can be written as follows:

$$v(\eta) = \frac{a_1 \exp(\eta) + a_0 + a_{-1}\exp(-\eta)}{b_2 \exp(2\eta) + b_1 \exp(\eta) + b_0 + b_{-1}\exp(-\eta) + b_{-2}\exp(-2\eta)} \tag{6}$$

We have set $c = 1$ and $q = 2$. Without compromising the generality we can assume $a_{-1} \neq 0$ and Eq. (6) can be simplified as

$$v(\eta) = \frac{a_1 \exp(\eta) + a_0 + \exp(-\eta)}{b_2 \exp(2\eta) + b_1 \exp(\eta) + b_0 + b_{-1}\exp(-\eta) + b_{-2}\exp(-2\eta)} \tag{7}$$

Substituting Eq. (7) into Eq. (5) and equating to zero the coefficients of all powers of $\exp(n\eta)$ we find a set of algebraic equations for a_0, a_1, b_2, b_1, b_0, b_{-1}, b_{-2}. Solving this system we obtain

$$\omega^2 = h^2 + k^2 + k^4$$

and the following coefficients:

$$a_0 = -2k^2 b_0, a_1 = k^4 b_0^2, b_1 = b_{-1} = 0, b_2 = \frac{a_1^2}{k^2 a_0}, b_{-2} = \frac{1}{k^2 a_0}$$

Substituting ω and the coefficients into Eq. (7), we obtain the following exact solution of the two-dimensional Boussinesq equation

$$v(x,y,t) = -\frac{2k^4 b_0 \exp\left(kx + hy - t\sqrt{h^2 + k^2 + k^4}\right)}{\left(1 + k^2 b_0 \exp\left(kx + hy - t\sqrt{h^2 + k^2 + k^4}\right)\right)^2}$$

4 Dispersive water waves equations

The problem of the propagation of long waves in shallow water is governed by a pair of coupled nonlinear partial differential equations [7]:

$$\begin{cases} u_t &= uu_x + h_x + \theta u_{xx} \\ h_t &= (hu)_x + \theta h_{xx} \end{cases} \tag{8}$$

Using the variable:

$$\eta = kx - \omega t$$

it is possible to lead Eq.s (8) to a couple of nonlinear ordinary differential equations:

$$\begin{cases} \omega u_\eta + kuu_\eta + kh_\eta + k^2\theta u_{\eta\eta} = 0 \\ \omega h_\eta + k(hu)_\eta + k^2\theta h_{\eta\eta} = 0 \end{cases} \tag{9}$$

Following the Exp-function method, we set:

$$u(\eta) = \frac{a_1 \exp(\eta) + a_0 + a_{-1}\exp(-\eta)}{b_2 \exp(2\eta) + b_1 \exp(\eta) + b_0 + b_{-1}\exp(-\eta) + b_{-2}\exp(-2\eta)} \tag{10}$$

and

$$h(\eta) = \frac{c_1 \exp(\eta) + c_0 + c_{-1}\exp(-\eta)}{d_2 \exp(2\eta) + d_1 \exp(\eta) + d_0 + d_{-1}\exp(-\eta) + d_{-2}\exp(-2\eta)} \tag{11}$$

Substituting Eq. (10) and Eq. (11) into Eq. (9) we obtain

$$\omega = k^2$$

and, solving the system, for dispersive water waves equations, we find:

$$u(x,t) = -\frac{2k\theta \exp(kx)}{\exp(kx) - b_{-2}\exp(k^2\theta t)}$$

and

$$h(x,t) = -\frac{4k^2\theta^2 b_{-2}\exp(k(x+k\theta t))}{\left(\exp(kx) - b_{-2}\exp(k^2\theta t)\right)^2}$$

5 Conclusions

In this paper we find exact solutions of two-dimensional Boussinesq equation and of the dispersive water waves equations using a simple and direct method called the Exp-function method. This is a straight and promising tool to solve non linear evolution equations arising in physics and engineering.

But, even if this scenario could be straightforward from one hand, the implementation of it is a difficult task, mainly for the amount of calculations.

In future we propose to solve the massive system of algebraic equations given by the Exp-function method using the method Gröbner basis of non linear algebra and numerical methods.

References

[1] L. Huibin and W. Kelin 1990 *J. Phys. A* **23** (1990).
[2] W. Malfliet *Am. J. Phys.* **60** (1992).
[3] S. Liao *Appl. Math. Comput.* **147** (2004).
[4] M. Dehghan and M. Tatari *Phys. Scr.* **73** (2006).
[5] J. H. He and X. H. Wu *Chaos, Soliton and Fractals* **30** (2006).
[6] R. S. Johnson *J. Fluid Mech.* **323** (1996).
[7] B. A. Kupershmidt *Comm. Math. Phys.* **99** (1985).

This page intentionally left blank

Modelling gravity-driven flow over uneven surfaces

K. A. Ogden[1], S. J. D. D'Alessio[1] & J. P. Pascal[2]
[1]*Department of Applied Mathematics, University of Waterloo, Canada*
[2]*Department of Mathematics, Ryerson University, Canada*

Abstract

This study concerns the gravity-driven two-dimensional laminar flow of a thin layer of fluid down a wavy inclined surface. Three mathematical models describing the unsteady two-dimensional flow evolution are presented and contrasted. The first is a shallow-water model, while the other two are integral-boundary-layer models representing non-hydrostatic approximations to the two-dimensional Navier-Stokes equations, which are valid for thin fluid layers. Various tests and simulations were conducted in order to assess the performance of the models. First, the instability threshold for the flat bottom case associated with each model was analytically determined and compared with the theoretical prediction based on the Navier-Stokes equations. Also for the flat bottom case, comparisons in neutral stability curves were made with existing experimental data. In addition, comparisons between two-dimensional numerical solutions of the full Navier-Stokes equations, obtained using the CFX software package, with simulations from the models were also investigated for a wavy bottom case. The wavy surface considered in this study corresponds to that of a sinusoidal profile. The emerging interfacial wave structure along with the combined effect of bottom topography and surface tension are discussed. Finally, critical Reynolds number predictions for cases including bottom topography are compared to existing experimental data.
Keywords: film flow, wavy incline, shallow-water and integral-boundary-layer models, numerical, experimental, analytical, CFX solver.

1 Introduction

There are many situations in which a model for flow down an inclined plane is applicable. Naturally occurring situations include mudslides and ice channels [1].

WIT Transactions on Engineering Sciences, Vol 69, © 2010 WIT Press
www.witpress.com, ISSN 1743-3533 (on-line)
doi:10.2495/AFM100261

As well, such models are useful for engineering applications such as aqueducts, dam spillways, and coatings in manufacturing [2]. Analytic models for this type of flow are useful because they help predict key features of the flow, such as under what conditions it will become unstable and how the shape of the free surface will develop after this happens. These are important predictions to make because the large roll waves that are formed when the flow becomes unstable can overflow channel walls or damage measurement equipment in engineering settings; in natural settings, these roll waves result in more destructive surges of flow due to the increased mass flow rate and momentum [2]. Therefore, models that give accurate predictions of these features of the flow are important, and could be used to design channels that can handle the waves that are likely to occur, or that can reduce the likelihood of roll waves forming.

Many previous studies focus on the case without bottom topography. Detailed analytical investigations include those by Ruyer-Quil and Manneville [3], who developed models based on weighted residual methods. They consider even-bottom surfaces, and develop first- and second-order models applicable to two and three dimensional cases. The problem has also been extended by Balmforth and Mandre [1], and D'Alessio et al. [2] to include bottom topography. Balmforth and Mandre use the shallow-water model, focussing on the turbulent version, while D'Alessio et al. apply a weighted residual model to the uneven bottom case.

In this study, three models that describe fluid flow over an uneven, inclined plane are compared. The problem setup and coordinate system are shown in Figure 1. These models are the shallow-water model (SWM), the integral-boundary-layer (IBL) model, and the weighted residual model (WRM). Model predictions for the critical Reynolds number for the onset of instability are compared with the theoretical value obtained from the Orr-Sommerfeld equation for the flat bottom case. Neutral stability curves resulting from the models are also compared with experimental data for the flat bottom case. As well, fully developed flows for various sets of parameters are compared with direct numerical simulations of the full

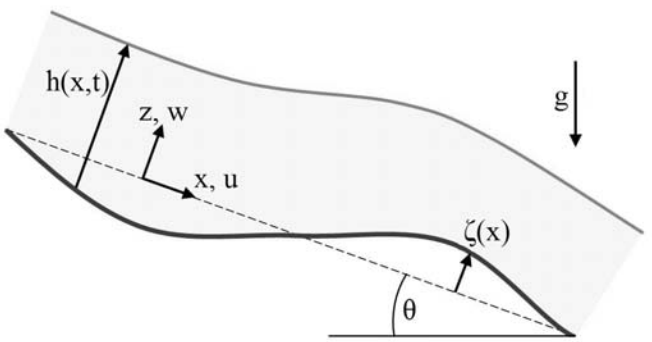

Figure 1: The coordinate system and flow setup.

Navier-Stokes equations using the computational fluid dynamics package CFX. In this comparison, bottom topography is included. The combined effect of surface tension and bottom topography on the stability is briefly discussed. Finally, the weighted residual model, which turns out to be the optimal model, is then compared to experimental results for flow over a wavy incline.

2 Description of models

Three models are considered in this study. They are the shallow-water model, the integral-boundary-layer model, and the weighted residual model. All three of the models are given below, with a brief description of how they are obtained.

As suggested by the name, the shallow-water model is founded on shallow-water theory and hence assumes that the fluid is incompressible and inviscid, and that the thickness of the fluid is much smaller than the characteristic length in the direction of the flow. It then follows that the pressure distribution is hydrostatic and that the streamwise velocity is depth independent. This model is limited to gentle inclines.

After these simplifications are made, three modifications are added to make the model more realistic. A flow factor multiplying the advective term is added; the value is empirically determined, and depends on whether the flow is laminar or turbulent. For the laminar model, a value of 4/5 is used [1]. A term partially accounting for viscosity and a bottom friction term are also added.

Two different forms of the shallow-water equations have been developed: one pertaining to laminar flow and the other to turbulent flow. The difference between the two is in the viscosity parameter of the added viscous term, the form of the bottom friction term, and the coefficient of the advection term. Balmforth and Mandre [1] give a thorough description of the two versions of the model. The laminar model is used in this study because flows having a Reynolds number of order unity are considered, and because the other two models are developed assuming laminar flow. The equations describing the laminar shallow-water model are given by

$$\frac{\partial h}{\partial t} + \frac{\partial q}{\partial x} = 0 \,, \tag{1}$$

$$\begin{aligned} \frac{\partial q}{\partial t} + \frac{\partial}{\partial x}\left(\frac{4}{5}\frac{q^2}{h} + \frac{\cot\theta}{2Re}h^2\right) &= -\frac{1}{5}\frac{q}{h}\frac{\partial q}{\partial x} - \frac{\cot\theta}{Re}h\frac{d\zeta}{dx} \\ &\quad + \frac{1}{\delta Re}\left(h - \frac{q}{h^2}\right) + \delta^2 hWe\frac{\partial^3}{\partial x^3}\left(\zeta + h\right) \\ &\quad + \frac{\delta}{Re}\left(\frac{\partial^2 q}{\partial x^2} - \frac{q}{h}\frac{\partial^2 h}{\partial x^2} - \frac{1}{h}\frac{\partial h}{\partial x}\frac{\partial q}{\partial x} + \frac{q}{h^2}\left(\frac{\partial h}{\partial x}\right)^2\right) \,. \end{aligned} \tag{2}$$

The non-dimensional flow variables are h, the height of the free surface from the bottom, and q, the mass flow rate. Here, θ denotes the angle of inclination of the surface, Re is the Reynolds number, defined as $Re = Q/\nu$, and We is the Weber number, defined as $We = \frac{\sigma H}{\rho Q^2}$, where Q is the non-dimensional characteristic

volume flow rate, H is the Nusselt thickness, ρ is the fluid density, σ is the surface tension coefficient, and ν is the kinematic viscosity of the fluid. The shallowness parameter, δ, is the ratio of the Nusselt thickness of the fluid to some characteristic length in the x direction, and is assumed to be small.

The integral-boundary-layer model is derived more rigorously from the Navier-Stokes equations. The non-dimensionalized continuity and momentum equations are

$$\frac{\partial u}{\partial x} + \frac{\partial w}{\partial z} = 0 \,, \tag{3}$$

$$\delta Re \left(\frac{\partial u}{\partial t} + u\frac{\partial u}{\partial x} + w\frac{\partial u}{\partial z} \right) = -\delta Re \frac{\partial p}{\partial x} + 3 + \delta^2 \frac{\partial^2 u}{\partial x^2} + \frac{\partial^2 u}{\partial z^2} \,, \tag{4}$$

$$0 = -Re\frac{\partial p}{\partial z} - 3\cot\theta + \delta\frac{\partial^2 w}{\partial z^2} \,. \tag{5}$$

Here, the advective terms in the z-momentum equation are neglected because they become third order in δ when the pressure is substituted into the x-momentum equation. The model is therefore second-order accurate in δ. This model more accurately accounts for the fluid viscosity and allows a non-hydrostatic pressure distribution, which are improvements over the shallow-water model.

At the free surface, we apply dynamic and kinematic conditions, given in non-dimensional form by

$$\left.\begin{aligned} 0 &= p - \frac{2\delta}{Re}\frac{\partial w}{\partial z} + \delta^2 We \frac{\partial^2}{\partial x^2}(h+\zeta) \\ 0 &= \frac{\partial u}{\partial z} - 4\delta^2 \frac{\partial}{\partial x}(h+\zeta)\frac{\partial u}{\partial x} + \delta^2 \frac{\partial w}{\partial x} \end{aligned}\right\} \text{ at } z = h+\zeta \,, \tag{6}$$

$$\left. w = \frac{\partial h}{\partial t} + u\frac{\partial (h+\zeta)}{\partial x} \right\} \text{ at } z = h+\zeta \,. \tag{7}$$

As well, the following no-slip conditions are imposed at the bottom surface:

$$u = w = 0 \;\text{ at }\; z = \zeta \,. \tag{8}$$

The pressure can be eliminated by integrating the z-momentum equation and using the first condition in eqn. (6) to find an expression for pressure, and then substituting this expression into the x-momentum equation. This leaves the continuity equation and a single momentum equation. The form of the streamwise velocity is then assumed based on the known steady flow over an even-bottom inclined plane, and modified to account for bottom topography defined by $\zeta(x)$. The profile is given by

$$u = \frac{3q}{2h^3}\left(2\left(h+\zeta\right)z - z^2 - \zeta^2 - 2h\zeta\right) \ . \tag{9}$$

The z dependence is then eliminated by integrating the equations across the fluid layer and applying the boundary conditions. The final form of the integral-boundary-layer model equations are

$$\frac{\partial h}{\partial t} + \frac{\partial q}{\partial x} = 0 \ , \tag{10}$$

$$\begin{aligned}\frac{\partial q}{\partial t} + \frac{\partial}{\partial x}\left(\frac{6}{5}\frac{q^2}{h} + \frac{3}{2}\frac{\cot\theta}{Re}h^2\right) &= \delta^2 hWe\frac{\partial^3}{\partial x^3}\left(h+\zeta\right) \\ &\quad -3h\frac{\cot\theta}{Re}\frac{\partial\zeta}{\partial x} + \frac{3}{\delta Re}\left(h - \frac{q}{h^2}\right) \\ &\quad +\frac{\delta}{Re}\left(\frac{9}{2}\frac{\partial^2 q}{\partial x^2} - \frac{6}{h}\frac{\partial h}{\partial x}\frac{\partial q}{\partial x} - \frac{3}{h}\frac{\partial q}{\partial x}\frac{d\zeta}{dx} + 3\frac{q}{h^2}\frac{\partial h}{\partial x}\frac{d\zeta}{dx}\right) \\ &\quad +\frac{\delta}{Re}\left(6\frac{q}{h^2}\left(\frac{\partial h}{\partial x}\right)^2 - 6\frac{q}{h^2}\left(\frac{d\zeta}{dx}\right)^2 - 6\frac{q}{h}\frac{\partial^2 h}{\partial x^2} - \frac{9}{2}\frac{q}{h}\frac{d^2\zeta}{dx^2}\right) \ .\end{aligned} \tag{11}$$

The weighted residual model is derived following a similar procedure to that used for the integral-boundary layer model. However, before integrating in the cross-stream direction, the equations are multiplied by a weighting function; in this case, a parabolic profile is used as the weighting function. In this way, a weighted average over the depth of the fluid is used. The resulting model equations are

$$\frac{\partial h}{\partial t} + \frac{\partial q}{\partial x} = 0 \ , \tag{12}$$

$$\begin{aligned}\frac{\partial q}{\partial t} + \frac{\partial}{\partial x}\left(\frac{9}{7}\frac{q^2}{h} + \frac{5}{4}\frac{\cot\theta}{Re}h^2\right) &= \frac{5}{6}\delta^2 hWe\frac{\partial^3}{\partial x^3}\left(h+\zeta\right) \\ &\quad +\frac{q}{7h}\frac{\partial q}{\partial x} - \frac{5h}{2}\frac{\cot\theta}{Re}\frac{d\zeta}{dx} + \frac{5}{2\delta Re}\left(h - \frac{q}{h^2}\right) \\ &\quad +\frac{\delta}{Re}\left(\frac{9}{2}\frac{\partial^2 q}{\partial x^2} - \frac{9}{2h}\frac{\partial h}{\partial x}\frac{\partial q}{\partial x} - \frac{5}{2}\frac{q}{h^2}\frac{\partial h}{\partial x}\frac{d\zeta}{dx} + 4\frac{q}{h^2}\left(\frac{\partial h}{\partial x}\right)^2\right) \\ &\quad +\frac{\delta}{Re}\left(-5\frac{q}{h^2}\left(\frac{d\zeta}{dx}\right)^2 - 6\frac{q}{h}\frac{\partial^2 h}{\partial x^2} - \frac{15}{4}\frac{q}{h}\frac{d^2\zeta}{dx^2}\right) \ .\end{aligned} \tag{13}$$

3 Model performance

To evaluate and compare the performance of the three models, four methods are employed. First, the critical Reynolds number at which the flow becomes unstable

is calculated for the flat bottom case, and compared to the known theoretical value. Second, the neutral stability curves for each model are compared to experimental data collected by Liu et al. [4]. Next, the evolution of the flow rate q, as predicted by the models, is compared to the solution of the full Navier-Stokes equations, where the solution to the full Navier-Stokes equations was obtained using the software package CFX. Finally, critical Reynolds number predictions for the weighted residual model for flow over a wavy bottom are compared to experimental results collected by Wierschem et al. [5]. Only the weighted residual model is considered in this final comparison because it is found to perform the best in the previous three tests.

The critical Reynolds number for a thin film flow down an even-bottom inclined plane has been determined by Benjamin [6] and Yih [7] from the corresponding Orr-Sommerfeld equation. The result is that the critical Reynolds number is:

$$Re_{crit} = \frac{5}{6}\cot\theta \ . \tag{14}$$

Performing a linear stability analysis on the shallow-water model, the integral-boundary-layer model, and the weighted residual model yields the following results:

$$Re_{crit}^{SWM} = \frac{5}{22}\cot\theta \ , \tag{15}$$

$$Re_{crit}^{IBL} = \cot\theta \ , \tag{16}$$

and

$$Re_{crit}^{WRM} = \frac{5}{6}\cot\theta \ , \tag{17}$$

respectively.

These results show that, of the three models considered, only the weighted residual model correctly predicts the critical Reynolds number. The integral-boundary-layer model predicts a critical Reynolds number slightly higher than the correct value, although it is still close. The shallow-water model gives a very poor prediction, significantly underestimating the critical Reynolds number.

To further evaluate the performance of the three models, the neutral stability curves for each of the models are compared to experimental data gathered by Liu et al. [4] and plotted in Figure 2.

As with the critical Reynolds number predictions, the weighted residual model most closely matches the experimental data. The integral-boundary-layer model is a slightly poorer predictor of the experimental data, although it gives a much better prediction than the shallow-water model. It should also be noted that the experimental data is for a very gentle incline, which is much more appropriate for the shallow-water model than for the integral-boundary-layer or weighted residual models; despite this, the weighted residual model does very well.

For the next comparison, numerical solutions using the models are compared to direct numerical simulations of the full Navier-Stokes equations. The full Navier-Stokes equations for the free surface flow down an inclined plane have been solved

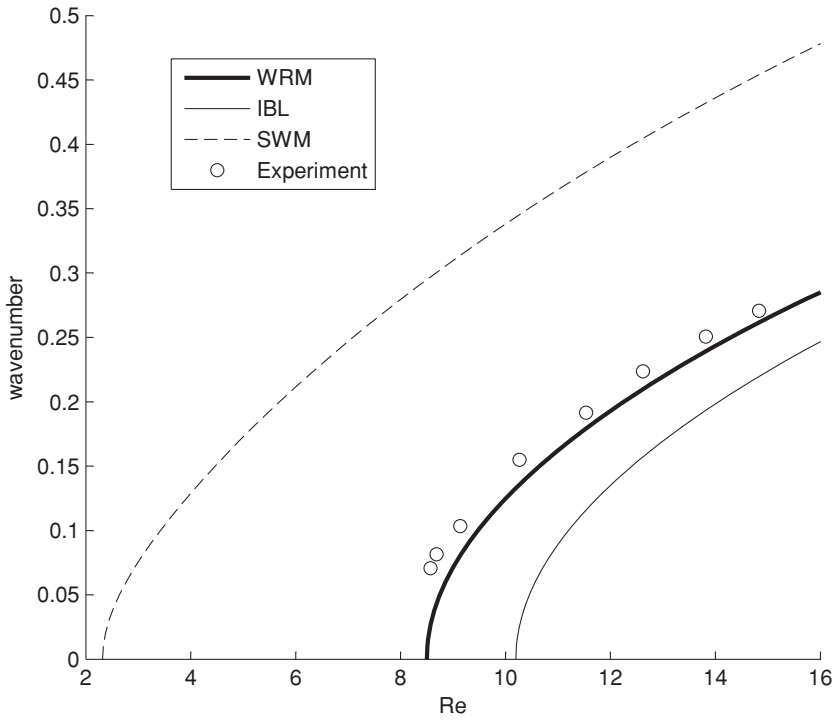

Figure 2: Comparison of neutral stability curves with experimental data for a glycerin-water solution with $\theta = 5.6\,^{\circ}$.

by employing CFX. This software package solves the full Navier-Stokes equations using a combination of finite volume and finite element methods [8]. The location of the interface is determined using a compressive volume fraction advection scheme [9].

The models considered in this study can also be used to predict the transient behaviour of the flow by numerically solving the equations. Using LeVeque's fractional step method [10], the unsteady equations for each model can be solved. When the steady-state solution, found using the bvp4c routine in matlab, is used as the initial condition and is perturbed, waves develop on the free surface. Eventually, characteristic features such as the number and height of the wave peaks in a domain of a given length are maintained. The wave characteristics predicted by the weighted residual and integral-boundary-layer models are compared to those found by solving the full Navier-Stokes equations. The shallow-water model is not included in this comparison because the inclination considered is too large for that model.

The comparison between the solutions to the full Navier-Stokes equations and the model equations is for a case without surface tension (i.e. $We = 0$). The angle of inclination is $33.7\,^{\circ}$, and the Reynolds number is 2.28. The number and

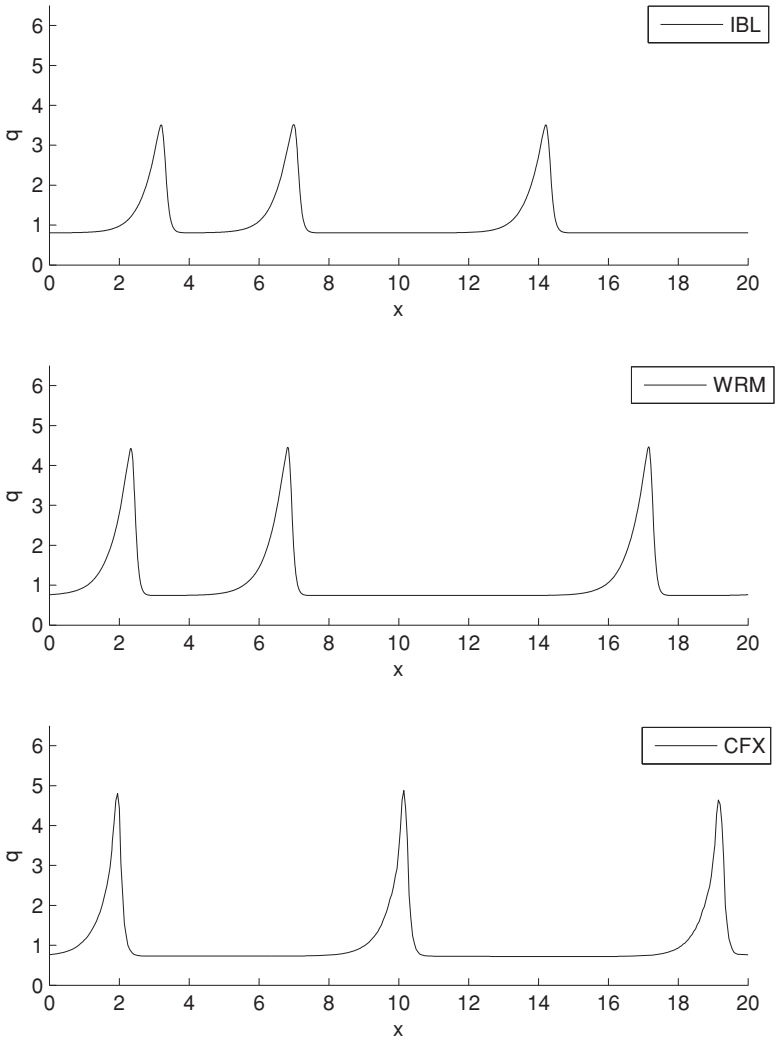

Figure 3: Fully developed roll waves for the IBL model, the WRM, and CFX; volume flow rate versus position along domain.

height of roll waves emerging from the weighted residual and integral-boundary-layer models are shown in Figure 3, where the non-dimensional volume flow rate is plotted against the position along the domain. The calculations for the same flow, resulting from the full Navier-Stokes equations using CFX, are also shown in Figure 3. Figure 4 shows the fluid height and bottom topography for both models and the CFX results, for the same set of parameters.

Comparing the figures, it can be seen that both the integral-boundary-layer and the weighted residual models correctly predict the number of roll waves in the

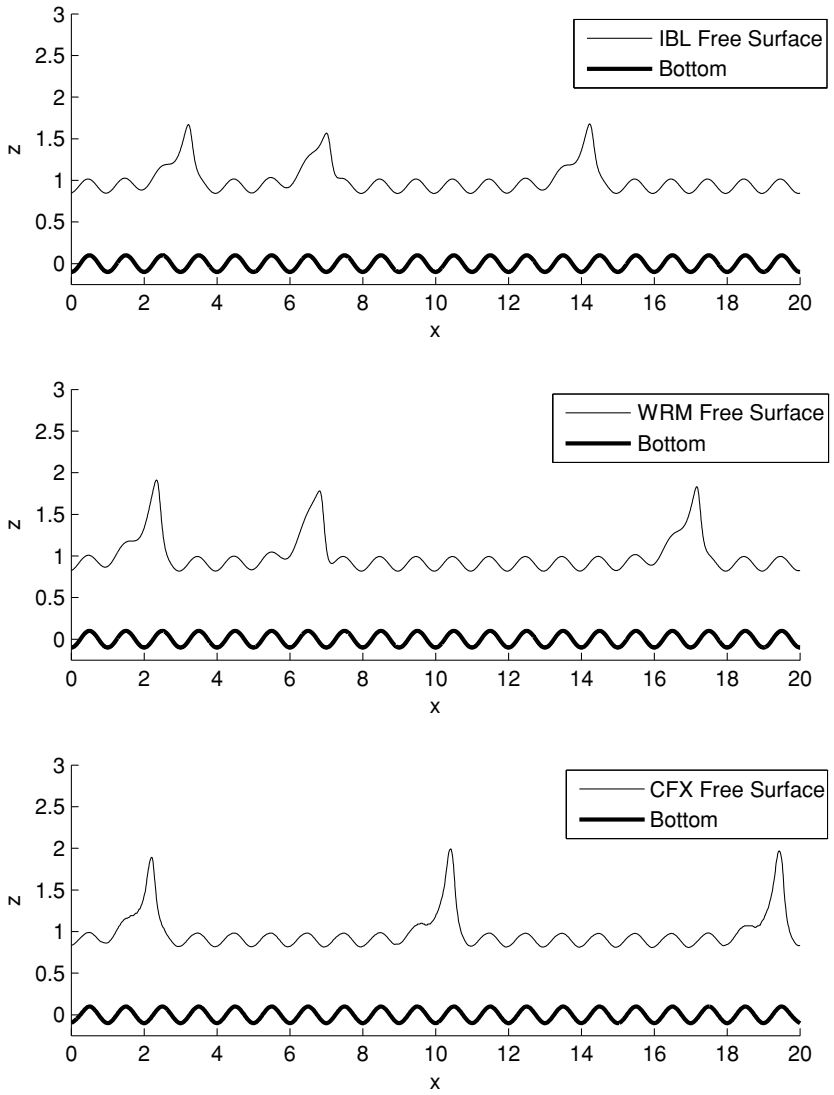

Figure 4: Fully developed roll waves for the IBL model, the WRM, and CFX; fluid height versus position along domain.

Comparing the figures, it can be seen that both the integral-boundary-layer and the weighted residual models correctly predict the number of roll waves in the domain. However, the weighted residual model more closely predicts the height of the waves.

For the case shown in Figure 3, tall sharp peaks emerge. If surface tension would have been included, the waves that would develop would be smoother and

Table 1: Comparison between experimental, numerical and theoretical values of Re_{crit} for a wavy-incline case with $\delta = 0.1$.

θ	Re_{crit}^{even}	Re_{crit}		
		Experimental	Numerical	Theoretical
15°	3.3	5.1 ± 0.4	(5.5,5.6)	5.6
30°	1.4	2.2 ± 0.2	(1.8,1.9)	1.7
40.7°	0.97	1.3 ± 0.1	(1.1,1.2)	1.1

wider. Surface tension and bottom topography also affect the stability of the flow by altering the critical Reynolds number. D'Alessio et al. [2] have shown that for small to moderate surface tension, bottom topography increases the critical Reynolds number of the flow while for larger surface tension and topography, the opposite occurs.

As a final confirmation of the validity of the weighted residual model, critical Reynolds number predictions are compared to experimental data for a wavy incline, collected by Wierschem et al. [5]. Table 1 contrasts the experimentally obtained critical Reynolds numbers with those from the weighted residual model for three different angles of inclination. Presented in the table are results from the numerical simulations along with theoretical values obtained from a linear stability analysis of the weighted residual model. Also listed in the table is Re_{crit}^{even}, the corresponding critical Reynolds number for an even bottom. The table shows that numerical predictions are almost all within the error of the experiment, and in close agreement with the theoretical values. This further demonstrates that the weighted residual model is the optimal model for flow over an incline with or without bottom topography.

4 Summary

This study compared the performance of three models for free surface flow down a wavy inclined plane. The simplest model is the shallow-water model, and it gives the poorest agreement with theory and experiments. The integral-boundary-layer model provides much better predictions in both areas, although the critical Reynolds number still does not match the theoretical value for an even bottom. The weighted residual model exactly predicts the theoretical critical Reynolds number, and also matches the experimental neutral stability curve very closely.

The integral-boundary-layer and weighted residual models were solved numerically and compared to direct numerical simulations of the full Navier–Stokes solutions, obtained using CFX. The weighted residual model performs slightly better than the integral-boundary-layer model since it yields better agreement in the height of the peaks.

Finally, the weighted residual model gives good predictions for the critical Reynolds number for flow over a wavy surface when compared to experimental data. Considering all four methods of comparison, the weighted residual model gives the best results over all.

Acknowledgements

Financial support for this research was provided by the Natural Sciences and Engineering Research Council of Canada.

References

[1] Balmforth, N. J. & Mandre, S., Dynamics of roll waves, *J. Fluid Mech.* **514**, pp. 1-33, 2004.
[2] D'Alessio, S.J.D., Pascal, J.P. & Jasmine, H., Instability in gravity-driven flow over uneven surfaces, *Physics of Fluids* **21**, pp. 062105-1 - 062105-11, 2009.
[3] Ruyer-Quil, C. & Manneville, P., Further accuracy and convergence results on the modeling of flows down inclined planes by weighted residual approximations, *Physics of Fluids* **14**, pp. 170-183, 2002.
[4] Liu, J., Paul, J.D. & Gollub, J.P., Measurements of the primary instabilities of film flows, *J. Fluid Mech.* **250**, pp. 69-101, 1993.
[5] Wierschem, A., Lepski, C., Aksel, N., Effect of long undulated bottoms on thin gravity-driven films, *Acta Mechanica* **179**, pp. 41-66, 2005.
[6] Benjamin, T.B., Wave formation in laminar flow down an inclined plane, *J. Fluid Mech.* **2**, pp. 554-574, 1957.
[7] Yih, C-S., Stability of liquid flow down an inclined plane, *The Physics of Fluids* **6**, pp. 321-334, 1963.
[8] ANSYS, Inc., *ANSYS CFX Solver Theory Guide, ANSYS CFX Release 11.0*, ANSYS Europe, Ltd, 2006, pp. 277-295.
[9] Zwart, P.J., Numerical modelling of free surface and cavitating flows, *VKI Lecture Series*, ANSYS Canada Ltd, 2005.
[10] LeVeque, R. J., *Finite volume methods for hyperbolic problems*, Cambridge University Press, Cambridge, UK, 2002.

This page intentionally left blank

Sizing of a plastic chamber with air-filled balls for water hammer control

A. Al-Khomairi & S. Ead
Civil Engineering Department, King Saud University, Saudi Arabia

Abstract

Water hammer in pipelines and pipe networks can result in pipe and equipment failures and economical/environmental losses. The use of a piece of flexible plastic pipe for water hammer control is discussed and experimental data for the use of such a device are presented. The device, referred to as a plastic chamber, reduces pressures resulting from water hammer. The flexibility of the plastic chamber allows radial expansion of its walls under pressure to accommodate the excess fluid and thereby reduce water hammer-induced pressure spikes. To enhance the performance of the plastic chamber, air-filled balls are inserted into the chamber. When a sudden pressure increase takes place, the air-filled balls shrink to reduce the pressure surge. Previous experimental data on the use of the plastic chamber and the air-filled balls (inserted in a rigid chamber) are analyzed. The effect of the plastic chamber on the reduction of water hammer was formulated as a function of a dimensionless parameter related to the plastic chamber and the pipe for which water hammer is to be controlled. Furthermore, the effect of the air-filled balls was formulated and found to be a function of an analogous dimensionless parameter related to the volume/inside pressure of the balls and pipe parameters. The two effects were combined in an empirical formula for the total reduction of water hammer when using a plastic chamber with air-filled balls. The procedure allows the required water hammer reducing device to be sized to achieve a target reduction of water hammer based on the parameters of the pipe, the plastic chamber and the air-filled balls.

Keywords: unsteady pipe flow, water hammer control, surge pressure control, water hammer damping.

WIT Transactions on Engineering Sciences, Vol 69, © 2010 WIT Press
www.witpress.com, ISSN 1743-3533 (on-line)
doi:10.2495/AFM100271

1 Introduction

Water hammer in pipelines and pipe networks can result in huge economical and/or environmental losses. Sudden valve closure, for instance, can generate high-pressure spikes that can damage the pipe and pipe equipment. Several methods have been used to control water hammer and reduce its effect on pipe networks. These include surge vessels, equilibrium tanks, pressure relief valves and suction lines around a booster pump. Other methods used for water hammer control for residential, commercial and light industrial applications include air chambers and water hammer arrestors. An air chamber consists of a short vertical section of pipe that is filled with trapped air. When a water hammer shock occurs, the air chamber acts as a shock absorber. After some time, the water pressure causes the air pocket to be absorbed by water rendering the device ineffective, and the water needs to be drained out of the device. A water hammer arrestor is similar to an air chamber but the air pocket in the arrestor is separated and sealed from the water by a piston with an "O" ring or diaphragm so that the air cannot be absorbed by water. The disadvantage of this device is that the moving piston makes it noisy.

Grundy and Fox [1] suggested the installation of in-line highly deformable tubes to reduce the effect of water hammer. Insertion of a high-density polyethylene (HDPE) polymeric pipe has also been suggested for water hammer suppression in simple pipe system [2]. Pezzinga [3] expanded on the topic by considering a polymeric pipe insertion in a pipe network. Al-Khomairi [4] provided a method of sizing the polymeric pipe insertion for a target water hammer reduction based on the parameters of the pipe and the insertion pipe. Different pipe sizes and insertion parameters/materials were considered. Al-Khomairi [5] presented a method using air-filled balls in a steel chamber for water hammer reduction. A steel chamber was used rather than a plastic chamber to isolate the effect of the chamber from the effect of the air-filled balls. This method also allows sizing of the pipe to achieve a target reduction in water hammer.

Al-Khomairi [4] showed that the ability of the polymeric pipe to reduce water hammer is a function of a dimensionless parameter R_D as follows:

$$R_D = \frac{\Delta \forall_D}{\Delta \forall_{max}} = \frac{1}{2}\frac{\rho a^2}{E_D}\frac{D_D}{e_D}\frac{\forall_D}{\forall_P}, \tag{1}$$

where ρ is the fluid density, a is the pressure wave velocity in the pipe, E_D is Young's modulus of elasticity for the polymeric pipe insertion, D_D is the diameter of the polymeric pipe insertion, a_D is the pressure wave velocity in the polymeric pipe insertion, $\forall_D$ is the volume of the polymeric pipe insertion, $\forall_P$ is the pipe volume and $\Delta\forall_D$ is the increase in volume of the polymeric pipe insertion due to a Δp increase in pressure. $\Delta\forall_{max}$ is the maximum fluid volume to be admitted for complete elimination of water hammer (during a time interval equal to $2L/a$) and is given by:

$$\Delta \forall_{\max} = Q, \quad t = Q(2L/a), \tag{2}$$

where Q is the discharge, t is the time required for the pressure wave to travel from the control valve to hit the boundary and come back to the valve, L is the pipe length and a is as defined earlier.

When using air-filled rubber balls inserted in a rigid steel chamber, this assembly works as a surge pressure absorber. To allow the pressure inside the balls to increase without affecting their volume, the balls are inserted in spherical retaining meshes before being inserted in the chamber. The device can be installed at the location expected to experience the most severe transient event (e.g., just upstream of a control valve) using a T connector with the pipe. Al-Khomairi [5] established a formula that relates the reduction in water hammer when using this device assembly to a function of a dimensionless parameter R_B (analogous to R_D discussed earlier) and is given by:

$$R_B = \frac{\Delta \forall_B}{\Delta \forall_{\max}}, \tag{3}$$

where $\Delta \forall_{\max}$ is as defined earlier and $\Delta \forall_B$ is the change in the volume of the ball(s) due to an increase in system pressure. The following equation has been developed by Al-Khomairi [5] to obtain $\Delta \forall_B$:

$$\Delta \forall_B = (h_{atm} + \Delta h)\forall_0 \left(\frac{1}{h_{P1} + h_{atm}} - \frac{1}{h_{P2} + h_{atm}} \right), \tag{4}$$
$$h_{P1} \text{ and } h_{P2} \text{ (gage)} \geq \Delta h,$$

where h_{atm} is the local atmospheric pressure head, Δh is the excessive amount of pressure head in the ball ($h_1 - h_0$), h_1 is the gage pressure head inside the ball as pre-determined from the experimental work, h_0 is the gage pressure head inside the ball when the ball is pressurized until it completely fills the spherical retaining mesh without exerting pressure on it, V_0 is the volume of the ball associated with h_0, h_{p1} is the steady-state system hydrostatic pressure head and h_{p2} is the pressure head following the spike caused by surge pressure.

The reduction in water hammer-induced pressure surges due to the use of a water hammer absorber is given by:

$$r = \frac{\Delta h_{WO} - \Delta h_W}{\Delta h_{WO}}, \tag{5}$$

where r is the fraction by which water hammer is reduced, Δh_{WO} is the pressure head increase due to water hammer evaluated when no device for water hammer reduction is used and Δh_W is the pressure head increase due to water hammer evaluated when the device for water hammer reduction is used to absorb the surge pressure.

To optimize the performance of the device, the two devices mentioned earlier can be combined by inserting plastic rubber balls (with retaining steel meshes) in a plastic chamber. Both the balls and the plastic chamber contribute to the performance of the device in water hammer mitigation. Thus, the water hammer reduction when using air-filled balls inserted in a plastic chamber is a function of R_D and R_B:

$$r = f(R_D, R_B). \tag{6}$$

2 Experimental setup

Two experimental runs were conducted for this study. A single-pipe system consisting of a recirculation tank, upstream pump, pipe, downstream control valve and pressure/flow measurements was used to conduct an extreme transient event experiment. Fig. 1 shows the experimental setup. The experimental work in this study was performed using the same apparatus used by Al-Khomairi [4]. The system and device parameters for the experimental work are: V (fluid velocity) = 2.88 m/s, Q = 76 lpm, D = 23.65 mm, L = 17.23 m, D_D = 110 mm, e_D = 3.2 mm, L_D (chamber length) = 700 mm and $E_D = 3.14 \times 10^9$ Pa. The chamber material used was uPVC. No air-filled balls were inserted in the plastic chamber. Using this experimental setup, fig. 2 shows the variables associated with eqn (5). Fig. 2(a) shows the transient event history following sudden and full closure of a downstream control valve without using a water hammer control device. Fig. 2(b) shows an identical transient event using a plastic chamber for water hammer control. It is clear that a pressure head spike as high as 218 m without the use of a chamber was reduced to 135 m when using the device.

Figure 1: The experimental setup.

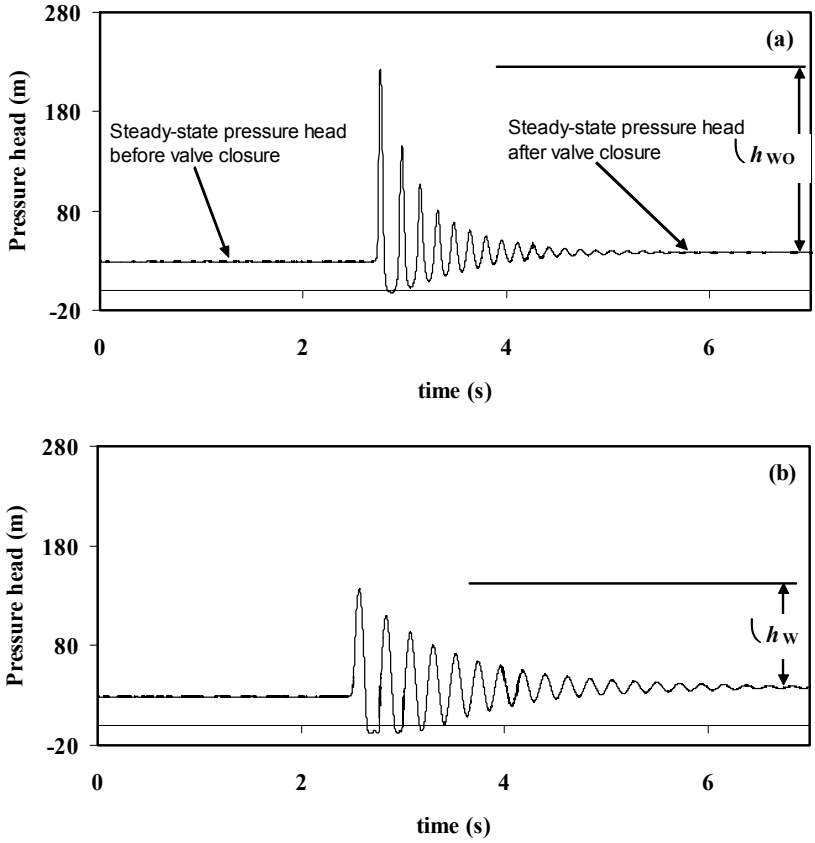

Figure 2: Pressure head history for a severe transient event: (a) without a plastic chamber and (b) with a plastic chamber.

3 Empirical formula

The empirical formula that was obtained in this study for the plastic chamber, the air-filled rubber balls and the combined effect of the two systems is explained in this section. Al-Khomairi [4] generated 69 data points using extensive experimental work to relate the ability of the plastic water hammer control device to reduce pressure surges to the dimensionless parameter R_D. To generate these data, the plastic chamber and the main pipe parameters were varied and included a wide range of parameter values. An analogous study [5] generated 86 data points relating the performance of the air-filled rubber balls to dimensionless parameters consisting of the relevant pipe and ball parameters. The water hammer reduction in this case was related to the dimensionless

parameter R_B. Inspecting the data for both studies revealed that a logarithmic trend line is the best-fit curved line to represent the data. Using regression analysis the empirical equation for the plastic chamber device is as follows:

$$r_D = 17.997 \ln(R_D) + 44.747, \tag{7}$$

where r_D is the % reduction in water hammer when using the plastic chamber for water hammer control and R_D is the dimensionless parameter associated with the chamber and the pipe as revealed in eqn (1).

By analogy, using regression analysis for air-filled balls placed in a rigid (steel) chamber, the following empirical equation is achieved for the device performance:

$$r_B = 11.488 \ln(R_B) + 62.968, \tag{8}$$

where r_B is the % reduction in water hammer when the device with air-filled balls is used to control water hammer and R_B is a dimensionless parameter representing the balls and pipe parameters as shown in eqn (3). Figs. 3 and 4 depict the resulting regression curves for the plastic chamber and the air-filled balls, respectively. It is logical that for both curves, with increased R_B or R_D, the reduction in water hammer approaches 100%.

It is possible to predict the performance of air-filled balls installed in a plastic chamber by combining the outcome of the two studies. The following equation can be used to find the combined reduction for the air-filled balls inserted in a plastic air chamber:

$$r_T = \left(1 - (1 - 0.01 r_D)(1 - 0.01 r_B)\right) \times 100, \tag{9}$$

where r_T is the total % reduction using the device that combines air-filled balls with a plastic chamber.

For example, a reduction of 30% by the plastic chamber and 40% by the air-filled balls means a reduction of 58% if the air-filled balls are placed in the plastic chamber.

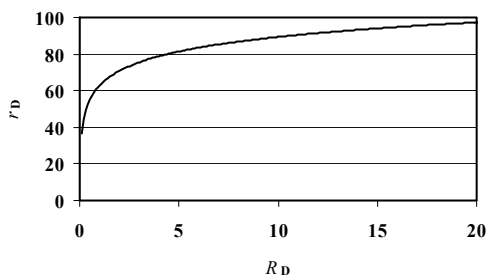

Figure 3: Pipe and plastic chamber: dimensionless parameter (R_D) versus % reduction (r_D) in water hammer-induced pressure surge.

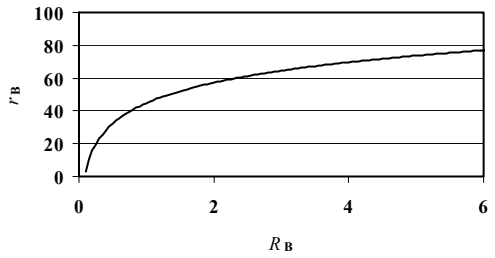

Figure 4: Pipe and air-filled balls: dimensionless parameter (R_B) versus % reduction (r_B) in water hammer-induced pressure surge.

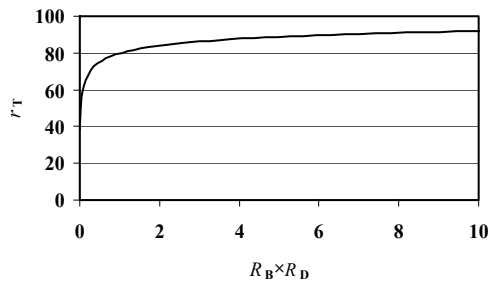

Figure 5: Percentage reduction in water hammer (r_T) due to the combined effect of air-filled balls (R_B) and the plastic chamber (R_D).

Plotting the product of the two variables, $R_D \times R_B$ versus the total reduction (r_T) provides a relationship between the parameters of the plastic chamber, air-filled balls (and pipe) and the total % reduction achieved by the device with the plastic chamber and the air-filled balls. Fig. 5 was obtained using the data from fig. 3, fig. 4 and eqn (9). The r_T axis scale was limited to a value of 10 to show a clearer picture of how the reduction changes for low $R_D \times R_B$ values. Fig. 5 can be used to predict the performance of the water hammer reducing device when air-filled balls are inserted in the plastic chamber. For example, computation of R_D and R_B based on the parameters of the pipe, plastic chamber and the balls allows one to use the curve to read the corresponding % reduction (r_D) for the device. Furthermore, it is possible to design a device with a plastic chamber and air-filled balls for a target % total reduction (r_T) value. From fig. 5 and a target r_T value, the corresponding $R_D \times R_B$ value can be read from the graph. The values of the parameter(s) that give the same $R_D \times R_B$ value can be selected. For example, if the parameters for the plastic chamber are fixed because of space limitations, the ball volume/pressure that would result in the required $R_D \times R_B$ value can be selected. It is also possible to use eqns (7), (8) and (9) instead of fig. 5 to determine the required parameters. If a plastic chamber is used without air-filled balls, eqn (7) or fig. 3 can be used to determine the design parameters.

However, eqn (8) or fig. 4 can be used for the analysis/design if air-filled balls are used in a rigid (e.g., steel) chamber for water hammer control.

4 Conclusions

The results of water hammer control in pipelines using two different methods are presented and analyzed. The first method uses a plastic chamber with a diameter much larger than the pipe for which water hammer is to be controlled. In the second method, air-filled rubber balls are inserted into a rigid (steel) chamber. Laboratory tests performed in earlier studies for both methods were analyzed. Regression analysis was performed on the data to achieve the most accurate empirical formula to determine the ability of each device to reduce water hammer as a function of dimensionless parameters related to the pipe, balls and plastic chamber.

A more effective method for water hammer mitigation would be to combine the effect of the two methods by inserting the air-filled rubber balls into a plastic chamber. An empirical formula was devised for the combined effect of the two methods on water hammer reduction. Equations and figures were established for each method and for the combined method to analyze device performance based on given pipe, balls and chamber pipe parameters. A target water hammer reduction can be achieved using these formula and graphs to design the device.

References

[1] Grundy, A.K. & Fox, J.A. The effect of compressible pipeliners on pressure transient generation. *Proceedings of the 3rd International Conference on Pressure Surges*. BHRA: Cranfield, UK, pp. 241–260, 1980.
[2] Pezzinga, G. & Scandura, P. Unsteady flow in installation with polymeric additional pipe. *Journal of Hydraulic Engineering* 121(11), pp, 802–811, 1995.
[3] Pezzinga, G. Unsteady flow in hydraulic networks with polymeric additional pipe. *Journal of Hydraulic Engineering 128(2)*, pp. 238–244, 2002.
[4] Al-Khomairi, A.M. Plastic water hammer damper. *Journal of Pipeline Systems Engineering and Practice* (submitted for publication).
[5] Al-Khomairi, A.M. Surge pressure suppression in pipelines using air-filled balls. *Journal of King Abdulaziz University* (submitted for publication).

Capture flows of funnel-and-gate reactive barriers without gravel packs

H. Klammler[1,2,3], K. Hatfield[1,2] & A. Kacimov[4]
[1]*Department of Civil & Coastal Engineering, University of Florida, USA*
[2]*Inter-Disciplinary Program in Hydrologic Science, University of Florida, USA*
[3]*Department of Environmental Science & Sustainable Development, Fed. University Bahia, Brazil*
[4]*Department of Soils, Water & Agricultural Engineering, Sultan Qaboos University, Oman*

Abstract

Permeable reactive barriers (PRBs) are a passive in-situ technology, which is based on the interception and physical, chemical and/or biological remediation of a contaminant plume through installation of reactive material in an aquifer. Previous work of the authors includes analytical approaches in two dimensions (horizontal plane) based on the conformal mapping technique that allows for the determination of the groundwater flow fields and capture zones of PRBs of different types. Solutions assume that the permeability k_r of the reactive material itself is high with respect to the surrounding aquifer permeability k_a or that highly permeable gravel packs are present to equilibrate the hydraulic heads at the up and down-gradient faces of the reactor. Respective results include a simple relationship $Q(R)$ between capture flow Q and reactor Darcian hydraulic resistance R. Based on the same technique, the present work gives an exact solution for funnel-and-gate (FG) and velocity equalization wall (VEW) PRBs without gravel packs for the particular case of $k_r = k_a$. Furthermore, a numerical finite difference study is performed to show that $Q(R)$ is a good approximation (with errors in the 1% range of maximum capture flow $Q(0)$) for FG and VEW

WIT Transactions on Engineering Sciences, Vol 69, © 2010 WIT Press
www.witpress.com, ISSN 1743-3533 (on-line)
doi:10.2495/AFM100281

PRBs of arbitrary geometric configurations and arbitrary values of k_r/k_a, even in the absence of highly permeable gravel packs at the reactor entrance and exit faces.

Keywords: PRB, groundwater, aquifer, contaminant plume, passive remediation, conformal mapping, Schwarz-Christoffel.

1 Introduction

Subsurface contaminant plumes transported by the (natural or induced) flow of groundwater represent a serious threat to ecosystems and human drinking water supplies. As opposed to hydraulically active pump-and-treat systems for contaminant remediation at the ground surface, [1], permeable reactive barriers (PRBs) are a passive technology, which has been successfully employed for in-situ remediation of contaminant plumes through installation of reactive materials in the pathway of a plume, [2]. Actual remediation may hereby be based on physical, chemical and/or biological processes during the residence/travel time of a contaminant particle inside the reactor. Critical parameters in PRB design and operation are (1) the capture flow or width, which determine the portion of groundwater flow and, hence, of the contaminant plume captured for treatment, as well as (2) contaminant residence time inside the reactor, which is directly related to the degree of remediation before initially contaminated groundwater exits the PRB and re-enters the aquifer. A variety of methods exist to optimize these two parameters under different conditions, two of which are represented in fig. 1. In the funnel-and-gate configuration (FG; fig. 1(a); [3]), impermeable funnel arms are deployed laterally extending into the aquifer in order to increase

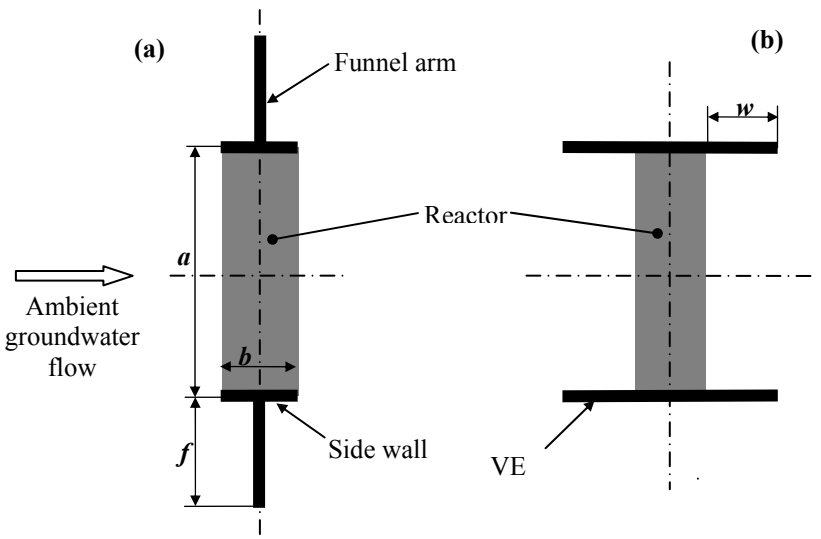

Figure 1: Horizontal cross sections (plan views) of (a) an FG and (b) a VEW PRB.

capture width for a given reactor. Alternatively, velocity equalization walls (VEWs; fig. 2(b); [4]) may be used to achieve more uniform contaminant residence time distribution across the reactor by avoiding flow singularities (i.e., the blow-up of the magnitude of the hydraulic gradient) near the reactor and, thus, providing largely uniform flow into, across and out of the reactor.

While numerical studies are more abundant in literature, e.g., [3, 4], previous work by the authors, [5–7], investigates different hydraulic aspects of these PRB configurations in a two-dimensional (horizontal) analytical framework by applying the theory of holomorphic functions, in particular, the conformal mapping technique. However, for arbitrary reactor conductivities results are valid only in the presence of highly permeable gravel packs at the up and down-gradient faces of the reactor, which provide for constant hydraulic head distributions throughout the gravel packs and, thus, strictly uniform flow across the reactor. The present work follows this conformal mapping approach and presents an exact analytical solution for the FG and VEW configurations of fig. 1 and the particular case of the reactor hydraulic conductivity k_r [L/T] being equal to the surrounding (homogeneous) aquifer conductivity k_a [L/T] without, however, assuming the presence of highly permeable gravel packs. Based on this exact solution and results of Klammler and Hatfield [5] for arbitrary k_r in the presence of gravel packs, an approximate solution is further presented for the capture flows of FG and VEW PRBs without gravel packs and for arbitrary k_r/k_a. The performance of the approximation is systematically validated against output from a numerical finite difference model (MODFLOW).

2 Theoretical approach

2.1 Exact solution for FG/VEW PRBs without gravel packs and $k_r = k_a$

Assuming that vertical flow components in a homogeneous aquifer and PRB reactor may be neglected (i.e., PRB structure stretching over full aquifer thickness) the flow field in the vicinity and inside a FG PRB of $k_r = k_a$ reduces to two-dimensional flow around the impermeable funnel and side wall structure of fig. 1a. By further assuming that the undisturbed flow field in the aquifer before PRB implementation is uniform with boundaries far away the boundary conditions at the PRB result as illustrated in figs. 2a and 2b for flow in x and y-directions (as indicated by the bold arrows), respectively. q_x and q_y [L^2/T] hereby denote the undisturbed depth integrated ambient groundwater fluxes far from the PRB. Due to symmetry, only the upper half plane is depicted, where thick continuous lines represent impermeable boundaries, thick dotted lines represent constant head boundaries and $z = x + iy$ [L] is the complex coordinate system of the physical plane ($i = \sqrt{-1}$ being the imaginary unit). Capital letters denote points (vertices) on the boundary of the flow domain (E_∞ being the point at infinity), which is symmetric about both the horizontal and vertical axes indicated in fig. 1. Shaded rectangles in figs. 1 and 2 are used to represent the reactor of width a [L] and length (in design flow direction) b [L]. f [L] denotes the length of a funnel arm. Since $k_r = k_a$ is assumed here, the exact shape of the reactor does not affect the resulting flow field as long as the impermeable funnel

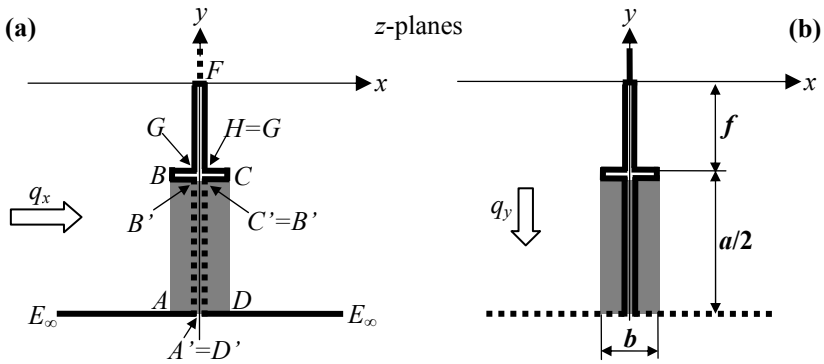

Figure 2: Boundary conditions in the physical z-plane for FG PRB with $k_r = k_a$ and flow in (a) x-direction and (b) y-direction.

structure is not modified. As a consequence, the VEW configuration of fig. 1b does not have to be treated separately and may be regarded as a particular case of the FG configuration with $f = 0$, for which flow always remains undisturbed (i.e., uniform) after PRB installation.

By applying the Schwarz-Christoffel function as discussed in Klammler and Hatfield [8] the flow domain above the boundaries of the z-plane in figs. 2a and 2b may be obtained by conformal mapping of the upper (auxiliary) τ_1-half-planes from figs. 3a and 3b, respectively, through

$$z(\tau_1) = c\int_0^{\tau_1} \frac{(\tau-\tau_{1B})(\tau-\tau_{1F})(\tau-\tau_{1C})}{\sqrt{(\tau-\tau_{1A'})(\tau-\tau_{1B'})(\tau-\tau_{1G})(\tau-\tau_{1H})(\tau-\tau_{1C'})(\tau-\tau_{1D'})}}\,d\tau. \qquad (1)$$

$\tau_{1A'}$ [-] hereby denotes the coordinate of vertex A' on the η_1-axis in figs. 3a and 3b, for example, and c [L] is a positive real scaling constant (no rotation between the τ_1 and z-planes). Adopting the lower integration limit in eqn. 1 as zero results in $\tau_{1F} = 0$ and symmetry further implies $-\tau_{1A'} = \tau_{1D'} = 1/k$, $-\tau_{1B'} = \tau_{1C'} = 1$, $-\tau_{1B} = \tau_{1C}$ and $-\tau_{1G} = \tau_{1H}$ with c accounting for the scaling imposed to achieve $\tau_{1C'} = 1$. With k [-] being a PRB shape parameter (so-called affix) in the sense of previous work, e.g., [5–7], eqn. 1 may be rewritten as

$$z(\tau_1) = c\int_0^{\tau_1} \frac{(\tau^2-\tau_{1C}^2)\tau}{\sqrt{\left(\tau^2-\frac{1}{k^2}\right)(\tau^2-1)(\tau^2-\tau_{1H}^2)}}\,d\tau, \qquad (2)$$

which may be reduced to an elliptic integral by substituting $u = \tau^2$. The unknown mapping parameters c, k, τ_{1C} and τ_{1H} may be determined by constructing a system of four non-linear equations by prescribing the physical coordinates of vertices A', B', B and G, for example. However, closed form solutions are generally difficult to obtain (this is known as the Schwarz-Christoffel parameter problem)

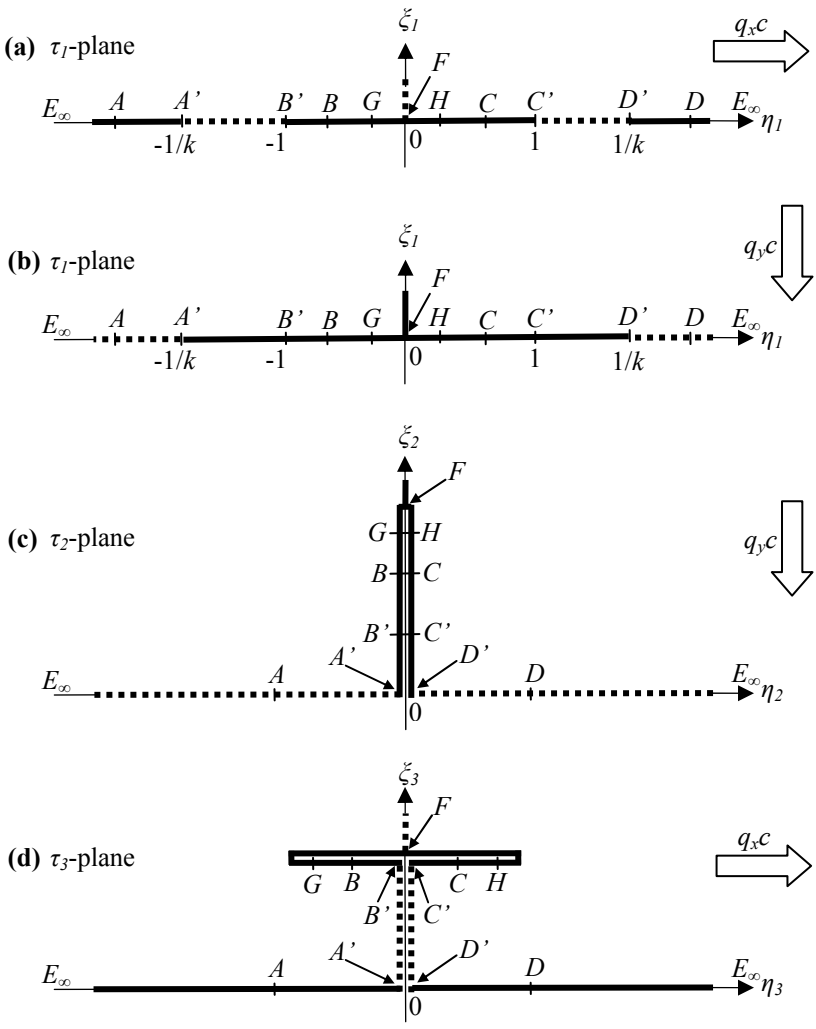

Figure 3: Boundary conditions in the τ_1, τ_2 and τ_3-planes for flow in x and y-directions.

and a Schwarz-Christoffel mapping toolbox [9] for MATLAB is used in the sequel to solve for the mapping parameters and to perform the mapping process (i.e., numerical evaluation and inversion of eqn. 2).

With this, the locations of all vertices in the τ_1-plane and the scaling constant c are known. Due to the fact that eqn. 2 stretches the flow domain at infinity by a factor of c ($dz/d\tau_1 = c$ for $\tau_1 \to \infty$) and in order to maintain continuity of flow between mapping planes, the magnitudes of the far fields (i.e., ambient fluxes q_x and q_y) are adjusted to cq_x and cq_y in the τ_1-plane of figs. 2a and 2b, respectively. By applying the mapping function

$$\tau_2(\tau_1) = \sqrt{\tau_1^2 - \frac{1}{k^2}}, \tag{3}$$

and regarding solutions of the square root in the upper τ_2-half-plane the flow domain of fig. 3c is obtained, which contains uniform flow in the y-direction. The corresponding complex potential may thus be written as

$$\Phi_y + i\Psi_y = q_y c i \tau_2, \tag{4}$$

where Φ_y and Ψ_y [L^3/T] are the potential and stream functions for flow in y-direction, respectively.

From Klammler and Hatfield [5; their figs. A1a and A1b] it is known that the τ_3-plane of fig. 3d may be obtained by

$$\tau_3(\tau_1) = \frac{1}{k}\left[E(\tau_1, k) - \frac{E(k)}{K(k)} F(\tau_1, k)\right], \tag{5}$$

where $K(k)$ and $F(\tau_1,k)$ are the complete and incomplete elliptic integrals of the first kind, respectively, and $E(k)$ and $E(\tau_1,k)$ are the complete and incomplete elliptic integrals of the second kind, respectively. The mapping parameter k is the so-called modulus of the elliptic integrals, [10]. The τ_3-plane meets the boundary conditions for uniform flow in x-direction and the corresponding complex is

$$\Phi_x + i\Psi_x = q_x c \tau_3. \tag{6}$$

The solutions of eqns. 6 and 4 are graphically represented in figs. 4a and 4b, respectively, in the form of flow fields for an example PRB of $b/a = 0.5$ and $f/a = 1$. Stream lines of constant Ψ are depicted as continuous, potential lines of constant Φ as dotted and stream lines delimiting the capture zone are bold. The flow field in fig. 4c for an arbitrary flow direction ($q_x = 2q_y$) is obtained by superposition (summation) of eqns. 4 and 6, which is a direct consequence of linearity of the governing Laplace equation for Φ and Ψ. It is seen that the solution not only consists of the flow field in the aquifer, but also the flow field inside the reactor (e.g., *ABCD* in fig. 2), which may be of interest for computation of contaminant residence times inside the reactor by the method of Klammler et al. [7].

Knowing that an ambient groundwater flow component q_y does not drive any flow across the reactor (i.e., across *A'B'* in fig. 2), the capture flow Q [L^3/T] is obtained as [5]

$$Q = \frac{q_x c \pi}{k K(k)}. \tag{7}$$

The thick continuous lines in fig. 5 depict the dimensionless capture width $Q/(aq_x)$ based on eqn. 7 as a function of b/a and f/a. As intuitively expected, $Q/(aq_x)$ increases as the relative funnel length f/a increases, independent of the reactor size b/a. In contrast, independent of f/a the dimensionless capture width

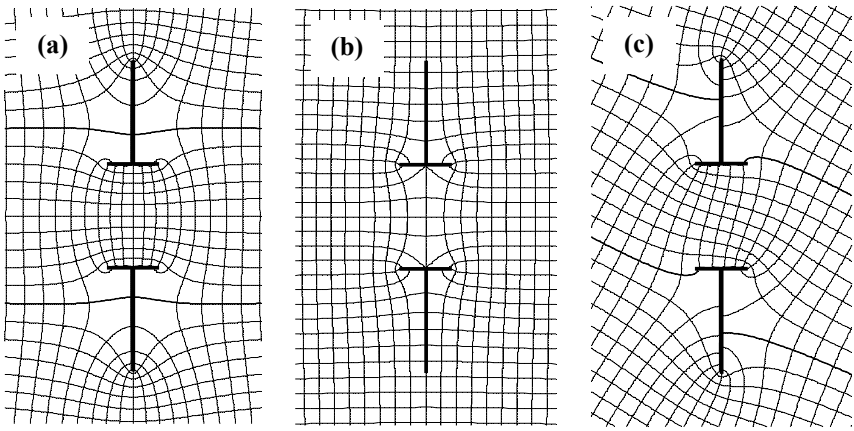

Figure 4: Example of flow nets for flow in (a) x-direction, (b) y-direction and (c) direction characterized by incident flow of $q_x = 2q_y$. b/a = 0.5 and f/a = 1.

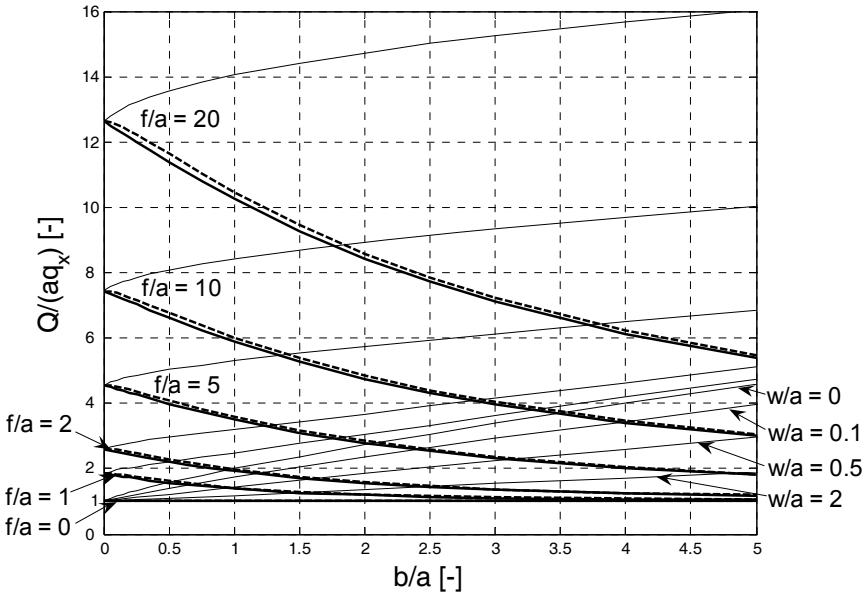

Figure 5: Dimensionless capture width $Q/(aq_x)$ as a function of b/a and f/a for $k_r = k_a$ and no gravel packs (thick continuous), $k_r = k_a$ with gravel packs (thick dashed) and $k_r >> k_a$ (thin continuous).

decreases with increasing b/a, i.e., as the impermeable side walls become longer. For $f/a << b/a$ the FG configuration approaches the VEW configuration of fig. 1b with $w = 0$ (or even w > 0 as long as $k_r = k_a$) and $Q/(aq_x)$ approaches unity.

2.2 Approximate capture flow for FG/VEW PRBs without gravel packs and arbitrary k_r/k_a

In general, and contrary to the assumption of the previous section, PRB reactors possess hydraulic conductivities different from the aquifer. For example, $k_r > k_a$ is typically a design goal in order to facilitate plume catchment, i.e., to increase Q. On the other hand, $k_r < k_a$ may be the case if reactive material is installed by direct subsurface injection instead of previous excavation. In addition to the exact solution of the previous section for $k_r = k_a$, an exact solution is known for $k_r >> k_a$, i.e., when the reactor itself is highly permeable. In this case it does not matter whether a gravel pack is actually deployed or not and the solution of Klammler and Hatfield, [5], as illustrated by the thin continuous lines in fig. 5 is directly applicable. Another exact solution may be obtained by the present approach for the absence of gravel packs and $k_r << k_a$. While this situation is obviously irrelevant for practice (impermeable reactor) it is noted that the presence or not of gravel packs in this case does not affect the capture flow $Q = 0$. Thus, in terms of capture flow, the solution of Klammler and Hatfield, [5], which considers the presence of head equilibrating gravel packs, is exactly valid in the limits of $k_r >> k_a$ and $k_r << k_a$, independent of the deployment or not of gravel packs.

For the intermediate case of $k_r = k_a$, fig. 5 compares dimensionless capture flows for no gravel packs (thick continuous lines; previous section) and with gravel packs (thick dashed lines; [5]). Maybe not so unsurprisingly, the agreement is very good with a maximum relative difference of approximately 3% for $b/a \approx 0.5$ and $f/a \approx 1$. The corresponding flow field for this "worst case" configuration is depicted in fig. 4a, where potential lines confirm a relatively constant head along the reactor-aquifer interfaces (i.e., *AB* and *CD* in fig. 2) even without deploying highly permeable gravel packs. Of course, this observation does not hold any longer in the presence of a significant flow component q_y, which, however, does not affect Q. Away from this worst case parameter configuration the influence of gravel packs on Q for $k_r = k_a$ becomes even smaller and goes to zero for either b/a, a/b, f/a or a/f approaching zero.

Based on the above observations that capture flow Q for FG and VEW PRBs without gravel pack is identical to or well approximated by Q of respective PRB types with gravel packs for the three cases of $k_r << k_a$, $k_r = k_r$ and $k_r >> k_a$, we propose that Q in the absence of gravel packs and for arbitrary k_r/k_a may be approximated by

$$Q \approx Q_{max} \frac{K(k_{gp})}{K(k_{gp})+RK(k_{gp'})} \tag{8}$$

as derived by Klammler and Hatfield, [5], for PRBs with gravel packs. Q_{max} is hereby the maximum capture flow corresponding to $k_r >> k_a$ (thin continuous

lines in fig. 5), $R = bk_a/(ak_r)$ [-] is a dimensionless hydraulic resistance of the reactor and k_{gp} [-] is the shape factor for PRBs with gravel packs from Klammler and Hatfield, [5; their fig. 4]. k_{gp} is used as the modulus of the complete elliptic integral or the first kind $K()$ in eqn. 8 with $k_{gp}' = \sqrt{1 - k_{gp}^2}$ [-] being the so-called complementary modulus [10].

3 Numerical validation and discussion of results

The validity and accuracy of the approximation postulated in eqn. 8 remains to be evaluated for finite values of k_r/k_a that are unequal to zero and one. For this purpose, a large (200 x 200 cells) two-dimensional finite difference model (MODFLOW) is used to perform a systematic numerical validation study. 60 model runs without gravel packs are conducted with all possible combinations of the following parameter sets: (1) k_r/k_a = {0.1, 1, 10, 100, 10^6}, (2) b/a = {0.1, 0.5, 2} and (3) f/a = {0, 1, 3} and w/a = {0.1}. Another 60 model runs are performed for the same PRB geometries (i.e., combinations of f/a, w/a and b/a), but with gravel packs of conductivity $10^6 k_a$ and with values of k_r/k_a adjusted such that the thickness of the gravel packs does not affect the reactor hydraulic resistance value R. The parameter ranges are chosen to encompass most practical situations as well as the "worst case scenario" for $k_r = k_a$ from fig. 5. The large value of $k_r/k_a = 10^6$ is used to generate a numerical version $Q_{max,n}$ of the analytical Q_{max}; differences between $Q_{max,n}$ and Q_{max} do not exceed 5% and may be attributed to numerical inaccuracies as well as effects of nearby boundaries required for the numerical method. In order to approximately correct for the latter, numerical capture flows reported in the sequel include a correction factor of $Q_{max}/Q_{max,n}$, i.e., an adjustment to honor the known analytical solution for $k_r >> k_a$.

Comparing the numerical output in the presence or not of gravel packs it is observed over the full range of the simulation study that the differences in respective capture flows (counted in the corresponding values of Q_{max}) are mostly below 1% and only exceed 3% in one case. This is a strong indication that the approximation of eqn. 8 is, in fact, appropriate and well within the error margins of typical field situations. This is further emphasized by fig. 6, which graphically compares analytical and numerical solutions for selected configurations. The continuous and adjacent dashed lines are analogs to respective lines in fig. 5 and represent analytical results from eqns. 7 and 8, respectively. Numerical output as indicated by the circular (no gravel packs) and star (with gravel packs) markers is in very good agreement, thus further validating eqn. 7. The remaining dashed lines correspond to $f/a = 1$ with k_r/k_a = 0.1 and 10 (with gravel packs from eqn. 8), which, by comparison with respective numerical output, validate the good performance of eqn. 8 also in the absence of gravel packs down to capture flows as low as approximately 5% of Q_{max}. Although little relevant for practice, no significant errors may be expected between this and the trivial (but exact) solution for $Q = 0$. As a consequence, eqn. 8 may be regarded as exact for the estimation of capture flows in the

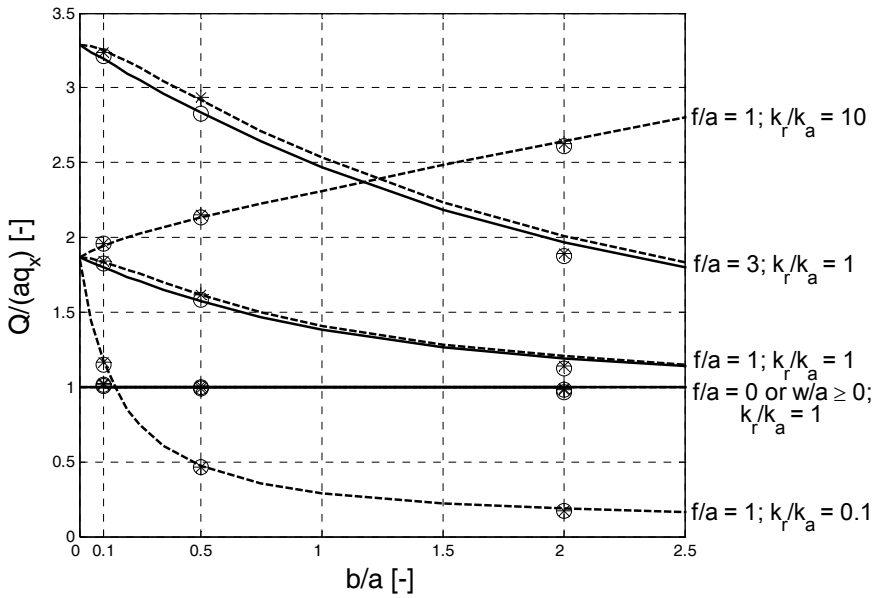

Figure 6: Comparison between analytical (lines) and numerical (markers) results. Continuous lines and circular markers are without gravel packs; dashed lines and star markers are with gravel packs.

presence of highly permeable gravel packs and as a good (errors in the 1% range of Q_{max}) approximation for capture flows of FG and VEW PRBs without gravel packs.

The small difference in capture flows between PRBs with gravel packs and without is a consequence of the fact that the hydraulic head along the reactor faces for flow in x-direction is relatively constant even without gravel packs. This is further supported by the fact that differences become even smaller as VEW of increasing length are added, i.e., as the hydraulic head at the reactor faces is even more forced to be constant. The presence of a flow component in y-direction does not affect capture flow, which is a pure function of q_x; capture width, in contrast, only remains unaffected when measured parallel to the y-direction. Even though to a quite limited extent, the presence or not of gravel packs does have an influence on capture flows. A closer look at the numerical results (or fig. 5) reveals the rather intuitive fact that gravel packs tend to increase Q. However, this is only true for low values of R up to a certain limit and above this limit deployment of gravel packs can actually decrease Q. We surmise that this is due to a "potentiating" effect of the low conductivity of gravel packs on the flow regime near the reactor. That is, for low values of R flow generally converges from the aquifer into the reactor and highly permeable gravel packs contribute to increase this flow convergence and, hence, capture flow. In contrast, for high values of R flow divergence, [5], around the reactor may occur and gravel packs contribute to further facilitate this phenomenon, thus, decreasing Q (however, this is not a typical design situation).

4 Summary

Unfortunately, groundwater contamination is currently a wide-spread (global) problem representing a serious threat to ecosystems including ourselves. Once a contaminant source and its down-gradient plume are identified, permeable reactive barriers (PRBs) provide a potential means for partial or full plume remediation with its particular advantages of being passive and in-situ, i.e., treatment occurs without pumping and in the aquifer. This is achieved by installation of a reactive material in the pathway of the contaminant plume, which performs a physical, chemical and / or biological remediation process before releasing the initially contaminated groundwater again into the aquifer. Engineering intervention into the subsurface by constructing a PRB belongs to the class of optimal design problems, with a hydraulic composite assembled as a meta-material (aquifer-wall-gravel pack, reactive material as hydraulic components of similar-dissimilar permeability) placed and structured in a certain manner with respect to the incident groundwater flow. A parameter of fundamental interest in the design and operation of a PRB is its capture flow, i.e., the portion of the ambient groundwater flow captured and treated. Previous analytical approaches by the authors are based on the assumption of the reactive material being much more permeable than the surrounding aquifer or, alternatively, the assumption that highly permeable gravel packs are present at the up and down-gradient faces of the reactor.

In the present work we investigate the influence of gravel packs on capture flows for funnel-and-gate (FG) and velocity equalization wall (VEW) PRBs. An exact analytical solution is presented for the flow field and the capture flow for the particular case of equal aquifer and reactor conductivities and no gravel packs. Graphical inspection of flow fields reveals that the hydraulic heads along the reactor-aquifer interfaces are relatively constant even without gravel packs and that maximum differences in capture flows with respect to the exact solution for gravel packs deployed are not larger than approximately 3%. Inspired by this, a systematic numerical simulation study considers a wide range of PRB geometries and reactor conductivities to confirm that capture flows of FG and VEW PRBs without gravel packs may accurately be approximated by the respective known solution (eqn. 8) for PRBs with gravel packs from Klammler and Hatfield, [5]. Errors of this approximation are found to be in the 1% range of the maximum capture flow Q_{max} for a highly permeable reactor, which is well within the range of uncertainty in field situations.

Evaluation of eqn. 8 is simple and requires determination of Q_{max} from the thin continuous lines of fig. 5 as a function of the geometric PRB dimensions b/a and f/a (for FG) or w/a (for VEW). The shape parameter k_{gp}, also being a function of the geometric PRB dimensions, is directly obtained from Klammler and Hatfield, [5; their "k" in fig. 4]. The values of the complete elliptic integrals of the first kind $K(k_{gp})$ and $K(k'_{gp})$ of modulus k_{gp} and k'_{gp}, respectively, are easily found from existing look-up tables, e.g., [10], or standard mathematical software. Finally, the dimensionless hydraulic reactor resistance R is a function of the reactor shape and conductivity as defined immediately after eqn. 8.

Acknowledgements

This research was partially funded by the Florida Water Resources Research Center under a grant from the U.S. Department of Interior (06HQGR0079) and NATO CELG grant 983197. The first author gratefully acknowledges support through a fellowship (DCR0001/2009) from the Brazilian National Council for Research and Development (CNPQ) and the Bahia State Research Foundation (FAPESB).

References

[1] Cunningham, J.A. & Reinhard, M., Injection-Extraction Treatment Well Pairs: An Alternative to Permeable Reactive Barriers. *Ground Water*, **40(6)**, pp. 599-607, 2002.

[2] EPA (Environmental Protection Agency), Capstone Report on the Application, Monitoring, and Performance of Permeable Reactive Barriers for Groundwater Remediation: Volume 1, Performance and Evaluation at Two Sites and Volume 2, Long-Term Monitoring of PRBs: Soil and Groundwater Sampling. EPA/600/R-03/045a and b, 2003.

[3] Starr, R.C. & Cherry, J.A., In-Situ Remediation of Contaminated Groundwater: The Funnel-and-Gate System. *Ground Water*, **32(3)**, pp. 465-476, 1994.

[4] Painter, B.D.M., Reactive Barriers: Hydraulic Performance and Design Enhancements. *Ground Water*, **42(4)**, pp. 609-617, 2004.

[5] Klammler, H. & Hatfield, K., Analytical Solutions for the Flow Fields near Funnel-and-Gate Reactive Barriers with Hydraulic Losses. *Water Resources Research*, **45**, W02423, 2009.

[6] Klammler, H., & Hatfield K., The Problem of Flow-by-Pass at Permeable Reactive Barriers. In: Geo-Environment and Landscape Evolution III, WIT Transactions on the Built Environment, vol. 100, edited by U. Mander, C. A. Brebbia, & J. F. Martin-Duque, pp. 15-24, 2008.

[7] Klammler, H., Hatfield, K. & Perminova, I.V., Groundwater and Contaminant Travel Time Distributions near Permeable Reactive Barriers. In: Water Resources Management V. WIT Transactions on Ecology and the Environment, vol. 125, edited by C.A. Brebbia & V. Popov, pp. 245-256, 2009.

[8] Klammler, H. & Hatfield, K., Analytical Solutions for Flow Fields near Continuous Wall Reactive Barriers. *Journal of Contaminant Hydrology*, **98(1-2)**, pp. 1-14, 2008.

[9] Driscoll, T.A., A MATLAB toolbox for Schwarz–Christoffel Mapping. *ACM Transactions on Mathematical Software*, **22**, pp. 168-186, 1996. (toolbox available under: www.math.udel.edu/~driscoll/SC/)

[10] Byrd, P.F., Friedman, M.D., *Handbook of Elliptic Integrals for Engineers and Physicists*, Springer, Berlin, 1954.

Airfoil cascades with bistable separation control

V. Tesař
Institute of Thermomechanics v.v.i.,
Academy of Sciences of the Czech Republic, Czech Republic

Abstract

To accommodate varying flow rate and shaft speed conditions, the airfoils arranged in cascades in hydrodynamic machines (turbines, pumps) should be variable. Mechanical articulation is expensive and complex, reducing reliability. The author investigated separation control by jets issuing from fixed stator blades shaped so that the flow past them is switched by short control-jet pulses between two alternative regimes differing in the resultant exit flow angle. Although applicable widely, in the tests the stator cascades were mostly used in simple rotor-less devices operating as a vortex-flow restrictor. Experiments were supplemented by extensive numerical flowfield solutions.
Keywords: separation control, airfoil cascade, Coanda effect.

1 Introduction: the role of airfoil cascades

Cascades, the periodic systems of airfoils, e.g. Scholz [1], are essential components of hydrodynamic machines, such as *pumps* or *turbines*. In these two machine types, energy conversion in one direction takes place, e.g. mechanical output is produced at the expense of decreasing hydraulic energy. The conversion actually usually involves two cascades, a fixed stator cascade and the other on the rotor connected with the rotating shaft. The energy transfer between the fluid flow and the mechanical work takes place in the rotor cascade. The stator (sometimes missing in machines that have to be cheap) either directs the flow into the turbine rotor or, in a pump or blower, converts the kinetic energy gained by the fluid in the rotor into the pressure rise. More complex conversions take place in machines with a pair of rotor cascades, each on its shaft (usually each also having its corresponding stator cascade). One of them has the role of a


WIT Transactions on Engineering Sciences, Vol 69, © 2010 WIT Press
www.witpress.com, ISSN 1743-3533 (on-line)
doi:10.2495/AFM100291

turbine and the other operates as a pump. With mechanical power transfer by a shaft connecting the two rotors, it is the case of a *turbo-charger*. On the other hand, in *couplings* and *torque converters* it is the fluid flow that transfers the power from the driving shaft to the driven one. There are also less common machines, such as *retarders*; in principle hydrodynamic couplings with fixed or absent output shaft, used to dissipate the mechanical input power. The *flow restrictors* have no rotor. They dissipate the input hydraulic power by vortex flow in a chamber located downstream from the stator.

Operating conditions of turbomachines are determined mainly by fluid flow rate and shaft rotational speed. In many applications they vary, sometimes in a wide range. Geometry of airfoils is designed for a particular working condition at which their efficiency attains a maximum. Deviations from this regime inevitably change the attack angle at which the fluid enters the cascade. This results in efficiency deterioration, especially if the attack angle is large enough for the airfoils to stall. Usually, the airfoil shapes are designed with some compromising so as to accept attack angle changes within a certain range, though the extent of this range is inevitably limited.

Acceptable efficiency, even with large variations of the flow rate, may be maintained- at least to a degree – by articulated vanes or blades. The standard solution (Fig. 1) is to vary the vane attack angle by mechanical actuators. Each vane is held in its bearing and all are connected to some actuation mechanism. This makes the machine more expensive – and yet the conditions cannot be ensured to remain ideal at all vane angular positions (this would require varying the vane shape and not just the attack angle). Nevertheless, efficiency

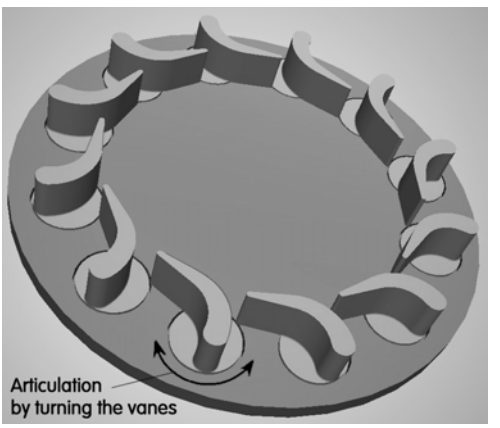

Figure 1: An example of a stator cascade with the classical mechanical articulation by turning the vanes. The necessary vane bearings and the actuation levels make this solution expensive and acceptable only for very large or very important turbo-machines. In the discussed solution, the vanes are fixed and their aerodynamic properties are varied by auxiliary control fluid flows.

improvement over non-articulated vanes is substantial. Apart from the compensation for flow rate or shaft speed variations, the actuator mechanism may serve as an input controlling the machine operation. In general, the mechanical articulation is justified only in machines handling large power levels. This is an unpleasant fact especially for very small turbomachines, belonging to microfluidics, e.g. Tesař [7]. Due to the small Reynolds number, efficiency of a microturbine is the critical factor and keeping it reasonably high by actuation of cascades would be particularly welcome.

Since there is a certain range of acceptable attack angles, a design capable of operating in two regimes is often acceptable. This may simplify the actuation somewhat. In the machines for power transfer between two shafts there is a solution using a gearbox connected to one of the shafts. This is not uncommon in car automatic transmissions, where it is acceptable (in spite of the gearbox cost) because of the long tradition of gearboxes in automobiles (and availability of the machine tools for manufacturing them). Experience shows that only two gear pairs may suffice despite the wide range of the car operating conditions.

2 Fluidic control of cascade flow

Characteristic feature of fluid flow control in aerodynamics is replacing the early solutions – with typical mechanical linkages and movable flaps or spoilers protruding into the flow – by fluid jets. This inspired author's investigations into the possibilities of similar development in the turbomachine cascades. The example in Fig. 2 is a historical early attempt (Tesař [2]) to replace mechanically articulated stator blades of a torque converter. In response to the control flows from the slit nozzles in the hollow blades, two flow regimes are possible. They

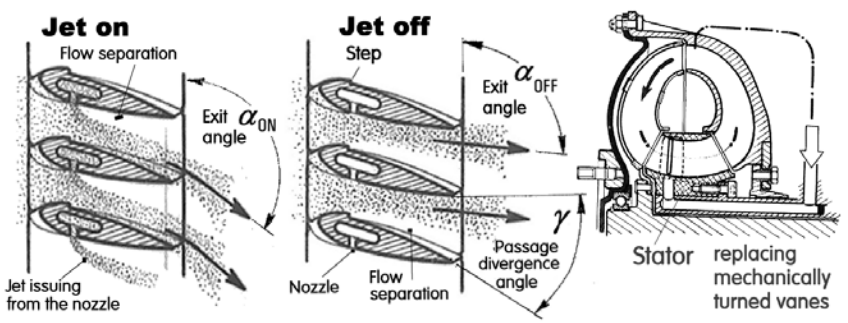

Figure 2: Cascade of airfoils with controlled separation in the passage between the blades. Divergence angle γ is too large for attachment to both walls. Without the control jets (centre), the flow separates (assisted by the step) from the dorsal wall. Jets from the slit nozzles (left) create the other regime, with the flow separating from the ventral side and leaving the cascade at a much larger angle α_{ON}.

differ in the angle α at which the flow leaves the cascade. The flow thus enters the rotating (pump) cascade immediately downstream at different angles of attack. If the rotor speed reaches a level at which, in the absence of the control flow, the attack angle is too large and the flow would separate from its blades, the separation is suppressed by switching the stator cascade to the other regime, with smaller attack angles.

The more recent designs – Fig. 3 presents an example of an application in the stator of a small radial centripetal turbine – retained the basic features of their forerunner from Fig. 2: the channel between the vanes causes the main flow to attach to one of the two walls further downstream. There are two regimes A and B. The inlets for the control flow are in the vanes, which tend to be unusually thick (a typical feature of airfoils with separation control). The fact that only two regimes are possible, and also that in both there is some separation, admittedly relegates this idea to less important machinery, especially of small size. It is an advantage that the fixed blades are much easier and cheaper to manufacture than their mechanically adjusted equivalents. Of course, availability of the control fluid flow, another limiting factor, is seldom a problem.

Later, essentially the same idea was applied to a valve presented Fig. 4. It was to be used in a filter for removal of particulate emissions from Diesel engine exhaust and operated at rather high temperatures. The filter clogs rather fast and has to be re-generated by burning the deposited carbon particles. During the regeneration the gas flow rate has to be decreased. This is achieved by temporary by-passing of the main gas flow through this turn-down valve. Designed according to Figs. 5 and 6, the valve contains no moving components and is therefore eminently suitable for the demanding conditions of operation at 350–600 ^{o}C.

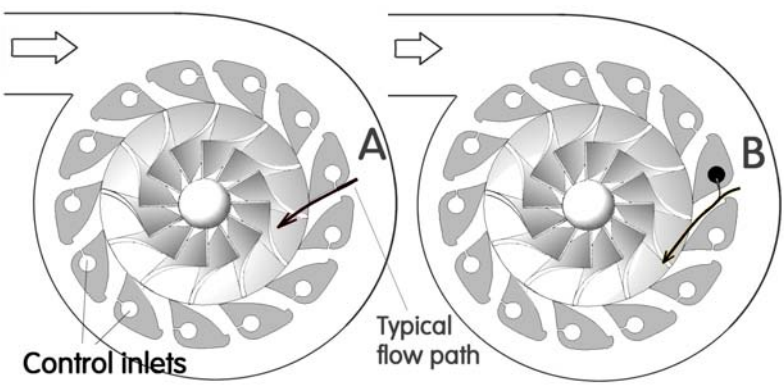

Figure 3: No-moving-part stator proposed for a small radial turbine. There are only two regimes (control flow ON or OFF). In both, the flow separates from one of the vane walls. Efficiency is better than with non-articulated vanes.

In this case, the cascade is bistable (while those in Figs. 2 and 3 were monostable). Again, the airfoils are rather thick – a feature common in airfoils with separation control by jets. They form an axial-flow stator that directs the flow passing between them either radially or tangentially into the vortex chamber. The divergence angle between the walls **m** and **n** (Fig. 6)

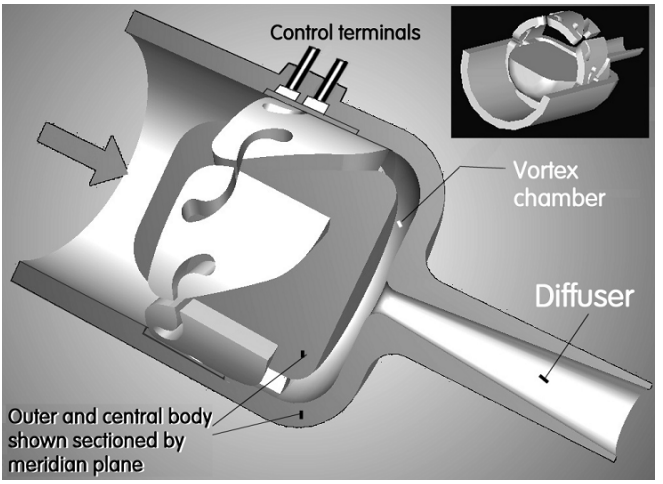

Figure 4: Jet-switched, axial flow stator cascade used to control the entry into vortex chamber in a no-moving-part turn-down valve, originally designed to reduce the Diesel engine exhaust gas flow in the re-generation phase of particulate emissions filter.

Figure 5: The stator cascade of six very thick, very short span airfoils from the previous Fig. 4. There is a control nozzle on both sides of the gap between the airfoils.

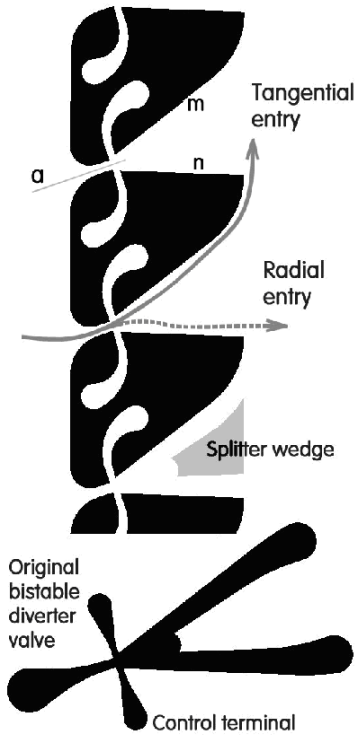

Figure 6: The cascade compared with (at the bottom) author's fluidic bistable valve VT30 described in by Tesař [4, 5]. The shape of the airfoils was actually designed starting from the geometry of the gaps between them.

is here as large as $\gamma = 40°$, symmetric with respect to the entrance axis **a**. The flow attaches either to the wall **m** or to **n.** If attached to **m** the flow enters the vortex chamber tangentially and its rotation velocity increases as the fluid proceeds towards the exit diffuser throat. The centrifugal effect then nearly stops the flow. If the flow is switched to attach to **n**, it passes radially through the vortex chamber. Without rotation, the pressure drop across the valve in this "open" state is small.

The airfoil design started from the geometry of the gap between them, using earlier author's experience [3–5] with the bistable fluidic diverter valves, as shown in Figs. 7, 8, and 9. Because the attachment to any of the two mutually opposing walls is stable, considerable saving is achieved of the control flow. For the switching, only very short control flow pulses suffice.

The problem with the valve of Fig. 4 was the complexity of the spatial geometry of the airfoils, Fig. 5, difficult to manufacture on standard machine tools when building the one-off laboratory model. This has led to the attention

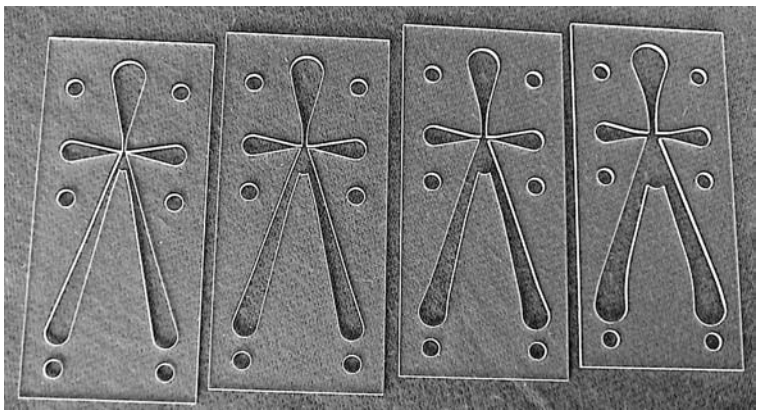

Figure 7: Perspex plates with family (note the different size of outlet diffusers) of laser-cut fluidic bistable unvented valves.

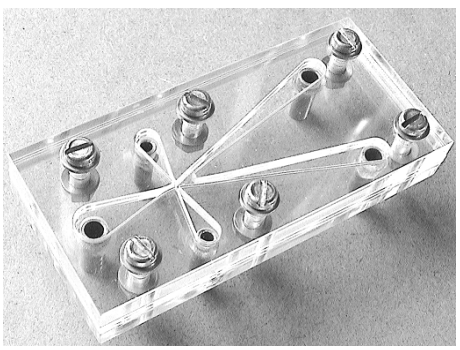

Figure 8: Laboratory model of author's fluidic diverter valve [3].

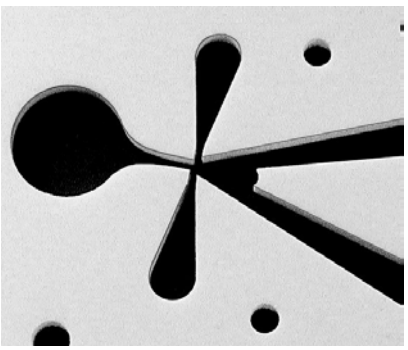

Figure 9: A detail of the key parts of the valve, the cavity for Coanda-effect attachments and interaction of the flows – in this case cut in Teflon [10].

later changed to the version with planar radial-flow cascade shown in Fig. 10, much easier to make – Fig. 11. It is again a rotor-less vortex valve. Because of most of its operating time spent in the CLOSED, tangential entry regime (the turning down is not complete), there is again the monostable behaviour. In contrast to the symmetric attachment walls in Fig. 6, here (Fig. 11) the preferential attachment wall **m** is aligned with the entrance axis a – while the other wall **n** was not only inclined at a large deviation angle but also separated by the large setback step. The advantage gained is the simplified control, needing

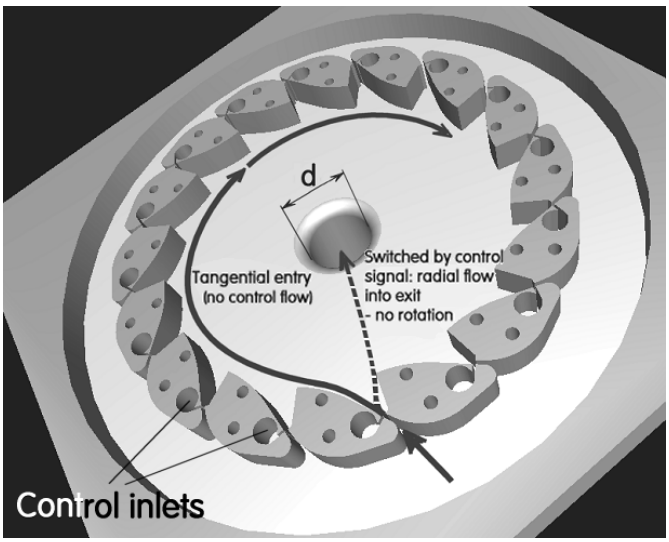

Figure 10: A cascade of the author's radial-flow airfoils in a monostable restrictor. The flow rotates so that the centrifugal acceleration turns it down – or is switched by control flows into the **OPEN** low-resistance state with radial entry into the vortex chamber.

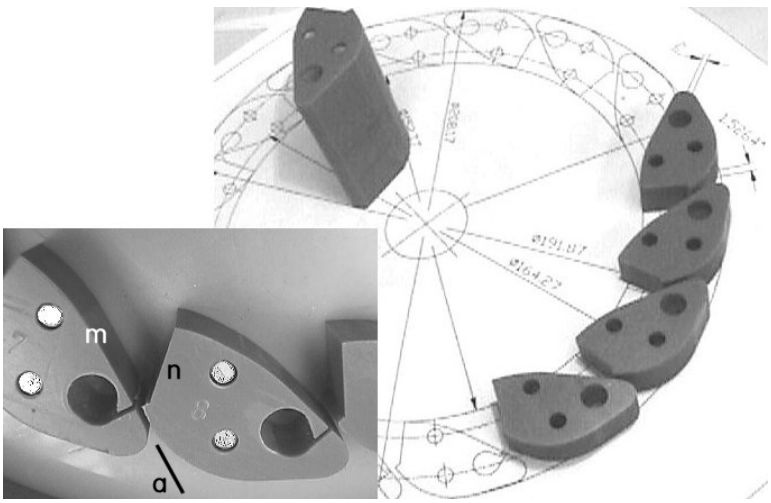

Figure 11: Left bottom corner: detail photograph of neighbouring airfoils (their punched workshop numbering may be noted), each held by a pair of steel pins. On the right, positioned on the workshop drawing, are airfoils during their manufacturing. Control nozzle slits were not yet made at this stage. The outer shapes were milled simultaneously in the stack of all 16 blades.

just a single control inlet. Of course, the attachment to **n** requires permanent control fluid flow to keep the valve OPEN. This was acceptable in the application to the Diesel engine filter where short re-generations (with the vortex valve open) take place between long-duration periods of sooth removal, during which no compressed air flow for the valve control is needed.

The monostability is obtained by giving to the wall **n** a large 41 deg deviation angle and also by separating it by the 1.8 mm separation step. The airfoils were cut from polyvinyl chloride plate 15 mm thick (nominally). The admittedly rather inefficient shape of the control nozzles was dictated by the available area inside the airfoils for placing the 9.8 mm dia circular control inlet chambers X and also by the method of cutting the nozzle slit. In another tested alternative, Fig. 12, controlling the main flow and not the by-pass, the role of the control was reversed: the flow into X is needed to keep the valve CLOSED during the re-generation. The performance in this version is somewhat better due to the flow from the control nozzle in the CLOSED regime interacting with the main flow in the OPEN state. There are two dominant cross sections in these restrictors: (a) the entrances into the inter-blade passages, of cross section bh (Fig.5), and (b) the vortex chamber exit. An efficient centrifugal action in the CLOSED regime requires the exit diameter to be as small as possible. On the other hand, the OPEN state requires a large exit area – or more exactly low dissipance [7, 14] of the exit, which may be achieved even with a small diameter by placing downstream from the exit a diffuser. An important design problem was the proper mutual relation between the two dominant cross sections. Early experiments suggested the optimum is reached with both areas equal. This remains a useful rough "*rule*

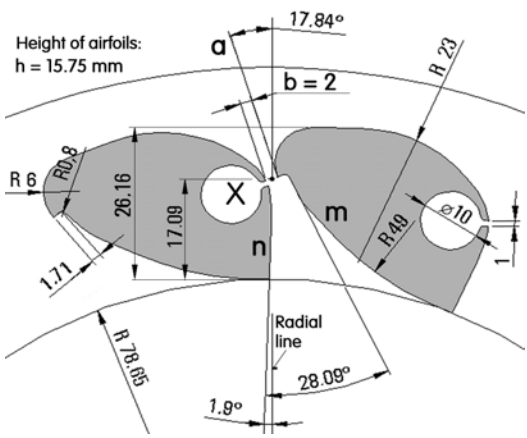

Figure 12: Geometry of the very thick airfoils used in another monostable variant of the vortex restrictor valve. In this case (note the position of the control X relative to the attachment walls m and n) the control flows switch the valve into the CLOSED, high-resistance regime.

of thumb", but a detailed discussion of the more exact solution of this matching problem is now available, using the approach discussed in Tesař [5]. Investigations performed with the monostable vortex restrictor having the cascade of the geometry shown in Fig. 12 and the exits as shown in Fig. 13 have shown the optimum conditions attained (Fig. 16) with the area of the exit diffuser throat somewhat smaller – only 76% of the total area 16 bh of the entrances. As with the vortex-type non-return valves [6],

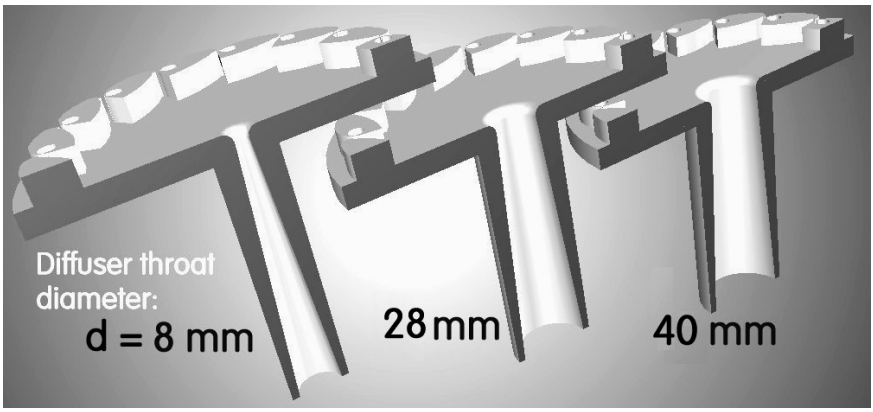

Figure 13: Investigations made to find the matching the cascade properties with those of the vortex-chamber exit. Various alternative exit diffusers were of identical 170 mm length.

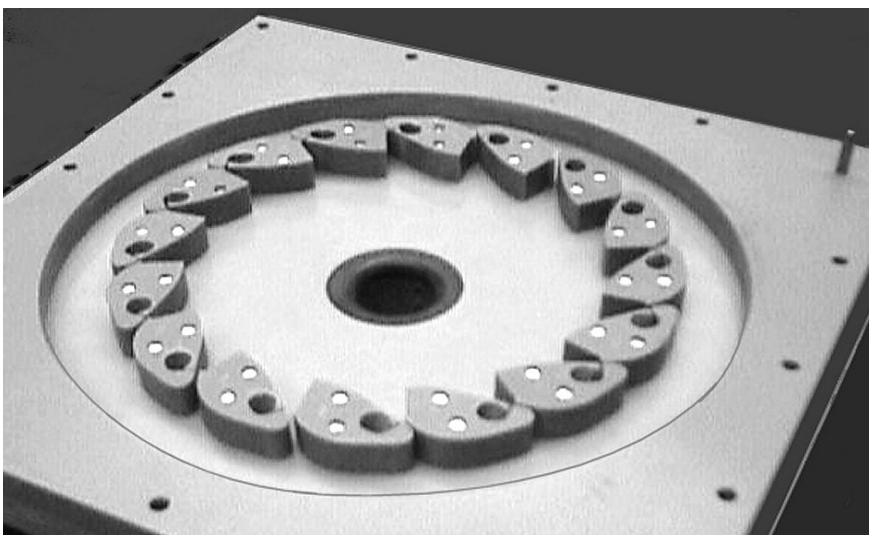

Figure 14: Photograph of the assembled monostable turn-down valve model with 16 airfoils and a large-diameter exit diffuser.

the turning-down action depends on the flow dynamics so that complete closure is not possible. Nevertheless, the demonstrated decrease shown in Fig. 16 to the value representing mere 3.6% of the magnitude in the OPEN state at the same pressure represents a good performance value, no doubt sufficient for most potential applications.

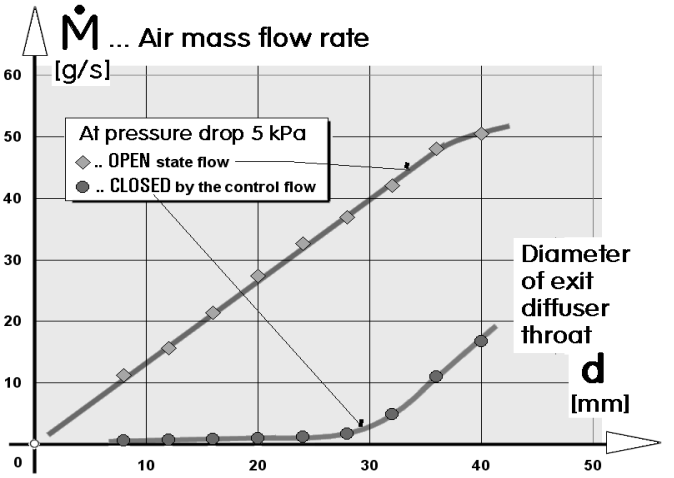

Figure 15: The two dependences on the exit diameter (the OPEN and CLOSED regimes) of the air flow rate through the restrictor with airfoils according to Fig. 12 at the same overall pressure drop 5 kPa.

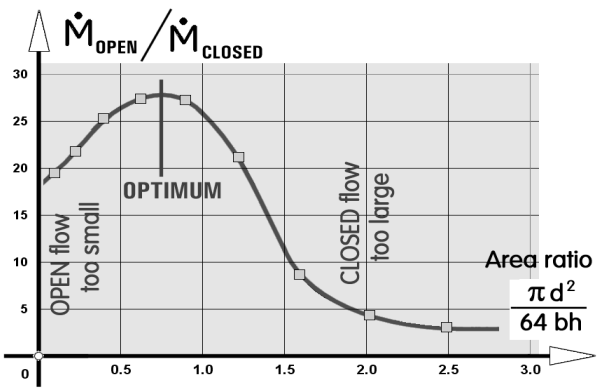

Figure 16: Ratio of flow rates in the two regimes at the same pressure drop, plotted as a function of the ratio of the two dominant cross section areas: the exit area and the area of the smallest cross sections in the channels between the airfoils.

3 Conclusions

Flow control is currently receiving most attention in the field of fluid dynamics. Apart from the control logic and sensor systems, considerable work is needed on the actuator side – devices enacting large-scale changes in the flowfield in response to small control signals, preferably exhibiting high reliability, robustness and low cost. Early developments based on mechanical linkages and movable bodies protruding into the flow tend to be replaced action of fluid jets. Most of this activity is currently in external aerodynamics – mainly for improving performance of flight vehicles. Present paper turns the attention to applying analogous ideas to internal aerodynamics – namely to airfoil cascades, the essential parts of energy converting hydrodynamic machines.

Acknowledgements

Gratefully acknowledged is support by grant IAA200760705 and by the research plan AV0Z20760514 received from the Grant Agency of the Academy of Sciences of the Czech Republic, and by the grant 101/07/1499 from GACR Czech Science Foundation.

References

[1] Scholz N., *Aerodynamics of Cascades* - in German, Braun, Karlsruhe, 1965
[2] Tesař V., *Machine converting energy between a mechanical motion and a fluid flow* – in Czech language, Czechoslovak Patent Nr. 230175, filed 10th April 1981
[3] Tesař V., Hung C.-H., Zimmerman W.: *No-Moving-Part Hybrid-Synthetic Jet Actuator*, Sensors and Actuators A, Vol. 125, p. 159, 2006
[4] Tesař V., *Mechanism of Pressure Recovery in Jet-Type Actuators*, Sensors and Actuators A-Physical, Vol. 152, p.182, 2009
[5] Tesař V., *Fluidic control of reactor flow – Pressure drop matching*, Chemical Engineering Research and Design, Vol. 87, p. 817, 2009
[6] Thoma D., *Non-return valve* - in German, VDI-Zeitschrift, Band 74, p. 1098, 1930.
[7] Tesař V., "*Pressure-Driven Microfluidics*", Artech House Publishers, Norwood, MA, USA, 2007
[8] Tesař V., "*Bistable turn-down power amplifier - Matching the two dominant cross sections*", Proc. of the 9-th 'Jablonna' International Fluidics Conference, Paper A-5, Jablonna, Poland, Sept. 1982
[9] Tesař V.: "*Arrangement for controlled transfer of rotational motion*" – in Czech language, Czechoslovak Patent Nr. 225603, filed 10th April 1981
[10] Tesař V.: "*Enhancing Impinging-Jet Heat or Mass Transfer by Fluidically Generated Flow Pulsation*", Chemical Engineering Research and Design, Vo. 87, p. 181, 2009I

[11] Tesař V.: "*Fluidic Valves for Variable-Configuration Gas Treatment*", Chemical Engineering Research and Design, Vol. 83 (A9), p. 1111, 2005
[12] Tesař V.: *"Fluidic Valve for Reactor Regeneration Flow Switching*", Chemical Engineering Research and Design, pp.1 -11, Part A, Vol, 82 (A3), 2004
[13] Tesař V.: "*Großmaßstäbliche fluidische Ventile für die Durchfluß-steuerung*" (Large-scale fluidic valves for flow control – in German), Messen-steuern-regeln Bd. 26, Nr. 4 1983
[14] Tesař V.: "*Characterisation of three-terminal fluidic elements and solution of bifurcated-flow circuits using the concept of equivalent dissipance*", Journal of Fluid Control / Fluidics Quarterly, Vol. 13, Nr. 2, June 1981
[15] Tesař V.: "*Valvole fluidiche senza parti mobile*" *(Fluidic valves without moving parts – in Italian),* Oleodinamica – pneumatica, pp. 216 –223, No 3 - Anno 39, marzo 1998

This page intentionally left blank

Surface forces and wetting features in drops and capillaries

M. G. Velarde[1] & V. M. Starov[2]
[1]*Instituto Pluridisciplinar, Universidad Complutense de Madrid, Spain*
[2]*Department of Chemical Engineering, Loughborough University, UK*

Abstract

Using the DLVO (Derjaguin, Landau, Verwey, Overbeek) theory, which accounts for quantum mechanics and electrostatics at the macroscopic level, the thermodynamic expressions for (thermodynamic) *equilibrium* contact angles of drops on solid substrates and menisci in solid wall capillaries are, operationally and unambiguously, expressed in terms of the corresponding Derjaguin pressure. The latter's *S*-shape is responsible for microdrops and other phenomena appearing on flat solid substrates.

Keywords: DLVO, Derjaguin pressure, surface forces, wetting, drops, capillaries.

1 Introduction: mechanics *versus* thermodynamics

In the study of the equilibrium of a *sessile* drop *partially* wetting a smooth, homogeneous, flat solid substrate, there have been numerous attempts to deduce the Young equation for the equilibrium *contact* angle, θ, [1-3]

$$\cos\theta = \frac{\gamma_{sv}^{0} - \gamma_{sl}}{\gamma}, \tag{1}$$

where γ_{sv}^{0}, γ_{sl}, γ are solid-vapor (of a *bare* solid surface), solid-liquid and liquid-vapor interfacial tensions, respectively. As reflected in most textbooks and scientific publications, traditional analyses use arguments either from thermodynamics or from mechanics, always insisting on eqn. (1) defining an "equilibrium" condition. As stated, eqn. (1) defines a *contact* angle, θ, that does

WIT Transactions on Engineering Sciences, Vol 69, © 2010 WIT Press
www.witpress.com, ISSN 1743-3533 (on-line)
doi:10.2495/AFM100301

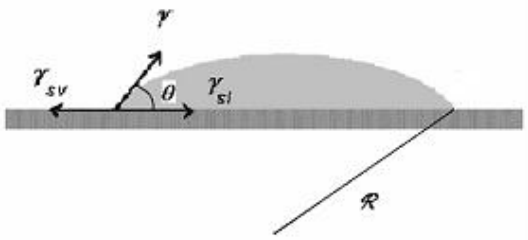

Figure 1: A sessile drop on a solid surface in apparent mechanical equilibrium. As shown, the angle θ defines, following Young, the *mechanical* equilibrium of tangential "forces".

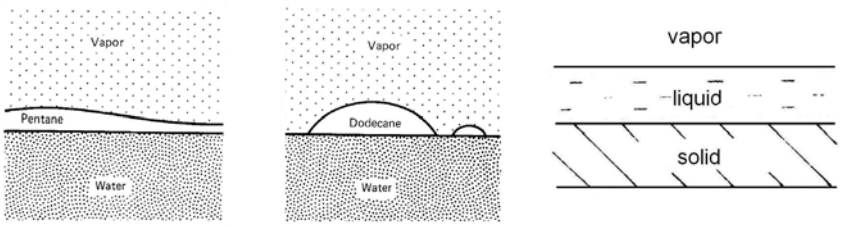

Figure 2: Wetting (left figure) and mostly non-wetting (center figure) liquid films and the "ideal" *complete* wetting case (figure on the right).

not depend on the vapor pressure in the ambient air or on the volume of the drop or on its radius of curvature, $\Re$. To be also noted is that neither γ_{sv}^{0} nor γ_{sl} can be measured [2].

However, to a useful first approximation, we have the Kelvin equation [2]

$$P_e = \frac{2\gamma}{\Re} = \frac{RT}{v_m} \ln \frac{p}{p_s}, \tag{2}$$

where v_m is the molar volume of the liquid, p_s is the pressure of the *saturated* vapor at the temperature *T*, *R* is the universal gas constant, *p* is the vapor pressure that is at equilibrium with the liquid in the drop, and P_e is the *excess* pressure inside the drop. As the right hand side of eqn. (2) must be positive the vapor pressure, *p*, must be above the pressure of the saturated vapor p_s (corresponding to a flat surface, $R \to \infty$). Hence the drop can be at equilibrium with *oversaturated* vapor pressure only. Thus, eqn. (2) determines a *single* radius of curvature of the liquid drop for each given value of *oversaturated* vapor pressure, *p*. Accordingly, the contact angle determined by eqn. (1) does not correspond to *thermodynamic* equilibrium. Note that, with *oversaturation*, the equilibration process demands quite long time intervals (on occasion up to hours). Surely most of the published data on measured contact angles actually

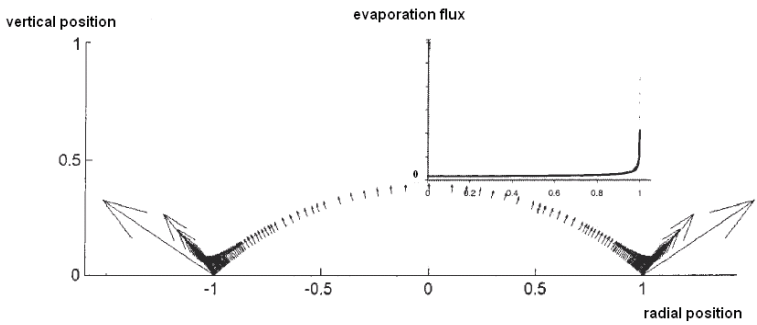

Figure 3: Evaporation flux along a sessile drop surface.

correspond to so-called (static) *advancing* contact angles, different from the *true* equilibrium value [2, 4, 5].

If eqn. (1) refers to *mechanical* equilibrium then, disregarding gravity effects, the drop is bound to retain a spherical shape down to the contact with the solid substrate, that is, down to the three-phase contact line where the thickness of the liquid vanishes. To be recalled is that a displacement of the three-phase contact line through the solid substrate as the liquid wets it is hard to explain. Indeed, according to standard hydrodynamics, the *tangential* friction force at the three-phase contact line *diverges* to infinite value. Another difficulty with eqn. (1), as it stands, is that evaporation seems to take place most vigorously in the vicinity of such three-phase contact line (fig. 2). This means that thermodynamic equilibrium is violated mostly just in the vicinity of the three-phase contact line [6, 7].

2 DLVO theory drops and capillaries

Starting with the work of Frumkin, Derjaguin and Landau, and Verwey and Overbeek, and Casimir, in the mid-XXth century, a useful approach (DLVO theory) to the problems raised by eqn. (1) [8-10] has been developed, thus leading to a sound thermodynamic derivation of the "true" equilibrium contact angle [4]. From the work of those authors it became clear that as the three-phase contact line belongs to the hundred nano-meter range then at such distances between two surfaces quantum mechanics and electrostatics intervene. When all their integrated molecular interactions are considered, this led to the introduction of so-called "surface forces" and the definition of a new form of pressure of significance in the study of thin liquid films and, in general, when two surfaces approach each other in vacuum or otherwise, as the "ideal" case illustrated in fig. 2. Originally, it was denoted as "disjoining" pressure though depending on the confronted surfaces and the medium separating them it could be either *disjoining* or *conjoining*. We shall call it Derjaguin pressure.

How much the action of Derjaguin pressure affects the liquid profile eventually deviating it from a spherical shape when approaching the three-phase

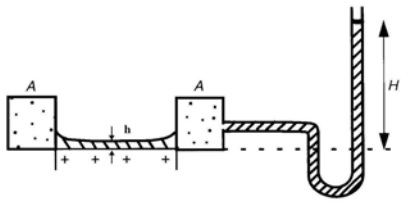

Figure 4: Measuring Derjaguin pressure (as proposed by Derjaguin, Churaev and Sheludko) using a porous container A: $\Pi(h) = -\rho g H$ (H may be positive or negative).

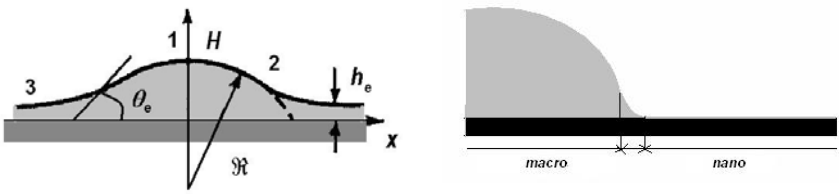

Figure 5: Exaggerated view (as $H >> h_e$) of a liquid drop *partially* wetting a solid substrate. $\Re$ is the radius of the "spherical" cap. In the left figure the angle θ_e can be considered as the contact angle at (thermodynamic) equilibrium corresponding (following Gibbs) to the minimum *excess* free energy of the system relative to the homogeneous flat thin liquid film. The right figure illustrates the spherical macro-region, the adsorbed nano-metric liquid film and the transition region.

contact line? How the (thermodynamic) *equilibrium* contact angle can be defined? These questions can be answered by considering the combined action of Laplace capillary ("surface tension") pressure and Derjaguin ("surface forces") pressure acting along the overall drop profile. The Laplace pressure is [2-5]

$$p_l - p_a = \frac{2\gamma}{\Re} \quad \text{or otherwise} \quad \frac{\gamma h''}{\left(1 + h'^2\right)^{3/2}} = P_e , \tag{3}$$

where for simplicity in two-dimensional geometry (a cylindrical drop) we have provided the value of $\Re$ in terms of the function h defining the drop profile. $P_e = p_a - p_l$ is negative for a drop and positive for a capillary.

To carry on the proposed task we must consider that at *thermodynamic* equilibrium the liquid in the drop must be at equilibrium with its own vapor (recall Kelvin equation), and also at equilibrium with the solid, both under the drop and around it, and the vapor must be at equilibrium with the solid substrate. The latter demands the existence of an adsorbed liquid film (of thickness h_e) on the solid surface as illustrated in fig. 5. A similar figure can be provided for a capillary with, however, opposite curvature [2, 4, 5].

Let us assume that we can maintain the *oversaturated* vapor condition over the solid substrate long enough until thermodynamic equilibrium is reached. Then the liquid molecules in the vapor are in equilibrium with the liquid molecules in the drop and with those in the adsorbed film on the solid surface. With either *partial* or *complete* wetting conditions, the presence of an adsorbed liquid layer on the solid substrate demands consideration of a new surface tension γ_{svh_e} of lower values than the surface tension of the *bare* solid surface, γ_{sv}^0. In view of the above, the expression for the *excess* free energy of the overall liquid layer over the solid substrate contains the *free* energies due to the spherical part of the drop and to the adsorbed liquid film with the transition zone:

$$\Phi_f = \gamma + P_e h_e + \int_{h_e}^{\infty} \Pi(h)dh + \gamma_{sl} - \gamma_{sv}^0 . \tag{4}$$

As earlier noted, P_e is a given Laplace *excess* capillary pressure and $\Pi(h)$ is the Derjaguin pressure for a given temperature.

We can rewrite the expression (4) as $\Phi_f = \gamma_{svh_e} - \gamma_{sv}^0$, by introducing

$$\gamma_{svh_e} = \gamma + P_e h_e + \int_{h_e}^{\infty} \Pi(h)dh + \gamma_{sl} , \tag{5}$$

as the interfacial tension (which is an *excess* free energy) of the solid substrate covered with the adsorbed liquid film. Then, inserting γ_{svh_e} rather than γ_{sv}^0 in Young equation (1) we get

$$\cos\theta_e = \frac{\gamma_{svh_e} - \gamma_{sl}}{\gamma} , \tag{6}$$

thus defining a contact angle at *thermodynamic* equilibrium. Consequently,

$$\cos\theta_e = \frac{\gamma + P_e h_e + \int_{h_e}^{\infty} \Pi(h)dh}{\gamma} \approx 1 + \frac{1}{\gamma}\int_{h_e}^{\infty} \Pi(h)dh , \tag{7}$$

if recalling the smallness of $h_e (H >> h_e)$ we neglect the term $P_e h_e / \gamma$. The latter equation is the Derjaguin-Frumkin equation for the (thermodynamic) *equilibrium* contact angle. It provides an operational definition relative to eqn. (1) which is conceptually unacceptable.

The argument is formally valid for both a drop and a capillary. As $-1 < \cos\theta_e < 1$, in the case of *partial* wetting (water and aqueous solutions over most solid substrates) the integral in the right hand side of eqn. (7) must be negative $\int_{h_e}^{\infty} \Pi(h)dh < 0$, and hence for *partial* wetting $S_- > S_+$ (actually, this condition defines *partial* wetting). Note that there are an infinite number of equilibrium contact angles for a drop on a solid substrate (each of them corresponds to a different value of the *oversaturated* vapor pressure in the

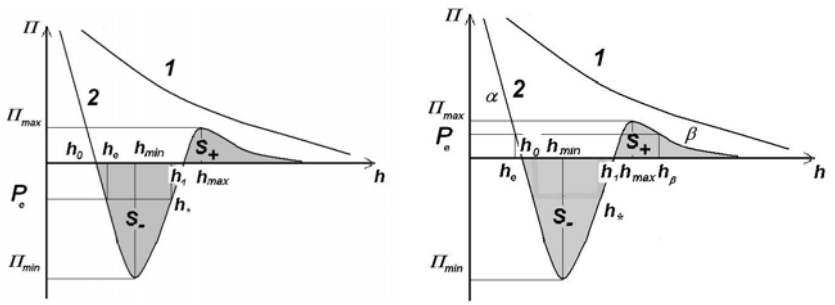

Figure 6: Derjaguin pressures, $\Pi(h)$, interpreted as isotherms corresponding to the cases of *complete* wetting (1) and *partial* wetting (2). The left figure is for drops and the right figure is for capillaries. In the latter the liquid film thicknesses, h_e, h_β and h_*, are thin flat films that for a given non-vanishing value of P_e could coexist at equilibrium with the central part of the meniscus in a capillary when $P_e < \Pi_{\max}$. However, only the first two are thermodynamically stable as $\frac{d\Pi(h)}{dh} < 0$ for either h_e or h_β. Hence h_* is unstable. For a drop as P_e is negative the left figure shows that there is only h_e and h_*, stable and unstable thicknesses, respectively. The values h_0 and h_1 denote the zeros of $\Pi(h)$ with no other meaning. For $h_{\min}$ and $h_{\max}$ see the main text.

surrounding air) but there is a single, uniquely defined equilibrium contact angle of the liquid meniscus in a *partially* wetted solid capillary for any *undersaturated* vapor pressure.

For completeness let us now focus on the capillary case. There are three solutions of equation $\Pi(h_e) = P_e > 0$ (fig. 6, right part, curve 2). Only those satisfying $\frac{d\Pi(h_e)}{dh} < 0$ are thermodynamically stable. The thinnest film h_e belongs to the so-called α-branch of the Derjaguin isotherm and it is *absolutely* stable. The thickest film, h_β, is a *metastable* solution, with a barrier $h_{\max}$, and belongs to the so-called β-branch. Then h_* corresponds to an unstable equilibrium flat film. On the surface of thin capillaries only equilibrium α-films are observed if $P_e > \Pi_{\max}$ where $\Pi_{\max}$ is the stability limit of β-films (fig. 6). This is the case for narrow enough capillaries. However, if $P_e < \Pi_{\max}$, the formation of *metastable* β-films is possible, and it has been observed experimentally.

The α-film is like an *adsorbing* film while the β-film is called a *wetting* film as it can be obtained by draining a thicker liquid layer. Generally, the free energy of α-films is lower than the free energy of β-films, ruling out spontaneous $\alpha \to \beta$ transitions. Typical α-films are the equilibrium films occurring when a hydrophilic surface is wetted with water. On the other hand, if more of the same liquid is added once the α-film is formed, disregarding gravity, it will not spread but rather it will form drops over the α-film (the fact that a liquid does not spread on itself is called *autophobicity*). Note that α or β-films may not exhibit interference colors when irradiated with white light and when they appear black they are usually called *black* films. In fact they do have *destructive* interference as two light rays/waves one reflected from the upper surface of the film and the other from the opposite surface, travel about the same path length but the second comes from the liquid film phase-shifted half a wavelength. These black liquid films were studied by Newton and it is customary to call the α-black film, a Newton black film, whereas the β-black film is called *common* black film. Aqueous soap solutions easily permit visualizing this phenomenon. Indeed, the transition from a thick film to a black film is easily demonstrated by allowing a vertical soap film supported on a horizontal frame to drain. Initially the whole film exhibits interference colors when illuminated, and then a dark boundary, separated from the colored area by a silvery band appears at the top and moves downward. This then divides into two areas occupied by black films. Note that a bi-layer of soap molecules is just a few nano-meters thick.

3 Non-flat equilibrium liquid films on flat surfaces: general thermodynamic approach

In a thick liquid film if its surface is curved or uneven, the Derjaguin and the Laplace (capillary) pressures acting together permit stable *non-flat* equilibrium shapes. Dictated by the *S*-shaped Derjaguin pressure, in the case of *partial* wetting, micro-drops, micro-depressions and spatially periodic (wavy) films could exist on homogeneous, flat solid substrates [11].

Let us insist in that eqn. (7) also shows that the equilibrium contact angle is completely determined by the shape of the disjoining pressure in the case of molecularly smooth solid substrates. There is no doubt that the surface roughness influences the apparent value of the contact angle. However, the roughness cannot result in a transition from *non-wetting* to *partial* wetting, or from *partial* wetting to *complete* wetting. The possible existence of non-flat equilibrium liquid films points to a scenario of rupture of "thick" metastable β-films and their transition to absolutely stable α-films.

Neglecting the action of gravity and, for simplicity, restricting again consideration to a *two-dimensional* capillary, the *excess* free energy of the system can be written as

$$\Phi = \int \left\{ \gamma\left(\sqrt{1+h'^2}-1\right) + P_e\left(h-h_e\right) + \int_h^\infty \Pi(h)dh - \int_{h_e}^\infty \Pi(h) \right\} dx \,, \tag{8}$$

where the coordinate x is taken along the flat solid surface of the wetted capillary. Such *excess* free energy is the *excess* over the energy of the same flat surface covered by a thermodynamically stable equilibrium α-film. Although such reference state results in an additive constant in expression (8), it is needed to study the liquid profile in a vicinity of the *apparent* three-phase contact line. Any liquid profile, $h(x)$, which gives the minimum value to the *excess* free energy, Φ, describes an equilibrium configuration. For a minimum we must have: (i) $\delta\Phi = 0$; (ii) if $f = \gamma\left(\sqrt{1+h'^2}-1\right) + P_e\left(h-h_e\right) + \int_h^\infty \Pi(h)dh - \int_{h_e}^\infty \Pi(h)$, then $\frac{\partial^2 f}{\partial h'^2} > 0$; (iii) as the solution is a curve, $h(x)$, the problem is in *functional* space and a *secondary variational* principle is needed [12]. This leads to a Jacobi equation $\frac{d}{dx}\frac{\gamma u'}{\left(1+h'^2\right)^{3/2}} + \frac{d\Pi(h)}{dh}u = 0$ whose solution cannot vanish when the unknown, x, is inside the region under consideration, except at the boundaries of the integration; and (iv) at the three-phase contact line, a smooth transition must occur from a non-flat liquid profile to a flat liquid film (*transversality* condition): $\left[f - h'\frac{\partial f}{\partial h'} \right]_{x=\Re} = 0$. The *actual* three-phase contact line, virtually located at the border of $\Re$ in fig. 5, corresponds to the intersection of the evolving liquid profile with the equilibrium liquid film of thickness, h_e, and not to the intersection with the solid substrate. Then $\left[\left(\sqrt{1+h'^2}-1\right) - \frac{h'^2}{\sqrt{1+h'^2}} \right]_{x=\Re} = 0$, or $\left[\frac{1}{\sqrt{1+h'^2}} \right]_{x=\Re} = 1$. The latter and hence the mentioned smooth transition occurs when $\left(h'\right)_{x=\Re} = 0$, or $h'\left(h_e\right) = 0$, hence $h' \to 0$, $x \to \infty$, where $x \to \infty$ means that it "tends to the end of the transition zone".

The first condition (i) yields

$$\frac{\gamma h''}{\left(1+h'^2\right)^{3/2}} + \Pi(h) = P_e \,, \tag{9}$$

which is the Laplace-Derjaguin equation. Indeed, the first term in the left hand side of eqn. (9) corresponds to the Laplace pressure and the second term to the Derjaguin pressure. Note that for a flat film the first term of the left hand side vanishes and hence $\Pi(h) = P_e$. If the thickness of the liquid is beyond the range of the surface forces action (above hundred nm) then eqn. (9) describes either a

flat liquid surface $(P_e = 0)$, or a spherical drop profile $(P_e < 0)$, or a curved meniscus profile $(P_e > 0)$. The second condition (ii) is always satisfied.

Direct differentiation of eqn. (9) yields $\frac{d}{dx}\frac{\gamma h''}{\left(1+h'^2\right)^{3/2}} + \frac{d\Pi(h)}{dh}\frac{dh}{dx} = 0$.

Accordingly, the solution of the Jacobi equation is $u = \text{const}\, h'$. Hence, there is stability if $h'(x_0) = 0$ with x_0 different from the boundary points; otherwise the system is unstable.

Integrating equation (9) we have: $\frac{1}{\sqrt{1+h'^2}} = \frac{C - P_e h - \int_h^\infty \Pi(h)dh}{\gamma}$, where C is an integration constant. Needless to say the right hand side must be positive. In the case of a meniscus in a flat capillary the integration constant, C, is determined from the condition that at the capillary center: $h'(H) = -\infty$, which gives $C = P_e H$, where here H is the half-width of the capillary. In the case of equilibrium drops the constant should be chosen using the condition that at the drop apex, $h = H : h'(H) = 0$, which results in $C = \gamma + P_e H$. An alternative way of getting the integration constant C is using the *transversality* condition.

A profile of the transition zone between a non-flat meniscus in a flat capillary and a thin α-film ahead of it in the case of *partial* wetting is depicted in fig. 7 (to be compared with fig. 6, right part, curve 2, for a flat meniscus). In the transition zone both Laplace and Derjaguin pressures act simultaneously. It appears that the liquid profile is not of uniform concavity from the vapor side, but changes curvature inside the transition zone.

In the transition zone (fig. 7, right part) all thicknesses appear from the very thick, outside the range of the Derjaguin pressure action, to the thin α-films.

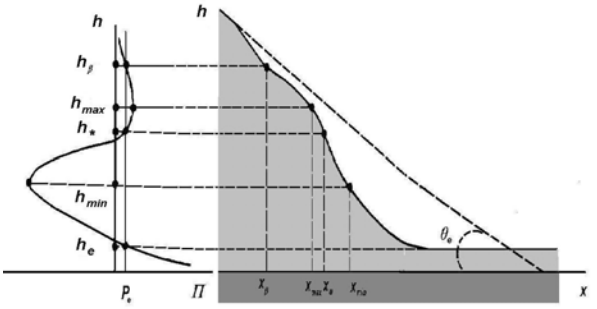

Figure 7: Partial wetting of a capillary. Enlarged view of the liquid profile inside the transition zone in "thick" capillaries. *S*-shaped disjoining pressure isotherm (left side) and the liquid profile in the transition zone (right side). Here h_e corresponds to the stable "thin" α-film, and h_β to "thick" t β-films as defined by $\Pi(h) = P_e > 0$.

Then the Jacobi equation condition (iii) above must be used rather than the stability condition (4) used in the case of *flat* films. Indeed, the transition zone is stable if $h'(x)$ does not vanish inside it. Such peculiar shape of the transition zone, where both the capillary pressure and the disjoining pressure are equally important, suggests looking for stable solutions other than flat liquid films of constant thickness.

4 Non-flat equilibrium films. Microdrops: the case $P_e > 0$ (undersaturation conditions)

Let us consider the possible existence of *microdrops*, i.e., drops with an apex height in the range of influence of the Derjaguin pressure [4, 11]. In this case the drop does not have a spherical part even at its apex, because its shape is everywhere distorted by the action of the surface forces. The *transversality* condition at $h = h_e$ gives $h'(h_e) = 0$, and hence the drop edge approaches the equilibrium film of thickness h_e on the solid surface at vanishing *microscopic* contact angle. This permits to fix the earlier mentioned integration constant $C = \gamma + P_e h_e + \int_{h_e}^{\infty} \Pi(h)dh$. Then, the microdrop profile (fig. 8; to be compared with fig. 6, left part, curve 2) follows from imposing $h' = -\sqrt{\dfrac{\gamma^2}{[\gamma - L(h)]^2} - 1}$,

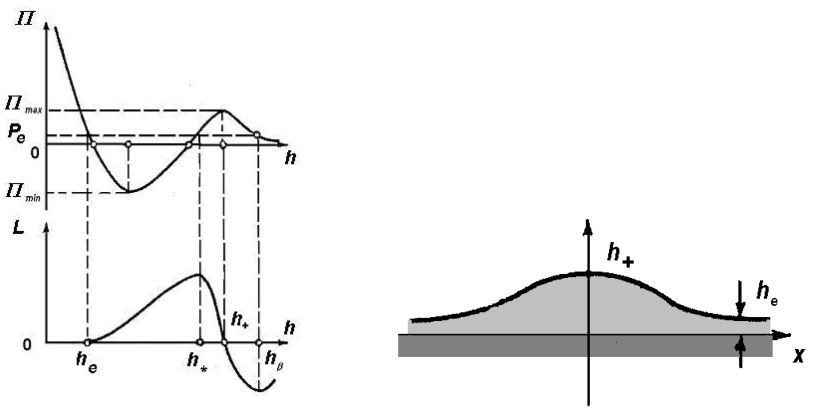

Figure 8: Microdrops. Left figure, *upper part*: *S*-shaped Derjaguin (pressure) isotherm; *bottom part*: $L(h)$ (see main text). The value $L(h_+) = 0$ determines the drop apex, h_+. Right figure: profile of an equilibrium microdrop. The apex of the microdrop is in the range of the Derjaguin pressure action, and hence the drop is not spherical even at the drop apex.

with $L(h) = P_e(h - h_e) - \int_{h_e}^{h} \Pi(h)dh$ and $0 \le L(h) \le \gamma$. The first equality corresponds to vanishing derivative, h', while the second one corresponds to the infinite derivative.

Let h_+ define the apex of the microdrop. The top part of the left fig. 8, shows the *S*-shaped dependence of the Derjaguin isotherm, $\Pi(h)$, while the bottom part shows the curve, $L(h)$, which is maximum or minimum when $P_e = \Pi(h)$. At the apex of the drop, when $h = h_+$, the first derivative must be zero, $h'(h_+) = 0$ and hence $L(h_+) = 0$. Take the origin placed at the center of the microdrop which corresponds to its formation at *undersaturation*, $P_e > 0$. In the range $0 < P_e < \Pi_{\max}$ the equation $P_e = \Pi(h)$ has *three* roots (fig. 8, left part); the smallest corresponds to the equilibrium flat α-film of thickness, h_e. For the existence of *microdrops* we must have: $h'' < 0$ at $h = h_+$ and $h'' > 0$ as $h \to h_e$, hence $h_* < h_+ < h_\beta$. Then $P_e(h_+ - h_e) = \int_{h_e}^{h_+} \Pi(h)dh$, whose solution, h_+, must satisfy the inequality $h_u < h_+ < h_\beta$ as illustrated in the bottom part of fig. 8, left part. As the left hand side is positive, so must be its right hand site. Hence, a *sufficient* condition for the existence of equilibrium microdrops is that $S_- < S_+$. This implies that the *S*-shaped Derjaguin (pressure) isotherm leads to an equilibrium contact angle of zero value. Consequently, *microdrops* at thermodynamic equilibrium are not possible if there is *partial* wetting, when $S_- > S_+$ or with *complete* wetting, when the Derjaguin pressure decreases in a monotonic way, as for example with $\Pi(h) = A/h^3$.

5 Concluding remarks

Summarizing, we have shown that the thermodynamics of drops and liquid films with curved menisci involves, for a given temperature, both the Laplace (capillary) pressure and the Derjaguin (surface forces) pressure. Once the Derjaguin (pressure) isotherm is known we can define, operationally and unambiguously, what do we mean by *complete* wetting, *partial* wetting and *non-wetting*. For the *partial* wetting case, the *S*-shaped Derjaguin isotherm, determines "true" *thermodynamic equilibrium* contact angles for drops of capillaries. Such *S*-shaped form is also responsible of the possible existence of microdrops, and even for micro-depressions and equilibrium periodic films on flat solid substrates.

Acknowledgement

This research was supported by the EU under Grant MULTIFLOW, FP7-ITN-2008-214919.

References

[1] Young, T., An essay on the cohesion of fluids. *Phil. Trans. Royal Soc. London*, **95**, pp. 65-87, 1805.
[2] Adamson, A.W. & Gast, A.P., *Physical Chemistry of Surfaces*, 6th ed., Willey: New York, 1997 (and references therein).
[3] de Gennes, P.G., Brochard-Wyart, F. & Quéré, D., *Capillarity and Wetting Phenomena. Drops, Bubbles, Pearls, Waves*, Springer-Verlag: New York, 2004.
[4] Starov, V.M., Velarde, M.G. & Radke, C.J., *Wetting and Spreading Dynamics*, Taylor & Francis /CRC: New York, 2007.
[5] Starov, V.M. & Velarde, M.G., Surface forces and wetting phenomena. *J. Phys. Cond. Matter*, **21**, pp. 464121-1-11, 2009.
[6] Starov, V.M. & Sefiane, K., On evaporation rate and interfacial temperature of volatile sessile drops. *Colloids & Surfaces A. Physicochem. Engng. Aspects*, **333**, pp. 170-174, 2009.
[7] Ajaev, V.S. Gambaryan-Roisman, T. & Stephan, P., Static and dynamic contact angles of evaporating liquids on heated surfaces. *J. Colloid Interface Sci.*, **342**, pp. 550-558, 2010.
[8] Derjaguin, B.V., Churaev, N.V. & Muller, V.M., *Surface Forces*, Consultants Bureau-Plenum Press: New York, 1987 (and references therein).
[9] Verwey, E.J.W. & Overbeek, J.Th.G., *Theory of the Stability of Lyophobic Colloids*, Elsevier: Amsterdam, 1948.
[10] Israelachvili, J.N., *Intermolecular and Surface Forces*, 2nd ed., Academic Press: London, 1991.
[11] Starov, V.M., Nonflat equilibrium liquid shapes on flat surfaces. *J. Colloid Interface Sci.*, **269**, pp. 432-441, 2004.
[12] Sagan, A., *Introduction to the Calculus of Variations*, Dover reprint: New York, chap. 7, 1992.

Power optimization of the complex pumping system

A. Alexandrescu
Department of Machine Manufacturing and Industrial Management, Technical University Gheorghe Asachi, Iasi, Romania

Abstract

This paper proposes a solution to the problem of reducing production costs for supplied domestic water, which directly affects the reduction of electric power consumption. The paper presents the methodology and the program of calculus for the transport's optimization of the water under pressure in the system of supply with water of Iasi city. The optimization process will take into account that the profitability of water distribution activity depends on the relationship between supply capability and operating costs. Therefore, the process depends on the volume of required investment, on the specific consumption electrical power for pumping, on the price of electricity, as well as on the volume of water billed on a monthly basis. The optimization calculation will use two target functions: total maximum efficiency and total electric power consumption required for transport of each cubic meter of supplied water, and cubic meter of sewage water, respectively. The mathematical methods may be improved by taking into account all active consumers in the network with simultaneous water requirements, at each moment of the day.

Keywords: adduction, flow, hydrophore, pipe network, pump, tank.

1 Introduction

The paper shows a determination method about the pumping installation's average global output in the adjustment situation through hydro – pneumatic heads. It is presented an analyze method about power and economical efficiency of the pumping installations equipped with only one type of pumps. The adaptation to variable regimes is done by the hydrophore's usage. The best power and economical performances will correspond to the pumping solution

WIT Transactions on Engineering Sciences, Vol 69, © 2010 WIT Press
www.witpress.com, ISSN 1743-3533 (on-line)
doi:10.2495/AFM100311

which ensures the covering of the request area flow, head (Q, H) with the best outturn.

The theoretical considerations are accompanied by the examples concerning an under pressure station from a collective system about supplying with urban water.

Profitability of water distribution activity depends largely on the relationships between operational capability and service costs, related to supplier's performance, volume of distributed water and effective operating costs [1]. The main variables that influence the total selling price are required investment value, specific consumption of electrical energy for pumping power, unit price of the electrical energy and total volume of monthly consumed water billed. The selection of rehabilitation and modernization measures must rely on market studies results that appropriately establish the quantities of water that may be distributed and billed. Present and future water requirements will be determined based on the analysis of actual operation data and on estimation of future trends in water consumption on national and international levels.

Authors used original mathematical algorithms to develop original computer programs that calculate, at each moment in time, depending on the number of active consumers connected simultaneously to the network, the functional parameters of the ensemble pumping station – hydrophore – pipe distribution network, as well as the available consumer parameters. This may be done in the hypothesis of a minimum price of cubic meter of pumped water.

The automatic calculation program defines the exploitations regimes for the overall output's installation to be maximum and the total typical energy consumed to be minimum on the work cycle ensemble.

2 Optimization problem's wording

The pumping efficiency is established by studying technical implications of modernization measures of the power station. Energy efficiency and economic efficiency for the pumping supply system are tightly connected to the proper choice of pumping device and appropriate operation of the hydraulic system. The best performances are obtained when, in order to meet the consumer requirement, the pumps are set to operate for regimes with efficiencies that are close to their maximum values. The equipment required for the pumping station must meet the operational characteristics of the network, as well as the relationships between the flow rate and specified hydraulic energy required by pumps, depending on various operational configurations.

The paper presents the authors efforts to find the optimum solutions to ensure proper servicing of consumers, 24 hours a day, and reduction of operation costs, proposing the following measures:

1. Rehabilitation of pumping stations, as the capacity of supply has to meet the requirements of the consumers and to take into account the present trend in domestic heating and hot water preparation by individual apartment heating units. The rehabilitation activity consists in replacing the present pumping devices with new ones that feature functional characteristics that correspond to

the present and future requirements of the consumers. These new devices will exhibit technologies present today on the worldwide market.

2. Modernize the pumping station to ensure the increase of energy efficiency and economic efficiency of the domestic and industrial water supply activity, that is, introduce the process automation for a reduced specific consumption of electric energy and reduced operational workforce.

To solve the optimization problem, the authors developed a general mathematical model that will emphasize the importance of the relationship between energy side and technological side of the analyzed process.

The calculation of the ensemble's overall output formed by the pumping station, the distribution network, consumers, loads into consideration the charge specific features which correspond to each ensemble's element, for the two work phases of hydrophore: fill up and emptying. It will correspond in (Q, H) plane by one specific feature of the network – consumer ensemble, for each combination (number, type, position) of active consumers.

It heads into consideration the head equal specific feature H_R, (H_D - head in pipes network origin; Q_D - flow in network origin; Q_R - network flow; α_n - heading grade on network):

$$H_{\mathrm{R}} = \frac{H_{\mathrm{D}} \cdot Q_{\mathrm{R}}^2}{\alpha_n^2 \cdot Q_{\mathrm{D}}^2};\ \alpha_n \in [0,\ 1 \div 1] \ . \tag{1}$$

The hydrophore's head in the analyze section (O) in filling stage $H_{(O)u}$ is shown by the following mathematical relation, (H_{gH} - hydrophore geometrical head; H_H - hydrophore head; $M_{rH,u}$ - hydrophore resistance hydraulic modulus for filling; $Q_{H,u}$ - hydrophore flow for filling):

$$H_{(\mathrm{O}),\mathrm{u}} = H_{\mathrm{gH}} + H_{\mathrm{H}} + M_{\mathrm{rH,u}}\, Q_{\mathrm{H,u}}^2 \ , \tag{2}$$

compared to the water level from the pumping station's aspiration basin, in the analyze section O, for filling up and:

$$H_{(\mathrm{O}),\mathrm{e}} = H_{\mathrm{gH}} + H_{\mathrm{H}} - M_{\mathrm{rH,e}}\, Q_{\mathrm{H,e}}^2 \tag{3}$$

for emptying, ($H_{(O),e}$ - hydrophore head in section O, emptying stage; $M_{rH,e}$ - hydrophore resistance hydraulic modulus for emptying; $Q_{H,e}$ - hydrophore flow for emptying). It was made a program of automatic calculation which can determinate the functional and energetic specific feature of hydraulic machines, for ordinary speed n and nominal speed n_o. The charge specific feature of the pumps can be designed as parabola with completely equation, or as parabola with incompletely equation, (H - pump head; H_{pf} - pump head; k_{pf} - pumps resistance hydraulic modulus) [7]:

$$H = H_{\mathrm{o}} + H_1 \cdot Q + H_2 \cdot Q^2 \ , \quad H = H_{\mathrm{pf}} - k_{\mathrm{pf}} \cdot Q^2 \ . \tag{4}$$

The gap between the flow delivered by a pump with discontinuous running and the one the network is really supplying (keeping head H in the range that ensures the prescribed quality of the supply), compensation capacity has to allow

the creation - between the minimal level, corresponding to the necessary pressure which keeps the minimal head requested by the network H_m, and the maximal level H_M, which is accepted through technical and energetic criteria and ensures the maximal superior limit head on the recommended operating range: $H_M = H_m + \Delta H$ of a serviceable water volume V_u. This value is calculated from the condition that imposes that, compared to the average pump flow Q_{pm} - on the recommended field (H_m, H_M), duration of the filling-emptying cycle T_c - between two successive pump start-ups - to be at least equal with a minimal admitted time T_e, which is specific to the chosen electric drive:

$$V_{\mathrm{u}} \geq \frac{Q_{\mathrm{pm}}.T_{\mathrm{c}}}{4}\ ;\ T_{\mathrm{c}} \geq T_{\mathrm{e}}\,. \tag{5}$$

The outturn specific feature of the pump written as parabola with equation without free term, (R_1 and R_2 are parabola constants):

$$R_{\mathrm{p}} = R_1.Q - R_2.\ Q^2\ . \tag{6}$$

The program calculates the resistance hydraulic modulus for any pipe - line network, taking notice of all singularity types. The head specific feature for pumping station H_{PS} has the following mathematical form, (M_{ro} - pipes network resistance hydraulic modulus; p - pumps number; Q_{PS} - pumping station flow):

$$H_{\mathrm{PS}} = H_{\mathrm{pf}} - \frac{K_{\mathrm{pf}} + M_{\mathrm{ro}}}{p^2}\ Q_{\mathrm{PS}}^2, \tag{7}$$

The mathematical expressions that define the flow and the head for pumping station – networks – hydrophore filling stage ensemble, in O section are:

$$Q_{\mathrm{PS\text{-}R\text{-}H,f}} = \sqrt{\frac{H_{\mathrm{pf}} - H_{\mathrm{g,R\text{-}H,u}}}{M_{\mathrm{R\text{-}H,u}} + \frac{K_{\mathrm{pf}} + M_{\mathrm{ro}}}{p^2}}}, \quad H_{\mathrm{PS\text{-}R\text{-}H,u}} = H_{\mathrm{pf}} - \frac{H_{\mathrm{pf}} - H_{\mathrm{g,R\text{-}N}}}{\frac{M_{\mathrm{R\text{-}H,u}}.p^2}{K_{\mathrm{pf}} + M_{\mathrm{ro}}} + 1}. \tag{8}$$

The power asked by network $N_{c,u}$ and the absorbed power by pump $N_{a,u}$ in the filling stage have the following mathematical relation:

$$N_{\mathrm{c,u}} = \gamma.\ Q_{\mathrm{PS-R-H,u}}\ .H_{\mathrm{(O),PS\text{-}R\text{-}H,u}}\ \ ,\ N_{\mathrm{a,u}} = \frac{\gamma.Q_{\mathrm{p,u}}.H_{\mathrm{p,u}}.p}{\eta_{\mathrm{p}}.\eta_{\mathrm{m}}}\ ;\ Q_{\mathrm{p,u}} = \frac{Q_{\mathrm{PS-R-H,u}}}{p}\ . \tag{9}$$

The total outturn of pumping aggregate – networks – hydrophore fill – up stage ensemble has the following mathematical relation:

$$\eta_{\mathrm{u,PA}} = \frac{N_{c,f}}{N_{\mathrm{a,f}}} = \eta_{\mathrm{p}}\ \eta_{\mathrm{m}}.\ \frac{1}{1 + \frac{K_{\mathrm{pf}} + M_{\mathrm{ro}}}{p^2}\ \frac{Q_{\mathrm{PS\text{-}R\text{-}H,u}}^2}{H_{\mathrm{(O),PS\text{-}R\text{-}H,u}}}}. \tag{10}$$

The hydrophore is acting in the network like a generator and has the following flow, in the emptying stage:

$$Q_{\mathrm{H,g}} = \sqrt{\frac{H_{\mathrm{g,H}} + H_H - H_{(\mathrm{O})}}{M_{\mathrm{rH,g}}}}. \tag{11}$$

It can be written these relations in accordance with the continuity equation, for the *O* section in the emptying stage of hydrophore:

$$Q_{(\mathrm{O}),\mathrm{H\text{-}SP,g}} = Q_{(\mathrm{O}),\mathrm{H,g}} + Q_{(\mathrm{O}),\mathrm{PS}}. \tag{12}$$

The flow and the head for pumping station – networks – hydrophore emptying stage ensemble, in *O* section are:

$$Q_{\mathrm{PS\text{-}R\text{-}H,g}} = \sqrt{\frac{H_{\mathrm{PS\text{-}H,g}}}{M_{\mathrm{PS\text{-}H,g}} + M_{\mathrm{R}}}}\ ; \quad H_{(\mathrm{O}),\mathrm{PS\text{-}R\text{-}H,g}} = H_{\mathrm{PS\text{-}H,g}} \left(1 - \frac{1}{1 + \dfrac{M_{\mathrm{R}}}{M_{\mathrm{PS\text{-}H,g}}}} \right) \tag{13}$$

The powers asked by network and pump, in the emptying stage have the following mathematical forms:

$$N_{\mathrm{c,g}} = \gamma \cdot Q_{\mathrm{PS\text{-}R\text{-}H,g}} \cdot H_{(\mathrm{O}),\mathrm{PS-R-H,g}}\ ; N_{\mathrm{a,g}} = \frac{\gamma \cdot Q_{\mathrm{p,g}} \cdot H_{\mathrm{p,g}} \cdot p}{\eta_{\mathrm{m}} \cdot \eta_{\mathrm{p}}}; Q_{\mathrm{p,g}} = \frac{Q_{\mathrm{PS-R-H,g}} - Q_{\mathrm{H,g}}}{p}. \tag{14}$$

The overall outturn of the pumping station – networks – hydrophore emptying stage ensemble, in *O* section has the following mathematical relation:

$$\eta_{\mathrm{g,PA}} = \frac{N_{\mathrm{c,g}}}{N_{\mathrm{a,g}}} = \frac{\eta_{\mathrm{m}}\ \eta_{\mathrm{p}}}{\left(1 - \dfrac{Q_{\mathrm{H,g}}}{Q_{(\mathrm{O}),\mathrm{PS\text{-}R\text{-}H,g}}} \right)} \cdot \frac{1}{\left[1 + \dfrac{k}{p^2\ H_{(\mathrm{O}),\mathrm{PS\text{-}R\text{-}H,g}}} \left(Q_{\mathrm{PS\text{-}R\text{-}H,g}} - Q_{\mathrm{H,g}} \right)^2 \right]} \tag{15}$$

The operational regimes for the pumping station supplies (ensemble of active pumps in the pumping station – open level tanks – slopes) will be analyzed taking into account required static heads, which vary in a pre-established range. This will emphasize the options to increase the designed flow rate, and determine energetic and economic characteristics of the typical operational regimes. One of the goals is to increase the transport capability of gravitational supplies. Energy employed to transport the fluid unit weight in the network unit length is given by the hydraulic head J_o – a parameter that influences every energetic and economic characteristic of the water transport and distribution ensemble pumping station – pipe network – consumer, $J_o = m.Q^{\gamma}.D^{-\beta}$. H_{t} represents the head loss in the discharge pipe for the pipe material, $H_t = m.L.Q^{\gamma}.D^{-\beta}$. To cover for the head losses in water transport of the annual volume W_o that is absorbed from the supply source [5], the energy required E'_p is:

$$E_{\mathrm{p}}^{'} = F.E_{\mathrm{p}};\ E_{\mathrm{p}} = \frac{W_{\mathrm{o}}.H_{\mathrm{o}}}{367.\eta_{\mathrm{h}}.\eta_{\mathrm{a}}} + \frac{1}{367}.\sum_{\mathrm{i=1}}^{\mathrm{n}} \frac{W_{\mathrm{i}}.H_{\mathrm{i}}}{\eta_{\mathrm{h}}^{\mathrm{i}}.\eta_{\mathrm{a}}^{\mathrm{i}}};\qquad (16)$$

Constant F is calculated with the form, (f, g - specific parameter; $p(q_i)$ - relative flow frequency; q_i - relative flow; β, γ - constant of hydraulic slope):

$$F = f^{-1}.g;\ f = \sum_{\mathrm{i}} q_{\mathrm{i}}.p\left(q_{\mathrm{i}}\right);\ g = \sum_{i}\ q_{\mathrm{i}}^{\gamma+1}\ .p\left(q_{\mathrm{i}}\right) \qquad (17)$$

The investment in constructions and devices I_p for pressurized transport is, (I_{Po} - investment in pumping station; i_p - investment coefficient in constructions and installations):

$$I_{\mathrm{p}} = I_{\mathrm{po}} + i_{\mathrm{p}}\ .N_{\mathrm{i}}\ . \qquad (18)$$

Processing the data acquired on the dependence between the investment in pipes I_R and the rated diameter D it follows that, (i_o - coefficient investment in pipe network; L - pipe length; n_N - upsetting pipe number; b - constant):

$$I_{\mathrm{R}} = n_{\mathrm{N}}\ .\ L.\ \left(i_{\mathrm{o}} + b\ .D^{\alpha}\right). \qquad (19)$$

The unitary cost of power energy p_o is different in the vertex period of head curve against basis period [2], (p_b - basis energy unitary cost; p_v - vertex energy unitary cost; t_p - pumping daily average time; t_{vp} - pumping daily average time in vertex period):

$$p_{\mathrm{o}} = p_{\mathrm{b}}\ .\left[1+\nu_{\mathrm{p}}\ .\left(m_{\mathrm{v}}-1\right)\right];\ \nu_{\mathrm{p}} = \frac{t_{\mathrm{vp}}}{t_{\mathrm{p}}};\ m_{\mathrm{v}} = \frac{p_{\mathrm{v}}}{p_{\mathrm{b}}}. \qquad (20)$$

The yearly average expenses quota in pumping station a_P" and the yearly average expenses quota in discharge pipe a_R" take into account different development rates for various economic domains that affect this analysis and all expenses are computed relative to the same moment in time: the first day of operation [2], (a_p - average overall quota in pumping station; a_r - average overall quota in pipe; r - monthly average rate for updating; t - recovery time of investment; T_r - existence standardised duration for the analysed system; u_a - annual average increase instalment; u_c - average parameter of cost annual increase; u_e - actualisation coefficient):

$$a_{\mathrm{p}}^{''} = a_{\mathrm{p}}^{'} + \frac{1}{T_{\mathrm{r}}},\ \ a_{\mathrm{p}}^{'} = a_{\mathrm{p}}.\frac{\sum_{\mathrm{k=1}}^{\mathrm{t}}\left(\frac{1+u_{\mathrm{a}}}{1+r}\right)^{\mathrm{k}}}{\sum_{\mathrm{k=1}}^{\mathrm{t}}\left(\frac{1+u_{\mathrm{e}}}{1+r}\right)^{\mathrm{k}}},\ \ T_{\mathrm{r}} = \sum_{\mathrm{k=1}}^{\mathrm{t}}\left(\frac{1+u_{\mathrm{e}}}{1+r}\right)^{\mathrm{k}}. \qquad (21)$$

$$a_{\mathrm{R}}^{''} = a_{\mathrm{R}}^{'} + \frac{1}{T_{\mathrm{r}}};\ a_{\mathrm{R}}^{'} = a_{\mathrm{R}}\ \frac{\sum_{k=1}^{t}\left(\frac{1+u_{\mathrm{c}}}{1+r}\right)^{k}}{\sum_{k=1}^{t}\left(\frac{1+u_{\mathrm{e}}}{1+r}\right)^{k}} \qquad (22)$$

The energy unitary specific consumption e_s depend of flow $Q_{H,u}$, head hydraulic power $H_{H,u}$ and outturn $\eta_{H,u}$ corresponding to mathematical relation:

$$e_s = \frac{N_{H,u} \cdot 10^3}{3600 \cdot \eta_{H,u} \cdot Q_{H,u} \cdot H_{H,u}}. \tag{23}$$

The optimization problem consists in identification of the proper values for pumping station operational parameters that will determine the minimum specific consumption averaged on yearly basis, abiding by the operational and constructional restrictions as well as assuming normalized section dimensions; some of these variables (*D, L, n, η*) have direct or indirect influences on device's proper operation [3]. The goal is to determine the values of the *D, L, n* parameters that minimize the economic target function *Z(D, n)*. This function is given by the equation (24):

$$Z = a''_p \cdot I_p + a''_R \cdot I_R + p_o \cdot E_p = a''_p \cdot \left(I_{po} + i_p \cdot m \cdot \frac{k \cdot Q_M^{\gamma+1} \cdot L}{\eta_{PA} \cdot n_N^{\gamma} \cdot D^{\beta}} \right) + a''_R \cdot n_N \cdot L \cdot$$
$$\cdot \left(i_o + b \cdot D^{\alpha} \right) + \frac{k \cdot m \cdot L \cdot Q_M^{\gamma} \cdot F \cdot W_o \cdot p_o}{D^{\beta} \cdot n_N^{\gamma} \cdot \eta \cdot 3600}. \tag{24}$$

The solution for the pair of variables (*D, n*) is given by the values that minimize the economic target function *Z(D, n)*; mathematically this means:

$$\frac{\partial Z}{\partial n} = 0; \frac{\partial Z}{\partial D} = 0 \tag{25}$$

The mathematical formulae for the optimum number of discharge pipes and for the optimum pipe diameter are:

$$n_o = \left[\left(\frac{\alpha \cdot \gamma}{\beta} - 1 \right) \cdot \frac{b^{\beta}}{i_o^{\alpha+\beta}} \right]^{\frac{1}{\alpha \cdot (\gamma+1)}} \cdot \left[\frac{k \cdot m \cdot \beta}{a''_R \cdot \alpha \cdot \eta} \cdot \left(i_p \cdot Q_M^{\gamma+1} \cdot a''_p + \frac{Q_M \cdot F \cdot W_o \cdot p_o}{3600} \right) \right]^{\frac{1}{\gamma+1}};$$
$$D_o = \left[\frac{k \cdot m \cdot \beta}{b \cdot \alpha \cdot \eta^{\gamma+1} \cdot a''_R} \cdot \left(a''_p \cdot i_o \cdot Q_M^{\gamma+1} + \frac{Q_M \cdot F \cdot W_o \cdot p_o}{3600} \right) \right]^{\frac{1}{\alpha+\beta}}. \tag{26}$$

The optimum pump type and dimensions (number of stages and rotational speed) is determined such as it may ensure the required flow rate, with specified head, for the highest value of efficiency; this value will become the reference maximum efficiency for pump selection.

For a given water supply system, with specified operational capacity, the same mathematical model is used, but this time the nominal diameter of the discharge pipe is known; it is possible to calculate an optimal flow Q_{opt} and then (with imposed conditions) the minimal annual average total cost. Then, comparing with the required supply capacity and analyzing previous data, the measures for modernizing and improving the studied water supply system may be chosen.

To make the best selection of a pump, it is useful to determine maximal efficiencies that can be reached by pumps having z = 1, 2, ..., k* stages, which, drive at different synchronism speeds, and may ensure the requested (Q, H) parameters. This is the method used to establish all functional and constructive pump characteristics and, also, the energetic performances required.

The selected pumps need match the required variables imposed by the water transport supply network. To reach this goal, pumps may be operated intermittently, or required flow rates may be compensated with a supplemental tank, that may be free level tank or air cushion tank (booster) that keeps constant operational pressure, ensuring also the network surge protection [6].

Efficiency of this control method is conditioned by satisfying the network requirements, maintaining the pump efficiencies in the neighbourhood of their maximal efficiency. Efficiency may be maintained at high levels if pump is properly sized and the compensation capacity is adequate. Also, it is mandatory to adequately operate the system composed of pumps, tank and network.

3 Experimental results

The optimization method is applied in the pumping station Codrescu, Iasi, for drinkable water, Figure 1. The pumping station is equipped with EP NK 64 x 4 pumps and rotational speed of n = 2900 rpm. Using several original mathematical algorithms, authors developed a computer program that calculates the functional parameters of the ensemble pumping station – hydrophore – pipe distribution network, as well as the available consumer parameters [4]. This may be accomplished at each moment in time, depending on the number of active consumers simultaneously connected to the supply network, in the hypothesis of a minimum price of cubic meter of pumped water.

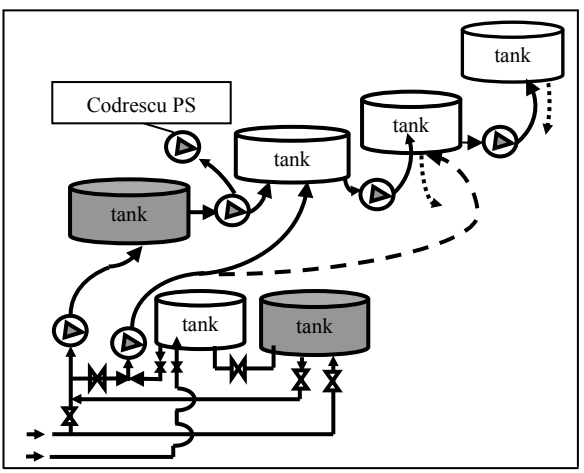

Figure 1: The drinkable water supply system scheme of Iasi city with Codrescu pumping station.

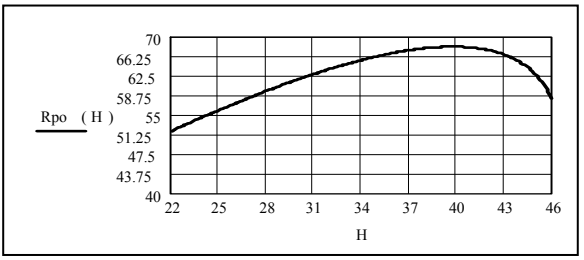

Figure 2: Nominal outturn variation R_{po} in accordance with head H for EP NK 64x4 pump.

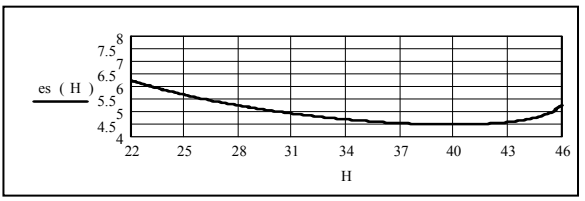

Figure 3: Unitary specific energy consumption variation e_s depending on head H, after the system's optimization.

Figure 2 shows the variation of outturn in accordance with pump's head $R_{po}(H)$.

The unitary specific energy consumption $e_s(H)$ for EP NK 64x4 pump depending on head, after the system's optimization are presented in Figure 3. The energy specific consumption e_s depend on the energy consumed in the period reference and water volume delivered in same period.

Figure 4 shows the working regimes of Codrescu pumping station at hydrophore heads H_H = 15 m, after the system's optimization. It is drawn outturn curves for $R_{H,u}$ = 50 ÷ 68%; also are drawn the variations of flow $Q_{H,u}$, head $H_{H,u}$, hydraulic power $N_{H,u}$ and unitary specific energy consumption variation e_s for different static head on hydrophore H_H at filling stage. The flow, power and unitary specific energy consumption variation depending on the hydrophore head, in filling stage, after the system's optimization are shown in Figure 5.

Codrescu pumping station working on hydrophore and outturn depending on flow Q, after system optimizations are presented in Figure 6. The recovery time of investment for the rehabilitation of Codrescu pumping station depend on the pumped water volume W_o and the monthly instalments number of credit engaged for the rehabilitation's achievement.

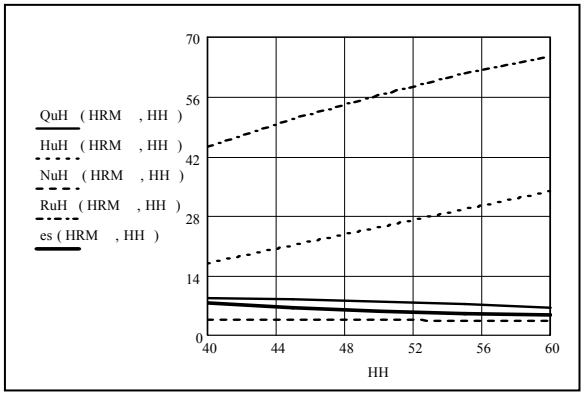

Figure 4: The working regimes of Codrescu pumping station with hydrophore head H_H = 15 m, at filling stage, after the system's optimization.

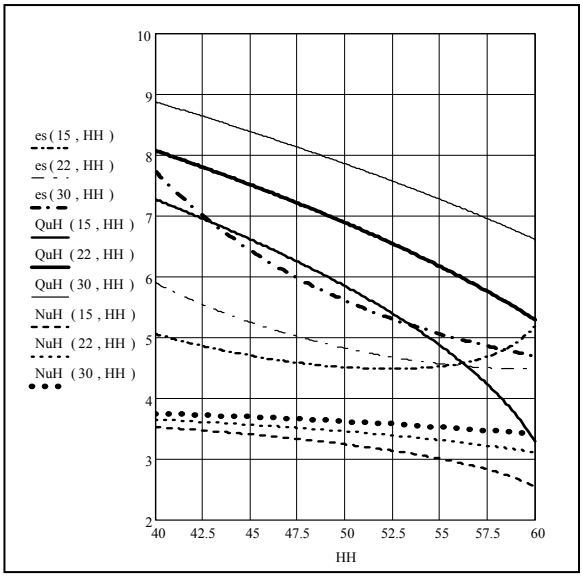

Figure 5: Flow, power and unitary specific energy consumption depending on hydrophore head, in filling stage, after the system's optimization.

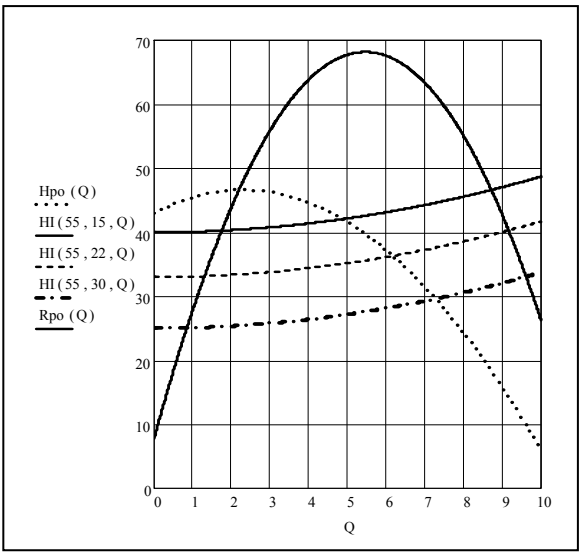

Figure 6: Codrescu pumping station working on hydrophore and outturn depending on flow Q, after the system's optimization.

4 Conclusions

The replacement of the existent equipment, that is obsolete from physical and technological point of view, must be done with new equipments with performances that will meet the requirements of an optimum operation from both energetic and economic perspectives. The water transport and distribution network must have the capability to meet the requirements of the consumers.

The insurance of efficient operation relies on automatic supervision and control of pumping installation, as well as automatic adjustments to variable consumer requirements.

The proposed analysis method is based on the system's mathematical modelling, simplified by analytic specific features of its components and the automated data processing system.

This analysis method has two objectives: the determination of the overall output about the pumping station – network – hydrophore – consumer's ensemble and the consumer's total typical energy e_s. The analyse was done to define the regimes of exploitation thus the overall output of the installation to be maximum, and the consumption of total specific energy to be minimum on the entire working cycle. Those two distinctive fazes of the hydrophore function (filling in/emptying) have been analysed depending on the loading grade of the network, α = (0,1 ÷ 1). The hydraulic system works with the following parameters: head H = (43 ÷ 73) m, flow Q = (5 ÷ 7,3) m^3/s, e_s = (4,5 ÷ 6,25)

kWh/m^3, η = (63 ÷ 68)%; these parameters are imposed by analysing with this method, through application of the software made by author.

If the consumers want to have a better water supplying regime (head H, flow Q and outturn η), the better parameters cannot be realised without increasing the total specific energy: meaning that the price of the water will grow up as well.

The research results are used for design optimization of the water supply installation for areas with various relief forms. The proposed method for energetic optimization allows a reduction with 10 ÷ 15% of the energy consumption required to operate the pumping station – network – hydrophore – consumers ensemble.

Acknowledgement

This work has been supported by the National Centre of Management Programmers, Bucharest, Romania, and financial contract No. 21-041/2007.

References

[1] Alexandrescu, A. & Popescu, D., The optimization of the pumping installation's working with the hydrophore, *Proc. of Computer Modelling in Engineering & Sciences*, Cap. 14, Fluid Flow & Heat Transfer, Pub. Tech Science Press, Encino, CA 91316, U.S.A. 208ICCES, 2003.

[2] Alexandrescu, A., Alexandrescu, S. A., & Alexandrescu, C. A., Contributions Regards the Optimization of the Hydraulic Systems for the Reduction of Energy Consumption, *Journal of International Research Publications*, *Materials, Methods and Technology*, Sunny Beach, Bulgaria, Vol. IV, pp. 24-33, 2008.

[3] Alexandrescu, A., Alexandrescu, S. A., & Alexandrescu, C. A., Contribution as for the optimization of the pumping stations, *Proc. International Conference on Computational & Experimental Engineering & Sciences*, ICCES0820071216415, Vol. 415, No. 1, Honolulu, Hawaii, U.S.A., pp. 1-11, 2008.

[4] Burns, M., Cottage Water Systems: An out – of – the City. Guide to Pumps, Plumbing Water, Purification and Privies, Hardcover, SUA, 2006.

[5] Douglass, H. M., *Conduit Fluid Flow*, Bloomington, IN, Ed. Mc Graw – Hill Science / Engineering / Math, USA, 2004.

[6] Klarbring, A., Petersson, J. & Torstenfelt, B., Karlsson, Topology optimization of networks, *Computer Methods in Applied Mechanics and Engineering,* Vol 192, Issue 35 – 36, S.U.A., pp. 3909 – 3932, 2005.

[7] Shun, D. L., Lee, C. C., *Water and Wastewater Calculations Manual*, Ed. Mc Graw – Hill Professional, New York, USA, 2002.

Section 4
Fluid structure interaction

This page intentionally left blank

Hydrodynamic loading on elliptic cylinders in regular waves

M. Rahman[1] & S. H. Mousavizadegan[2]
[1]*Retired Professor of Dalhousie University, Halifax, Canada*
[2]*Faculty of Marine Tech., Amirkabir University of Tech., Tehran, Iran*

Abstract

This paper deals with an elliptical cylinder in regular waves and investigation is made to determine the exciting forces and moments exerted on this body in regular waves. We have used the potential theory formulation in this case under the assumption that the viscous effects are negligible. An analytical solution to the linear wave diffraction problem, in terms of the infinite series of Mathieu's function, for a fixed vertical cylinder of elliptical cross-section in water of finite depth d has been presented. Further, Mathieu functions were simplified by taking the characteristic number s to be independent of the parameter q. The values of these simplified forms of Mathieu functions are substituted in the closed form approximations for the force and moment components for small eccentricity e of the cylinder, and the results thus obtained are compared with the existing results in the previous literature. The comparison shows good agreement except for $e = 0.9$ and $e = 1.0$. The limiting case of the circular cylinder, obtained by taking $e = 0$, has also been studied. The horizontal and vertical forces for the circular and elliptical cylinder for angle of incidence $\alpha = 0°$ and $90°$ have been compared.
Keywords: hydrodynamics, loading, forces and moments, elliptic cylinders, regular waves, finite depth oceans, diffraction, scattering.

1 Introduction

The determination of wave forces on offshore structures is essential to study the effects of waves, wind and current on them. The offshore structures should experience minimal movement to provide a stable work station for operations such as drilling and production of oil. The solution to the problem of ocean wave interaction with offshore structures is usually very complex. In many cases, only

WIT Transactions on Engineering Sciences, Vol 69, © 2010 WIT Press
www.witpress.com, ISSN 1743-3533 (on-line)
doi:10.2495/AFM100321

an approximate solution is sought. Some of the mathematical techniques required for the hydrodynamic problem associated with the design of offshore structures are analytical while many are numerical in nature. While the evolution of computers has made the numerical methods more advantageous over the classical analytical methods, numerical methods alone cannot find absolute success without being complemented by either analytical methods or at least experiments; in this sense analytical methods become a cost efficient and handy technique for designers in most cases.

The diffraction of plane waves by circular cylinders and ribbons is well known and adequately documented in the literature. Both situations are the limiting cases of the corresponding elliptical-cylinder problem. Many studies have been done on the interaction of electromagnetic or sound waves with an elliptic cylinder of infinite length. The solution to the problem of diffraction of electromagnetic waves by an elliptic cylinder and the corresponding Mathieu function series solution was originally given by Sieger [4]. This paper attracted scant attention, owing possibly to a lack of physical applications, and to analytical difficulties; for the Mathieu functions could not be treated in a straight forward way like Bessel functions or Legendre polynomials.

Chen and Mei [1] investigated the problem of scattering of linear progressive waves by an elliptic cylinder. They obtained the various force and moment coefficients in terms of Mathieu function series and presented extensive numerical results for arbitrary wavelengths using a computer program developed by Clemm [2] for the Mathieu functions.

In the present work the theory developed by Williams [5] has been used to obtain the force and moment coefficients on the surface of a fixed elliptic cylinder in water of finite depth for various angles of incidence and for a wide range of eccentricities ranging from 0.1 to 1.0. While deriving the approximate expressions for the force and moment coefficients for small eccentricity Williams [5] has adopted the notations of McLachlan [3] while in the present analysis simplified forms of Mathieu functions given.

2 The coordinate system

Consider a fixed, rigid vertical cylinder of elliptical cross-section in water of finite depth d (Figure 1). The coordinate system is fixed with the x-axis along the still water surface and the z-axis pointing vertically upwards along the axis of the cylinder. Since the objective of this investigation is to study the potential flow around an elliptical cylinder in the x-y plane, therefore, the elliptical coordinate system would be the appropriate and logical choice. The elliptical coordinates are denoted by (ξ, η, z) where $\xi =$ constant and $\eta =$ constant are families of confocal ellipses and hyperbolae, intersecting orthogonally, with common foci ($\pm c$, 0).

The elliptical coordinates (ξ, η, z) can be related to the Cartesian coordinates (x, y, z) by using the following transformation. $x = c\cosh\xi\cos\eta$, $y = c\sinh\xi\sin\eta$ and $z = z$. The semi-major and minor axes of the ellipse are given as follows. $a = c\cosh\xi$ and $b = c\sinh\xi$. The eccentricity of the ellipse can be expressed as

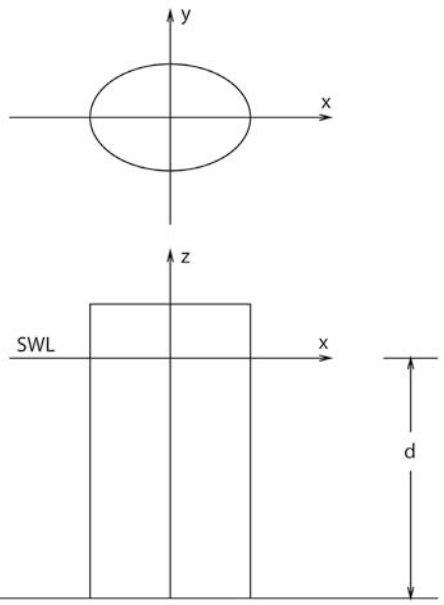

Figure 1: Definition sketch for an elliptic cylinder.

$e = \sqrt{1-(b/a)^2}$. The focal distance is given by $c = \sqrt{a^2 - b^2}$. If we keep focus, c, fixed and let eccentricity $e \to 1, \xi \to 0$, the elliptical cylinder transforms to a line of length $2c$. Alternatively, if we allow $e \to 0, \xi \to \infty$, then $a \to b$, the ellipse will transform to a circle with radius $r = (x^2 + y^2)^{\frac{1}{2}}$.

3 Mathematical formulation

A simple and concise mathematical model to study the potential flow around an elliptic cylinder can be constructed by using the well known general assumptions which govern any flow around a solid geometry. To facilitate this, we consider an inviscid, homogeneous and incompressible fluid and the flow around the object to be irrotational. By virtue of these assumptions, Euler's and the continuity equations can be simplified to yield Laplace's equation. Let $\Phi(\xi, \eta, z, t)$ denote the total fluid potential and let $z = \gamma(\xi, \eta, t)$ be the equation of the free surface, where (ξ, η, z) are the elliptical coordinates. Then everywhere in the region of the flow, the fluid motion is governed by Laplace's equation.

$$\nabla^2 \Phi(\xi, \eta, z, t) = 0 \tag{1}$$

where ∇ is the Laplacian operator.

The velocity potential is subject to the following linearized boundary conditions:

Bottom boundary condition:

Assuming the floor of the ocean to be flat, the boundary condition at the ocean bottom states that the vertical component of the velocity is zero at the bottom

$$\frac{\partial \Phi}{\partial z} = 0 \quad \text{at } z = -d; \tag{2}$$

Body surface boundary condition:

On the surface of the body the velocity of the fluid must be equal to zero

$$\frac{\partial \Phi}{\partial \xi} = 0 \quad \text{on } \xi = \xi_o \tag{3}$$

Dynamic free surface boundary condition:

The dynamic free surface condition is derived from the Bernoulli equation, on the assumption that the atmospheric pressure outside the fluid is constant.

$$g\gamma - \frac{\partial \Phi}{\partial t} = 0 \quad \text{on } z = 0 \tag{4}$$

Kinematic free surface boundary condition:

The kinematic condition states that a particle lying on the free surface will continue to remain on the surface. Mathematically,

$$\frac{\partial \gamma}{\partial t} + \frac{\partial \Phi}{\partial z} = 0 \quad \text{on } z = \gamma \tag{5}$$

Equation (5) is a concise form of kinematic free surface boundary condition from which the nonlinear terms have been omitted. The dynamic and the kinematic free surface boundary conditions can be combined together to yield one equation which is known as free surface boundary condition,

$$\frac{\partial^2 \Phi}{\partial t^2} + g\frac{\partial \Phi}{\partial z} = 0 \quad \text{on } z = 0 \tag{6}$$

Radiation condition:

In addition to the above boundary conditions, there is the Sommerfeld radiation condition to be discussed. This radiation condition is introduced after splitting the total velocity potential Φ as the sum of an incident wave potential Φ_I and the scattered wave potential Φ_S that is

$$\Phi = \Phi_I + \Phi_S \tag{7}$$

At large distance from the cylinder the scattered potential must be an outgoing wave i.e Φ_S must satisfy the radiation condition, namely

$$\frac{\partial \phi_S}{\partial r} \pm ik_1\phi_S = 0 \quad \text{as } r \to \pm\infty \tag{8}$$

where $\Phi_s = Re(\phi_s e^{-i\sigma t})$ and k_1 is the incident wave number. Here Re stands for the real part, σ is the wave frequency and ϕ_s the complex wave potential.

4 Solution of Laplace's equation in elliptical coordinates

Laplace's equation in cartesian coordinates (x, y, z) is written as:

$$\nabla^2\Phi = \frac{\partial^2\Phi}{\partial x^2} + \frac{\partial^2\Phi}{\partial y^2} + \frac{\partial^2\Phi}{\partial z^2} = 0 \tag{9}$$

The above equation can be expressed in terms of elliptical coordinates (ξ, η,z) by using the transformation stated in section 2:

$$\frac{\partial^2\Phi}{\partial\xi^2} + \frac{\partial^2\Phi}{\partial\eta^2} + c^2(\sinh^2\xi + \sin^2\eta)\frac{\partial^2\Phi}{\partial z^2} = 0 \tag{10}$$

To obtain a solution to equation (10) we write

$$\Phi(\xi,\eta,z) = F(\xi)G(\eta)Z(z) \tag{11}$$

where, F(ξ) is a function of ξ, G(η) is a function of η and Z(z) is a function of z alone. Defining a new positive constant s and the parameter q as $s = l^2 + \frac{p^2c^2}{2}$ and $q = \frac{p^2c^2}{4}$, the Laplace's equation can be written as

$$\frac{d^2G}{d\eta^2} + (s - 2q\cos 2\eta)G = 0 \tag{12}$$

and

$$\frac{d^2F}{d\xi^2} - (s - 2q\cosh 2\xi)F = 0 \tag{13}$$

Equation (12) and (13) are known as the canonical forms of Mathieu's equation and modified Mathieu's equation respectively. The solution to equation (12) consists of the periodic Mathieu functions

$$G(\eta) = [ce_n(\eta,q), se_n(\eta,q)] \tag{14}$$

where $ce_n(\eta,q)$ and $se_n(\eta,q)$ are respectively the even and odd Mathieu functions of order n and argument η, while the solution to equation (13) consists of the modified (or radial) Mathieu functions

$$F(\xi) = [Ce_n(\xi,q), Se_n(\xi,q); Fey_n(\xi,q), Gey_n(\xi,q)] \tag{15}$$

of the first and second kind of order n and arguments ξ. These and other variety of Mathieu functions are defined in McLachlan . The functions $ce_n(\eta,q)$ and $se_n(\eta,q)$ can be expressed as a series of cosine and sine terms. Also, the functions $Ce_n(\xi,q)$ and $Se_n(\xi,q)$ can be written as a series of Bessel's function J_n of the first kind, while the functions $Fey_n(\xi,q)$ and $Gey_n(\xi,q)$ can be written as a series

of Bessel's function Y_n of the second kind. Thus solution of equation (10) which is periodic in η and has a real exponential behaviour in z will consist of the product of equation (11) with any linear combination of products of equations (14) and (15) which have the same value of s and q, namely

$$[\exp(pz), \exp(-pz)][(Ce_n(\xi,q), Fey_n(\xi,q))ce_n(\eta,q), \\ (Se_n(\xi,q), Gey_n(\xi,q))se_n(\eta,q)]$$

5 A close form analytical solution

In this section a closed form solution to the linear diffraction problem is obtained for a fixed vertical cylinder of elliptic cross-section extending from the seabed and piercing the free surface. This type of analysis, was initially done by Chen and Mei [1], and then by Williams [5]. A complete derivation of the velocity potential Φ and expressions for the force and moment coefficients is presented here, in terms of Mathieu functions. For the following analysis, the usual assumption of inviscid, incompressible fluid and irrotional flow is made. A linear simple harmonic wave of time period T, wave length L, wave height H and angular frequency σ is incident at an angle α to the major-axis upon a vertical cylinder of elliptic cross-section in water of finite depth d. The incident wave upon arriving at the structure undergoes significant diffraction. The incident waves are assumed to be of small height as compared to their lengths in a finite water depth so that the linear theory may be used. The coordinate system and the mathematical formulation along with the boundary conditions have already been discussed. Then, the potential due to the linear incident wave is given by

$$\Phi_I = \frac{gH}{\sigma}\frac{\cosh k_1(z+d)}{\cosh k_1 d} Re\left[e^{-i\sigma t}\exp\{ik_1(x\cos\alpha + y\sin\alpha)\}\right] \tag{16}$$

where Re stands for the real part, x and y are given in section 2 and g is the acceleration due to gravity. In terms of Mathieu functions (see McLachlan [3, p.207]),

$$\begin{aligned}\Phi_I = \frac{2gH}{\sigma}&\frac{\cosh k_1(z+d)}{\cosh k_1 d} \\ &Re\left[e^{-i\sigma t}\sum_{n=0}^{\infty}\left\{A_0^{2n}\frac{Ce_{2n}(\xi,q)ce_{2n}(\eta,q)ce_{2n}(\alpha,q)}{ce_{2n}(0,q)ce_{2n}(\frac{\pi}{2},q)}\right.\right. \\ &+ qB_2^{2n+2}\frac{Se_{2n+2}(\xi,q)se_{2n+2}(\eta,q)se_{2n+2}(\alpha,q)}{se'_{2n+2}(0,q)se'_{2n+2}(\frac{\pi}{2},q)} \\ &- iq^{\frac{1}{2}}A_1^{2n+1}\frac{Ce_{2n+1}(\xi,q)ce_{2n+1}(\eta,q)ce_{2n+1}(\alpha,q)}{ce_{2n+1}(0,q)ce'_{2n+1}(\frac{\pi}{2},q)} \\ &\left.\left.+\ iq^{\frac{1}{2}}B_1^{2n+1}\frac{Se_{2n+1}(\xi,q)se_{2n+1}(\eta,q)se_{2n+1}(\alpha,q)}{se'_{2n+1}(0,q)se_{2n+1}(\frac{\pi}{2},q)}\right\}\right]\end{aligned} \tag{17}$$

In order to find an expression for the scattered potential Φ_S we introduce the modified Mathieu functions of the third and fourth kinds denoted by $Me_n^{(1)}$, $Ne_n^{(1)}$ and $Me_n^{(2)}$, $Ne_n^{(2)}$ which can be expressed as:

$$\begin{aligned} Me_n^{(1),(2)} &= Ce_n(z,q) \pm iFey_n(z,q) \\ Ne_n^{(1),(2)} &= Se_n(z,q) \pm iGey_n(z,q) \end{aligned} \tag{18}$$

where Fey_n and Gey_n are the even and odd modified Mathieu functions of the second kind respectively.

Thus, the scattered potential Φ_S is taken to be of the form

$$\begin{aligned} \Phi_S = \frac{2gH}{\sigma}\frac{\cosh k_1(z+d)}{\cosh k_1 d} \\ Re\left[e^{-i\sigma t}\sum_{n=0}^{\infty}\left\{c_{2n}Me_{2n}^{(1)}(\xi,q)ce_{2n}(\eta,q)ce_{2n}(\alpha,q)\right.\right. \\ + c_{2n+1}Me_{2n+1}^{(1)}(\xi,q)ce_{2n+1}(\eta,q)ce_{2n+1}(\alpha,q) \\ + s_{2n+2}Ne_{2n+2}^{(1)}(\xi,q)se_{2n+2}(\eta,q)se_{2n+2}(\alpha,q) \\ \left.\left. + \ s_{2n+1}Ne_{2n+1}^{(1)}(\xi,q)se_{2n+1}(\eta,q)se_{2n+1}(\alpha,q)\right\}\right] \end{aligned} \tag{19}$$

where c_{2n}, c_{2n+1}, s_{2n+2} and s_{2n+1} are coefficients to be determined. The total velocity potential is obtained by adding the incident potential Φ_I and scattered potential Φ_S

$$\Phi = \Phi_I + \Phi_S \tag{20}$$

Thus, using equation (17) and (19), we obtain:

$$\begin{aligned} \Phi = \frac{2gH}{\sigma}\frac{\cosh k_1(z+d)}{\cosh k_1 d} \\ Re\left\{e^{-i\sigma t}\sum_{n=0}^{\infty}\left[\left\{\frac{A_0^{2n}Ce_{2n}(\xi,q)}{ce_{2n}(0,q)ce_{2n}(\frac{\pi}{2},q)} + c_{2n}Me_{2n}^{(1)}(\xi,q)\right\}\right.\right. \\ \times ce_{2n}(\eta,q)ce_{2n}(\alpha,q) \\ + \left\{\frac{qB_2^{2n+2}Se_{2n+2}(\xi,q)}{se'_{2n+2}(0,q)se'_{2n+2}(\frac{\pi}{2},q)} + s_{2n+2}Ne_{2n+2}^{(1)}(\xi,q)\right\} \\ \times se_{2n+2}(\eta,q)se_{2n+2}(\alpha,q) \\ + \left\{\frac{-iq^{\frac{1}{2}}A_1^{2n+1}Ce_{2n+1}(\xi,q)}{ce_{2n+1}(0,q)ce'_{2n+1}(\frac{\pi}{2},q)} + c_{2n+1}Me_{2n+1}^{(1)}(\xi,q)\right\} \\ \left.\left. \times ce_{2n+1}(\eta,q)ce_{2n+1}(\alpha,q)\right.\right. \end{aligned}$$

$$+\left\{\frac{iq^{\frac{1}{2}}B_1^{2n+1}Se_{2n+1}(\xi,q)}{se'_{2n+1}(0,q)se_{2n+1}(\frac{\pi}{2},q)}+s_{2n+1}Ne^{(1)}_{2n+1}(\xi,q)\right\}$$
$$\times se_{2n+1}(\eta,q)se_{2n+1}(\alpha,q)\Bigg]\Bigg\} \tag{21}$$

To determine the coefficients, $c_{2n}, c_{2n+1}, s_{2n+2}$ and s_{2n+1} we use the boundary condition that the water-particle velocity normal to the surface of the cylinder is zero. Thus we obtain

$$\Phi=\frac{2gH}{\sigma}\frac{\cosh k_1(z+d)}{coshk_1d}$$
$$\sum_{n=0}^{\infty}\Bigg[\left\{\frac{A_0^{2n}ce_{2n}(\eta,q)ce_{2n}(\alpha,q)Ee_{2n}(\xi,q)Ve_{2n}(\xi_0,q)}{ce_{2n}(0,q)ce_{2n}(\frac{\pi}{2},q)}\right\}\cos(\sigma t-\beta_{2n})$$
$$+\left\{\frac{qB_2^{2n+2}se_{2n+2}(\eta,q)se_{2n+2}(\alpha,q)Ue_{2n+2}(\xi_0,q)De_{2n+2}(\xi,q)}{se'_{2n+2}(0,q)se'_{2n+2}(\frac{\pi}{2},q)}\right\}$$
$$\times\cos(\sigma t-\gamma_{2n+2})$$
$$+\left\{\frac{q^{\frac{1}{2}}A_1^{2n+1}ce_{2n+1}(\eta,q)ce_{2n+1}(\alpha,q)Ee_{2n+1}(\xi,q)Ve_{2n+1}(\xi_0,q)}{ce_{2n+1}(0,q)ce'_{2n+1}(\frac{\pi}{2},q)}\right\}$$
$$\times\sin(\beta_{2n+1}-\sigma t)$$
$$+\left\{\frac{q^{\frac{1}{2}}B_1^{2n+1}se_{2n+1}(\eta,q)se_{2n+1}(\alpha,q)Ue_{2n+1}(\xi_0,q)De_{2n+1}(\xi,q)}{se'_{2n+1}(0,q)se_{2n+1}(\frac{\pi}{2},q)}\right\}$$
$$\times\sin(\sigma t-\gamma_{2n+1})\Bigg] \tag{22}$$

6 Forces and moments on the elliptical cylinder

We shall now derive the formulae for force F(F_x, F_y) and moment M(M_x, M_y and M_z). Here x, y and z represent the components along the three coordinate axes respectively. The pressure normal to the surface of the elliptic cylinder is given by the linearized Bernoulli equation. Thus if p denotes the pressure, ρ the fluid density and g the acceleration due to gravity, then

$$p=\rho\Phi_t-\rho gz \quad \text{on } \xi=\xi_0 \tag{23}$$

Then F_x and F_y are given by the formula

$$F_x^{(1)}=\int_S p\,(\hat{n}\cdot\hat{x})\;dS \qquad F_y^{(1)}=\int_S p\,(\hat{n}\cdot\hat{y})\;dS \quad \text{on } \xi=\xi_0 \tag{24}$$

where S denotes the wetted surface of the body, $\hat{n}$ is the unit normal in the outward direction to the surface of the cylinder and dS is the elementary area.

The solution of the first order forces can be written after considerable mathematical manipulation,as follows using $F_x = \epsilon F_x^{(1)}$ and $h = \epsilon H$ is the first order wave height. Thus

$$F_x = -\frac{8\rho g h \tanh k_1 d \sinh \xi_0}{k_1^2} \sum_{n=0}^{\infty} \Bigg[ce_{2n+1}(\alpha, q) ce_{2n+1}(0, q) \\ ce'_{2n+1}\left(\frac{\pi}{2}, q\right) Ve_{2n+1}(\xi_0, q) \cos(\beta_{2n+1} - \sigma t) \Bigg] \tag{25}$$

$$F_y = \frac{8\rho g h \tanh k_1 d \cosh \xi_0}{k_1^2} \sum_{n=0}^{\infty} \Bigg[se_{2n+1}(\alpha, q) se'_{2n+1}(0, q) \\ se_{2n+1}\left(\frac{\pi}{2}, q\right) Ue_{2n+1}(\xi_0, q) \cos(\gamma_{2n+1} - \sigma t) \Bigg] \tag{26}$$

The moments M_x and M_y about the x and y axes respectively, taken about the sea-bed $z = -d$ are

$$M_x = \int_S (z + d)\, p\, (\hat{n} \cdot \hat{y})\, dS$$

$$M_y = \int_S (z + d)\, p\, (\hat{n} \cdot \hat{x})\, dS \quad \text{on } \xi = \xi_0 \tag{27}$$

The twisting moment M_z about z-axis is

$$M_z = \int_S p\, (x\, \hat{n} \cdot \hat{y} - y\, \hat{n} \cdot \hat{x})\, dS \quad \text{on } \xi = \xi_0 \tag{28}$$

Following the same procedure as we did in obtaining F_x, we can write

$$M_x = \frac{8\rho g h (k_1 d \tanh k_1 d + \operatorname{sech} k_1 d - 1)}{k_1^3} \cosh \xi_0 \\ \sum_{n=0}^{\infty} \left[se_{2n+1}(\alpha, q) se'_{2n+1}(0, q) se_{2n+1}\left(\frac{\pi}{2}, q\right) Ue_{2n+1}(\xi_0, q) \cos(\gamma_{2n+1} - \sigma t) \right] \tag{29}$$

$$M_y = \frac{-8\rho g h (k_1 d \tanh k_1 d + \operatorname{sech} k_1 d - 1)}{k_1^3} \sinh \xi_0 \\ \sum_{n=0}^{\infty} \left[ce_{2n+1}(\alpha, q) ce_{2n+1}(0, q) ce'_{2n+1}\left(\frac{\pi}{2}, q\right) Ve_{2n+1}(\xi_0, q) \cos(\beta_{2n+1} - \sigma t) \right] \tag{30}$$

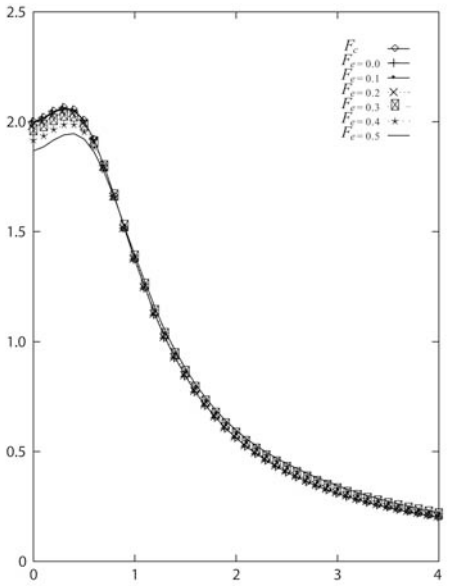

Figure 2: Comparison of the maximum non-dimensional horizontal forces for the elliptical and circular cylinder as a function of $k_1 a$ for $\alpha = 30^0$.

$$M_z = \frac{8\rho g h \tanh k_1 d}{k_1^3}$$
$$\sum_{n=0}^{\infty}\left[se_{2n+2}(\alpha,q)se'_{2n+2}(0,q)se'_{2n+2}\left(\frac{\pi}{2},q\right)Ue_{2n+2}(\xi_0,q)\sin(\sigma t-\gamma_{2n+2})\right] \tag{31}$$

Extensive numerical results for the forces and moments on an elliptical cylinder have been presented in graphical form for a wide range of relevant parameters by Chen and Mei [1]. As said earlier, calculation of the Mathieu functions and associated coefficients requires considerable computational effort, and, also, the convergence of the series expressions for the force and moment components is slow for large values of q.

7 Results and conclusions

The solution of Mathieu's equation led to a closed form expression for velocity potential on the surface of the elliptic cylinder in water of finite depth ; it is this velocity potential which is used to extract the formulae for the non-dimensional forces and overturning moments exerted by a linear progressive wave incident on the surface of the cylinder. Therefore, the values of maximum non-dimensional forces F(F_x, F_y) and overturning moment M_z will be used as the

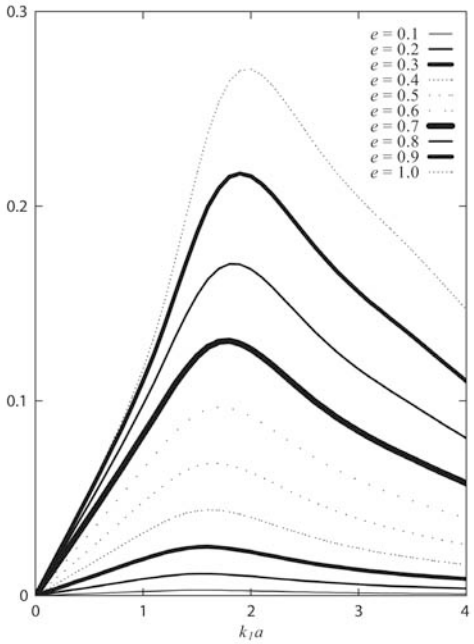

Figure 3: Maximum non-dimensional overturning moment as a function of k_1a M_z for $\alpha = 60^0$.

basis of discussion and comparison with the previous study of Williams [5]. The calculations of the aforementioned forces and moments require the evaluation of the special functions such as Mathieu functions which eventually necessitate the computations of the Bessel functions of integer order and positive real arguments. For simplicity these functions were computed by using the commercially available IMSL subroutine. A simple computer code is then developed to obtain the forces and overturning moments for the previous and present investigation.

Figure 2 shows the comparison of the maximum non-dimensional horizontal forces plotted against the non-dimensional wave number k_1a for the angles $\alpha = 30^\circ$ and for eccentricities ranging from 0.0 to 0.5. The maximum of these forces occurs at zero wave number and decreases with increasing wave number k_1a. In general, the forces appear to decline nearly exponentially with increasing wave numbers greater than 1.0. The effect of the angle of inclination α with respect to the incident wave seems to be more dramatic and clearly visible on the two components of the forces. It is found (not shown here) at the $\alpha = 30^\circ$, the ratio of max$|F_x|$ and max$|F_y|$ is approximately 2 at $k_1a = 0$ while it becomes 0.8 for $\alpha = 45^\circ$ for $e = .1, .2, .3$. It is also found that the ratio of the max$|F_x|$ to the max$|F_y|$ decreases with increasing eccentricity. For example, at $k_1a = 0$ and $\alpha = 30^\circ$, the ratio of max$|F_x|$ to max$|F_y|$ is approximately 2.0 for $e = 0.1$ which

becomes 0.5 for $e = 1.0$. For $\alpha = 45°$, max$|F_x|$ and max$|F_y|$ coincide for $k_1 a$ exceeding 2.0.

A sample curve depicted in Figure 3 shows the overturning moment max$|M_z|$, plotted against the non-dimensional wave number $k_1 a$ for $\alpha = 30°$. The figure contains max$|M_z|$ curves for different eccentricities ranging from $e = 0.1$ to $e = 1.0$. It is found that the values of max$|M_z|$ for the previous and present study are identical. The turning moment M_z is zero for zero wave number. Further it increases monotonically to attain a peak value at $k_1 a \approx 1.9$ for most eccentricities and then starts declining. For $\alpha = 30°$, the peak value of max$|M_z|$ at $e = 1.0$ is observed to be an order of magnitude higher than its value at $e = 0.1$. This feature is loosely preserved for other angles of inclination as well. Similar trends are also observed for the peak values of max$|M_z|$ for other angles of incidence.

References

[1] Chen, H.S. and Mei, C.C. (1971). Scattering and Radiation of Gravity Waves by an elliptical cylinder, Parsons Lab., Dept. of Civil Eng. M.I.T. Tech. Report, No. 140.

[2] Clemm, D.S. (1969). Algorithm 352, Characteristic Values and Associated Solutions of Mathieu's Differential Equation (s22), Comm. Assoc. Comp. Machinery, 12, No. 7.

[3] McLachlan, N.W. (1964). *Theory and Applications of Mathieu Functions*, The Dover Publications, Inc., New York.

[4] Sieger, B. (1908). *Annalen Der Physik* Vol 27, pp. 626–664.

[5] Williams, A.N. (1982). The Linear Theory of Wave Diffraction by a Vertical Cylinder of Elliptic Cross-Section in Water of Finite Depth, Fluid Dynamics Report, 3/82.

Wave effect on the trajectory of a high-speed rigid body in a water column

P. C. Chu & C. Fan
Naval Ocean Analysis and Prediction Laboratory Naval Postgraduate School, Monterey, California, USA

Abstract

Waves form when the water surface is disturbed, for example, by wind or gravitational forces. During such disturbances energy and momentum are transferred to the water mass and sea-state is changed. For shallow water regions, the bottom topography affects the waves dramatically. Waves may cause an evident slant of the ocean surface with a large inclination angle of about 55^{o}. When a high-speed rigid body strikes the wavy ocean surface, the random ocean slope largely affects its underwater trajectory. Identification of such an effect is a key point in the prediction of a fast moving rigid body in a water column. The probability density equation (PDF) of the ocean wave slopes was used to generate the stochastic surface slope. A 6-degree of freedom (DOF) model of a fast-moving rigid body is used with the stochastic sloping surface as its water-entry condition. The PDFs of the body location and orientation are obtained from results of 6-DOF model runs. From temporal change of these PDFs, the wave effect on the trajectory of a high-speed underwater rigid body has been identified.
Keywords: body-flow interaction, 3D bomb trajectory prediction, 6-DOF model, STRIKE35, random waves, probability density function.

1 Introduction

Movement of a fast-moving rigid body such as a bomb through a water column has been studied recently [1–3]. These studies have been motivated by a new concept of using a general purpose bomb such as the Mk-84 for mine/maritime improvised explosive device (IED) clearance in order to reduce the risk to

WIT Transactions on Engineering Sciences, Vol 69, © 2010 WIT Press
www.witpress.com, ISSN 1743-3533 (on-line)
doi:10.2495/AFM100331

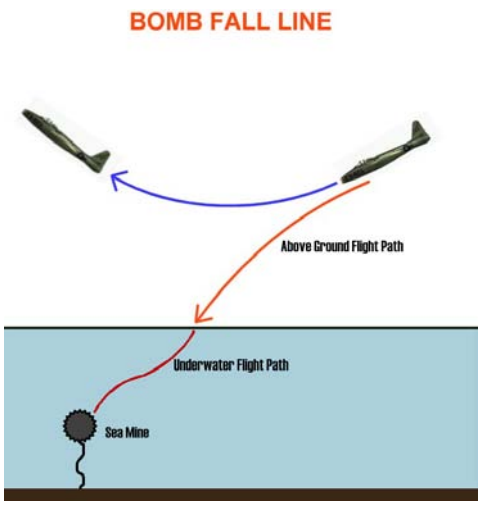

Figure 1: The concept of airborne sea mine/maritime IED clearance.

personnel and to decrease the sweep timeline without sacrificing effectiveness (Fig. 1). The horizontal distance (r) (or called trajectory deviation) between surface impact point and the bomb location varies with depth in different types of trajectories. This parameter draws attention to the naval research due to the threat of mine and maritime IED. Prediction of trajectory deviation of an underwater bomb contributes to the bomb breaching for mine and maritime IED clearance in surf and very shallow water zones with depth shallower than 12.2 m (i.e., 40 ft), shallow water zones (12.2 – 91.4 m, i.e., 40-300 ft), and deep zones (deeper than 91.4 m, i.e., 300 ft) according to U.S. Navy's standards. The bombs' trajectory drift is required to satisfy the condition, $r \leq 2.1$ m, for the validity of mine clearance using bombs [5].

In coastal oceans, waves form when the water surface is disturbed, for example, by wind or gravitational forces. During such disturbances energy and momentum are transferred to the water mass and sea-state is changed. For very shallow and shallow water regions, the bottom topography affects the waves dramatically and causes a significant change in surface slope. When bomb strikes on the wavy ocean surface, a scientific problem arises: How does randomly changing ocean-surface slope affect the underwater bomb trajectory and orientation? Or what is the probability density function of the underwater bomb trajectory deviation due to random sea surface slope? The major task of this paper is to answer these questions. Stochastic features of the sea slope are simply described in Section 2. A recently developed six degrees of freedom (6-DOF) model at the Naval Postgraduate School for predicting underwater bomb location and trajectory is depicted in Section 3. Ensemble 6-DOF modelling to get PDF of trajectory deviation from the stochastically changing sea surface slope is described in Section 4. The conclusions are presented in Section 5.

2 PDF of ocean surface slope

Wave height and wave period are approximately independent of each other for either wind waves or swells, but not for mixed waves. From mixed wave records, Gooda [8] found that there is a strong correlation between wave height and wave period. In fact, the correlation is mainly caused by the two or more groups of notable waves with different characteristic wave heights and periods in the mixed waves. With the independent assumption between wave amplitude and wave period (or wavelength), the PDF of averaged wave slope s scaled by its standard deviation σ (the real slope is s* = sσ) is obtained from the PDF of wave length and PDF of wave amplitude [9],

$$p(s) = \frac{n}{(n-1)} s \left[1 + \frac{s^2}{(n-1)} \right]^{-(n+2)/2}, \tag{4}$$

where n is the peakedness coefficient which is determined by both the spectral width of the gravity waves, and the ratio between the gravity wave mean-square slope and the detectable short wave mean-square slope. Generally speaking, the peakedness of slopes is generated by nonlinear wave–wave interactions in the range of gravity waves; and the skewness of slopes is generated by nonlinear coupling between the short waves and the underlying long waves. For n = 2, the PDF of the wavelength corresponds to the Rayleigh distribution. For n = 10, the PDF in (4) fits the Gram Charlier distribution [10], very well in the range of small slopes. As $n \to \infty$, the PDF of the wavelength tends to the Gaussian distribution [9]. Fig. 2 shows four typical surface-slope characteristics: (a) n =2, (b) n = 4, (c) n = 10, and n = 100. It is seen that There is almost no difference in PDF between n = 10 and n = 100.

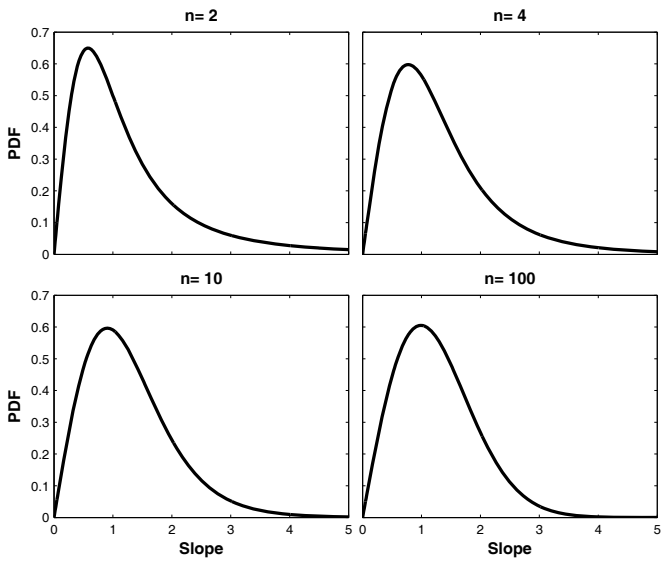

Figure 2: The s-PDFs for various surface characteristics: (a) n = 2, (b) n = 4, (c) n = 10, and (d) n = 100.

3 A 6-DOF model (STRIKE35)

Recently, a 6-DOF model has been developed at the Naval Postgraduate School for predicting underwater bomb location and trajectory. It contains three parts: momentum equation, moment of momentum equation, and semi-empirical formulas for drag, lift, and torque coefficients [11–13]. The momentum equation of a rigid body is given by

$$m\frac{d\mathbf{u}}{dt} = \mathbf{F}_g + \mathbf{F}_b + \mathbf{F}_d + \mathbf{F}_l, \tag{5}$$

where m is the mass of the rigid body, $\mathbf{u}$ is the translation velocity of the centre of mass,

$$\mathbf{F}_g = -mg\mathbf{k}, \quad \mathbf{F}_b = \rho\Pi g\mathbf{k}, \tag{6}$$

are the gravity and buoyancy force; Π is the volume of the rigid body; $\mathbf{k}$ is the unit vector in the vertical direction (positive upward): and g is the gravitational acceleration. $\mathbf{F}_d$ is the drag force; and $\mathbf{F}_l$ is the lift force. The moment of momentum equation is given by

$$\mathbf{J} \bullet \frac{d\mathbf{\Omega}}{dt} = -\sigma\mathbf{e} \times \left(\rho\Pi g\mathbf{k}\right) + \mathbf{M}_h, \tag{7}$$

where $\mathbf{\Omega}$ is the rigid-body's angular velocity vector; σ is the distance between centre of volume (o_v) and centre of mass (o_m), which has a positive (negative) value when the direction from o_v to o_m is the same (opposite) as the unit vector $\mathbf{e}$; $\mathbf{M}_h$ is the hydrodynamic torque due to the drag/lift forces; and $\mathbf{J}$ is the gyration tensor.

The drag/lift/torque coefficients should be given before running the 6-DOF model. These coefficients depend on various physical processes such as water surface penetration, super-cavitation, and bubble dynamics. A diagnostic-photographic method has been developed [4] to get semi-empirical formulae for calculating the drag/lift/torque coefficients for underwater bombs with dependence on the Reynolds number (Re), angle of attack (α), and rotation rate along the bomb's major axis (Ω) [4],

$$C_d = 0.02 + 0.35e^{-2\left(\alpha - \pi/2\right)^2}\left(\frac{\mathrm{Re}}{\mathrm{Re}^*}\right)^{0.2} + 0.008\Omega\sin\theta, \tag{8}$$

$$C_l = \begin{cases} 0.35\sin\left(\theta_1\right)\left(\dfrac{\mathrm{Re}}{\mathrm{Re}^*}\right)^{0.2} & \text{if } \alpha \le \dfrac{\pi}{2} \\ 0.1\sin\left(\theta_2\right) - 0.015\Omega\left(\dfrac{\mathrm{Re}}{\mathrm{Re}^*}\right)^2 \sin\left(\theta_2^{0.85}\right) & \text{if } \alpha > \dfrac{\pi}{2} \end{cases} \tag{9}$$

$$C_m = \begin{cases} 0.07\sin(2\alpha)\left(\dfrac{\mathrm{Re}^*}{\mathrm{Re}}\right)^{0.2} & \text{if} \quad \alpha \le \dfrac{\pi}{2} \\ 0.02\sin(2\alpha)\sqrt{\left(\dfrac{\mathrm{Re}}{\mathrm{Re}^*}\right)} & \text{if } \alpha > \dfrac{\pi}{2} \end{cases} \tag{10}$$

Here, $\mathrm{Re}^* = 1.8 \times 10^7$, is the critical Reynolds number, and

$$\theta \equiv \left(\pi^{2.2} - \left(\pi - |\pi - 2\alpha|\right)^{2.2}\right)^{\frac{1}{2.2}} \mathrm{sign}(\pi - 2\alpha), \tag{11}$$

$$\theta_1 = \pi\left(\frac{2\alpha}{\pi}\right)^{1.8}, \theta_2 = 2\pi\left(\frac{2\alpha}{\pi} - 1\right)^{0.7}. \tag{12}$$

4 PDF of bomb's horizontal drift

Let the bomb be dropped in the vertical direction to the slanted sea surface characterized by an averaged slope ($s^* = \sigma s$) in a wave period, here $s^* = \tan\mu$ (see Fig. 3). Consider a 5-time of s* value as the interval [0, 5s*] for the change of the surface slope. This interval [0, 5s*] is divided into I equal sub-intervals,

$$\sigma s_i = \frac{5is^*}{I}, \quad i = 0,1,2,...,I, \tag{13}$$

with the corresponding inclination,

$$\mu_i = \arctan(\sigma s_i) = \arctan\frac{5is^*}{I}, \quad i = 0,1,2,...,I. \tag{14}$$

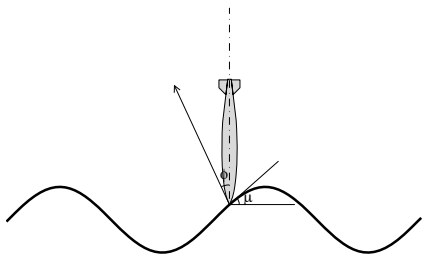

Figure 3: Ocean surface inclination angle (μ) and bomb impact angle (φ) relative to the normal direction of the surface.

For a given parameter n in the s-PDF, the probability for s^* taking values between σs_{i-1} and σs_i is calculated by

$$P_i \equiv \mathrm{Prob}(s_i \le s \le s_{i+1}) = \int_{s_i}^{s_{i+1}} p(s)ds. \tag{15}$$

The 6-DOF model is integrated I times (called ensemble integration) from the surface impact speed (V) and various μ_i values to get the bomb horizontal drift $\hat{r}_i$ (i = 0, 1, …, I) at depth z = -H. The series $\{\hat{r}_i,\ i = 0, 1, \ldots, I\}$ might not be in monotonically increasing or decreasing order. Therefore, it is reorganized into monotonically increasing order $\{r_j\ , j = 0, 1, \ldots, J\}$ with $J \leq I$. The inequality is due to an interval $[r_j, r_{j+1}]$ of the horizontal drift corresponding to m intervals $\{[s_{i1}, s_{i1}+1],\ [s_{i2}, s_{i2}+1], \ldots, [s_{im}, s_{im}+1]\}$ of the surface slope (Fig. 4).

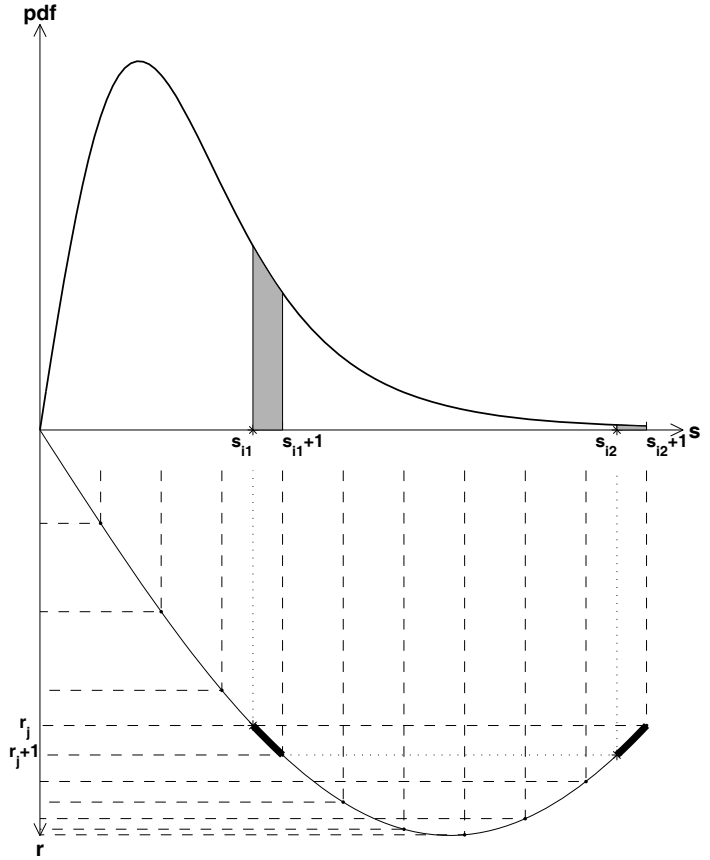

Figure 4: Calculation of the probability for the bomb's horizontal drift r taking values between r_j and r_{j+1} from m intervals of surface slope s. Here, m = 1, and m = 2.

The probability for the bomb's horizontal drift r taking values between r_j and r_{j+1} is calculated by

$$Q_j \equiv \text{Prob}(r_j \leq r \leq r_{j+1}) = \int_{s_{i1}}^{s_{i1+1}} p(s)ds + \int_{s_{i2}}^{s_{i2+1}} p(s)ds + \ldots + \int_{s_{im}}^{s_{im+1}} p(s)ds \quad (16)$$

The probability density between r_j and r_{j+1} is calculated by

$$p_j = \frac{Q_j}{r_{j+1} - r_j}. \tag{17}$$

From p_j, we can obtain the PDF of r, or called the r-PDF. Dependence of r-PDF on depth can be identified from the ensemble integration (I = 100) of the 6-DOF model with given bomb's surface impact speed (V = 300 m/s), s^* = 0.2 (i.e., σ = 0.2), and n = 2 (i.e., large peakedness in the s-PDF). The calculated r-PDF (Fig. 5) is positively skewed for shallow depth (H = 12.2 m, i.e., 40 ft), reduces the skewness as depth increases to 50 m, becomes negatively skewed as the depth exceeding 91.4 m (i.e., 300 ft).

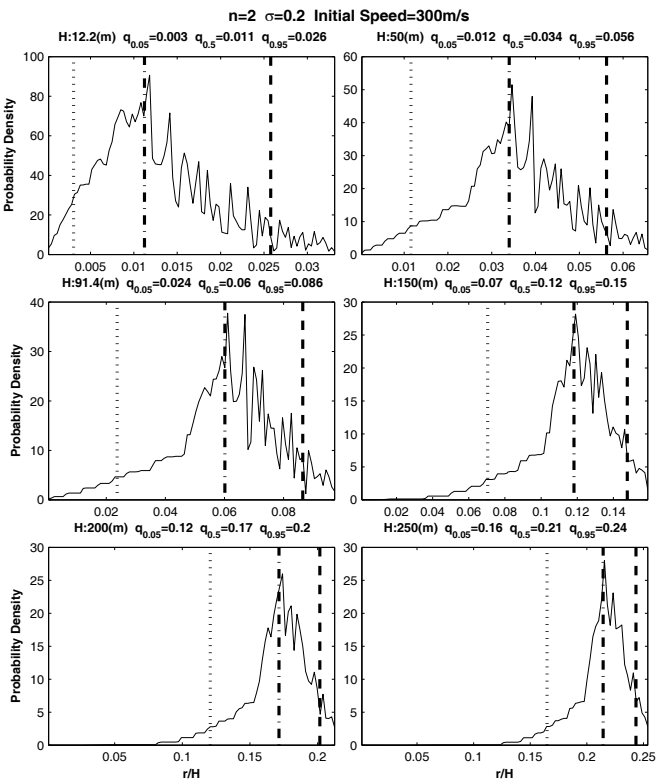

Figure 5: Probability distribution of the bomb's horizontal drift (scaled by the depth) r/H with n = 2, σ = 0.2, and V = 300 m/s for various depth: (a) 12.2 m (i.e. 40 ft), (b) 50 m, (c) 91.4 m (i.e., 300 ft), (d) 150 m, (e) 200 m, and (f) 250 m.

The negative skewness strengthens as depth deeper than 91.4 m. The horizontal axis in all the panels Fig. 5 is the non-dimensional horizontal drift r/H. The median (50 percentile $q_{0.5}$) of the horizontal drift (r) is 0.16 m at the depth z = -12.2 m, 1.7 m at z = -50 m, 5.4 m at z = -91.4 m (300 ft), 18.0 m at z = -150 m, 34.0 m at z = -200 m, and 52.5 m at z = -250 m (Table 1). Here z is the vertical coordinates with z = 0 corresponding to the water surface. Thus, down to the depth of 50 m, the median value of the horizontal drift is always less than the Navy's criterion, i.e., 2.1 m. The 95 percentile ($q_{0.95}$) of the horizontal drift (r) represents a reasonable estimation (with 95% of confidence) of the distance between bomb and mine/maritime IED when the bomb maneuvering in the water column. If this value is smaller than 2.1 m, according to the Navy's standard, the bomb will effectively 'kill' the mine/maritime IED. It is 0.32 m at the depth z = -12.2 m, 2.8 m at z = -50 m, 7.86 m at z = -91.4 m (300 ft), 22.5 m at z = -150 m, 40.0 m at z = -200 m, and 60.0 m at z = -250 m (Table 2). The 5 percentile ($q_{0.05}$) of the horizontal drift (r) represents the minimum distance (likely) between bomb and mine/maritime IED when the bomb maneuvering in

Table 1: The median horizontal drift (unit: m) of an underwater bomb at various depths obtained from ensemble integration of the 6-DOF model with various input parameters.

Depth (m)	Case 1: V = 300 m/s n = 2 σ = 0.2	Case 2: V = 300 m/s n = 100 σ = 0.2	Case 3: V = 300 m/s n = 2 σ = 1.0	Case 4: V = 200 m/s n = 2 σ = 0.2
12.2	0.16	0.16	0.37	0.17
50.0	1.7	1.8	3.1	2.5
91.4	5.4	5.7	8.6	8.9
150.0	18.0	18.0	22.5	25.5
200.0	34.0	34.0	42.0	44.0
250.0	52.5	55.0	62.5	65.0

Table 2: The values of $q_{0.95}$ for the horizontal drift (unit: m) of an underwater bomb at various depths obtained from ensemble integration of the 6-DOF model with various input parameters.

Depth (m)	Case 1: V = 300 m/s n = 2 σ = 0.2	Case 2: V = 300 m/s n = 100 σ = 0.2	Case 3: V = 300 m/s n = 2 σ = 1.0	Case 4: V = 200 m/s n = 2 σ = 0.2
12.2	0.32	0.27	0.54	0.17
50.0	2.8	2.55	4.0	3.6
91.4	7.86	7.40	10.05	10.97
150.0	22.5	21.0	25.5	28.5
200.0	40.0	38.0	46.0	48.0
250.0	60.0	60.0	67.5	70.0

Table 3: The values of $q_{0.05}$ for the horizontal drift (unit: m) of an underwater bomb at various depths obtained from ensemble integration of the 6-DOF model with various input parameters.

Depth (m)	Case 1: V = 300 m/s n = 2 σ = 0.2	Case 2: V = 300 m/s n = 100 σ = 0.2	Case 3: V = 300 m/s n = 2 σ = 1.0	Case 4: V = 200 m/s n = 2 σ = 0.2
12.2	0.13	0.05	0.15	0.04
50.0	0.6	0.80	1.8	1.05
91.4	5.48	7.40	5.76	5.30
150.0	10.5	12.45	18.0	18.0
200.0	24.0	26.0	34.0	32.0
250.0	40.0	45.0	55.0	55.0

the water column. It is 0.13 m at the depth z = -12.2 m, 0.6 m at z = -50 m, 5.48 m at z = -91.4 m (300 ft), 10.5 m at z = -150 m, 24.0 m at z = -200 m, and 40.0 m at z = -250 m (Table 3).

5 Conclusions

The PDF of the horizontal drift of underwater bomb trajectory (i.e., r-PDF) due to stochastic ocean surface slope is obtained through ensemble integration of the 6-DOF model recently developed at the Naval Postgraduate School. For a bomb dropping in the vertical direction to a slanted sea surface, the input parameters of the 6-DOF model are the bomb's surface impact speed (V), and surface slope. The surface slope is a random variable depending on two parameters: (a) averaged slope within a wave period (σ), and (b) peakedness of the s-PDF (n).

The s-PDF is discretized into I intervals (in this paper, I = 100). For given values of (V, σ, n), the 6-DOF model is integrated I times with different values of the surface slope from the s-PDF to obtained I values of the horizontal drift at various depth. The r-PDF is then constructed from these r values. The r-PDF has the following features:

(1) The r-PDF varies with depth. Usually, the r-PDF is positively skewed for very shallow water (H = 12.2 m, i.e., 40 ft), and negatively skewed down below. Increase of the peakedness parameter of the s-PDF (n) or the averaged surface slope in a wave period (σ) reduces the positive skewness at the very shallow water and enhances the negative skewness. Decrease of the bomb's surface impact speed (V) enhances the peakedness of the r-PDF. Three measures were calculated ($q_{0.05}$, $q_{0.5}$, and $q_{0.95}$) from the r-PDF.

(2) The values of $q_{0.95}$ are small for all cases at a very shallow depth (z = -12.2 m, i.e., 40 ft) with a maximum value of 0.54 m for the initial conditions of (V = 300 m/s, n = 2, σ = 1.0). This value (0.54 m) is much smaller than the critical value of 2.1 m for effectively 'killing' the mine/maritime.

(3) The values of $q_{0.95}$ are all larger than 2.1 m when the depth deeper than 50 m. This indicates that to extend the bomb breaching technology from very shallow water (12.2 m depth) to shallow water (12.2 m – 91.4 m) needs more studies.

Acknowledgements

The Office of Naval Research Breaching Technology Program (Grant Number: N0001410WX20165, Program Manager: Brian Almquist) supported this study. The authors thank Mr. Kennard Watson from the Naval Surface Warfare Center Panama City Division for very useful comments and helps.

References

[1] Chu, P.C., and G. P. Ray, 2006, "Prediction of high-speed rigid body maneuvering in air-water-sediment," *Adv. Fluid Mech.*, **6**, edited by M. Rahman and C.A. Brebbia, WIT Press (ISBN-1-84564-163-9), 43-52.

[2] Ray G. P., 2006. *Bomb Strike Experiments for Mine Clearance Operations*. MS Thesis in Meteorology and Physical Oceanography, Naval Postgraduate School, Monterey, California, pp. 197.

[3] Chu, P.C., Fan, C.W., and Gefken, P.R., 2008, "Semi-empirical formulas of drag/lift coefficients for high-speed rigid body maneuvering in water column," *Adv. Fluid Mech.*, **7**, edited by M. Rahman and C.A. Brebbia, WIT Press (ISSN-1743-3533), 163-172.

[4] Chu, P.C., Fan, C.W., and P. R. Gefken, 2010. "Diagnostic-photographic determination of drag/lift/torque coefficients of high speed rigid body in water column," *ASME J. Appl. Mech*., **77**, 011015-1- 011015-15.

[5] *Humes, G., 2007. Technology Transition Agreement, EC SHD-FYO6-03 FNC Product: Standoff Assault Breaching Weapon Fuze Improvement*. pp.10.

[6] Kinsman, B., 1965, *Wind Waves*, Prentice-Hall Inc., Englewood Cliffs, New Jersey, Library of Congress Catalog Card Number: 64-10136, pp. 676.

[7] Dare, A., Landsberg, A., Kee, A., and Wardlaw, A., 2003, "Three-dimensional modeling and simulation of weapons effects for obstacle clearance," *DoD User Group Conf*., Bellevue, Washington, 09-13 June, pp. 9.

[8] Gooda, Y., 1977, "The analysis on the joint distribution of period and wave height from the records of wave observations (in Japanese)," *Technol. Res. Data Estuaries,* **272,** 1–19.

[9] Liu, Y., Yan, X.-H., Liu, W.T., and Hwang, P.A., 1997, "The probability density function of ocean surface slopes and its effects on radar backscatter," *J. Phys. Oceanogr*., **27**, 782-797.

[10] Cox, C. S., and Munk, W. H., 1954, "Measurement of the roughness of the sea surface from photographs of the sun's glitter," *J. Opt. Soc. Amer.,* **44,** 838–850.

[11] Chu, P.C., and Fan, C.W., 2006. "Prediction of falling cylinder through air-water-sediment columns," *AMSE J. Appl. Mech*., **73**, 300-314.
[12] Chu, P.C., and Fan, C.W., 2007, "Mine impact burial model (IMPACT35) verification and improvement using sediment bearing factor method," *IEEE J. Ocean. Eng.*, **32** (1), pp. 34-48.
[13] Chu, P.C., 2009, "Mine impact burial prediction from one to three dimensions," *ASME Appl. Mech. Rev.*, **62** (1), 010802 (25 pages), DOI: 1115/1.3013823.

This page intentionally left blank

Dispersion relation of flow-induced wave of a flexible web subjected to fluid flow in a narrow gap

M. Watanabe, G. Kudou & K. Hara
Department of Mechanical Engineering, Aoyama Gakuin University, Japan

Abstract

This paper deals with a theoretical stability analysis of a flow-induced wave generated in a flexible web subjected to fluid flow in a narrow gap. The flexible web is subjected to both fluid flow and in-plane tensile force. The flow-induced wave occurs to the flexible web resulting from fluid-structure interaction between out-of-plane motion of the flexible web and the fluid flow. The effect of the fluid flow and tensile force on the stability of the wave is examined. The theoretical results show that traveling-wave type unstable wave occurs to the flexible web due to the fluid flow in the narrow gap, and clarify the dispersion relation of the flow-induced wave of the web, i.e., phase velocity (traveling-wave speed) and growth rate of the wave, which are as a function of the flow velocity and tensile force. The theoretical results are verified by experiments on the most unstable wave number and critical flow velocity.

Keywords: flow-induced wave, flexible web, dispersion relation, fluid-structure interaction.

1 Introduction

In the manufacturing process of flexible materials, such as a paper, sheet and plastic films, the flexible materials are subjected to a fluid flow in a narrow gap for non-contact support and drying. However the interaction of the thin film with the fluid flow causes an unstable wave. The flow-induced wave reduces the process efficiency and generates noise, in some case, causes fatigue failure to the thin film.

WIT Transactions on Engineering Sciences, Vol 69, © 2010 WIT Press
www.witpress.com, ISSN 1743-3533 (on-line)
doi:10.2495/AFM100341

Up to this time, many studies on the stability of leakage-flow-induced vibrations and sheet flutter have been reported. Inada and Hayama [1, 2] studied leakage-flow-induced vibrations of translational one-degree-of-freedom system, and clarified the instability mechanism of these systems theoretically. Nagakura and Kaneko [3] examined the stability of a cantilever beam subjected to the leakage fluid flow by employing the modal analysis method, and they verified the theoretical results comparing with experimental results.

Some studies on the flow induced vibration and flow induced wave of a flexible sheet have been reported [4–9]. Chang and Moretti [8] studied flow induced vibration of free edges of thin films by using a traveling-wave analysis based on the incompressible potential-flow. In their study, previous studies of edge flutter on two-dimensional waves expands to a more realistic three-dimensional problem, and the simple closed form solutions of the critical flow velocity are presented. Watanabe and Kobayashi [9] studied the stability and dynamic characteristics of a moving flexible sheet with shear fluid flow. In their study, unstable wave occurs to the flexible sheets as a type of traveling-wave due to the shear fluid flow.

This paper presents the theoretical stability analysis of the flow-induced wave generated in the web subjected to the fluid flow in the narrow gap. In the stability analysis, tensile force is applied to the web, and the web is subjected to air flow in a narrow gap. The analytical results show the stability and wave characteristics of the flow-induced wave, phase velocity and growth rate of the wave.

2 Theoretical stability analysis

2.1 Modeling and coordinate system

Fig. 1 and Fig. 2 show a traveling wave motion and an analytical model of the web subjected to the fluid flow together with the stationary coordinate system *xyz* and geometrical parameters considered in this model. The web is set in the middle of the narrow gap filled with fluid and is subjected to the fluid flow in *y*-direction. Tensile force is applied to the web. The equilibrium gap width in steady state is a constant, H_0, and thickness of the web is h. The uniform tensile

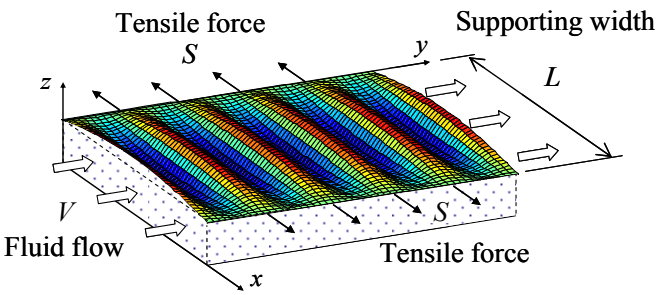

Figure 1: Traveling wave motion generated in the web (thin film).

force per unit width S is applied in x-direction. The fluid flow and tensile force are crossed at a right angle.

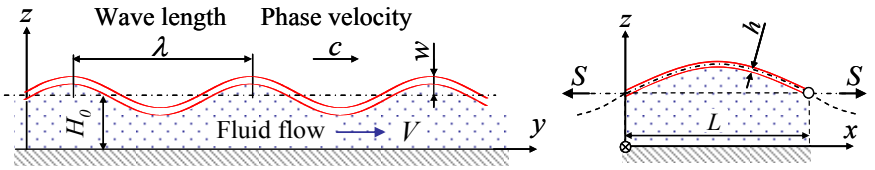

Figure 2: Analytical model of the flow-induced wave.

2.2 Basic equation of structural motion and fluid flow

The equation of motion of the web subjected to the fluid flow is derived in terms of the transverse displacement w and with respect to the stationary coordinate system xyz as follows:

$$\rho h\frac{\partial^2 w}{\partial t^2}+C_s\frac{\partial w}{\partial t}+-S\frac{\partial^2 w}{\partial x^2}+\frac{h^3}{12}(E+E^*\frac{\partial}{\partial t})(\frac{\partial^4 w}{\partial x^4}+2\frac{\partial w^4}{\partial x^2\partial y^2}+\frac{\partial^4 w}{\partial y^4})=f, \quad (1)$$

where E is Young's modulus, C_s and E^* are the external and internal structural damping coefficients, respectively. f is fluid force acting on the web surface per unit area. ρ and h are the density and thickness of the thin film, respectively.

The equations of motion of the fluid flow around the web are derived by integrating the continuity and momentum equations of fluid motion over the gap width H_0 as follows:

$$\frac{\partial H}{\partial t}+\frac{\partial}{\partial y}(HV)=0, \quad (2)$$

$$\frac{\partial}{\partial t}(HV)+\frac{\partial}{\partial y}(HV^2)+\frac{H}{\rho_f}\frac{\partial P}{\partial y}+\frac{12\mu}{\rho_f}(V-V_0)-\frac{1}{2}(f_s-f_w)V^2=0, \quad (3)$$

where V is mean flow velocity over the gap width between the web and side wall. V_0 is steady flow velocity of the fluid flow in the narrow passage. μ is fluid viscosity. f_s and f_w are fluid friction coefficients on the surface of the web and side wall, respectively, and are assumed to be obtained as follows [10]:

$$f_s=f_w=\frac{1}{4}\{1.14-2\log_{10}(\frac{\varepsilon_H}{D_H}+\frac{21.25}{\mathrm{Re}^{0.9}})\}^{-2}, \quad (4)$$

where the friction coefficients f_s and f_w depend on the Reynolds number Re and the roughness of surface ε_H. The Reynolds number is defined as $\mathrm{Re}=VD_H/\nu_f$, where $D_H=2H_0$, μ_f is kinematic viscosity of the fluid and ε_H is roughness of the side wall respectively.

2.3 Wave equation

In this section, a linear wave equation of bending wave motion of the web coupled with the fluid flow in the narrow gap is derived from the basic equations of motion of the web and fluid flow.

The gap width H between the web and side wall is obtained using the steady equilibrium gap width H_0 and transverse displacement w of the web as follows:

$$H(x,y,t) = H_0 + w(x,y,t). \tag{5}$$

Similarly, the flow velocity and fluid pressure are obtained by summation of the steady and unsteady terms as follows:

$$V(y,t) = V_0 + \Delta v(y,t), \tag{6}$$

$$P(x,y,t) = P_0(y) + p(x,y,t), \tag{7}$$

where V_0 and Δv are steady and unsteady flow velocities, and P_0 and p are steady and unsteady fluid pressures, respectively. Here the unsteady fluid pressure is induced by the motion of the web.

Substituting eqn. (5), (6) and (7) into the basic eqn. (2) and (3), the basic equations of the fluid flow are linearized with respect to the unsteady terms as follows:

$$\frac{\partial \hat{w}}{\partial T} + \frac{\partial \Delta\hat{v}}{\partial Y} + \hat{V}\frac{\partial \hat{w}}{\partial Y} = 0, \tag{8}$$

$$\begin{aligned}\frac{\partial \Delta\hat{v}}{\partial T} + \hat{V}\frac{\partial \hat{w}}{\partial T} + 2\hat{V}\frac{\partial \Delta\hat{v}}{\partial Y} + \hat{V}^2\frac{\partial \hat{w}}{\partial Y} + \frac{12\hat{\mu}\hat{h}}{\hat{\rho}}\Delta\hat{v} \\ + (f_w - f_s)\hat{V}\Delta\hat{v} + \frac{1}{2}(f_s - f_w)\hat{V}^2\hat{w} + \frac{\hat{h}}{\hat{\rho}}\frac{\partial \hat{p}}{\partial Y} = 0,\end{aligned} \tag{9}$$

where each term is expressed by dimensionless parameters by defining the following quantities:

$$T_0 = \sqrt{\frac{\rho h H_0^4}{D}}\ ,\ U_0 = \frac{H_0}{T_0}\ ,\ T = \frac{t}{T_0}\ ,\ \hat{V} = \frac{V_0}{U_0}\ ,\ \hat{L} = \frac{L}{H_0}\ ,\ \hat{w} = \frac{w}{H_0}\ ,$$

$$X = \frac{x}{H_0}\ ,\ Y = \frac{y}{H_0}\ ,\ \hat{h} = \frac{h}{H_0}\ ,\ \Delta\hat{v} = \frac{\Delta v}{U_0}\ ,\ \hat{\rho} = \frac{\rho_f}{\rho}\ ,\ \hat{S} = \frac{SH_0^2}{D}\ ,\ \hat{p} = \frac{H_0^3}{D}p\ , \tag{10}$$

$$\hat{\mu} = \mu\sqrt{\frac{H_0^2}{\rho h D}}\ ,\ \hat{C}_s = C_s\sqrt{\frac{H_0^4}{\rho h D}}\ ,\ \hat{f} = \frac{H_0^3}{D}f\ ,\ \varepsilon = \frac{E^*}{E\,T_0}\ ,\ D = \frac{Eh^3}{12}.$$

Similarly, the dimensionless basic equation of the web is obtained from eqn. (1) using the dimensionless parameters as follows:

$$\frac{\partial^2 \hat{w}}{\partial T^2} + \hat{C}_s\frac{\partial \hat{w}}{\partial T} - \hat{S}\frac{\partial^2 \hat{w}}{\partial X^2} + (1 + \varepsilon\frac{\partial}{\partial T})(\frac{\partial^4 \hat{w}}{\partial X^4} + 2\frac{\partial^4 \hat{w}}{\partial X^2 \partial Y^2} + \frac{\partial^4 \hat{w}}{\partial Y^4}) = \hat{f}(X,Y,T), \tag{11}$$

where $\hat{f}$ denotes the dimensionless fluid force obtained from the dimensionless unsteady fluid pressure $\hat{p}$ using following relationship:

$$\hat{f}(X,Y,T) = \hat{p}(X,Y,T). \tag{12}$$

From these linearized equations, eqn. (8), (9) and (11), a linear wave equation of bending wave motion of the web coupled with the fluid flow is obtained as follows:

$$\begin{aligned}&(\frac{\partial}{\partial T}+\hat{V}\frac{\partial}{\partial Y})^2\hat{w}+\gamma(\frac{\partial}{\partial T}+\frac{\partial}{\partial Y})\hat{w}\\&=\frac{1}{\beta}\frac{\partial^2}{\partial Y^2}\{\frac{\partial^2\hat{w}}{\partial T^2}+\hat{C}_s\frac{\partial\hat{w}}{\partial T}-\hat{S}\frac{\partial^2\hat{w}}{\partial X^2}+(1+\varepsilon\frac{\partial}{\partial T})(\frac{\partial^4\hat{w}}{\partial X^4}+2\frac{\partial^4\hat{w}}{\partial X^2\partial Y^2}+\frac{\partial^4\hat{w}}{\partial Y^4})\},\end{aligned} \tag{13}$$

where β, γ and δ are defined by the following dimensionless parameters:

$$\beta=\frac{\hat{\rho}}{\hat{h}},\qquad \gamma=\frac{12\hat{\mu}\hat{h}}{\hat{\rho}}+(f_w-f_s)\hat{V},\ \delta=\hat{V}-\frac{\alpha}{\gamma}, \tag{14}$$

where α is defined by the following dimensionless parameters:

$$\alpha=\frac{1}{2}(f_s-f_w)\hat{V}^2. \tag{15}$$

From eqn. (13), it is found that the wave equation is composed two fluid-wave equations expressed by first and second-order differential equations and the structural wave equation derived from the equation of motion of the web. The first fluid-wave equation is derived from the inertia term of the basic equation of the web and the continuity equation of the fluid flow. The second fluid-wave equation is derived from the viscosity and friction loss terms of the basic equation of the web and the continuity equation of the fluid flow.

Moreover, in eqn. (13), γ denotes a dimensionless parameter of the viscosity and friction loss of the fluid. β denotes a dimensionless parameter which has the effect of the fluid-waves on the structural wave of the web. If β is large, the fluid-waves are dominant compared with the structural wave traveling in the web. On the other hand, if β is small, the structural wave is dominant compared with the fluid-waves. Thus, it is found that the dimensionless parameter β is one of the most important parameter for the dynamic characteristics and stability of the wave.

2.4 Dispersion relation and stability analysis

In this section, the dispersion relation of the wave is derived from the wave equation, eqn.(13), to investigate the dynamic characteristics, phase velocity (traveling-wave velocity) and growth rate of the wave. The transverse displacement *w* of the web is expressed as follows:

$$\hat{w}=\hat{w}_0\sin(\frac{\pi X}{\hat{L}})\exp\{i(\hat{\omega}T-kY)\}. \tag{16}$$

Substituting eqn. (16) into the wave eqn. (13), the dispersion relation of the wave is obtained as follows:

$$(\beta + k^2)\hat{\omega}^2 - 2k\beta\hat{V}\hat{\omega} - [\gamma\beta + \hat{C}_s k^2 + k^2\varepsilon\{(\frac{\pi}{\hat{L}})^2 + k^2\}^2]i\hat{\omega} + [\beta k^2\hat{V}^2 - k^2\{(\frac{\pi}{\hat{L}})^2 + k^2\}^2 - \hat{S}k^2(\frac{\pi}{\hat{L}})^2] + i\gamma\beta\delta k = 0. \quad (17)$$

The stability and dynamic characteristics of the wave generated in the web are dependent on the complex root, $\hat{\omega}$ obtained from eqn. (17), where $\mathrm{Re}[\hat{\omega}]/k$, real part of $\hat{\omega}$ divided wave number *k*, is denotes the phase velocity of the wave. If $\mathrm{Re}[\hat{\omega}]/k$ is positive, the wave is forward wave which propagates in the same direction as the fluid flow, and if $\mathrm{Re}[\hat{\omega}]/k$ is negative, the wave is backward wave which propagates in the opposite direction as the fluid flow. Moreover, $-\mathrm{Im}[\hat{\omega}]$, negative imaginary part of $\hat{\omega}$, denotes the growth rate of the wave. If $-\mathrm{Im}[\hat{\omega}]$ is positive, the wave grows exponentially in time, that is, an unstable wave occurs, and if $-\mathrm{Im}[\hat{\omega}]$ is negative, the wave is stable.

3 Analytical parameters

Table 1 shows parameters used in the calculation for the stability analysis. These parameters correspond to the experimental parameters used in the other experimental study. In the calculations, the web is thin film and is made of PET, and the fluid in the gap between the web and side wall is air. Moreover, the external and internal structural damping coefficient are assumed $C_s = 10.0$ Ns/m^3 and $E^* = 1.0\times10^3$ Ns/m^2. In this conditions, dimensionless parameters are $\beta = 2.46\times10^{-1}$, $\hat{C}_s = 1.65\times10^{-2}$, $\varepsilon = 9.01\times10^{-5}$ and $\hat{S} = 2.40\times10^3$.

Table 1: Parameters used in the calculation.

Material of the web	PET	Tensile force S [N/m]	50 ~ 200
Fluid	Air	Young's modulus E [Pa]	3.0×10^9
Gap width H_0 [m]	5.0×10^{-3}	Web density ρ [kg/m^3]	1.4×10^3
Web width L [m]	0.3 ~ 0.6	Fluid density ρ_f [kg/m^3]	1.1
Web thickness h [m]	16.0×10^{-6}	Fluid viscosity μ [Ns/m^2]	18.2×10^{-6}

4 Analytical results

4.1 Phase velocity and growth rate of wave

Fig. 3 (a) and (b) show the phase velocity $\mathrm{Re}[\hat{\omega}]/k$ and growth rate $-\mathrm{Im}[\hat{\omega}]$ of the wave generated in the web subjected to the fluid flow in the narrow passage

as a function of the flow velocity $\hat{V}$. In this figure, three types of curve denote the results of wave number $k = 1.2, 1.6, 2.0$, respectively. From Fig. 3(a), it is seen that there are forward and backward waves for each wave number at the flow velocity of zero, and vary with increasing flow velocity. The phase velocity of the backward wave progressively goes to zero. After the phase velocity of the backward wave has become zero, the backward wave becomes forward wave, and its phase velocity increases as the flow velocity increases. From Fig. 3(b), it is seen that unstable (flow-induced) waves occurs because growth rate of the forward wave becomes positive, and that the waves occur as a type of traveling wave.

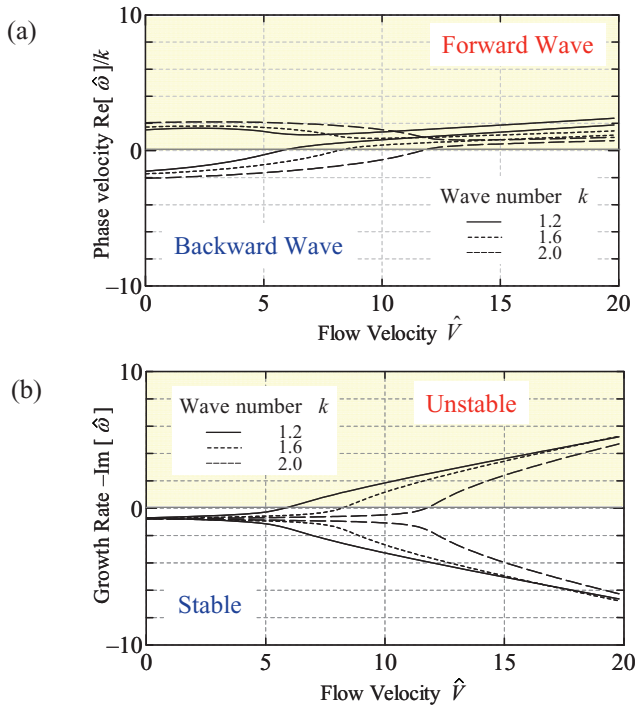

Figure 3: Phase velocity $\mathrm{Re}[\hat{\omega}]/k$ and growth rate $-\mathrm{Im}[\hat{\omega}]$ with changing flow velocity $\hat{V}$.

4.2 Unstable region

Fig. 4(a) shows the unstable region of the wave with changing the flow velocity as a function of the tensile force $\hat{S}$. In this figure, four types of curve denote the result of the tensile force $\hat{S} = 1.2\times10^3 \sim 4.8\times10^3$. It can be seen that the unstable region of wave number becomes narrower with increasing the tensile force, and

the critical flow velocity increases with increasing the tensile force. The unstable region of the wave number becomes broader with increasing the fluid flow. Moreover, it can be seen that the most unstable wave number is about $k = 0.5$. Fig. 4(b) shows the unstable region of the wave with changing the flow velocity as a function of the web supporting width. In this figure, four types of curve denote the results of the web supporting width $\hat{L} = 60 \sim 120$. It can be seen that the unstable region of wave number becomes broader with increasing the web supporting width, and the critical flow velocity decreases with increasing the web supporting width. The unstable region of the wave number becomes broader with increasing the flow velocity.

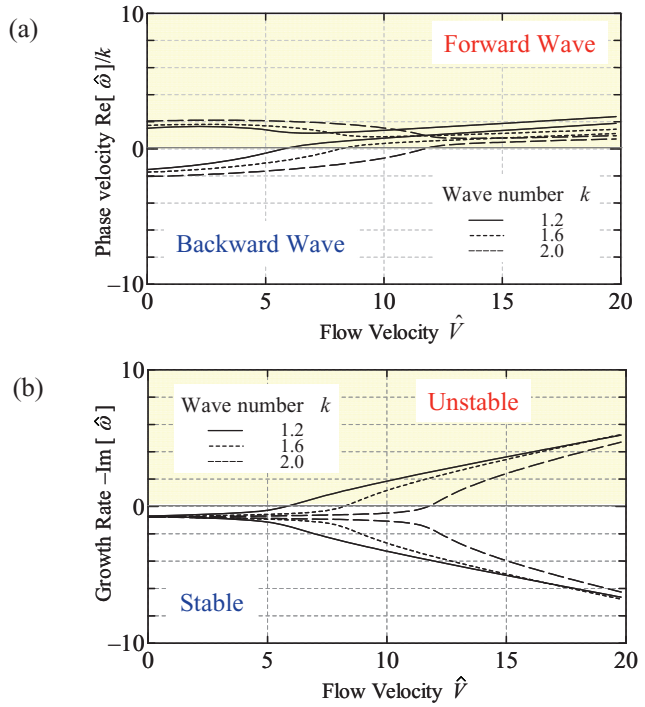

Figure 4: Unstable region with changing tensile force applied to the web $\hat{S}$ and supporting width $\hat{L}$.

5 Conclusions

The theoretical stability analysis of the flow-induced wave generated in the web subjected to the fluid flow in the narrow gap was developed. In the stability analysis, the effect of the fluid flow, tensile force, and web supporting width on the stability were examined and the dispersion relation of the flow-induced wave were clarified. The following main conclusions were obtained:

(1) The flow-induced traveling wave occurs in the web due to the fluid flow in the narrow gap when the flow velocity becomes higher.
(2) The unstable region of wave number becomes narrower with increasing the tensile force, and becomes broader with increasing the flow velocity. The critical flow velocity increases with increasing the tensile force.
(3) The unstable region of wave number becomes broader with increasing the web supporting width, and the critical flow velocity decreases with increasing the web supporting width.
(4) The flow-induced wave is generated in which the wave number is about $k = 0.5$.

References

[1] F. Inada and S. Hayama, A Study on Leakage-Flow-Induced Vibrations (1st Report, Fluid-Dynamic Forces Acting on the Walls of a One-Dimensional, Narrow, Tapered Passage), *JSME Int. J. Series III*, **31**, pp.39-47, 1998.
[2] F. Inada and S. Hayama, A Study on Leakage-Flow-Induced Vibrations. Part 1: Fluid-Dynamic Forces and Moments Acting on the Walls of a Narrow Tapered Passage, *Journal of Fluids and Structures*, **4**, pp.395-412, 1990.
[3] H. Nagakura and S. Kaneko, The Stability of a Cantilever Beam Subjected to One-Dimensional Leakage Flow (in Japanese), *Transactions of the JSME. Series C*, **58** (546), pp.352-259, 1992.
[4] C. A. Evrensel and A. Kalnins, Response of Compliant Slab to Inviscid Incompressible Fluid Flow, *Journal of Acoustical Society of America*, **78**, pp.2034-2041, 1985.
[5] R. J. Hansen and D. J. Huston, C. C. Ni, An Experimental Study of Flow-Induced Waves on a Flexible Surface, *Journal of Sound and Vibration*, **68**, pp.317-334, 1980.
[6] P. W. Carpenter and A.D.Garrad, The Hydrodynamic Stability of Flow Over Kramer-Type Compliant Surface. Part 1. Tollmien-Schlichting Instabilities, *Journal of Fluid Mechanics*, **155**, pp.465-510, 1985.
[7] P. W. Carpenter and A. D. Garrad, The Hydrodynamic Stability of Flow Over Kramer-Type Compliant Surface. Part 2. Flow-Induced Surface Instabilities, *Journal of Fluid Mechanics*, **170**, pp.199-232, 1986.
[8] Y. B .Chang and P. M. Moretti, Flow-Induced Vibration of Free Edges of Thin Film, *Journal of Fluids and Structures*, **16**, pp.989-1008, 2002.
[9] M. Watanabe and N. Kobayashi, Dynamics and Stability Analysis of Axially Moving Web Subjected to Shear Fluid Flow in Narrow Space (in a Case of Finitely Long Space) (in Japanese), *Transaction of the JSME. Series C*, **67**(664), pp.3722-3729, 2001.
[10] F. Axisa and J. Antunes, Flexural Vibrations of Rotors Immersed in Dense Fluids Part I, Theory, *Journal of Fluids and Structures*, **6**, pp.3-21, 1992

This page intentionally left blank

Fluid/structure interaction analysis using the Smoothed Particle Hydrodynamic method

D. Delsart[1], N. Toso-Pentecôte[2], A. Vagnot[3], L. Castelletti[4], U. Mercurio[5] & S. Alguadich[5]
[1]*Office National d'Etudes et de Recherches Aérospatiales (ONERA), France*
[2]*German aerospace Center (DLR), Institute of Structures and Design, Germany*
[3]*EUROCOPTER, Airframe Stress Department, France*
[4]*Politecnico di Milano, Dipartimento di Ingegneria Aerospaziale, Italy*
[5]*CIRA ScpA, Centro Italiano ricerche Aerospaziali, Italy*

Abstract

Works presented in this paper have been performed within the GARTEUR Action Group AG15 "Improvement of SPH methods for application to helicopter ditching" whose overall objective is aimed at assessing analytical tools for the simulation of helicopter impacts on water. It particularly focused on the Smoothed Particle Hydrodynamic (SPH) formulation, which consists of a gridless Lagrangian method and whose main interest, with respect to fluid/structure interaction issues, relies upon the absence of connectivity between the "particle elements", thus permitting it to cope with large deformations without generating mesh distortion problems. In the first step, the SPH method was evaluated through the simulation of droplet impact tests onto a rigid plate, performed at two impact velocities (1 m/s and 5 m/s); numerical results were analysed in terms of force and impulsion data and proved to conveniently fit with the test results. In the second step, water impact tests on simple shapes were simulated, including tests on triangular and cylindrical rigid shapes, performed at the Politecnico Di Milano, and vertical drop tests of a deformable metallic cylinder performed at CIRA. For the considered structures and impact conditions, the simulations permitted one to draw a general conclusion in terms of prediction capacities regarding deformations, accelerations and pressure data.

Keywords: smooth particles hydrodynamics, water, impact.

WIT Transactions on Engineering Sciences, Vol 69, © 2010 WIT Press
www.witpress.com, ISSN 1743-3533 (on-line)
doi:10.2495/AFM100351

1 Introduction

In the field of aircraft ditching modelling, classical solutions for fluid/structure interaction simulation, based on Finite Element Lagrange or even ALE (Arbitrary Lagrange Euler) formulations, face well-known limitations [1] – mesh distortions leading to numerical instabilities (negative volumes) and high CPU consumption (time step decrease) that make the modelling of specific threats – such as water ingress through a failed structure – almost impossible. The present works, carried out within the GARTEUR Action Group AG15, investigate a more recent formulation based on SPH (Smooth Particles Hydrodynamics) formulation that permits one to get rid of most of the numerical issues insofar the media behaviour is no longer modelled through elements deformation, but through particles inter-displacement. Different codes available among the AG15 partners are thus investigated and the present paper gives an overview of some of the achieved results. As a first step to evaluate the SPH formulation, laboratory tests consisting of droplet impacts onto a rigid plate are considered, with the measured output limiting to the force generated by the droplet on the rigid support. In the second step, the SPH method is applied to the modelling of impact tests of simple structures, including rigid and deformable shapes, for an impact velocity range relevant with crash issues. Such tests permit one to evaluate the capacity of the method to predict standard observables, such as acceleration and pressure data.

2 Smoothed Particle Hydrodynamic method

The Smoothed Particle Hydrodynamics method is a gridless Lagrangian method, whose corner stones are two approximations, namely the kernel approximation and the particle approximation. The estimate $\langle A(\vec{\mathbf{r}})\rangle$ of $A(\vec{\mathbf{r}})$ called the kernel approximation is derived from the following identity:

$$\left\langle \mathbf{A}(\vec{\mathbf{r}})\right\rangle = \int_{\Omega} \mathbf{A}(\vec{\mathbf{r}}')\,\delta(\vec{\mathbf{r}}-\vec{\mathbf{r}}')\,\mathbf{d}\mathbf{r}' \tag{1}$$

$$\int_{\Omega} \delta(\vec{\mathbf{r}}-\vec{\mathbf{r}}')\mathbf{d}\vec{\mathbf{r}}' = 1 \text{ (delta function)} \tag{2}$$

where $A(\vec{\mathbf{r}})$ may be any scalar vector or tensor material property, $\vec{\mathbf{r}}$ is the position vector in space and Ω the domain of integration. Eqn (1) shows that the "value at a point" of a continuous function over a continuous domain could be extracted from its integral by using a delta function as a "filter". Assuming now that the delta function is replaced by another function $W(\vec{\mathbf{r}})$, which spans a certain "range" but still obeys the basic delta function property $\lim_{\mathbf{h}\to 0} \mathbf{W}(\vec{\mathbf{r}}-\vec{\mathbf{r}}',\mathbf{h}) = \delta(\vec{\mathbf{r}}-\vec{\mathbf{r}}')$, then eqn (1) yields

$$\left\langle \mathbf{A}(\vec{\mathbf{r}})\right\rangle = \int_{\Omega} \mathbf{A}(\vec{\mathbf{r}}')\,\mathbf{W}(\mathbf{r}-\vec{\mathbf{r}}',\mathbf{h})\,\mathbf{d}\mathbf{r}' \tag{3}$$

Eqn (3) is similar in appearance to eqn (2) except for the function W, which is called the kernel function and the range of influence it spans is controlled by the "smoothing length" h. It means that the value of a function at a point contains information not just about that point but also about the range around that point that the kernel in question is spanning. Therefore, a "smoothing" of the domain has taken place, hence the term "smoothed" particle hydrodynamics.

The particle approximation implies that the domain around the point in question where we seek to define the value of a function is not continuous. Instead it consists of a number of "topologically unconnected finite elements" called particles in order to distinguish them from the classical finite elements, which have a pre-defined and rigid topological connection ("connectivity" defined at the input level). The consequence of this approximation is the replacement of the integral by a summation over a finite number of particles, which are also interpolation points, and the modification of the algebra to account for the "number density" of the domain (i.e. how many particles can be found within a given domain volume defined by the kernel). This is expressed as below:

$$\left\langle \mathbf{A}(\vec{\mathbf{r}}) \right\rangle = \sum_{\mathbf{j}=1}^{\mathbf{J}} (\mathbf{m_j} / \boldsymbol{\rho}_\mathbf{j})\, \mathbf{A_j}\, \mathbf{W}(\left|\vec{\mathbf{r}} - \vec{\mathbf{r}}_\mathbf{j}\right|, \mathbf{h}) \tag{4}$$

where $A_j = A(\vec{r}_j)$, m_j and ρ_j are respectively the mass and material density associated with the particle j, $\vec{r}_j$ the position vector of particle j and J the number of particles that are within the region of influence of a given particle at a given time. Eqn (4) indicates that the contribution of each particle within the kernel range (taking into account its number density) is summed over all the particles in order to produce the smoothed value of a function at a point. In order for the kernel and particle approximations to be pragmatic, the choice of the kernel function should be such that following properties are satisfied:

- Compact form i.e. acting over a finite range, zero outside that range
- Positive within this range,
- Respecting the "delta function properties",
- Monotonically decreasing,
- Degenerating in the limit to a delta function.

One should note that the first two requirements listed above are the same for the classical interpolation functions of the FE method. Therefore, the kernel should be seen as a form of interpolation function. A more detailed discussion regarding the kernel choice, the control of the smoothing length and other numerical issues can be found in [2]. Figure 1 illustrates graphically the similarity between the FE and the SPH approximations. A patch of 9 elements is shown in both the FE and the equivalent SPH approximation. The interpolation functions have been overlaid upon the central element of the FE mesh while the kernel of the central particle has been "sketched" as spanning its neighbours in the SPH mesh.

The main advantage of the SPH method is the absence of connectivity between the "particle elements", which therefore permits to treat large

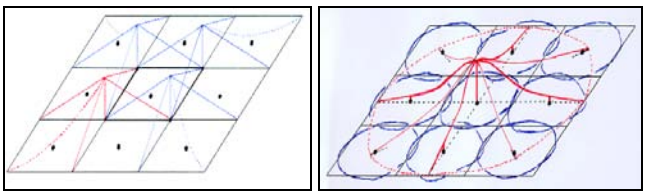

Figure 1: Comparison between a) FE and b) SPH (9 elements patch modelling).

deformation. In particular, problems of mesh distortion and tangling common with the standard Finite-Element method can be avoided. Furthermore, as both FE and SPH are Lagrangian techniques, penalty contact algorithms already available for the Finite-Element method can also be used to define contacts between SPH particles and classical Finite-Elements. However, a major drawback of this method is the very high computation time due to the necessary search for neighbours around each of the particles, which should occur periodically. Based on these facts, one strategy to simulate the impact of structures on water is to combine SPH (in the impact area) and classical finite-element solids (around the impact area) to model the water continuum, with the transition from particles to solid elements defined as a tied interface. This strategy enables to limit the number of particles and consequently positively influences the computation time.

3 Simulation of droplet impact tests on rigid plates

3.1 Droplets impact tests onto a rigid plate

In a preliminary step to evaluate the SPH method, impact tests of a droplet onto a rigid plate have been performed. The circular aluminium plate (Ø20 mm) was mounted on a low capacity piezo-electric load cell to record the evolution of the impact force. Water droplets were generated by a needle permitting to control the droplet diameter and could be dropped from a height up to 2 m thus permitting to cover an impact velocity range from 0,5 up to 5 m/s. In the present paper, two impact velocities are considered – 1.05 and 5.17 m/s – with a Ø=4.2 mm droplet as illustrated in the following figure with the measured force versus time (pictures on the right are for the 5.17 m/s impact velocity).

3.2 Simulation results of the droplet impact test at 5.17 m/s

The droplet is meshed with a hexagonal network defined with an inter-particle distance of $0.1x\sqrt{2}$ so as to obtain a smoothing length equal to 0.1, thus leading to a model with 54694 particles. Two simulations are performed, for 2 values of the friction coefficient – 0 and 0.2 – of the contact interface managing the interaction between the droplet and the plate (modelled with shell elements fully constrained in displacement and rotation) and are run over a 2 ms duration. The numerical force/time curves are post-treated from the contact interface normal

force and are presented in the following figure, together with the corresponding experimental data (the animation pictures correspond to the simulation with the friction coefficient set to 0). Results show that the profile of the force/time signal is well predicted by the simulations though its magnitude tends to be globally overestimated. One also notes that the friction coefficient does not affect the droplet behaviour as both simulations lead to super-imposable results.

In Table 1, results are analysed in terms of maximum force and time of appearance of this maximum force, and in terms of maximum impulsion (integral of the force/time signal). This shows that the magnitude of the maximum force is in good agreement with the test data but is postponed compared to the experiment, while the impulsion is largely over-estimated, as a consequence of the global overestimation of the force signal.

3.3 Results of the simulation of droplet impact at 1.05 m/s

Two simulations are also conducted at 1.05 m/s, for 2 values of the friction coefficient, and are run over a 6 ms run time, with the same parameters as for the

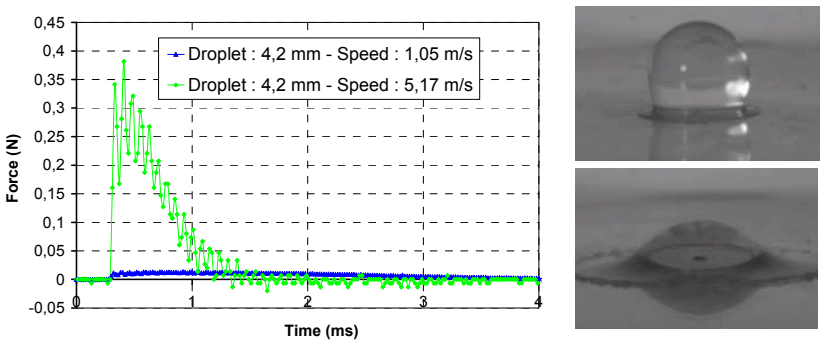

Figure 2: Results of the impact tests of a Ø=4.2mm droplet on a rigid plate.

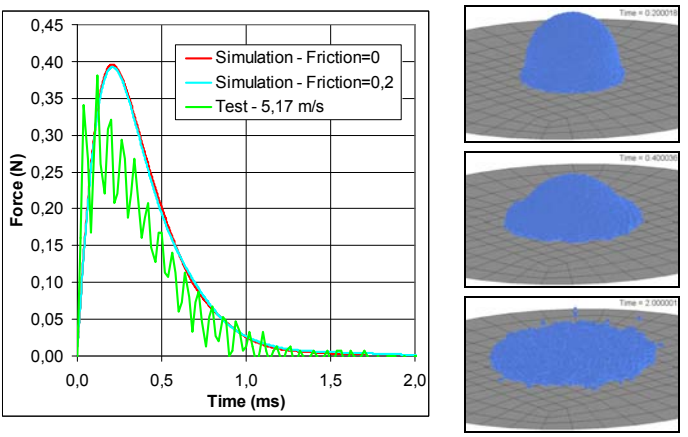

Figure 3: Comparison of the experimental/numerical results at 5.17 m/s.

Table 1: Comparison of the experimental/numerical data at 5.17 m/s.

Simulation	Max Force (N)	Time of Max Force (ms)	Impulsion (N.ms)
Simulation – Friction=0	0.3956	0.2060	0.1972
Simulation – Friction=0,2	0.3923	0.2080	0.1970
Test	0.3815	0.1200	0.1430

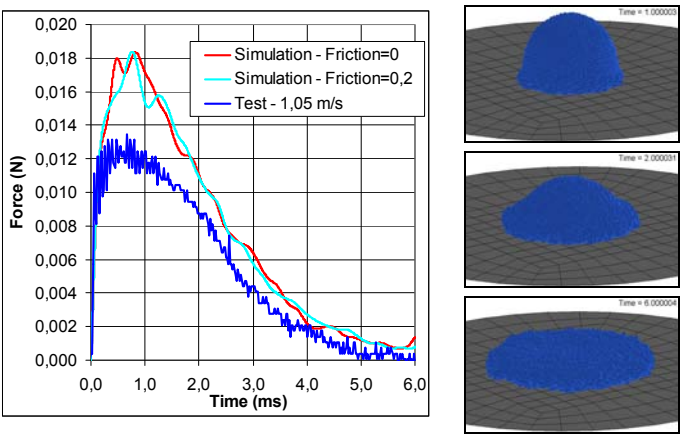

Figure 4: Comparison of the experimental/numerical results at 1.05 m/s.

Table 2: Comparison of the experimental/numerical data at 5.17 m/s.

Simulation	Max Force (N)	Time of Max Force (ms)	Impulsion (N.ms)
Simulation – Friction=0	0.0183	0.8220	0.0441
Simulation – Friction=0,2	0.0184	0.7560	0.0438
Test	0.0134	0.6600	0.0315

5.17 m/s velocity. One observes that the simulations also conveniently predict the profile of the force/time signal but again globally overestimate its magnitude.

The analysis of the maximum force and impulsion shown in the following table confirms the above conclusions, with an overestimation of the maximum force and impulsion values.

4 Simulation of impact tests of simple structures

4.1 Impact tests on triangular and cylindrical rigid shapes – Politecnico Di Milano (PM)

Politecnico Di Milano performed guided tests with triangular (1m long and 0.4m wide for a 37 Kg weight) and cylindrical (1m long and 0.25 m wide for a 33 Kg

weight) rigid articles, in a 22 m height drop-tower installed upon a 8m diameter pool [3]. Specimens were equipped with 3 accelerometers (2 at corners and 1 in the middle of one edge) in order to control the article incidence at the impact and new enhanced pressure transducers (8 for the triangle and 6 for the cylinder) designed and manufactured at PM – metallic cylindrical end-cups including a thin membrane equipped with a diaphragm strain gauge on its internal face (with the possibility to modify to membrane thickness to adjust the sensor sensitivity). In addition to these accelerations and pressures measurements, results also included pictures/videos.

Preliminary tests were conducted to assess the test configuration and equipments, for a large impact velocity range (up to 12.5 m/s for the triangular shape and 7.7 m/s for the cylindrical shape). Finally, two impact velocities were selected for the final test program – 4.4 m/s and 7.7 m/s – with 3 tests planned for each velocity and shape. The following figure illustrates typical results for one test on the triangular shape at the 4.4 m/s impact velocity, noting that the pressure transducers and accelerometers provided repeatable measurements between the 3 performed tests. To evaluate the test data relevance, a comparison with analytical results obtained using Von Karman's formulas for rigid body water impacts was performed and showed good correlation. Finally, it was observed that the trend of both pressure and acceleration measurements were rather linear with the drop-height.

4.2 Simulation results of the impact tests on triangular and cylindrical rigid shapes

Only the simulations of the 4.4 m/s impact test of the triangle shape and the 7.7 m/s impact test of the cylindrical shape are presented in the following paragraph. For computation cost reasons, 1/4 of the pool is considered, with appropriate symmetry boundary conditions. The water basin is modelled by combining SPH particles in the impact area and solid Finite Elements around, modelled with an isotropic elastic plastic hydrodynamic material law. In the

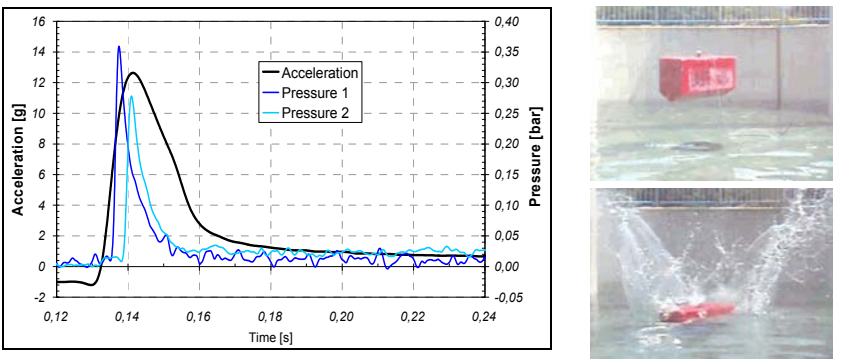

Figure 5: Impact on water of the triangular shape – V_{impact}=4.4 m/s (Politecnico Di Milano test facility).

simulations, pressures are measured from the forces measured by dedicated contact interfaces managing the interaction between the particles and a set of shell elements representing the pressure sensor surface. Therefore, the SPH density was determined so as to obtain a relevant number of "particles" interacting with each pressure transducers, which led to a water model containing 150000 SPH particles and 14000 solid elements.

As for the droplet tests simulation, two values (0 and 0.2) of the friction coefficient between the particles and the structure are considered.

In Figure 6, the measured acceleration time history of the wedge impacting on water at 4.4 m/s is depicted with the simulation results. As it can be seen, variation of the friction does not show any significant influence on the acceleration in that case. The simulation predicts an acceleration peak of 14 g whereas the measured acceleration peak amounts to 13 g. Acceleration peaks agree well between test and analysis. Nevertheless, it can be observed that the calculated acceleration peak is delayed compared to the measured one. Regarding the pressure time histories, measured pressure peaks are between 0.37 and 0.41 bar, whereas calculated ones are in the range 0.28–0.35 bar; the simulation is therefore also able to predict the order of magnitude of the pressure.

Finally, Figure 6 shows an animation picture taken during the impact and especially illustrates the capacity of the SPH model to conveniently reproduce the formation of a splash around the impacting structure. Concerning the

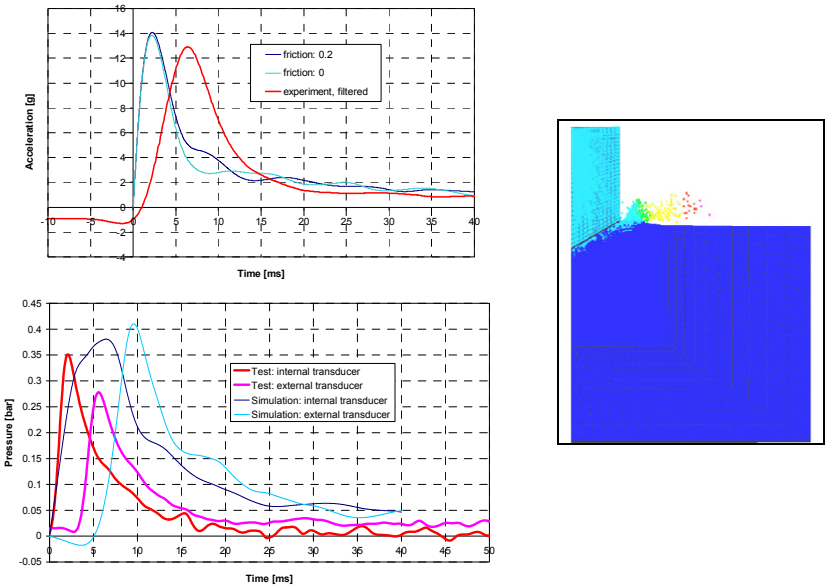

Figure 6: Comparison between test and simulation (CFC60 filter) for the 4.4 m/s impact of a wedge.

cylinder impacting on water, similar comparisons to the wedge case between test and simulation are performed. Figure 7 shows that the simulation is also able to predict well the acceleration peak (37 g in the test – 36 and 40 g in the simulations). Both peaks in the simulations correspond to two different frictions in the definition of the contact between the cylinder and the water continuum. Contrary to the case with the wedge, the value of the friction coefficient slightly influences the acceleration peak (17%) – this is also observed for the impact velocity of 4.2 m/s, which is not presented in this paper. It is presumed that the cylinder due to its geometry (surface tangent at impact parallel to the water surface) presents a higher drag than the wedge when entering water and therefore leads to higher friction forces acting on the structure surface compared to the wedge. Figure 7 also shows that the order of magnitude of the pressures is satisfactorily predicted by the simulation.

Finally, the animation picture proves the capacity of the method to conveniently reproduce the formation of a splash, which is, in the cylinder case, intrinsically topologically different from the wedge case.

4.3 Impact tests on a deformable cylindrical shape - CIRA

CIRA conducted vertical drop tests on water of a deformable metallic structure. The tests article consisted of a half-cylinder made of 2 mm thick steel skin stiffened with metallic frames (resulting in a 66 Kg weight) and was tested in the CIRA-LISA (Laboratory for Impact tests on Aerospace Structures) drop tower

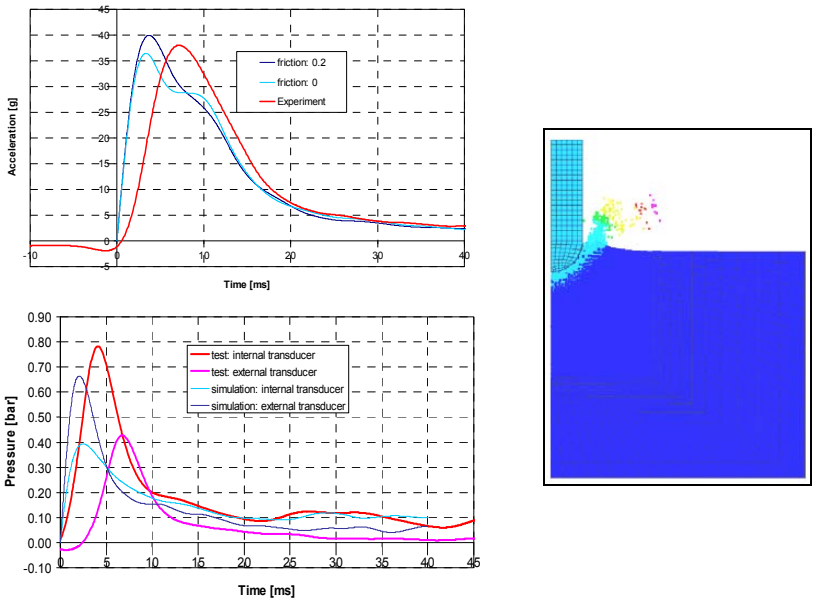

Figure 7: Comparison between test and simulation (CFC60 filter) for the 7.7 m/s impact of a cylinder.

facility. The tests were performed at 3 increasing velocities (3m/s, 8m/s and 10 m/s), with the specimen fixed to a trolley (174 Kg) which was guided during its free fall.

In a preliminary step, the test configurations (specimen thickness, mass and impact velocities) were identified from numerical analysis, with the objective to obtain tested specimens with or without residual deformation. Tests exhibited the targeted behaviours insofar the 2 m/s impact velocity led to no residual deformation of the specimen skin, while the 8 m/s and 10 m/s permitted to obtain increasing residual deformation. Results delivered by CIRA included acceleration (4 accelerometers fixed on the upper side of the article) and pressures (7 transducers distributed on the external side of the skin, at stiffened and un-stiffened areas) measurements, high speed videos and the residual deformation of the article (mapping at referenced points of the deformed skin).

Finally, as a support to the numerical works, CIRA additionally conducted dynamic mechanical characterisation tests on the steel material constitutive of the skin, for a strain-rate range up to 60 s^{-1}. This tensile tests campaign permitted to identify the reference static mechanical properties and the strain rate influence of the steel material.

4.4 Simulation results of the impact tests on a deformable cylindrical shape

The specimen is modelled with shell elements associated to an elastic plastic material model taking into account strain rates, with its parameters identified from the dynamic characterisation tests performed at CIRA. The water media is modelled by combining SPH particles in the impact area and solid Finite Elements around, leading to a water model containing 62100 SPH particles and 22400 solid elements.

The comparison with the test data is performed in terms of acceleration (nodal acceleration at nodes located at the accelerometers position), pressures (simulated pressures are extracted from dedicated contact interfaces between the water media and selected shell elements on the skin) and residual deformation of the tank.

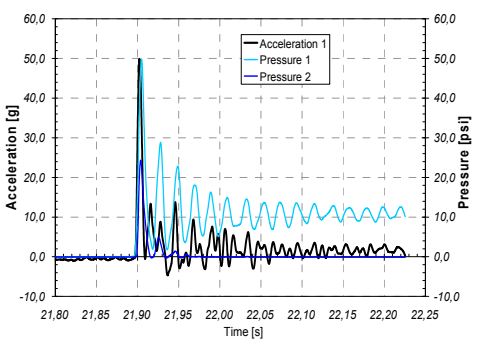

Figure 8: Impact on water of a deformable cylindrical shape – V_{impact}=10 m/s (CIRA's LISA test facility).

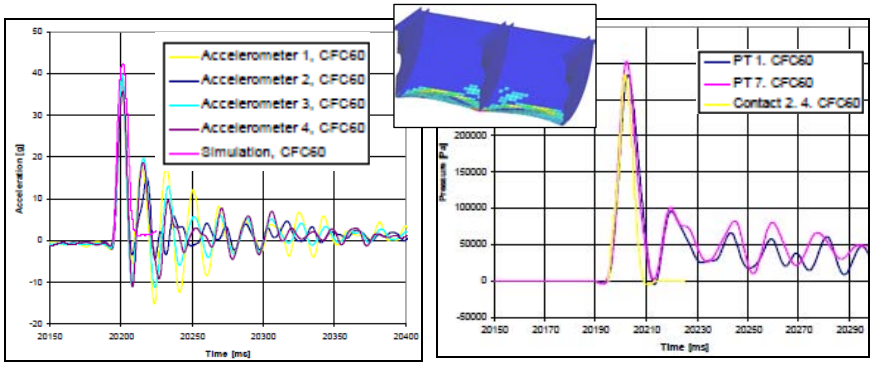

Figure 9: Numerical/experimental comparison for the 8 m/s impact test.

The simulations for the 3 impact velocities lead to quite similar conclusions, hereafter summarized and illustrated in Figure 9 for the 8 m/s impact velocity:

- The deformations of the test article are slightly over-predicted by the code (conservative analysis).
- Accelerations are conveniently predicted.
- Pressures are well predicted at soft areas i.e. where the test article deforms.
- Pressures are systematically over-predicted at stiff or slightly deformable areas (a refinement of the SPH network shall permit a better prediction).

5 Conclusion

These works performed within the GARTEUR Action Group AG15 aimed at evaluating the capacity of the SPH formulation to simulate fluid/structure interaction, with the objective to apply the method to the modelling of helicopter ditching [4]. In a preliminary step, one major goal of the group consisted in generating an experimental database including laboratory tests and tests on simple shapes, in order to collect relevant data for the validation of numerical models. Based on this experimental database, numerical works have established the relevance of the SPH formulation to represent the physics involved in fluid/structure interaction phenomenon and to predict the order of magnitude of most experimental observables (force, acceleration and pressure), however noting a tendency to some overestimation according to the considered data. Finally, SPH simulations also proved to be free of numerical instability and runnable over large run times, thus constituting one significant advantage compared to classical Finite-Element methods when modelling highly deformable media.

Acknowledgements

The authors wish to acknowledge the members of the GARTEUR Action Group AG15 “Improvement of SPH methods for application to helicopter ditching” for

their support to the activities performed within the project. Authors also acknowledge the European Commission, the French Ministry of Defense and the Région Nord-Pas-de-Calais for their financial support to the present works.

References

[1] Langrand, B., Bayart, A-S., Chauveau, Y. & Deletombe, E., *Assessment of multi-physics FE methods for bird impact modelling – Application to a metallic riveted airframe*, Int. Journal of Crashworthiness, 7(4), pp. 415-428, 2002.

[2] Groenenboom, P.H.L., *Numerical Simulation of 2D and 3D Hypervelocity Impact Using the SPH Option in PAM-SHOCK*, Int. J. Impact Engng, Vol. 14, 1993, pp. 255-265.

[3] Anghileri, M., Castelletti, L., Francesconi, E., Pittofrati, M., Milanese, A., *Rigid Body Water Impact: Experimental Tests and Numerical Simulations Using SPH Method*, AHS2007.

[4] Toso-Pentecôte, N., Delsart, D., Vagnot, A., *Assessment of the SPH method: Simulation of simple body shapes impacting on water and a PUMA helicopter ditching*, ODAS Symposium - October 2009 – Berlin Germany.

Environmental impacts on coastal structures with a case evaluation of armor stone protection at Keweenaw Waterway, USA

M. Zakikhani[1], D. W. Harrelson[1], J. G. Tom, J. A. Kissane[2], M. K. Allis[3] & J. E. Kolber[4]
[1]*The U.S. Army Engineer Research and Development Center, USA*
[2]*U.S. Army Corps of Engineers, Chicago District, USA*
[3]*U.S. Army Corps of Engineers, Detroit District, USA*
[4]*U.S. Army Corps of Engineers, Buffalo District, USA*

Abstract

The evaluation of armor stone performance as a viable construction material is essential to increasing the longevity of maritime structures used to protect harbors, coastal areas and navigable waterways from damaging waves and other forces. The environmental parameters have led to the armor stones deteriorating faster than laboratory testing indicates. This paper provides an overview of the decomposition of the four rock types (limestone, granite, quartzite, and concrete) over the five field inspections. The meteorological variables were used to calculate the number of freeze-thaw events that occurred over the time period. The water wave height data were used to calculate stone deterioration from wave actions. The results from the field observations, together with the meteorological analysis, were used to help better parameterize the numerical model and assist in identifying problems in scalability from laboratory test samples to field samples.

Keywords: hydrodynamic forces, response of structures, fluid dynamics, armor stone durability, great lakes, numerical modeling, laboratory testing.

1 Introduction

Degradation of armor stone placed in coastal navigation areas in the United States Great Lakes has occurred as the result of a number of interacting and interrelated natural factors, such as seasonal weather changes, and repeated

WIT Transactions on Engineering Sciences, Vol 69, © 2010 WIT Press
www.witpress.com, ISSN 1743-3533 (on-line)
doi:10.2495/AFM100361

cycles of temperature (e.g., flowing water, wetting and drying, wave action, freeze and thaw, etc.). This study was proposed to evaluate the importance of various factors in armor stone durability, consider the relevance of test procedures and possibly develop scaling factors and test methods that will be more representative of the materials used. It also provides guidelines for the personnel involved in source selection activities, so they may be more consistent across the organization. The research provides a better understanding of the relationship between the standard tests used in stone specifications and the performance of stone in the structures. Several investigations have developed standard field and laboratory procedures for careful comparisons of stone of similar, if not identical, properties. Previous investigations have been directed at considering the causes, based on comparison of different types of stone used in different structures. Much of the testing performed on stone submitted as material for erosion protection is based on the protocols used to evaluate concrete aggregate and sub-grade stone materials – that is, tests designed for use on material orders of magnitude smaller than armor stone of several tons. Acceptance of sources is then based on a combination of test results, performance records, and quarry inspections.

As a secondary objective, beyond evaluating testing, the results of this study and the previous work on armor stone durability would be used to develop guidelines for future armor stone selection procedures with respect to ranking of stone types, excavation methods and geologic characteristics of the materials available within a region. These guidelines could also be considered when developing documents, such as "Engineering Considerations during Construction", for use in evaluating proposed sources.

Three sites, Burns Harbor, Cleveland Harbor and Keweenaw Waterway were selected for evaluation of armor stone performance. Index stones were placed in the structures and monitored over the study period. Samples from quarries used in shoreline projects were designated and tested using existing ASTM or testing protocols contained in existing stone specifications that stipulate the size of samples. These test results were compared to tests of larger size samples to consider the effects of scale. In addition, larger samples were placed in structures so that they may be subjected to the conditions that cause weathering of armor stone and the results of their performance have been compared to the laboratory results. To consider the combined effects of environmental stresses on armor stone, testing were done to evaluate the performance of stone subjected to both freezing and thawing and wetting and drying. This testing was performed on the same samples rather than independently, as is more typically done. The combined testing realistically simulates the environmental conditions in the structure. In addition, by including stone of different rock types (i.e. igneous, metamorphic and sedimentary), the relative scaling effects can be evaluated to determine whether the scaling factors, if they exist, are constant or variable by rock type. After evaluating monitoring data, a determination was made as to the relative comparability of scaled laboratory test results and material durability in coastal projects in the Great Lakes, and recommendations made as to the appropriate laboratory tests for future stone specifications.

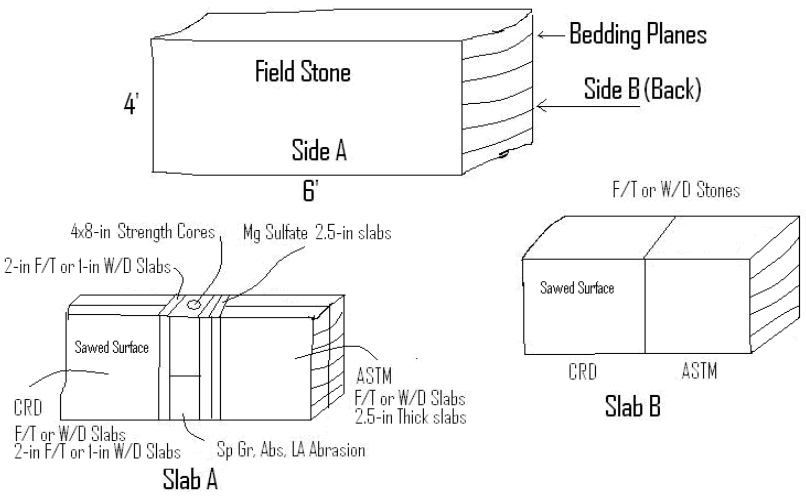

Figure 1: Drawing of the cutting lines and test specimens.

2 Field sampling and monitoring

To determine qualified samples for this study, several quarry sites that have historically supplied material for shoreline protection in and around the Great Lakes Region were visited. The five samples received represent two of five material types proposed for the entire investigation. Samples identified as MCNP 1, 2, 3 are stone discard pieces from stones placed in the field for monitoring from the Hayton Quarry. Each sample consisted of two slabs, each approximately 4-ft by 6-ft by 1-ft, from the original stone and was assigned Concrete and Materials Branch Serial No. 070103, 070104, and 070105, respectively. The smaller, thinner slabs are further identified as Slab A and the larger thicker, more massive slabs are further identified as Slab B (fig. 1). Samples identified as MCNP 4 and 5 are also discard pieces from stones placed in the field from Valders Quarry. These samples also consisted of two slabs, each approximately 4-ft by 6-ft by 1-ft, and was assigned CMB Serial No. 070106 and 070107, respectively. The samples proposed for Phase I of this investigation are the CMB Serial No. 070104 (MCNP-2) and 070105 (MCNP-3).

3 Numerical modeling

3.1 Estimation of degradation rate

Latham [1] provided a simple approach to estimate reduction in armor rock weights as results of several environmental and other impacts. Factors affecting the degradation rate are the intrinsic material properties of the rock source, the

production-influenced geometric properties of the armors tine, the environmental boundary conditions at the coastal site, and the armor layer design concepts used. The parameters affecting stone degradation rates are provided in table 1.

Table 1: Degradation-rate factors for armor stone (post-construction).

Type of factor	Controlling factor			Parameter
Intrinsic material properties of the rock	Mineralogy	Rock fabric strength	Resistance to weathering	K_s *(see* X_6*)*
	Micro-texture		abrasion	K_s
	Weathering grade		Type-II impact breakage	K_s*(see* X_4*)*
	Block integrity	Block strength due to existence of macro-flaws	Type-I impact breakage	*(see* X_4*)*
Production influenced geometric properties	Block size (W_{50})			X_1
	Block grading (W_{85}/W_{15})			X_2
	Initial shape (P_R)			X_3
Environmental boundary conditions	Incident wave energy (e.g. $H^2_S T^2_m$ or H_s)			X_4
	zone of structure			X_5
	Meteorological effects			X_6
	Water-borne attrition agents			X_7
Factors influenced by design of armor layer	Concentration of wave attack (slope angle+ tidal range)			X_8
	Armor stone mobility in design concept (e.g. $Hs/\Delta D_{n50}$)			X_9

W_{50} is the median weight of blocks. W_{85} and W_{15} are the 85 and 15 percent lighter by weight values. PR is the Fourier Asperity Roughness parameter. HS and Tm are the significant (i.e. average of the highest one third waves) wave height and mean wave period. Δ is the buoyant density of rock relative to sea water and D_{n50} is the nominal size of W_{50} block.

Source: Latham [1]

To determine degradation rate for a given armor stone, a sample of the material is tested in an abrasion mill simulation of the wear process. This provides a graph of weight versus laboratory time. Laboratory time is converted to years on site using an equivalent wear time factor, which is derived from a product of nine weighted parameters (see table 1). The effects of fracturing and spalling as well as abrasion are included.

3.1.1 Example of degradation model

The rock samples are used in the abrasion mill to create plot of fractional weight loss versus revolutions (fig. 2). This graph gives the typical loss in asperity roughness observed in milling tests. The equivalent wear time factor, X is calculated as product of all ratings.

$$X = \prod_1^9 X_i \tag{1}$$

The value X is then used to convert number of years in service to thousands of revolutions in mill. Using fig. 1 and the number of revolutions, W/W_0 (W = final stone weight; W_0 = initial stone weight) will be estimated and finally the reduction in weight will be calculated.

As an example input parameters for two site situations are given in table 2 (Latham [1]): (i) for a 3 ton, basalt in tropical climate, medium grading, dynamic design, and (ii) for 4.5 ton, temperate climate, narrow grading, static design.

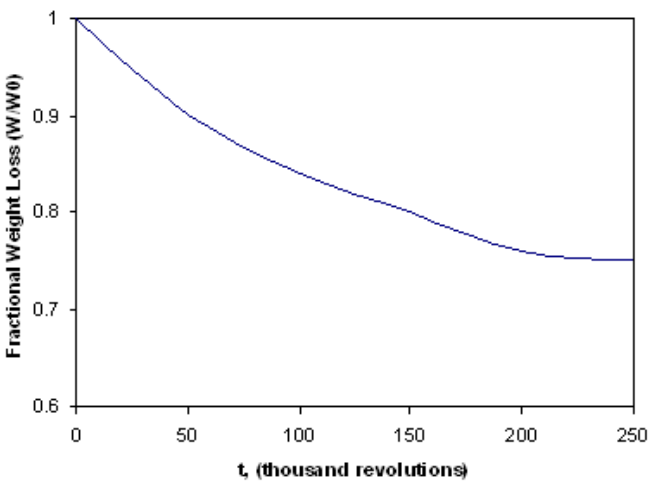

Figure 2: Abrasion mill test results for a specific type of armor stone.

Table 2: Example site situation summary.

		Ratings	
Parameter		(i)	(ii)
X_1	size	0.72	0.84
X_2	grading	1.0	1.2
X_3	shape	1.5	1.5
X_4	wave energy	2.0	2.0
X_5	zone	1.0	1.0
X_6	climate	0.2	1.0
X_7	attrition	1.0	1.0
X_8	concentration of attack	1.5	1.0
X_9	block mobility	1.0	2.0
X		0.6	6.0

3.2 Characterization of rock heterogeneity

Liu et al. [2] describes a statistical approach (homogeneity index) to characterize the heterogeneity in rock. According to this article, the Weibull distribution (Weibull [3]; Hudson [4]) describes very well the experimental data for the distribution of microstructures within rock. Therefore, the Weibull statistical distribution is used to characterize the rock heterogeneity. The Weibull distribution may be simplified as:

$$Q(\sigma) = \int_0^{\sigma} P(x)dx = 1 - \exp\left[-\left(\frac{\sigma}{\sigma_0}\right)^m\right] \tag{2}$$

where Q is a simplified form of Weibull distribution, σ is the elemental parameter (MPa), P is the Weibull probability density function, m is the shape parameter describing the scatter of σ and describes the heterogeneity of rock, and σ_0 is the mean value of the physical-mechanical parameters of the specimen (elemental parameter).

The most recommended method for calculating the homogeneous index m (Curtis and Juszczyk [5]; Davies [6]) is to rank strength (σ) data from smallest to largest and the assignment of respective Q (σ) values according to the following:

$$Q(\sigma) = \frac{i}{N+1} \tag{3}$$

Where i is the rank and N is the total number of specimens. According to Equation 3, the Weibull distribution can be liberalized into the following form:

$$y = \ln\left[\ln\left(\frac{1}{1-Q(\sigma)}\right)\right] = m\ln\sigma - m\ln\sigma_0 = Ax + B \tag{4}$$

where y=ln [ln {1/[1-Q (σ)]}], A=m, x=ln σ, and B=-m ln σ_0. With reference to this equation, a plot of lnσ against ln [ln {1/[1-Q (σ)]}] gives the line-relationship and the slope of the line is the homogeneous index m. The best estimate of the homogeneous m may be obtained using the linear least squares (LLS) techniques (Davies [6]):

$$m = A = \frac{n\sum xy - \sum x \sum y}{n\sum x^2 - (\sum x)^2} \tag{5}$$

where ∑, x and y in the equations are abbreviations for $\sum_{i=1}^{n}$, x_i and y_i, respectively.

One of the attractive aspects of the Weibull distribution is the presence of the shape parameter, which allows this function to take a wide variety of shapes. For m = 1; this distribution is exponential; at about m = 1.5; the distribution is nearly log-normal; and at about m= 4, it closely approximates a normal distribution. Since the shape parameter m is a measure of the element parameter variability, it can be considered as a homogeneity index. The larger the index m is, the more homogeneous is the rock. When m tends to infinity, the variance tends to zero and an ideal homogeneous rock is obtained.

3.3 Estimation of freeze-thaw intensity

The intensity of freezing and thawing depends on the freezing temperature, the duration of the freezing cycle, the available moisture, the slope direction (geographic area properties), degree of saturation, and permeability (rock properties) (Lienhart [7]). The first four of these parameters depend on geographic area and the last two factors are merely rock properties. Linehart [7] describes the calculation of some terms that can be used to calculate intensity and frequency of freeze-thaw cycles.

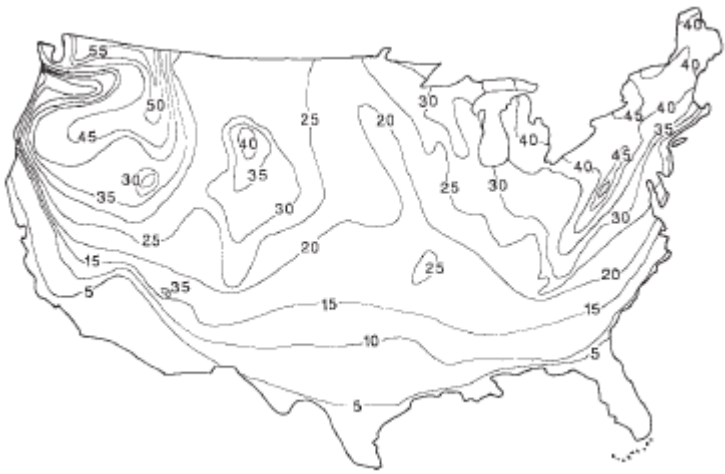

Figure 3: Isoline map of the moist freeze-thaw index for the United States.

The National Oceanic and Atmospheric Administration (NOAA) climate data are used to calculate mean number of freezing cycle days for each month. These monthly freezing cycle days could then be added to find the mean number of freezing cycle days per year. Since the presence of moisture is significant in the freeze-thaw durability environment it was decided multiply the percent days of precipitation of 0.01 inch or more during the freezing cycle month by mean number of freezing cycle days per year and the product was termed moist freeze-thaw index. Fig. 3 shows isoline map of the moist freeze-thaw index for the United States using Lienhart method.

3.4 Design

The design process for the determination of riprap and armor stone sizes is complex, particularly for the various geometries of channel protection, and is beyond the scope of this article. Various factors must be considered in order to fully understand how the design parameters have an indirect effect on stone performance, and two of the more useful of the design equations will be reviewed to demonstrate the influence of these factors.

Hudson and Fairhurst [8] developed the best known of the design equations for determination of acceptable armor stone size to resist damage from a given wave system based on hydraulic modeling studies. The equation is as follows:

$$W = H^3 w_r / K_d (Sr - 1) cot\theta \tag{6}$$

where W is the weight of the armor unit, H is the average wave height of the highest 10 percent of all waves, w_r is the unit mass of the stone, K_d is a damage coefficient, S_r is the specific gravity of the stone, and θ is the angle of the slope of the armor stone.

Hudson and Fairhurst [8] present the results of an extensive series of experiments conducted to obtain basic information on the stability, K_d of rubble-mound breakwaters. These equations along with other design formulations have been used in this study.

4 Overview of Keweenaw waterway

The Keweenaw waterway is located on Michigan's Upper Peninsula, USA. The waterway was completed in 1860's. It connects Lake Superior with Portage and Torch Lake. The waterway has been used by shipping companies in the early days to transport copper and other goods. The waterway experiences some of the harshest weather conditions in the great Lakes region with large fluctuations in temperature and high wind and wave action due to large fetch. The local weather has led to stones deteriorating faster than laboratory testing indicates.

Ten index stones were placed within the toe of the western structure: five lime stones, two granites, two quartzites and one cement. The weather data consist of hourly surface observations from Houghton county memorial airport, hourly buoy observations from NOAA buoys and hourly wave data from GLERL GLCFS.

Freeze-thaw effects have potential to increase rate of deterioration. Water gets into natural and man-made cracks of the stones. When water freezes in these cracks, it causes them to expand, increasing its size and exerting more pressure on surrounding areas. Subsequent thawing leaves larger areas for the process to repeat itself. Two published methods of freeze-thaw cycle techniques were used for this study. The first method is described by Lienhart [7] and the second one is modified form of Arnold et al. [9].

Results of the freeze-thaw cycle calculation indicate that the site observation data are consistent with both methods. Maximum number of freeze-thaw events occur during seasonal changes, such as the late fall and early spring. Most intense period occurred in the winter and month of November. Freeze-thaw cycle had a little correction with the overall rate of the stone degradation.

Waves impacting the structure can cause stone to move around, potentially increasing the rate of deterioration. Hudson and Fairhurst [8] equation is used to determine the minimum weight of a stone to ensure weight of stone to ensure structure stability for a given wave condition. Wave heights had a strong correlation with the degradation of cement.

5 Summary and conclusion

The project described here is a multi-year research effort. To date we have completed part of the study. The results presented here are not conclusive. The reader should look for future publications of this research project. Currently, ten index stones have been placed at Keweenaw Waterway and eight index stones at Cleveland Harbor. The Keweenaw samples consist of ten stones, five lime stones, two quartzites, two granites and one cast concrete block. All Keweenaw index stones (except the cast concrete) were cut into roughly rectangular shapes producing a 5–6 ton stone. The concrete block was cast into approximately the same dimensions as the other cut stones. Cleveland Harbor's index stones consist four cut stones; two sandstones and two lime stones and four cast concrete blocks (with varying concrete mixtures). These stones also rectangular in shape average about 9 tonnes in weight. The index stones placed in Keweenaw Waterway and Cleveland Harbor are currently being monitored for rock mass-loss and degradation. Additionally, specific macroscopic features being monitored include vugs, stylolites and fossils in the limestones and fractures, joints and cracks in the quartzite and granites. Petrographic analysis of various microscopic features is continuing as part of the laboratory efforts.

A total of four rounds of monitoring have been conducted at Keweenaw Waterway. Field observations on these samples indicate that in general the stones are weathering from the edges inward towards the center of the stone. The cast concrete block has shown the most weathering with measurable deterioration and mass-loss beginning along its edges (and some corners) that is progressing towards the center of the stone. This trend is less evident in the other index stones, but four rounds of observations indicate that although stone deterioration and mass-loss is less than for the concrete block, it is still progressing in a similar manner.

The limestones, quartzites, and granites have had little measurable rock mass-loss and display no clear trends, but numerous macroscopic features including fractures and joints on all rock types and vugs and stylolites found in the limestones are being monitored for change and a time line for a stone deterioration index is underway.

Several of the Keweenaw index stones displayed ice abrasion during their first winter (2006). This abrasion occurred mainly as scoring of the rock at its waterline due to ice movement. One stone, a quartzite, was moved (displaced to the toe of the structure) during a large storm event in October of 2006, but recovered and replaced on the structure in August 2007.

The field observations and laboratory testing will be used to construct a "stone durability index model" that will be useful in determining the life cycle of large (type A) armor stone. The model will integrate field observations and laboratory testing into a common index that will predict percent rock mass-loss and deterioration rate.

References

[1] Latham, J-P., Degradation model for rock armour in coastal engineering. *Quarterly Journal of Engineering Geology*, 24, pp. 101-118, 1991.

[2] Liu, H.Y., Roquete, M., Kou, S.Q. & Lindqvist, P.-A. , Characterization of rock heterogeneity and numerical verification. *Engineering Geology*, 72, pp. 89–119, 2004.

[3] Weibull, W., A statistical distribution function of wide applicability. *J. Appl. Mech.*, pp. 293–297, 1951.

[4] Hudson, R. Y., *Design of Quarry-Stone Cover Layers for Rubble-Mound Breakwaters*, U.S. Army Engineer Waterways Experiment Station Research Report No. 2-2, Vicksburg, MS, 39 p., 1958.

[5] Curtis, R.V. & Juszczyk, A.S., Analysis of strength data using two- and three-parameter Weibull models. *J. Mater. Sci.,* 33, 1151– 1157, 1988.

[6] Davies, I.J., Empirical correction factor for the best estimate of Weibull modulus obtained using linear least square analysis. *J. Mater. Sci. Lett.,* 20, 997– 999, 2001.

[7] Lienhart, D.A., The geographic distribution of intensity and frequency of freeze-thaw cycles. *Bulletin of the Association of Engineering Geologists*, **25(4)**, pp. 465-469, 1988.

[8] Hudson, J.A., Fairhurst, C., Tensile strength, Weibull's theory and a general statistical approach to rock failure. *The Proceedings of the Civil Engineering Materials Conference*, Held in Southampton 1969, pp. 901– 904, 1969.

[9] Arnold, J. G., Allen, P. M. , Ramanarayanan, T. S. , Srinivasan, R., Muttiah, R. S., The Geographical distribution of freeze/thaw and wet/dry cycles in the United States, *Environmental & Engineering Geoscience*, **2(4),** pp. 596-603, 1996.

Numerical simulation of reservoir fluctuation effects on the nonlinear dynamic response of concrete arch dams

M. A. Hariri Ardebili & H. Mirzabozorg
Department of Civil Engineering,
K. N. Toosi University of Technology, Iran

Abstract

Fluid-structure interaction problems occur in many engineering structures, such as dams, gates, offshore structures, storage tanks, piping systems, etc. Analysis of such interaction problems is important for the safe and economic design of future structures and the safety and performance evaluation of present ones. In the present study, reservoir fluctuation effects on the nonlinear dynamic response of concrete arch dams are investigated. The structure nonlinearity is originated from material nonlinearity due to tensile cracking and compression crushing of mass concrete using the William-Warnke failure surface in principal stress state (Smeared Crack Model). The reservoir is assumed to be compressible and foundation rock is modeled as a mass-less medium. The DEZ concrete arch dam in Iran, with a height of 203m, is selected as the case study. The system is executed using records based on the response spectrum of the dam site. It is found that fluid-structure interaction has significant structural effects on the system such that, when the reservoir level is increased, almost all structural responses of the dam body, such as crest displacement, velocity and acceleration, decrease until a special level and growth is significantly made for reservoir maximum level in the linear model. In addition, principal stresses on upstream and downstream faces increase significantly with reservoir dewatering. On the other hand, responses of the dam in the nonlinear model have special intricacies, but the extension of cracked areas in both upstream and downstream faces develop meaningfully by decreasing the reservoir water level and there is good argument between stress results in the linear and nonlinear models.

Keywords: concrete arch dam, fluid-structure interaction, reservoir fluctuation effect, smeared crack model.

WIT Transactions on Engineering Sciences, Vol 69,
www.witpress.com, ISSN 1743-3533 (on-line)
doi:10.2495/AFM100371

1 Introduction

Interaction between dams and impounded water is one of key factors affecting the seismic response of arch dams during earthquakes. When the dam–reservoir system is subjected to an earthquake, hydrodynamic pressure in excess of hydrostatic pressure occurs on the upstream face due to vibration of the dam body and water in the reservoir. The magnitude of hydrodynamic pressure effect on the response of arch dams depends on the water level in the reservoir, which is governed by the reservoir operation regime. Sometimes the reservoir may be dewatered to visit the upstream face or to repair probable damages or because of drought and it has been found that these states can considerably affect the response of arch dams during earthquakes. The importance of hydrodynamic effects on the behavior of arch dams subjected to earthquake ground motions has long been recognized by investigators, such as Chopra [1], Chwang [2], Fok and Chopra [3], Hung and Chen [4], Fahjan et al. [5]. They studied dam-reservoir systems with different geometrical features of the dam body and the pertinent reservoir. In Fok and Chopra's studies, complex frequency functions were used to define dam–reservoir interactions and concrete material was assumed to be linearly elastic. They found that hydrodynamic pressure plays an important role on the dynamic response of arch dams. In these studies, the reservoir was generally considered to be empty or full. Proulx et al. [6] investigated experimentally and numerically the variation of resonant frequencies of EMOSSON arch dam for four different water levels. Akkose et al. [7] studied reservoir water level effects on the nonlinear dynamic response of arch dams. In their investigation, concrete is idealized as elasto-plastic material using the Drucker-Prager model and the reservoir was modeled with Lagrangian fluid finite elements. They found that reservoir water level effects must be considered in the nonlinear analysis of arch dams.

There are several approaches to simulate the stress–strain relationship of mass concrete under various stress states. In this regard, theories based on plasticity and fracture mechanics approaches have been developed and used in most engineering analyses. In addition, several researches have been conducted to study the dynamic behavior of concrete arch dams. Kuo [8] suggested an interface smeared crack approach to model contraction joints and used this technique for the dynamic analysis of arch dams. Hall [9] proposed a simple smeared crack model to simulate contraction joints, while diagonal cracking is neglected in his work. Espandar and Lotfi [10] applied non-orthogonal smeared crack and elasto-plastic approaches to the Shaheed Rajaee arch dam in Iran. Mirzabozorg et al. [11] utilized a damage mechanics approach to conduct seismic nonlinear analysis of concrete gravity dams in 2D space, including dam-reservoir interaction effects. In 2005, Mirzabozorg and Ghaemian [12] developed a model based on the smeared crack approach in 3D space. In their work, they analyzed 3D models, including dam-reservoir interaction effects, and considered the nonlinear behavior of the structure.

In the present study, reservoir level fluctuation effects on the nonlinear seismic response of a high arch dam, including dam-reservoir-foundation

interaction, is investigated utilizing the Eulerian approach in the fluid domain and the Lagrangian approach in the solid domain. The dam body is modeled, defining concrete material properties and considering the smeared crack method entitled NL-SCM, and dam-reservoir-foundation interaction is taken into account. In the conducted analyses, the height of water in the reservoir is considered in four various levels so that in the first analysis 28.9%, in the second 52.1%, in the third 79.9% and in the last one 96.9% of the total height of the dam body is filled in order to study responses of the modeled system.

2 Constitutive models for concrete material nonlinearity

In theories based on continuum crack, the fracture is idealized to propagate as a blunt front smeared over an entire element or a certain band width of the element. After initiation of the fracture process, determined by a suitable constitutive model, the pre-crack material stress-strain relation is replaced by an orthotropic relation with a material reference axis system aligned with the fracture direction. One of the most important branches of continuum crack is the nonlinear – smeared crack model (NL-SCM), which considers concrete nonlinear characteristics.

The behavior of concrete elements is assumed to be linear elastic until it reaches ultimate strength (Figure 1) and the elasticity modulus of concrete is considered as the average, E, instead of the linear actual, E_0. Stress increases linearly along with an increase in strain. In this step, each reloading of elements

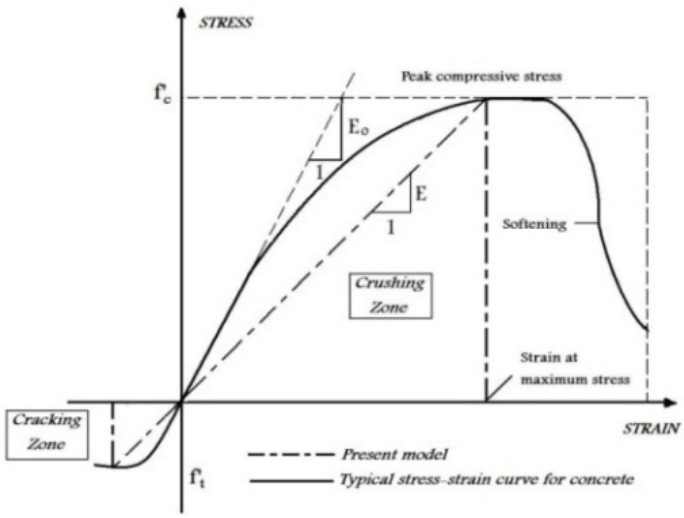

Figure 1: Typical uniaxial compressive/tensile stress-strain curve for concrete.

leads to elastic returning of strain. The tension failure of concrete is characterized by a gradual growth of cracks, which join together and finally disconnect larger parts of the structure. It is a usual assumption that forming cracks is a brittle process and the strength in the tension-loading direction abruptly goes to zero after big cracks.

In the utilized model, cracking occurs based on the William-Warnke 5-parameter failure model. According to this theory, cracking occurs when a combination of principal stresses in any direction lies outside the biaxial failure surface. After cracking, the elastic modulus of the element is set to zero in the direction parallel to the principal tensile stress direction. In this model cracking is permitted in three orthogonal directions at each integration point. When cracking occurs at an integration point, the stress-strain relation is modified by defining a weak plane normal to the crack direction, which is unable to endure any tensile stresses.

3 Finite element formulation of reservoir

Hydrodynamic pressure distribution within a reservoir is governed by the pressure wave equation. Assuming water is linearly compressible and neglecting viscosity, the small-amplitude irrotational motion of water is governed by the 3D wave equation given as:

$$\nabla^2 P(x,y,z) = \frac{1}{c_\bullet^{\,2}} \ddot{P}(x,y,z,t) \tag{1}$$

where P is hydrodynamic pressure and c_0 is the velocity of the pressure wave in the water.

For earthquake excitation, conditions at the boundaries of dam-reservoir, reservoir-foundation, reservoir-far-end and reservoir-free-surface as, shown in figure 2, are governed as given in following sections.

3.1 Dam-reservoir boundary condition

At the surface of fluid-structure, there must be no flow across the interface. This is based on the fact that the face of concrete dams is impermeable.

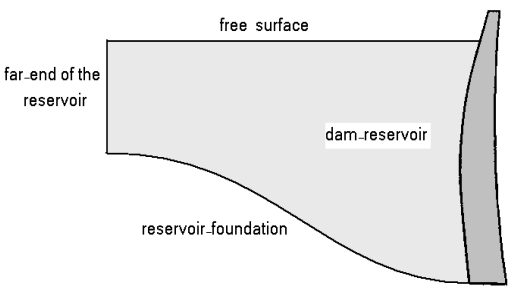

Figure 2: Boundary conditions for dam-reservoir-foundation.

$$\frac{\partial P(x,y,z,t)}{\partial n} = -\rho a^{s}{}_{n}(x,y,z,t) \tag{2}$$

in which a^{s}_{n} is normal acceleration of the dam body on the dam-reservoir interface and n is the normal vector on the face. The superscript s refers to structure.

3.2 Reservoir-foundation boundary condition

If there is no energy absorption on the reservoir bottom and sides, the same boundary condition represented in eqn (2) is used. The reservoir bottom absorption effect can be implemented with eqn (3).

$$\frac{\partial P(0,t)}{\partial n} = -\rho a_{n}(t) + q\frac{\partial P(0,t)}{\partial t} \tag{3}$$

where q is the admittance coefficient and the relation between q and the wave reflection coefficient, α, is expressed as:

$$\alpha = \frac{1-qc_{\bullet}}{1+qc_{\bullet}} \tag{4}$$

3.3 Free-surface boundary condition

In high reservoirs, surface waves are negligible and hydrodynamic pressure on the reservoir surface is taken as zero.

3.4 Reservoir-far-end boundary condition

For modeling far-end truncated boundary, viscous boundary called as Sommerfeld boundary condition is utilized given as eqn (5).

$$\frac{\partial P}{\partial n} = -\frac{1}{c_{\bullet}}\frac{\partial P}{\partial t} \tag{5}$$

4 Numerical simulation of the model

DEZ dam is a high double curvature arch dam with a peripheral joint separating the dam body from its concrete saddle structure (PULVINO foundation). Its total height (maximum height above the foundation) is 203m and the height of the main body is 186m. Thickness of the dam at crest is 4.5m and its maximum thickness at base is 21m.

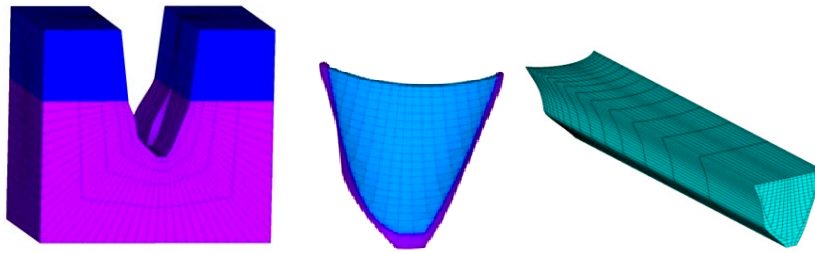

Figure 3: Finite element model of the dam, foundation and reservoir.

Finite element idealization prepared for dam, foundation rock and reservoir is presented in figure (3). Model consist 792 8-node solid elements for modeling concrete dam and saddle and 3770 elements for modeling foundation region. In addition, reservoir is modeled using 3660 Eulerian fluid elements.

Isotropic elasticity of mass concrete in static and dynamic conditions is 40GPa and 46GPa and Poisson's ratio are 0.2 and 0.14, respectively. Density of mass concrete is 2400 Kg/m^3. Uniaxial crushing and cracking strength for mass concrete under static loads are 35MPa and 3.4MPa and under seismic loads are raised to 36.5MPa and 5.1MPa respectively. Also, isotropic elasticity of foundation rock in saturated and unsaturated regions is reported as 13GPa and 15GPa. Furthermore, reservoir water density is assumed 1000kg/m^3, sound velocity is 1440m/s in water and wave reflection coefficient for reservoir around boundary is taken as 0.8.

5 Loading history

Applied loads are dam body self-weight, hydrostatic pressure in various water levels and earthquake load. It is worth noting that thermal loads is not considered in the current article because of the main object of the study which is considering fluctuation effects of the reservoir water level. The β-Newmark method is utilized to solve the coupled nonlinear problem of dam-reservoir-foundation model.

The system is excited at foundation boundaries using TABAS earthquake records. Total time duration of earthquake is 48.9s. For specifying significant duration of excitation, Arias intensity on Husid diagram was used and time interval between 10% and 80% of Arias intensity (totally 70%) was selected. With this method significant time duration is obtained to be 10s (as shown in figure 4). Moreover structural damping is taken to be 10% of critical damping.

6 Discussion of results

Considering great importance of natural vibration modes, 30 first periods of dam-reservoir-foundation system in four different water levels was extracted. As seen in figure 5, natural period grows associated with reservoir impounding

which is because of added mass to the system. Differences between modes are meaningful for ten first modes. Water levels in reservoir are considered as 56, 101, 155 and 188 m that stand to level I, level II, level III and level IV to investigate reservoir level fluctuation effects on dynamic responses of the selected arch dam.

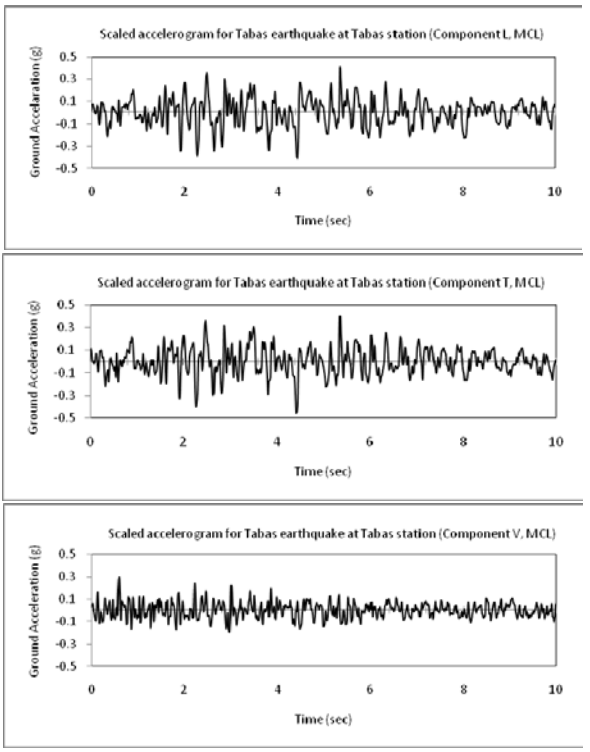

Figure 4: TABAS earthquake in TABAS station.

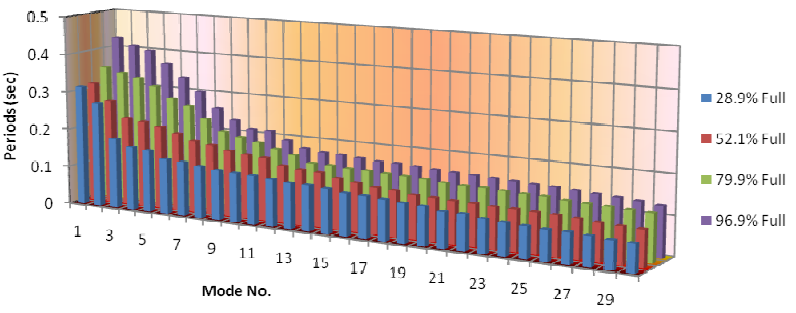

Figure 5: Comparison of dam periods at four different reservoir levels.

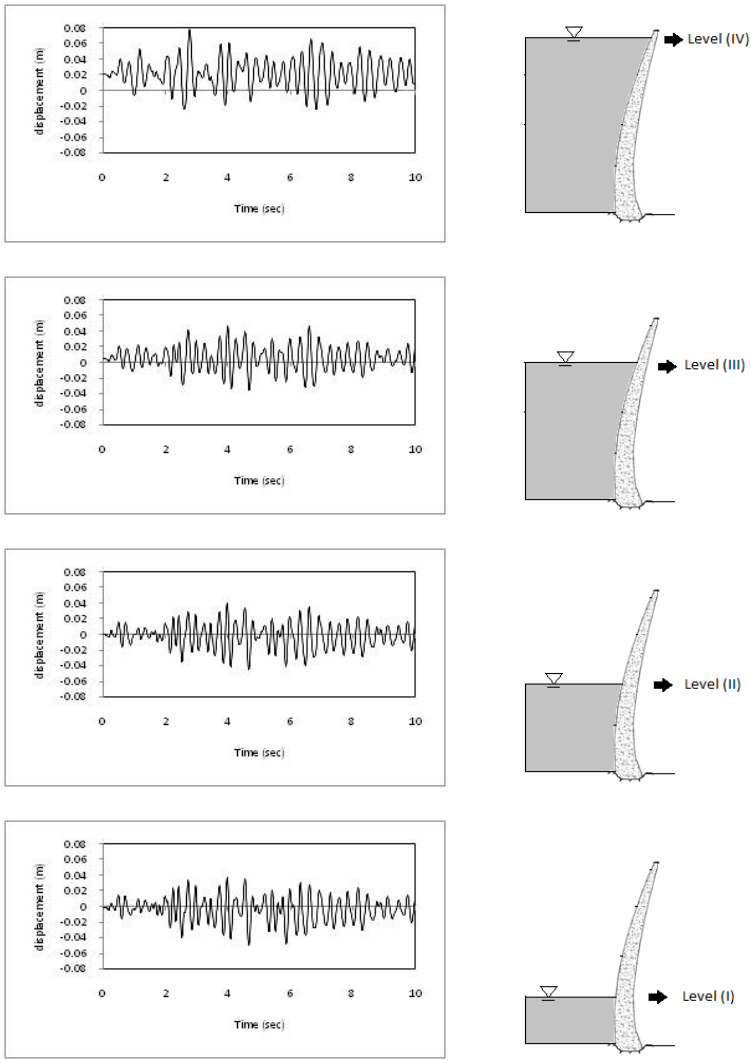

Figure 6: Time-history of US/DS displacement for the center of the crest.

6.1 Crest displacement

Time-history of crest displacement at central cantilever in four considered reservoir water levels is shown in figure 6. As can be seen, when the reservoir level is decreased, crest displacement shifts toward upstream direction. The crest experiences maximum displacement in downstream direction when the reservoir level is set to be at level IV.

Table 1: Absolute max velocity of crest points in the stream direction.

	Center point (m/s)	Left quarter point (m/s)	Right quarter point (m/s)
Level (IV)	1.093	0.779	0.766
Level (III)	1.064	0.697	0.700
Level (II)	1.087	1.133	0.832
Level (I)	1.157	1.142	0.850

Table 2: Absolute max acceleration of crest points in the stream direction.

	Center point (m/s^2)	Left quarter point (m/s^2)	Right quarter point (m/s^2)
Level (IV)	24.00	25.35	26.65
Level (III)	27.54	22.66	28.37
Level (II)	31.75	33.88	25.08
Level (I)	40.64	35.80	25.96

6.2 Crest velocity

Table 1 represents absolute max velocity of crest points in stream direction corresponding to various reservoir levels. As can be found, raising reservoir levels from I to III leads to decreasing in total velocities, but to sudden increasing from level III to IV. Maximum velocities can be seen at level I as well. The reason can be attributed to free movement of the upper parts of the dam body.

6.3 Crest acceleration

Table 2 represents absolute max acceleration of crest points in stream direction. As shown, in the central point the acceleration increases regularly by decreasing reservoir level and it is followed approximately in left quarter point but accelerations remain the same in the right quarter point for all levels except level III where the maximum acceleration has greater value than the rest.

6.4 Bottom pressure

Table 3 represents hydrostatic, absolute max of hydrodynamic and total pressures at bottom of the dam body for different reservoir levels. As shown,

Table 3: Hydrostatic, absolute max of hydrodynamic and total pressures at the base level.

	Hydrostatic pressure(MPa)	Hydrodynamic pressure(MPa)	Total pressure (MPa)
Level (IV)	1.647	0.357	2.005
Level (III)	1.324	0.300	1.624
Level (II)	0.794	0.326	1.120
Level (I)	0.353	0.253	0.606

absolute max of hydrodynamic pressure in level IV is more than the rest and in level I is less than the others. Between these levels hydrodynamic pressure varies between maximum and minimum amounts and generally, total pressure grows with increasing reservoir level.

6.5 Cracked areas

Cracked areas for upstream and downstream faces of the dam body for various water levels are shown in figure 7. In each level two various situations corresponding to static and seismic analyses are shown. As it is found, cracking status of the dam body becomes critical by reservoir dewatering. Generally it is the case for upper parts of upstream and downstream faces, in vicinity of pulvino and some areas around bottom of the dam body. In static condition, cracked areas for levels I, II and III are the same and limited only to a few elements, but in level IV the number of cracked elements show a little increasing. On the other hand, seismic analyses with various reservoir levels shows increase in number of cracked elements and also changes in pattern of cracked areas according to reservoir dewatering.

7 Conclusion

In the present paper, effect of reservoir level fluctuation on nonlinear seismic response of a high concrete arch dam is considered. Mass concrete is assumed to able cracking and crushing in tension and compression, respectively. Reservoir medium is assumed compressible and foundation rock is flexible. Four levels are chosen for studying and FE model of dam-reservoir-foundation is excited using an earthquake record scaled based on response spectrum of the dam site. It is found that dewatering the reservoir leads to increasing absolute maximum velocity and acceleration along the crest and moving the crest toward upstream direction.

In addition, when the reservoir is impounded, the number of cracked elements and the extension of cracked regions are less than the cases when the reservoir water level is low.

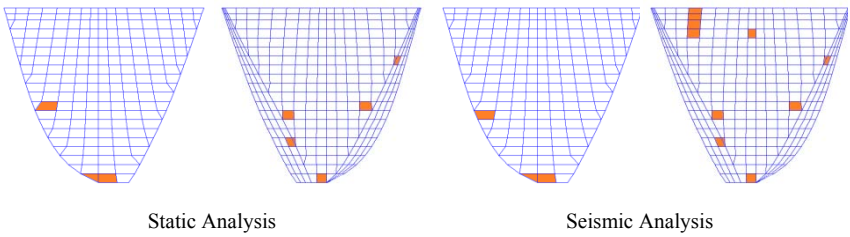

Static Analysis Seismic Analysis

Level IV

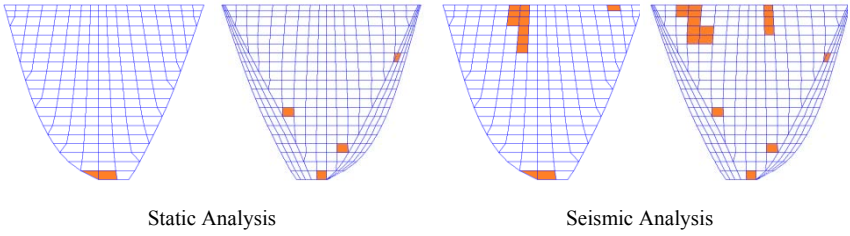

Static Analysis Seismic Analysis

Level III

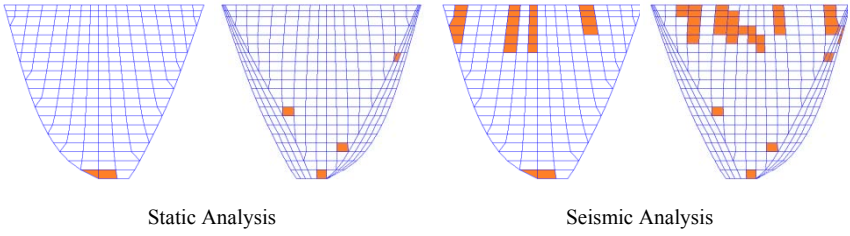

Static Analysis Seismic Analysis

Level II

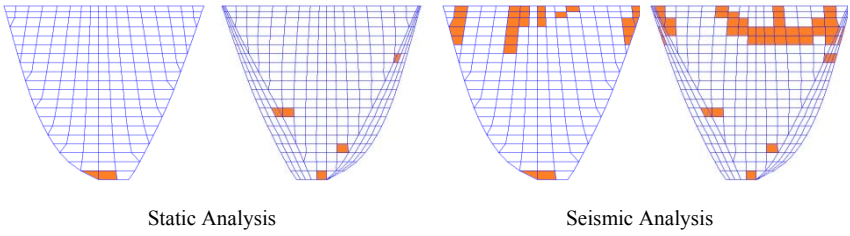

Static Analysis Seismic Analysis

Level I

Figure 7: Cracked areas in upstream and downstream faces of the dam body.

References

[1] Chopra, A.K., Hydrodynamic pressures on dams during earthquakes. ASCE: Journal of Engineering Mechanics, 93, 1967.
[2] Chwang, A.T., Hydrodynamic pressures on sloping dams during earthquakes, part 2: exact theory, Journal of Fluid Mechanics, 87(2), 1978.
[3] Fok, K.L. & Chopra, A.K., Hydrodynamic and foundation flexibility effects in earthquake response of arch dams. Journal of Structural Engineering, 112(8), pp. 1810–1828, 1986.
[4] Hung, T.K. & Chen, B.F. Non-linear hydrodynamic pressure on dams. ASCE: Journal of Engineering Mechanics. 106(6), pp. 1372-1391, 1990.
[5] Fahjan, Y.M., Borekci, O.S., & Erdik, M., Earthquake-induced hydrodynamic pressures on a 3D rigid dam-reservoir system using DRBEM and a radiation matrix, International Journal of Numerical Methods in Engineering, 56, pp. 1511-1532, 2003.
[6] Proulx, J., Paultre, P., Rheault, J., & Robert, Y., An experimental investigation of water level effects on the dynamic behavior of a large arch dam. Earthquake Engineering and Structural Dynamics, 30, pp.1147–1166, 2001.
[7] Akkose, M., Bayraktar, A., Dumanoglu, A.A., Reservoir water level effects on nonlinear dynamic response of arch dams. Journal of Fluids and Structures, 24, pp. 418–435,2008
[8] Kuo, JSH., On the nonlinear dynamic response of arch dams to earthquakes—I. Fluid–structure interaction: Added-mass computations for incompressible fluid. II. Joint opening nonlinear mechanism: Interface smeared crack model. PhD thesis, University of California, Berkeley, 1982.
[9] Hall J.F., Efficient non-linear seismic analysis of arch dams, Earthquake Engineering and Structural Dynamic, 27, pp.1425–1444, 1998.
[10] Espandar, R. & Lotfi V., Comparison of non-orthogonal smeared crack and plasticity models for dynamic analysis of concrete arch dams, Computers & Structures, pp. 1461-1474, 2002.
[11] Mirzabozorg, H., Ghaemian M. & Kianoush M.R., Damage mechanics approach in seismic analysis of concrete gravity dams including dam-reservoir interaction, European Earthquake Engineering, XVIII(3), pp.17-24, 2004.
[12] Mirzabozorg, H., & Ghaemian M., Nonlinear Behavior of Mass Concrete in Three-dimensional Problems Using Smeared Crack Approach, Earthquake Engineering & Structural Dynamics, 34, pp.247-269, 2005.

Fluid–structure simulation of a viscoelastic hydrofoil subjected to quasi-steady flow

R. L. Campbell, E. G. Paterson, M. C. Reese & S. A. Hambric
Penn State Applied Research Laboratory, USA

Abstract

Fluid–structure interaction simulations are performed for a flexible hydrofoil subjected to quasi-steady flow conditions. The hydrofoil is fabricated from a polymeric material that exhibits viscoelastic effects, causing the hydrofoil to change shape while subjected to the fluid loads. The time-dependent deformations and loads will be compared in the future to empirical results from upcoming water tunnel tests. The fluid–structure interaction simulations are performed using a tightly coupled partitioned approach, with OpenFOAM as the flow solver and a finite element solver for the structural response. The codes are coupled using a fixed-point iteration with relaxation. The flow is modeled as laminar and quasi-steady. Simulations indicate the hydrofoil angle of attack (AOA) changes from zero to a negative value as the material relaxes. The approach used here is being developed for application to a blood pump that has a performance closely tied to blade deformation through the impeller tip clearance.
Keywords: fluid–structure interaction, viscoelasticity, hydrofoil, OpenFOAM.

1 Introduction

The area of fluid–structure interaction (FSI) modeling has been very active in recent years, as evidenced by the numerous papers in the literature (see, for example, the review by Tezduyar and Sathe [1]). The dramatic advances in affordable computational resources coupled with improved modeling capability for both fluid and solid structures over the past two decades have made feasible coupled fluid/solid simulations for real-world engineering applications. While FSI simulations have been an area of research since the late 1970s (see Felippa et al. [2]), there still exist several challenges before these simulations will be


WIT Transactions on Engineering Sciences, Vol 69, © 2010 WIT Press
www.witpress.com, ISSN 1743-3533 (on-line)
doi:10.2495/AFM100381

routinely applied to real-world engineering applications (Tezduyar and Sathe [1] and Longatte et al. [3]).

The present application is related to a flexible blood pump impeller with a tip clearance (i.e., the clearance between the blade tips and the pump housing) that is very sensitive to blade deflections. The impeller is fabricated from a polymer that has a time-dependent response to applied loads (creep) and enforced displacements (stress relaxation), and therefore requires the use of a viscoelastic material model. The influence of blade deformation on pump performance is expected to be very strong because of the anticipated tip gap changes.

The approach to solving this problem involves several steps. The first step is to implement a FSI solver capable of modeling the nonlinear, time dependent polymeric material behaviour. Verification and validation of this solver is the second step and will be performed using a simple hydrofoil constructed of the same polymer as the blood pump impeller, and subjected to flow in a water tunnel for which net blade loads and blade deformation will be measured. The modeling approach will then be modified and updated as necessary and then applied to the actual rotating impeller of the blood pump. Time-dependent performance predictions of the pump will be compared to empirical results. The focus of the current paper is the fluid–structure simulations of the simple polymeric hydrofoil operating in the water tunnel test section.

2 Problem description

A single hydrofoil constructed of a polymeric material is affixed in a water tunnel test section with zero angle of attack (AOA). The hydrofoil is a modified NACA series 66 with $a = 0.8$ camber [4] and thus has nonzero lift at zero AOA. The upstream flow boundary is modeled as a uniform inflow with a velocity of 2 m/s and the downstream flow boundary is modeled with a zero pressure condition. The no-slip condition is applied at all other fluid boundaries. The foil is constrained at the root and is subjected to fluid pressures at the fluid/solid interface, $\Gamma_{F/S}$. A schematic of the setup is shown in figure 1. The test section has a length (L) of 0.762 m, width (W) of 0.508 m, and height (H) of 0.114 m. The distance from the inlet to the foil leading edge is 0.356 m. The foil has a chord length (c) of 0.050 m and a span (s) of 0.100 m.

The Reynolds number, based on hydrofoil chord, for this flow is approximately 100,000 and the critical Reynolds number for transition to turbulence is on the order of 200,000. Therefore, it is reasonable to employ a laminar flow model for the first attempt at modeling this problem.

3 Fluid–structure simulation approach

The governing equations for continuum mechanics (both fluids and solids), cast in an arbitrary Lagrangian Eulerian (ALE) form, are as follows. Mass conservation

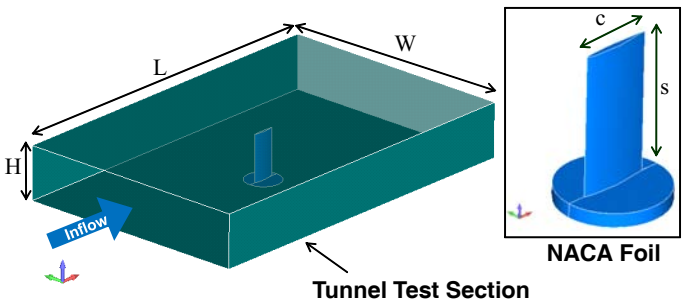

Figure 1: Flow over a cantilevered modified NACA 66 hydrofoil with uniform inflow conditions.

is governed by the continuity equation:

$$\frac{\partial \rho}{\partial t} + \nabla \cdot \left[\rho \left(\boldsymbol{v} - \boldsymbol{v}^{ale}\right)\right] = 0, \tag{1}$$

where ρ is mass density, $\boldsymbol{v}$ is the particle velocity, and $\boldsymbol{v}^{ale}$ is the grid point velocity. For a Lagrangian implementation, $\boldsymbol{v}^{ale} = \boldsymbol{v}$, and for an Eulerian implementation, $\boldsymbol{v}^{ale} = 0$. Performing a force balance and making use of the continuity equation leads to the following momentum equations:

$$\rho \frac{\partial \boldsymbol{v}}{\partial t} + \rho \left[\left(\boldsymbol{v} - \boldsymbol{v}^{ale}\right) \cdot \nabla\right] \boldsymbol{v} = \nabla \cdot \boldsymbol{\sigma} + \rho \boldsymbol{b}, \tag{2}$$

where $\boldsymbol{\sigma}$ is the stress tensor and $\boldsymbol{b}$ is the body force.

The current effort makes use of a segregated approach, wherein each domain is modeled separately and employs different solvers. The fluid domain solver for this problem employs a finite volume discretization while the solid domain solver uses a finite element discretization. The use of a segregated approach enables the governing equations to be cast in different primitive variables: velocity for the fluid solver and displacement for the structure, as is traditional for each of these domains.

Because the fluid and solid time scales are much shorter than the viscoelastic relaxation (discussed below in Section 3.2) timescale, a quasi-steady simulation is used in this work. It is therefore not necessary to include the temporal components in the continuum equations shown above, but they are included for the sake of completeness. Note, however, that the solution time does play a role in the viscoelastic material model response.

While the governing equations for each domain (eqns (1) and (2)) are identical, the constitutive relationships required for closure of the equations differ, as described below along with the coupling requirements at the fluid/solid interface.

3.1 Flow solver

OpenFOAM is the flow solver of choice for this effort because it facilitates custom integration with third-party solvers, has a pre-existing, robust mesh motion capability, and it is freely available through the GNU General Public License. The automatic mesh motion solver for the current problem makes use of a variable diffusion coefficient with quadratic dependence on the distance from the moving boundary (i.e., $\gamma = 1/l^2$), see Jasak and Tuković [5]. The flow for this problem is approximated as incompressible and laminar, and the stress-strain closure is modeled as Newtonian:

$$\boldsymbol{\sigma} = -p\boldsymbol{I} + 2\mu\boldsymbol{S}, \tag{3}$$

where p is the thermodynamic pressure, μ is the absolute viscosity, $\boldsymbol{I}$ is the second rank unity tensor, and $\boldsymbol{S}$ is the strain-rate tensor.

3.2 Structural solver and solid model

The structural solver employed for this work uses a Lagrangian finite element (FE) implementation, which means the mesh velocity is equivalent to the material velocity, $\boldsymbol{v}^{ale} = \boldsymbol{v}$. The momentum equation (eqn 2) becomes:

$$\rho\frac{\partial^2\boldsymbol{u}}{\partial t^2} = \nabla\cdot\boldsymbol{\sigma} + \rho\boldsymbol{b}, \tag{4}$$

where $\boldsymbol{u}$ are the material displacements.

One of the important aspects of the current problem is the time dependency of the polymeric material. The time dependency is a result of a viscous-like material behaviour. The material also exhibits elasticity in that it will not continue to flow unbounded with the application of a finite stress. The viscoelasticity model employed for this work follows an approach similar to that used by the commercial software Abaqus (see the Abaqus User's Manual [6]) and derived in a similar manner by Kaliske and Rothert [7]. This model is for linear viscoelastic materials (which does not mean the time response of the material is linear, but rather the stress is proportional to strain at any given time: $\varepsilon\left[c\sigma(t)\right] = c\varepsilon\left[\sigma(t)\right]$, where c is a constant) and uses the approximation that shear and volumetric behavior are independent. Experimental evaluation of the current material suggests that only the shear terms need to be modified by the viscoelastic model, which is consistent with most material behavior as reported by Kaliske and Rothert [7] and also in the Abaqus Manual [6].

The underlying material model is that of the Generalized Maxwell Element, which consists of Maxwell elements (i.e., a spring and dashpot in series) in parallel with a Hooke element (i.e., a spring) as shown in figure 2. The spring stiffness shown in this figure represents the material stiffness at infinite time (i.e., after all of the viscoelastic forces have diminished to zero). Each of the Maxwell elements are represented by a term in a Prony series (a series of the form $\sum_{i=1}^{N}\gamma_i e^{-t/\tau_i}$) representation of the material, which is further described below.

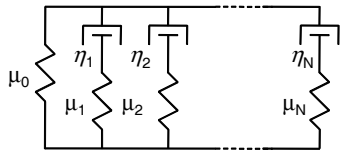

Figure 2: General Maxwell element with N components.

The stress is decomposed into hydrostatic and deviatoric components in order to isolate the viscoelastic effect from the volumetric terms:

$$\boldsymbol{\sigma}^{n+1} = \kappa \text{ tr } \boldsymbol{\varepsilon}^{n+1} \boldsymbol{I} + \text{dev } \boldsymbol{\sigma}^{n+1}, \tag{5}$$

where κ is the bulk modulus, tr $\boldsymbol{\varepsilon}^{n+1}$ is the trace of $\boldsymbol{\varepsilon}^{n+1}$, and dev $\boldsymbol{\sigma}^{n+1}$ is the deviatoric part of the material stress tensor for the current $(n+1)$ time step. The deviatoric part of the stress takes on the following form:

$$\text{dev } \boldsymbol{\sigma}^{n+1} = \text{dev } \boldsymbol{\sigma}_0^{n+1} + \sum_{i=1}^{N} \boldsymbol{h}_i^{n+1}, \tag{6}$$

where $\boldsymbol{\sigma}_0$ is the elastic stress tensor and $\boldsymbol{h}_i$ are the internal stress variables that come from the so called *heredity integral*:

$$\boldsymbol{h}_i(t) = \int_o^t \gamma_i e^{-\frac{t-s}{\tau_i}} \frac{\partial \boldsymbol{\sigma}_0(s)}{\partial s} \text{ds}. \tag{7}$$

Splitting this integral into parts that are known (i.e., time period $[0,\ t^n]$) and unknown (i.e., time period $[t^n,\ t^{n+1}]$), and using the approximation $\frac{\partial \boldsymbol{\sigma}_0(t)}{\partial t} \approx \frac{\boldsymbol{\sigma}_0^{n+1} - \boldsymbol{\sigma}_0^n}{\Delta t}$, the internal stress variables at the next time step are approximated as follows:

$$\boldsymbol{h}_i^{n+1} \approx e^{-\frac{\Delta t}{\tau_i}} \boldsymbol{h}_i^n + \gamma_i \frac{1 - e^{\frac{-\Delta t}{\tau_i}}}{\frac{\Delta t}{\tau_i}} \left[\text{dev } \boldsymbol{\sigma}_0^{n+1} - \text{dev } \boldsymbol{\sigma}_0^n\right], \tag{8}$$

where γ_i are the normalized relaxation constants, τ_i are the relaxation times, and $\Delta t = t^{n+1} - t^n$ is the time step. Both γ_i and τ_i represent terms of a Prony series and are determined from empirical data as described below.

Important for nonlinear finite element analyses using an implicit formulation with a Newton algorithm is the material stiffness tensor. The tensor is computed as follows for the viscoelastic material:

$$\boldsymbol{\mathcal{C}}^{n+1} = \kappa \boldsymbol{I}\boldsymbol{I} + 2\mu_0 \left[1 + \sum_{i=1}^{N} \gamma_i \frac{1 - e^{-\frac{\Delta t}{\tau_i}}}{\frac{\Delta t}{\tau_i}}\right] \left(\boldsymbol{\mathcal{I}} - \frac{1}{3}\boldsymbol{I}\boldsymbol{I}\right), \tag{9}$$

where $\boldsymbol{\mathcal{I}}$ is the fourth rank unity tensor.

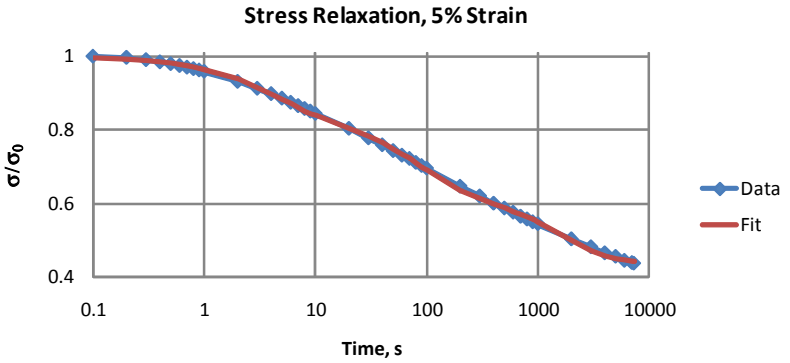

Figure 3: Stress relaxation data and the resulting Prony series curve fit.

Table 1: Prony series stress relaxation parameters.

Component, i	γ_i	τ_i
1	0.1484	4.130
2	0.2115	$8.195\text{x}10^{1}$
3	0.1993	$1.610\text{x}10^{3}$

Relaxation constants and times, γ_i and τ_i, are determined from empirical stress relaxation data of tensile test samples. The polymeric material used in this work has a 95 A Shore hardness and is from the Hapflex line of materials purchased from Hapco, Inc., Massachusetts USA. The constants are determined by a least-squares fit to uni-axial tensile stress relaxation data shown in figure 3 along with the resulting fit. The parameters used to create this fit are provided in table 1. The remaining parameters required for the structural model are the long term modulus, E_0, and Poisson's ratio, ν. The material is assumed to be nearly incompressible and thus $\nu = 0.49$ is used in the simulations. The long term modulus has been estimated from empirical data to be $E_0 = 30.4$ MPa.

The finite-element solver used for this effort has been been implemented by the authors in the form of a C/C++ program that can easily be combined and compiled with OpenFOAM. The use of a separate finite-element solver instead of the existing structural finite volume solver in OpenFOAM is a matter of preference.

3.3 Coupling approach

The algorithm defining the solution procedure is provided in figure 4. As indicated in this figure, a fixed-point iteration is performed with under-relaxation to ensure the fluid pressures and solid displacements are tightly converged before moving on to the next time step.

The under-relaxation approach employs the Aitken Δ^2 method [8] to define the dynamic relaxation coefficient. The coefficient is calculated as follows:

$$\omega_i = -\omega_{i-1} \frac{\boldsymbol{r}_i^T (\boldsymbol{r}_{i+1} - \boldsymbol{r}_i)}{|\boldsymbol{r}_{i+1} - \boldsymbol{r}_i|^2}, \tag{10}$$

where $\boldsymbol{r}_i = \hat{\boldsymbol{u}}_{\Gamma_{F/S},i} - \boldsymbol{u}_{\Gamma_{F/S},i-1}$ and $\hat{\boldsymbol{u}}_{\Gamma_{F/S},i}$ are the computed fluid/structure interface displacements for iteration i. The prediction of the displacements for the current iteration is then $u_{\Gamma_{F/S},i} = u_{\Gamma_{F/S},i-1} + \omega_i \left(\hat{u}_{\Gamma_{F/S},i} - u_{\Gamma_{F/S},i-1}\right)$, as indicated in the coupling algorithm of figure 4. The iteration stops when $|\boldsymbol{r}_i|/\sqrt{n} < \epsilon$, where n is the length of $\boldsymbol{r}_i$ and ϵ is the error tolerance.

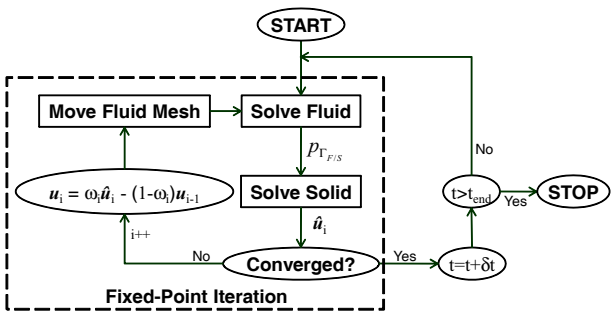

Figure 4: Implicit coupling scheme with under-relaxation.

4 Simulation results

The important variables to monitor for the current simulation are blade deflection and net blade load because these will be measured during the upcoming water tunnel tests. Sample results for the blade deflection, shown by blade tip sections, are provided in figure 5. The net blade forces, from integrating the fluid pressures over $\Gamma_{F/S}$ are shown in figure 6. This figure shows results for a baseline model and the viscoelastic model. The baseline model uses a constant constitutive relationship wherein the modulus represents the material response to an instantaneously applied load.

The blade AOA at the tip section changes from zero at the start of the simulation to increasingly negative values, reaching -8.1° at $t = 360\,s$. The blade lift (lift = $-F_y$) decreases to zero after about $50\,s$ of operation, and then continues to decrease with time as indicated in figure 6. This figure also shows the large difference in force magnitude between the baseline and viscoelastic models and the strong temporal dependence of the viscoelastic model. Note that the the first $360\,s$ of operation are shown in this figure. Results have been computed for longer times and indicate the system is nearly at a steady state condition after approximately one hour of operation.

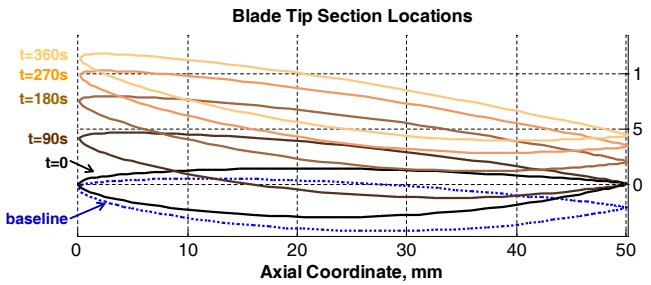

Figure 5: Blade tip section deflections; curves show results from different simulation times; baseline model response shown by dotted curve.

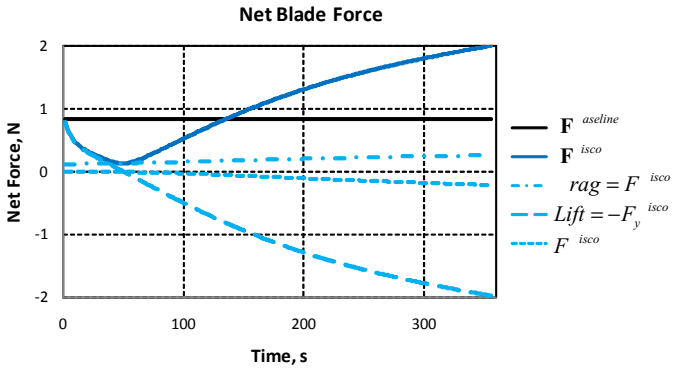

Figure 6: Net blade forces for baseline (using the instantaneous modulus) and viscoelastic models.

5 Summary and conclusions

Tightly coupled FSI simulations have been used for a single hydrofoil subjected to quasi-steady flow to model the effects of a viscoelastic hydrofoil operating in a water tunnel test section. The fluid domain is discretized using the finite volume approach, and solved using OpenFOAM. The flow is modeled as incompressible, laminar, and steady. The moving mesh in the fluid domain is accomplished through the tetrahedral decomposition approach with Laplace smoothing, as implemented in OpenFOAM. The solid domain is discretized with finite elements and solved using an author-written solver that is compiled with the OpenFOAM solver to facilitate data transfer necessary for the domain coupling. Simulation results for blade deformations and loads with respect to time show the dramatic effect of employing the viscoelastic constitutive relationship instead of an equivalent material modulus. The AOA

of the blade monotonically decreases from zero to increasingly negative values (reaching -8.1° at $t = 360\,s$), with concomitant decreases in blade lift. It can be concluded that the inlet flow velocity of $2\,m/s$ should be satisfactory for use in the water tunnel test to provide blade deformations and forces large enough to be easily measured.

References

[1] Tezduyar, T.E. & Sathe, S., Modelling of fluid-structure interactions with the space-time finite elements: solution techniques. *International Journal for Numerical Methods in Fluids*, **54(6-8)**, pp. 855–900, 2007.

[2] Felippa, C., Park, K. & Farhat, C., Partitioned analysis of coupled mechanical systems. *Computer Methods in Applied Mechanics and Engineering*, **190(24-25)**, pp. 3247–3270, 2001.

[3] Longatte, E., Verreman, V. & Souli, M., Time marching for simulation of fluid–structure interaction problems. *Journal of Fluids and Structures*, 2008.

[4] Brockett, T., Minimum pressure envelopes for modified NACA-66 sections with NACA a= 0.8 camber and Buships type I and type II sections. Technical Report 1780, David Taylor Model Basin, U.S. Navy, 1966.

[5] Jasak, H. & Tuković, Z., Automatic mesh motion for the unstructured finite volume methodupt. *Transactions of FAMENA*, **30(2)**, pp. 1–20, 2006.

[6] Hibbitt, K., Sorenson. ABAQUS user's manual, version 6.6, 2006.

[7] Kaliske, M. & Rothert, H., Formulation and implementation of three-dimensional viscoelasticity at small and finite strains. *Computational Mechanics*, **19(3)**, pp. 228–239, 1997.

[8] Küttler, U. & Wall, W., Fixed-point fluid–structure interaction solvers with dynamic relaxation. *Computational Mechanics*, **43(1)**, pp. 61–72, 2008.

This page intentionally left blank

Section 5
Multiphase flow

This page intentionally left blank

Visualization of ultrasonic cavitation in visible and IR spectra

A. Osterman[1], O. Coutier-Delgosha[2], M. Hocevar[1] & B. Sirok[1]
[1]*Faculty of Mechanical Engineering, University of Ljubljana, Slovenia*
[2]*Arts et métiers ParisTech, Centre de Lille, France*

Abstract

Ultrasonic cavitation was generated with ultrasound of 33 kHz in a small closed water tank, containing about one liter of water. Cavitation was experimentally observed simultaneously with high-speed cameras in IR and visible spectra. Cameras were capturing images of the same observation area. From the images obtained time-dependent velocity fields were calculated for both cameras. Velocity calculation was based on pattern and similitude recognition between pairs of consecutive images. Images from the visible spectrum were also processed in order to detect the individual graphical objects presumably linked with cavitation collapses. As a result, correlations between velocity fields from each camera and correlations between velocity fields and cavitation collapses were determined. Strong correlations were found in all cases. Additionally, a delay was found for the velocities from the camera in the visible spectrum when compared to the thermographic results. Also the behavior of the correlation between cavitation collapses and velocities was in some cases found to be dependent on whether the velocities were from the images taken in the visible or the IR spectrum.
Keywords: cavitation, ultrasound, IR thermography, velocity fields, correlation, bubble collapse, visualization.

1 Introduction

Ultrasonic cavitation has many applications (Mason and Lorimer [1], Brennen [2]) and an obvious question that arises when one is dealing with it, is what is happening inside. In search for a non-trivial answer, an experimental approach to measure basic flow quantities seems appropriate, since currently available

WIT Transactions on Engineering Sciences, Vol 69, © 2010 WIT Press
www.witpress.com, ISSN 1743-3533 (on-line)
doi:10.2495/AFM100391

numerical methods cannot sufficiently handle a phenomenon of such complexity as found in practical use in industrial processes, medicine etc. [3–6], although the experimental approach has also some limitations. As cavitation actually consists of bubble collapses, often very fast sensors are needed. Additionally, it is desirable to use non-intrusive methods to preserve a true cavitating fluid flow (Franc and Michel [7]), such as visualization [8–14].

This paper presents several new approaches to cavitation. First, it describes thermovision method applied to measure cavitation thermal effects. On a scale of a single bubble very high temperatures can occur during the compression stage of cavitation collapse (Rae *et al.* [15], Kim *et al*. [16]) and temperature delay is a known phenomenon during cavitation growth (Brennen [2], Franc and Michel [7]). Also in case of cryogenic liquids local temperature drops are reported (Ishii and Murakami [17]). However, proper experimental measurements of temperatures are very scarce (Dular *et al*. [18]) and few experimental data of that kind are available (Fruman *et al*. [19]).

Secondly, algorithm for determination of velocity fields based on experimental visualization results is presented, so that velocities near solid boundaries in cavitating water are obtained. The algorithm works similarly to PIV (Stanislas *et al*. [20]) but no seeding particles are needed. Thirdly, detection of collapses of cavitating bubbles is presented, which are then identified as a driving factor for measured velocity fields.

Cavitation was generated in an ultrasonic cleaning device, filled with water. For visualization, high-speed cameras that work in IR and visible spectra were used. They were synchronized and were taking images of the same observation area. Detection of collapses of bubbles was based on images from a high-speed camera operating in the visible spectrum. Presented results show that there is good agreement between velocity fields from both cameras and that velocity magnitude is in proportion with the number of cavitation collapses.

2 Experimental set-up

Experimental set-up is presented in figure 1. Cavitation was generated in a closed container of an ultrasonic cleaning device, partially filled with water. It was generated with a piezoelectric transducer oscillating at 33 kHz. A vessel containing approx. 1 liter of untreated tap water was just partially filled, then air-tightly closed with a lid, having an acrylic-glass tube (opened just at the bottom end) attached to it. When the tube was inserted in the water so that its open end was below the initial water level, it was possible to raise the water level above the edge of the vessel by evacuating the air through a valve at the top of the tube. On the upper end of the tube an observation window was mounted. Such set-up was necessary to obtain free space for laser sheet illumination needed for visualization in the visible spectrum. Through the observation window two synchronized cameras running at 66 Hz were taking images of the same observation area in sequences of approx. 20 s. A sapphire glass window was chosen because it is transparent in both IR and visible spectra (Edmund Optics [21]), which were the operating ranges for our cameras.

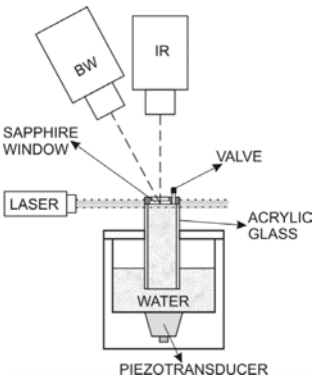

Figure 1: Experimental set-up.

A thermographic camera CMT384SM Thermosensorik, operating in the IR spectrum ranging from 1.5 to 5 μm was used. Resolution was set to 384x288 pixels and exposition time was 1 ms. Temperature fields were taken at the water–sapphire window interface because in the measured spectrum water is not transparent to IR (Hale and Querry [22]). It was checked that 20 μm thick water film was completely opaque for the measured part of the IR radiation. The uncertainty of the mean water operating temperature was ±0.15 K. More important in our case is that the uncertainty of temperature changes in a single point, relative to the operating temperature, was only ±0.03 K.

The camera for visualization in the visible spectrum was Basler Scout scA640-70gm (resolution 640x480 pixels, exposition time 1 ms). Illumination for the camera was provided by a collimated laser Quantum Ventus 520 (527 nm, 700 mW), generating approx. 1 mm thin laser light sheet. It was positioned in parallel with the observation window, with its front and back edges still illuminated.

3 Image processing

With both cameras being synchronized, series of images were taken. Thermocamera images (TC) were representing temperature fields, while the camera in visible spectrum took black-and-white images (BW) of particles in the illuminated layer of water. Example of TC and BW images is shown in figure 2.

To obtain further information about the observed cavitation, images were processed in several ways. First, brightness and contrast values of the raw images were modified so that useful information covered the larger part of the 8-bit span of grayscale images. Secondly, velocity fields were calculated. An example of an obtained velocity field is shown in figure 3. Additionally, large objects were detected on BW images. Time series of velocities and frequency of large objects were then filtered. The same filter was used in all instances. On these series correlation was applied to quantify their relationships and interdependence.

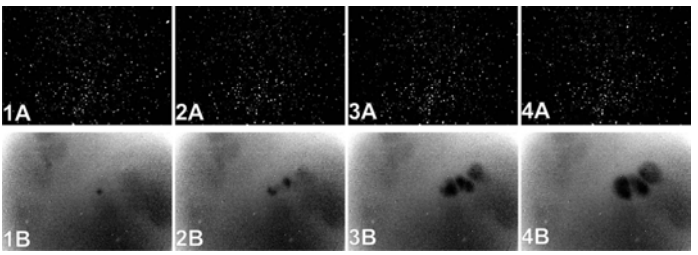

Figure 2: Example of series of BW (A) and TC (B) images (time between frames is 15 ms, frame size is 13x19 mm).

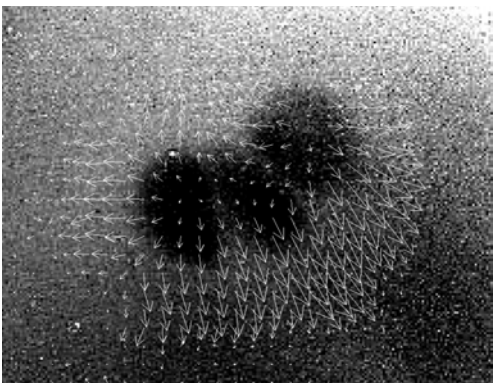

Figure 3: Example of instantaneous velocity field superposed on TC image.

3.1 Velocity field calculation

An algorithm for the estimation of displacement and, consequently, velocity was developed. To estimate displacement and velocity from two consecutive images, 2D image cross correlation was applied. All procedures in a selected region of interest were applied in two consecutive images (one pair) in the image sequence. Velocity was calculated from displacement according to camera frame rate and image pixel size.

Measurement uncertainty of PIV measurements is in the range of 1% (Stanislas *et al*. [20]). We estimate that using our algorithm for the velocity measurements the same level of uncertainty is achieved.

3.1.1 Selection of interrogation windows

Velocity estimation was performed in a selected matrix of 34x22 locations in the first image of the chosen pair. A set of interrogation windows of different sizes was extracted from the first image for every selected location.

The best results were obtained for the starting size of interrogation window of 45x45 pixels, reducing to the final size of 35x35 pixels with a step size of 2 pixels. Interrogation window was moved across the second (consecutive) image in both horizontal and vertical direction. A rate of successful searches and

accurate space localization were considered. By defining smaller interrogation windows, not enough details from images were included, producing scattered results. By using larger windows, velocity field was averaged too much and the details of local velocities were lost.

3.1.2 Selection of best finds

For each interrogation window size up to 5 locations were found in the second image, ordered by the similarity of the pattern in relation to the pattern of the template of the first image. The similarity was quantified with 2D cross-correlation. The one that was selected had the highest correlation coefficient where the distance from the template was smaller than a selected value of 15 pixels. Additionally, locations were also rejected on the basis of the lowest allowed normalized correlation limit, set to 0.5. A value of 1 corresponded to exactly the same patterns in both templates. These limitations served to prevent that the determination of displacements and velocity vectors would be very different from those of their neighbors.

3.2 Large object detection

From observation of BW images the existence of two types of objects was apparent: a vast majority of small moving objects and very few large objects that appeared on only one image and disappeared on another. It was assumed that the first ones show laser light dissipation on microbubbles of undissolved gas and solid impurities while the second ones actually show cavitation bubble collapses. In figure 4 three examples are provided, taking three consecutive images (A, B, C), showing for each example the same observation area through time.

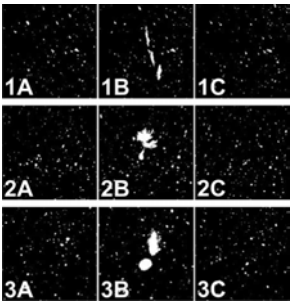

Figure 4: Examples of sequences of consecutive images (A–C) containing collapse structures (B).

It is clearly visible that in B-images some objects are significantly bigger than the others and that they are not present in either A or C images. The actual shapes of these collapse-related objects probably show some parts of bubble splashing against a solid wall (Tong *et al*. [23]) which was in our case the sapphire observation window. Shapes may be more or less deformed circles due to the existing velocity field, pressure gradients, interaction with other bubbles

etc., causing that the microjet is not perpendicular to the window. In some cases several large objects together in the same image may also indicate secondary collapse(s) (Bai *et al*. [24]).

The relationship between the number of detected objects and their area is shown in figure 5. Distributions for a random single image (gray circles) and for the average of the whole sequence (little black squares) are presented, where the number of objects in one image is counted. Note the logarithmic scales that were used because the number of objects so drastically reduces with their increased area. The number of objects that is smaller than unity represents that they are not present on every image. To determine if an object is large several thresholds for object area were used, set from 10 to 50 pixels with a step of 5 pixels. Within this range, the frequency of large objects reduces for approximately a thousand times.

Using the obtained classification of detected objects, the appearance of collapse-related objects in time in a certain region in each BW image was analyzed. This is presented in figure 6. The left image (A) shows the original BW image. From all objects detected in it, only the ones with their area greater than a given threshold were preserved, and are shown in the image (B). The concentric circles around a chosen point define search areas. Radii were increased from 20 to 120 pixels with 20-pixel steps. For each area, the number of included (fully or partially) objects (e.g. objects 1-3) was calculated.

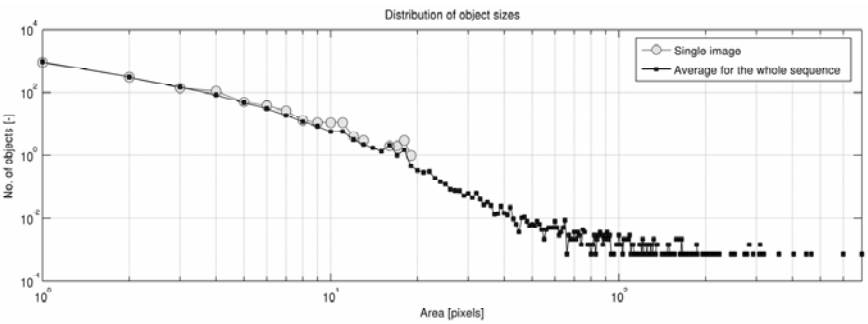

Figure 5: Distribution of frequency of objects with regard to their size.

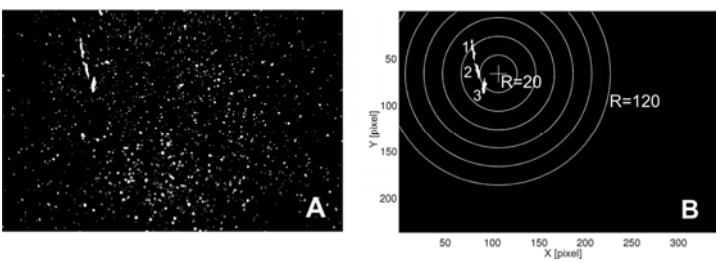

Figure 6: Determination of collapse-related objects (1-3) from original images (A) and their counting inside circular searched areas (B).

In order to continue, time series of these quantities were obtained by computing velocity fields and presence of large objects for each image.

3.3 Filtering

Spatial representation of computed velocity magnitudes in one moment in time are presented in figure 7. The left image stands for the velocities from the BW image, whereas the right image is for the velocities from corresponding TC image.

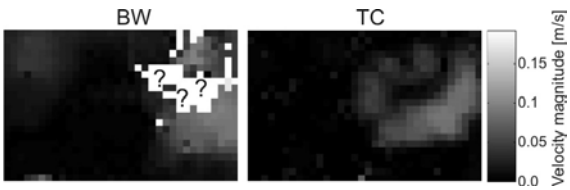

Figure 7: Spatial representation of velocity magnitudes in one moment for both cameras.

When there is insufficient correlation, no velocity in a point is obtained. Generally, in BW series more velocities were missed than in TC series. This is represented in figure 7 where in some areas there are question marks. For computational purposes the velocities in these points were fixed to zero, although they often appeared near the areas with the highest velocities. To compensate this, a low-pass filter (in temporal sense) was applied. A 1st order Butterworth filter was chosen as such filters are monotonic and have maximally flat magnitude response in the passband (Bianchi and Sorrentino [25]). Cutoff

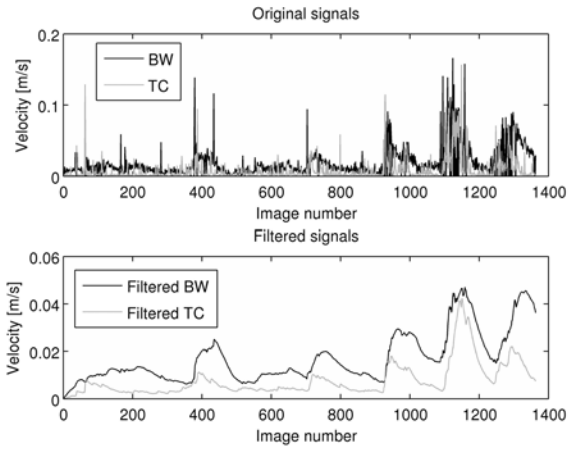

Figure 8: Comparison between original and filtered time series of velocities in a single point.

frequency, for which the magnitude response of the filter was $\sqrt{1/2}$, was set to 0.33 Hz. Original and filtered signals of temporal velocity magnitudes in one point are presented in figure 8.

The same filter was applied to the data concerning the counting of large object appearance. First, the same phase shift was produced, and secondly, the original data were ill-conditioned for comparison with velocity time series because they consisted of sporadic integers. This was greatly improved after the filter was applied.

4 Results

Some comparisons between BW and TC velocities were already presented in figure 7 (spatial distribution) and figure 8 (time series). In figure 7, velocities are higher on the right side of each image and have similar magnitudes (where defined), as can be seen from gray levels. In figure 8, velocities in one point are displayed as time series, where time advancement is indicated by image number. General course is the same for both BW and TC, although TC values are smaller. Measured velocities are mostly in order of a few cm/s. The comparison of temporal signals also shows that TC signal slightly precedes BW signal (note the positions of peaks). This is presented in more detail in figure 9, where computed correlations between BW and TC signals are shown.

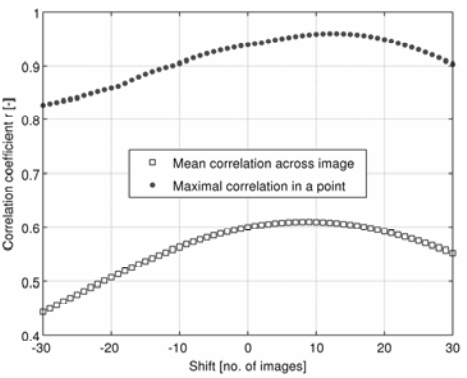

Figure 9: Correlation of velocity signals, shifted in time.

Correlation r was calculated as

$$r = \frac{N\sum XY - \left(\sum X\right)\left(\sum Y\right)}{\sqrt{\left[N\sum X^2 - \left(\sum X\right)^2\right]\left[N\sum Y^2 - \left(\sum Y\right)^2\right]}}, \quad (1)$$

where N is the number of images in a series which is in further analysis the same as the number of data in X or Y, which are vectors of compared quantities (e.g. velocities, number of objects, average brightness etc.) at a chosen position in an image.

While the maximum of the best correlation obtained across the image for a single point is reached when signals are shifted for 13 images (TC delayed for 0.2 s), the maximum for mean correlation (mean from all correlations, not from mean velocity) was for 9-images shifted signals (TC delayed for 0.14 s).

In the next step, velocities were compared to collapses (as related by large objects). In figure 10 normalized velocity courses in a single point together with the normalized number of large objects found around that point are shown. Velocities are chosen for the same point as presented in figure 8. A location of the point is shown with a cross in figure 6 (B). In figure 10 results for the search area of radius 40 pixels are presented, while the minimal object size was set to 20 pixels.

Good general agreement can be observed, especially between TC signal and the number of objects, considering that such different quantities are compared.

The effects of the search area radius and the minimal object size on the correlation between the velocities and the number of objects were investigated and the results are shown in figure 11. Correlation for frequency of large objects compared to BW velocities is shown on the left side and for TC velocities on the right side. While increasing the minimum object area causes the correlation to

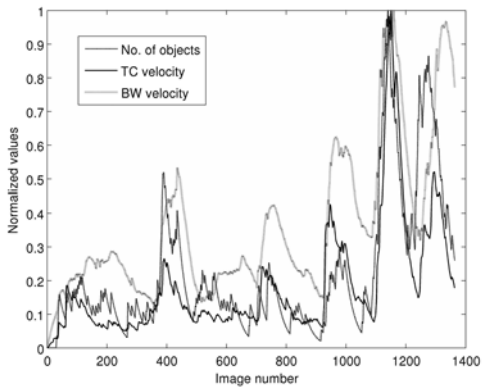

Figure 10: Comparison between velocities and number of objects for time signal in a single point.

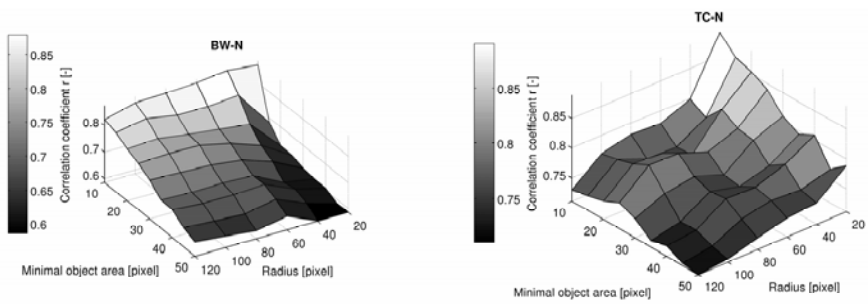

Figure 11: Correlation between velocities and number of objects.

diminish in both cases, the effect of the search area radius is not the same. On the left (BW), the correlation generally grows with increased radius and decreases slowly just for small object areas, while on the right (TC), the correlation decreases with increasing radius of the search area almost over the whole range of values. However, for both cases the best correlation is obtained for the smallest search radius and the smallest minimal object area.

5 Discussion

By using a relatively new experimental approach to cavitation (Dular *et al*. [18]), cavitation thermal effects were successfully measured. Temperature drops were in range of a few tenths of kelvin, lasting for a few tenths of a second. Spatial scales were in range of millimeters. Due to physical properties of water which is not transparent in the measured part of IR spectrum, temperatures at the water-observation glass interface were measured.

By taking into account the finite thickness of the observing layer of water illuminated with laser light sheet (BW case) which was thicker than the observed interface between water and sapphire window (TC case), it can be also explained why measured TC velocities were smaller than BW velocities, because further away from the observation window the effect of solid wall due to viscosity gets smaller and velocities are higher.

A short note about the cameras: frames were taken at 66 Hz with 1 ms exposure time. It was estimated that the frame rate of both cameras is sufficiently high. The increased frame rate would not significantly contribute to better results, especially not in TC case, whereas in BW case it is expected that in the critical moments around collapses, velocities could be found more often. The real advantage of higher frame rate is in better detection and observation of collapses themselves (BW images), where additional information on collapse shape may be useful for prediction of velocity field orientation or direction of thermal effect spreading etc.

As untreated tap water was used, many of very small objects were related to light reflections on undissolved gas bubbles and on other particles, not connected with cavitation. It is believed that by using filtered and degassed water many of these small objects would disappear. While this provides better initial images for large object detection and quantification, it would be a great drawback for velocity field calculation because the searching algorithm would lack handles for detecting similar patterns.

6 Conclusions

Experimental investigation of cavitation, generated in an ultrasonic cleaning device at 33 kHz was done based on visualization with two synchronized high-speed cameras, operating in visible and IR spectra, and was further supported with image processing tools. An algorithm was developed to determine temporal velocity fields from visualization images on the basis of similarity searching. Another tool was used to determine individual objects in the images from camera

recordings in visible spectrum. Detected objects were depending on their sizes, connected with cavitation collapses, and several comparisons between velocity fields from both cameras and frequency of collapses were done, quantified by correlation.

The main findings are listed below:

1) Measured velocities resulting from ultrasonic cavitation were in a range of a few cm/s. Similar values were obtained from the analysis of visible and IR images, but velocities were generally higher in the first case.
2) Good agreement between spatial and temporal distributions of velocities was obtained from the analysis of visible and IR images, where for the time series from visible images, velocity information was delayed for about 0.14 s.
3) Cavitation thermal effects were successfully measured, although usually neglected, and were proved useful for cavitation analysis. They were measured in the form of time dependent temperature fields, displaying temperature drops in range of a few tenths of kelvin, lasting for a few tenths of a second and with characteristic lengths in range of millimeters.
4) From the images in visible spectrum individual objects were identified and connection between large objects and cavitation collapses was made. From distribution of object sizes it was determined that large objects occur very seldom, e.g. the smallest appear approx. million times more frequently than the greatest, while the ratio of their sizes is in a range of one to hundred.
5) Good agreement between presence of large objects and velocity magnitude was found, from which a conclusion was drawn that cavitation collapses are driving measured stirring of water. The obtained correlation was higher when frequency of large objects was compared with velocities from IR images.

References

[1] Mason, T. J. & Lorimer, J. P., *Applied Sonochemistry*: Wiley-VCH, 2002.
[2] Brennen, C. E., *Cavitation and Bubble Dynamics*: Oxford University Press, 1995.
[3] Bretz, N. *et al*, Numerical simulation of ultrasonic waves in cavitating fluids with special consideration of ultrasonic cleaning. *Proc. of IEEE Ultrason. Symp.,* pp. 703–706, 2005.
[4] Servant, G. *et al*, Numerical simulation of cavitation bubble dynamics induced by ultrasound waves in a high frequency reactor. *Ultrason. Sonochem.,* **7**, pp. 217–227, 2000.
[5] Yasui, K. *et al*, FEM calculation of an acoustic field in a sonochemical reactor. *Ultrason. Sonochem.,* **14 (5)**, pp. 605–614, 2007.
[6] Osterman, A., Dular, M. & Širok, B., Numerical Simulation of a near-wall bubble collapse in an ultrasonic field. *J. of Fluid Science and Technology,* **4 (1)**, pp. 210–221, 2009.

[7] Franc, J.-P. & Michel, J.-M., *Fundamentals of cavitation*: Kluwer Academic Publishers, Netherlands, 2004.
[8] Dähnke, S., Swamy, K.M. & Keil, F.J., A comparative study on the modeling of sound pressure field distributions in a sonoreactor with experimental investigation. *Ultrason. Sonochem.,* **6**, pp. 221–226, 1999.
[9] Price, G.J., Harris, N.K. & Stewart, A.J., Direct observation of cavitation fields at 23 and 515 kHz. *Ultrason. Sonochem.,* **17 (1)**, pp. 30–33, 2010.
[10] Leighton, T.G., Bubble population phenomena in acoustic cavitation. *Ultrason. Sonochem.,* **2 (2)**, pp. 123–136, 1995.
[11] Moussatov, A., Granger, C. & Dubus, B., Cone-like bubble formation in ultrasonic cavitation field. *Ultrason. Sonochem.,* **10**, pp. 191–195, 2003.
[12] Birkin, P.R., Delaplace, C.L. & Bowen, C.R., Electrochemical and photographic detection of cavitation phenomena within a variable frequency acoustic field. *J. Phys. Chem. B,* **102**, pp. 10885–10893, 1998.
[13] Chen, H. *et al*, High-speed observation of cavitation bubble cloud structures in the focal region of a 1.2 MHz high-intensity focused ultrasound transducer. *Ultrason. Sonochem.,* **14**, pp. 291–297, 2007.
[14] Chen, H., Li, X. & Wan, M., The inception of cavitation bubble clouds induced by high-intensity focused ultrasound. *Ultrasonics,* **44**, pp. e427–e429, 2006.
[15] Rae, J. *et al*, Estimation of ultrasound induced cavitation bubble temperatures in aqueous solutions. *Ultrason. Sonochem.,* **12**, pp. 325–329, 2005.
[16] Kim, K.Y., Byun, K.-T. & Kwak, H.-Y., Temperature and pressure fields due to collapsing bubble under ultrasound. *Chem. Eng. J.,* **132**, pp. 125–135, 2007.
[17] Ishii, T. & Murakami, M., Comparison of cavitating flows in He I and He II. *Cryogenics,* **43**, pp. 507–514, 2003.
[18] Dular, M. *et al*, Local thermal effects of ultrasound induced cavitation. *Proc. of 6th Int. Symp. on Cavitation CAV2006,* 2006.
[19] Fruman, D.H., Reboud, J.L. & Stutz, B., Estimation of thermal effects in cavitation of thermosensible liquids. *Int. J. of Heat Mass Transf.,* **42**, pp. 3195-3204, 1999.
[20] Stanislas, M. *et al*, Main results of the second international PIV challenge. *Exp. Fluids,* **39**, pp. 170–191, 2005.
[21] Edmund Optics, Sapphire windows technical images, http://www.edmundoptics.com
[22] Hale, G. M. & Querry, M. R., Optical constants of water in the 200 nm to 200 μm wavelength region". *Appl. Opt.,* **12**, pp. 555–563, 1973.
[23] Tong, R.P. *et al*, The role of 'splashing' in the collapse of a laser-generated cavity near a rigid boundary. *J. Fluid Mech.,* **380**, pp. 339–361, (1999).
[24] Bai, L. *et al*, A high-speed photographic study of ultrasonic cavitation near rigid boundary. *J. of Hydrodynamics,* **20 (5)**, pp. 637–644, 2008.
[25] Bianchi, G. & Sorrentino, R., *Electronic filter simulation and design*: McGraw-Hill, 2007.

Question for Euler–Lagrange type simulator from a view point of macroscopic properties of gas-liquid multiphase flow

K. Ueyama
Department of Environmental and Energy Chemistry,
Faculty of Engineering, Kogakuin University, Tokyo, Japan

Abstract

Corrections to the conventional two-fluid model equations are briefly illustrated, showing the general expression of the two-fluid model equation without any restriction on averaging, the general expression of the interaction term with 'inside-out' property, and the corrected two-fluid model equation with a new and novel term reflecting the 'inside-out' property of the interaction term.

On the basis of the corrected two-fluid model equation, several questions are stated and discussed for Euler–Lagrange type simulator with respect to the moving velocity of individual drop and fluctuating motion of drops, and new concepts for Euler–Lagrange and Euler–Euler type of simulators are proposed focusing on the fluctuating motion of drops, which is one of the representative phenomena in the dispersed multiphase flow.

Keywords: fluctuating motion of drops, dispersion of drops, Euler–Lagrange type simulator, Euler–Euler type simulator.

1 Introduction

Recently, a flaw in the basis of the conventional two-fluid model equation based on volume-averaging was revealed [8]. It was shown that the restriction, that the control volume must be between the drop size and the scale of macroscopic variations, was unrealistic for treating multiphase flow with spatial variation of macroscopic properties, and the two-fluid equation has been derived without any restriction on averaging, by combining volume-averaging and time-averaging. The most important founding in the work is that the interaction term has "inside-

WIT Transactions on Engineering Sciences, Vol 69, © 2010 WIT Press
www.witpress.com, ISSN 1743-3533 (on-line)
doi:10.2495/AFM100401

out" property, which has been over looked for more than 40 years since the appearance of the two-fluid model equations based on volume-averaging [1,9]. The "inside-out" property causes significant corrections to the conventional two-fluid model equations.

This work comprises three sections. In the first section, the derivation of the corrected two-fluid model equation is briefly illustrated. In the second section, questions for the previous Euler–Lagrange type simulators are stated and discussed with respect to the moving velocity of each drop obtained in the simulator, and the contribution of fluctuating motion of drops to the macroscopic property of the multiphase flow. In the third section, new concepts for Euler–Lagrange type and Euler–Euler type simulators are proposed focusing on the contribution of fluctuating motion of drops on the controlling mechanism of spatial distribution of the dispersed phase.

2 Revision for the two-fluid model equation [8]

2.1 Interaction term without any restriction on averaging

Supposing dispersed two phase flow, eqn. (1) was obtained by successively volume-averaging and time-averaging the Navier-Stokes equation for the continuous phase in an entire volume of the continuous phase in a control volume V .

$$\frac{\partial}{\partial t}\left\{(1-\varepsilon)\overline{\rho_c \mathbf{u}_c}^{c}\right\}+\nabla\cdot\left\{(1-\varepsilon)\overline{\rho_c \mathbf{u}_c \mathbf{u}_c}^{c}\right\}-(1-\varepsilon)\overline{\rho_c}^{c}\mathbf{g}+\nabla\left\{(1-\varepsilon)\overline{P_c}^{c}\right\}+\nabla\cdot\left\{(1-\varepsilon)\overline{\boldsymbol{\tau}_c}^{c}\right\} \quad (1)$$
$$=-\lim_{V\to\mathbf{x}_0}\frac{1}{V}\overline{\mathbf{F}_{R,S}^{V}}^{\Lambda}$$

Here, ρ_c, $\mathbf{u}_c$, P_c and $\boldsymbol{\tau}_c$ are density, velocity vector, static pressure and stress tensor, respectively, of the continuous phase. A notation $\mathbf{F}_{R,S}^{V}$ on the right hand side is a sum of forces acting on drop surfaces in the control volume , and notations $\overline{q}^{\Lambda}$ and $\overline{q}^{c}$ mean time-averaged values of physical quantity q for total time length of averaging Λ and total time length during which the continuous phase covers the point of interesting Λ_c, respectively, as defined by eqns. (2) and (3).

$$\overline{q}^{\Lambda}(\mathbf{X},t)=\frac{1}{\Lambda}\int_{t-\frac{\Lambda}{2}}^{t+\frac{\Lambda}{2}} q(\mathbf{X},t)dt \quad (2)$$

$$\overline{q}^{c}(\mathbf{X},t)=\frac{1}{\Lambda_c}\int_{\Lambda_c} q(\mathbf{X},t)dt \quad (3)$$

A notation $\mathbf{X}$ is a position vector and a notation $\int_{\Lambda_c} q(\mathbf{X},t)dt$ means time integral of $q(\mathbf{X},t)$ for duration when the point $\mathbf{X}$ is covered by the continuous

phase. A notation ε in eqn. (1) is a local hold up of the dispersed phase defined as a ratio of Λ_d to the total time-averaging duration Λ, where Λ_d is a total tine duration during which the point of interest is occupied by the dispersed phase. Hence, $(1-\varepsilon)$, in eqn. (1) is a local holdup of continuous phase. Following relations hold, where suffices c and d mean continuous and dispersed phase, respectively.

$$\Lambda = \Lambda_c + \Lambda_d \tag{4}$$

$$\varepsilon = \frac{\Lambda_d}{\Lambda} \tag{5}$$

$$\overline{q_c}^{\Lambda}(\mathbf{X},t) = (1-\varepsilon)\overline{q_c}^{c}\mathbf{X}(\mathbf{x},t) \tag{6}$$

$$\overline{q_d}^{\Lambda}(\mathbf{X},t) = \frac{1}{\Lambda}\int_{t-\frac{\Lambda}{2}}^{t+\frac{\Lambda}{2}} q_d(\mathbf{X},t)dt = \frac{1}{\Lambda}\int_{\Lambda_d} q_d(\mathbf{X},t)dt = \varepsilon\,\overline{q_d}^{d}(\mathbf{X},t) \tag{7}$$

A notation $\lim_{V\to\mathbf{X}_0}$ on the right hand side of eqn.(1) means to take a limit value when the control volume converges to a point $\mathbf{X}_0$. Terms on the left hand side of eqn. (1) are given at a point $\mathbf{X}_0$ to which the control volume V converges. The right hand side of eqn. (1) is the interaction term without any restriction on averaging. Eqn. (1) shows that the interaction term in the two-fluid model equations based on time-averaging is time-averaged force acting on drop surfaces in an infinitesimal size of control volume.

2.2 'Inside-out' property of interaction term

The value of

$$\overline{\mathbf{F}_{R,S}^{V}}^{\Lambda} = \frac{1}{\Lambda}\int_{t-\frac{\Lambda}{2}}^{t+\frac{\Lambda}{2}} \mathbf{F}_{R,S}^{V}\,dt$$

for a control volume sufficiently smaller than a drop size was rigorously analysed for the dispersed two-phase flow with homogeneous size of drops with radius R, and eqn. (8) was obtained as a limit for the infinitesimal control volume.

$$\begin{aligned}&\lim_{V\to\mathbf{X}_0}\frac{1}{V}\overline{\mathbf{F}_{R,S}^{V}}^{\Lambda}\\ &= -\frac{1}{\Lambda}\int_0^{2\pi} d\phi\int_0^{\pi} d\theta\left[\sin\theta\,\mathbf{n}(\theta,\phi)\cdot\Delta\overline{\mathbf{T}_c^{\Lambda}}(\mathbf{X}_0-R\,\mathbf{n}(\theta,\phi),R,\theta,\phi)\lambda_R(\mathbf{X}_0-R\,\mathbf{n}(\theta,\phi))R^2\right]\\ &\quad -\frac{1}{\Lambda}\int_0^{2\pi} d\phi\int_0^{\pi} d\theta\left[\sin\theta\,\mathbf{n}(\theta,\phi)\cdot\overline{\mathbf{T}_c}^{c}(\mathbf{X}_0)\lambda_R(\mathbf{X}_0-R\,\mathbf{n}(\theta,\phi))R^2\right]\end{aligned} \tag{8}$$

Here, $\mathbf{T}_c(\mathbf{X}:R,\theta,\phi)$ is defined by eqn. (9) below, where $\mathbf{I}$ denotes the unit tensor: A notation $(\mathbf{X}:R,\theta,\phi)$ means a position in a spherical coordinate system $\{r,\theta,\phi\}$ with its origin at point $\mathbf{X}$. Notations $\mathbf{n}(\theta,\phi)$ and $\lambda_R(\mathbf{X})$ are

$$\mathbf{T}_c(\mathbf{X}:R,\theta,\phi)=P_c(\mathbf{X}:R,\theta,\phi)\mathbf{I}+\boldsymbol{\tau}_c(\mathbf{X}:R,\theta,\phi) \tag{9}$$

unit vector on the r-axis to the direction (θ,ϕ) and a duration in which the center of a drop with radius R is in unit volume assigned at point $\mathbf{X}$, respectively. A notation $\Delta\mathbf{T}_c^{\Delta}$ is the difference between time-averaged values of $\mathbf{T}_c$ at angular coordinates (θ,ϕ) on the surface, which is $\overline{\mathbf{T}_c^{\Delta}}(\mathbf{X}-R\mathbf{n}(\theta,\phi):R,\theta,\phi)$, and that at the same position in the bulk, which is $\overline{\mathbf{T}_c}^{c}(\mathbf{X})$, as defined by eqn. (10), which was introduced to utilize the knowledge on the drag force, lift force and virtual mass

$$\Delta\overline{\mathbf{T}_c^{\Delta}}(\mathbf{X}-R\mathbf{n}(\theta,\phi):R,\theta,\phi)=\overline{\mathbf{T}_c^{\Delta}}(\mathbf{X}-R\mathbf{n}(\theta,\phi):R,\theta,\phi)-\overline{\mathbf{T}_c}^{c}(\mathbf{X}) \tag{10}$$

force. The sum of them, $\overline{\mathbf{f}_d^{\Delta\mathbf{T}}}(\mathbf{X}_0)$, is given by eqn. (11). Knowledge on the drag force, lift force and virtual mass force can be applied to $\overline{\mathbf{f}_d^{\Delta\mathbf{T}}}$.

$$\overline{\mathbf{f}_d^{\Delta\mathbf{T}}}(\mathbf{X}_0)=-\int_0^{2\pi}d\phi\int_0^{\pi}d\theta\left[\sin\theta\,\mathbf{n}(\theta,\phi)\cdot\Delta\overline{\mathbf{T}_c^{\Delta}}(\mathbf{X}_0:R,\theta,\phi)R^2\right] \tag{11}$$

To consider the first term on the right hand side of eqn. (8), the positions where the values of $\Delta\overline{\mathbf{T}_c^{\Delta}}$ and λ_R are specified were exchanged. That is;

$$\begin{aligned}
&-\frac{1}{\Delta}\int_0^{2\pi}d\phi\int_0^{\pi}d\theta\left[\sin\theta\,\mathbf{n}(\theta,\phi)\cdot\Delta\overline{\mathbf{T}_c^{\Delta}}(\mathbf{X}_0:R,\theta,\phi)\lambda_R(\mathbf{X}_0)R^2\right] \\
&=-\frac{\lambda_R(\mathbf{X}_0)}{\Delta}\int_0^{2\pi}d\phi\int_0^{\pi}d\theta\left[\sin\theta\,\mathbf{n}(\theta,\phi)\cdot\Delta\overline{\mathbf{T}_c^{\Delta}}(\mathbf{X}_0:R,\theta,\phi)R^2\right] \\
&=\frac{V_d\lambda_R(\mathbf{X}_0)}{\Delta}\frac{1}{V_d}\overline{\mathbf{f}_d^{\Delta\mathbf{T}}}(\mathbf{X}_0)\approx\frac{\Delta_d(\mathbf{X}_0)}{\Delta}\frac{1}{V_d}\overline{\mathbf{f}_d^{\Delta\mathbf{T}}}(\mathbf{X}_0)=\varepsilon(\mathbf{X}_0)\frac{1}{V_d}\overline{\mathbf{f}_d^{\Delta\mathbf{T}}}(\mathbf{X}_0)
\end{aligned} \tag{12}$$

The last expression on the right hand side of eqn. (12) is the same as the conventional interaction term. The intrinsic properties of the interaction term in the two-fluid model equations is visible in eqn. (8), which differs clearly from the conventional interaction term in its 'inside-out' property.

2.3 Revised two-fluid model equation

The 'inside-out' property can be treated by using Taylor expansion to shift the points where $\Delta\overline{\mathbf{T}_c}^{c}$ and λ_R are specified. Upon neglecting higher order terms, eqn (13) was finally obtained.

$$\begin{aligned}
&\lim_{V\to\mathbf{X}_0}\frac{1}{V}\overline{\mathbf{F}_{R,S}^{V}}^{\Delta} \\
&\approx\varepsilon(\mathbf{X}_0)\frac{\overline{\mathbf{f}_d^{\Delta\mathbf{T}}}(\mathbf{X}_0)}{V_d}-cR\left(\frac{\partial\varepsilon}{\partial Z}\right)\Bigg|_{\mathbf{X}_0}\frac{\overline{\mathbf{f}_d^{\Delta\mathbf{T}+}}(\mathbf{X}_0)-\overline{\mathbf{f}_d^{\Delta\mathbf{T}-}}(\mathbf{X}_0)}{V_d}+(\nabla\varepsilon)\big|_{\mathbf{X}_0}\overline{P_c}^{c}(\mathbf{X}_0)+(\nabla\varepsilon)\big|_{\mathbf{X}_0}\cdot\overline{\boldsymbol{\tau}_c}^{c}(\mathbf{X}_0)
\end{aligned} \tag{13}$$

The first term on the right hand side of eqn. (13) is the same as the conventional interaction term. Standard analyses of the drag force, lift force and virtual mass force for a single drop in a flow field can now be applied to $\overline{\mathbf{f}_d^{\Delta\mathbf{T}}}(\mathbf{X}_0)$.

The second, third and fourth terms in eqn. (13) was introduced to compensate for the discrepancy between $\lim_{V\to\mathbf{X}_0}\frac{1}{V}\overline{\mathbf{F}_{R,S}^{V}}^{\Lambda}$ and the conventional interaction term $\varepsilon(\mathbf{X}_0)\frac{\overline{\mathbf{f}_d^{\Delta\mathbf{T}}}(\mathbf{X}_0)}{V_d}$.

The Z axis in the second term on the right hand side of eqn. (13) is chosen to the direction of $\nabla\varepsilon$, and $\overline{\mathbf{f}_d^{\Delta\mathbf{T}+}}(\mathbf{X}_0)$ and $\overline{\mathbf{f}_d^{\Delta\mathbf{T}-}}(\mathbf{X}_0)$ are forces acting on the two hemispherical surfaces of the drop having positive and negative values of Z respectively. The parameter c represents the effects of the weight function, $\cos\theta$, in the surface integration over the hemisphere surface, and is between 0 and 1. This term becomes significant for flow having steep gradients of the local holdup and averaged velocity.

The third term on the right-hand side of eqn. (13) is similar to the result of Kolev [4] in rearranging surface integrals for two-fluid model equations based on volume-averaging, which is crucial to excluding local holdup from the differential operator ∇ in the static pressure term in the two-fluid model equation.

The fourth term on the right hand side of eqn. (13) arises from the definition of the force acting on a drop, $\overline{\mathbf{f}_d^{\Delta\mathbf{T}}}$, given by eqn. (11), since $\Delta\overline{\mathbf{T}_c^{\Lambda}}$, which is the difference between time- averaged values of tensor, $\mathbf{T}_c = P_c\mathbf{I} + \boldsymbol{\tau}_c$, on a drop surface and in the bulk of the continuous phase, was taken to define the force acting on a drop $\overline{\mathbf{f}_d^{\Delta\mathbf{T}}}$. This term makes a small modification the shear stress term in the two-fluid model equation.

Finally, the two-fluid model equation is given as eqn. (14).

$$\begin{aligned}&\frac{\partial}{\partial t}\left\{(1-\varepsilon)\overline{\rho_c\mathbf{u}_c}^{c}\right\}+\nabla\cdot\left\{(1-\varepsilon)\overline{\rho_c\mathbf{u}_c\mathbf{u}_c}^{c}\right\}\\&=-\varepsilon\frac{\overline{\mathbf{f}_d^{\Delta\mathbf{T}}}}{V_d}-(1-\varepsilon)\left(\nabla\overline{P_c}^{c}\right)-(1-\varepsilon)\left(\nabla\cdot\overline{\boldsymbol{\tau}_c}^{c}\right)+(1-\varepsilon)\overline{\rho_c}^{c}\,\mathbf{g}+cR\left(\frac{\partial\varepsilon}{\partial Z}\right)\frac{\overline{\mathbf{f}_d^{\Delta\mathbf{T}+}}(\mathbf{X}_0)-\overline{\mathbf{f}_d^{\Delta\mathbf{T}-}}(\mathbf{X}_0)}{V_d}\end{aligned}\tag{14}$$

Eqn. (14) is derived without any restriction on averaging, to which the accumulated knowledge on the drag force, lift force and virtual mass force can be applied.

3 Question for Euler–Lagrange type simulator

In the preceding section, it has been revealed that the conventional two-fluid model equations based on volume-averaging passed over the "inside-out" property of the interaction term due to the restriction on the size of the control volume. It has been also shown that we have eqn. (14) as the two-fluid model equation without any restriction on averaging, to which the accumulated knowledge on the drag force, lift force and virtual mass force can be applied. It

is worth noting here that eqn. (14) is obtained by combining volume-averaging and time-averaging, and the result, eqn. (14), is based on time-averaging. This means that we have to keep in mind that the averaged physical quantities in the two-fluid model equation are to be based on time-averaging. In this section, several questions for the conventional Euler–Lagrange type simulators are made and discussed from a view point of macroscopic properties of gas-liquid multiphase flow.

3.1 Over-view of dispersed two-phase flow and questions for Euler–Lagrange type simulator

In a bubble column operated in the recirculating turbulent flow regime, it is well known that the flow field in the columns is fully developed turbulent flow with distributed size of vortices up to the order of column diameter [3,7]. Bubbles are rising in highly turbulent liquid flow with considerable scale of fluctuating motion induced by the vortices. The well-known parabolic distribution of gas holdup in bubble columns operated in this flow regime [3,7] has been a hot target for numerical studies, and has not been successively realized yet [10]. The reason why bubbles are gathering in the central region of the column may be attributed to the lift force, and almost all of the previous works have been focused on the force acting on a drop, such as Tomiyama coefficient for the lift force [5], the dispersion force [2], and so on.

In Euler–Lagrange type simulators, a trail of each drop is followed by an equation of motion for each drop, to which accumulated knowledge on the forces acting on a drop is applied. The values of moving velocity of drops thus obtained are "averaged" values, because the flow field of the surrounding fluid described by the two-fluid model equation is averaged one. Several questions arise here: What kind of "mean" value is the moving velocity obtained from the equation of motion? Can we ignore the contribution of fluctuating motion of drops to the macroscopic property of the multiphase flow? What kind of forces should be accounted on the equation of motion for a drop? Let us discuss these questions next.

3.2 Equation of motion for a drop

The equation of motion for a drop is given by Newton's law, which is a balance between the acceleration term and the sum of forces acting on the drop. The force acting on an entire surface of a drop is the contribution of a tensor $\mathbf{T}_c$ acting on the drop surface, however, the sum of the drag force, lift force and virtual mass force is given by eqn (11) as $\overline{\mathbf{f}_d^{\Delta\mathrm{T}}}(\mathbf{X}_0)$ which is assigned for the contribution of $\Delta\overline{\mathbf{T}_c^{\Delta}}$ on the drop surface. Hence, the contribution of $\overline{\mathbf{T}_c^{\Delta}}(\mathbf{X}_0{:}R,\theta,\phi) - \Delta\overline{\mathbf{T}_c^{\Delta}}(\mathbf{X}_0 : R,\theta,\phi) = \overline{\mathbf{T}_c}^{c}(\mathbf{X}_0 + R\mathbf{n}(\theta,\phi))$ should be accounted in addition to the force $\overline{\mathbf{f}_d^{\mathrm{T}}}(\mathbf{X}_0)$, to account all the forces acting on the drop surface. That is;

$$\begin{aligned}\overline{\mathbf{f}_b}(\mathbf{X}_0) &= -\int_0^{2\pi} d\phi \int_0^{\pi} d\theta \left[\sin\theta\, \mathbf{n}(\theta,\phi)\cdot \overline{\mathbf{T}_c}^{c}(\mathbf{X}_0 + R\mathbf{n})R^2\right] \\ &= -\int_{V_d} \nabla\cdot\left(\overline{P_c}^{c}\mathbf{I} + \overline{\boldsymbol{\tau}_c}^{c}\right) dV \approx V_d\left(\nabla \overline{P_c}^{c}\right)_{\mathbf{X}_0} + V_d\left(\nabla\cdot\overline{\boldsymbol{\tau}_c}^{c}\right)_{\mathbf{X}_0}\end{aligned} \tag{15}$$

Here, V_d is volume of a drop and $\int_{V_d} dV$ means an integration over V_d.

The force $\overline{\mathbf{f}_b}(\mathbf{X}_0)$ given by eqn. (15) is regarded as buoyancy force, because the second term on the right hand side of the last expression in eqn. (15) can be neglected comparing with the first term.

The accumulated knowledge on the drag force, lift force and virtual mass force tells that the sum of those forces can be expressed as a function of liquid velocity $\mathbf{u}_c$ and moving velocity of a drop $\mathbf{u}_p$, as eqn. (16). The function H can

$$\mathbf{f}_d^{\Delta\mathbf{T}} = H\left(\mathbf{u}_c, \mathbf{u}_p\right) \tag{16}$$

be easily found in text books or literatures in this research field. Since we have an intention to utilize the two-fluid model equation, which is described in terms of time-averaged physical quantities, together with eqn. (16), let us expect that eqn (17) hold for the time-averaged velocity field of liquid $\overline{\mathbf{u}_c}^{c}$ and averaged moving velocity of a drop $\overline{\mathbf{u}_p}$.

$$\overline{\mathbf{f}_d^{\Delta\mathbf{T}}} = H\left(\overline{\mathbf{u}_c}^{c}, \overline{\mathbf{u}_p}\right) \tag{17}$$

Here, $\overline{\mathbf{f}_d^{\Delta\mathbf{T}}}(\mathbf{X}_0)$ is a sum of the drag force, lift force and virtual mass force acting on a drop defined by eqn. (11). The averaged moving velocity of a drop $\overline{\mathbf{u}_p}$ is regarded as moving velocity of a drop defined by eqn. (17) for the flow field of the time-averaged velocity of the continuous phase $\overline{\mathbf{u}_c}^{c}$.

Now, we have eqn. (18) as the equation of motion for a drop.

$$\frac{d}{dt}\left(\rho_d V_d \overline{\mathbf{u}_p}\right) = H\left(\overline{\mathbf{u}_c}^{c}, \overline{\mathbf{u}_p}\right) + \overline{\mathbf{f}_b} + \rho_d V_d \mathbf{g} \tag{18}$$

Here, $\overline{\mathbf{f}_b}$ is buoyancy force acting on the drop.

It is worth noting here that the dispersion force [2] does not appear on the right hand side of eqn. (18) because it was introduced in modifying Reynolds stress in the second term on the left hand side of eqn. (14). The term is acceptable in the two-fluid model equation, but does not appear in the equation of motion for a drop.

4 Proposal for Euler–Lagrange and Euler–Euler types of simulators

The second term on the left hand side of eqn. (14) can be expressed in terms of time-averaged velocity field of continuous phase by using $\kappa-\varepsilon$ model, for instance, probably with the dispersion force. The fifth term on the right hand

side of eqn. (14) cannot be treated at present due to the lack of knowledge, however, it should be resolved for the practical use sooner or later. Let us skip to the utilization of eqn. (14) for the simulator of multiphase flow.

4.1 Euler–Lagrange type of simulator

Since the averaged moving velocity of a drop, $\overline{\mathbf{u}}_p$, is regarded as moving velocity of a drop defined by eqn. (17) for the flow field of the time-averaged velocity of the continuous phase, the actual moving velocity of a drop, $\mathbf{u}_p$, is given as eqn. (19).

$$\mathbf{u}_p = \overline{\mathbf{u}}_p + \mathbf{u}'_p \tag{19}$$

Here, $\mathbf{u}'_p$ is fluctuating component of moving velocity of a drop induced by turbulent vortices in surrounding fluid, which should play a key role in the simulator to control the distribution of local holdup of the dispersed phase through dispersion phenomena of drops.

Eqns. (14) and (18), and eqn. (20) which follows are basic equations for the Euler–Lagrange type of simulator.

$$\rho_c \frac{\partial}{\partial t}(1-\varepsilon) + \nabla \cdot \left\{(1-\varepsilon)\overline{\mathbf{u}_c}^c\right\} = 0 \tag{20}$$

Eqn. (20) is the time-averaged equation of continuity for the continuous phase [6].

Supposing that spatial distributions of $\overline{\mathbf{u}_c}^c$ and $\overline{P_c}^c$, and averaged moving velocity, $\overline{\mathbf{u}}_p$, and position of individual drop are known at time $t = t_1$, the spatial distributions of $(1-\varepsilon)\overline{\mathbf{u}_c}^c$ at the next time step $t = t_1 + \Delta t$ can be calculated from eqn. (14). The position of individual drop at the next time step is given by adding $\Delta t\, \mathbf{u}_p = \Delta t\left(\overline{\mathbf{u}}_p + \mathbf{u}'_p\right)$ to the position vector of each drop, then the spatial distribution of ε at $t = t_1 + \Delta t$ can be obtained. Then, the value of $\overline{\mathbf{u}_c}^c$ at $t = t_1 + \Delta t$ can be calculated, and the value of $\overline{\mathbf{u}}_p$ at the next time step $t = t_1 + \Delta t$ is given by eqn. (18). The spatial distribution of $\overline{P_c}^c$ at the next time step are determined so that the spatial distributions of $\overline{\mathbf{u}_c}^c$ and $\overline{P_c}^c$ satisfy both eqns (14) and (20).

How to give the value of the fluctuating component $\mathbf{u}'_p$ to each drop is not known at present, however the trial and error approach in the numerical experiments to realize the distribution of the dispersed phase seem to be useful to obtain effective suggestion for the fluctuating motion.

4.2 Euler–Euler type of simulator

The contribution of fluctuating motion of drops to the controlling mechanism of the distribution of local holdup of the dispersed phase can also be treated by introducing dispersion coefficient in stead of fluctuating velocity. Since the time-averaged velocity of the dispersed phase $\overline{\mathbf{u}_c}^c$ includes contributions of both averaged moving velocity of drops $\overline{\mathbf{u}_p}$ and dispersion of drops due to fluctuating moving velocity $\mathbf{u}'_p$, we have eqn. (21).

$$\varepsilon\,\overline{\mathbf{u}_d}^d = \varepsilon\,\overline{\mathbf{u}_p} - D_\varepsilon\left(\nabla\varepsilon\right) \tag{21}$$

Here, D_ε is a dispersion coefficient of drops. A notation $\overline{q}^d$ means time-averaged values of physical quantity q for total time length during which the dispersed phase covers the point of interesting.

Equation of continuity for the drop phase time-averaged for the dispersed two-phase flow is obtained as eqn. (22) [6].

$$\frac{\partial}{\partial t}\varepsilon + \nabla\cdot\left(\varepsilon\,\overline{\mathbf{u}_d}^d\right) = 0 \tag{22}$$

Introducing eqn. (21) into eqn. (22), eqn. (23) is obtained.

$$\frac{\partial}{\partial t}\varepsilon + \nabla\cdot\left(\varepsilon\,\overline{\mathbf{u}_p}\right) = \nabla\cdot\left\{D_\varepsilon\left(\nabla\varepsilon\right)\right\} \tag{23}$$

Eqn. (24) also holds as the Navier-Stokes equation for the dispersed phase time-averaged for dispersed multiphase flow [6].

$$\begin{aligned}&\frac{\partial}{\partial t}\left(\varepsilon\,\overline{\rho_d\mathbf{u}_d}^d\right) + \nabla\cdot\left(\varepsilon\,\overline{\rho_d\mathbf{u}_d\mathbf{u}_d}^d\right) - \varepsilon\,\overline{\rho_d}^d\,\mathbf{g} + \nabla\left\{\varepsilon\,\overline{P_d}^d\right\} + \nabla\cdot\left\{\varepsilon\,\overline{\boldsymbol{\tau}_d}^d\right\}\\ &= \lim_{V\to\mathbf{x}_0}\frac{1}{V}\overline{\mathbf{F}_{R,S}^{V}}^{A}\end{aligned} \tag{24}$$

From eqns. (14) and (24), eqn. (25) is obtained.

$$\begin{aligned}0 = {}&\frac{\partial}{\partial t}\left\{\left(1-\varepsilon\right)\overline{\rho_c\mathbf{u}_c}^c\right\} + \frac{\partial}{\partial t}\left(\varepsilon\,\overline{\rho_d\mathbf{u}_d}^d\right) + \nabla\cdot\left\{\left(1-\varepsilon\right)\overline{\rho_c\mathbf{u}_c\mathbf{u}_c}^c\right\} + \nabla\cdot\left(\varepsilon\,\overline{\rho_d\mathbf{u}_d\mathbf{u}_d}^d\right)\\ &-\left(1-\varepsilon\right)\overline{\rho_c}^c\,\mathbf{g} - \varepsilon\,\overline{\rho_d}^d\,\mathbf{g} + \nabla\,\overline{P_c}^c + \nabla\cdot\left\{\left(1-\varepsilon\right)\overline{\boldsymbol{\tau}_c}^c\right\} + \nabla\cdot\left\{\varepsilon\,\overline{\boldsymbol{\tau}_d}^d\right\}\end{aligned} \tag{25}$$

Here, the values of static pressure time-averaged for dispersed and continuous phases are assumed to be the same.

Eqns. (14), (17), (20), (23) and (25) are basic equations for the Euler–Euler type simulator. Once we know the spatial distributions of time-averaged velocity of the continuous phase $\overline{\mathbf{u}_c}^c$, the average moving velocity of a drop $\overline{\mathbf{u}_p}$, time-averaged static pressure for the continuous phase $\overline{P_c}^c$ and local holdup of the dispersed phase ε, we can calculate the spatial distributions of them at the next time step, by using eqns. (14), (17), (20), (23) and (25).

Accumulated knowledge on the dispersion coefficient D_ε is poor at present; however, the trial and error approach in the numerical experiments to realize the distribution of the dispersed phase is an effective approach to investigate the fluctuating motion.

5 Conclusion

Corrections to the conventional two-fluid model equations have been briefly illustrated, showing eqn. (1) as the general expression of the two-fluid model equation without any restriction on averaging, eqn. (8) as the general expression of the interaction term with 'inside-out' property, and eqn. (14) as the corrected two-fluid model equation with a new and novel term comprising the product of the local gradient of holdup and the difference between the forces acting on a hemispherical surface of the drop cut by a plane perpendicular to the local holdup gradient[8].

Questions for the previous Euler–Lagrange type simulators have been stated and discussed with respect to the moving velocity of each drop obtained in the simulator and the contribution of fluctuating motion of drops to the macroscopic property of the multiphase flow. It has also been shown in the discussion that the contribution of fluctuating motion of drops on the macroscopic properties of multiphase flow cannot be treated in the previous Euler–Lagrange type simulator because both the two-fluid model equation and the equation of motion for a drop are relations between time-averaged velocity field of surrounding fluid and averaged moving velocity of a drop.

Concepts of Euler–Lagrange type and Euler–Euler type simulators are proposed focusing on the contribution of fluctuating motion of drops to the controlling mechanism of spatial distribution of the dispersed phase. It was shown that the fluctuating motion of drops, which cannot be treated in the two-fluid model equation and the equation of motion of a drop, may play a key role in controlling the spatial distribution of local holdup of dispersed phase.

Symbols

D_ε:	dispersion coefficient of drops	$[m^2 \cdot s^{-1}]$
$\overline{\mathbf{f}_b}$:	force acting on drop surface due to tensor $\mathbf{T}_c$ time-averaged for bulk of the continuous phase, which nearly equals to the buoyancy force as defined by eqn. (15).	$[kg \cdot m \cdot S^{-2}]$
$\mathbf{f}_d^{\Delta\mathbf{T}}$:	contribution of the difference between the values of $\mathbf{T}_c$ at the drop surface and in bulk of the surrounding fluid, on an entire surface of single drop, which is the sum of the drag, lift and virtual mass forces for a single drop in a flow field	$[kg \cdot m \cdot S^{-2}]$

$\overline{\mathbf{f}_d^{\Delta\mathbf{T}}}$:	contribution of $\Delta\overline{\mathbf{T}_c^{\Lambda}}$ on an entire surface of a drop, given by eqn (19)	$[kg \cdot m \cdot s^{-2}]$
$\overline{\mathbf{f}_d^{\Delta\mathbf{T}+}}$:	force due to $\Delta\overline{\mathbf{T}_c^{\Lambda}}$ acting on a hemispherical surface of a drop with positive value of Z	$[kg \cdot m \cdot s^{-2}]$
$\overline{\mathbf{f}_d^{\Delta\mathbf{T}-}}$:	force due to $\Delta\overline{\mathbf{T}_c^{\Lambda}}$ acting on a hemispherical surface of a drop with negative value of Z	$[kg \cdot m \cdot s^{-2}]$
$\mathbf{F}_{R,S}^{V}$:	sum of forces acting on drop surfaces in a control volume	$[kg \cdot m \cdot s^{-2}]$
$\mathbf{g}$:	vector of gravitational acceleration	$[m \cdot s^{-2}]$
$\mathbf{I}$:	unit tensor	$[-]$
$\mathbf{n}(\theta,\phi)$:	unit vector along the r axis in spherical coordinate system directed to (θ,ϕ)	$[-]$
P:	static pressure	$[Pa]$
q:	physical quantity	
r:	radial coordinate in spherical coordinate system	$[m]$
R:	radius of a drop	$[m]$
S:	surface of a control volume	$[m^2]$
t:	time	$[s]$
$\mathbf{T}_c$:	tensor composed of static pressure and shear stress tensor, defined as eqn. (9)	$[kg \cdot m^{-1} \cdot s^{-2}]$
$\overline{\mathbf{T}_c^{\Lambda}}$:	mean value of tensor $\mathbf{T}_c$ for duration Λ, at a fixed angular coordinate on drop surface	$[kg \cdot m^{-1} \cdot s^{-2}]$
$\mathbf{u}$:	velocity vector	$[m \cdot s^{-1}]$
$\mathbf{u}_p$:	moving velocity vector of a drop	$[m \cdot s^{-1}]$
$\overline{\mathbf{u}}_p$	averaged moving velocity vector of a drop, defined by eqn (26)	$[m \cdot s^{-1}]$
$\mathbf{u}'_p$	fluctuating moving velocity vector of a drop	$[m \cdot s^{-1}]$
V:	volume of the control volume	$[m^3]$
V_d:	volume of a drop	$[m^3]$
$\mathbf{X}$, $\mathbf{X}_0$:	position vector in Cartesian coordinate	$[m]$
Z:	coordinates in Cartesian coordinate system	$[m]$
Δt:	time step in numerical calculation	$[s]$
ε:	local hold up of the dispersed phase, defined by eqn (8)	$[-]$
ϕ, θ:	coordinates in spherical coordinate system	$[radian]$
$\lambda_R(\mathbf{X})$:	duration in which the center of a drop with radius R is in unit volume assigned at point $\mathbf{X}$	$[s \cdot m^{-3}]$

Λ :	total duration for time averaging	$[s]$
Λ_d :	total time during which the dispersed phase occupies the point of interest	$[s]$
Λ_c :	total time during which the continuous phase occupies the point of interest	$[s]$
ρ :	density	$\left[kg \cdot m^{-3}\right]$
$\boldsymbol{\tau}$:	shear stress tensor	$[Pa]$

Suffixes and other notations

c :	continuous phase
d :	dispersed phase
$^{-\Lambda}$:	time-averaged value for total duration for time-averaging, Λ
$^{-c}$:	time-averaged value for duration Λ_c
$^{-d}$:	time-averaged value for duration Λ_d

References

[1] Anderson, T. B. and R. Jackson, A fluid mechanical description of fluidized bed, *Ind. Eng. Fundam.*, **6**, 527-534, 1967

[2] Bertodano, M. L., R. T. Lahey and O. C. Jones, Phase distribution in bubbly two-phase flow in vertical ducts, *Int. J. Multiphase Flow*, **20**, 805-818, 1994

[3] Hills, J.H., Radial non-uniformity of velocity and voidage in a bubble column, *Trans. Inst. Chem. Engrs.*, **52**, 1-10, 1974.

[4] Kolev, N. I., Multiphase Flow Dynamics, 3rd ed., 51-54, Springer-Verlag Berlin Heidelberg, 2007

[5] Tomiyama, A., Y. Nakahara, Y. Adachi and S. Hosokawa, Shapes and rising velocity of single bubbles rising through an inner subchannel, *J. Nuclear Science and Technology*, **40**, 136-142, 2003

[6] Ueyama, K. and T. *Miyauchi, Time-averaged Navier-St*ok**es** equations as Basic Equations for multiphase flow, *Kagakukogaku Ronbunshu*, **2**, 595-601, 1976.

[7] Ueyama, K. and T. Miyauchi, Properties of recirculating turbulent two phase flow in gas bubble columns, *AIChEJ.*, **25**, 258-266, 1979.

[8] Ueyama, K., A study of two-fluid model equations, submitted to *J. Fluid* Mechanics

[9] Whitaker, S., Diffusion and dispersion in porous media, *AIChE Journal*, 13, 420-427, 1967

[10] Zhang, X. and G. Ahmadi, Eulerian-Lagrangian simulations of liquid-gas-solid flows in three-phase slurry reactors, *Chem. Eng. Sci.*, **60**, 5089-5104, 2005.

Control of a magnetic fluid drop moving in a viscous fluid inside a cylinder

M. Shinohara
Gifu National College of Technology, Japan

Abstract

An investigation has been made of the dynamic behaviour of a magnetic fluid drop settling in a viscous fluid inside a vertical cylinder in response to impressed magnetic fields. Two coils were placed so as their axes coincided with the cylinder axis in order to provide the magnetic field for the tests. The Reynolds number Re (Re = av_z/ν) is in the range of 0.001–0.037. Here, a is the scale of the magnetic fluid drop, v_z is the settling velocity of the drop and ν is the kinematic viscosity of the machine oil. Near the upper coil, the centre of the drop is forced upwards, but the velocity of the drop is not always decreased. At the middle point between the two coils, the drop tends to extend along the field. Due to the change of the shape of the drop, the drag on the drop is reduced and the velocity of the drop is increased.

Keywords: low Reynolds number, magnetic fluid, cylindrical wall, viscous fluid.

1 Introduction

A magnetic fluid is a homogeneous colloidal suspension of magnetic particles in a solvent. Various physical phenomena relating to the flows of magnetic fluids have been studied by Rosensweig [1].

A number of interesting phenomena are exhibited by the magnetic fluids in response to impressed magnetic fields [2–4]. A certain interest is shown to magnetic fluids as carriers of drug. The magnetic field can pilot the path of a magnetic fluid drop in the body, bringing drugs to a target site [5], and the drugs can be retained there for as long as necessary. This means that it is important to investigate the motion of a magnetic fluid drop travelling inside a tube in an external magnetic field.

WIT Transactions on Engineering Sciences, Vol 69, © 2010 WIT Press
www.witpress.com, ISSN 1743-3533 (on-line)
doi:10.2495/AFM100411

This paper is concerned with the motion and the formation of a magnetic fluid drop settling in a stagnant viscous fluid inside a vertical cylinder under the influence of a magnetic field. First, we seek the difference of the settling velocity between magnetic fluid drop and an iron sphere under the influence of a magnetic field. The surface of the magnetic fluid drop is free, then the shape of the drop is deformed by the applied magnetic field and the settling velocity of a drop is changed. The shape of the iron sphere does not change and the velocity of it depends on the magnetostatic force. Second, it is shown that the velocity of the magnetic fluid varies at the middle point between two coils only due to the change of the shape of the magnetic fluid drop.

2 Experimental method

The experimental apparatus is shown in Fig. 1. A vertical glass cylinder about 150cm long and of internal diameter 2.0cm is used. To eliminate the optical distortion in viewing a particle or a drop through the cylinder, a square section duct made of transparent plates was set outside the cylinder. Another square section duct was set outside this square section duct. Water of constant temperature circulates between these two square section ducts. The temperature of the room was controlled by an air-conditioner not to vary more than $\pm 1^{o}$C

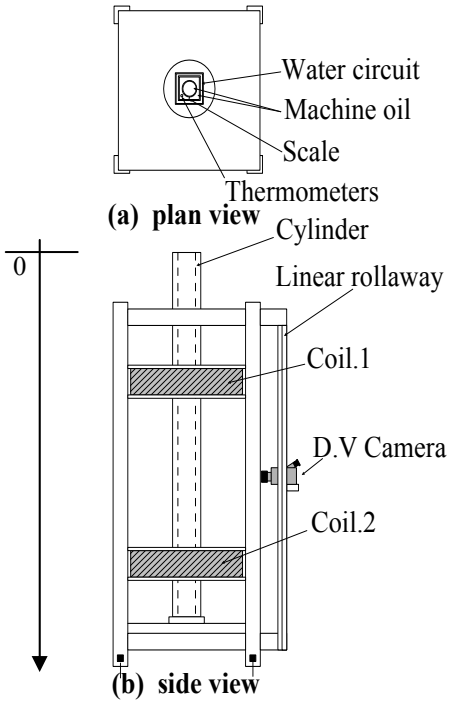

Figure 1: Experimental apparatus.

from the set point. Three thermometers were inserted between the cylinder and inner square section duct at upper, middle and lower points. Before each run, the temperatures of three thermometers were read to 0.1°C. The temperature variation was checked whether it was less than 0.1°C. Two coils, arranged as a Helmholtz pair, placed as their axes to be coincide with the cylinder axis and provided the magnetic field for the tests. The current supply was measured by an ammeter.

The magnetic field between the coils was measured by using a gaussmeter with Hall probe. The magnetic fluid used in the experiments was water-based ferricolloid W-40 (density 1.392 g/cm^3). The stagnant fluid used in the experiment was machine oil. Spheres are of the ball bearing with a diameter 0.982mm (density 7.79 g/cm^3). Its accuracy was checked and error was less than 1μm. The test section, 30 cm long, was located in the central section of the 150cm long glass cylinder to reduce any errors due to end effects. A pipette is used for injection of the magnetic fluid drop. The volume of the drop ranged from 0.26 to 2.10mm^3. After the drop or the iron sphere had fallen down through the upper coil 1, the current was supplied and the magnetic field was imposed. The positions of the particle or drop, the shape of the drop, and the time were recorded by a digital video camera. The velocities of iron spheres and magnetic fluid drops were calculated from the time data and the trajectory data. The velocity of a sphere or drop under no magnetic field is recorded above the upper coil 1.

3 Experimental results

In Fig. 2 and Fig. 3, the vertical component of magnetic field and the gradient of it between two coils are shown.

The current supply I to two coils was 3A or 7A. The upper and lower coils are at the vertical position z=40cm and 70cm respectively.

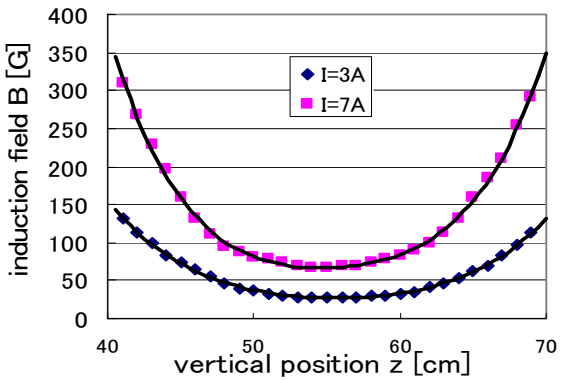

Figure 2: Magnetic field.

Settling velocities of iron spheres and magnetic fluid drops were calculated from the time data and the trajectory data. Figure 4 shows the settling velocity v_z of a single iron sphere normalized with respected to the mean velocity of an iron sphere. When the current (4A) was supplied to two coils, the velocity of a single iron sphere varies in proportion to the gradient of the magnetic field. This

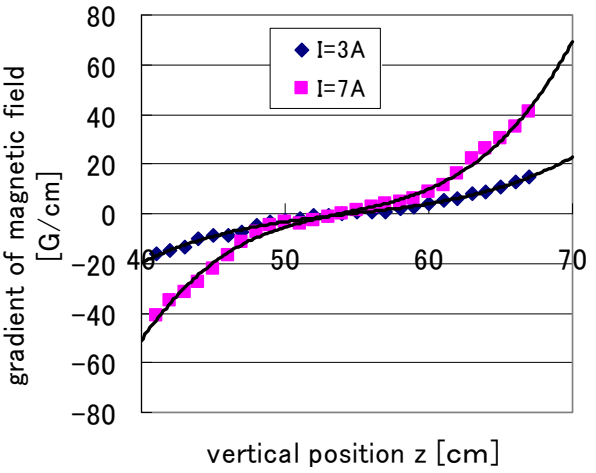

Figure 3: Gradient of a magnetic field.

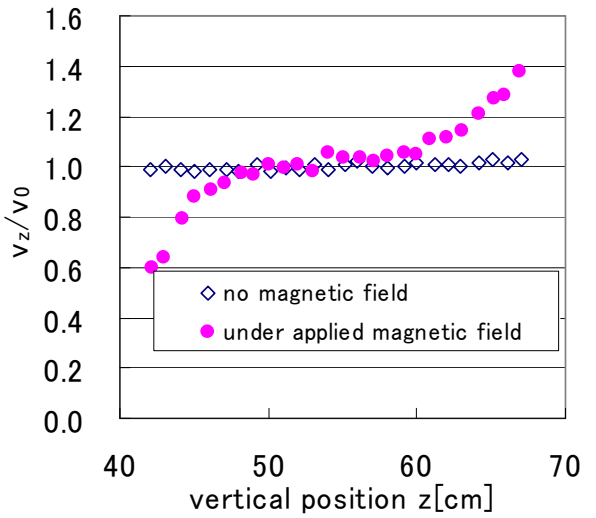

Figure 4: Settling velocity of a single iron sphere.

phenomenon occurs as an iron sphere is subjected to the force $\mu_0 \boldsymbol{M} \cdot \nabla H$, where μ_0 is the permeability of free space, $\boldsymbol{M}$ is the magnetization and H is the magnetic field.

At the place right below the upper coil, the magnetostatic force acts on the iron sphere upward. On the other hand, at the place right above the lower coil, the magnetostatic force acts on the iron sphere downward. At the middle point between two coils, the iron sphere experiences no magnetostatic force.

In the present experiment, Reynolds numbers (=0.03-0.06) are very low and Stokes's law may be applied. When a sphere moves in a fluid under the magnetic field, it experiences the drag, gravitational, magnetic and buoyancy force.

$$\frac{4}{3}\pi a^3 \rho_1 \frac{d^2 z}{dt^2} = \{(\rho_1 - \rho_2)g + \mu_0 \boldsymbol{M} \cdot \nabla H\}\frac{4}{3}\pi a^3 - 6\pi\rho_2 \nu \frac{dz}{dt} a \tag{1}$$

In the eqn (1), ρ_1 (=7.79) and ρ_2 (=0.875) are the density of iron and that of the machine oil respectively, z is the vertical position of the sphere, and g is the gravitational acceleration. When there is no magnetic field, it is easy to solve this equation and the time to reach 99% of the terminal velocity is obtained as 0.02 second.

Figure 5 shows the settling velocity v_z of a magnetic fluid drop. At the place right below the upper coil, the magnetostatic body force $\mu_0 \boldsymbol{M} \cdot \nabla H$ acts on the magnetic fluid drop upward. However, at that place the velocity of magnetic fluid drops of volume 0.821 and 1.997 mm^3 were faster than those at middle

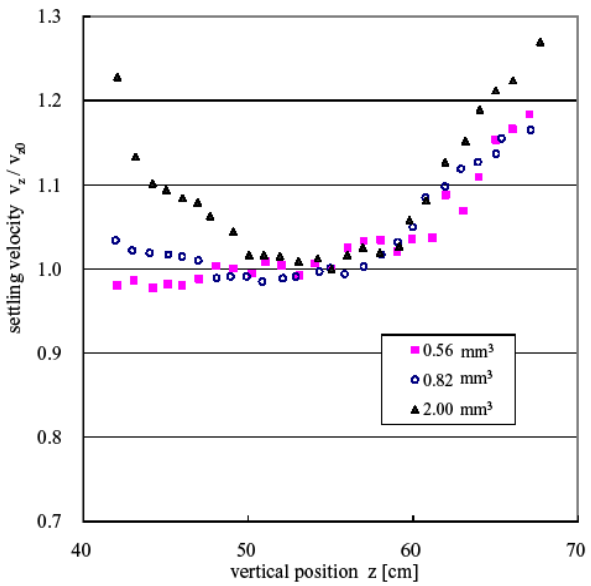

Figure 5: Settling velocity of a magnetic fluid drop.

point. Initial shapes of magnetic fluid drops were sphere with volumes 0.56, 0.82 and 2.00 mm^3 and the current I supply to two coils was 2A. The velocity is normalized with respect to the velocity v_0 at the middle point between two coils.

Figure 6 shows the shapes of a settling magnetic fluid drop of volume 1.12mm^3 settling in the machine oil inside a cylinder. The right figure shows the deformation of a magnetic fluid drop under the influence of a magnetic field.

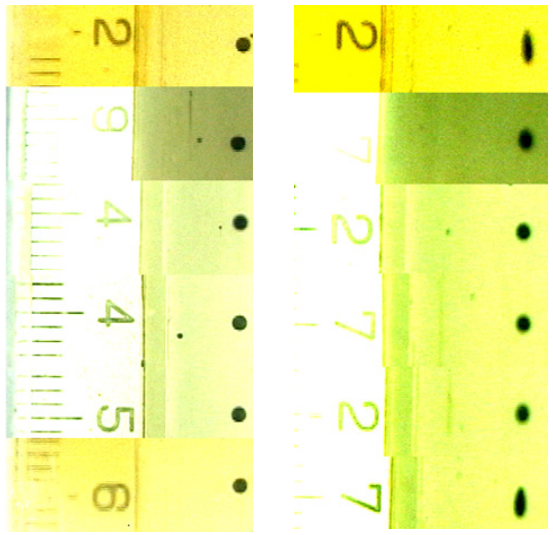

under no magnetic field

under the influence of a magnetic field

Figure 6: Shapes of a settling magnetic fluid drop (volume 1.12mm^3).

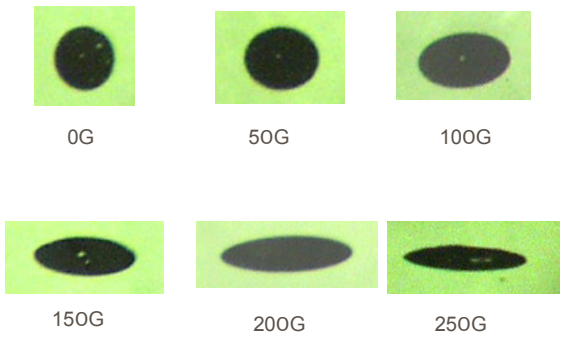

Figure 7: Change of the shape of a magnetic fluid drop (0.36cm^3) under the horizontal magnetic field.

The current supply I to two coils was 2A. Near the upper and lower coils, the drop elongated. This deformation reduced the drag on the drop and it was accelerated.

Change of the shape of a magnetic fluid drop under the magnetic field is shown in Fig. 7. It extended along the magnetic field. In order to avoid the influence of gravity, a horizontal uniform magnetic field was applied to a magnetic fluid drop.

At the middle point between two coils, the external uniform magnetic field cannot force the centre of the magnetic fluid drop inertia. However, due to the magnetic pressure jump takes place on the drop surface, the drop tends to extend along the field. Due to the change of the shape of the drop, the drag on the drop is reduced and the velocity of the drop is increased.

Figure 8 shows the velocity change of the magnetic fluid drop of the same volume 0.81mm^3 at the middle point between two coils as the magnetic field was

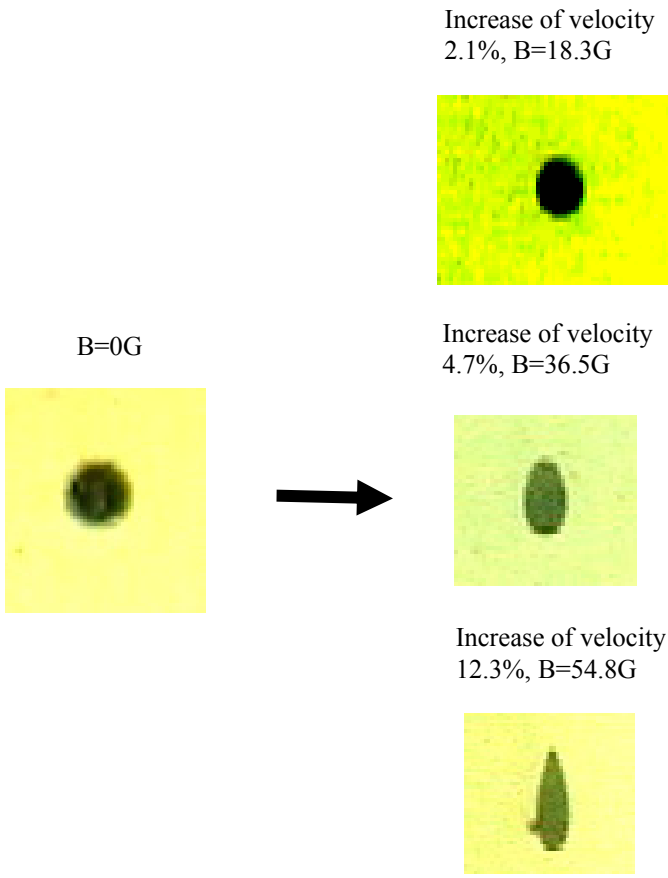

Figure 8: Increase of velocity under the magnetic field at the middle point between two coils (volume 0.81mm^3).

raised. Due to the change in the shape of the drop, the drag on the drop is reduced and the velocity of the drop is increased.

Figure 9 shows the velocity change of the magnetic fluid drop when the same magnetic field is applied at the middle point between two coils for various volumes of magnetic fluid drops. When the external uniform magnetic field is applied, a magnetic pressure jump $\mu_0 M_n^2/2$ takes place on the drop surface. This pressure jump is balanced by increasing the surface curvature at the upper and lower points. The curvature of the larger drop is smaller than that of the smaller drop with the similar shape. Then the larger drop elongated remarkably and the drag on it is reduced.

The velocity change of the magnetic fluid drop when various magnetic fields are applied at the middle point between two coils for various volumes of magnetic fluid drops is shown in Fig. 10. The velocity of larger drop changed more than that of smaller drop.

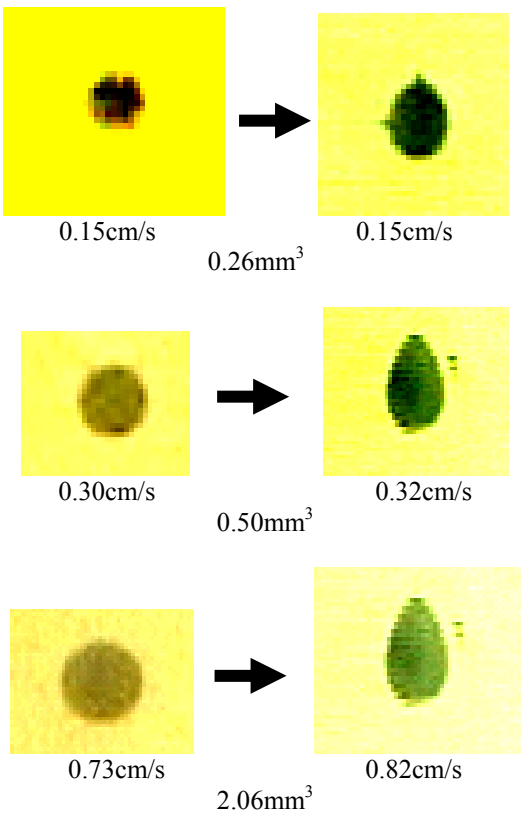

Figure 9: Change in the shape and the velocity of the magnetic fluid drop when the magnetic field [B=18.3G] is applied.

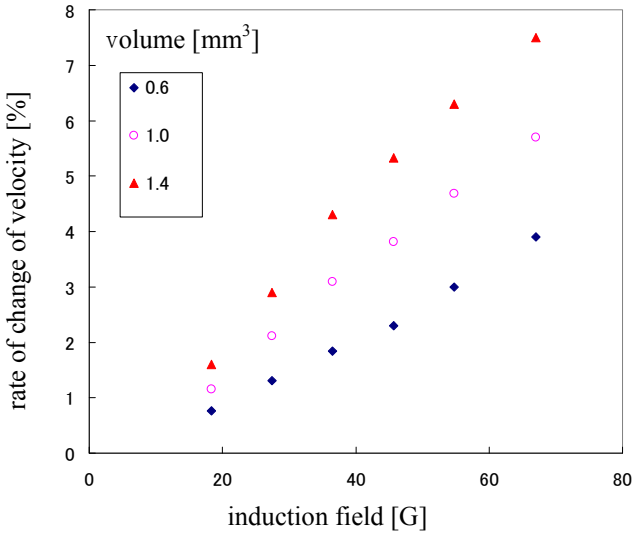

Figure 10: Change of the velocity of the magnetic fluid drop.

4 Conclusion

In the present work experimental results have been obtained on the velocity change of a settling magnetic fluid drop in an incompressible viscous fluid inside a vertical circular cylinder under the influence of the magnetic field.

Near the upper coil, the centre of the drop is forced upwards, but for the extension of the drop and the drag reduction, the velocity of the drop is not always decreased. Near the lower coil, however, the centre of the drop is forced downwards, for the extension of the drop and the drag reduction, the velocity of the drop is increased significantly.

The velocity of a single iron sphere varies in proportion to the gradient of the magnetic field.

At the middle point between two coils, the external magnetic field cannot force the centre of the magnetic fluid drop inertia. However, due to the magnetic pressure jump takes place on the drop surface, the drop tends to extend along the field. Due to the change in the shape of the drop, the drag on the drop is reduced and the velocity of the drop is increased. The velocity change of the magnetic fluid drop when various magnetic fields are applied at the middle point between two coils for various volumes of magnetic fluid drops is obtained. The velocity of a larger drop changed more than that of a smaller drop.

References

[1] Rosensweig, R. E. *Ferrohydrodynamics*, Cambridge Univ. Press, Cambridge, 1985.

[2] Bashtovoy, V. G., Berkovsky, B. M. and Vislovich, A. N. *Introduction to thermomechanics of magnetic fluids*, Springer-Verlag, 1987.
[3] Sero-Guillaume, O. E. and Bernardin, D. Note on a Hamiltonian formalism for the flow of a magnetic fluid with a free surface, J. Fluid Mech., **181**, pp. 381-386, 1987.
[4] Sero-Guillaume, O. E., Zouaoui, D. and Bernardin, D. The shape of a magnetic liquid drop, J. Fluid Mech., **241**, pp. 215-232, 1992.
[5] Morimoto, Y., Akimoto, M., and Yotsumoto, Y., Dispersion state of protein-stabilized magnetic emulsions., Chem. Pharm. Bull. , **30**, pp. 3024-3027, 1982.

The development and water-air two-phase test results of an electrical submersible pump visualization prototype

F. E. Trevisan & M. G. Prado
Department of Petroleum Engineering, University of Tulsa, USA

Abstract

Artificial lift systems are extensively used in the petroleum industry in order to enhance or even initiate the production of oil wells that present insufficient energy to produce naturally. The Electrical Submersible Pump (ESP) is one of the many existing artificial lift techniques and consists of assembling several diffuser type centrifugal pumps in series.

It is common in petroleum field applications to have an inflow of natural gas into the pump intake, which compromises pump performance and reliability. Trying to better understand the interaction between the gas and liquid inside centrifugal pumps is still a challenge and the current investigation tries to help understand this subject.

This research describes the development of a visualization prototype built using original ESP components, applying minimal mechanical and geometrical modifications, with the intent of acquiring visual evidence of the flow patterns that occur inside the pump. Because of these minimal changes to the original pump geometry, the prototype was proven to operate according to the original pump catalogue performance, implying that its hydraulic behaviour was maintained.

Water-air two phase experiments were conducted at different rotational speeds (15, 20, 30 Hz) and non-slip void fractions (up to 5%) while the liquid rate was kept constant at 60% of the maximum rate at the defined shaft speed. High speed video footage was gathered, as well as differential pressure measurements.

The authors identified four water-air flow patterns inside the impeller channels: Dispersed Bubbles, Agglomerated Bubbles, Gas Pocket and Segregated Gas. By comparing the images with the differential pressure data, it

WIT Transactions on Engineering Sciences, Vol 69, © 2010 WIT Press
www.witpress.com, ISSN 1743-3533 (on-line)
doi:10.2495/AFM100421

was confirmed that pump two-phase homogeneous flow head prediction is quite accurate under the Dispersed Bubble pattern. It was concluded that the Agglomerated Bubble pattern is responsible for the initial head degradation and that the surging event coincides with the Gas Pocket structure, indicating that this is an interface instability problem.

Keywords: centrifugal pump, flow visualization, two-phase flow, surging, flow patterns.

1 Introduction

The Electrical Submersible Pump (ESP) is one of the many existing artificial lift techniques used in the petroleum industry. It consists of a series of small diameter diffuser type casing centrifugal pumps. ESPs are mainly known for their capacity of handling high volumes and are widely used. Their applications vary from producing high productivity oil wells onshore and offshore to dewatering coal bed methane and gas wells.

The use of ESPs, or any other centrifugal pump for that matter, on liquid single phase applications is well understood and the knowledge necessary for these situations is consolidated. However, as is common in the petroleum industry, the presence of a compressible phase, such as natural gas, will also modify the hydraulic performance of these types of pump.

Several studies have been conducted to visualize and simulate pump performance under the presence of free gas; the majority of these studies focus on centrifugal pumps used by the nuclear industry, motivated by the flux of water and water vapour in their systems. Murakami and Minemura [1] used a semi-open type pump with transparent casing. The observed flow patterns were recorded photographically, and bubble diameter measurements could be made inside the impeller. Patel *et al.* [2] also observed two-phase flow in centrifugal pumps by testing a 1/20 scale prototype of a primary coolant pump used in nuclear reactors, to measure bubble sizes. Sekoguchi *et al*. [3] used a pump equipped with a closed radial-flow impeller to visualize the flow patterns and also installed eight needle tip void probes to measure bubble frequency and later examined the slip ratio between the fluids.

ESPs, however, are different from these pumps, they are smaller in diameter, they are diffuser-type rather than volute-type design and consist of several stages, whereas single-staged pumps are used in the nuclear industry. ESP two-phase investigations started with Lea and Bearden [4] by performing tests on three different impeller designs, two radial and one mixed flow type. The authors also used two different fluid combinations, first water and air and later diesel oil and carbon dioxide. Sachdeva [5] proposed a one-dimensional model for single and two-phase performance of an ESP. In his work, derivation of the governing equations was done and later solved numerically. Pessoa [6] published an extensive experimental investigation with two-phase flow performance of a mixed flow type impeller ESP. Duran [7] performed two-phase experiments on an Electrical Submersible Pump with water. The objective of the experiments

was to measure the performance of a specific stage, observing its pressure increment at several stage intake pressures and water and air flow rates.

More recently, flow modelling complemented by visualization in these types of centrifugal pumps have been investigated by Estevan [8] who used an ESP impeller and a modified Plexiglas diffuser to observe air-water flow inside the pump. The author noticed that accumulation of gas in the pressure side of the blade and two distinct flow patterns occurring at different sections of the impeller. Estevan used the visual observations to develop a one-dimensional model. Barrios [9] also built a visualization prototype based on an ESP impeller and modified diffuser design. The author used a high speed camera to observe the flow patterns and take bubble size measurements in order to complete the proposed one-dimensional model. Later, Gamboa [10] built a visualization prototype to obtain images used to explain the hydraulic behaviour and illustrate the flow pattern map developed through pressure generation data, collected in a large scale experiment. Both pumps used had the same geometrical properties; the visualization prototype was built by minimally altering the large scale pump stages. However, because of this minimal alteration, the author could only observe the impeller discharge and diffuser intake.

These previous work indicated that there was a trade-off between visualization and geometrical integrity. Therefore the objective of this work was to develop a visualization prototype that allowed two-phase flow visualization inside the impeller with minimum alteration on the pump geometrical properties, thus unchanging its hydraulic performance.

By building such prototype water single phase tests were conducted to validate this premise. Water-air two-phase flow tests were later conducted where pressure generation data and high speed video footage of the flow patterns inside the impeller were collected.

2 Experimental description

2.1 Prototype development

The visualization prototype had the primary intent of imitating the hydraulic behaviour of an actual ESP. This could only be obtained by introducing minimal geometrical alterations to actual ESP stages while installing visualization windows. The original pump stage from which the prototype was developed was the Baker Huges Centrilift FC1600 model. It was chosen for its large radius, which provided reasonable viewing area, and for its low capacity, which respected flow loop limitations. Figure 1 presents a sketch of proposed alterations.

It can be observed that only the entrance (lower section) of the top diffuser was modified. Figure 2 presents the development of this component; on the left is the original diffuser, in the middle this piece is shown with the necessary alterations and on the right it is shown with the Plexiglas installed. The lower external walls were machined off, exposing the diffuser's internal blades and channels entrance. The Plexiglas piece installed recreated the original external wall geometry and accommodated the upper mechanical seal.

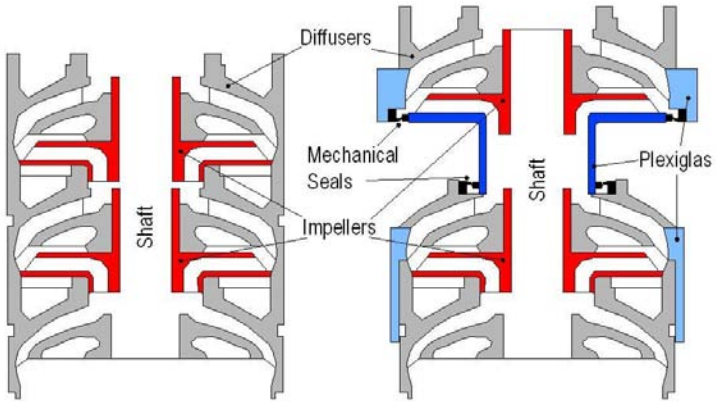

Figure 1: Original ESP (left) modified ESP (right).

Figure 2: Top diffuser development process.

Figure 3: Impeller development process.

Figure 3 presents the impeller development process. On the left is the original piece, in the middle is the impeller with its bottom shroud removed and on the right the piece is shown with the Plexiglas installed, with the mechanical seals' stainless steel rings in place. The original impeller entrance diameter and the original shroud angles were preserved when building the Plexiglas attachment.

The bottom diffuser had the most modifications of all components. In order to accommodate the lower mechanical seal and improve the visualization window, its top section was removed and internal diameter enlarged, however the internal channels fluid discharge remained intact. The external wall was machined off, exposing the lower sections of the diffuser blades and channels; however, the

Plexiglas window installed on the lower part of this component had to accommodate the impeller and diffuser from the stage bellow. Figure 4 presents the original diffuser and in its final state.

The entrance diffuser assembly process is presented in Figure 5, where an unaltered stage was assembled prior to the visualization stage.

The mechanical seals used were custom built for this application. They consisted of a stainless steel ring, installed on the top and bottom of the impeller Plexiglas shroud, and a lip seal design made out of PolyShell®-03 (graphite filled PTFE) placed at the top diffuser entrance and bottom diffuser discharge.

In order to hold all the components sealed in place and connected to the stand that held the motor, a PVC casing was machined for both upper and lower diffusers. Figure 6 presents a sketch of these components as well as the pressure taps location used for head generation data collection. This information was collected only for the visualization stage (between taps PT1 and PT2).

2.2 Experimental loop and procedure

In order to make the necessary measurements, an ESP visualization prototype was installed in a closed circuit loop. Figure 7 provides a graphical representation of the experimental facility built.

Figure 4: Bottom diffuser development process.

Figure 5: Entrance stage assembly process.

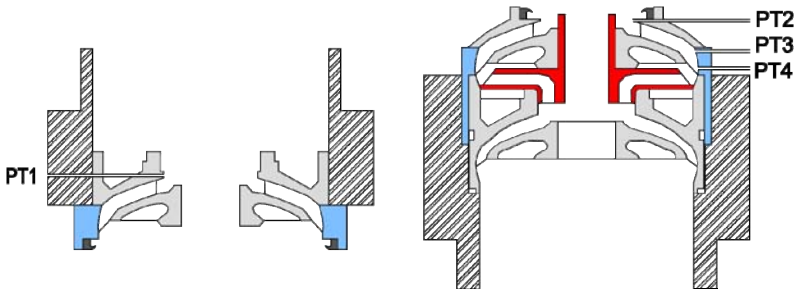

Figure 6: Prototype PVC casing sketch, upper section (left) and lower section (right).

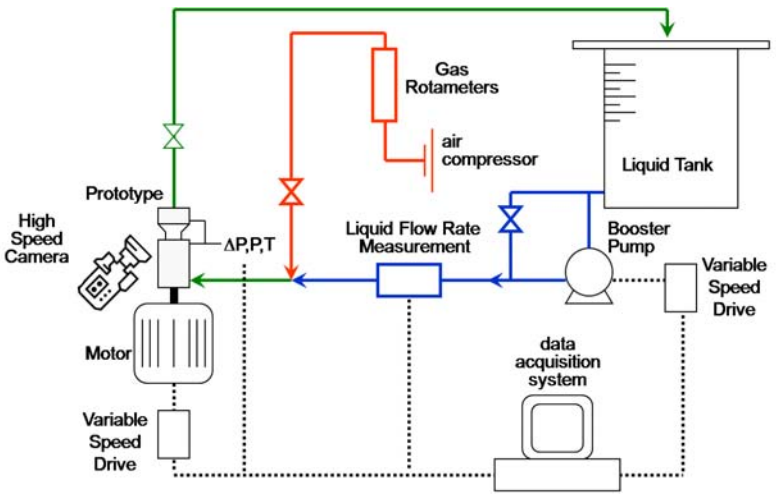

Figure 7: Visualization loop configuration.

The two-phase testing procedure was based on previous experience and followed the so called "Surging Test" method, in which the pump rotational speed, visualization stage inlet pressure and liquid flow rate are kept constant while the gas flow rate is increased and the pressure increment generated by the visualization stage is measured. The liquid flow rate used for each test was determined as 60% of the maximum liquid rate at the specified shaft speed. This value is commonly used in the industry as a high efficiency pump operational point.

The non-slip void fraction, given by the ratio between the gas flow rate and the total mixture flow rate, varied from 0 to 5%. Three different shaft speeds were used during the two-phase tests: 15, 20 and 30 Hz.

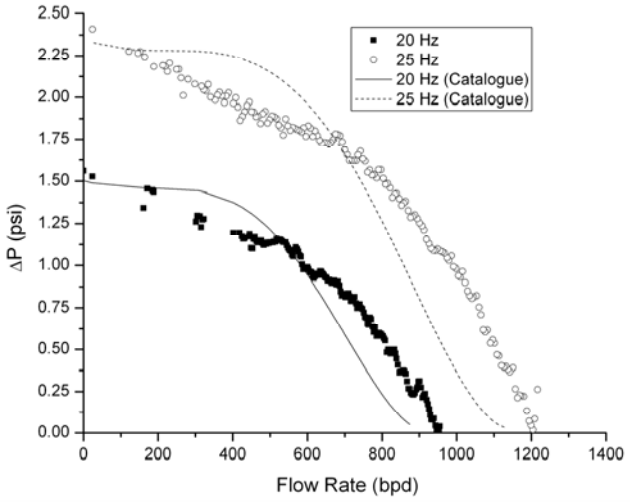

Figure 8: Prototype versus catalogue performance.

3 Results and analysis

3.1 Single-phase tests

The first experiments conducted were single-phase tests at two different rotational speeds: 20 and 25 Hz. The purpose of these experiments was to characterize the pump, comparing it to its original design catalogue behaviour.

From the comparison presented in Figure 8, it can be seen that the prototype presents a similar behaviour as the original pump, especially at the shut-in pressure and at values around the 60% of the maximum flow rate. However, some minor differences can be observed which may be explained by the different recirculation patterns inside original ESP and prototype, especially because the first presents a floating impeller and the second a fixed impeller.

Shut-in and open flow single phase tests were also conducted with the intent to prove that the prototype obeyed the Affinity Laws, thus proving that it operated as a centrifugal device. Figure 9 presents the experimental points as well as the quadratic fit line and linear fit line found for the shut-in pressures and maximum flow rates, respectively.

3.2 Two-phase tests

Based on the high speed video footage taken during the water and air two-phase flow tests, four flow patterns were identified and their descriptions are as follows.

Bubbly Flow: At low gas flow rates, independent of the liquid rate or rotational speed, this pattern was observed. It consists of small air bubbles rising

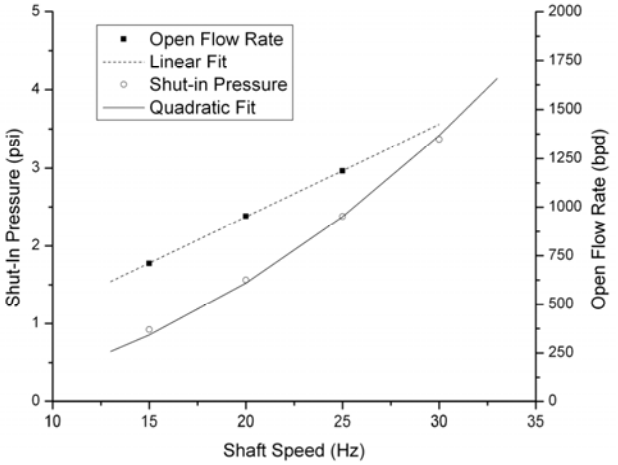

Figure 9: Water shut-in and maximum flow rates versus rotational speed.

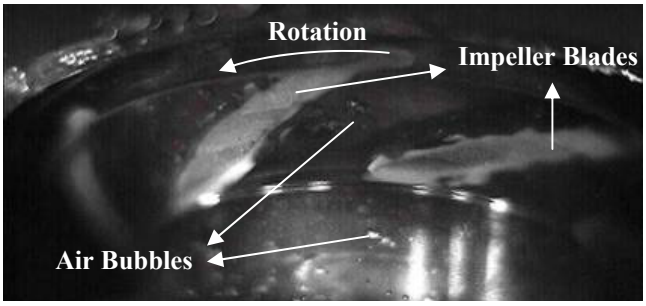

Figure 10: Bubbly flow pattern.

through the impeller entrance and being redirected when entering the impeller channels. Figure 10 presents a still image obtained from the high speed video.

The gas rate influenced mainly the quantity of bubbles observed, while their size and shape varied from spherical for smaller entities to prolate ellipsoidal for larger units. Eventually even larger bubbles were seen with an irregular shape rising through the impeller entrance; however, they would break up into smaller units upon reaching the impeller channel.

Agglomerated Bubbles: This flow pattern was obtained by increasing the gas flow rate once at the bubbly flow pattern. It is characterized by the presence of agglomerated bubbles at the impeller blade leading end and pressure side. Figure 11 presents the impeller channels under this flow pattern.

Gas Pocket: By further increasing the gas flow rate, it was noticed that the gas pocket formed by bubble coalescence from the previous flow structure. This larger stationary entity occupied a significant section of the impeller channel, restricting the liquid's flow path. The stationary bubble gas-liquid interface was

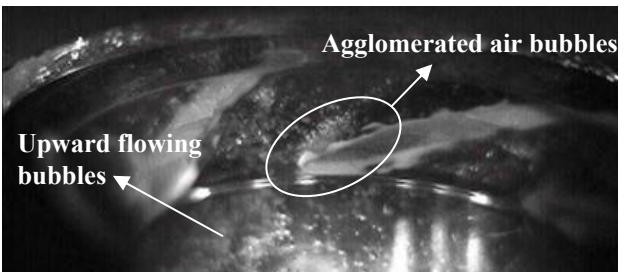

Figure 11: Agglomerated bubbles.

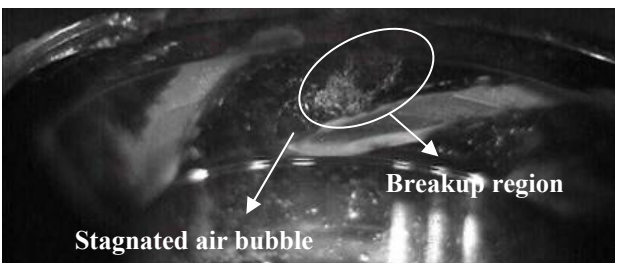

Figure 12: Gas pocket pattern.

observed to be unsteady, indicating instability. Gas bubbles rising through the impeller entrance were dragged with the water through its reduced flow area or coalesced with the stationary gas pocket which led to break up at its trailing end. Figure 12 presents a photograph of this observed pattern.

It was also observed that some larger bubbles, with irregular shape, rose through the impeller entrance. However, in this case, instead of breaking up as in previous cases, they either coalesced with the gas pocket or passed through the impeller channel intact. This indicates that the stationary gas bubble reduces the kinetic energy transferred to the liquid, which causes the larger bubbles not to break up.

Segregated Gas: By further increasing the gas flow rate, it was possible to observe that the gas pocket had been extended to the impeller outer radius. As before, the gas-liquid interface remained unstable, indicating bubble break up at the stationary element's trailing end. Figure 13 presents the described flow structure.

By following the experimental procedure described previously, differential pressure data was collected for the surging tests at rotational speeds of 15, 20 and 30 Hz. Figure 14 presents the information collected by plotting on the horizontal axis the no-slip void fraction and on the vertical axis the normalized differential pressure.

This figure shows the effect of rotational speed on the pump two-phase performance. At low void fraction values, all curves present relatively small deviations from its homogeneous flow prediction, since at these gas rates the air

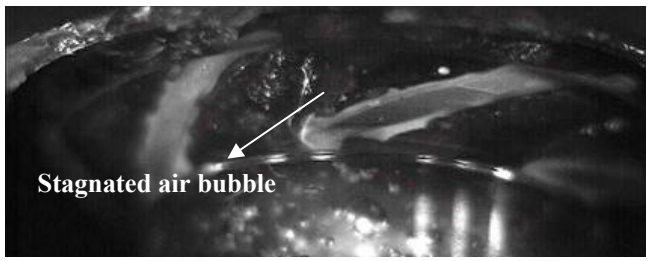

Figure 13: Segregated gas pattern.

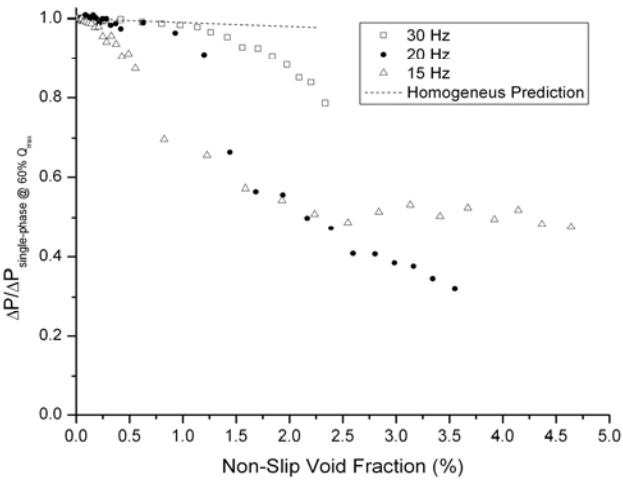

Figure 14: Water-air surging test results.

bubbles are predominantly small and flow with the liquid. By increasing air injection, a non-linear, but continuous, deviation from the homogeneous prediction is observed. Further increase of the no-slip gas fraction caused the surging phenomenon to occur, indicated by the curves sudden inclination change and in this case seen as a discontinuity. It can be observed that at 15 and 20 Hz the surging occurs at void fractions of 0.55 and 1.3%, respectively, while on the 30 Hz curve surging was not reached.

By combining the same plot style as Figure 14 with the flow pattern identification used previously, Figure 15 was obtained. This graph indicates adequate association of the Bubbly Flow pattern with the homogeneous model prediction. It can also be observed that the Agglomerated Bubbles pattern, where slip between the phases was observed, is strongly associated with head degradation thus deviation from the homogeneous predictions.

It can also be seen that the two occurrences of the Gas Pocket pattern correspond to void fractions of 0.55 and 1.44 for rotational speeds of 15 and

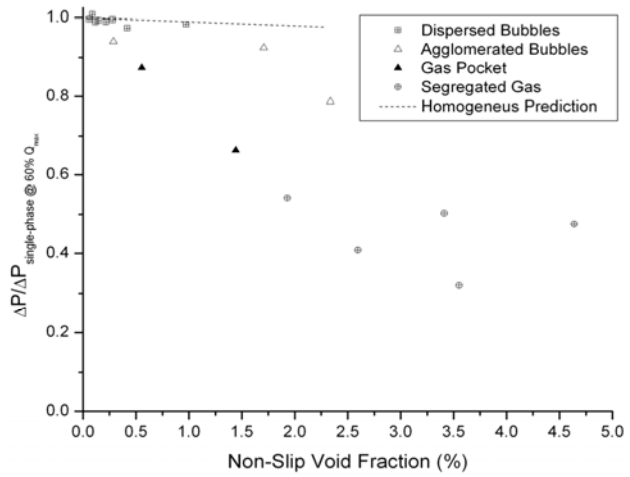

Figure 15: Flow pattern occurrence on data.

20 Hz, respectively, previously identified as surging points. However, for 15 Hz it corresponds to a pre-surging state, while for 25 Hz for a post-surging condition. This indicates that this pattern holding the pre-surging differential pressure is an unstable equilibrium point. Thus, the surging phenomenon is a shift on the equilibrium position to a lower differential pressure value, allowing the same flow pattern to occur at two different differential pressure conditions.

The Segregated Gas flow structure is responsible for the most head degradation measured. In this case, the stationary gas bubble alters the impeller geometry seen by the liquid, drastically depredating performance.

4 Conclusions

From this research the following conclusions could be made: a visualization prototype was successfully built with minor geometrical alterations to the original ESP design, imposing a very similar hydraulic performance; the liquid turbulence maintains small air bubble diameters, which are dragged with the water through the impeller; slip between the phases occurs in the Agglomerated Bubbles pattern, observed in the video footage and in head degradation data; surging phenomenon occurs in the Gas Pocket pattern. The images and data indicate that it is a transient phenomenon event and probably do to interfacial instability.

Acknowledgements

The present work was supported by CNPq, a Brazilian Government entity dedicated to scientific and technological development. The authors also would like to thank Baker Hughes Centrilift for their material and technical support.

References

[1] Murakami and Minemura. Effects of Entrained Air on the performance of a centrifugal pump. *Bulletin of the JSME*., Vol. 17, No 110, August 1974 (1st report).
[2] Patel, Bharatan and Runstadler, Peter Jr. Investigations into the Two-Phase Behavior of Centrifugal Pumps. Polyphase Flow in Turbomach, Symp presented at Winter Annual Meeting of the ASME. Dec 10-15 1978.
[3] Sekoguchi K., Takada S and Kanemori Y. Study of Air-Water Two-Phase Centrifugal Pump by Means of Electric Resistivity Probe Technique for Void Fraction Measurement (1st Report). *Bulletin of JSME.* Vol. 27, No 227, May 1984.
[4] Lea J. F. and J. L. Bearden. "Effect of Gaseous Fluids on Submersible Pumps" paper presented at SPE 55th Annual Fall Technical Conference and Exhibition, SPE 9218, (September 1980).pp: 2922-2930.
[5] Sachdeva R. Performance of electrical Submersible pump in Gassy Wells. SPE Paper. 22767. 55.
[6] Pessoa, R. "Experimental Investigation of Two-Phase Flow Performance of Electrical Submersible Pump Stages", MS Thesis, The University of Tulsa (2001).
[7] Duran, Javier. "Pressure Effects on ESP Stages' Air-Water Performance", M.Sc. Thesis, The University of Tulsa (2003)
[8] ESTEVAM, Valdir. A Phenomenological Analysis about centrifugal pump in two-phase flow operation. *Campinas: Faculdade de Engenharia Mecânica, Universidade Estadual de Campinas,* 2002. 265 p. Thesis (PhD)
[9] Barrios, Lisset. "Visualization and Modelling of Multiphase Performance inside an ESP". PhD Dissertation, The University of Tulsa (2007)
[10] Gamboa, Jose. "Prediction of the Transition in Two-Phase Performance of an Electrical Submersible Pump". PhD Dissertation, The University of (2008)

Simulation of multiphase flows with variable surface tension using the Lattice Boltzmann method

S. Stensholt
University of Bergen, Department of Mathematics, Norway

Abstract

Methods for implementing variable surface tension on two popular Lattice–Boltzmann models, the original gradient-based chromodynamic model, and the Shan–Chen model, are explored and examined. The experiment, inspired by the work of Greenspan, consists of reducing the surface tension at two poles of a circular droplet due to a diffusive solute (surfactant). Both Lattice Boltzmann models are able to simulate the expected initial deformation where the droplet is stretched along the pole axis, and contracts at the equator. We observed no furrowing to the droplet, which verifies the work of He and Dembo who concluded that variation in surface tension cannot alone account for such furrowing. We were able to simulate the process as the surfactant diffuses over the entire interface and the spatial variation in surface tension vanishes. The droplet reverts back to its original circular shape with the overall surface tension reduced. Variable surface tension is easier to implement with the chromodynamic model. The physically direct Shan–Chen model, which has superior isotropic qualities, can also be used for variable surface tension. However, coordinating the decline of the surface tension with the reduction in the separation forces is a more delicate matter, and the diffusivity of the interface increases if the surface tension is weakened.
Keywords: Lattice Boltzmann, variable surface tension, droplet deformation.

1 Introduction

The study of fluid flow with variable surface tension has seen multiple applications, including biological fields related to cell division [4–6], and oil reservoir dynamics.

WIT Transactions on Engineering Sciences, Vol 69, © 2010 WIT Press
www.witpress.com, ISSN 1743-3533 (on-line)
doi:10.2495/AFM100431

In this article, we apply the Lattice Boltzmann method to study this effect. We consider two popular models, the chromodynamic method, and the Shan–Chen method.

In order to simulate the effects of microemulsions, lattice Boltzmann models with amphiphile surfactants are largely based on the free energy model of Orlandini *et al.* [7], see for example references [8–11]. The model used here is simpler, since the purpose is primarily to investigate the deformative effects of surface tension rather than the effects on the interface structure. Lattice Boltzmann methods with variable surface tension have also been employed by Farhat and Lee [12] in order to simulate the biconcave shape of red blood cells.

If the surface tension is constant, all droplets will attain a circular shape, but if surface tension varies along the interface, the interface curvature will be greater where the surface tension is low. By manipulating the surface tension, it is possible to create deformations to an initially circular droplet.

In this article we employ an experiment based on that conducted by Greenspan [3], where surface tension-reducing surfactant is applied to two poles of a droplet. The expected deformation is an elongation along the axis and a contraction at the equator. Greenspan even demonstrated furrowing to the droplet, although Sapir and Nir [13], He and Dembo [4], and Li and Lubkin [14] were unable to produce deformations as large as this.

Our main goal with conducting this experiment is to demonstrate the validity of our variable surface tension methods. In addition we wish to illustrate the relative ease with which a solute surfactant can be applied in the method.

2 Lattice Boltzmann method

The Lattice Boltzmann method was introduced by McNamara and Zanetti [15] as an extension to the lattice gas cellular automata. The method can alternately be derived by discretizing the Boltzmann equation [16]. The first method to extend the method to handle multiphase flows was introduced by Gunstensen *et al.* [1] in 1991, and an alternate method was proposed by Shan and Chen in 1993 [2].

Our interest is in two component multiphase flow. The components are labelled "red" (superscript R) and "blue" (superscript B). An arbitrary component is labelled superscript s, while we let $\hat{s}$ represent the other component.

Lattice Boltzmann methods aim to simulate the evolution of the discrete distribution functions $f_i^s(\boldsymbol{x}, t)$, which tells how many particles of mass 1 are moving along vector $\boldsymbol{e}_i$ at site $\boldsymbol{x}$ at time t. Summing the distribution function over all i will yield the mass density, summing $f_i^s \boldsymbol{e}_i$ over all i will yield the particle momentum. As long as we are away from the interface, we use the ideal gas equation

$$p = (\rho^R + \rho^B)c^2, \tag{1}$$

for pressure where $c^2 = \frac{1}{3}$ is the square of the speed of sound.

We have employed the D2Q9 lattice [17], which has two dimensions and nine possible velocities at each site, given by

$$\boldsymbol{e_i} = \begin{cases} (0,0), & i = 0, \\ \left(\cos\frac{(i-1)\pi}{2}, \sin\frac{(i-1)\pi}{2}\right)\Big) & i = 1,\ldots 4, \\ \sqrt{2}\left(\cos[\frac{(i-5)\pi}{2} + \frac{\pi}{4}], \sin[\frac{(i-5)\pi}{2} + \frac{\pi}{4}]\right) & i = 5,\ldots 8. \end{cases} \tag{2}$$

The equation to update the distribution function is given by

$$f_i^s(\boldsymbol{x} + \boldsymbol{e}_i, t+1) = f_i^s(\boldsymbol{x}, t) + \Omega(f_i^s, f_i^{s_1}, f_i^{s_2}, \ldots), \tag{3}$$

where the first terms handle propagation (streaming) of particles, while the collision term Ω deals with interparticle collisions, including the generation of surface tension and phase separation.

In the chromodynamic model by Gunstensen, the process is to first create surface tension by increasing the proportion of particles moving normal to the interface, and then enforce phase separation through a recolouring step. Central to this idea is the concept of the color gradient $\boldsymbol{F}$

$$\boldsymbol{F}(\boldsymbol{x}, t) = \sum_{i=1}^{8} \boldsymbol{e}_i(\rho^R(\boldsymbol{x} + \boldsymbol{e}_i) - \rho^B(\boldsymbol{x} + \boldsymbol{e}_i)). \tag{4}$$

The collision operator Ω^s can be written as $\Omega^s = \Omega 3^s[\Omega 1^s + \Omega 2^s]$ [18], where $\Omega 1^s$ is the single relaxation time (BGK [19]) operator

$$\Omega 1^s = -\frac{1}{\tau^s}(f_i^s - f_i^{s(eq)}), \tag{5}$$

with local equilibrium distribution $f_i^{s(eq)}$ given by

$$f_i^{s(eq)}(\boldsymbol{u^s}) = w_i\rho\left(1 + \frac{3(\boldsymbol{e}_i \cdot \boldsymbol{u^s})}{c^2} + \frac{9(\boldsymbol{e}_i \cdot \boldsymbol{u^s})^2}{2c^4} - \frac{3}{2}\frac{(u^s)^2}{c^2}\right) \tag{6}$$

where $\boldsymbol{u}^s$ is the macroscopic velocity of component s. The weights w_i are $w_0 = 4/9, w_{1,\ldots,4} = 1/9, w_{5,\ldots 8} = 1/36$. Surface tension is generated by $\Omega 2$ and is given by [20]

$$\Omega 2_i^s = \frac{A}{2}|\boldsymbol{F}|\left(w_i\frac{(\boldsymbol{e}_i \cdot \boldsymbol{F})^2}{|\boldsymbol{F}|^2} - B_i\right), \qquad i = 0,\ldots,8, \tag{7}$$

with A being a parameter for surface tension, and B_i are the constants $B_0 = -4/27, B_{1,\ldots,4} = 2/27$ and $B_{5,\ldots,8} = 5/108$. Surface tension is proportional to the parameter A in (7), and a variation in surface tension can therefore be conveniently applied by adjusting A.

The recolouring algorithm, which accounts for phase segregation, can be applied through the formula given by Latva-Kokko and Rothman [21]

$$\Omega 3_i = \begin{cases} f_i^R &= \phi^R f_i + \phi^R \phi^B f_i^{eq}(\rho, 0)\cos\theta, \\ f_i^B &= \phi^B f_i - \phi^R \phi^B f_i^{eq}(\rho, 0)\cos\theta \end{cases}, \tag{8}$$

where ϕ^R and ϕ^B are the fraction of particles which are red and blue respectively.

In the Shan–Chen model, the collision operator is basically the BGK operator (5), but the velocity $\boldsymbol{u}^s$ used to calculate f_i^{eq} is perturbed to $\boldsymbol{u'}^s$ by a repulsive force between particles of opposite color

$$\rho \boldsymbol{u'}^s = \rho \boldsymbol{u}^s - \psi^s(\boldsymbol{x}, t) G \sum_{i=1}^{8} w_i \psi^{\hat{s}}(\boldsymbol{x} + \boldsymbol{e}_i, t)\boldsymbol{e}_i, \tag{9}$$

where ψ^s simply can be defined as ρ^s in the multicomponent model. The parameter G controls surface tension and phase separation. If G is large enough, the separation forces will overcome the diffusion and yield separate phases. The critical value of G for separation is a function of the proportion of each phase [22].

The Shan–Chen model does not conserve momentum on each individual site as the chromodynamic model does, but if we maintain symmetry between two interacting sites we maintain global conservation of momentum [23]. A practical drawback to the Shan–Chen model is the difficulty in determining the surface tension *a priori*. The surface tension generally rises with G, but it is not a convenient proportional relationship as there was for the chromodynamic model [24].

For both the chromodynamic and Shan–Chen models, solute flow is implemented by introducing a third component with its own distribution function g. This component evolves according to an equation like (3), with a relaxation time τ^g which controls its diffusivity, but it does not contribute to the calculation of $\boldsymbol{u}$ [25]. In order to keep the solute on the interface, we implemented a force perturbing the solute's velocity $\boldsymbol{u}$ to $\boldsymbol{u'}$ by

$$\boldsymbol{u'} = \boldsymbol{u} + a\left(\sum_{i=1}^{8} w_i \phi^R(\boldsymbol{x} + \boldsymbol{e}_i)\phi^B(\boldsymbol{x} + \boldsymbol{e}_i)\boldsymbol{e}_i \right), \tag{10}$$

where a is a positive constant which we set to 10. This is large enough to keep almost all the solute on the surface, but not so large that it destabilizes the model.

For both models, the surface tension can be found by measuring the radius r and pressure difference Δp between a circular droplet's interior and exterior. The surface tension parameter σ is then given by Laplace's law $\sigma = r\Delta p$.

3 Simulation and discussion

In our simulation, we started with an initially stable droplet of radius 10.4 in units of grid spacing. For the chromodynamic test, we set the parameter $A = 0.10$ while

we set the parameter $G = 2.0$ for the Shan–Chen model. These choices yield almost the same initial pressure difference of $\Delta p = 0.122$ for the chromodynamic model and 0.121 for the Shan–Chen model.

At $t = 0$ a surfactant solute is applied at two nodes, at opposite ends of the droplet, with an initial concentration of $C = 1$. Following the lead of Greenspan, we attempt to let the reduction in surface tension be proportional to the concentration of surfactant, although we do not let it go below zero. The new and reduced parameter for the chromodynamic test is therefore

$$A(\boldsymbol{x}) = \max(0, A_0 - \zeta C(\boldsymbol{x})), \tag{11}$$

where the parameter ζ controls how effective the solute is at reducing the surface tension.

Reducing the surface tension in the Shan–Chen model is a more delicate matter. As mentioned in section 2, maintaining symmetry between sites is essential, so introducing a spatial variation to the parameter G in equation (9) by

$$G(\boldsymbol{x}) = \max(0, G_0 - \gamma C(\boldsymbol{x})). \tag{12}$$

would violate the conservation of momentum unless $C(\boldsymbol{x})$ is constant in space. However, we can achieve a result similar to (12) by multiplying the ψ^s values in (9) with a factor $d(\boldsymbol{x})$, where $0 < d < 1$ reduces the surface tension and $d > 1$ increases the surface tension. If we set

$$d(\boldsymbol{x}) = \max(0, \sqrt{1 - \gamma C(\boldsymbol{x})/2}), \tag{13}$$

we have the same result with constant C as (12) would have given us.

As mentioned, σ is not proportional to G, since much of the separation force is used to overcome diffusion. Chin *et al.* did however indicate a linear relationship between G and σ for moderate G, and some experiments we have conducted indicate that σ is roughly proportional to $G - 1/\rho$. We therefore estimate that surface tension vanishes when

$$C \geq \frac{1}{\gamma}\left(G - \frac{1}{\overline{\rho}}\right), \tag{14}$$

where $\overline{\rho}$ is the average density, equal to 1 in our experiments. We set the parameters $\zeta = 2.5$ and $\gamma = 25$ so that both these models give zero surface tension for $C \geq 0.04$. The relaxation time τ^g for the solute species is 1. The evolution of the droplets' shapes and surfactant concentrations are shown in figures 1 and 2 for the tests with the chromodynamic and Shan–Chen models respectively.

In the chromodynamic model, the deformations are relatively small, but are clearly noticeable at $t = 150$. When the surfactant is evenly distributed, there is no longer any variation in surface tension, and the droplet reverts back to the original circular shape, as seen for $t = 500$. At $t = 2000$ (not pictured) the pressure difference has dropped to 0.0107 (we recall that $\Delta p = 0.0122$ at $t = 0$).

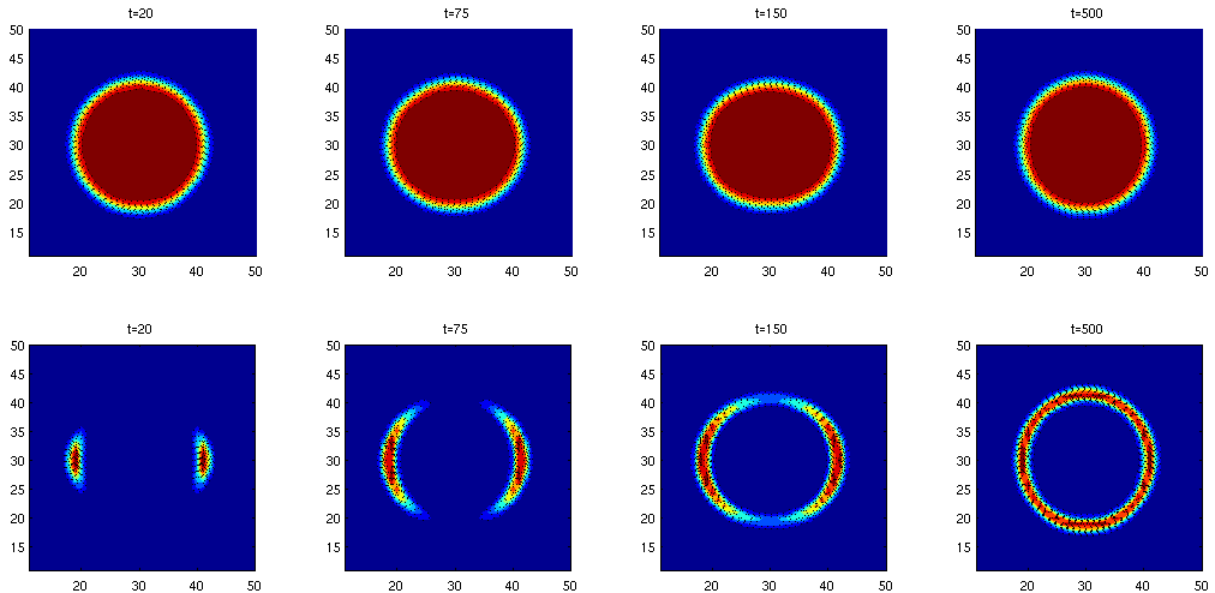

Figure 1: Evolution of the droplet (top) and concentration of surfactant (bottom) for the test with the chromodynamic model. Snapshots taken at $t = 20$, $t = 75$, $t = 150$, and $t = 500$.

WIT Transactions on Engineering Sciences, Vol 69, © 2010 WIT Press
www.witpress.com, ISSN 1743-3533 (on-line)

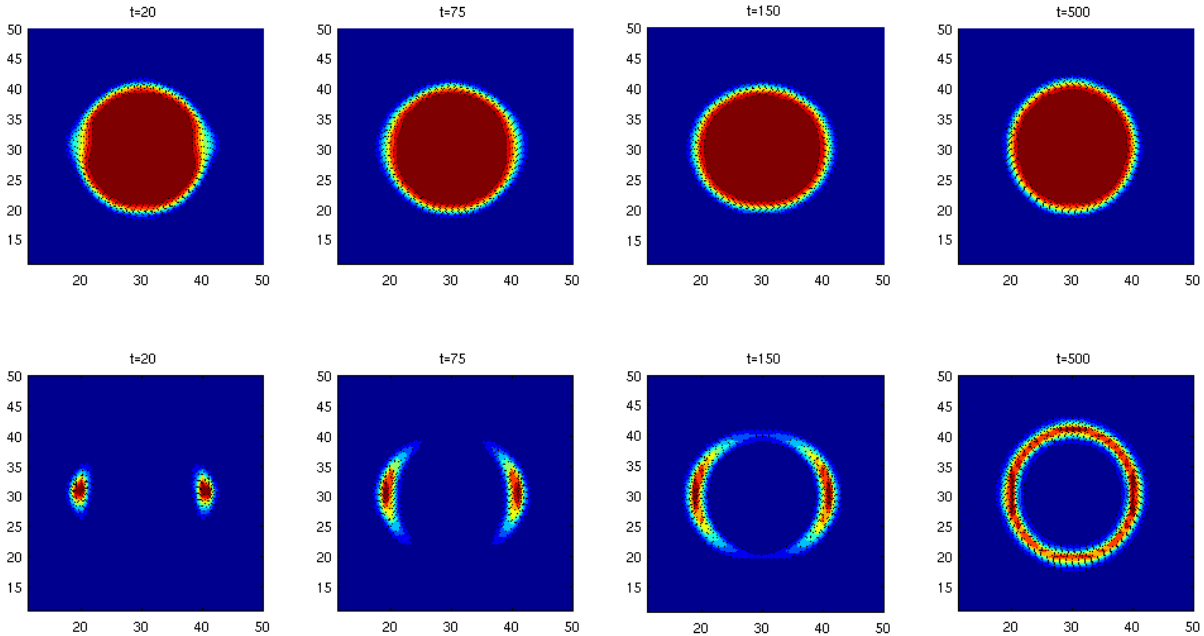

Figure 2: Evolution of the droplet (top) and concentration of surfactant (bottom) for the test with the Shan–Chen model. Snapshots taken at $t = 20$, $t = 75$, $t = 150$, and $t = 500$.

WIT Transactions on Engineering Sciences, Vol 69, © 2010 WIT Press
www.witpress.com, ISSN 1743-3533 (on-line)

A major difference between the chromodynamic method and the Shan–Chen method is that the former scheme enforces surface tension and phase separation in separate operations, (7) and (8), while these effects are intimately coupled together in the Shan–Chen method through the forcing terms in (9). Therefore, in figure 2 we see diffusion occurring between the red and blue phases once the surfactant is applied.

The final reduction in pressure difference was almost identical to that observed from the chromodynamic model, with the pressure difference dropping from 0.0121 at $t = 0$ to 0.0108 at $t = 2000$ when the droplet has restabilized.

When the surface tension is weakened at the poles of the droplet, there will be a flow towards the weakened interface, reducing the number of particles at the equator. The result is an elongation along the polar axis and a contraction of the equator [3]. This expected deformation was successfully reproduced by our experiment. Greenspan also observed the droplet's reversion to circular shape with a reduced surface tension as the surfactant diffused over the entire interface.

Neither droplet showed any signs of furrowing or cleavage to the droplet, and the deformation was in both cases fairly small. Although Greenspan's laboratory experiment did show furrowing for certain cases, He and Dembo [4] showed that surface tension variation alone cannot account for such furrowing.

4 Conclusion

We have demonstrated ways to implement variable surface tension with both the chromodynamic and Shan–Chen lattice Boltzmann models. Comparing the two models, we think variable surface tension is easier to implement with the chromodynamic model because of the convenient relationship between the surface tension and the parameter A in (7). Implementing variable surface tension with the Shan–Chen model is nonetheless possible if we keep in mind the need to maintain symmetry between sites, and remember that the surface tension vanishes when the concentration exceeds the inequality (14).

The Shan–Chen model is known to possess superior isotropic qualities, and adherence to Laplace's law [26]. Weakening the surface tension in the Shan–Chen method does entail weakening of the phase separation as well, which produces a diffusive interface as observed in figure 2 (top left).

The purpose of our method was to simulate the effects of variable surface tension, not any emulsification process. In order to simulate emulsification, the free energy method is a more circumspect approach, although a more complex representation of the surfactant can be used for the Shan–Chen model, as seen for example in references [27] and [28].

The deformations we observed are relatively small, affirming the conclusions found by He and Dembo [4] who found that surface tension variations alone will generally not yield large deformation or furrowing.

Lattice–Boltzmann methods allow for easy simulation of solutes, a feature which we exploited by implementing the surfactant as a solute.

Acknowledgements

The author thanks his advisors Alf Øien and Magne Espedal for helpful discussions and for reviewing the manuscript.

References

[1] Gunstensen, A.K., Rothmann, D.H., Zaleski, S. & Zanetti, G., Lattice Boltzmann model of immiscible fluids. *Phys Rev A*, **43(8)**, pp. 4320–4328, 1991.
[2] Shan, X. & Chen, H., Lattice Boltzmann model for simulating flows with multiple phases and components. *Phys Rev E*, **47(3)**, pp. 1815–1820, 1993.
[3] Greenspan, H.P., On the Deformation of a Viscous Droplet Caused by Variable Surface Tension. *Stud Appl Math*, **57(1)**, pp. 45–58, 1977.
[4] He, X. & Dembo, M., Numerical simulation of oil-droplet cleavage by surfactant. *Journal of Biomechanical Engineering*, **118(2)**, pp. 201–209, 1996.
[5] Greenspan, H.P., On The Dynamics of Cell Cleavage. *J theor Biol*, **65**, pp. 79–99, 1976.
[6] Lubkin, S.R. & Li, Z., Force and deformation on branching rudiments: cleaving between hypotheses. *Biomechan Model Mechanobiol*, **1(1)**, pp. 5–16, 2002.
[7] Orlandini, E., Swift, M. & Yeomans, J., A Lattice Boltzmann Model of Binary-Fluid Mixtures. *Europhys Lett*, **32(6)**, pp. 463–468, 1995.
[8] Lamura, A. & Gonnella, G., Modeling the Dynamics of amphiphilic fluids. *Internat J Modern Phys C*, **9(8)**, pp. 1469–1478, 1998.
[9] Lamura, A., Gonnella, G. & Yeomans, J., A lattice Boltzmann model of ternary fluid mixtures. *Europhys Lett*, **45(3)**, pp. 314–320, 1999.
[10] Theissen, O. & Gompper, G., Lattice-Boltzmann study of spontaneous emulsification. *Eur Phys J B*, **11**, pp. 91–100, 1999.
[11] Furtado, K., Pooley, C.M. & Yeomans, J.M., Lattice Boltzmann study of convective drop motion driven by nonlinear chemical kinetics. *Phys Rev E*, **78**, p. 046308, 2008.
[12] Farhat, H. & Lee, J., Simulation of RBCs Bioconcave shape Using 2-D Lattice Boltzmann. *Nanotechnology 2008*, NSTI Nanotech, volume 3, pp. 433–437, 2008.
[13] Sapir, T. & Nir, A., A Hydrodynamic Study of the Furrowing Stage During Cleavage. *Physicochemical Hydrodynamics*, **6**, pp. 803–814, 1985.
[14] Li, Z. & Lubkin, S.R., Numerical analysis of interfacial two-dimensional Stokes flow with discontinuous viscosity and variable surface tension. *Int J Numer Meth Fluids*, **37**, pp. 525–540, 2001.
[15] McNamara, G.R. & Zanetti, G., Use of the Boltzmann Equation to Simulate Lattice-Gas Automata. *Phys Rev Letters*, **61(20)**, pp. 2332–2335, 1988.
[16] He, X. & Luo, L.S., A priori derivation of the lattice Boltzmann equation. *Phys Rev E*, **55(6)**, pp. 6811–6817, 1996.

[17] Qian, Y., D'Humieres, D. & Lallemand, P., Lattice BGK Models for Navier-Stokes Equation. *Europhys Lett*, **17(6)**, pp. 479–484, 1992.
[18] Tölke, J., Krafczyk, M., Schulz, M. & Rank, E., Lattice Boltzmann simulations of binary fluid flow through porous media. *Philos Trans R Soc Lond Ser A Math Phys Eng Sci*, **360**, pp. 535–545, 2002.
[19] Bhatnagar, P.L., Gross, E.P. & Krook, M., A model for collision processes in gases. i. small amplitude processes in charged and neutral one-component systems. *Phys Rev*, **94(3)**, pp. 511–525, 1954.
[20] Reis, T. & Phillips, T.N., Lattice Boltzmann model for simulating immiscible two-phase flows. *J Phys A Math Theor*, **40**, pp. 4033–4053, 2007.
[21] Latva-Kokko, M. & Rothman, D.H., Diffusion properties of gradient-based lattice Boltzmann models of immiscible fluids. *Phys Rev E*, **71**, p. 056802, 2005.
[22] Shan, X. & Doolen, G., Diffusion in a multicomponent lattice Boltzmann equation model. *Phys Rev E*, **54(4)**, pp. 3614–3620, 1996.
[23] Marconi, S., Chopard, B. & Latt, J., Reducing the compressibility of a Lattice Boltzmann fluid using a repulsive force. *Internat J Modern Phys C*, **14(8)**, pp. 1015–1026, 2003.
[24] Chin, J., Boek, E.S. & Coveney, P.V., Lattice Boltzmann simulation of the flow of binary immiscible fluids with different viscosities using the Shan-Chen microscopic interaction model. *Philos Trans R Soc Lond Ser A Math Phys Eng Sci*, **360**, pp. 547–558, 2002.
[25] Kang, Q., Zhang, D., Chen, S. & He, X., Lattice Boltzmann simulation of chemical dissolution in porous media. *Phys Rev E*, **65**, 2002.
[26] Hou, S., Shan, X., Zou, Q., Doolen, G.D. & Soll, W.E., Evaluation of Two Lattice Boltzmann Models for Multiphase Flows. *J Comput Phys*, **138**, pp. 695–713, 1996.
[27] Chen, H., Boghosian, B.M., Coveney, P.V. & Nekovee, M., A Ternary Lattice Boltzmann Model for Amphiphile Fluids. *Proceedings: Mathematical, Physical and Engineering Sciences*, **456(2000)**, pp. 2043–2057, 2000.
[28] Nekovee, M., Coveney, P.V., Chen, H. & Boghosian, B.M., Lattice-Boltzmann model for interacting amphiphilic fluids. *Phys Rev E*, **62(6)**, pp. 8282–8294, 2000.

Tetra-marching procedure for high order Level Contour Reconstruction Method

I. Yoon & S. Shin
Department of Mechanical and System Design Engineering, Hongik University, Korea

Abstract

Direct numerical simulation of the multiphase flow on a fixed Eulerian grid became increasingly popular due to its simplicity and robustness. Lately, there have been efforts to construct hybrids from existing well-known methods including VOF, Level Set, and Front Tracking with the intention of overcoming the inherent drawbacks of each method. The Level Contour Reconstruction Method is one of the hybrid type methods, which combines the Front Tracking and Level Set characteristics. By introducing a high order interpolation kernel during interface reconstruction, we could reconstruct the interface very accurately and smoothly compared to linear interpolation of a given distance function field. The high order reconstruction procedure can be undertaken, generally, with the same rectangular shaped Eulerian grid structure as the flow computation. With this rectangular shaped grid, there can be more than two lines in a single cell during the reconstruction. In this paper, we introduce the tetra-marching reconstruction procedure which can eliminate ambiguity of drawing contour lines between multiple edge points in a single cell during high order reconstruction. We tested several benchmarking simulations of interface evolution and found that high order reconstruction with a tetra-marching procedure enables the fidelity of the reconstructed interface, which is continuous and smooth even with a highly distorted interface.

Keywords: interface reconstruction, front tracking, level set, tetra-marching, numerical simulation.

WIT Transactions on Engineering Sciences, Vol 69, © 2010 WIT Press
www.witpress.com, ISSN 1743-3533 (on-line)
doi:10.2495/AFM100441

1 Introduction

Multiphase flow is an ubiquitous process used for diverse engineering applications. Due to the small length and time scale associated with multiphase flow, a numerical technique can be an ideal tool for identifying underlying physics compared to experiment. Lately, methods using a fixed Eulerian grid with an additional advection scheme to track the interface motion, e.g. VOF [1], Level Set [2], and Front Tracking [3], has drawn great attentions. Despite the success of each method, it is still a formidable task to come up with an accurate, reliable, and yet simple method which can model complex interfacial dynamics, especially for three-dimensional simulation. The Level Contour Reconstruction Method (LCRM) [4–7] which combines the advantage of the Front Tracking and Level Set method has been devised to overcome some drawbacks pertaining to each method. Similar efforts can also be found in various hybrid type methods including CLSVOF(Level Set+VOF) from Sussman and Puckett [8], particle Level Set (Level Set+Lagrangian marker particle) from Enright *et al.* [9], and Aulisa *et al.* [10] who combines markers and the VOF method.

The LCRM is basically a Front Tracking type method which tracks implicitly connected individual interface elements (lines for 2D and faces for 3D). Implicit connectivity of the interface elements make it possible to eliminate the burden of bookkeeping of the logistic information of neighbouring elements which incurs a large memory and calculation cost. At the same time, it takes advantage of the Level Set method since the interface can also be represented by an Eulerian function field (e.g. distance function) which can be computed directly from a given interface location. Reconstruction of the interface at a certain level of the distance function enables us to model the merging and pinch off of interfaces naturally and automatically as in the Level Set method. During the original reconstruction procedure [4], the interface was relocated by linear interpolation from the given distance function field. We found that linear interpolation generates a continuous but not smooth interface after reconstruction. High order LCRM [6] has been introduced to increase the accuracy and smoothness of the reconstructed interface since a small disturbance originated from linear reconstruction can cause instability of the solution requiring frequent interface reconstruction, especially with a low resolution.

In general, the reconstruction procedure can be undertaken within the same rectangular shaped Eulerian grid structure as flow computation. In the case of highly deformable interface evolution, the phase front can elongate to form a thin filament and approach too close to each other. High order reconstruction makes it possible to relocate this subtle feature accurately but can also generate the ambiguity of drawing contour lines in a rectangular cell since there can be more than two lines with an attenuated interface. Without a complex algorithm, there can be small holes along, with a narrow gap of the elongated interface. This effect is usually negligible since reconstruction will be performed regularly but might cause solution instability where surface tension plays a dominant role. In this paper, we introduce the tetra-marching procedure which

can eliminate ambiguity to draw lines between multiple edge points in a single cell during high order reconstruction.

2 Numerical formulation

2.1 Governing equations

The single field form of the governing equations for multi fluid motion including phase change can be expressed as:

$$\nabla \cdot \mathbf{u} = 0 \tag{1}$$

$$\rho\left(\frac{\partial \mathbf{u}}{\partial t} + \mathbf{u} \cdot \nabla \mathbf{u}\right) = -\nabla p + \rho \mathbf{g} + \nabla \cdot \mu(\nabla \mathbf{u} + \nabla \mathbf{u}^{\mathrm{T}}) + \mathbf{F} \tag{2}$$

$$\frac{\partial T}{\partial t} + \mathbf{u} \cdot \nabla T = \alpha \nabla^2 T \quad \begin{pmatrix} \alpha = \alpha_L \ \textit{in liquid phase} \\ \alpha = \alpha_G \ \textit{in gas phase} \end{pmatrix} \tag{3}$$

here, **u** is the velocity, p is the pressure, **g** is the gravitational acceleration, and **F** is the local surface tension force at the interface which can be described by the hybrid formulation [5, 7] as:

$$\mathbf{F} = \sigma \kappa_H \nabla I \tag{4}$$

where σ is the surface tension coefficient (assumed constant here), I is the indicator function, a Heaviside function which varies from zero to one near the interface. The indicator function also has been utilized to describe material property at each phase. κ_H is the curvature field calculated on the Eulerian grid given by:

$$\kappa_H = \frac{\mathbf{F}_L \cdot \mathbf{G}}{\sigma \mathbf{G} \cdot \mathbf{G}} \tag{5}$$

where

$$\mathbf{F}_L = \int_{\Gamma(t)} \sigma \kappa_f \mathbf{n}_f \delta_f (\mathbf{x} - \mathbf{x}_f) \mathrm{d}s \tag{6}$$

$$\mathbf{G} = \int \mathbf{n}_f \delta_f (\mathbf{x} - \mathbf{x}_f) ds \tag{7}$$

here, $\mathbf{n}_f$ is the unit normal from the interface, $\mathbf{x}_f$ is a location of the interface, and $\delta_f(\mathbf{x}\text{-}\mathbf{x}_f)$ is a dirac delta distribution that is non-zero only at the interface. ds is the length or area of the element, and κ_f is twice the mean interface curvature computed in a Lagrangian fashion.

The indicator function can be obtained using a distance function which has been computed directly from a given interface front [7]. This additional hybridization with the Level Set technique enables us to compute an accurate distance function as well as to locate the minimum distant point on the interface from grid node of interest. This information then allows us to calculate a

compact curvature field based on the curvature at a minimum distance point on the interface. This compact curvature field can further reduce the parasitic current to a significantly lower level [7]. The more detailed procedure for calculating the compact curvature field can be found in [4–7].

The interface is advected in a Lagrangian fashion by integrating

$$\frac{\mathrm{d}\mathbf{x}_f}{\mathrm{d}t} = \mathbf{V} \tag{8}$$

where $\mathbf{V}$ is the interface velocity vector interpolated at $\mathbf{x}_f$. The energy equation (eqn (3)) has been solved using the sharp interface technique [11] and a detailed solution procedure and discretization of the governing equations can be found in [4–7].

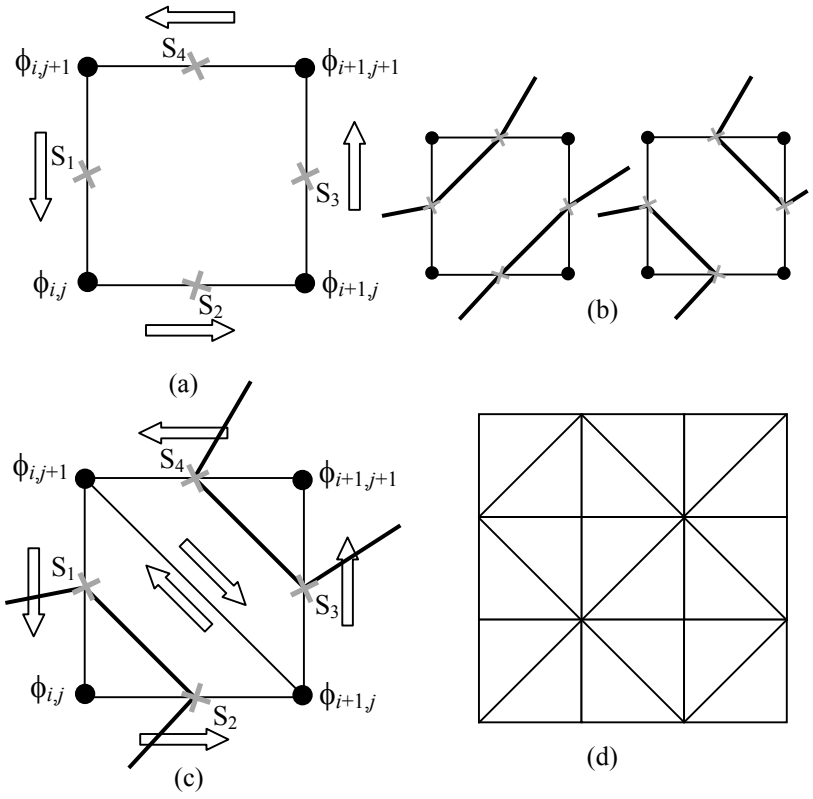

Figure 1: Two-dimensional interface generation procedure for the LCRM (a) original LCRM using a rectangular cell (b) ambiguity in the interface reconstruction with a rectangular cell (c) tetra-marching reconstruction with a triangular cell (d) alternative orientation of triangular cells for interface connectivity.

2.2 High order reconstruction method

The original LCRM [4] used linear interpolation kernel to create contour lines or faces from given indicator or distance function field. Here we will briefly explain the basic procedure of the original LCRM in 2D. As you can see from fig. 1, we try to search the specific contour level of the function ϕ, e.g. zero value in the case of distance function, along with the grid cell edges. If we find two points on the edges of the grid cell ($\phi_{i,j}\cdot\phi_{i,j+1}<0$ and $\phi_{i,j}\cdot\phi_{i+1,j}<0$), we draw a contour line between those two points (S_1 and S_2). After sweeping all grid cells considered, the reconstructed interfaces will share the same end points thus we can achieve implicit connectivity of the interface.

We found that linear interpolation generates a small disturbance since it cannot guarantee smoothness of the interface but only connectivity. Moreover, mass can redistribute from the high curvature region to the lower curvature region by enforcing global mass conservation during interface reconstruction. These slight discrepancies in the interface points can induce undesirable results where the exact location of the interface is extremely important. Thus high order reconstruction [6] was introduced and we will briefly summarize the main idea.

The distance function $\phi(i, j)$ (fig. 1(a)) where the specific value, i.e. zero, represents the interface position can be modified by adding a trial function, $\psi(i, j)$, as follows:

$$\phi^H(\mathbf{x}) = \sum_g \left[\phi(i,j) + \psi(i,j)\right] S(\mathbf{x} - \mathbf{x}_g) \tag{9}$$

here, $\mathbf{x}$ is the evaluation point, $\mathbf{x}_g$ is the grid cell centre, $S(\mathbf{x}\text{-}\mathbf{x}_g)$ is the interpolation kernel composed of B-splines for smoothness of function values, suggested by Torres and Brackbill [12]. The summation is performed across a small multiple of the mesh, usually four grid cells wide, in each x, y direction.

The trial function has been added since the zero contour level of the original distance function itself cannot describe exactly the original interface location. We have used the same B-spline type interpolation kernel for trial function:

$$\psi(i,j) = \sum_{N_p} \delta I_p S(\mathbf{x}_g - \mathbf{x}_p) \tag{10}$$

here, $\mathbf{x}_p$ is the location of the original interface points before reconstruction, δI_p is the increment needed at the original interface points, and the integral has been performed over all interface elements. This trial function makes the zero contour level of eqn (9) lies exactly on top of the original interface location. The method is very simple and has a comparable accuracy to other methods using complicated smoothing procedures. The basic idea of high order LCRM is similar to the Point Set method of Torres and Brackbill [12] except that their indicator function has been computed directly from the interface elements. The detailed procedure for high order reconstruction can be found in [6].

2.3 Tetra-marching procedure

The reconstruction procedure can be undertaken, in general, with the same rectangular shaped Eulerian grid structure as flow computation. With this rectangular shaped grid, there can be more than four points (S_1, S_2, S_3, and S_4) at four edges of the reconstruction cell as described in fig. 1(a) when the interface stretches severely to form a thin filament ($\phi_{i,j+1}>0$, $\phi_{i+1,j}>0$, $\phi_{i,j}<0$, $\phi_{i+1,j+1}<0$). In this case, there can be ambiguity of drawing contour lines in a single cell during the reconstruction procedure as in fig. 1(b). Special formulation of the interface reconstruction is required for the rectangular shaped reconstruction domain. For two-dimensional simulation, this can be done with a relatively simple procedure but it will be an overwhelming task for three-dimensional simulation.

Drawing a line or surface from given data is an iso-surface extraction process which has been a major concern for volume visualization of the scattered data set from a medical image such as a CT and MRI scan. Marching cubes technique [13] is the most popular procedure for extracting surface from cubical grid data. 256 cube configurations are possible but it can be reduced to 15 unique cases using symmetry and reflective condition. The look-up table has been generated with vertex data then reconstruction has been performed to each cube in a marching direction.

Lately, Carneiro *et al* [14] proposed the tetra-cubes reconstruction method which does not use a look-up table to extract iso-surface data from a medical image thus eliminating the choice from 15 possible interfacial geometries in the case of rectangular shaped geometry. Similarly, interface reconstruction does not have to coincide with the rectangular grid cell as primary variables of velocity and pressure for the LCRM. We will start with 2D reconstruction for simplicity. The ambiguity of drawing lines from multiple edge points can be avoided by using a triangular reconstruction grid as in fig. 1(c). There can be only one line from each triangular cell of interest for 2D simulation. We also need to make the reconstructed interface share the same end points between neighbouring cells. To make the reconstructed interface continuous, a triangular grid has been oriented in an alternative fashion as shown in fig. 1(d).

Three-dimensional reconstruction is basically the same as a two-dimensional one. As can be seen from fig. 2 (a), we first reconstructed edge lines from 6 faces wrapping the cubic cell. These lines will compose the line edges of the reconstructed 2D surface element. As pointed out earlier [13], there can be 15 possibilities of interface location with a given distance function value at 8 vertices. This problem can be also avoided by using a tetrahedral mesh [14] instead of a cubic one. In the case of the tetrahedral cell, there can be two possible interface geometries after reconstruction as in fig. 2(b). The first one is the triangular element which does not need any modification. The second is the rectangular element which has been modified to triangles by subdividing in the direction of the longest distance between edge points. Even if we use a tetrahedral cell for interface reconstruction, we still need to orient the tetrahedral cell carefully to guarantee connectivity of the reconstructed interface elements. We try to use a given Cartesian cubical cell for fluid computation as our basic

reconstruction cells and subdivide this to five tetrahedral cells as in fig. 3(a). The five sub-cells have been reoriented to match the reconstructed edges at cube faces of the neighbouring cell as in the two-dimensional case (fig. 3(b)). By using zigzag orientation of the tetrahedral cells [14], we can construct continuous surface elements after reconstruction.

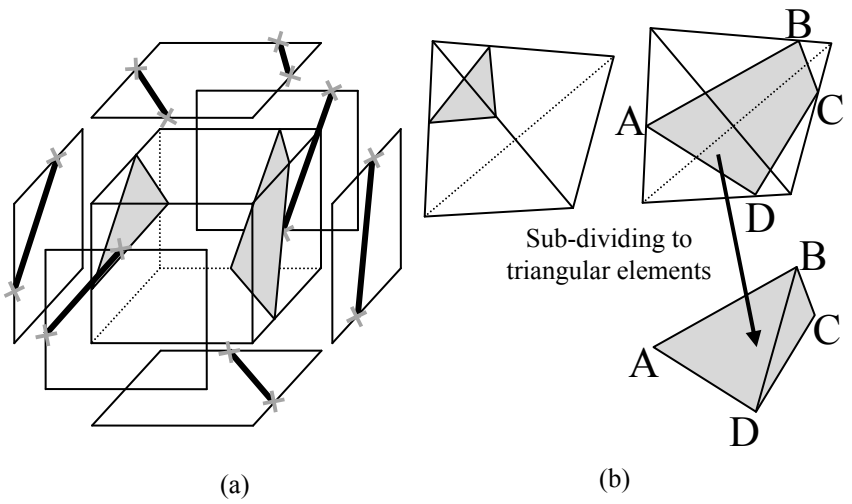

Figure 2: Three-dimensional interface generation procedure for the LCRM (a) original LCRM using a Cartesian rectangular cell (b) tetra-marching reconstruction using a tetrahedral cell.

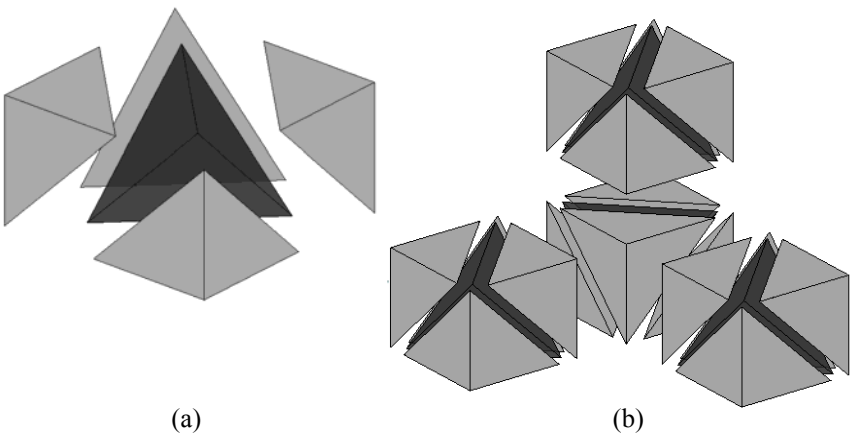

Figure 3: Three-dimensional interface generation procedure for the LCRM (a) tetrahedral cell generation from a rectangular cell (b) zigzag orientation of a tetrahedral cell for interface connectivity.

3 Results and discussion

3.1 Geometry tracking test

We first tested the "vortex in a box" problem introduced by Bell *et al* [15]. The test can demonstrate the method's ability to accurately resolve thin filaments on the scale of a grid cell. A circle of radius 0.15 is placed at (0.5, 0.75) using a 64×64 grid resolution in unit domain. The velocity field is defined by:

$$\mathbf{v}(\mathbf{x}) = 2\begin{bmatrix} -\sin^2(\pi x)\sin(\pi y)\cos(\pi y) \\ \sin^2(\pi y)\sin(\pi x)\cos(\pi x) \end{bmatrix} \tag{11}$$

The resulting velocity field stretches out the circle into a very long, thin spiral filament which progressively wraps itself toward the centre of the box. In this case the interface elements become highly elongated by the flow and a reconstruction procedure becomes essential for an accurate simulation. Fig. 4 shows the interface at $t = 3$. Reconstruction has been performed at every 100th time step and a total number of 30 reconstructions have been performed for the simulation. As can be seen from fig. 4(a), the fine structure of the interface has been successfully captured but the reconstructed interface does not have complete connectivity near the thin filamentary region using a rectangular shaped reconstruction cell with high order reconstruction. We have not provided any logical algorithm when ambiguity of drawing interface arises. Fig. 4(b) shows tetra-marching reconstruction of the interface at an identical time as in Fig. 4 (a). The interface has been well connected without any additional algorithm.

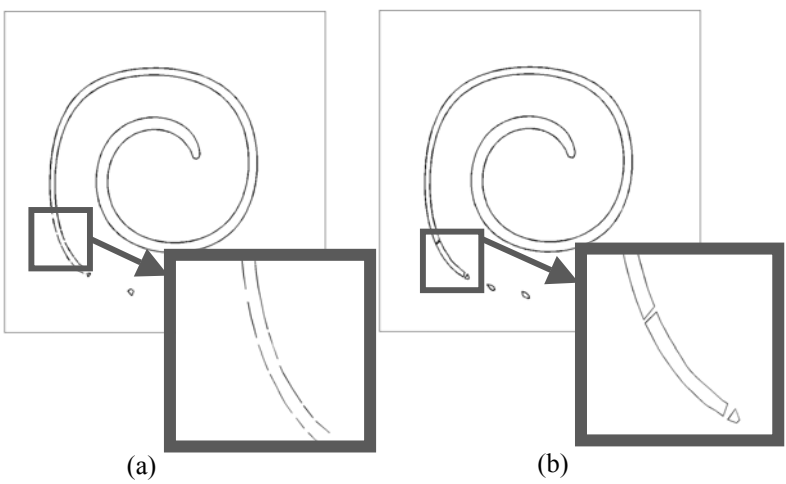

Figure 4: Comparison of reconstruction accuracy (a) original LCRM using rectangular cell (b) tetra-marching reconstruction using triangular cell.

3.2 Nucleate boiling with convective flow

We have simulated nucleate boiling with fluid convection to validate reconstruction accuracy during severe deformation of the interface in 3D. The governing equations (1) to (3) can be non-dimensionalized by appropriate scales of length $l_o=(\sigma/g(\rho_L-\rho_G))^{1/2}$, velocity $U_o=(gl_o)^{1/2}$, temperature $\rho_G L_o/\rho_L c_L$ (measured from T_{sat}), and pressure $\rho_L U_o^2$ (measured from the ambient system pressure P_∞). The problem can then be characterized by the Reynolds, *Re*, Peclet, *Pe,* Jakob, *Ja* and Weber, *We*, numbers as well as the property ratios which can be defined as follows:

$$Re=\frac{\rho_L U_o l_o}{\mu_L}, We=\frac{\rho_L U_o^2 l_o}{\sigma}, Pe=\frac{k_L}{\rho_L c_L U_o l_o}, Ja=\frac{T_{sat} c_L}{L_o} \tag{12}$$

$$\rho^*=\frac{\rho_G}{\rho_L}, k^*=\frac{k_G}{k_L}, \mu^*=\frac{\mu_G}{\mu_L}, c^*=\frac{c_G}{c_L} \tag{13}$$

here ρ is density, μ is viscosity, k is thermal conductivity, c is specific heat, T is temperature and L_o is the latent heat of vaporization. A more detailed description of numerical formulation can be found in [4, 16]

During nucleate boiling, individual bubbles will directly contact the heated wall so proper modelling of the contact line motion becomes very important. The detailed physics of the contact region regarding contact line motion is still poorly understood thus we applied a simple Navier-slip model [11]. The interface can move freely between the advancing and receding angle and the contact angle has been fixed to a constant angle of 120^o if the contact angle is greater than the prescribed advancing angle of 120^o and, vice versa, to a receding angle of 60^o. We also used a simplified form of the microlayer evaporation model proposed by Son [17] which uses algebraic formulation based on geometric constraint instead of solving a nonlinear differential equation.

Initially, four hemispherical cap shaped bubbles in different sizes of 1.0, 1.05, 1.1, and 1.15 are placed at each centre of the four quadrants of the bottom wall where a no-slip velocity boundary condition has been used (small window of fig. 5). A periodic boundary condition has been applied to both the *x* and *y* direction and moving wall boundary condition with 3 m/s in the *x* direction is used for the top wall. To allow vaporization, fluid is also allowed to exit at the top boundary where the pressure is specified to be zero. The temperature field is initially zero everywhere except the rigid bottom wall where a constant non-dimensional temperature of 108 applied. Temperature at the top wall boundary has been specified as -532. We have chosen to use the properties of water at atmospheric condition thus our simulation parameters will be ρ^*=0.0006237, μ^*=0.04353, k^*=0.03694, c^*=0.4847, *Re*=1334.2, *We*=1.0, *Pe*=0.0004268, and *Ja*=0.6972, The box size of 4.2×4.2×6.3 with a 40×40×60 grid resolution has been used for the simulation.

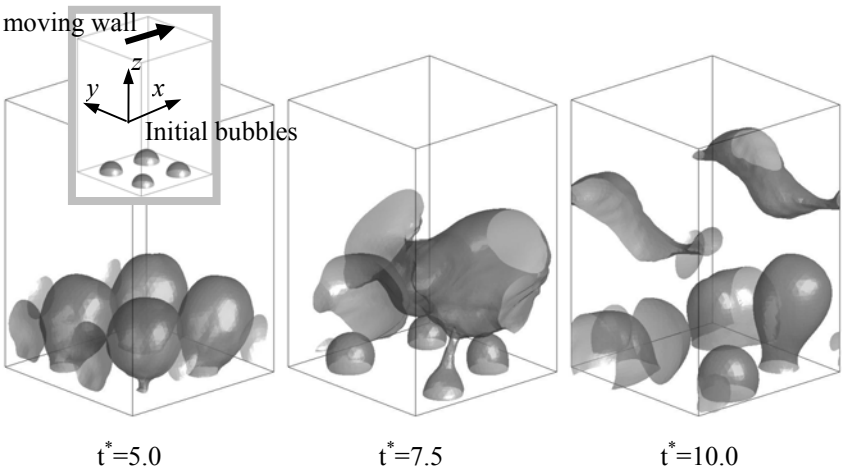

Figure 5: Nucleate boiling with multiple bubbles under fluid convection.

As can be seen from fig. 5, multiple bubbles are growing independently at the start and merging to form a larger bubble. A merged bubble is finally pinched off from the bottom surface then experiencing the condensation from the top boundary temperature condition. The interface undergoes severe transition of the topological evolution. At t*=7.5, there exists a thin filamentary vapour column right before pinch off and the tetra-marching procedure can generate a closed interface after reconstruction. There is also a complicated merging process of the interfaces at the middle section of the domain. We found that the tetra-marching reconstruction procedure can generate perfectly interconnected elements as well as a naturally and automatically merged interface after reconstruction. More quantitative research of nucleate boiling including surface heat transfer is necessary and currently underway.

4 Conclusion

The LCRM is one of the hybrid type interface methods for multiphase flows which combines some essential features of the Front Tracking and Level Set techniques. While retaining an explicitly tracked interface using interfacial elements, the distance function calculated from a given interface location plays a crucial role in periodic reconstruction of the interface elements.

By adopting high order reconstruction, we can maintain an excellent mass conservation and interface fidelity. However, there can be ambiguity during interface reconstruction in the case of a rectangular shaped reconstruction cell. Despite the fact that this local disconnection of the interface will not cause complete breakdown of the simulation, it generates a relatively large error where the interface evolves into a thin filamentary shape. The tetra-marching procedure can create a perfectly interconnected interface near the very tail of a filamentary

shaped interface. The procedure is simple and easily applicable for both 2D and 3D simulations without any complex algorithm. It can handle complicated interface evolution in a straightforward manner. Several tests including interface evolution in a vortex field and three-dimensional nucleate boiling problems with convective flow with a large surface deformation have been performed and the tetra-marching reconstruction procedure showed an accurate reconstruction capability compared to the original method.

References

[1] Scardovelli, R. & Zaleski, S., Direct numerical simulation of free-surface and interfacial flow, *Ann. Rev. Fluid Mech*., **31** , pp 567-603, 1999

[2] Osher, S. & Fedkiw, R.P., Level set methods: An overview and some recent results, *J. Comput. Phys.*, **169**, pp 463-502, 2001.

[3] Tryggvason, G., Bunner, B., Esmaeeli, A., Juric, D., Al-Rawahi, N., Tauber, W., Han, J., Nas, S. & Jan, Y.J., A front tracking method for the computations of multiphase flow, *J. Comput. Phys*. 2001; **169**: 708-759.

[4] Shin, S. & Juric, D., Modeling three-dimensional multiphase flow using a level contour reconstruction method for front tracking without connectivity, *J. Comput. Phys*., **180**, pp 427-470, 2002.

[5] Shin, S., Abdel-Khalik, S.I., Daru, V. & Juric, D., Accurate representation of surface tension using the level contour reconstruction method, *J. Comput. Phys*., **203**, pp 493-516, 2005.

[6] Shin, S. & Juric, D., High order level contour reconstruction method, *Journal of Mechanical Science and Technology*, **21**, pp 311-326, 2007.

[7] Shin, S., & Juric, D., A hybrid interface method for three-dimensional multiphase flows based on front tracking and level set technique, *Int. J. Numerical Methods in Fluids*, **60(7)**, pp 753-778, 2009.

[8] Sussman, M. & Puckett, E.G., A coupled level set and volume-of-fluid method for computing 3D and axisymmetric incompressible two-phase flows, *J. Comput. Phys*., **162**, pp 301-337, 2000.

[9] Enright, D., Fedkiw, R., Ferziger, J. & Mitchell, I., A hybrid particle level set method for improved interface capturing, *J. Comput. Phys*., **183**, pp 83-116, 2002.

[10] Aulisa, E., Manservisi, S. & Scardovelli, R., A mixed markers and volume-of-fluid method for the reconstruction and advection of interfaces in two-phase and free-boundary flows, *J. Comput. Phys*., **188**, pp 611-639, 2003.

[11] Liu, H., Krishnan, S., Marella, S. & Udaykumar, H. S., Sharp interface Cartesian grid method II: a technique for simulating droplet interactions with surfaces of arbitrary shape, *J. Comput. Phys*., **210**, pp 32-54, 2005.

[12] Torres, D.J. & Brackbill, J.U., The point-set method: front-tracking without connectivity, *J. Comput. Phys*., **165**, pp 620-644, 2000.

[13] Timothy, S.N. & Hong, Y., A survey of the marching cubes algorithm, Computers and Graphics, **30**, pp 854-879, 2006

[14] Carneiro, B.P., Silva, C.T. & Kaufman, A.E., Tetra-Cubes: an algorithm to generate 3D isosurfaces based upon tetrahedral, *Anais do IX SIBGRAPI*, pp 205-210, 1996.
[15] Bell, J.B., Colella, P. & Glaz, H.M., A second-order projection method for two-phase flow consisting of separate compressible and incompressible regions, *J. Comput. Phys*., **85**, pp 257-283, 1989.
[16] Juric, D. & Tryggvason, G., Computations of boiling flows, *Int. J. Multiphase Flow*, **24**, pp 387-410, 1998.
[17] Son, G., Numerical simulation of bubble motion during nucleate boiling, *Transaction of the KSME B.*, **25(3)**, pp 389-396, 2001.

A qualitative model of flashing across an aperture with a pressure differential

G. C. Polanco[1], A. E. Holdo[2] & G. Munday[3]
[1]*Universidad Simón Bolívar,*
[2]*Venezuela Narvik University College,*
[3]*Norway Coventry University, UK*

Abstract

Many industries use materials that are stored above their atmospheric pressure boiling points (superheated liquids) which can form two-phase mixtures upon their accidental release to the environment at ambient conditions. The behaviour and the characteristics of these liquid-gas mixtures during a superheated liquid release due to the breaking of the metastable state can significantly affect the hazard zone and the mitigation steps that can be taken to minimize the release impact for the hydrocarbon industry or the quality of the combustion, or explosions inside the diesel engines. The dependence of the whole process over the initial parameter values as the pressure, the temperature and others factors, which can created, for some cases, a complete breaking of the liquid core into droplets at the same time that it is going out of container like unstable jet, or a complete one phase liquid jet, is recreated by an empirical model based on the flashing process similarity and a damped second order system. Results of this model agreed with some available experimental data.

Keywords: superheated liquids, empirical model, flashing process.

1 Introduction

Flashing is the violent phase change of a super-heated liquid when it is exposed to a pressure gradient generated by the pressure difference between the vessel or pipe line and the atmospheric pressure, due to vessels or pipelines faults. During the brief depressurisation of the liquid breaks into droplets at the same time that it is going out of container trough an opening like unstable jet, as consequence of the altering of the metastable state of the superheated liquid stored.

WIT Transactions on Engineering Sciences, Vol 69, © 2010 WIT Press
www.witpress.com, ISSN 1743-3533 (on-line)
doi:10.2495/AFM100451

Experimental research has found that for distances closer to the opening, liquid regions and large droplets are still superheated, so, they continuously break-up or evaporate in a section known as the expansion region; after this section, the droplet velocity decreases due to effects of the entrainment of air into the internal energy balance of the jet, and this new region is known as the entrainment region [8].

Flashing process is a non isentropic process in which mechanics and thermodynamics mechanisms interact generating a particular type of jet, with certain characteristics of phase velocities, temperature and mass flow. These two mechanisms work together but there is not an equal and constant predominance of any of them along the whole process. The identification of the predominance of a particular mechanism in different situations is used to characterize the type of jet formed. The fluid properties, such as, the viscosity and density, and their dependency with temperature or pressure together with the difference between the ambient conditions and the superheated initial condition of the fluid make an important contribution to the final characteristics of a flashing jet. The potential hazard of a vessels leak of metastable fluid is directly related with the fluid conditions and the mechanism predominant under certain circumstances.

2 Qualitative model of flashing: physics considerations

Phase change process presented in flashing needs to rich a minimum level of energy in order to appear, due to the significant difference in the internal energy of liquid and vapour phases of the same fluid. Assuming that the flashing occurs at most just outside of the opening, an analytical model of flashing across an aperture with pressure change is proposed to determine the type of jet resulting after the leak takes place.

To understand the characteristics of the different types of jet, it was necessary to establish in advance the number of cases to take into account. There are three main different types of jet, known as: liquid jet, mixture jet and gas jet with droplets [7, 9, 10]. The proposed model is based on the compilation of the individual influences of pressure differences, temperature differences and fluid properties. The pressure-temperature relationship in a fluid at saturation conditions shows that there is a variable dependence on temperature over changes in pressure for a particular pressure ratio. When the pressure increases and becomes closer to the critical point the dependence of temperature on pressure decreases. The region limited by the spinodal line, which represents the theoretical range of superheat that the fluid can achieve decreases, when the temperature or pressure values become closer to the critical condition. Larger values of temperature or pressure increase the thermal and pressure energy in the fluid, which in case of any release to ambient atmospheric conditions will need to be dissipated by the jet on its way out. The dissipation of larger quantity of energy generates a more violent phase change inside the jet because larger amount of energy have to be dissipated over a short distance. In its way, out the vessel, the fluid pressure and temperature suffer changes due to the interaction between the fluid and the ambient, from the vessel pressure value to the ambient

pressure at sufficient long distances from the opening. When the pressure difference changes, it produces a velocity variation and liquid density variation, that can be characterized by the Reynolds number, which is the ratio of the resulting inertial force and the viscous force. The Jacob number, *Ja*, defined as the ratio of the energy supplied by the superheated liquid and fluid latent heat, h_{fg}. The ratio of the constant heat coefficient, C_p, and the latent heat drives the speed of the heat transfer phenomenon by conduction mean over evaporation phenomenon. Clearly, the Jacob number increases as a result of rising pressure due to the decrease of enthalpy and the increase of the C_p with the pressure rise and also with the temperature difference.

The resistance of the liquid to keep itself together as a liquid jet before it stars to break-up by any external (surface instabilities or waves) or internal (nucleation) means to the jet is represented by the Weber number, defined as the ratio of inertial force and surface tension force. It can be expected that the Weber number will increase as result of the effect of the square exponent of the velocity, which increases with pressure difference, as well as, with the decrease of the surface tension with pressure rise. It suggests the existence of a critical Weber number that drives the growth of the nucleated bubbles inside the fluid [11].

The liquid density to gas density ratio can be used as measure of how much energy is necessary to overcome the phase change barrier through evaporation, which at least must correspond to latent heat of the fluid. Small density ratios indicate that less energy must be added to the system to achieve the evaporation than for higher density ratios. The boiling mechanisms inside of the fluid will depend on the introduction of sufficient kinetic energy for the molecules inside the fluid to change from liquid to vapour state.

A previous study performed by Skripov et al. [12] has confirmed that fluid properties as surface tension, specific volume, specific heat, viscosity and thermal conductivity of a superheated liquid follow the same trend as the properties at saturation point, however, the information under this condition is not often available. Due to fluid temperature will go below the boiling point only after some distance downstream of the opening within the jet, named Minimum Temperature Distance, the fluid properties at the injection temperature, T_{inj}, will be delimit by the properties value at the boiling temperature, T_b, as shown by eqn (1). The values of the main properties of the liquid phase as density, ρ_l, viscosity, μ_l , surface tension, σ_l , and coefficient at constant pressure, C_p , will be in all the cases limited by the value of the properties at the boiling temperature.

$$\left.\begin{aligned} \rho_l\left(T_{inj}\right) &< \rho_l\left(T_b\right) \\ \mu_l\left(T_{inj}\right) &< \mu_l\left(T_b\right) \\ \sigma_l\left(T_{inj}\right) &< \sigma_l\left(T_b\right) \\ C_p\left(T_{inj}\right) &> C_p\left(T_b\right) \end{aligned}\right\} \; for\; T_{inj} > T_b \tag{1}$$

Therefore, the properties values used to compute all non-dimensional numbers involved in a flashing problem will be assumed as the properties at the boiling point.

Resulting flashing jet also depends on geometrical considerations. The geometry of the nozzle as well as the piping system used in every experimental setting could affect the final output of the flashing jet. The diameter, the length and the shape of the nozzle have been taken as major characteristic parameters to be considered [6, 8, 13, 14]. Nozzle diameter, length and shape and the wall's roughness e, will influence the discharge coefficient [15]. For instance, the discharge coefficient of a nozzle with sharper edges will be larger than for a nozzle with chamfered edges, and therefore, a nozzle with sharper edges will produce a larger pressure drop in the flow, as well as, larger disturbances in the flow field.

The nozzle diameter also affects total mass flow rate discharged and the area available to conduct the heat transfer inside the fluid. The cross sectional area of the fluid is drastically reduced from inside the tank to the exit passing through the nozzle. The smaller nozzle diameter will cause a reduction of the fluid heat transfer area, making it difficult for the fluid to keep the same conduction heat transfer rate on its way out, augmenting the possibilities of a violent and explosive flashing process. The nozzle length determines the period of time required by a fluid with certain velocity to flow trough the nozzle. It can promote the formation of heterogeneous nuclei inside the nozzle due to the increase of the contact between the fluid and the internal surface irregularities of the nozzle [16]. If, it is the case that the fluid can still be liquid at the exit of the nozzle, then the length will affect the type and size of perturbation or instabilities presented in the jet surface, as product of the internal flow pattern. In cases of two-phase discharges the length is an important factor in the determination of the two phase flow pattern inside a pipe [6, 17–19].

3 Model's development

It is seen that nucleation has a significant effect on flashing as the initial process that produces the breaking of the liquid continuum [20]. Nuclei are the starting point of gas bubbles inside the liquid and they are in turn responsible for the liquid transformation into droplets after the release. The total nucleation is responsible for all the vapour in the jet [21, 22].

The proposed model is a one dimensional model based on a second order system which accounts for damping forces and stiffness forces over the nucleation process of a system driven by temperature and pressure differences at conditions where phase change occurs for liquids [23].

There are similarities between the parameters that influence the nuclei generation process and the physical parameters that take part in the motion generation within a damped second order system and the type of response that the system can have under certain circumstances. For instance, both systems need to achieve a minimum level of energy to initiate the process, the type of response of the whole system to the velocity of the changes, the behaviour of the

system will change drastically depending on the output of the system. It possible to think that, every case of leakage has the possibility to experience nucleation at different levels: explosive, very weak or none. The possibilities of the actual system response will be determined by the interaction between the parameters involved in the stiffness coefficient and the dissipation coefficient.

Based on those similarities the variable to be considered as the modelled parameter for the model proposed is the number of bubble clusters generated, called N. The nucleation rate of bubble clusters $\dot{N}$, is determined from the balance of those parameters by the second derivative of the numbers of nuclei, $\ddot{N}$. The letters K^* and C^* of eqn (2) represent the stiffness and damping coefficient by unit mass. The stiffness coefficient per unit mass and damping coefficient per unit mass will be named here after as the production coefficient and the dissipation coefficient of the nucleation system. So, the left hand side term of the eqn (1) represents the number of bubbles per squared second instead that the acceleration defined as distance per squared second.

$$\ddot{N} = -C^* \dot{N} - K^* N \tag{2}$$

The model development was centred in the determination of the equivalent coefficients to the spring and the damped component of a damped second order system. The production coefficient represents the interaction of all parameters that potentially promote of the nucleation process. The potential of the liquid to nucleate is assumed to be a function of the degree of superheat, pressure difference, diameter and length of the nozzle as well as properties of the fluid. However, the relative magnitudes of the temperature and the pressure of the fluid with respect to the critical parameters of the flow are also important variables to take into account. The critical point represents the maximum potential energy contained in the flow. The closer the fluid is to the critical conditions, the lesser energy is needed to produce a phase change. Whilst, the dissipation coefficient represents the influence of the parameters that tries to slow down the nucleation. The influence of a particular variable is not exclusively in favour or against nucleation, there are some variables having a relevant role in both aspects. As result of the analysis of experiment data it is clear that the influence of a particular variable depends on its proportion respect to a reference value, as for instance the critical conditions values of a substance or the standard atmospheric conditions. The expression developed for these two coefficients are represented in eqns (3) and (4).

$$K^* = g_o C_D d^{1.25} \frac{l}{d} \left(p_{inj} - p_o \right) \sqrt{\frac{T_{inj} - T_b}{T_{inj}}} \frac{1}{\rho_g} \tag{3}$$

$$C^* = g_1 T_b \frac{d}{l} + g_2 \frac{\rho_{liq}}{\rho_{gas}} \frac{p_c}{p_o} \frac{e}{d} \frac{\left(T_c - T_{inj} \right)}{T_{inj}} \frac{C p \left(T_c - T_{inj} \right)}{L} \left(\frac{\sigma}{\mu} \sqrt{\frac{\rho_l}{2 p_0}} \right) \frac{\left(p_c - p_{inj} \right)}{\rho_g} \frac{\left(p_c - p_{inj} \right)}{L} \tag{4}$$

Note that production coefficient as natural number is only defined for temperatures higher that the boiling temperature.

The criterion used to establish the characteristics of the resulting type of jet is the same used in a damped second order system which is given by the resolution of the eqn (2). Then, when a leak takes place the system is suddenly exposed to a pressure gradient between the inside and outside of the vessel. The answer of the system can be identified as under damped, damped or over damped. Every condition is associated with an equation that shows the relationship between the production coefficient K^* and dissipation coefficient C^*, as shown in eqns (5), (6) and (7), respectively.

An over-damped system the liquid will stay liquid even after the nozzle. It is represented by eqn (5):

$$4K^* < C^{*2} \quad over\ damped \tag{5}$$

A damped system will correspond to the case where the liquid has vapour bubbles inside of the core region is present after the nozzle. It is represented by eqn (6):

$$4K^* = C^{*2} \quad damped \tag{6}$$

An under damped system will correspond to the full atomized case, where the remaining liquid is present as droplets after the nozzle. It is represented by eqn (7):

$$4K^* > C^{*2} \qquad under\ damped \tag{7}$$

The definition of the *sign* parameter is introduced to normalize the output of the model. A positive unity value of *sign* parameter means the system achieves flashing condition and a negative unity value means the system do not achieve flashing condition.

$$sign = \frac{4K^* - C^{*2}}{abs\left(4K^* - C^{*2}\right)} \tag{8}$$

To finish the model, the incorporation of three dimensional constant named g_0, g_1 and g_2 expressed in eqns (3) and (4) was needed. The units of the constants are consistent with the complete equation of balance of nucleation, nucleation second and first derivative and the nucleation itself. The values of these constants are the product of an empirical and numerical work of the experimental set of data available for hydrocarbons and water [6, 8, 11, 13, 24–28].

The nucleation is expressed by the number of nuclei created and considering that it is not a proper unit then the units of the whole equation will be number of nuclei per squared second. Then, the unit of the production coefficient is the inverse squared second and the unit of the dissipation coefficient is the inverse of second. The numerical values were deducted taken all parameters involved in the international system unit (SI). The values are quite close each other due to the intension of the model is basically to catch the behaviour of the different fluid on the actual expression of every term rather that the numerical values of the constants used [23].

4 Results

In this section the results corresponding to two different cases of hydrocarbons are shown. The first case cover the experiment made by Johnson and Woodward [9] using chlorine as working fluid.

The first three columns of the Table 1 contain the original for the first case and the fourth column contains the results of the application of the *sign* parameter, eqn (8), for all the chlorine cases tested. This set of data allows testing the influence of the pressure, the pressure, and the effects of the nozzle characteristics on the release exit. The *sign* parameter corresponding to the cases of temperature of 289.63 K did not appear, due to the production and dissipation coefficients were not defined for temperature values smaller than the boiling temperature of the fluid.

Table 1: Model results for CFC11. Source: [9].

Pressure [kPa]	Temperature [K]	Observations	*sign*
161,800	297.90	Liquid stream remained together until vertical movement of stream was dominant.	1.0
163,500	308.95	No break-up of liquid stream visible	1.0
168,100	289.63	Liquid stream breaks up during vertical portion of trajectory into large drops and globs of liquid. Considerable splashing of liquid when it contacts the capture surface.	-
190,400	314.40	Liquid stream begins to break up about 0.3 m from release point	1.0
224,100	319.94	Near the release point, the stream appears thicker and slightly more broken up.	1.0
254,900	324.77	Stream appears more broken up from 2 m on.	1.0
269,700	327.32	No vapour pockets were visible in stream. Break-up of liquid stream occurred, but more uniformly than 330 K liquid.	1.0
302,000	330.71	Definite liquid break-up about 0.2 m from release point.	-1.0
362,500	338.37	Majority of liquid stream is being blown apart by vapour formation. The entire stream is broken apart about 20 percent of the time.	-1.0
366,700	338.42	Liquid stream begins to break-up near the release point. Complete shattering of the stream occurs occasionally.	-1.0
392,700	341.09	Stream break-up occurs about 2-3 cm from release point.	-1.0
470,600	348.81	Liquid stream has completely broken up. Visible drops appear infrequently.	-1.0
554,100	354.96	No large drops visible. Complete stream break-up within 1-2 cm (0.5-inch) of release point.	-1.0

Figure 1 shows the influence of the temperature of the type if jet generated after the nozzle, since a complete liquid jet to a fully sprayed one. Figure 2 shows the pressure effect on the jet type. Although both jets contain droplets after the nozzle, the spray angle is larger for the larger pressure. Figure 3 shows the effects on the jet of the change in diameter of the nozzle. In this particular case it can be see that the jet flashing location becomes closer to the nozzle, changing the profile at the exit of the nozzle since a liquid jet discharge to a complete sprayed jet.

The effect of the length of the nozzle, is normally represented by the length diameter ratio, instead the actual value. Figure 4 shows three cases of 850 kPa and 20°C for L/D, 0, 2 and 7 respectively.

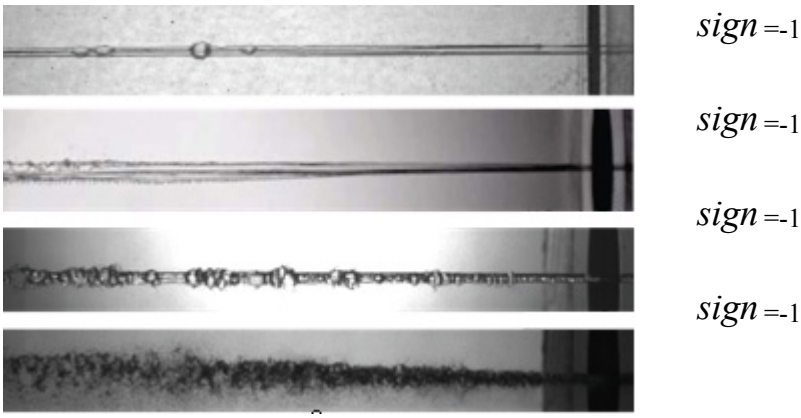

Figure 1: Photograph of a flashing jet from a nozzle diameter of 1mm and fixed pressure of 85.000 KPa, showing the test corresponding to five distinct temperatures, 13, 14, 18.5 and 20.2°C respectively. Source: [5].

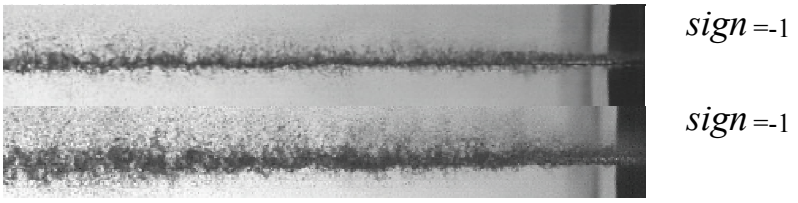

Figure 2: The effects of two pressure values, 850 kPa and 1250 Pa in a flashing jet. Temperature = 20°C, nozzle diameter = 1 mm. Source: [5].

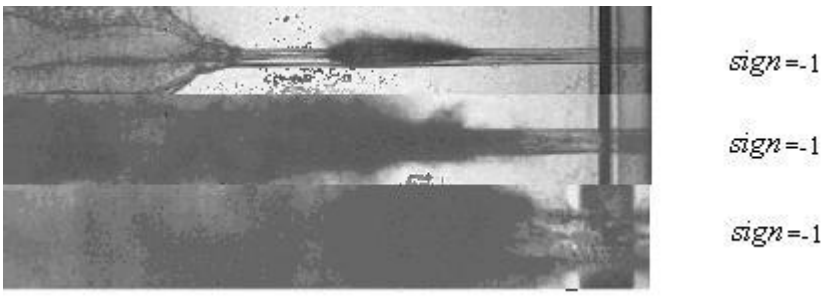

Figure 3: Flashing jet from three nozzle diameters (2 mm, 3mm and 4mm respectively). All cases tested at 850 kPa and 13°C. Source: [5].

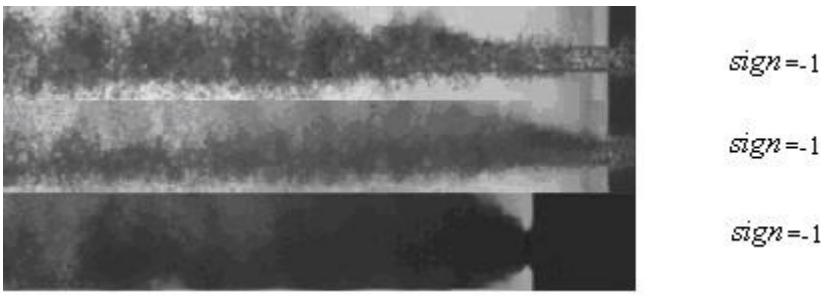

Figure 4: Flashing jet from a nozzle of 2 mm, 850 kPa and 20°C for L/D= 0, 2 and 7 respectively. Source: [5].

The type of regime achieve by the fluid after the release is an indication of how strong the nucleation rate was inside the fluid. The stronger the nucleation is, the breaking of the liquid core will be more extreme and the droplets generated tend to be smaller.

5 Discussions

The general trend of the experimental information is reproduced by the present model. The information shown in Table 1 highlights the quality of the obtained results. The output of the model reproduces the experimental observations reported in the original work.

The present model predicts that all the cases of R134a will produce a flashing jet. However, the experimental evidence is, in some cases, ambiguous. The criterion will depend on the accuracy in identifying a liquid with visible bubbles inside the jet or a complete liquid jet. It is important to mention that the order of magnitude of the reduced pressure range evaluated for the R134a cases is about 0.20 after . This value of reduced pressure is larger than any other experimental setting, where the common range for the evaluated reduced pressure is about 0.04. Therefore the dissipation coefficient has a smaller value which is overcome

for the production coefficient. The model is capable of reproducing the experimental observations related to basic influences of diameter increases, pressure increase, length increase, and temperature increase.

A good agreement was also obtained for experiments using water, . The model fails to predict the liquid discharges corresponding to the data reported by Miyatake et al. [14]. The discrepancies between the result and the observations reported can be related to presence of a large length diameter ratio, up to a maximum of L/D =78.2. When, the length of the nozzle becomes large in comparison with the diameter, then the temperature effect becomes stronger since the pressure energy is mainly used to overcome the viscous losses through the nozzle and the viscous forces in the nozzle walls affects the force balance in the fluid. This alters the physics of the system modelled. In this case the surface tension will not be the major force acting on nucleation. Therefore, the assumptions used to develop the expression of the production and dissipation coefficients do not apply in a correct way for this experimental data.

6 Conclusions

A one dimensional model of flashing from an aperture has been developed. This model uses the nucleation process as the major process within flashing jet. This model called production dissipation model covers the study of flashing occurs it or not, and it is capable of reproducing the effects on the jet of the change of diameter and length of the nozzle, as well as, the variation in temperature and pressure and their relative position to the critical temperature or pressure of the fluid.

The occurrence of a flashing jet can be determined by the model based on the force balance between the promoting forces and dissipation forces of nucleation, in a similar way to a second order damped system. This balance take into account individual effect of the problem parameters, such as initial pressure and temperature as well as geometry dimensions represented by dimensionless parameters as Reynolds number, Jacob number, Weber number, ratio of density, friction factors or discharge coefficient. This model can be used for both water and hydrocarbons fluids. The solution of the model will determine the behaviour of the system as sub-damped (flashing jet), damped or over damped system (liquid jet).

The model allows the inclusion of the friction factor or dimensionless roughness, as important parameter in the nucleation process sue to its important as a potential nuclei sources, which are not normally included in any other work presented in the literature.

If was found that the different behaviour of water and hydrocarbon is based on the appreciable difference of their properties. In particular the liquid density and gas density ratio of hydrocarbons and water, which represents the quantity of energy needed to overcome the phase change barrier by evaporation and differences in surface tension.

References

[1] Deaves, D.M., et al., Modelling of catastrophic flashing releases. *Journal of Hazardous Materials* (A88): p. 1-32, 2001.

[2] Michaella, M., N. Piccinini, and A. Poggio, Analysis of an LPG accidental release. *Process Safety and Environmental Protection*. **82**: p. 128-131, 2004.

[3] Lee, C.S. and S.W. Park, An experimental and numerical study on fuel atomization characteristics on high-pressure diesel injection sprays. *Fuel*. **81**: p. 2417-2423, 2002.

[4] Diek, H. and R.L. Roberts, The determination of the sauter mean droplet diameter in fuel nozzle sprays. *Applied optics*. **9**(9): p. 2007-2014, 1970.

[5] Yildiz, D., P. Rambaud, and J.v. Beek. *Break-up, droplet size and velocity characterisation of a two-phase flashing R134A jet*. in *5th International Conference on Multiphase Flow*. Yokohama, Japan. 2004.

[6] Park, B.S. and S.Y. Lee, An experimental investigation of the flash atomization mechanism. *Atomatization and Sprays*. **4**: p. 159-179, 1994.

[7] Peter, E.M., A. Takimoto, and Y. Hayashi, Flashing and shattering phenomena of superheated liquid jets. *JSME International Journal*. **37**(2): p. 313-321, 1994.

[8] Yildiz, D., *Dynamics of two-phase flashing jets*. VKI Lectures Series. Belgium: von Karman Institute for Fluid Dynamic. 2003

[9] Johnson, D.W. and J.L. Woodward, *RELEASE A Model with data to predict aerosol rainout in accidental releases*. Center for chemical process safety. New York: American Institute of Chemical Engineers. 1999

[10] Lin, S.P. and R.D. Reitz, Drop and spray formation from liquid jet. *Annual Review Fluid Mechanics*. **30**: p. 85-105, 1998.

[11] Brown, R. and L. York, Sprays formed by flashing jets. *American Institute of Chemical Engineers*. **8**(2): p. 149-153, 1962.

[12] Skripov, V.P., et al., *Thermophysical properties of liquids in metaestable (superheated) state*. Amsterdam: Gordon and Breach Science Publisher. 1988

[13] Reitz, R.D., A photographic study of flashing-boiling atomization. *Aerosol, Science and Technology*. **12**: p. 561-569, 1990.

[14] Miyatake, O., et al., An experimental study of spray flash evaporation. *Desalination*. **36**(2): p. 113-128, 1981.

[15] Potter, M., D. Wiggert, and M. Hondzo, *Mechanics of fluids*. Second Edition ed: Prentice Hall Inc. 1997

[16] Yan, F. and M. Giot, A nucleation model for superheated liquids in adiabatic vessel and pipes. p. 323-331, 1989.

[17] Barnea, D., O. Shoham, and Y. Taitel, Flow pattern transition for downward inclined two phase flow; horizontal to vertical. *Chemical Engineering Science*. **37**(5): p. 735-740, 1982.

[18] Barnea, D., O. Shoham, and Y. Taitel, Flow pattern transition for vertical downward two phase flow. *Chemical Engineering Science*. **37**(5): p. 741-744, 1982.

[19] Barnea, D., et al., Flow pattern transition for gas-liquid flow in horizontal and inclined pipes. Comparison of experimental data with theory. *International Journal of Multiphase Flow*. **6**(3): p. 217-225, 1980.
[20] C Cartes, M.G.C.a.R.S., Van der waals normal form for a one-dimensional hydrodynamic model. *Physics Review*. **70**(031302-1/8), 2004.
[21] R Ramanathan, Y.K.M., K. K. Gupta, Agam K Jha and S. S. Singh, A comparative study of two models of QCP-Fireball formation. *eprint arXiv:hep-ph/0502046,* 2005.
[22] D. L. Frost, R.B., and J. Nerenberg, *TP 12123E. Small-Scale BLEVE Tests with Refrigerant-22*. 1995, Transportation Development Centre: Quebec. p. 48.
[23] Polanco, G., *Phase change within flows from breaches of liquefied gas pipelines*. 2008, Coventry: Coventry.
[24] Solomon, et al., Flow and atomization in flashing injectors. *Atomization Spray Technology*. **1**: p. 53-76, 1985.
[25] Hervieu, H. and T. Veneau, Experimental determination of the droplet size and velocity distributions at the exit of the bottom discharge pipe of a liquefied propane storage tank during a sudden. *Journal of Loss Prevention in the Process Industries*. **9**(6): p. 413-425, 1996.
[26] Bolle, L.a.D.-Z., P., Experimental and theoretical analysis of flashing water flow through a safety valve. *Journal of Hazardous Materials*. **Vol. 46.**: p. pp. 105-116, 1996.
[27] Gemci, T., et al., Experimental study of flash atomization of binary hydrocarbon liquid. *International Journal of Multiphase Flow*. **30**: p. 395–417, 2004.
[28] Gemci, T., et al., Flash atomization of water / acetone solutions. *Atomization and Sprays*. **14**: p. 459-475, 2004.

Section 6
Applications in biology

This page intentionally left blank

Modelling nanoparticle transport in an animal exposure chamber: a comparison between numerical and experimental measurements

F. Morency & S. Hallé
Département de Génie Mécanique, École de Technologie Supérieure, Canada

Nanoparticles transport in an exposure chamber is investigated using computational fluid dynamics (CFD). This exposure chamber is used to assess the lung toxicity in rats resulting from the inhalation of airborne NPs. The mathematical model for airflow is based on the three-dimensional Reynolds-averaged Navier-Stokes equations with turbulence modelling. Simulations of airborne NPs are based on assumptions such that their motions are similar to the ones of a single sized diameter distribution of a passive contaminant.
Keywords: nanoparticles, CFD, exposure chamber, passive contaminant.

1 Introduction

The evaluation of the potential hazards for human health associated with inhalation or other form of contact with nanoparticles (NPs) is a question of much interest in the scientific community. Indeed, the phenomenal emergence of various types of nanotechnologies led many governmental agencies to present discussion papers on the safe use of nanometric scale particles, herein called NPs. These international reports are unanimous in supporting proactive measures to ensure the safety of workers exposed to NPs [1, 2].

One of the basic elements for the risk assessment evaluation in a work environment consists in an adequate characterization of the degree of exposure. In the case of exposition to airborne NPs, numerical simulations could be used advantageously as a tool to safely predict these exposure levels. In order to achieve this though, the development of models is still required. It is expected that these models once validated will make it possible to predict the behaviour of airborne NPs in a workplace environment, to evaluate the effective exposure of

WIT Transactions on Engineering Sciences, Vol 69, © 2010 WIT Press
www.witpress.com, ISSN 1743-3533 (on-line)
doi:10.2495/AFM100461

humans to these NPs, and to safely assess the associated risks. This will in turn make it possible to design efficient ventilation and/or filtering systems which would make it possible to contain and to recover from an accidental release of undesirable NPs.

In that perspective of developing reliable models to simulate the transport and dispersion of airborne NPs, the objective of this paper is to present numerical results for a simple model of NPs dispersion in an animal exposure chamber. This exposure chamber will be used in further works to assess the lung toxicity in rats resulting from the inhalation exposures to airborne titanium dioxide (TiO_2) NPs.

More specifically, air flow simulation results are presented in the exposure chamber for which the NPs are assumed to behave as a passive contaminant. First, a complete description of the exposure chamber is provided. Then, the mathematical model for the air flow in the exposure chamber is detailed. Finally, some numerical results will be compared with experimental measurements made in the real chamber.

2 Exposure chamber

An exposure chamber is a device used to assess the toxicity of aerosols or gases during inhalation studies with laboratory animals. These inhalation studies, if carried out under controlled conditions, can simulate potential exposure conditions of humans at workplaces [3]. Controlled conditions mean that the level exposure must be uniform in space and time. The technical performance of our exposure chamber is critical for the credibility of an inhalation studies since non-uniform TiO_2 concentration will lead to a **non-uniform dose delivery** to the rats.

Fig. 1 presents the experimental set-up that will be used for the in vivo study. The exposure chamber (Unifab, Kalamazoo, USA) is 0.5 m^3 in volume. The chamber is equipped with 2 inlets located in the upper part and one outlet located in the lower part. As indicated in fig. 1, airborne TiO_2 NPs are delivered into the chamber by a 24-jets Collison nebulizer. The aerosol, from inlet 2, is then mixed and diluted by filtered fresh air admitted into the chamber via inlet 1. A round deflector plate in the upper part ensures thorough and even distribution of air. In any case, the concentration of airborne NPs should be kept as uniform as possible in the zone delimited by the deflector at the top and the grid at the bottom. Such exposure rooms are usually design to work as a mixing chamber and therefore create a complex 3D air flow.

This exposure chamber is design for whole-body exposure studies. To adapt the actual chamber for a node-only system, seven holes were drilled on one side. These holes were tapped to receive each a 4.8 cm nominal Plexiglas pipe. The central tube is connected to a DUST Track and a Dekati sampling system (sampling rate = 20 l/min).

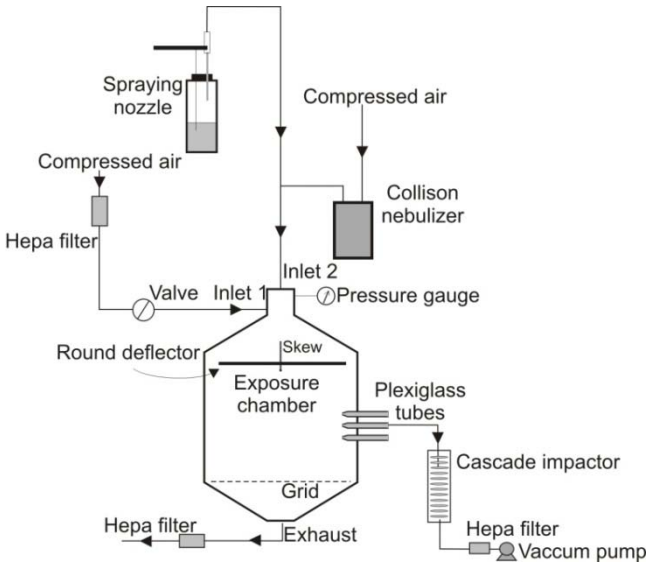

Figure 1: Schematic view of the experimental set-up.

3 Mathematical model

3.1 Governing equations for the air flow

Air flow within the exposure chamber is modelled by the three-dimensional Reynolds-averaged Navier-Stokes (RANS) equations using the eddy viscosity (ϑ_t) assumption. The mass conservation equation, eqn. (1), and the momentum conservation equation, eqn. (2), are:

$$\frac{\partial U_i}{\partial x_i} = 0 \tag{1}$$

$$U_j \frac{\partial U_i}{\partial x_j} = -\frac{1}{\rho}\frac{\partial P}{\partial x_i} + \frac{\partial}{\partial x_j}\left[(\vartheta + \vartheta_t)\left(\frac{\partial U_i}{\partial x_j} + \frac{\partial U_j}{\partial x_i}\right)\right]. \tag{2}$$

For the airflow studied in this paper, turbulent flow regime is present into the chamber. These turbulent effects are modelled by the *k*-ω turbulence model. In the *k*-ω model, the eddy viscosity is function of the turbulent kinetic energy (*k*) and the specific dissipation rate (ω). Both variables can be determined by solving two additional transport equations. More details on the *k*-ω turbulence model are available in Wilcox [4].

3.2 Governing equations for the nanoparticles transport

Airborne NPs are subjected to numerous physical phenomena that shape their size distribution in space and time. Coagulation leads to a reduction of the total number of particles, to an increase in the average particle diameter, and to an increase in the number of molecules in the particles. Growth of the particle

occurs by gas-to-particle conversion. Sedimentation resulting from the gravity field also occurs, with the particle settling velocity depending on particle size.

However, under certain hypothesis, NPs distribution can be considered constant in space and time: i) for low NPs concentration, no coagulation or agglomeration of NPs will occur [5] and thus aerosol distribution is not altered; ii) for the exposure chamber, there is no gas-to-particle conversion; iii) sedimentation or settling of NPs is negligible in the global dispersion process, as current studies indicate [6, 7].

Moreover, because of their low concentration, NPs have no effects on the air flow and behave as a passive contaminant. This approximation is widely used for clean room design [8, 9].

In the exposure chamber, the generated NPs distribution is well represented by a single mean aerodynamic diameter. Several aerosol generation tests were performed by changing the input air pressure. The aerosol size distribution data obtained from a cascade impactor (Electrical Low Pressure Impactor, Dekati Inc.) located at inlet 2, show a maximum concentration of airborne TiO_2 in the order of 9.40×10^6 particles/cm^3 with a relatively narrow size distribution around a mean aerodynamic diameter of 26 nm (fig. 2).

Under the assumptions stated above, the transport of a turbulent diffusing passive contaminant in a velocity field can be solved either using a Lagrangian approach, as in the studies of Wang et al. [10] and Horender et al. [11]. Another possibility is to solve an Eulerian model governed by the Reynolds averaged mass transport equation for the contaminant:

$$\frac{\partial(\rho Z_A)}{\partial t} + \frac{\partial(\rho Z_A U_j)}{\partial x_j} = \frac{\partial}{\partial x_j}\left[\left(\rho D_j + \frac{\mu_t}{Sc_t}\right)\left(\frac{\partial Z_A}{\partial x_j}\right)\right] \tag{3}$$

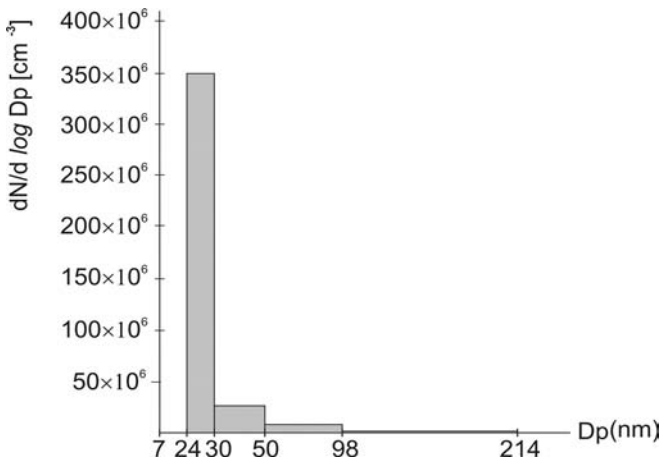

Figure 2: Experimental size distribution of airborne TiO_2 NPs at inlet 2.

In eqn. (3), Z_A is the ratio of the contaminant mass fraction to the total mass, D_j is the NPs Brownian diffusion coefficient and the turbulent Schmidt number

(Sc_t) represent the ratio of the eddy viscosity to the eddy diffusivity. The turbulence in the exposure chamber will generate diffusion effects which are orders of magnitude higher than Brownian diffusion. These turbulent diffusion effects are characterize by the turbulent Schmidt number which is usually close to unity; therefore Sc_t was fixed to 0.9. However, the intensity of turbulence becomes negligible near surfaces and the Brownian diffusion is the dominant mechanism in that region.

In a previous paper, Morency et al. [12], compared three Brownian diffusion models for NPs. They shown the models proposed by Friedlander [13] and Hinds [5] give almost identical diffusion coefficients while the diffusion coefficients obtain by the Gussman's model [14] are slightly lower. In the current study, D_j was fixed to 6.0×10^{-9} m^2/s according to the value predicted by the Friedlander's model for a NP diameter of 30 nm.

In the present study, the set of coupled eqns (1, 2 and 3), are solved by a finite volume method using the commercial software FLUENT version 6.3. An Eulerian approach, similar to the one proposed here, has been used by other researchers such as Zhang et al. [15], to study NPs deposition in human tracheobronchial region or by Kumar et al. [16], to study NPs concentration in an urban street canyon.

3.3 Computational domain and boundary conditions

Fig. 3 shows a three-dimensional view of the exposure chamber computation domain. The model width (Δx), length (Δy) and height (Δz) are 67.4 cm, 67.4 cm and 115.3 cm respectively. Diameter of the two inlets is 3.8 cm. In order to limit

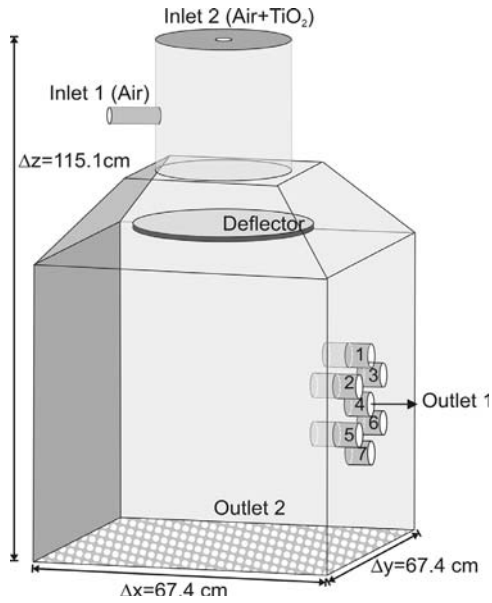

Figure 3: Computational domain

the computational time, the bottom part of the exposure chamber was not considered in the numerical model. Therefore, the grid located at the bottom is modeled as an outlet vent in FLUENT. An outlet vent is an infinitely thin surface with a pressure drop proportional to the dynamic pressure of the flow. The velocity distribution at inlet 1 and 2 are considered uniform. No-slip conditions are imposed at wall for the velocity components.

The contaminant mass fraction to the total mass (Z_A) imposed at inlet 2 is determined from the experimental size distribution of airborne TiO_2 NPs. We have:

$$Z_A = \frac{\left[n \times {}^{\pi}/_{6} (D_p)^3 \times \rho_{TiO2}\right]}{[total\ mass\ in\ 1\ cm^3]} \tag{5}$$

with n=9.40×10^6 particles/cm^3, ρ_{TiO2} = 3895 kg/m^3 (anatase TiO_2) and D_p = 26.4×10^{-9} m, the mass fraction at inlet 2 is set to 2.89×10^{-7} kg/kg.

3.4 Diffusional losses of nanoparticles

Diffusion is the largest force acting on NPs in the laminar region of the boundary layer. Airborne NPs will disperse rapidly and will diffuse toward solid surfaces who act as a sink. Constant removal of NPs from the air by deposition on solid surfaces leads to significant diffusion losses in the exposure chamber.

It is not possible to develop an analytical expression to predict the loss of NPs for a complex three dimensional flow pattern such as the one observed in the exposure chamber. In a straight tube, NPs transport efficiency can be determined by the following relation [17]:

$$\eta_{diffusion} = e^{-[\xi Sh]}, \tag{6}$$

where $\xi = \frac{\pi DL}{Q}$. Key parameters determining the transport efficiency are the tube diameter (D), the tube length L, the Reynolds number based on flow rate Q (Re_d) and the particles diffusion coefficient (D_j). For a tube with fully developed turbulent flow conditions, Friedlander [13] proposed a relation to determine the Sherwood number (Sh):

$$Sh = 0.0118\, Re_d^{7/8} \left[\frac{\mu}{\rho_{air} D_j}\right]^{1/3}. \tag{7}$$

NPs transport and diffusion in a turbulent pipe flow are calculated within FLUENT in order to compare the numerical results with Friedlander's relation. Fig. 4 presents the axisymmetric computational domain used in FLUENT. A constant velocity of 5 m/s is imposed at inlet with a density of 1.225 kg/m^3, for Re_d=3423. For this flow condition, the entry length region spans less than 5% of the total pipe length.

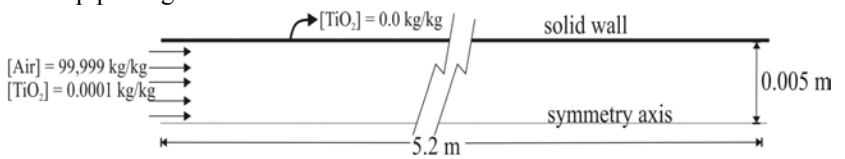

Figure 4: Tube flow geometry.

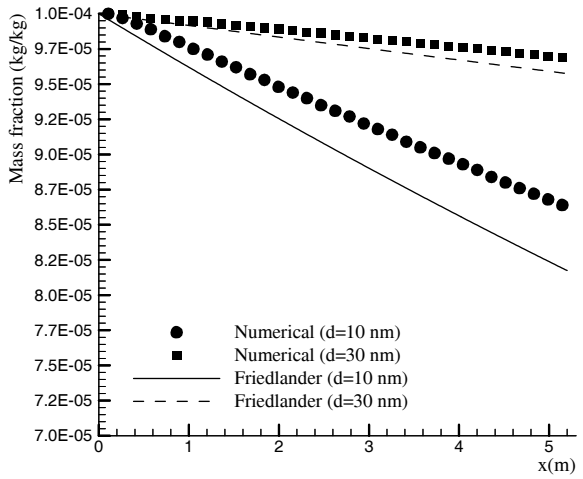

Figure 5: Mass fraction of airborne NPs in turbulent tube flow as a function of length.

Fig. 5 compares numerical transport efficiencies calculated by FLUENT to the ones obtained using eqn. (6). Results for NPs diameters of 10 nm and 30 nm are plotted. The numerical transport efficiencies are slightly higher than the correlation, around 6% of error in the worst case. The error band for the correlation is not known, but it can be expected to be similar to the one commonly admitted for heat transfer correlations, around 30%.

4 Results

In this study, NPs were treated as a passive contaminant. This approximation is based on the hypothesis that the aerosol size distribution is not altered by coagulation. Fig. 6 presents the mass fraction distribution of NPs in the cylindrical part of the exposure chamber. Two-dimensional **slice,** at y=0.0 m, shows the mixing of fresh air from inlet 1 with airborne NPs from inlet 2. Initial mass fraction of 2.89×10^{-7} kg/kg at inlet 2 decreased to an average value of 1.0×10^{-7} kg/kg at the cylinder bottom end (z=0.0 m). Assuming spherical particle of 26 nm in diameter, this mass fraction correspond to 3.3×10^{6} particles/cm^3. According to Hinds [5] for an initial concentration of 5×10^{6} particles/cm^3, the time require to halve the number of particles by coagulation, is in the order of five minutes. With the actual ventilation rate of 143.5 l/min, the NPs residence time is estimated to 3½ minutes, and it seems reasonable to neglect the coagulation of NPs as a first approximation.

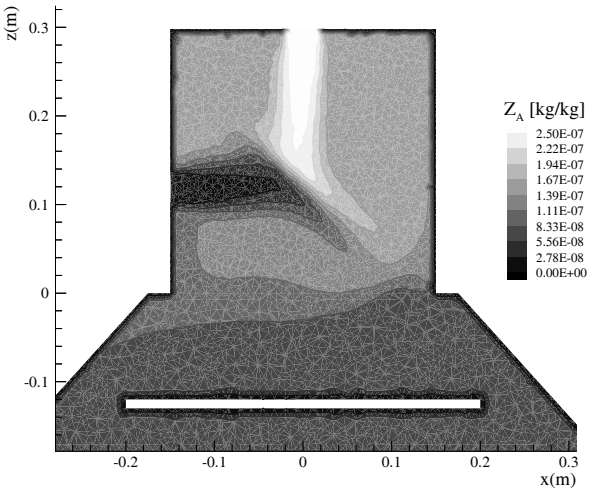

Figure 6: Mass fraction distribution in the cylindrical zone.

As stated in section 2, exposure rooms are design to work as a mixing chamber. Thus, the concentration of airborne NPs should be as uniform as possible in the animals breathing zone. Fig. 7 shows the two-dimensional mass fraction distribution in the Plexiglas tubes region. Predicted mass fraction present not significant variation in spite of the disturbances in the velocity distribution observe in Fig. 8. Central tube used for aerosol sampling created a suction zone with a velocity reaching 0.5 m/s while the air velocity near tube 1 and 7 (Fig. 3) remain close to zero.

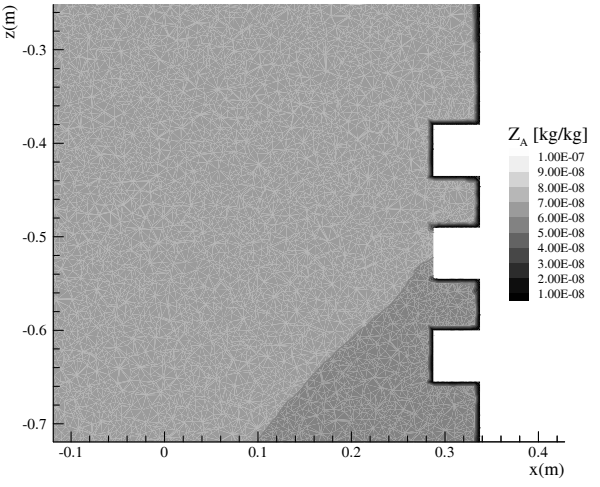

Figure 7: Mass fraction distribution in the breathing zone.

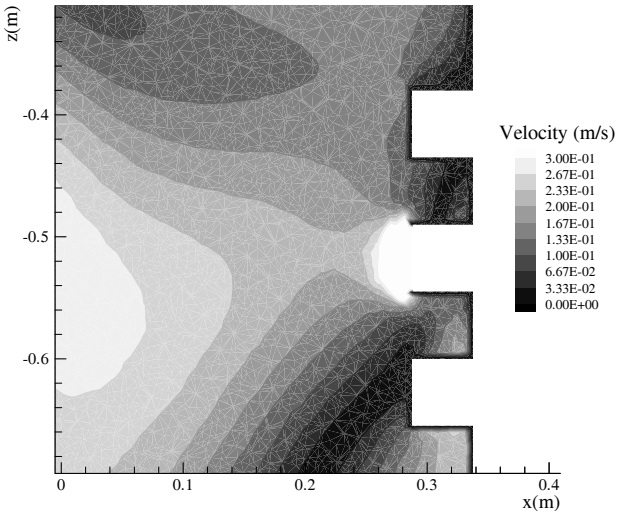

Figure 8: Velocity distribution in the breathing zone.

Table 1 presents the predicted mass fraction of NPs in the exposure chamber at seven location points. These seven points are respectively located on the centerline of each of the Plexiglas tube at 1cm from the tubes tip. For the simulated ventilation and aerosol generation conditions, the NPs concentration in the rats breathing zone is fairly uniform. The averaged mass fraction is 6×10^{-8} kg/kg with a standard deviation of 0.13×10^{-8} kg/kg. Table 1 also shows the measured mass fraction at the sampling tube (tube 4). Although the location of the Dekati sampling system probe is known approximately, the agreement between the experimental and predicted mass fraction is excellent.

Table 1: Comparisons of the predicted and measured mass fraction.

Tube (Fig. 3)	**1**	**2**	**3**	**4**	**5**	**6**	**7**
Z_A ($\times10^{-8}$ kg/kg) (numerical)	6.12	6.15	5.90	6.02	6.04	5.80	5.92
Z_A ($\times10^{-8}$ kg/kg) (measured)				5.59			

5 Conclusion

This study focuses on airborne NPs transport and diffusion in an exposure chamber. Based on the assumption that NPs behave as a passive contaminant, the conclusions can be summarized as follows:

a) Comparison between correlations and numerical simulations shown that diffusional losses of airborne NPs can be taken into account by imposing a zero mass fraction at solid walls.
b) The upper part of the exposure chamber act as a mixing chamber which create favorable flow conditions to disperse uniformly the NPs from inlet 2 and to prevent coagulation.
c) Mass fraction in the animal's breathing zone is uniform with a standard deviation at the seven Plexiglas tubes tips of only 2%.
d) The agreement between the measured and predicted mass fraction at the sampling tube is remarkable.

References

[1] Aitken, R. J., Creely, K. S., & Tran, C. L., Nanoparticles: An occupational hygiene review. Health & Safety Executive Research Report 274, 2004.
[2] Ostiguy, C., Roberge, B., Menard, L., & Endo, C.-A., Guide de bonnes pratiques favorisant la gestion des risques relies aux nanoparticules de synthèse. IRSST Guide technique R-586, 2008.
[3] Pauluhn, J., Overview of Inhalation Exposure Techniques: Strengths and Weakness. *Experimental and Toxicologic Pathology,* **57**, pp. 111-128, 2005.
[4] Vorbau, M., Hillemann, L., & Stintz, M., Method for the charcterization of the abrasion induced nanoparticle release into air from surface coatings. *Aerosol Science,* **40**, pp. 209-217, 2009.
[5] Hinds, W. C., *Aerosol Technology: Properties, Behavior, and Measurement of Airborne Particles*. John Wiley & Sons: New York, 1999.
[6] Lechner, M. D. &Mächtle, W., Determination of the Particle Size Distribution of 5-100-nm Nanoparticles with the Analytical Ultracentrifuge: Consideration and Correction of Diffusion Effects. *Progr. Colloid Polym. Sci.,* **113**, pp. 37-43, 1999.
[7] Hervé-Bazin, B., *Les nanoparticules - Une enjeu majeur pour la santé au travail ?* ed. INRS, EDP Sciences: Les Ulis, 2007.
[8] Hu, S. C., Chuah, Y. K., & Yen, M. C., Design and Evaluation of a Mini-Environment for Semi-Conductor Manufacture Processes. *Building and Environment,* **37**, pp. 201-208, 2002.
[9] Zhao, B. &Wu, J., Numerical Investigation of Particles Diffusion in a Clean Room. *Indoor and Built Environment,* **14(6)**, pp. 459-479, 2005.
[10] Wang, X., Gidwani, A., Girshick, S. L., & McMurry, P. H., Aerodynamic focusing of nanoparticle: II. Numerical simulation of particle motion through aerodynamic lenses. *Aerosol Science and Technology,* **39(7)**, pp. 624-636, 2005.
[11] Horender, S., Lipowsky, J., Sommerfeld, M., Schwerin, M., & Badeke, K.-U., Deposition of SiO2 nanoparticles produced in a turbulent H2/O2 Flame. *Aerosol Science and Technology,* **42(11)**, pp. 873-883, 2008.

[12] Morency, F., Hallé, S., Dufresne, L., & Emond, C., "Evaluation of Diffusion Models for Airborne Nanoparticles Transport and Dispersion," in *Advances in Fluid Mechanics VII*, Ashurst, England, 2008.
[13] Friedlander, S. K., *Smoke, Dust, and Haze - Fundamentals of Aerosol Dynamics*. Oxford University Press: New York, 2000.
[14] Gussman, R. A., On the Aerosol Particle Slip Correction Factor. *J. Appl. Meteorol.,* **8**, pp. 999-1001, 1969.
[15] Zhang, Z., Kleinstreuer, C., & Kim, C. S., Airflow and nanoparticle deposition in a 16-generation tracheobronchial airway model. *Annals of Biomedical Engineering,* **36(12)**, pp. 2095-2110, 2008.
[16] Kumar, P., Garmory, A., Ketzel, M., Berkowicz, R., & Britter, R., Comparative study of measured and modelled number concentrations of nanoparticules in an urban street canyon. *Atmospheric Environment,* **43**, pp. 949-958, 2009.
[17] Brockman, J. E., *Sampling and transport of aerosol, Aerosol measurements: principles, techniques and applications*. 2nd edition, eds. P. A. Baron and K. Willeke, Wiley-InterScience Inc.: New-York, 2001.

This page intentionally left blank

The influence on Dobutamine docking of blood flow around the sinoatrial node

A. K. Macpherson[1], S. Neti[1], M. Averbach[2], P. A. Macpherson[3], C. Chu Takositkanon[1] & M. Chaney[4]
[1]*Institute of Biomedical Engineering and Mathematical Biology, Lehigh University, USA*
[2]*Division of Cardiology, St Lukes Hospital, USA*
[3]*Department of Applied Technology, Rogers State University, USA*
[4]*Department of Surgery, College of Physicians & Surgeons, Columbia University, USA*

Abstract

Traditionally, the docking of drugs onto cell receptors has been considered to occur from the capillaries into the interstitial fluid and thence to the cell receptor. In patients that are unable to exercise, pharmacologic stress testing is performed, either with vasodilatory agents (e.g. adenosine) or Dobutamine, which is a pro-inotropic and chronotropic drug. This drug docks with the sinoatrial node (SAN) in the upper right atrium of the heart near the superior vena cava. Due to its unique location it is exposed to both the blood flow coming from the right ventricle as well as the flow in the interstitial fluid. The SAN in the human has a surface area of approximately 4.6 mm^2 and 0.1-0.2 mm thick and hence has a large surface area to volume ratio. The flow on the outside was simulated by a multiscale model consisting of a continuum flow, a Monte Carlo region and at the inner surface a molecular dynamics model. The simulation of the interstitial fluid contains more unknowns than the external flow. The SAN is relatively thin and thus it does not contain as many capillaries as would be found in normal tissue. The drug molecular dimensions are such that the Dobutamine can readily pass through the spaces between the capillary molecules, usually approximately 40 microns. Due to the number of unknowns involved with the capillary solution a continuum solution involving a diffusion coefficient based on the Lebas molecular volume was undertaken to obtain the order of magnitude of the

WIT Transactions on Engineering Sciences, Vol 69, © 2010 WIT Press
www.witpress.com, ISSN 1743-3533 (on-line)
doi:10.2495/AFM100471

docking. It was found that the number of drug molecules docking on the surface was much greater than the number docking through the interstitial fluid.
Keywords: sinoatrial, Dobutamine, drug docking, bloodflow, drug diffusion.

1 Introduction

One method to evaluate for underlying coronary artery disease is to perform stress testing. Often, myocardial stress is achieved by the patient walking on a treadmill or riding a stationary bicycle while being monitored. In patients that are unable to exercise, pharmacologic stress testing is performed, either with vasodilatory agents (e.g. adenosine) or Dobutamine, which is a pro-inotropic and chronotropic drug. Dobutamine (the drug) is injected in the patients arm and is absorbed by the sinoatrial nodes (SA) in the right ventricle. There are receptors on the SA onto which the drug docks. The docking process involves certain atoms on the drug interacting with appropriate atoms in receptor.

There are three possible mechanisms for the drug to affect the membrane, figure 1 [1]. One is by direct docking with the receptor (a), the second is by entering the membrane and then diffusing through the membrane to dock with

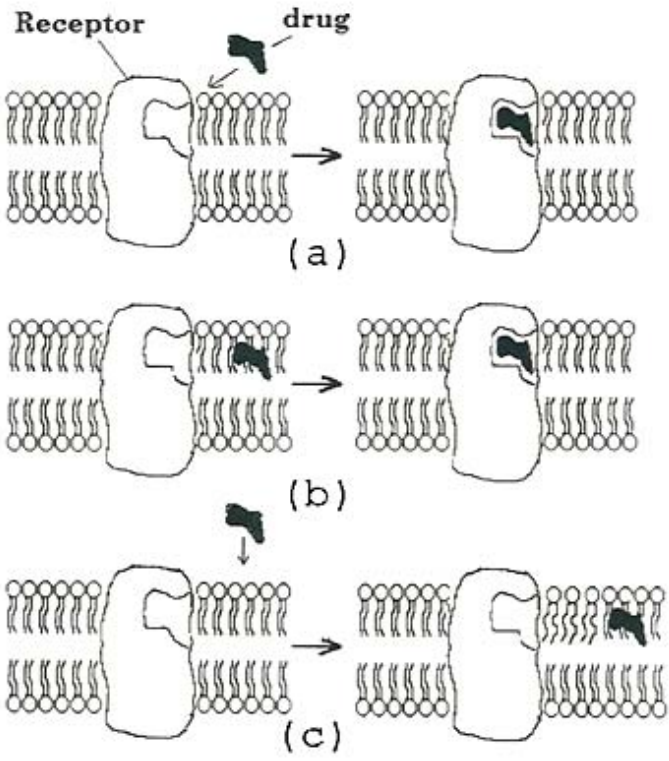

Figure 1: Mechanisms for the drug affect on the membrane.

the receptor (b). The third is by interacting directly with the membrane. Probably all three mechanisms are involved. However for the present work only the direct action is considered. The SA are the pace makers of the heart and the effect of the Dobutamine is to increase the heart rate. In undertaking an analysis of the effects of the drug it is important to know how much of the drug that is injected is absorbed by the cells. The SA nodes are located at the entrance to the superior vena cava past which the blood flows to the left ventricle. Blood also flows through the interior of the SA via the capillary network. In the present case the ratio of surface area to volume ratio is much larger than in most drug docking situations. Thus it would appear possible that a larger percentage of the drug could be absorbed at the surface as opposed to the usual mechanism by diffusion from the capillary bed. The present paper examines this proposition.

2 Method of calculation

Probably the earliest experimental work on Dobutamine docking on beta 1 sites is [13]. Here experiments were undertaken on dogs and it was found that the main effect was '*direct action on beta 1 cardiac receptors*'. The effect on beta 2 and alpha sites was slight. The same view has been confirmed many times since and generally persists today.

The Chemical Computing Group's MOE molecular modeling software (Montreal, Quebec, http://www.chemcomp.com) was used for protein construction, visualization and docking calculations. The structure of the human beta 1 adrenergic receptor was based on sequence homology with the known X-ray structure of turkey beta 1 receptor, complexed with Cyanopindolol (2VT4, Protein Data Bank). The FASTA routine within Biology WorkBench 3.2 (http://workbench.sdsc.edu) was used for sequence alignment and revealed an E score = 1.8e-65, and pair-wise identity of 77.5% (ungapped), over 345 amino acid residues. The final structure of the complex was achieved by molecular dynamics simulation and minimization using the Merck Molecular Force Field (MMFF94x) and parameter set, as supplied within MOE program. Specifically a non-bonded cut-off was set at 12.0 Angstoms. Solvation effects were incorporated using the Born implicit model. As it does not appear that the docking of Dobutamine has been studied experimentally a probable binding site was calculated. The Dobutamine structure was built and minimized. It was positioned initially by superimposing it with the Cyanopindolol molecule as observed complexed within the turkey beta 1 structure.

An additional and supporting approach for determining the potential Dobutamine site was guided by using the Alpha Site Finder methodology [14], a feature of the Chemical Computing Group's MOE molecular modeling software. The algorithm calculates and displays potential regions of tight atomic packing on a protein surface. Both methods were in agreement and established a starting point for docking studies using the MOE Flex algorithm. The best binding site was based on a number of scoring functions (AEC scoring, Affinity DG scoring, HB scoring and London DG scoring (http.//chemcom.com for detailed definition). The result of our docking study based on the best score is shown in

figure 2. The appropriate amino acid sites on the receptor are shown, which indicate a tightly closed and energetically bound ligand. It be seen that there are five possible residue sites on the Beta 1 receptor that are in close contact and contribute to its binding of Dobutamine. Ser 212 and Ser 215 form H-bonds with the meta and the ligand's para-hydroxyls (1.6 A and 1.8 A, respectively). An amino salt- bridge interaction is formed with Asp 121 (1.2 A), along with an H-bond to Asn 329 (1.5 A). The Gly 98 backbone carbonyl is observed to form an H-bond with Dobutamine's other para-hydoxyl group (1.5 A). Also contributing to the stabilization of Dobutamine binding are the hydrophobic and aromatic residues that form hydrophobic and pi-stacking interactions with the ligand's aromatic system.

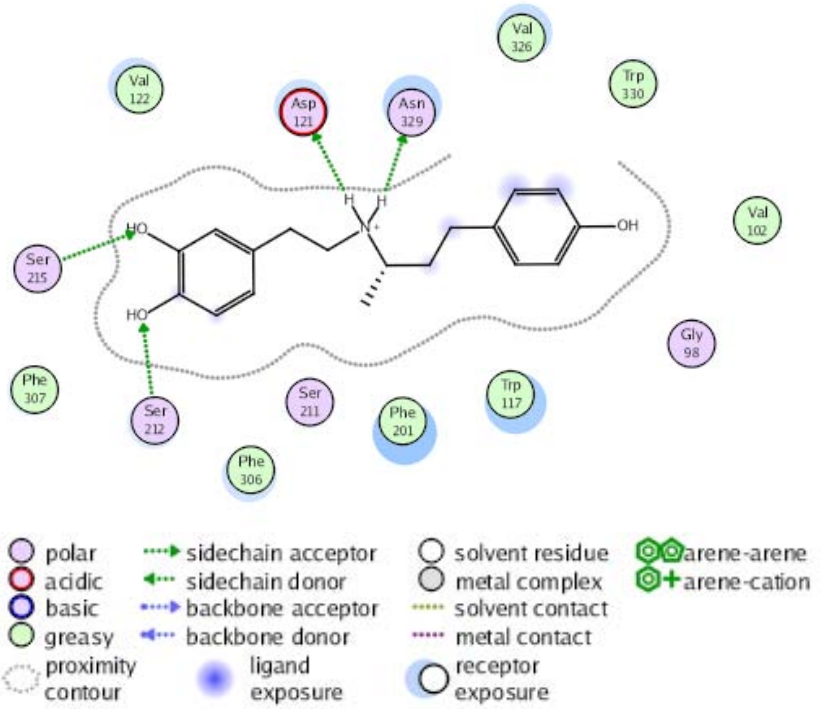

Figure 2: A Two-Dimensional Beta 1 – Dobutamine contact map. Close contacts (less than 3.5 Ang) are displayed indicating those Beta 1 residues that are responsible for binding Dobutamine. The legend indicates the type of interaction, residue properties, ligand and receptor exposure, as well as the proximity countour. Residue numbers refer to human Beta 1.

The external blood flow calculations were undertaken using a multiscale model [5] which was modified for the present calculations. The flow in the region most distant from the surface was a continuum region, the interaction at

the blood cell size level is a Monte Carlo process and the interactions with the receptors are undertaken using a direct simulation method known as molecular dynamics.

Continuum Scale: As details on neither the dimensions of the right atrium nor the blood flow velocity were available the continuum level solution could not be undertaken. Thus average values were chosen from [6]. The value used was 7.0 x 10^9 Å/sec.

Blood cell scale: The Monte Carlo method has been described previously in [5] so it will only be briefly reviewed here. The Monte Carlo region of interest 12000Å x 4000Å x 3000Å was divided into 100 cells. The method involves separating the motion into a collisional exchange of information and a convective information exchange. The blood is considered to be composed of water, erythrocyte, albumin, and Dobutamine. As the medium is a liquid then the collisional information was undertaken using the Landau equation.

The initial assignment of particle positions is random in the three directions. The velocities of the particles were set with a Maxwellian distribution appropriate to the temperature

The solution starts by taking a Monte Carlo fraction of the molecules. In the present case the fraction was 1/20. The change of velocity was undertaken using the Landau equation which in the test particle form below has been described as *a generalized diffusion equation in velocity space* [6]. Expressed in a non-dimensional form it becomes

$$\partial\phi_\tau = \partial_{v_r}(-F_r + 0.5\partial_s T_{rs})\phi \tag{1}$$

where $\boldsymbol{\phi}$ is the velocity distribution, the v_r differentiation is with respect to the non-dimensional velocity v/2kT, subscript $\boldsymbol{\tau}$ is differentiation with respect to the non-dimensional time defined below.

$$\boldsymbol{F_r} = -8\boldsymbol{v}^{-1}\boldsymbol{G}(\boldsymbol{v})\boldsymbol{v_r} \tag{2}$$

$$\boldsymbol{T_{rs}} = 2\boldsymbol{v}^{-1}\boldsymbol{H}(\boldsymbol{v})\boldsymbol{\delta_{rs}} + 2\boldsymbol{v}^{-3}\boldsymbol{E}(\boldsymbol{v})\boldsymbol{v_r}\boldsymbol{v_s} \tag{3}$$

and H,G and E are tabulated [6]. The non-dimensional time [7] is

$$\boldsymbol{t} = \frac{\boldsymbol{\beta}^{3/2}\boldsymbol{Bn}}{\boldsymbol{m}^{1/2}}\boldsymbol{\tau} \tag{4}$$

where $\boldsymbol{m}$ is the mass, $\boldsymbol{n}$ the number density, $\boldsymbol{\beta}$=1/kT and $\boldsymbol{B}$ is defined as

$$\boldsymbol{B} = 8\boldsymbol{\pi}^5 \int_0^{l_m} \boldsymbol{l}^3 \boldsymbol{V_l} \boldsymbol{dl} \tag{5}$$

The force on a particle will consist of a drag due to G(v) and a random force due to H(v). The interaction time scale is as defined in equation (5). The convective step is then implemented. This is achieved by choosing a short length

of time ΔT. The particles then move with the velocity **v** attained at the end of time ΔT for a distance **v** ΔT. New cells are then formed and the process repeated. The boundary conditions as described above are applied at the end of each time step ΔT. The value of ΔT was determined as follows [8]. Within a cell containing N particles the particle with the largest total interaction cross section σ_i is chosen for collision where

$$\boldsymbol{\sigma}_i = \sum_{j=1}^{N} \frac{\left|\boldsymbol{c}_i - \boldsymbol{c}_j\right|}{\boldsymbol{c}_i} \boldsymbol{\sigma}_{oij} \tag{6}$$

The cross section is very difficult to calculate in the present case as the particles are so large. Thus two possible interactions were considered. In one case the particles were considered to carry a charge and the collision cross section σ_{oij} is given in terms of the deflection angle χ_m. In the other case, the particles were considered to be hard spheres. The two cases were compared to judge the importance of the cross sectional approximation. The procedure then continues by choosing two colliding particles and time t calculated by

$$t_i = -\xi^*(n)/(\sigma_i N) \tag{7}$$

where ξ is a random number between 0 and 1, n is the number of molecules in the cell, N is the number density. This process is repeated for all cells.

The geometry for the calculation of the diffusion of the Dobutamine in the sinus node is complex as shown in figure 3 from [9]. The arrows point to capillaries. The length of the centre arrow is approximately 50 μm long. The distance between the capillaries are then 48μm and 81μm. An accurate calculation of a docking process would require detailed knowledge concerning the cell structure, the location of the interstitial fluid, the capillary lengths, the number of capillaries normally active etc., within the limits discussed below the diffusion equation

$$\frac{\partial C_N}{\partial t} = D \frac{\partial^2 C_N}{\partial^2 x} \tag{8}$$

can be approximately solved. Although the diffusion process is three dimensional [5], due to the uncertainties in the present case only a one dimensional solution will be considered.

The molecular dynamics region was the region above the surface and below the Monte Carlo region. The beta 1 receptor molecule rises approximately 50Å above the cell surface. Thus the lower surface of the Monte Carlo region was placed at 57Å above the cell surface. If a Dobutamine molecule entered the molecular dynamics region it was allowed to proceed at its current velocity to the cell surface. The density of beta 1 receptors of beta 1 receptors was obtained from [10] as 7.7 pmol/mL. Assuming that 30% of the receptors would be activated at a given time a random number was generated and if it was greater than the probability of hitting a receptor a collision was considered to occur. An

arbitrary impact parameter was chosen for the Dobutamine molecule as well as an arbitrary rotational angle. The molecule was then the allowed to proceed through the molecular dynamics region till it intercepted the receptor. If the appropriate atoms on the Dobutamine were within 3Å of a docking site, as shown in figure 2, then a docking was considered to occur. At this time the receptor was removed from the cell as thus the density of receptors in the cell was reduced. New Dobutamine molecule was introduced at the midpoint of the region of interest.

3 Results

The external flow was calculated as described above. Due to the small number of Dobutamine molecules in the blood it is impossible to perform the calculations using the full number of water and erythrocyte molecules. This arises as with a Monte Carlo fraction of 20 there are only two Dobutamine molecules in the region of interest. The number of albumin molecules was set at the correct value. However even using the Monte Carlo fraction of 20 the number of water and erythrocyte molecules would be so large that only a super computer using parallel processing could undertake such a calculation The code was run with the different numbers of water and erythrocyte molecules and it was found that provided the numbers were greater than 50 there did not appear to be any significant changes in the results. In the present calculations the number of water and erythrocyte molecules were set at 500 each. The result of the calculations is shown in table 1.

Table 1: External flow docking of Dobutamine with Beta 1 receptors.

Number of Dobutamine molecules docking/μm^2	Time Ionic Cross Section Secs.	Time Hard Sphere Cross Section Secs
2000	.03382	0.0139
4000	.07355	0.0515
6000	.09979	0.1148

It can be seen that the assumptions made about the collision cross section is relatively unimportant. This arises because it is only used to calculate the time advance and not the collisional change of velocity.

As described above the docking within the cells is very complex. There does not appear to be experimental values for the diffusion coefficient (D) for Dobutamine. One method of estimating D is from [11]

$$D = k\frac{1.474x10^{-15}}{\mu^{1.14}V_B^{0.589}} \tag{9}$$

where D is the diffusivity in m^2/sec, μ is the viscosity in kg/m.sec and V_B is the LeBas molar volume in m^3/mol. Taking the solvent as water the viscosity is 1.08e-3 kg/m.sec, k=1 and the Le Bas volume is 1.053e-2 giving a diffusivity of 3.42 $x10^{-10}$ m^2/sec. The diffusion coefficient can also be estimated from the Stokes –Einstein relation $D=kT/(6\pi\upsilon r)$. This gives the value of D as 3.90 $x10^{-10}$ m^2/sec for diffusion in water. A value of $3.5x10^{-10}$ m^2/sec will be used.

Based on figure 3 the solution of equation (8) would not be very accurate. However an order of magnitude for the time involved can be obtained from an approximation of equation (8).

$$t=\lambda^2/D \tag{9}$$

where λ is a typical diffusion length scale. The diffusion length that is significant is the distance from a capillary to a cell. Considering the dimensions discussed above a length of 25 μm would be appropriate. Thus an order of magnitude calculation of the time for diffusion can be obtained as 0.18 sec. The docking calculation would then increase the time due to the availability of receptors and the orientation of the drug as described for the external flow. From figures 2 and 3 [9] the dimensions of the nodal cells and the capillaries range between 4μmi and 8μm. Thus as well as interstitial fluid there is considerable tissue such as mitochondrial cells. In this case the viscosity may be an order of magnitude greater [12] giving a diffusivity of $0.25x10^{-10}$ m^2/sec. The thickness of the sinus nodes is approximately 200μm. Thus there are approximately 5 layers of cells through the nodes.

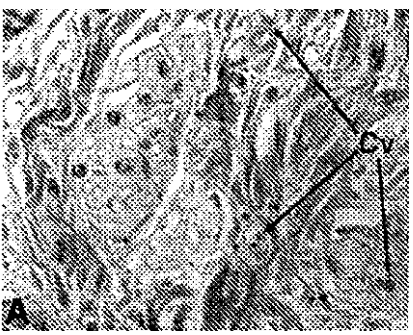

Figure 3: Sinus node histologic section from figure 1 [9].

4 Conclusions

Comparing equation 9 and table 1 the docking of Dobutamine on the sinus nodes mainly occurs on the blood side of the nodes. It would be expected that the drug would be mainly absorbed within 1 second of the Dobutamine being distributed around the body. The release time of the Dobutamine from the receptor is known. In order that there remain sufficient receptors available for the

Dobutamine to dock with, then a release time of less than half a second would appear to be conservative. Thus the present values for the docking time may be reasonable.

This result arises because of the high blood flow past the nodes. A similar situation likely occurs in the ventricles although to a lesser degree. In most situations diffusion is likely to be the principal mechanism.

References

[1] Mavromoustakos T, Daliani I and Matsoukas 1999 The application of biophysical methods to study Drug Discovery and Design: Medical Aspects Ed J. Matsoukas and T. Mavromoustakos, IOS press, Amsterdam, 13-24.

[2] Goodsell, D.S. and Olson, AJ. (1990) "Automated Docking of Substrates to Proteins by Simulated Annealing". Proteins: Structure, Function, and Genetics 8:195-202.

[3] Morris, G.M., Goodsell, D.S., Huey, R and Olson, AJ. (1996) "Distributed Automated Docking of Flexible Ligands to Proteins: Parallel Applications of AutoDock 2.4". J. Computer-Aided Molecular Design 10:293-304.

[4] Morris, G.M., Goodsell, D.S., Halliday, RS, Huey, R, Hart, W.E., Belew, RK., Olson, AJ. (1998) "Automated docking using Lamarckian genetic algorithm and an empirical binding free energy function." J. Compo Chem. 19:1639-1662.

[5] Macpherson AK and Neti S 2001 "A rapid procedure for initial drug evaluation", Phys. In Med. and Biol.46,6

[6] Sloth E, Kruse M, Houlind KC, Petersen EM, Hasenkam JM, "The impact of ischemic heart disease on main pulmonary flow blood flow patterns : a comparison between magnetic resonance phase velocity mapping and transesophagel colour Doppler" Cardiovascular Research 37,377-385,1997.

[7] Chandrasekhar, S. "Principles of Stellar Dynamics", Uni. of Chicago Press, Chicago, 1942.

[8] Ruth, D.W. 1972 "A Monte Carlo simulation of the impulsively started piston problem, M.S. Thesis, University of Manitoba, Dept. of Mech. Eng., Winnipeg, Canada

[9] Balescu R. Equilibrium and Non Equilibrium Statistical Mechanics, John Wiley, New York, 1990.

[10] Hurlé A, Sánchez-Quintana D, Ho S.Y., Bernabeu E, Murillo M, Climent V Capillary Supply to the sinus Node in Subjects with Long-Term Atrial Fibrillation, The annals of thoracic surgery,89, 1, 38-43, 2010.

[11] Tsukamoto1.T et al 'Decreased Myocardial b-Adrenergic Receptor Density in Relation to Increased Sympathetic Tone in Patients with Nonischemic Cardiomyopathy ",The Journal of Nuclear Medicine, 48, 11, Nov 2007 177-182

[12] Lyman, W.J., Reehl, W.F., Rosenblatt, D.H. (eds.) (1990) Handbook of chemical property estimation methods, American Chemical Society, Washington DC, USA.

[13] Meulemans A, Paycha F, Hannoun P, Vulpillat M, Measurement and Clinical and Pharmacokinetic Implications of Diffusion Coefficients of Antibiotics in Tissues, Antimicrobial Agents and Chemotherapy, Aug 1989, 1286-1290.
[14] Tuttle RR, Mills J. Dobutamine: development of a new catecholamine to selectively increase cardiac contractility. Circ Res. 1975 Jan;36(1):185-96

Section 7
Electronic components cooling

This page intentionally left blank

Enhancement of conjugate heat transfer from electronic chips with a rotating tri-vane assembly

R. I. Bourisli
Department of Mechanical Engineering, Kuwait University, Kuwait

Abstract

The enhancement of heat transfer from heat-dissipating devices is investigated. The laminar convection-conduction heat transfer from five heat-generating block in a channel at different Reynolds numbers is numerically simulated using the finite volume method. Newly proposed tri-vane structures with constant angular velocities are placed near the upper downstream corners of the blocks. The vanes in the structures drive significant portions of the core channel flow into the dead zones between the blocks. An optimum angular velocity for the structure is shown to exist, giving a reduction in maximum temperature of 16.3% at $\mathrm{Re} = 1000$. The location of the optimum angular velocity was shown to bifurcate because of the influence of the natural frequency of the structure. It is concluded that this effect can have a positive effect on the overall heat transfer from the blocks.
Keywords: Heat transfer enhancement, corrugated channel, heated blocks, rotating vanes, optimum angular velocity.

1 Introduction

The problem of enhancing heat transfer in channels with geometrical inhomogeneities is of great interest to engineers from both the theoretical and practical points of view. Flow in a channel with heat-dissipating elements, for example, is found in many engineering devices such as compact heat exchangers, oxygenators, dialyzers, nuclear reactor cores, and cooling systems of electronic equipment. In most of these applications the design requires that the maximum temperature of the heat-dissipating components be maintained below a certain temperature in order increase device efficiency and reliability and avoid failure [1].

WIT Transactions on Engineering Sciences, Vol 69, © 2010 WIT Press
www.witpress.com, ISSN 1743-3533 (on-line)
doi:10.2495/AFM100481

A simple way of accomplishing this objective is to increase the flow rate and thus the rate of heat removal. While this solution is acceptable for low flow-rate devices, the ensuing noise, vibration and pressure drop requirement deems it impractical for many moderate-to-high flow-rate devices.

A common alternative is to modify the channel topology so as to enhance heat transfer from thermally stagnant zones. Among these strategies are altering the configuration of the heated elements [2,3] and adding cylinders and deflectors [4,5] in the channel. In most cases, while moderate heat transfer enhancement is observed relative to the basic configuration, new, thermally-stagnant zones develop in the channel. Additionally, the size and location of the new objects have to be optimized carefully to effect the highest gain in heat transfer for the effort spent.

The effect of adding a streamwise, pulsating component to the flow on the heat transfer has also been proposed by a number of researchers [6–8]. The enhancement in heat transfer was strongly dependent on whether the Strouhal number matched the natural frequency of vortex formation and ejection from inter-block cavities. Enhancements are also directly related to the amplitude of the pulsation, which could not be increased indefinitely. On top of that, the fact that additional power and some sort of variable-frequency pump was required takes away from the practicality of such strategy. Some researchers used oscillating objects, such as plates and cylinder, within the channel to help break the eddies formed between heated blocks [9, 10]. The same dependence on frequency was observed but with much better heat transfer than when the flow itself is oscillated.

One popular approach among researchers is to use vanes or deflectors to alter the dynamics of the flow around heated blocks [11, 12]. Specifically, the vanes lead the cooling fluid into the relatively stagnant zones between the block in order to increase heat transfer from the hidden surfaces, which are normally not greatly affected by the core flow in the channels. While fluid acceleration between the vanes and blocks results in the elimination of large recirculation zones, and thus in heat transfer enhancement, new recirculation zones soon develop, namely between the deflected flow and the upstream surface of the next block in line. The aim of this research is to investigate the utility of adding a rotational velocity component to the vane structure such that the flow is continuously altered. To maintain the effect throughout the rotation period, a tri-vane structure, consisting of three outward-facing identical vanes, is used.

2 Problem formulation

The conjugate conduction/convection problem considered is that of a 2-D, transient, incompressible, Newtonian flow in a channel of height H. The fluid flows over five homogeneous $w \times h$ blocks with constant thermal conductivity k_s, heated from below with a uniform heat flux, simulating electronic chips. The distance from the inlet to the upstream face of the first block is L_i and the distance from the downstream face of the last block to the exit is L_e. The inter-block spacing is s. The adiabatic tri-vanes structures are formed by three identical spline curves inscribed in a circle of radius d. The center of the circle is located a distance x

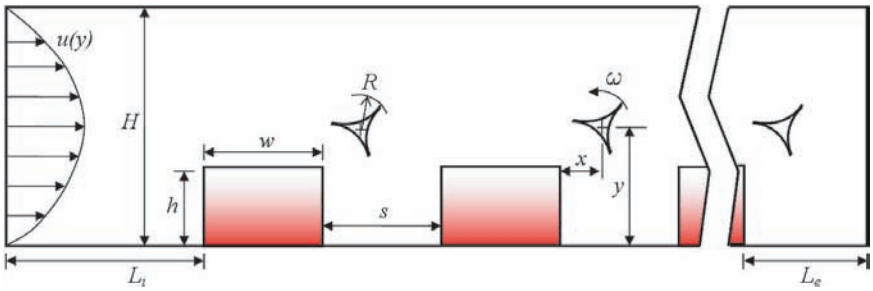

Figure 1: Schematic of the problem showing key dimensional variables.

from the upper left corner of the block, at height y from the bottom surface of the channel. The structure rotates with a constant angular velocity ω. The fluid has density ρ, viscosity μ, thermal conductivity k_f and Prandtl number Pr. It enters the channel with a parabolic, fully-developed profile, $u_i(y)$, and exits with the same profile to zero gage pressure. All properties are assumed constant, and viscous dissipation and body forces are neglected. Figure 1 shows a schematic drawing of the problem showing key geometrical features.

Fluid flow is governed by the 2-D, transient, incompressible Navier-Stokes equations, while energy flow is governed by the transient, 2-D heat equation. These equations can be non-dimensionalized using the following quantities,

$$u^* \equiv \frac{u}{U}, \quad v^* \equiv \frac{v}{U}, \quad x^* \equiv \frac{x}{H}, \quad y^* \equiv \frac{y}{H}, \quad p^* \equiv \frac{pH}{\mu U}, \quad t^* \equiv \frac{tU}{H}$$

$$k^* \equiv \frac{k_s}{k_f}, \quad \theta \equiv \frac{T - T_{in}}{q''H/k_f}, \quad Re_H \equiv \frac{\rho U H}{\mu}, \quad \mathrm{Pr} \equiv \frac{c_p \mu}{k_f}$$

where u and v are the Cartesian velocity components, μ is the dynamic viscosity, c_p is the specific heat, k_f, k_s, and k^* are the fluid, solid and dimensionless thermal conductivities, respectively, and T_{in} and θ are the inlet and dimensionless temperatures, respectively. The resulting nondimensional Navier-Stokes equations are,

$$\frac{\partial u^*}{\partial x^*} + \frac{\partial v^*}{\partial y^*} = 0 \tag{1}$$

$$Re_H \left(\frac{\partial u^*}{\partial t^*} + u^* \frac{\partial u^*}{\partial x^*} + v^* \frac{\partial u^*}{\partial y^*} \right) = -\frac{\partial p^*}{\partial x^*} + \frac{\partial^2 u^*}{\partial x^{*2}} + \frac{\partial^2 u^*}{\partial y^{*2}} \tag{2}$$

$$Re_H \left(\frac{\partial v^*}{\partial t^*} + u^* \frac{\partial v^*}{\partial x^*} + v^* \frac{\partial v^*}{\partial y^*} \right) = -\frac{\partial p^*}{\partial y^*} + \frac{\partial^2 v^*}{\partial x^{*2}} + \frac{\partial^2 v^*}{\partial y^{*2}} \tag{3}$$

and the nondimensional energy equation for the fluid is,

$$\frac{\partial \theta_f}{\partial t^*} + u^* \frac{\partial \theta_f}{\partial x^*} + v^* \frac{\partial \theta_f}{\partial y^*} = \frac{1}{Re_H \, \mathrm{Pr}_f} \left(\frac{\partial^2 \theta_f}{\partial x^{*2}} + \frac{\partial^2 \theta_f}{\partial y^{*2}} \right) \tag{4}$$

and for the solid blocks,

$$\frac{\partial \theta_s}{\partial t^*} + \frac{\partial^2 \theta_s}{\partial x^{*2}} + \frac{\partial^2 \theta_s}{\partial y^{*2}} = 0 \tag{5}$$

The fluid enters the domain with the fully-developed profile $u_i(y)$ and temperature T_i. At the channel exit, zero streamwise velocity and temperature gradients are imposed. The exposed parts of the lower and upper channel walls are assumed adiabatic with the no-slip boundary condition prescribed. The five blocks experience a constant heat flux of magnitude q'' W/m^2 through their bottom surfaces. The no-slip boundary condition is prescribed at the left, right and upper surfaces of blocks. Thermally, these interfaces between the blocks and the flow have temperature and heat flux continuities and experience conjugate heat transfer. The boundary conditions can be summarized as follows:

Inlet:

$$u^* = 6y^*(1 - y^*), \quad v^* = \theta_f = 0 \tag{6}$$

Exit:

$$\frac{\partial u^*}{\partial x^*} = \frac{\partial v^*}{\partial y^*} = \frac{\partial \theta_f}{\partial x^*} = 0 \tag{7}$$

Exposed channel walls:

$$u^* = v^* = \frac{\partial \theta_f}{\partial y^*} = 0 \tag{8}$$

Blocks bases:

$$q'' = 1 \tag{9}$$

Exposed blocks surfaces:

$$u^* = v^* = 0, \quad \theta_f = \theta_s, \quad \frac{\partial \theta_f}{\partial \mathbf{n}^*} = k^* \frac{\partial \theta_s}{\partial \mathbf{n}^*} \tag{10}$$

Finally, the five tri-vane structures were created and meshed separately and then merged with the channel and block geometry/mesh using the T-Grid software. The five (tri-vane) separate continua were given a constant rotational component of magnitude ω, acting as a temporal boundary condition. A *sliding mesh* technique was used to ensure continuity of flow between the two main channel and tri-vanes regions.

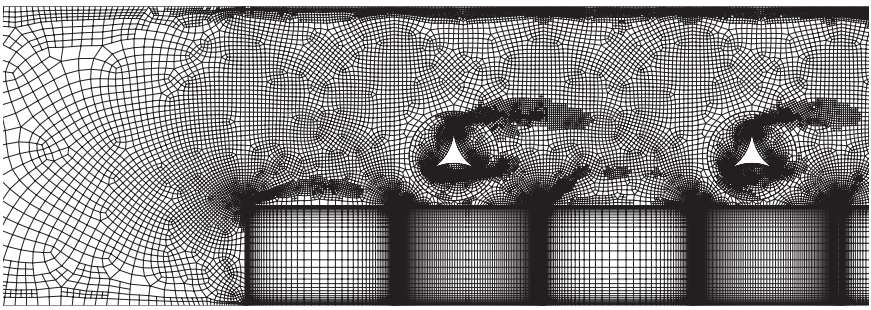

Figure 2: Part of the mesh used showing the effect of adaption.

2.1 Discretization technique

The governing equations and boundary conditions were discretized using the finite volume technique [13]. The power law scheme was used to discretize the momentum and energy equations while a first-order upwind scheme was used for the continuity (pressure) equations. A 1st-order, implicit formulation was used for the transient term. The problem of flow over five heated blocks without vanes was examined using a series of meshes, ranging from 80,000 to 197,900 cells. The maximum dimensionless temperature and the area-weighted average Nusselt number values for the first and fifth blocks were used to assess the quality of the mesh. For meshes larger than 170,000 cells, changes in all three quantities cease to be greater than 1%. In most results reported here, 180,500 cells were used. A series of mesh adaption modifications were performed at different intervals within a rotation period to ensure that the mesh is optimized with respect to high velocity and temperature gradients. A partial view of a sample resulting mesh, showing the effect of adaption, is shown in Figure 2. The consistency of the numerical algorithm was tested by comparing its results for a single block to the "steady" ones of Young and Vafai [2]; excellent agreement between the two methods/grids was observed, judging by the maximum temperature and local Nusselt number distributions reported.

3 Results and discussion

Simulations were performed at Reynolds numbers 250, 500 and 1000 for a fluid with Prandtl number 0.72. The heat flux was taken to be $q'' = 1$ W/m^2. In all, nine rotational speeds for the tri-vanes were tested: $\omega = 0.63$, 1.05, 1.26, 1.57, 2.09, 3.14, 4.19, 5.03 and 6.28 rad/s, corresponding to rotation periods of 10, 6, 5, 4, 3, 2, 1.5, and 1.25 1, seconds, respectively. The tri-vane geometry, nondimensionlized by H, has $d = 0.2$, $x = 0.2$ and $y = 0.5$. The equations of motion were discretized and solved as aforementioned. Due to the coupled nature of the problem, a coupling of the pressure, momentum and energy equations was necessary at each time step of each of the 27 cases tested. This resulted in

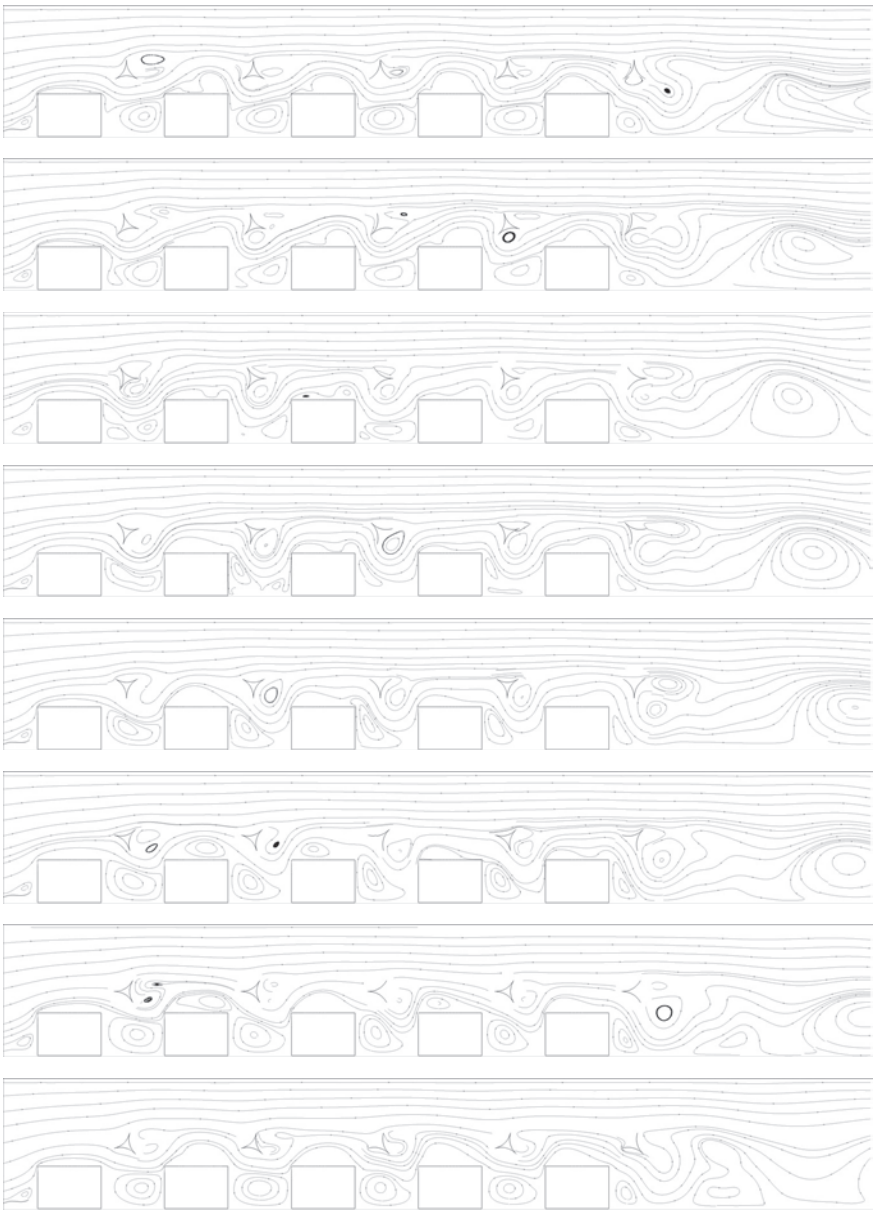

Figure 3: Streamlines through one third of a period, Re $= 1000$.

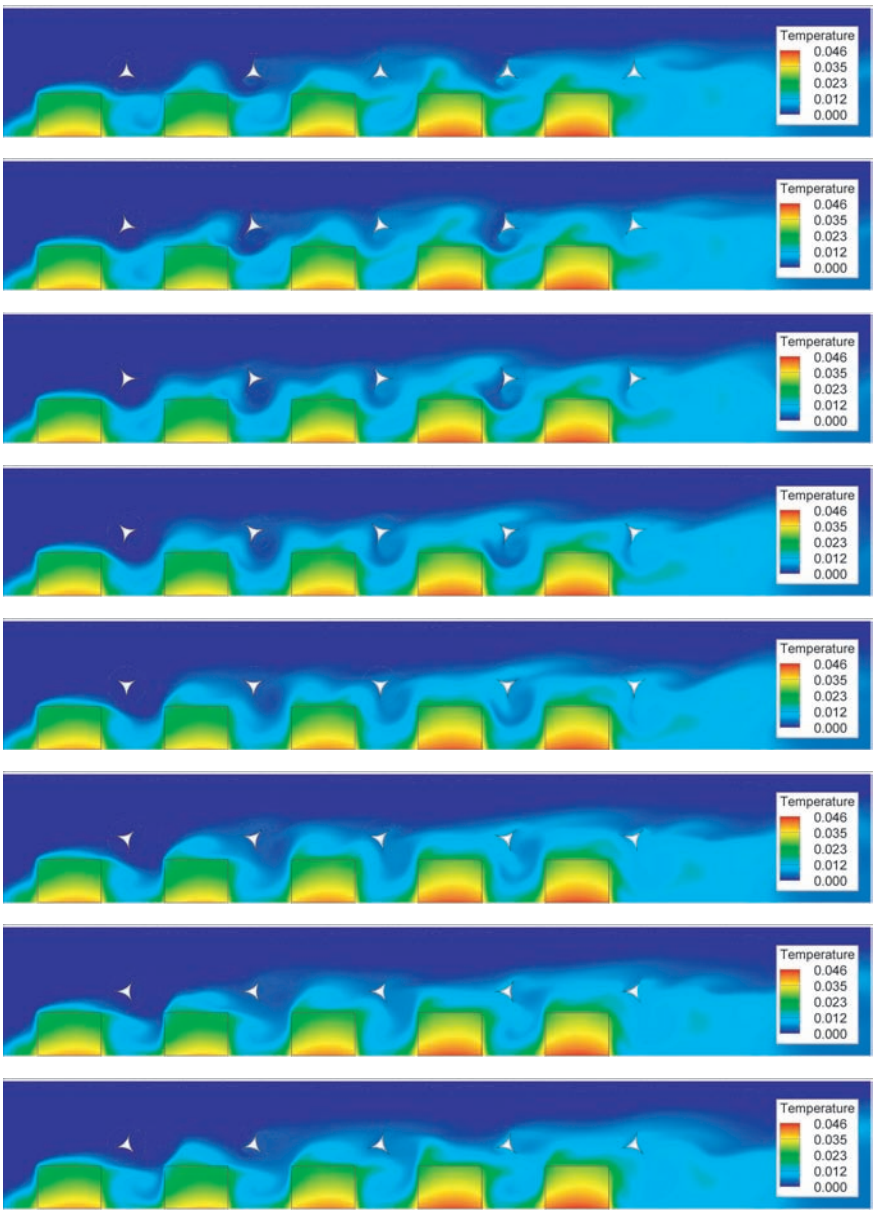

Figure 4: Temperature contours through one third of a period, Re = 1000.

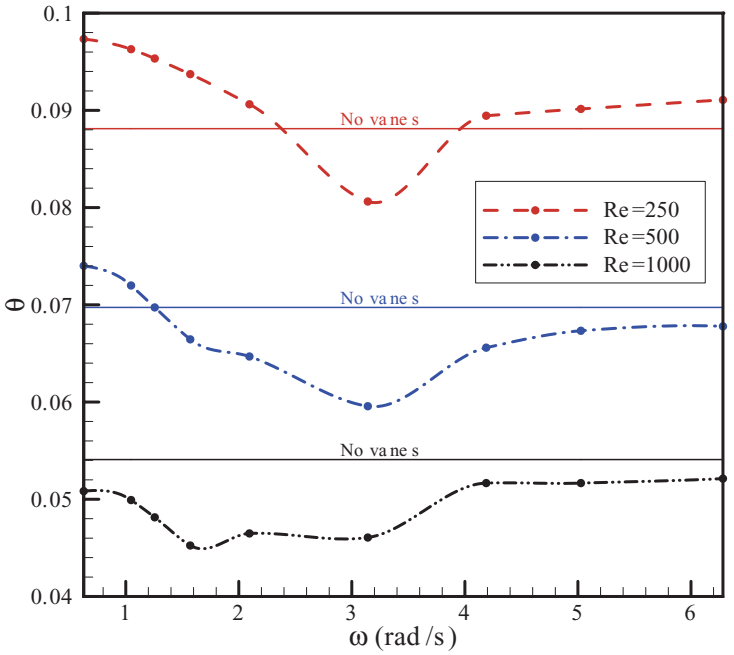

Figure 5: Maximum temperature, θ_{max}, among the blocks vs. angular velocity, ω.

extremely long (computational) simulation times before cyclic steady state was reached, even though the physical flow became cyclically steady after a relatively short amount of (physical) time.

Figures 3 show the evolution of the streamlines in the channel through one third of a period. Due to the circumferential symmetry of the structure, one third of a complete period is sufficient to draw conclusions. The dynamic nature of the flow is evident through the intermittent flow of fluid from the core into the stagnant regions between the blocks. Large eddies do not form in the grooves and reduce the Nusselt number over the sides of the blocks. Additionally, and more importantly, when the vane facing the block rotates away, an eddy is given a chance to form momentarily before it is swept away by the next vane. This prevents stagnant zones in the whole channel and results in the fluid passing over the next upper surface with even higher momentum.

Figures 4 show the concurrent temperature contours in the channel. The effect of eddy formation and ejection is clearly visible in the areas between blocks, where cold fluid, almost at the temperature of the core flow, penetrates deep into the grooves, carrying with it a large portion of the heat. The penetration of the cool fluid to the bottom of the grooves is of paramount importance because of their proximity to the heat source.

The effect of the angular velocity, ω, on the maximum temperature in the five blocks, θ_{max}, is shown in figure 5 at the three Reynolds numbers considered. As

expected, the effectiveness of the tri-vanes, rotating or not, does not enhance heat transfer at low Reynolds numbers. This can be attributed to the fact that at such Reynolds numbers, the flow lacks the required momentum to drive itself into the grooves as the vanes intended. At the same time, the existence of the structure over any block hinders the core flow from attaining its usual core velocity over the top surface of the next block in line, thereby reducing heat transfer. At Re$= 250$, only one rotational velocity was successful in reducing the maximum temperature compared to the basic grooved channel. It is expected, but not verified, that this optimum will quickly disappear as the Reynolds number is reduced further. For moderate-to-high (laminar) Reynolds numbers, the use of the tri-vane structures clearly reduces the maximum temperature in the heat-generating blocks. In fact, for Re $= 1000$, any value of ω results in a reduction in the maximum temperature for the shape studied. In general, reductions in the maximum temperature amongst the blocks were 8.50%, 14.6% and 16.3%, for $\mathrm{Re} = 250$, 500, and 1000, respectively.

An important observation can be made regarding the value of the optimum ω as Re increases. Interestingly, the clear optimum observed for the Re $= 500$ case gradually bifurcates into two co-optima as the Reynolds number is increased. It is known that in static mode, heat transfer from obstacles placed in a channel is maximized when the frequency of oscillation/rotation is synchronous with the natural frequency of vortex shedding, a phenomenon known as *lock-on* [14]. It is also reasonable to assume that heat transfer is not maximized over all surfaces simultaneously. We observe here that the resultant effect of the tri-vanes is to force the large vortices to take a different route than the usual one. Thus, the bifurcation can be explained by the fact that the periodicity of vortex shedding is severely disrupted by the rotation of the tri-vanes in such a way that it artificially overrides the natural lock-on and forces the flow into dead zones, normally unattended by the undisturbed flow. In other words, the asynchronous rotation (with respect to the natural frequency) can become so pronounced as to "unexpectedly" enhance heat transfer from different block surfaces, thereby doing more good than harm.

4 Conclusions and future work

In this research, enhancement of the laminar convection-conduction heat transfer from five heat-generating blocks in a channel is investigated numerically using the finite volume method. A rotating tri-vane structure was used to drive the flow into the grooves between the blocks. The result was a noticeable decrease in the maximum temperature in the blocks. The periodic diversion of the core channel flow into the grooves prevents sustaining large, stagnant eddies. Reductions in the maximum temperature in the blocks were as high as 16.3% for $\mathrm{Re} = 1000$. An optimum angular velocity for the tri-vanes was shown to exist. It is believed that the rotational velocity "throws off" the natural frequency of vortex shedding. This dilatation of the lock-on effect was shown to have a positive effect on the overall heat transfer from the blocks. For future work in this area, more laminar cases can be simulated to draw more physical conclusions. It is also interesting to see if

effects of the tri-vanes is as pronounced in the turbulent regime. The tri-vanes, or similar shapes, that move with variables velocities should also be investigated.

References

[1] Teo, J., Thermal cycling aging effect on the reliability and morphological evolution of SnAgCu solder joints. *IEEE Transactions on Components and Packaging Technologies*, **30**, pp. 279–284, 2007.
[2] Young, T.J. & Vafai, K., Convection flow and heat transfer in a channel containing multiple heated obstacles. *International Journal of Heat and Mass Transfer*, **41**, pp. 3279–3298, 1998.
[3] da Silva, A.K., Lorenzini, G. & Bejan, A., Distribution of heat sources in vertical open channels with natural convection. *International Journal of Heat and Mass Transfer*, **48(8)**, pp. 1462–1469, 2005.
[4] Herman, C. & Kang, E., Comparative evaluation of three heat transfer enhancement strategies in a grooved channel. *Heat and Mass Transfer*, **37**, pp. 563–575, 2001.
[5] Korichi, A., Oufer, L. & Polidori, G., Heat transfer enhancement in self-sustained oscillatory flow in a grooved channel with oblique plates. *International Journal of Heat and Mass Transfer*, **52**, p. 11381148, 2009.
[6] Moon, J.W., Kim, S.Y. & Cho, H.H., Frequency-depedent heat transfer enhancement from rectangular heated block array in a pulsating channel flow. *International Journal of Heat and Mass Transfer*, **48**, pp. 4904–4913, 2005.
[7] Korichi, A. & Oufer, L., Heat transfer enhancement in oscillatory flow in channel with periodically upper and lower walls mounted obstacles. *International Journal of Heat and Fluid Flow*, **28**, p. 10031012, 2007.
[8] Alawadhi, E.M. & Bourisli, R.I., The role of periodic vortex shedding in heat transfer enhancement for transient pulsatile flow inside wavy channels. *Int Journal of Natural Sciences and Engineering*, **1(2)**, pp. 79–85, 2009.
[9] Fu, W.S. & Tong, B.H., Numerical investigation of heat transfer characteristics of the heated blocks in the channel with a transversely oscillating cylinder. *International Journal of Heat and Mass Transfer*, **47**, pp. 341–351, 2004.
[10] Florio, L.A. & Harnoy, A., Use of a vibrating plate to enhance natural convection cooling of a discrete heat source in a vertical channel. *Applied Thermal Engineering*, **27**, pp. 2276–2293, 2007.
[11] McGarry, M., Campo, A. & Hill, D., Numerical simulations of heat and fluid flow in grooved channels with curved vanes. *Numerische Heat Transfer, Part A*, **46**, pp. 41–54, 2004.
[12] Luviano-Ortiz, L., Hernandez-Guerrero, A., Rubio-Arana, C. & Romero-Mendez, R., Heat transfer enhancement in a horizontal channel by the addition of curved deflectors. *International Journal of Heat and Mass Transfer*, **51**, pp. 3972–3984, 2008.

[13] Patankar, S.V., *Numerical Heat Transfer and Fluid Flow*. Series in Computational Methods in Mechanics and Thermal Sciences, McGraw Hill: New York, 1980.
[14] Mahir, N. & Altaç, Z., Numerical investigation of convective heat transfer in unsteady flow past two cylinders in tandem arrangements. *International Journal of Heat and Fluid Flow*, **29**, pp. 1309–1318, 2008.

This page intentionally left blank

Experimental study of the turbulent flow around a single wall-mounted prism obstacle placed in a cross-flow and an impinging jet

Y. Masip, A. Rivas, A. Bengoechea, R. Antón,
G. S. Larraona & J. C. Ramos
Thermal and Fluids Engineering Division, Mechanical Department, TECNUN-University of Navarra, San Sebastián, Spain

Abstract

This paper describes the experimental part of an electronics cooling research project. To undertake the experiments a test rig has been designed and assembled which represents a channel made by two parallel printed circuit boards (PCBs). Different arrangements of heated prismatic bodies can be mounted on the walls of the channel simulating electronic components. These bodies are cooled combining a channel cross-flow and impinging jets issuing from the walls. The working fluid is air and the maximum Reynolds number (calculated respect to the channel height) is 13740. The test rig has been designed to take flow measurements using different experimental techniques such as hot wire anemometry (HWA), particle image velocimetry (PIV) and infrared imaging (IR). Experimental data on fluid flow features around electronic components will be used to develop and validate turbulence models that will be implemented in Computational Fluid Dynamics simulations.

The presented results are two preliminary experimental studies to analyse the influence of the component height (h) and the Reynolds number on the flow structure around the component. The first study was made with the component in a cross flow without impinging jet and in the second study an impinging jet was added to the cross flow. The Reynolds numbers employed are close to those used in applications within the electronics industry. The measurement mean (U, V), *rms* velocity (u_{rms}, v_{rms}) profiles in three main regions of the flow, namely, the wake, the upper and the side region have been obtained using the hot wire anemometry. From theses measurements the lateral flow separation, reattachment points and recirculation have been studied.
Keywords: electronic cooling, cross flow, impinging jet, wall-mounted prism.

WIT Transactions on Engineering Sciences, Vol 69, © 2010 WIT Press
www.witpress.com, ISSN 1743-3533 (on-line)
doi:10.2495/AFM100491

Nomenclature

H, W	Channel height and width (mm)	U_{max}	Maximum Velocity at centerline of the channel (m/s)
L, h	Obstacle width and height (mm)	U_j	Impinging Jet Velocity (m/s)
h/L	Obstacle aspect ratio	x,y,z	Streamwise, Vertical and Spanwise coordinates (mm)
Re_H	Channel Reynolds number ($=U_mH/\nu$)	ν	Fluid kinematic viscosity (m^2/s)
Re_i	Impinging jet Reynolds number ($=U_jD/\nu$)		
U_m	Channel Bulk velocity (m/s)		

1 Introduction

Thermal management of electronic systems is one of the bottlenecks in today's electronics industry. The increasing clock speeds and miniaturization implies a huge increase of the heat dissipation per unit area in electronic systems. It is a real challenge to cool electronic components in an efficient way, since the heat transfer in electronic components depends strongly on characteristics of the flow field around them. That is the reason why the flow and heat transfer around small-scale three-dimensional blocks, which simulated electronic components, has aroused great interest.

Flows over isolated, wall-mounted cubes have been subject to several past investigations. Castro and Robins [1] measured the flow velocity around a single cube mounted on a flat plate with different oncoming boundary layer flows. It was shown that the extent of the wake recirculation and the size of the vortex on top of the obstacle were strongly dependent on the boundary layer thickness of the oncoming flow. Ogawa et al. [2] studied the flow and mass diffusion around a cube considering the concentration and flow patterns on and around the cube. The concentration patterns were shown to be strongly dependent upon the flow patterns, and in particular, on the existence of reverse flow at the source location.

The flow around a single wall-mounted cube in a fully developed turbulent channel flow was investigated experimentally by Hussein and Martinuzzi [3], Larousse et al. [4], Martinuzzi [5] and Martinuzzi and Tropea [6]. The Reynolds number was Re_h=40000, based on the cube height (h = 25mm) and the bulk velocity, and the channel height-to-cube ratio was 2. The major flow features were well described, namely the horseshoe vortex induced at the leading face of the cube, the arc-shaped vortex in the wake, the flow recirculations at the top and the side faces. Further, the studies included a detailed description of the Reynolds stresses and other higher order moments. It was found that the horseshoe vortex region was unstable but non-periodic which caused bimodal

velocity distributions. Moreover, vortex shedding was detected in the wake of the cubical obstacle. Meinders [7] and Meinders et al. [8–10] reported on the flow field characteristics (e.g.: flow separation and reattachment at the top and side faces of the cube) of a single wall-mounted cube (h=15mm) in a developing turbulent channel flow for a Reynolds number range of $2750<Re_h<4970$.

The literature review of Schofield and Logan [11] showed that a consensus exists for the general flow features around a single wall-mounted prism. The features include the horseshoe vortex, the wake vortex and the top and side vortices, which are indicated in Figure 1. These flow features are not only observed for a single prism in turbulent channel flows, but are also representative for configurations of multiple prisms. The flow field in front of the obstacle is characterized by the horseshoe vortex, indicated with **A**, which originates at the base of the windward stagnation region and extends downstream along the channel floor past the sides of the prism. The separation of the top shear layer resulted in a bound recirculation ("top vortex", indicated with **B**). The side vortex is indicated with **C**. An arc-shaped vortex was typically found in the wake of the obstacle ("wake vortex"). This wake vortex, indicated with **D**, was confined by the solid walls and the fluid flowing along the side and the top faces.

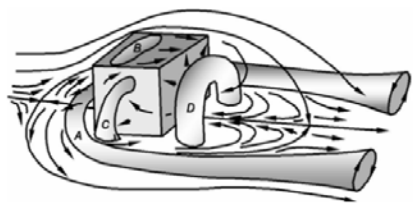

Figure 1: Schematic representation of the flow features a surface-mounted obstacle by Martinuzzi and Tropea (From [6] with permission).

In cooling of electronic components, forced channel flow between PCBs is frequently used as a cooling technique [7]. Using forced channel flow excessive flow rates will be required to manage the whole thermal load of the electronic system. One possible alternative to face this problem is using an impinging jet over the most dissipating component combined with a low-velocity channel flow (see Rundström and Moshfegh [12]). Impinging jets are used for many industrial applications where high heat and mass transfer rates are required. In addition to their industrial applications, turbulent impinging jets have great scientific interest due to the particular characteristics of this flow. Extensive experimental and numerical research has been carried out to predict the flow and heat transfer in the stagnation region of an impinging jet.

This paper presents an experimental study about the influence of the obstacle height and Reynolds number on the flow field structure. The component used is located in a cross flow for the first case and in the second case the component is placed in a cross flow adding an impinging jet. The flow features determined for the first case were the reattachment point on the top and downstream of the trailing face of the component and the lateral separation. Moreover, a

comparison with the results found in the literature was performed. In the second case two principal regions, the upper zone and the wake were studied.

2 Experimental setup

2.1 Test section description

The experiments were performed in an open circuit wind tunnel specifically designed for electronics applications. This wind tunnel was built following the criteria found in Mehta and Bradshaw [13], Westphal [14], Barlow et al. [15]. As can been seen in Figure 2, the wind tunnel consisted of different assembled pieces, namely input cone, honeycomb, screens, contraction, test section, diffuser, filters, laminar flow element and centrifugal fan.

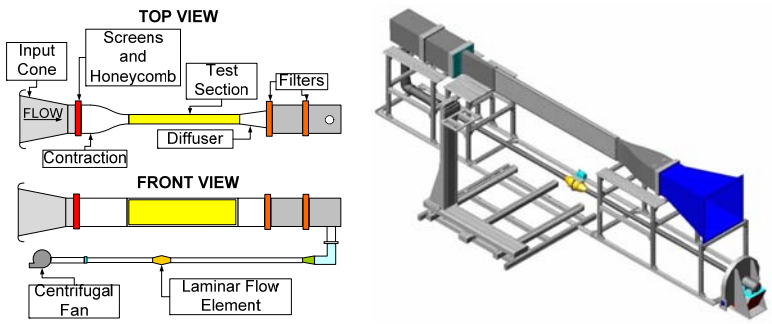

Figure 2: View of the wind tunnel.

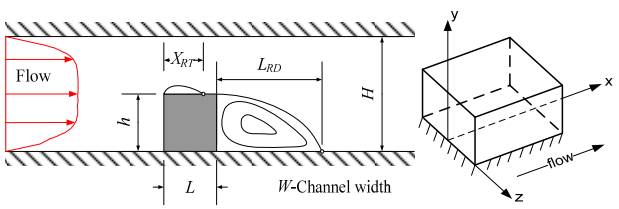

Figure 3: Sketch of the side view of the test-section with a single wall-mounted obstacle and local coordinate system of the obstacle.

The honeycomb and fine screens were used to eliminate the large turbulence scales and to straighten the flow. The channel (test section) has internal dimensions of 2000x30x300 mm^3. A sketch of the test section with the coordinate system employed is given in Figure 3. The *x*-axis and *y*-axis refer to the streamwise and the normal direction respectively. The *z*-axis points out of the image, referring to the spanwise direction. The diffuser is used for the transition between a section of high velocity and one of low velocity. The filters are used to eliminate the strange particles conveyed by the air and to avoid damage of the

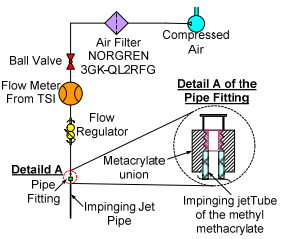

Figure 4: Sketch of the control system of the flow for the impinging jet.

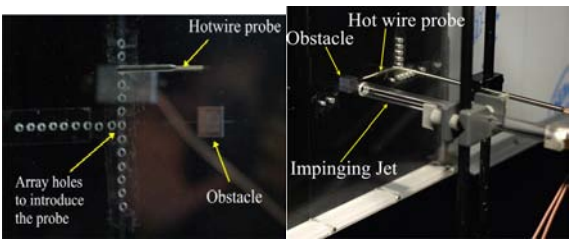

Figure 5: Photograph of the test-section with a single wall-mounted obstacle during the hot wire measurements.

laminar flow element. The laminar flow element is used to measure the volumetric flow that circulating through wind tunnel. The centrifugal fan has a variable-frequency driver so that different flow rate can be achieved.

The test section has been designed and assembled to represent a channel made by two parallel PCBs. Different arrangements of heated prismatic bodies can be mounted on the walls of the channel simulating electronic components. The walls are made of a transparent material (methyl methacrylate) to have optical access to the test section. This setup provides the possibility to assemble and disassemble the walls with little effort. The front wall has an array of holes to introduce the support of the hot wire probe. Also one plate can be changed in order to use the impinging jet. The impinging jet enters to the test section through a rigid tube sufficiently long to obtain fully developed flow. The flow rate of the impinging jet is controlled by means of a flow meter, valve and flow regulator to maintain the required working conditions, see Figure 4. A photograph of the test section with both setups is shown in Figure 5.

A computer application has been developed in Labview 8 to control and monitor the working flow rate through both the channel and the impinging jet.

2.2 Measurement equipment and uncertainty analysis

Mean velocity and second order statistic were measured with a HWA. This equipment includes a Streamline Calibrator, Streamline Module (type 9010), A/D board to convert analogical signal into digital and Probe (X- probe type 55P61 two-dimensional velocity component). The probe used has the possibility of measuring two-dimensional flows, where the velocity vector stays within ±45º with respect to the probe axis (see Jorgensen [16]). Due to the rotational symmetry of the sensing element (Bruun [17]), the cylindrical hot-wire probe cannot detect negative velocities. Therefore, the location of small recirculation regions will be estimated from the Reynolds stresses in the wake downstream of the trailing face and over the top face [1].

The uncertainty value of the calibration equipment has been provided by the manufacturer and is 1%. The data acquisition is related to A/D board resolution

which has an uncertainty of 0.13% calculated following Jorgensen [16]. The uncertainties related to experimental conditions depend on the ambient conditions and the probe positioning. The ambient conditions are measured automatically by the equipment. The positioning uncertainty ($\Delta\theta$) relates to the alignment of the probe in the experimental setup after calibration. This value is estimated from measurements in the centerline of the channel being approximately $\Delta\theta \approx 2.5^{\circ}$. Finally, the total uncertainty is approximately 2.7%.

The volumetric air flow rate was measured by a laminar flow element with a total accuracy, including the pressure transducer, of ± 0.87% of the reading. The humidity, atmospheric pressure and ambient temperature were recorded in order to make corrections.

2.3 Channel and impinging jet flow conditions

The features of the oncoming flow in the channel are found upstream of the obstacle at a far plane where the flow is unperturbed by the latter. The measurements are made for Reynolds numbers close to those used in electronics industry applications, namely Re_H=3410, 4560, 5752 and 8880 with respect to channel height and bulk velocity. The mean velocity and Reynolds stress profiles in the channel are measured 120 mm upstream of the front face of the obstacle. A typical profile at the centerline of the channel is given in Figure 6. The analysis of the velocity and Reynolds stresses shows that the channel flow is under development. In the case of the impinging jet it is impossible to measure the velocity profile at the jet inlet with the hot wire because the probe introduced in the tube alters the flow stream.

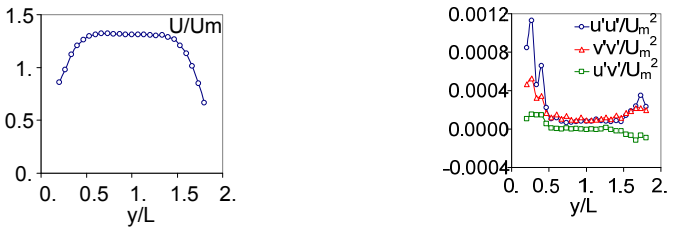

Figure 6: Profile of the dimensionless streamwise velocity and Reynolds stresses in the normal direction at x/L=-8 at z/L=0 for Re_H=8880.

3 Test procedure

Hot wire measurements were performed in different planes x/L, y/L and z/L (see Table 1) for the wake, top and side regions around of the obstacle respectively.

The planes are chosen in such a way the measurements can be taken as close as possible to the obstacle and it was able to locate the hot wire probe. The flow and turbulence fields have been built from measurements obtained in a large number of points. The employed spatial resolution in the y-axis direction has been 1 mm. The combination of the resolution, the measuring planes and the Reynolds numbers produces 6360 points where mean velocity, Reynolds stresses

and higher order moments in x and y directions were measured. These values are the average of 5000 samples taken at a frequency of 1 kHz. The impinging jet measurements are taken in the central plane z/L=0. It is important to highlight that due to the hot wire probe diameter (3mm) it is impossible to measure in the near-wall region. It is one of the main limitations in employing this intrusive technique.

Table 1: Measurement plane positions.

Wake (z/L)=0 x/L	Upper (z/L)=0 x/L	Side (x/L)=0.5 z/L
1.1	0	0.9
1.5	0.25	1
2	0.5	1.5
3	0.75	2
5	1	2.5
		3

4 Results and discussion

4.1 Case 1

The first experimental study is about the flow field around a prismatic obstacle mounted on the wall of the flow channel. In this study all components have constant width and length $L=H/2$=15 mm but different height (h) namely 5, 10, 15 mm. The aim of this study is to determine the influence of the height of the obstacle and the Reynolds number on the flow structure around the component. The flow separation on the sides of the obstacle and the reattachment point downstream from the trailing face zones have been studied in this case.

4.1.1 Wake of the obstacle

The mean flow pattern in the wake recirculation region is dominated by an arc-shaped vortex as shown in Figure 1. This vortex was produced by separation of the shear layer at the top trailing edge and reattached downstream of the trailing face. In this situation it is possible to obtain the reattachment point and hence the recirculation length to characterize the wake. The mean velocity (U/U_m) and Reynolds normal stress (u_{rms}^2/U_m^2) profiles are given several y/L locations in the symmetry plane z/L=0 in Figures 7 and 8 respectively.

The reattachment length depends on the interaction between the shear layer released at the trailing edge of the component and the main stream. The bulk flow forces the shear layer to reattach at the floor of the channel downstream of the back face. Normally, the reattachment point is found where the negative velocities disappear in the wake. The reattachment point can be estimated in the region that the Reynolds stresses present maximum values (e.g. Figure 8) and the velocity profile stabilizes [1]. This parameter is important because the recirculation in the wake is located between the reattachment point and the

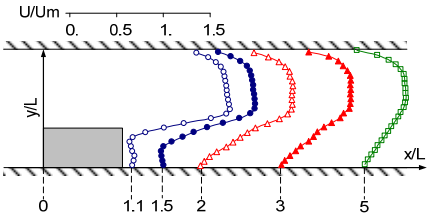

Figure 7: U/U_m at z/L=0, h=10mm, Re_H=8880.

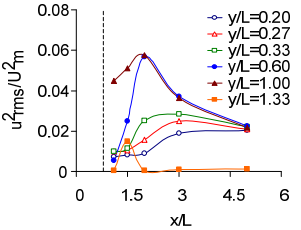

Figure 8: u_{rms}^2/U_m^2 at z/L=0, h=10mm, Re_H=8880.

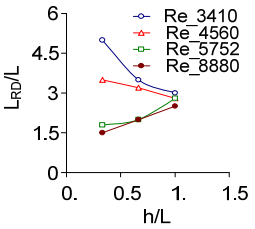

Figure 9: Length of reattachment as function of h/L and Re_H.

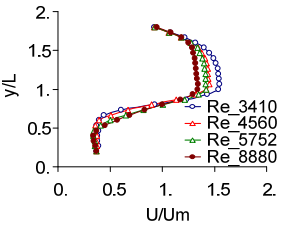

Figure 10: U/U_m for different Reynolds numbers for h=10mm at x/L=1.5.

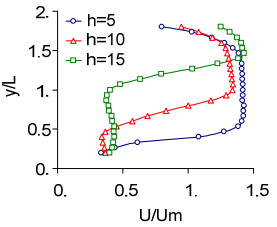

Figure 11: U/U_m for different component heights at x/L=1.5 and Re_H=8880.

trailing face and it is limited in the vertical plane by the shear layer. The region of maximum values depends of the obstacle height and occurs approximately at y/h= 0.9-1.2. The normalized reattachment length (L_{RD}/L) is plotted as a function of the aspect ratio (h/L) and Reynolds number in Figure 9, where it can be seen that as the value of h/L increases the reattachment length shows almost no change with the Reynolds number. In the case of components with low height, the Reynolds number has a major influence in the reattachment length (Figures 10 and 11 show this fact).

4.1.2 Top face of the obstacle

The top face is characterized by a bound vortex in the vicinity of the leading edge. Figure 1 shows this vortex type. A shear layer appears due to the flow

detachment at the leading edge of the component. The flow reattaches almost at the trailing edge and it is possible to identify the point of reattachment because in this region are found the maximum values of the Reynolds stress, given in Figure 13. In the case of height 5 mm this point is almost undetectable, although it occurs at the same location. The central zone of the upper recirculation is observed over the top face at x/L=0.5 plane where the velocities are minimum for the three obstacles used, see Figure 12. The normal Reynolds Stress profiles show maxima approximately at y/h=1-1.2, which coincides with areas of local production of turbulence for the three heights caused by the reattach of the flow.The influence of Reynolds number and component height on the velocity profile is shown in Figures 14 and 15 respectively. The Reynolds number does not have a significant influence on the flow near the top of the component. However, the increase of height causes a variation in the flow structure.

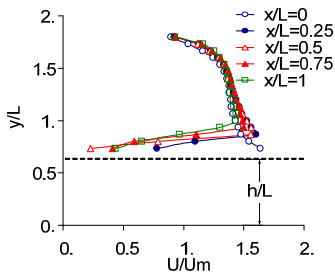

Figure 12: U/U_m in the top of the obstacle at z/L=0, h=10mm, Re=5752.

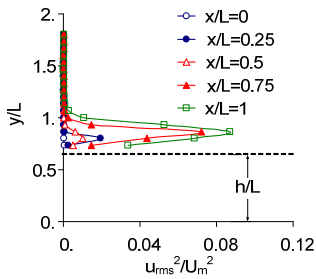

Figure 13: u_{rms}^2/U_m^2 in the top of the obstacle at z/L=0, h=10mm, Re=5752.

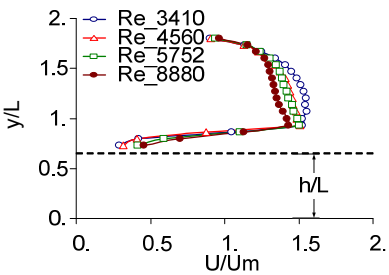

Figure 14: U/U_m for different Reynolds numbers at x/L=0.75 and h=10mm.

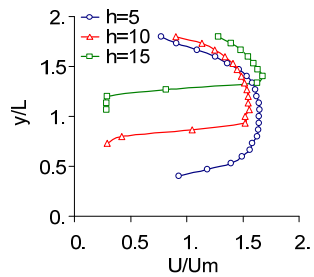

Figure 15: U/U_m for different component heights at x/L=0.75 and Re=3410.

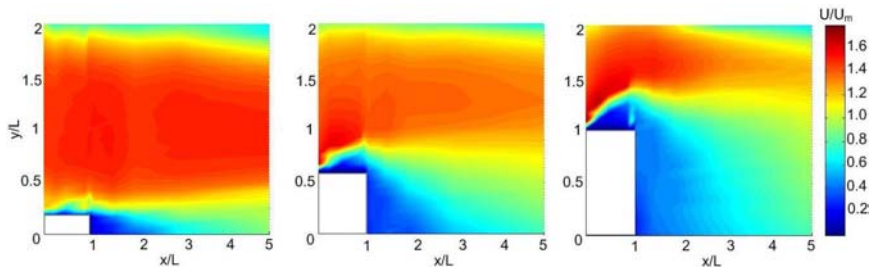

Figure 16: Contours of the U/U_m for the component h=5, 10 and 15 mm respectively at z/L=0 and Re=5752.

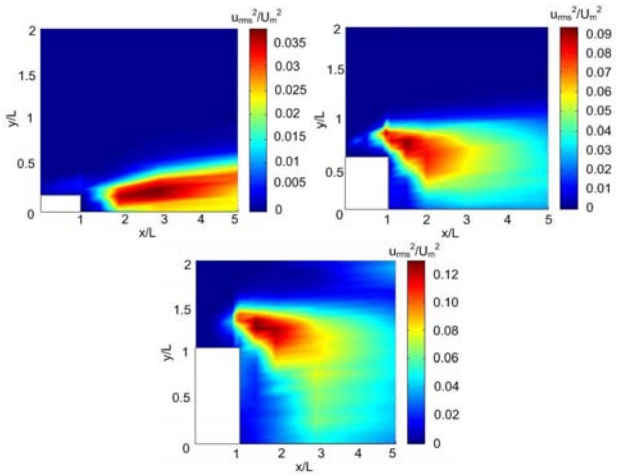

Figure 17: Contours of the u_{rms}^2/U_m^2 for the component h=5, 10 and 15 mm respectively at z/L=0 and Re=5752.

Figures 16 and 17 depict the velocity and normal Reynolds stress contours for the three component heights built from measurements. These pictures show the shear layer shedding at the leading edge and the approximate reattachment point in the wake.

4.1.3 Side of the obstacle

The flow at both sides of the obstacle is dominated by a side vortex close to the leading edge, confined by the main stream and the obstacle. An important parameter is the lateral separation (Zs) which allows establishing the zone perturbed by the horseshoe vortex. This vortex appears due to the impact of the flow with the front face of the obstacle. The velocity and Reynolds stress profiles for the lateral region are given in Figures 18 and 19 respectively. In Figure 20 the influence of the component height on the velocity profile is shown, and this influence is significant because a larger height increases both the blockage and the separation of the flow, causing decrease in the velocity on the sides of the

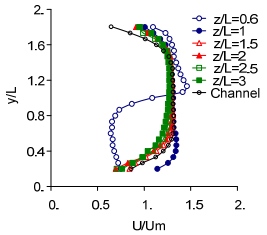

Figure 18: U/U_m in the side at plane x/L=0.5, h=15mm and Re=8880.

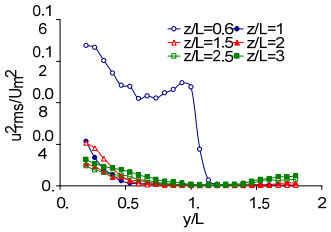

Figure 19: Of u_{rms}^2/U_m^2 in the side at x/L=0.5, h=15mm and Re=8880.

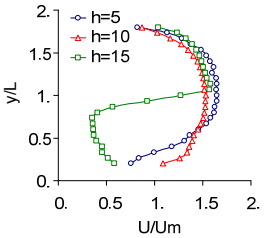

Figure 20: U/U_m for different component heights at x/L=0.5, z/L=0.6 and Re=3410.

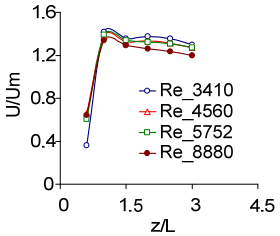

Figure 21: U/U_m for different Reynolds numbers for h=15mm at x/L=0.5, y/L=0.6.

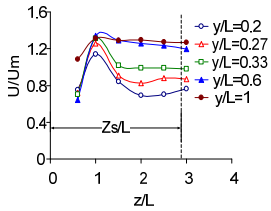

Figure 22: U/U_m at the lateral face at x/L=0.5, h=15mm and Re=8880.

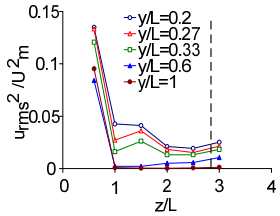

Figure 23: Reynolds stresses at x/L=0.5, h=15 and Re=8880.

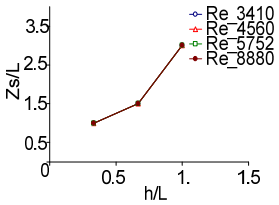

Figure 24: Length of the spanwise separation as function of h/L.

component. The Reynolds number almost shows no effect on the velocity profile in the side, see Figure 21.

The lateral separation is found from measurements of the mean velocities and normal Reynolds stresses given in Figures 22 and 23 respectively for six spanwise planes. The Reynolds stress profiles show their maximum values in the vicinity of the obstacle wall, at approximately y/h=0.9 for the three obstacle heights. The estimation of this separation is found from the point at which the velocity profile is uniform and the Reynolds stress profile decreases and almost remains at the same value. In Figures 22 and 23 the profiles keep a stable value from the broken line and the distance to this point coincides with the length of the lateral separation.

In Figure 24 the normalized spanwise separation length (Zs/L) is plotted as a function of the aspect ratio and the Reynolds numbers. It can be seen that the lateral separation length increases with the increasing obstacle height. The curves for all Reynolds numbers are almost superimposed indicating that the latter does not have a significant influence on the lateral separation.

4.1.4 Comparison with the literature

The single component in the cross flow case discussed in this study differed in several aspects from the case of Martinuzzi and Tropea [6]. The component in the present study is placed in a developing turbulent channel using different Reynolds numbers, while Martinuzzi and Tropea considered a fully developed channel flow for a Reynolds number which is almost one order of magnitude higher Re_H=80000. However, the channel-height-to-cube-size ratio was equal in both studies (H/h=2).

The present study has found a reattachment flow on the top face of the component that was absent in the fully developed case [7]. Further, the flow reattachment at the channel floor downstream from the component occurs at a larger distance away from the trailing face than in the fully developed channel flow.

Profiles of the mean velocity U/U_{max} are compared in Figure 25 with the results from Martinuzzi and Tropea. The coordinate is scaled with the component width. The differences in the proximity of the component face are caused by use of the hot wire. The agreement in the other regions is good.

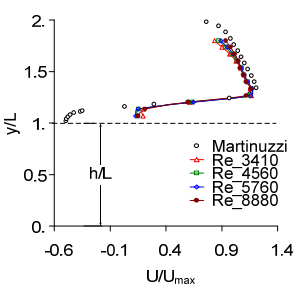

Figure 25: Comparison between the present study and the literature result: traverses of U/U_{max} in the z/L=0 and x/L=0.5.

4.2 Case 2

The second experimental case is the study of the flow around a wall-mounted component in a cross-flow adding an impinging jet. This configuration represents a simplified case of an electronics cooling device. The sketch of the flow under consideration is shown in Figure 26. It consists of two fluid streams: the first is a channel flow over a single wall-mounted cube, and the second is a round jet impinging perpendicular and centred on the cube. The Reynolds number of the channel flow is Re_H = 3410, based on its bulk velocity U_m = 1.66 m/s and the channel height $2h$ = 30 mm. The Reynolds number of the impinging jet is Re_j = 3936, based on its bulk velocity U_j = 4.79 m/s. These Reynolds numbers and velocity ratios correspond roughly to real electronics cooling systems. The obstacles employed have equal width, length and height (L=h=15 mm).

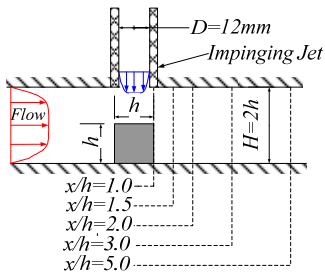

Figure 26: Sketch of the experimental setup and measurements *xy*-planes.

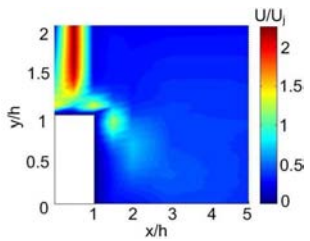

Figure 27: Contours of the U/U_j^2 in the *xy*-plane, z/L=0.

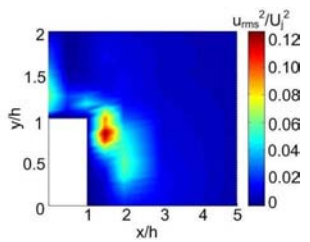

Figure 28: Contours of the u_{rms}^2/U_j^2 in the *xy*-plane, z/L=0.

The velocity field is illustrated by contour plots of the velocity and Reynolds stress in the *xy*-plane at the centre of the channel (see Figures 27 and 28) obtained from measurements. The flow field shows a complex behaviour and there are several flow-related phenomena that can affect the cooling performance, for example the position of the stagnation point on top of the component and the separation of the flow at the trailing edge of the component.

The cross-flow affects to the impinging jet and the separation from the top of the cube. The impinging jet creates a downstream flow with a zone of the

Reynolds stress that is high (approximately at y/h=0.9) due to the shear layer and vortex shedding in the impingement process. The recirculation is almost not detected in the region behind the rear side of the cube due the low values employed for the Reynolds number. The stagnation region over the top face is detected where the velocity values and the Reynolds stresses are almost insignificant.

The cross-flow affects to the impinging jet and the separation from the top of the cube. Downstream the impinging jet creates a zone of high Reynolds stress approximately at y/h=0.9 due to the shear layer and vortex shedding in the impingement process. Due to the low value of the Reynolds number, the recirculation in the region behind the trailing face of the obstacle is difficult to detect. The stagnation region over the top face is detected where the velocity values and the Reynolds stresses are very low.

Figure 29 shows the normalized x-velocity component (U/U_j) as a function of the vertical distance (y/h). Each diagram represents different locations in the x-direction at z/h=0. The first diagram corresponds to the zone where the flow is accelerated by the impact of the jet on the top of the component. This result is in agreement with the experimental study of Tummers et al. [18]. The region where the flow is accelerated have almost identical values due to the interaction of the shear layer (see second diagram in Figure 29).

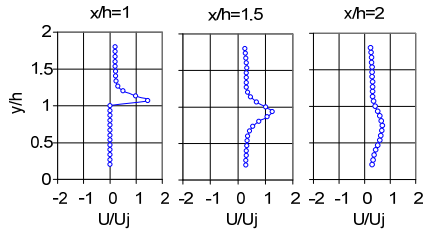

Figure 29: *x-velocity* components (U/U_j) in the *xy*-plane, z/h=0.

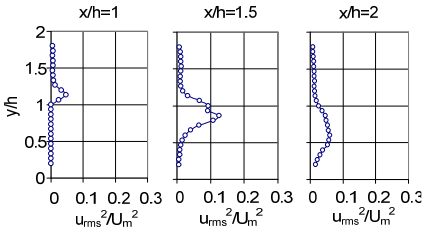

Figure 30: Reynolds stress (u_{rms}^2/U_j^2) in the *xy*-plane, z/h=0.

Figure 30 shows the normalized Reynolds stress (u_{rms}^2/U_j^2) as a function of the vertical distance (y/h) at the centreline. The Reynolds stresses at x/h=1 show a maximum value over the top face. This zone corresponds with the interaction between the impinging jet flow and the top face of the obstacle (see the first diagram in Figure 30). The maximum value of Reynolds stresses is found approximately at x/h=1.5 and y/h=0.9 (see the second diagram in Figure 30) which indicates where there exists a maximum production of u_{rms}^2/U_j^2. This occurs as a result of the interaction between the shear layer released by the impinging jet over the top face and the cross flow in the wake downstream of the trailing face.

5 Conclusions

The flow around an obstacle with different heights (h=5, 10 and 15 mm) was studied experimentally employing several Reynolds numbers. This study has shown that for high height the reattachment length downstream of the trailing face remains almost unchanged for the Reynolds numbers. However, for small height the Reynolds numbers has a high influence on the L_{RD}, in this case when the Reynolds numbers decrease the reattachment length increase. For the studied obstacle heights, points which have the maximum values of Reynolds stresses exit in the wake and top of the obstacle, their positions are a function of the obstacle height. In the case of the wake, these points are located at y=1.2 of the channel floor downstream of the trailing face. At the top face of the component it appears approximately 0.2h above this face.

The lateral separation length increases with the obstacle height. The Reynolds number has no influence on the lateral separation. The normal Reynolds stresses show their maximum values close to the side faces, approximately 0.9h above the channel floor where the highest turbulence production was found, due to the shear layer interaction.

In the case of impinging jet and cross flow combination the measurements indicate the presence of a stagnation point at the centre of the top face of the obstacle and regions of turbulence production downstream of the trailing face. The downstream region of the trailing face have high Reynolds stresses at approximately x/h=1.5 and y/h=0.9. This region corresponds to the maximum turbulence production due to the shear layer and vortex shedding. These observations agree with those found in other studies.

Acknowledgements

This research was funded by Ministerio de Ciencia e Innovacion, Spain Government through program CICYT D+I (DPI2008-05349). The support of Cátedra Fundación Antonio Aranzabal-Universidad de Navarra and Linköping University (Sweden) is also gratefully acknowledged.

References

[1] Castro, I.P., Robins, A.G. *The flow around a surface-mounted cube in uniform and turbulent streams*. J. Fluid Mech. 79 (2), pp.307-335, 1977.

[2] Ogawa, Y., Oikawa, S., Uehara, K. *Field and wind tunnel study of the flow and diffusion around a model cube-II. Near field and cube surface flow and concentration patterns*. Atmospheric Environment. 17 (6), pp. 1161-1171, 1983.

[3] Hussein, H.J., Martinuzzi, R.J. *Energy balance for turbulent flow around a surface mounted cube placed in a channel*. Phys. Fluids 8 (3), pp. 764-780, 1996.

[4] Larousse, A., Martinuzzi, R., Tropea, C. *Flow around surface-mounted, three-dimensional obstacles*. In: Eighth Symposium on Turbulent Shear Flows. TU-Munich/Germany, vol. 1, pp. 1441-1446, 1991.

[5] Martinuzzi, R.J. *Experimentelle Untersuchung der Umstroming wandgebundener, rechteckiger, prismatischer Hindernisse*. Ph.D. Thesis, Erlangen, Germany.
[6] Martinuzzi, R.J., Tropea, C. *The flow around surface mounted, prismatic obstacles placed in a fully developed channel flow*. J. Fluids Eng. 115, pp. 85-92, 1993.
[7] Meinders, E.R. *Experimental study of heat transfer in turbulent flows over wall-mounted cubes*. Ph.D. Thesis, Faculty of Applied Sciences, Delft University of Technology, Delft, Netherlands, 1998.
[8] Meinders, E.R., van der Meer, T.H., Hanjalic, K., Lasance, C.J.M. *Application of infrared thermography to the evaluation of local convective heat transfer on arrays of cubical protrusions*. Int. J. Heat and Fluid Flow 18 (1), pp. 152-159, 1997.
[9] Meinders, E.R., van der Meer, T.H., Hanjalic, K. *Local convective heat transfer from an array of wall-mounted cubes*. Int. J. Heat and Mass Transfer 41 (2), pp. 335-346, 1998.
[10] Meinders, E.R., Martinuzzi, R., Hanjalic, K. *Experimental study of the local convective heat transfer from a wall-mounted cube in turbulent channel flow*. Int. J. Heat and Mass Transfer 45, pp. 465-482, 2002.
[11] Schorfield, W.H., Logan, E. *Turbulent shear flow over surface mounted obstacles*. J. of Fluids Engineering, pp. 113, 405, 1990.
[12] Rundström, D., Moshfegh, B. *RSM and v^2-f study on the flow behavior of an impinging jet in a cross-flow on a wall-mounted cube*. Progress in Computational Fluids Dynamics, vol7, No.6. pp. 311-322, 2007.
[13] Mehta, R.D., Bradshaw, P. *Design Rules for Small Low Speed Wind Tunnels*. Aeronautical Journal, pp. 443-449, 1979.
[14] Westphal, R.V. *Wind tunnel design. Proceedings, Thermal measurements in electronic cooling*. (K. Azar, editor), Boca raton, Florida, pp. 321-347, 1997.
[15] Barlow, J.B., Rae, Jr. W.H., Pope, A. *Low-speed wind tunnel testing*. John W. & Sons, INC, New York. 3rd edition, 1999.
[16] Jorgensen, F. E. *How to measure turbulence with hot wire anemometers*. Dantec Dynamic, Publication no.: 9004U6151. Denamark, pp. 40-44, 2002.
[17] Bruun, H. H. *Hot-wire anemometry principles and signal analysis*. Oxford Science Publications, pp234-239, 1995.
[18] Tummers, M. J., Flikweer, M. A., Hanjalic, K., Rodink, R. & Moshfegh, B. *Impiniging Jet cooling of a wall mounted cubes*. Engineering Turbulence Modelling and Experiments 6, pp. 773-791, 2005

Author Index

Solitary Waves in Fluids

Edited by: ***R.H.J. GRIMSHAW****,*
Loughborough University, UK

After the initial observation by John Scott Russell of a solitary wave in a canal, his insightful laboratory experiments and the subsequent theoretical work of Boussinesq, Rayleigh and Korteweg and de Vries, interest in solitary waves in fluids lapsed until the mid 1960s with the seminal paper of Zabusky and Kruskal describing the discovery of the soliton. This was followed by the rapid development of the theory of solitons and integrable systems. At the same time came the realization that solitary waves occur naturally in many physical systems, and play a fundamental role in many circumstances.

This text describes the role that soliton theory plays in fluids in several contexts. After an historical introduction, the book is divided into five chapters covering the basic theory of the Korteweg-de Vries equation, and the subsequent application to free-surface solitary waves in water, internal solitary waves in coastal ocean and the atmospheric boundary layer, solitary waves in rotating flows, and planetary solitary waves with applications to the ocean and atmosphere. The remaining chapters examines the theory and application of envelope solitary waves and the nonlinear Schrödinger equation to water waves.

Series: Advances in Fluid Mechanics, Vol 47
ISBN: 978-1-84564-157-3
eISBN: 978-1-84564-265-5
2007 208pp £70.00